CARBON DIOXIDE ACTIVATION AND SUBSEQUENT REDUCTION TO VALUE-ADDED CHEMICALS AND FUELS ON GRAPHITIC CARBON NITRIDE SURFACES

Thesis submitted to the
Cochin University of Science and Technology
in partial fulfillment of the requirements for the degree of
Doctor of Philosophy
under the **Faculty of Environmental Studies**

Submitted by
Hariprasad N
(Reg. No. 4403)

Research Guide: Dr. M. V. Harindranathan Nair

School of Environmental Studies
Cochin University of Science and Technology

February 2024

Author Hariprasad N
Research Scholar
School of Environmental Studies
Cochin University of Science and Technology
Cochin-682022
Email: hariprasadmandur@gmail.com

Research Guide Dr. M. V. Harindranathan Nair
Associate Professor (Retired)
School of Environmental Studies
Cochin University of Science and Technology
Cochin-682022
Email: harinathses@gmail.com

Mentor Prof. Balasubramanian Viswanathan
Chair Professor
National Centre for Catalysis Research
Department of Chemistry
Indian Institute of Technology Madras
Chennai-600036
Email: bviswanathan@gmail.com

Research Centre National Centre for Catalysis Research
Department of Chemistry
Indian Institute of Technology Madras
Chennai-600036

CERTIFICATE

I, Dr. Harindranathan Nair, hereby certify that Hariprasad N. completed the PhD program under my supervision at the School of Environmental Studies, Cochin University of Science and Technology. The candidate has carried out research work entitled, CARBON DIOXIDE ACTIVATION AND SUBSEQUENT REDUCTION TO VALUE-ADDED CHEMICALS AND FUELS ON GRAPHITIC CARBON NITRIDE SURFACES, with dedication and a strong commitment to excellence. This research was based on Carbon Dioxide Capture and Utilization. I have closely monitored the progress of the candidate's research work, and I am satisfied that the candidate has met the academic requirements and standards of the PhD program satisfactorily. The candidate showed a high motivation level and a deep understanding of the research topic.

I am confident that the candidate's research has met the criteria for original and significant contributions to the field of Photon-assisted Catalysis. The findings of this research have been presented clearly and concisely, and have been thoroughly discussed and evaluated. I have also reviewed the final version of the PhD thesis and have satisfied that it meets the expected standards of a PhD thesis. The thesis has been written clearly and concisely, and formatted and structured according to the university's guidelines. I am confident that the candidate has the skills and knowledge necessary to pursue a successful career in academia or industry, and I am proud to have supervised the candidate's research work. In conclusion, I strongly endorse this PhD thesis for examination.

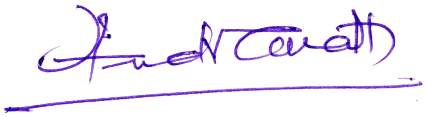

Dr. M. V. Harindranathan Nair
Associate Professor (Retired)
School of Environmental Studies
Cochin University of Science and Technology
Cochin-682022
Email: harinathses@gmail.com
Date: February 2, 2024

CERTIFICATE OF PLAGIARISM CHECK

This is to certify that the thesis entitled “CARBON DIOXIDE ACTIVATION AND SUBSEQUENT REDUCTION TO VALUE-ADDED CHEMICALS AND FUELS ON GRAPHITIC CARBON NITRIDE SURFACES” submitted by Hariprasad N (Reg. No. 4403) in partial fulfillment of the requirements for the degree of Doctor of Philosophy at Cochin University of Science and Technology has undergone a plagiarism check using iThenticate, a reputable plagiarism detection tool available in our university library.

The plagiarism check revealed that the thesis had been thoroughly examined for originality, and the percentage of detected similarity was 3%

Based on the results obtained from the plagiarism check, it was confirmed that the content of the thesis complies with the academic integrity standards set forth by the Cochin University of Science and Technology.

Date: 02/02/2024

Dr. M. V. Harindranathan Nair
Associate Professor (Retired)
School of Environmental Studies
Cochin University of Science and Technology
Cochin-682022

DECLARATION

I, Hariprasad N., declare that this thesis titled CARBON DIOXIDE ACTIVATION AND SUBSEQUENT REDUCTION TO VALUE-ADDED CHEMICALS AND FUELS ON GRAPHITIC CARBON NITRIDE SURFACES is a record of the original work carried out by me under the supervision of Dr. Harindranathan Nair. The research was conducted in accordance with the guidelines and regulations of the Cochin University of Science and Technology.

I declare that the material presented in this thesis results from my research and that all sources used have been adequately acknowledged and referenced. I have not submitted this thesis, either in whole or in part, to any other academic institution to award any degree or diploma.

I have taken reasonable care to ensure that the work contained in this thesis is accurate and free from errors. However, I accept that the contents of this thesis are open to further scrutiny and investigation, and that I assume full responsibility for any errors or omissions.

I also declare that the research work carried out and the material presented in this thesis have not been published elsewhere, and do not infringe upon any other person's rights.

Hariprasad N
February 2, 2024

DEDICATION

I dedicate this thesis to my late father Narayanan Embran N. K, a retired agricultural officer, passed away before the submission of this work. He was a constant source of love, support, and encouragement throughout my life, and his passing left a profound void in my life. Despite his absence, his influence and spirit guided me in everything I do.

My father was my greatest supporter and was advocated throughout my research journey. He believed in me when others did not, and provided the financial support I needed to complete my studies, even when my fellowship ended. One of the most remarkable things about my father was his unwavering dedication to my success even in the face of adversity.

When he was admitted to the hospital for a few months, I had the privilege of caring for him. Despite his struggles, he was constantly worried about me and my work and often asked if my studies would be delayed. He even made arrangements for financial support during his unconsciousness, ensuring that I would have the necessary resources to continue my work.

I dedicate this thesis to my late father's memory, and I hope it will serve as a lasting tribute to his legacy and as a testament to his unwavering love and support. I am forever grateful for his contributions and the sacrifices he made to support my success.

I wonder if I can be a human being, as loving and caring as you were.

Rest in peace, Acha. I love you.

Hariprasad Narayanan
February 2, 2024

ACKNOWLEDGEMENTS

The successful completion of a PhD thesis is the culmination of a long and challenging journey, and I am deeply grateful to everyone who has supported and guided me along the way. This thesis would not have been possible without invaluable contributions and support.

I wish to express my sincere gratitude to my research guide, Dr. Harindranathan Nair, for his guidance, support, and encouragement throughout the research process. Even though I had to change my research guide during my journey, Hari Sir was instrumental in providing the direction and guidance I needed to complete this thesis. His expertise, dedication, and patience inspired me and motivated me.

I want to extend my sincere gratitude to my initial guides, Prof. Suguna Yesodharan and Prof. E. P. Yesodharan, for introducing me to the field of photocatalysis and providing me with a solid foundation to build upon. The work I did in their lab was valuable, and it gave me the skills and knowledge to pursue independent research. I am grateful for their guidance and support, which allowed me to better understand photocatalysis and its many opportunities. Their contributions to my education and development as a researcher are always remembered and appreciated.

I express my deepest gratitude to my mentor, B. Viswanathan, for his invaluable support and guidance throughout my research. BV has been an inexhaustible source of inspiration, and his vast experience and knowledge in the field have been critical in shaping my research. Despite several challenges during my research journey, BV has always been there to offer unwavering support and guidance. His dedication and commitment to my research were crucial to my success. BV's insights and feedback helped me refine my research methodology, analyze data, and interpret the results accurately. I would also like to thank BV for his patience and understanding when I faced personal and professional difficulties. His constant encouragement and motivation motivated me to achieve my research goal. I would also like to acknowledge the efforts of BV to create a supportive research environment that allowed me to grow and learn. His mentoring style has been instrumental in honing my research skills and developing my critical thinking abilities. I am deeply grateful for his continuous support and mentorship that shaped my research career. I would also like to highlight that BV is not just a mentor but also a father figure. He has always been approachable and empathetic towards me, and his guidance has extended beyond research-related issues. BV has always provided me with emotional support and advice whenever needed. Moreover, weekend discussions played a crucial role in shaping my research abilities. I am grateful to acknowledge that, during these discussions with BV, I learned how to approach scientific problems critically, effectively communicate scientific ideas, and significantly refine my research skills through BV's valuable comments and suggestions. In addition to research, BV has motivated me to learn new skills such as LaTeX and computer languages. He encouraged me to take online courses to enhance my skills, and his guidance was instrumental in expanding my knowledge. I want to add that BV has been one of the few people who have constantly shown concern about delays in my PhD process. He has always been aware of the importance of the timely completion of research work, and his constant reminders and encouragement have motivated me to stay on track and focus on

my goals. Finally, I would like to thank BV for his unwavering belief in me, which has given me the confidence to pursue my research goals relentlessly. His guidance and support have been invaluable, and I will always cherish the memories of our research journey.

I would like to express my heartfelt gratitude to Prof. K.R. Krishnamurthy and Prof. S. Sivasankar, for his unwavering support and guidance throughout my research.

I would also like to extend my sincerest thanks to the service engineers, Mr. Ranjith & Mr. Narasimhan, and the Perkin Elmer team, who provided invaluable support for fixing the issue. Their prompt response and willingness to share their expertise were instrumental in resolving the problem and ensuring the smooth execution of my research.

We would like to express our sincere gratitude to Prof. P. Selvam for his support during my research. His generosity in allowing me to use departmental facilities was invaluable, and I am deeply grateful for the funding he provided during the post-covid period.

I extend my heartfelt gratitude to the National Centre for Catalysis Research, IIT Madras, for providing me with the necessary resources and facilities to carry out this research. The support and encouragement of the faculty and staff have been instrumental to my success.

I would like to express my deep gratitude to Arunima Balachandran, who has been a pillar of support throughout my research career. The unique outlook of my dissertation can be mainly attributed to her immense support in characterizing materials. I am also grateful for the collaboration developed between the two laboratories. I cannot express enough gratitude to Arunima for her support, friendship, and encouragement.

I want to express my deepest gratitude and appreciation to Nitha P R for her unwavering support throughout the journey of writing this thesis. Her presence and encouragement have been instrumental in helping me overcome the difficulties I faced. Nitha stood on my side, offering her unwavering support and understanding during these challenging days. Her compassion and empathy gave me solace and motivation to get back on track. To Nitha, I extend my deepest love and appreciation to be my source of inspiration and support. This thesis would not have been possible without her belief in me and her willingness to stand by my side at every step of the way. Her encouragement, understanding, and love have been my driving force, and I am forever indebted to her for her unwavering commitment.

I would also like to thank the technical staff of the Department of Chemistry at IIT Madras and the office staff of the School of Environmental Studies for their immense support during my research. Their technical expertise and administrative support have been invaluable to my academic pursuits, and I cannot thank them for their contributions.

Additionally, I would like to thank the faculty members from the School of Environmental Studies, including Prof. Rajathi Sivalingam, Prof. Bright Singh, and Prof. Ammini Joseph, for their guidance and support throughout my research journey. Their expertise and mentorship have been instrumental in shaping my academic career and I am grateful for the opportunities they have provided me with.

I want to acknowledge the invaluable support and assistance provided by the

following individuals throughout my research journey: Girish Kumar K K, Anupama Aravind, Sudheesh K V, Bhavya Kachiprath, Pragin C, Honey Mary Joseph, Shijin Chandran, Sithin N V, Durgam Sharada, Venugopal, Shivraj Kumar, Sundaravelu, Sujeethkumar, Krishnadas, Manila, Velu Jeyalakshmi, Venkat Rajalingam, Divya Unnikrishnan, Shibin O M, Veena Vijayan, Anju S G, Manu Mohan, Shijeesh M R, Ajay, Akhilesh and Vidya.

I owe my success to my family's unconditional love and support, and I am honored to have outstanding family members who have always been there for me. I thank them from the bottom of my heart for their contributions to my research and for being a great source of inspiration and motivation.

Finally, I would like to express my sincere gratitude to all those who supported and guided me throughout my journey and helped me complete this thesis. I am deeply grateful for their contributions and support and I am confident that their influence will continue to guide me in my future endeavors.

Hariprasad Narayanan
February 2, 2024

ABSTRACT

This doctoral thesis presents a comprehensive investigation into the synthesis, characterization, and photon-assisted catalytic performance of graphitic carbon nitride (g-C_3N_4) materials for carbon dioxide (CO_2) reduction and water splitting. The research addresses the critical need for sustainable energy solutions and CO_2 utilization in the face of global climate change.

The study employs a multi-faceted approach, exploring various synthesis methods including one-pot, crucible-based, ionothermal, and supramolecular-assisted eutectic techniques. A wide array of advanced characterization methods, such as X-ray diffraction, spectroscopic techniques, and electron microscopy, are utilized to elucidate the structural, electronic, and surface properties of the synthesized materials.

Novel analytical approaches, including derivative spectroscopy and machine learning algorithms, are introduced to enhance the understanding of structure-property-performance relationships. The research introduces innovative parameters, such as normalized surface concentration (NSC%) and light absorption efficiency per unit surface area (DP/SA), to provide deeper insights into photon-assisted catalytic activity.

The thesis is structured into two main sections, examining a total of 18 g-C_3N_4 systems. The first part investigates the impact of precursors and crucible materials on the photon-assisted catalytic performance of g-C_3N_4. The second part explores the synthesis of g-C_3N_4 derivatives using molecular salt- and supramolecular-assisted pathways, including the iono-thermal synthesis of lithium polytriazine imide (Li-PTI) and nickel-incorporated g-C_3N_4 frameworks. Key findings reveal the crucial role of surface functionalities, crystallinity, and electronic structure in determining the photon-assisted catalytic activity of g-C_3N_4 materials. The research demonstrates that factors such as synthesis atmosphere, precursor selection, and incorporation of metal ions significantly influence the CO_2 reduction performance.

The thesis concludes by proposing new design criteria for photon-assisted catalytic systems, emphasizing the importance of considering both catalyst characteristics and effective illumination. It highlights the need for a paradigm shift in approach, suggesting that the wavelength and intensity of incident photons should be tailored to the specific properties of the photon-assisted catalyst.

This comprehensive study contributes to the fundamental understanding of g-C_3N_4 photon-assisted catalysts and provides valuable insights for the rational design of efficient materials for CO_2 reduction and solar fuel production. The findings have significant implications for the development of sustainable energy technologies and environmental remediation strategies.

PREFACE

The global imperative to mitigate climate change and reduce our dependence on fossil fuels has never been more urgent. This thesis addresses this critical challenge by exploring innovative solutions for sustainable energy production, with a particular focus on the photon-assisted reduction of carbon dioxide (CO_2) into valuable chemicals and fuels. At the heart of this research lies the exploration of graphitic carbon nitride (g-C_3N_4) as a promising photocatalyst for CO_2 reduction. Through a series of carefully designed experiments and in-depth analyses, this work delves into the intricate relationships between material synthesis, structural properties, and photocatalytic performance.

The thesis begins with a comprehensive review of the fundamental principles and current state of the art in photon-assisted CO_2 conversion. It then progresses through a systematic investigation of various aspects of g-C_3N_4 photocatalysts, including the impact of precursor selection, the role of crucible materials in synthesis, and innovative approaches such as ionothermal and supramolecular-assisted eutectic synthesis methods. A key strength of this research lies in its multifaceted analytical approach. By employing a wide array of advanced characterization techniques and introducing novel parameters such as normalized surface concentration (NSC%) and light absorption efficiency per unit surface area (DP/SA), this work provides unprecedented insights into the structure-property-performance relationships of g-C_3N_4 materials.

Moreover, this thesis challenges conventional wisdom in the field of photon-assisted catalysis. It questions the adequacy of traditional efficiency measures and proposes new approaches for assessing the true activity of photocatalytic systems. The work emphasizes the critical importance of considering both catalyst characteristics and effective illumination in designing efficient photon-assisted catalytic processes. The findings presented herein not only contribute to the fundamental understanding of g-C_3N_4 photocatalysts but also offer practical guidelines for the rational design of more efficient materials for CO_2 reduction. Furthermore, this research opens new avenues for exploration in the field of solar fuel production, particularly in the areas of material synthesis and catalytic system design.

As we stand at the crossroads of environmental sustainability and energy security, the insights and methodologies developed in this thesis aim to accelerate progress towards viable solutions for CO_2 utilization and renewable energy production. It is my hope that this work will serve as a valuable resource for researchers and practitioners in the field, inspiring further innovations in sustainable energy technologies.

This thesis represents not just the culmination of years of dedicated research, but also a call to action for the scientific community to reevaluate and refine our approaches to photon-assisted catalysis. As we continue to face the challenges of climate change, the pursuit of efficient and sustainable energy solutions remains more critical than ever.

Prof. B. Viswanathan
Dr. M. V. Harindranathan Nair

Contents

List of Tables

List of Figures

LIST OF ACRONYMS

PCET Proton Coupled Electron Transfer

WGSR Water-Gas Shift Reaction

DAC Direct Atmospheric Capture

UV Ultraviolet

CPC Compound Parabolic Concentrator

CFC Chlorofluorocarbon

B.E.T Brunauer–Emmett–Teller

IEP Isoelectric Point

PZC Point of Zero Charge

SRH Shockley-Read-Hall

MOT Molecular Orbital Theory

HOMO Highest Occupied Molecular Orbital

LUMO Lowest Unoccupied Molecular Orbital

PCM Polarizable Continuum Model

B3LYP Becke, 3-parameter, Lee-Yang-Parr

cc-pVTZ Correlation-Consistent Polarized Valence Triple-Zeta

NHE Normal Hydrogen Electrode

PEC Photoelectrochemical

DET Direct Electron Transfer

PRET Plasmonic Resonant Energy Transfer

HEIE Hot Electron Injection Efficiency

TOF Turnover Frequency

HER Hydrogen Evolution Reaction

OER Oxygen Evolution Reaction

M-O Bond Metal-Oxygen Bond

ROS Reactive Oxygen Species

DOS Density of States

XPS X-ray Photoelectron Spectroscopy

UPS Ultraviolet Photoelectron Spectroscopy

DRS Diffuse Reflectance Spectroscopy

TOC Total Organic Carbon

PTFE Polytetrafluoroethylene

XRD X-ray Diffraction

PXRD Powder X-ray Diffraction

CAM Melamine Cyanurate

GoF Goodness of Fit

BETSI BET Surface Identification

SESAMI Script to Estimate the Surface Area of Materials from their Isotherms

GUI Graphical User Interface

ESW Excess Sorption Work

AIF Adsorption Information File

ASTM American Society for Testing and Materials

USP United States Pharmacopeia

ISO International Organization for Standardization

LASSO Least Absolute Shrinkage and Selection Operator

DIS Derivative Isotherm Summation

SDIS Second Derivative Isotherm Summation

KE Kinetic Energy

BE Binding Energy

VB Valence Band

CB Conduction Band

FESEM Field Emission Scanning Electron Microscopy

EDS Energy-Dispersive X-ray Spectroscopy

EDX Energy-Dispersive X-ray Spectroscopy

EDXS Energy-Dispersive X-ray Spectroscopy

XEDS Energy-Dispersive X-ray Spectroscopy

EDXA Energy Dispersive X-ray Analysis

EDAX Energy Dispersive X-ray Analysis

EDXMA Energy Dispersive X-ray Microanalysis

IUPAC International Union for Pure and Applied Chemistry

SSNMR Solid State Nuclear Magnetic Resonance

RF Radio Frequency

NMR Nuclear Magnetic Resonance

PL Photoluminescence

STP Standard Temperature and Pressure

UV-DRS Ultraviolet Diffuse Reflectance Spectroscopy

GC Gas Chromatography

HP High-Pressure

VP Vapour Pressure

ppm Parts per Million

FID Flame Ionization Detector

TCD Thermal Conductivity Detector

CP-MAS Cross Polarization-Magic Angle Spinning

TMS Tetramethylsilane

MW Molecular Weight

DP D Parameter

SA Surface Area

NSC Normalized Surface Concentration

MSAIS Molten-Salt-Assisted Ionothermal Synthesis

FD First Derivative

SD Second Derivative

IE Ionization Energy

EA Electron Affinity

SAM Second Absorption Maximum

FWHM Full Width Half Maximum

LR Linear Regression

PTI Poly Triazine Imide

K-M Kubelka-Munk

STD Standard Deviation

FQE Formal Quantum Efficiency

AQE Apparent Quantum Efficiency

"For every human problem, there is a neat simple solution. And it is always wrong![†]"

– H. L. Mencken

[†]This perspective underscores the importance of rigorous scientific principles and evidence-based approaches in addressing sustainable development challenges. It emphasizes the need for careful consideration and critical evaluation of scientific evidence when developing technological solutions, rather than relying on oversimplified answers.

Chapter 1

Energy-Matters

Since the dawn of civilization, humans have relied on various energy resources to fulfill their needs. Following the industrial revolution, quality of life and, consequently, energy demand increased. Currently, we are heavily dependent on the fossil fuel industry to meet our current demand. Although many believe that fossil fuels comprise only petrol and diesel, this is not the case. Petrol and diesel are two petroleum products derived from crude oil, and the remainder is utilized to synthesize a myriad of value-added chemicals and fuels, which serve as precursors for the majority of the synthetic goods available in the market[1, 2]. For example, consider the case of a professor sitting in an office. The following are some petroleum products that are in direct contact on a daily basis:

- Stationery: Writing instruments such as pens, pencils, markers, and erasers may contain petroleum derivatives, such as polyethylene, polypropylene, or styrene.
- Electronics: Computers, monitors, printers, phones, calculators, and other electronic devices that utilize petroleum-based plastics for casings, circuit boards, and wires.
- Furniture: Furniture pieces such as chairs, desks and shelves, including polyurethane foam, nylon fabric, and plastic components derived from petroleum.
- Cleaning supplements: Disinfectants, hand sanitizers, and cleaning products often contain alcohols or other petroleum-derived chemicals.
- Personal Items: Your backpack, wallet, watch, coffee mug, or other personal belongings may include plastic, nylon, or polyester, which are derived from petroleum.

The notion that the transition to renewable energy in the transportation and energy sectors is insufficient to address this issue[†]. Fossil fuels are also a primary

[†]However, transitioning from traditional to renewable energy sources is difficult. Although solar panels and electric cars may appear to be ideal green solutions, their production often relies on fossil fuels. A complex chain of events, extending from the mining of silicon for solar panels to the extraction of lithium for batteries, is not always eco-friendly.

However, it is important not to dismiss these advancements as mere "greenwashing." A more

source of industrial platform chemicals, which are the precursors of most value-added products and goods available in the market. Consequently, in the event of a comprehensive shift toward renewable energy, it is recommended that industrial platform chemicals be manufactured from non-fossil fuel sources that utilize renewable resources.

When making decisions regarding the appropriate energy sources for a transition, it is crucial to adhere to certain criteria to ensure human peace. Specifically, the distribution of energy resources must be equitable and balanced among all nations. If this principle is not upheld, it is likely to result in disputes and conflicts between countries. Furthermore, the state of the resource in question must also be considered, that is, whether it is solid, liquid, gas, or any other form. It is imperative that they are easily storable and transportable. Moreover, the resource should not be confined to a specific location; rather, its distribution should be uniform and ensured, and exploitation should be decentralized. Resource management must be universal [†].

It is important to highlight earth-abundant molecules, including dinitrogen, carbon monoxide, carbon dioxide, and water, because they have the potential to produce high-energy content, sustainable fuels, and chemicals. Consequently, they can contribute to addressing the energy needs of the universe. This process is deemed efficient for transforming chemical energy into electricity, which has led to the development of modern energy-conversion devices, such as fuel cells, batteries, and supercapacitors[3]. Although attempts have been made for over 50 years to convert water into fuel hydrogen using available energy vectors, such as solar energy or alternate electricity sources, such as wind energy or hydroelectricity, the efficiency of energy conversion remains unfavorable. The development of economically viable and distributed fuel conversion systems is long way off[4].

1.1 Carbon Dioxide as an Energy Resource

The primary drivers of the increase in atmospheric carbon dioxide (CO_2) concentration are the inefficient conversion of fossil carbon into usable energy and excessive human energy consumption. It is estimated that only approximately 32 percent of fossil carbon is effectively converted into useful energy, with the remaining portion being released into the atmosphere as heat. The extensive use of fossil fuels depletes their resources, which, in turn, increases the atmospheric CO_2 levels[5]. However, the extent to which carbon dioxide (CO_2) contributes to climate change

balanced approach is needed to assess the progress that has been made rather than focusing solely on the obstacles that remain. The development of sustainable mining practices and alternative materials is rapidly progressing, paving the way for cleaner production. Furthermore, an increasing number of charging stations and parts of the grid are being powered by renewable energy sources. Although the shift was gradual, it is undeniable.

Evaluating these technologies solely based on their current limitations fails to recognize their vast potential. Each solar panel harnessing the power of the sun and each electric car gliding silently represents a step towards a future free from dependence on fossil fuels. Although challenges still exist, it is essential to acknowledge the remarkable progress that has already been made and the thrilling possibilities that lie ahead[2]

[†]The principles discussed herein were greatly enhanced by a productive weekend group discussion with Professor B. Viswanathan. All documentation related to the discussion, including reports and presentations, was accessible through the website `http://catalysis.eprints.iitm.ac.in/`

remains the subject of debate, it is imperative to transition away from fossil fuels and towards renewable energy sources in order to conserve natural resources [6].

Human activity, commonly referred to as anthropogenic forcing, introduces approximately 38 gigatons of anthropogenically generated carbon dioxide into the atmosphere annually. This amount surpasses the capacity of the natural carbon cycle to absorb it through the process of photosynthesis, which produces approximately 800 gigatons of CO_2 per year. However, the natural carbon cycle cannot effectively manage excess CO_2 generated by human activity. Thus, it is essential to establish an artificial CO_2 cycle that can be integrated with the natural carbon cycle to facilitate the efficient and precise production of goods[7].

The primary challenge confronting carbon capture and utilization technologies is the utilization of CO_2 for the production of industrial platform chemicals and fuels, which would restrict the exploitation of fossil fuels to below their annual generation rate, while preserving fossil carbon energy for future generations. Given the rising demand for energy, it is essential to adopt alternative energy sources that lower CO_2 emissions and minimize environmental impacts. Fossil carbon energy is readily transportable to any location, whereas perennial energy sources and their derivatives have limited distribution potential and are not available continuously [8].

Applications of carbon dioxide are typically categorized into two groups: conversion and utilization. While utilization involves the use of carbon dioxide as a technical fluid without undergoing chemical conversion, conversion refers to the chemical transformation of carbon dioxide into other products. Three classes of carbon dioxide reactions can be identified based on the energetics and state of the carbon dioxide molecule [9]. The first class involves the addition of a full carbon dioxide molecule to compounds that are either exergonic or moderately endergonic, with carbon remaining in the oxidation state of 4. Examples of such compounds include carbonates, polycarbonates, carbamates, and polyurethanes[10]. The second class consists of intermediate-energy processes that decrease the oxidation state of carbon by forming C-C bonds without the use of hydrogen. The third class of reactions requires the provision of energy and hydrogen to decrease the oxidation state of carbon to -4 in CH_4[11].

The available energy determines the most suitable class of CO_2 reaction. Certain reactions within the first class can only be accomplished using energy derived from fossil fuels. However, as the use of renewable energy sources has increased, new third-class reactions have become more feasible[11]. Since 1987, the strategy of utilizing CO_2 as a resource rather than a waste product, which mimics natural processes, has gained popularity[12]. The transformation of CO_2 and water into valuable products using solar energy, such as oxygen and high-energy hydrocarbons, presents a significant scientific challenge for the future, as highlighted by recent research[13].

This study focuses on a highly efficient fuel conversion process that utilizes CO_2 as the primary carbon source. However, the necessity of hydrogen in this process results in higher CO_2 emissions than those being fixed, making the production of fuels from CO_2 unfeasible in the context of fossil fuel energy. To produce hydrocarbon unit in the form of C_nH_{2n+2}, it is necessary to produce (n+1) units of hydrogen through the Water-Gas Shift Reaction (WGSR) during syngas production. This results in the release of the (n+1) units of CO_2. Owing to the significantly

larger size of the fuel market compared to the chemical market, CO_2 is utilized as a carbon source for fuel production[11].

The considerable size of the fuel market makes CO_2 a potential carbon source for fuel production. However, in a fossil fuel-dependent energy framework, converting CO_2 into fuels is impractical because of the necessity of hydrogen generation, which generates more emissions than is fixed, and the emissions from the separation and synthetic processes render the process unworkable. Nonetheless, a novel framework centered on photovoltaics is anticipated to emerge, enabling extensive industrial use of the methanation reaction[14, 15]. This would accelerate the conversion of fossil CO_2 into fuels and bring us closer to a "Man-made C-Cycle." An alternative method for converting CO_2 into fuel involves employing solar energy and Direct Atmospheric Capture (DAC) technology[16]. This approach mimics natural photosynthesis, but is more efficient. The utilization of solar energy for the conversion of carbon dioxide into fuel relies on constant energy sources. However, the consumption of fossil fuels is unsustainable; therefore, alternative energy sources are required. Although this process is more efficient than natural photosynthesis, it is not currently commercially competitive with technologies that rely on fossil fuels. To make this process economically viable, it is necessary to optimize the selectivity and chain elongation of long-chain hydrocarbons. In the medium term, this may lead to the production of cost-competitive fuel. To achieve the desired outcome, it is essential to avoid the use of fossil fuels[17].

Traditional methods for transforming carbon dioxide into fuels, such as chemocatalysis and thermal processes, may be supported by a more innovative approach that employs photovoltaic technology in conjunction with electrolysis. However, one challenge with hydrogen produced through electrolysis is the need for effective and safe storage, owing to the mismatch between hydrogen production and utilization. An alternative strategy that can address this issue is the Man-Made C-cycle approach, which utilizes Proton Coupled Electron Transfer (PCET) in water as a reducing agent for CO_2 to convert solar energy into fuel. This approach has the potential to be both practical and cost-effective.

The production of hydrogen through photoelectrochemical, photocatalytic and photosynthetic methods has been hampered by several energy barriers, including the selection of suitable, cost-effective, and stable semiconductors, owing to the requirement of overvoltage and energy-intensive manufacturing processes. The current technologies available for the reduction of dinitrogen (Haber process) or carbon monoxide (Fischer-Tropsch Process) are energy-intensive and thus unfavorable from an energy conversion perspective [18]. Furthermore, conversion of these molecules requires the development of new infrastructure. In contrast, reduction in carbon dioxide can result in the production of hydrocarbon fuels and chemicals that are compatible with the current energy vector[19, 20]. There are several possibilities for producing chemicals and fuels, as illustrated in Figure 1.1 & 1.2, respectively[21].

In the future, engineered semiconductors incorporating n-p-type materials could be used for CO_2 and water coprocessing to prevent exciton collapse. Studies have reported light efficiencies of >10% using this approach[22, 23]. Although there are environmental and energy benefits to using water as a reductant, the low efficiency of the carbon reduction reaction remains a challenge because of issues with the reaction mechanism [24–26].

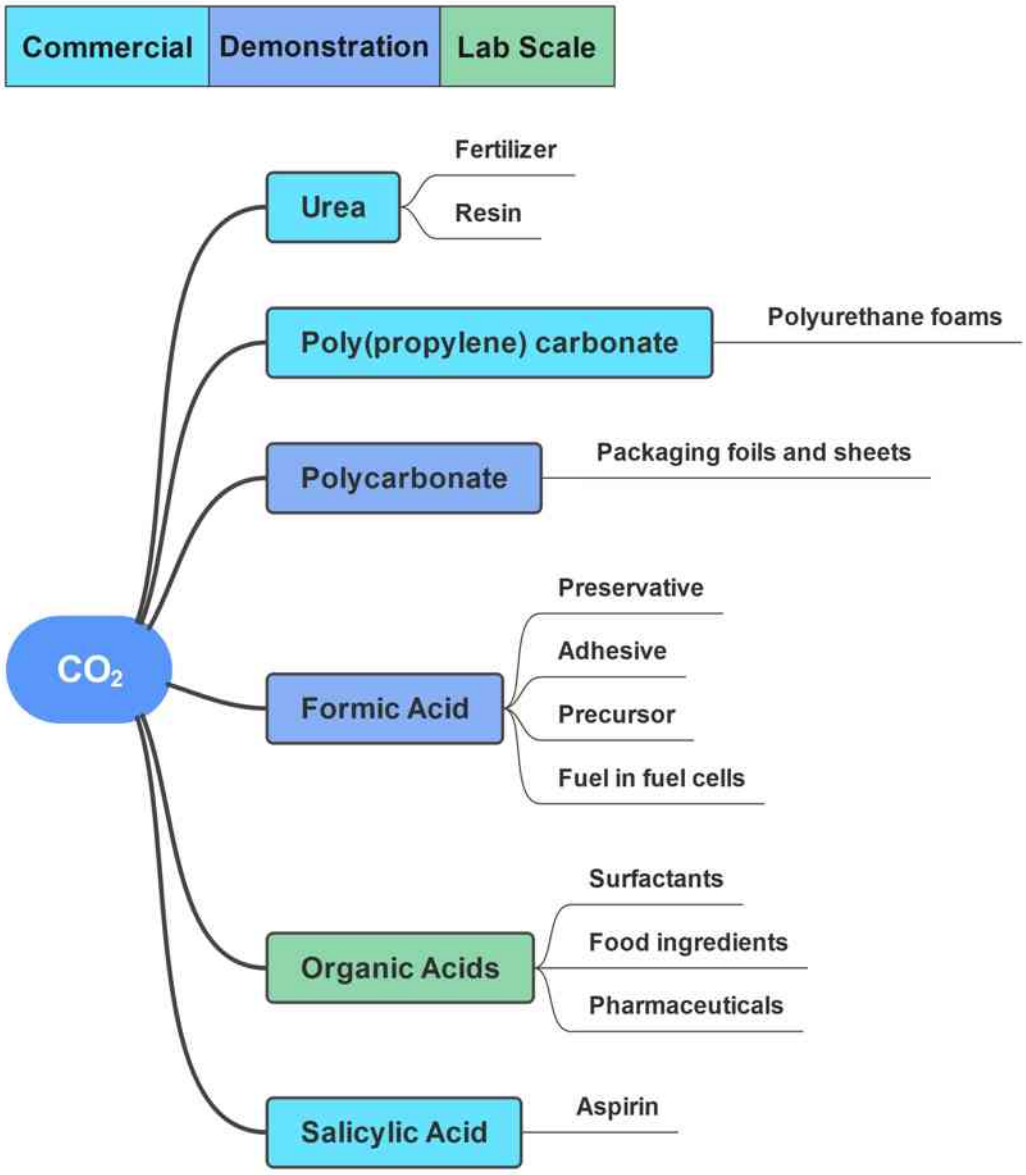

Figure 1.1: Illustrates the products obtained from CO_2-based synthesis, as presented in a report by the International Energy Agency (IEA) in 2019 [21].

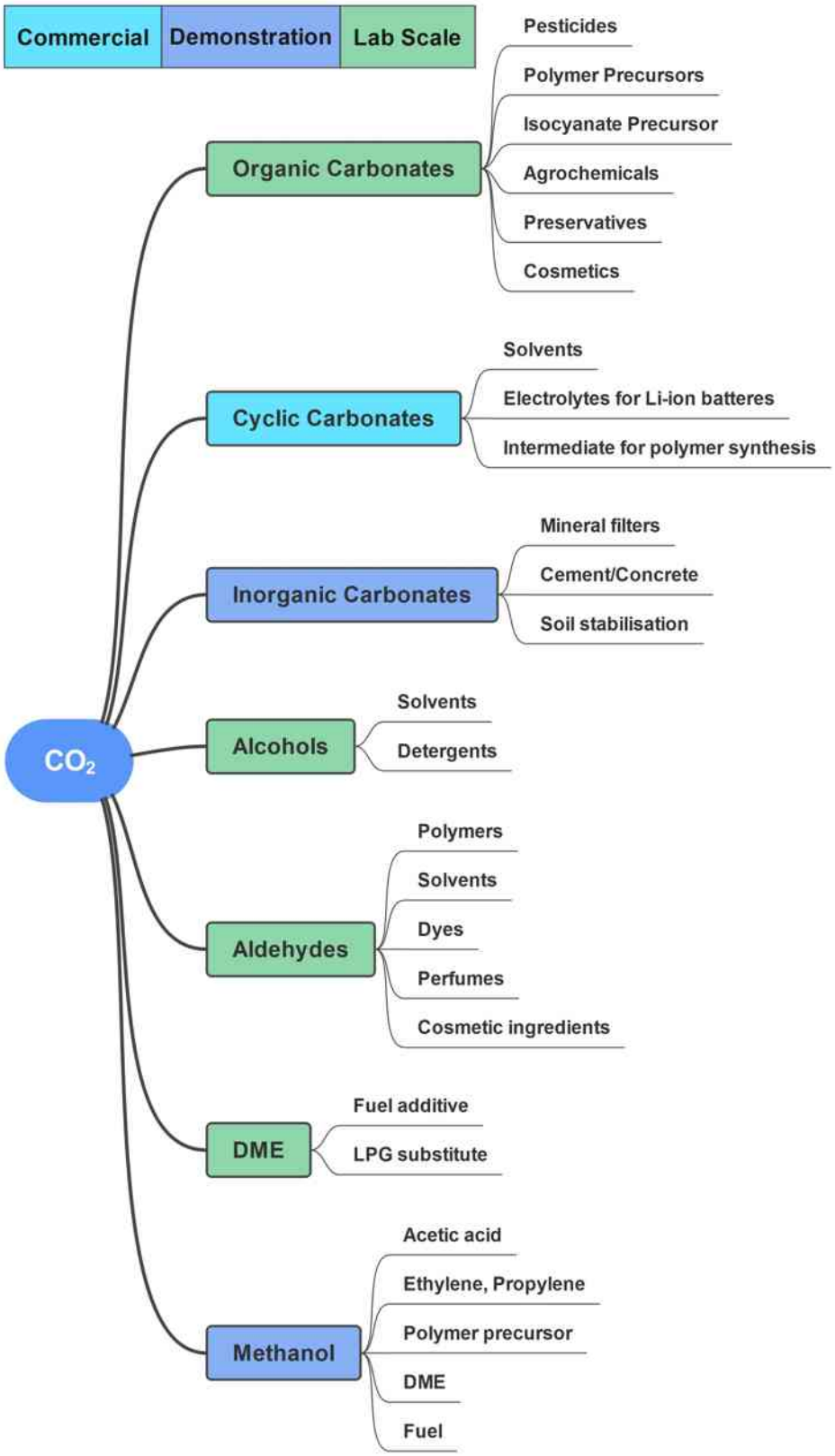

Figure 1.2: The figure shows a comprehensive overview of various synthesized products derived from carbon dioxide, providing valuable insights into the potential applications and outcomes of CO_2 utilization strategies[21].

1.2 Solar Energy

The Earth receives an enormous amount of energy from the sun, with nearly $4.3 \times 10^{20}\,\mathrm{J\,h^{-1}}$ being absorbed by the planet. However, the Earth's energy requirements are approximately $4.3 \times 10^{16}\,\mathrm{J\,h^{-1}}$, which means that harnessing just one hour of solar energy could provide the Earth with enough energy for nearly $9200\,\mathrm{h}$ or over a year. The availability of solar energy as a freely accessible energy source is always tempting for humans; however, there is always a catch. Scientific methodologies have been developed to harness solar energy in various ways, including the conversion of waste products, such as carbon dioxide, into valuable chemicals and fuels. However, the process of converting waste products into fuels is more challenging than that of converting water into fuel because of the higher free energy change of $689\,\mathrm{kJ\,mol^{-1}}$. Despite this limitation, efforts to convert carbon dioxide into chemicals and fuels using solar energy have recently gained considerable attention. The chemical, electrocatalytic, and biochemical routes can also be used for this conversion. However, the photon-assisted catalytic route has received the most attention because of its similarity to artificial photosynthesis [27][28].

The conversion of solar energy is difficult, and a high barrier is associated with the conversion process and its technical implementation. Photovoltaic research involves the conversion of solar energy into electricity, which is associated with storage and transportation problems. The efficiency of photovoltaic cell reached the desired levels for technical implementation, but the process economics were high. Solar cells are pollution-free, which means that they do not emit carbon dioxide into the atmosphere. Hence, it is also referred to as carbon-neutral technology. In reality, solar cells or other solar energy conversion processes are not carbon-neutral technologies. The creation and appending parts of solar cells are made using fossil fuel energy, and it also causes the emission of CO_2, sulfur hexafluoride, and Chlorofluorocarbon (CFC)-like greenhouse gases, which possess 23,700 and 10000 times higher global warming potential than carbon dioxide, respectively[29]. Other solar energy conversion processes also depend on fossil fuels as the production materials. The main advantage of photon-assisted catalysis is that its carbon dioxide footprint is comparatively low compared with that of other carbon dioxide conversion techniques.

Carbon dioxide reduction was more active in the presence of Ultraviolet (UV) light in the spectrum. Because the penetration depth of UV light into the semiconductor is low compared to that of visible light, the recombination is uniform. Natural sunlight contains approximately 3-6% UV light, which varies with time, latitude, and season[30, 31]. Exploring UV light alone from sunlight can resolve the entire issue even though the percentage is low.

Although a few studies have utilized natural sunlight as an energy source, Varghese et al. reported the highest yield among these studies[32]. The yield was influenced by the wavelength of the incident light, and the maximum efficiency was observed at a wavelength of $254\,\mathrm{nm}$ compared with that at $354\,\mathrm{nm}$[33, 34].

The effect of irradiation with ultraviolet light, with a wavelength below $315\,\mathrm{nm}$, on the photochemical reaction of gaseous products, such as methane, carbon monoxide, and formaldehyde, is initiated through free radical reactions. Additionally, the interpretation of product analysis may be affected. The increased product

yield below $254\,\mathrm{nm}$ can be attributed to the photochemical reactions occurring in the gaseous phase of the reaction system. Methane, produced by the photon-assisted catalytic reduction of carbon dioxide combined with hydroxyl radicals, forms a variety of products, including HCHO, CO, CO_2, and other gaseous products. These products also undergo photochemical reactions at wavelengths below $315\,\mathrm{nm}$[35, 36]. Therefore, it cannot be assumed that all detected gaseous products were formed directly from CO_2 or carbon artifacts and that the photochemical dissociation of methane itself contributed to the formation of CO and HCHO.

Dissociation occurs in carbon dioxide molecules when exposed to high-energy ultraviolet radiation, resulting in the production of carbon monoxide. This was the main source of carbon monoxide in the upper atmosphere. To alleviate the issue of UV irradiation, it is possible to place the lamp horizontally on the liquid reaction system, which prevents direct interactions between the gaseous products and UV light.

The amount of energy received at the top of the hemisphere is approximately $1360\,\mathrm{Wm}^2$ because of the spherical and rotating nature of Earth. This energy spreads out, resulting in an average of $340\,\mathrm{Wm}^2$[37]. The same issue also applies to the liquid-phase photon-assisted catalytic reduction of carbon dioxide, where the photons reaching the surface of the solvent do not equal the energy absorbed by the photocatalyst. Instead, photons undergo multiple scattering, similar to that in atmosphere. As a result, the majority of the photon flux reaching Earth's surface is not available for photon-assisted catalytic reaction systems[38].

Undoubtedly, the energy reaching the Earth's surface varies from that reaching the top of the atmosphere. The intensity of sunlight is subject to changes due to a range of environmental factors, including geographical location, time of year, latitude, aerosol concentration, and cloud cover[30]. Aa appropriate reactor design is essential to optimize the utilization of available sunlight [39–43]. The role of a photoreactor is to capture solar radiation and direct it towards the photocatalyst surface. Consequently, if the reactor design is unsuitable, even the champion photocatalyst may be insufficient. A reactor must be constructed such that it transmits more irradiated light, even in the presence of diffused sunlight. Innovative reactor designs for CO_2 reduction have also been developed. Recently, photocatalytic hydrogen generation has been achieved using a Compound Parabolic Concentrator (CPC) under direct solar irradiation in the presence of wastewater as a sacrificial reagent[44]. CPC technology has the advantage of concentrating all types of radiation, regardless of whether they are diffused into the central tube containing the photocatalyst and substrates. This type of reactor can be used on cloudy days and effectively directs diffused light towards the photocatalytic reactor. Moreover, it does not require any solar tracking facilities; all that is required is positioning the CPC at an angle equivalent to the latitude of its location[45]. The usefulness of this type of reactor configuration has yet to be examined for the reduction of both aqueous and gaseous CO_2 forms. Typically, CO_2 reduction is performed in a batch-type reactor, which provides superior yields, but is not suitable for pilot plant-scale operations. Koci et al. explored the influence of the reactor geometry on the photoreduction of CO_2 using two annular batch reactors[46]. The results showed that the product yield was influenced by the reactor diameter and volume of the liquid phase and that perfect mixing did not occur in the annular reactor. The highest product yield was obtained when the lamp was placed near the

surface of the liquid in the reactor. These findings demonstrate that the macroscopic parameters have a significant impact on the photon-assisted catalytic reduction of CO_2. Additional research is necessary to overcome the obstacles associated with solar energy utilization[47]. The successful utilization of CO_2, water, and sunlight requires collaboration between scientists from various disciplines[48].

1.3 Motivation

The purpose of this thesis is to address the pressing need to reduce dependence on fossil fuels. These fuels not only deplete finite resources but also contribute significantly to environmental issues, particularly the increase in atmospheric carbon dioxide (CO_2). As we face the challenges of transitioning to sustainable energy sources, there is a crucial opportunity to convert CO_2 from problematic by-products into a valuable resources.

This study focused on exploring innovative solutions for sustainable energy production, specifically the conversion of CO_2 into useful chemicals and fuels. This thesis aims to contribute to the development of efficient and environment friendly technologies by investigating the properties of materials such as graphitic carbon nitride (g-C_3N_4) and understanding the underlying mechanisms of CO_2 photoreduction. The ultimate goal is to pave the way for a more sustainable future by harnessing solar energy to convert CO_2 into valuable resources and to mitigate the environmental impact of fossil fuel consumption.

1.4 Relevance of the Work

This study is of great importance for both contemporary and future energy frameworks. Given the growing concerns about climate change and environmental sustainability, it is imperative to shift from energy systems reliant on fossil fuels to more sustainable alternatives. The research on transformation of carbon dioxide (CO_2) into valuable chemicals and fuels aligns perfectly with this objective, thereby reducing the detrimental environmental consequences associated with fossil fuel consumption.

As the demand for energy continues to increase, it is essential to diversify energy sources and adopt sustainable practices. The focus of this research on utilizing solar energy for carbon dioxide photoreduction provides a forward-thinking solution. This study contributes to the development of efficient and scalable technologies for sustainable energy generation by investigating the potential of materials, such as graphitic carbon nitride, and elucidating their mechanistic complexities.

As countries endeavor to attain carbon neutrality and diminish greenhouse gas emissions, the findings of this study hold promise in delivering eco-friendly energy alternatives. The capacity to transform CO_2 into valuable items addresses environmental issues and provides a pathway for repurposing a substance that was previously viewed as waste.

This research is pertinent to present global endeavors to combat climate change and aligns with the long-term objectives of establishing sustainable and environmentally responsible energy practices. The implications of this study have the

potential to shape the trajectory of energy technologies and make a substantial contribution to a sustainable and durable energy future.

1.5 Objectives

1. Study the Role of Material Properties: Investigate the influence of various material properties, particularly focusing on surface functionalities, nanoporous characteristics, and crystalline properties, on the photon-assisted reduction of carbon dioxide. The examined photocatalyst was graphitic carbon nitride (g-C_3N_4).
2. Explore Other Systems: Extend the investigation to encompass other systems, including metallic and bimetallic g-C_3N_4 configurations, to explore their potential as photocatalysts for carbon dioxide reduction.
3. Mechanistic insights: A comprehensive understanding of the reaction mechanisms involved in carbon dioxide activation and reduction is of paramount importance. This objective is to unveil the underlying chemical processes and reaction intermediates responsible for the transformation of carbon dioxide into valuable products.

Achieving these goals will not only further the field of photon-assisted catalysis but will also open up new areas of investigation beyond the realm of material development. The originality of this study lies in the innovative approach that connects the chemical, physical, and photophysical properties of the developed materials, thereby facilitating a comprehensive understanding of their catalytic potential. This study aims to make a substantial contribution to sustainable energy solutions and to the utilization of carbon dioxide as a valuable resource for producing valuable organic compounds and fuels.

1.6 Structure of the Thesis

- Chapter 1 Energy - Matters
- Chapter 2 The Conversion of Carbon Dioxide into Chemicals and Fuels
- Chapter 3 Experimental Methods
- Chapter 4 Understanding the Role of Surface Functionalities in the Photon-Assisted Reduction of Carbon Dioxide on Graphitic Carbon Nitride (g-C_3N_4) Surfaces
- Chapter 5: On the Role of Nature of Crucible on the Properties of Graphitic Carbon Nitride (g-C_3N_4) Surface in the Photon-Assisted Reduction of Carbon Dioxide
- Chapter 6: Exploring the Iono-Thermal Synthesis Route for Graphitic Carbon Nitride: Structural Insights and Solar Fuel Applications

- Chapter 7: Supramolecular Assisted Eutectic Synthesis of Graphitic Carbon Nitride for Photon-Assisted Reduction of Carbon Dioxide
- Chapter 8 Conclusions and Perspectives

1.7 Innovation in Methodology

This thesis introduces a significant innovation in the pioneering application of derivative spectroscopy for a comprehensive understanding of the material properties of CO_2 photoreduction. This represents a major breakthrough in catalysis research as it is an unprecedented advancement. Derivative spectroscopy is an innovative analytical approach that allows the simultaneous examination of optical properties and surface area characteristics. This cutting-edge methodology provides a more nuanced understanding of the complex interplay between material features and catalytic performance. To express this, a novel parameter, termed the D parameter, was introduced, which facilitates the direct comparison of product yields. This key innovation serves as a bridge between optical properties and surface area metrics, offering a unified measure to assess catalytic efficiency. The introduction of the D parameter enhances the precision and clarity of evaluating material performance in CO_2 photoreduction. Furthermore, machine learning techniques have been applied to study the Brunauer–Emmett–Teller (B.E.T) surface area, marking a significant departure from the traditional approaches. The integration of advanced computational methods into surface area analysis provides a more nuanced and efficient understanding of material characteristics. This enhances the accuracy and efficiency of the surface area determination, contributing to the methodological innovation of this thesis.

The application of Rietveld refinement represents a noteworthy methodological advancement in terms of structural elucidation. This sophisticated approach enables precise determination of crystallographic structures, thereby facilitating a more comprehensive understanding of the materials under investigation. In this thesis, a range of innovative methodologies are introduced, including derivative spectroscopy, D parameter calculation, machine learning for B.E.T surface area analysis, and Rietveld refinement for structural elucidation. These methodological innovations not only contribute to progress in catalysis research but also significantly enhance the accuracy, efficiency, and depth of material characterization in the context of CO_2 photoreduction.

References

[1] Ozin, G.; Ghoussoub, M., *The Story of CO_2 Big Ideas for a Small Molecule*; University of Toronto Press: Toronto, 2020.

[2] Mertens, J.; Breyer, C.; Arning, K.; Bardow, A.; Belmans, R.; Dibenedetto, A.; Erkman, S.; Gripekoven, J.; Léonard, G.; Nizou, S.; Pant, D.; Reis-Machado, A. S.; and Jaap Vente, P. S.; Webber, M.; Sapart, C. J. Carbon capture and utilization: More than hiding CO_2 for some time. *Joule* **2023**, *7*, 442–449.

[3] Viswanathan, B., Chapter 16 - Energy Conversion Routes: An Evaluation In *Energy Sources*, Viswanathan, B., Ed.; Elsevier: Amsterdam, 2017, pp 369–376.

[4] Viswanathan, B., Chapter 1 - Introduction In *Energy Sources*, Viswanathan, B., Ed.; Elsevier: Amsterdam, 2017, pp 1–28.

[5] Nocito, F.; Dibenedetto, A. Atmospheric CO_2 mitigation technologies: carbon capture utilization and storage. *Current Opinion in Green and Sustainable Chemistry* **2020**, *21*, New Synthetic methods: Selected papers from the 4^{th} Green and Sustainable Chemistry Conference, 34–43.

[6] Aresta, M. Do Bio-Ethanol and Synthetic Ethanol Produced from Air-Captured CO_2 Have the Same Degree of "Greenness" and Relevance to "Fossil C"? *Molecules* **2022**, *27*.

[7] Aresta, M.; Nocito, F., Large Scale Utilization of Carbon Dioxide: From Its Reaction with Energy Rich Chemicals to (Co)-processing with Water to Afford Energy Rich Products. Opportunities and Barriers In *An Economy Based on Carbon Dioxide and Water: Potential of Large Scale Carbon Dioxide Utilization*, Aresta, M., Karimi, I., Kawi, S., Eds.; Springer International Publishing: Cham, 2019, pp 1–33.

[8] Aresta, M.; Dibenedetto, A., The CO_2 Revolution In *The Carbon Dioxide Revolution: Challenges and Perspectives for a Global Society*; Springer International Publishing: Cham, 2021, pp 219–228.

[9] Aresta, M.; Dibenedetto, A.; Angelini, A. The changing paradigm in CO_2 utilization. *Journal of CO_2 Utilization* **2013**, *3-4*, 65–73.

[10] Aresta, M.; Dibenedetto, A.; Quaranta, E. State of the art and perspectives in catalytic processes for CO_2 conversion into chemicals and fuels: The distinctive contribution of chemical catalysis and biotechnology. *Journal of Catalysis* **2016**, *343*, Catalytic CO_2 conversion processes to fuels and other small molecules, 2–45.

[11] Aresta, M.; Dibenedetto, A. Carbon Recycling Through CO_2-Conversion for Stepping Toward a Cyclic-C Economy. A Perspective. *Frontiers in Energy Research* **2020**, *8*, 159.

[12] Aresta, M., The Carbon Dioxide Problem In *Carbon Dioxide as a Source of Carbon: Biochemical and Chemical Uses*, Aresta, M., Forti, G., Eds.; Springer Netherlands: Dordrecht, 1987, pp 1–22.

[13] Dibenedetto, A.; Marcolongo, D. M.; Aresta, M., Conversion of CO_2 to Fuels In *Reference Module in Earth Systems and Environmental Sciences*; Elsevier: 2022.

[14] Aresta, M.; Dibenedetto, A.; Angelini, A. The changing paradigm in CO_2 utilization. *Journal of CO_2 Utilization* **2013**, *3-4*, 65–73.

[15] Aresta, M.; Dibenedetto, A.; Angelini, A. Catalysis for the Valorization of Exhaust Carbon: from CO_2 to Chemicals, Materials, and Fuels. Technological Use of CO_2. *Chemical Reviews* **2014**, *114*, PMID: 24313306, 1709–1742.

[16] Wang, X.; Song, C., Capture of CO_2 from Concentrated Sources and the Atmosphere In *An Economy Based on Carbon Dioxide and Water: Potential of Large Scale Carbon Dioxide Utilization*, Aresta, M., Karimi, I., Kawi, S., Eds.; Springer International Publishing: Cham, 2019, pp 35–72.

[17] Marcolongo, D. M.; Aresta, M.; Dibenedetto, A., Chapter Nine - Stepping toward the carbon circular economy (CCE): Integration of solar chemistry and biosystems for an effective CO_2 conversion into added value chemicals and fuels In *Recent Highlights I*, Hubbard, C. D., van Eldik, R., Eds.; Advances in Inorganic Chemistry, Vol. 78; Academic Press: 2021, pp 289–351.

[18] Aresta, M.; Nocito, F.; Dibenedetto, A., Chapter Two - What Catalysis Can Do for Boosting CO_2 Utilization In Song, C., Ed.; Advances in Catalysis, Vol. 62; Academic Press: 2018, pp 49–111.

[19] Scibioh, M. A.; Viswanathan, B., Chapter 1 - CO_2 Conversion—Relevance and Importance In *Carbon Dioxide to Chemicals and Fuels*, Scibioh, M. A., Viswanathan, B., Eds.; Elsevier: 2018, pp 1–22.

[20] Scibioh, M. A.; Viswanathan, B., Chapter 10 - Perspectives—CO_2 Conversion to Fuels and Chemicals In *Carbon Dioxide to Chemicals and Fuels*, Scibioh, M. A., Viswanathan, B., Eds.; Elsevier: 2018, pp 475–482.

[21] (IEA), I. *Putting CO_2 to Use*; tech. rep., License: CC BY 4.0; Paris: IEA, 2019.

[22] Liu, C.; Colón, B. C.; Ziesack, M.; Silver, P. A.; Nocera, D. G. Water splitting–biosynthetic system with CO_2 reduction efficiencies exceeding photosynthesis. *Science* **2016**, *352*, 1210–1213.

[23] Lewis, N. S.; Nocera, D. G. Powering the planet: Chemical challenges in solar energy utilization. *Proceedings of the National Academy of Sciences* **2006**, *103*, 15729–15735.

[24] Aresta, M.; Dibenedetto, A.; Quaranta, E., The Carbon Dioxide Molecule In *Reaction Mechanisms in Carbon Dioxide Conversion*; Springer Berlin Heidelberg: Berlin, Heidelberg, 2016, pp 1–34.

[25] Narayanan, H.; Viswanathan, B.; Nair, H. On the current status of the mechanistic aspects of photocatalytic reduction of carbon dioxide. *Indian Journal of Chemistry-Section A (IJCA)* **2017**, *56*, 251–269.

[26] Narayanan, H.; Viswanathan, B.; Yesodharan, S. Photocatalytic reduction of carbon dioxide: Issues and prospects. *Current Catalysis* **2016**, *5*, 79–107.

[27] Viswanathan, B., Reduction of Carbon Dioxide: Photo-Catalytic Route to Solar Fuels In *Materials and Processes for Solar Fuel Production*, Viswanathan, B., Subramanian, V. R., Lee, J. S., Eds.; Springer New York: New York, NY, 2014, pp 211–233.

[28] Viswanathan, B., Chapter 10 - Electro-Catalytic Reduction of Carbon Dioxide In *New and Future Developments in Catalysis*, Suib, S. L., Ed.; Elsevier: Amsterdam, 2013, pp 275–295.

[29] Zehner, O., *Green Illusions: The Dirty Secrets of Clean Energy and the Future of Environmentalism*; University of Nebraska Press: 2012.

[30] Folli, A.; Bloh, J. Z.; Strøm, M.; Pilegaard Madsen, T.; Henriksen, T.; Macphee, D. E. Efficiency of Solar-Light-Driven TiO_2 Photocatalysis at Different Latitudes and Seasons. Where and When Does TiO_2 Really Work? *The Journal of Physical Chemistry Letters* **2014**, *5*, 830–832.

[31] National Renewable Energy Laboratory Solar Resource Data and Tools `https://www.nrel.gov/grid/solar-resource/renewable-resource-data.html`.

[32] Varghese, O. K.; Paulose, M.; LaTempa, T. J.; Grimes, C. A. High-Rate Solar Photocatalytic Conversion of CO_2 and Water Vapor to Hydrocarbon Fuels. *Nano Letters* **2009**, *9*, 731–737.

[33] Matthews, R. W.; McEvoy, S. R. A comparison of 254 nm and 350 nm excitation of TiO_2 in simple photocatalytic reactors. *Journal of Photochemistry and Photobiology A: Chemistry* **1992**, *66*, 355–366.

[34] Koci, K.; Zatloukalova, K.; Obalova, L.; Krejcikova, S.; Lacny, Z.; Capek, L.; Hospodkova, A.; Solcova, O. Wavelength Effect on Photocatalytic Reduction of CO_2 by Ag/TiO_2 Catalyst. *Chinese Journal of Catalysis* **2011**, *32*, 812–815.

[35] Seinfeld, J. H.; Pandis, S. N., *Atmospheric Chemistry and Physics: From Air Pollution to Climate Change*, Third; John Wiley & Sons, Inc.: 2016.

[36] Manahan, S. E., *Environmental Chemistry*, Eleventh; CRC Press: 2022.

[37] Burch, S.; Harris, S. Climate Literacy: Navigating Climate Change Conversations The University of British Columbia.

[38] Smith, Y. R.; Subramanian, V.; Viswanathan, B., Photo-electrochemical and photo-catalytic conversion of carbon dioxide In *Photo-Electrochemistry and Photobiology for Sustainability.* Kaneco, S., Viswanathan, B., Katsumata, H., Eds.; Union Press: 2012, pp 155–181.

[39] Ola, O.; Maroto-Valer, M. Review of material design and reactor engineering on TiO_2 photocatalysis for CO_2 reduction. *Journal of Photochemistry and Photobiology C: Photochemistry Reviews* **2015**, *24*, 16–42.

[40] De Richter, R. K.; Ming, T.; Caillol, S. Fighting global warming by photocatalytic reduction of CO_2 using giant photocatalytic reactors. *Renewable and Sustainable Energy Reviews* **2013**, *19*, 82–106.

[41] Nguyen, T.-V.; Wu, J. C. Photoreduction of CO_2 to fuels under sunlight using optical-fiber reactor. *Solar Energy Materials and Solar Cells* **2008**, *92*, 864–872.

[42] Tahir, M.; Tahir, B.; Amin, N. S. Photocatalytic CO_2 reduction by CH_4 over montmorillonite modified TiO_2 nanocomposites in a continuous monolith photoreactor. *Materials Research Bulletin* **2015**, *63*, 13–23.

[43] Braham, R. J.; Harris, A. T. Review of Major Design and Scale-up Considerations for Solar Photocatalytic Reactors. *Industrial & Engineering Chemistry Research* **2009**, *48*, 8890–8905.

[44] Villa, K.; Domènech, X.; Malato, S.; Maldonado, M. I.; Peral, J. Heterogeneous photocatalytic hydrogen generation in a solar pilot plant. *International Journal of Hydrogen Energy* **2013**, *38*, 12718–12724.

[45] Romero, M.; Blanco, J.; Sánchez, B.; Vidal, A.; Sixto Malato; Cardona, A. I.; Garcia, E. Solar Photocatalytic Degradation of Water and Air Pollutants: Challenges and Perspectives. *Solar Energy* **1999**, *66*, 169–182.

[46] Kočí, K.; Reli, M.; Kozák, O.; Lacný, Z.; Plachá, D.; Praus, P.; Obalová, L. Influence of reactor geometry on the yield of CO_2 photocatalytic reduction. *Catalysis Today* **2011**, *176*, Special issue dedicated to APAC 2010, 212–214.

[47] Rodriguez, C. A.; Modestino, M. A.; Psaltis, D.; Moser, C. Design and cost considerations for practical solar-hydrogen generators. *Energy Environ. Sci.* **2014**, *7*, 3828–3835.

[48] Schmalensee, R., *The future of solar energy: an interdisciplinary MIT study*; Energy Initiative, Massachusetts Institute of Technology: 2015.

Chapter 2

The Conversion of CO_2 into Chemicals and Fuels

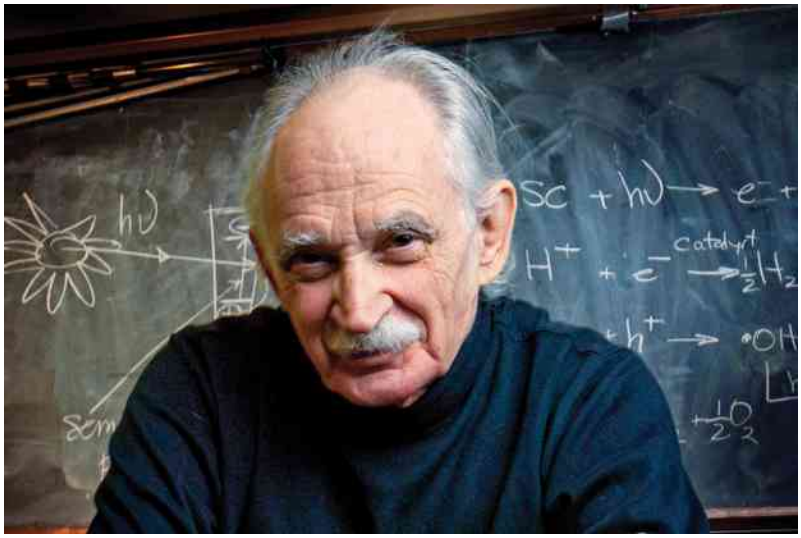

This chapter is dedicated to the memory of Allen J. Bard, Department of Chemistry at The University of Texas at Austin, whose pioneering contributions to electrochemistry, especially semiconductor photoelectrochemistry, have profoundly influenced the field and inspired countless researchers.

Abstract

Photon-assisted reduction of CO_2 to value-added chemicals and fuels presents a promising approach for mitigating climate change while producing renewable energy carriers. This comprehensive review examines the fundamental principles, material design strategies, reaction mechanisms, and practical challenges of photon-assisted CO_2 conversion. We begin by exploring the essential concepts of semiconductor physics and the interfacial phenomena that underpin photon-assisted processes. The review critically assesses various material engineering approaches, including doping, heterojunction formation, and plasmonic metal incorporation, highlighting their benefits and limitations. A detailed analysis of the proposed reaction pathways and intermediates is presented, with an emphasis on the role of the CO_2 radical anion and the influence of the reaction environment.

We also address key practical challenges such as competing reactions, stability issues, and the impact of carbonates and carbonates in aqueous systems. In this review, we highlight recent advances in this field, including the emergence of metal-free catalysts and novel in situ characterization techniques. Finally, we offer perspectives on future research directions and the potential for practical implementation of photon-assisted CO_2 reduction technologies. This review aims to provide researchers with a critical understanding of the current state of the art and guide future efforts in developing efficient and sustainable photon-assisted systems for CO_2 utilization.

2.1 Introduction

Despite significant progress over the past four decades, no economically viable technology or process currently exists for the direct conversion of carbon dioxide into valuable chemicals and fuels [1–4]. Efficient carbon dioxide conversion remains a challenge, as highlighted in the Department of Energy (DOE) status report, which identifies the difficulties related to CO_2 conversion processes[5]. One of the key challenges is the scarcity of catalysts capable of utilizing abundant solar energy and inexpensive reducing agents to form chemical bonds, enabling rapid and selective cleavage of C-O bonds and the production of C-H bonds in fuel products.

The photoreduction of carbon dioxide occurs via two pathways: the formation and subsequent hydrogenation of $^{-\bullet}CO_2$ and proton-coupled electron transfer reactions. Proton-assisted electron addition is preferred because of the lower energy barrier for CO_2 hydrogenation products. The Latimer-Frost diagram (Figure 2.1), which correlates the net free energy change with electron transfer, can identify thermodynamically unstable species that can be converted into stable species such as formaldehyde, which can be converted into carbon monoxide and methanol[6].

Although insights from natural photosynthesis are valuable, they are insufficient for fulfilling the ambitions of Ciamician's vision[7]. The process of converting CO_2 to glucose via photosynthesis is complex and difficult to apply in an industrial setting. Developing CO_2 reduction technology requires a deep understanding of the underlying principles of the CO_2 reduction process, which is beyond current technological capabilities [8–10].

In the context of photon-assisted reduction, it is essential to note that only initiation from the photon source is required, without conversion to electricity. Moreover, the adsorption of the substrate on the photocatalyst surface significantly reduces the overpotential required for the reduction process. Photon-assisted catalytic or photochemical pathways are considered the preferred approach for solar energy conversion because they utilize carbon dioxide and water as precursors for reduction, converting them into products in the ambient atmosphere. In aqueous media, hydrogen evolution is more favorable than CO_2 reduction, and the presence of oxygen and reactive oxygen species increases the chance of reverse oxidation of the reduction products[11, 12]. Consequently, various proton source alternatives have been explored[13].

Figure 2.2 highlights the critical role that CO_2 conversion technologies play in achieving Ciamician's vision and addressing current environmental and energy-

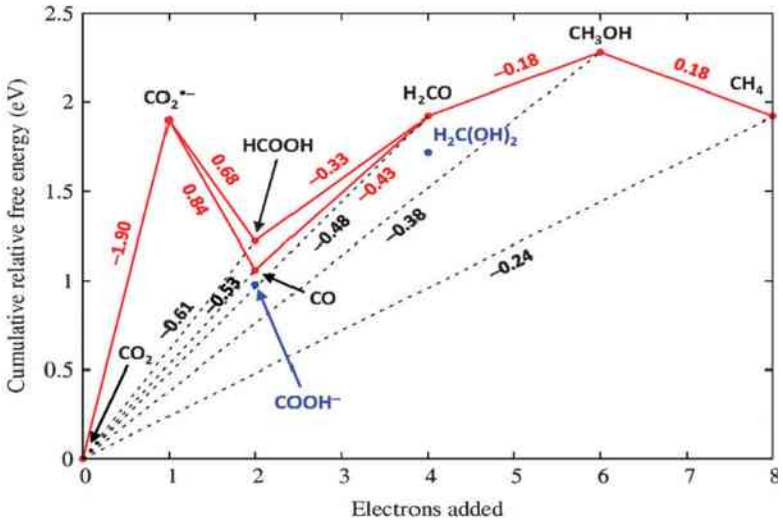

Figure 2.1: A schematic representation of the Latimer–Frost diagram, illustrating the multi-electron, multi-proton reduction of carbon dioxide (CO_2) in a homogeneous aqueous solution at a pH of 7. Any species that lies above the straight line connecting two adjacent points (such as $CO_2^{\bullet-}$, located between CO_2 and HCOOH) is considered thermodynamically unstable with respect to disproportionation [6]. Reproduced from *Chem. Soc. Rev. 2012, 41, 2036–2051. ©2012 Royal Society of Chemistry.*

related issues. Although these technologies cannot solve the problem of atmospheric CO_2 accumulation, they can help reduce the volume of CO_2 produced from point sources, enabling the carbon-neutral use of chemicals[14]. However, achieving these targets is challenging, and the development of effective CO_2 conversion processes remains a priority for addressing these issues[15].

The process of photon-assisted conversion of carbon dioxide can be approached in two ways: (1) gaseous-phase reduction, which involves the direct treatment of $CO_{2(g)}$ with a photocatalyst surface using hydrogen, typically in the form of water vapor; and (2) liquid-phase reduction, which involves the reduction of carbon dioxide in an aqueous solution or other solvent medium in the presence of a dispersed photocatalyst. A conventional depiction of the gaseous-phase CO_2 reduction mechanism is shown in Figure 2.3, and is commonly used to interpret the mechanisms of aqueous-phase CO_2 reduction. However, in the case of aqueous-phase CO_2 reduction, the process is influenced by competing and different radical reactions in the reaction system. Therefore, it is necessary to make corrections to describe the types of interfacial reactions involved in the CO_2 reduction process. The photon-assisted CO_2 reduction process encompasses all processes occurring at the semiconductor surface interface, which creates competition and ultimately reduces the efficiency (Figure 2.3). Despite the significance of competitive reactions in the CO_2 reduction process, most studies have overlooked their exact roles.

Conducting a comprehensive analysis of the difficulties related to CO_2 reduction photocatalysis, it is clear that the underlying mechanisms of carbon dioxide reduction have not been extensively studied, and existing theories are insufficient to explain most of the processes associated with CO_2 photoreduction.[16, 17] Consequently, there is an immediate need to re-evaluate the established theories

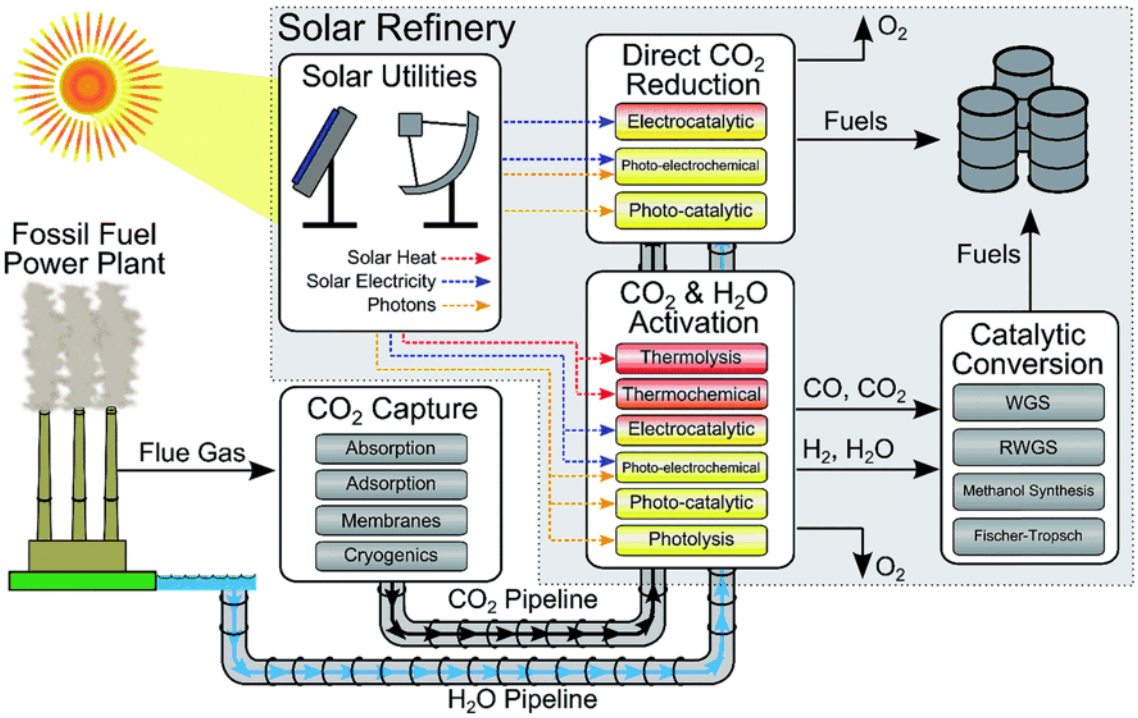

Figure 2.2: Simplified overview of solar fuel production: Solar energy, alongside CO_2 and H_2O, undergoes conversion in solar refineries to produce usable fuels. Two main methods involve direct solar-driven CO_2 reduction or solar activation of CO_2/H_2O, followed by catalytic conversion. Temperature requirements are color-coded (red = high temperature, yellow = ambient temperature) [15]. *Reproduced with permission from Herron, J. A.; Kim, J.; Upadhye, A. A.; Huber, G. W.; Maravelias, C. T., Energy & Environ. Sci. 8 (2015) 126–157. ©2015 Royal Society of Chemistry.*

on CO_2 activation and the subsequent conversion into fuels or fuel precursors. This attempt aims to reconsider the present understanding of the mechanism underlying semiconductor-mediated photon-assisted catalytic reduction of CO_2[16, 18].

2.2 Clarifying the Difference between Photocatalytic and Photosynthetic Processes

The utilization of solar energy to drive chemical transformations has been a major focus of research in recent decades, with the aim of developing sustainable technologies for energy production and environmental remediation. Two fundamental approaches have emerged: photocatalysis and photosynthesis. Although these terms are often used interchangeably in the literature, they represent distinct processes with different thermodynamic requirements and device architectures. This section elucidates the key differences between photocatalytic and photosynthetic systems, their classification, and the implications for their optimization and practical application [19].

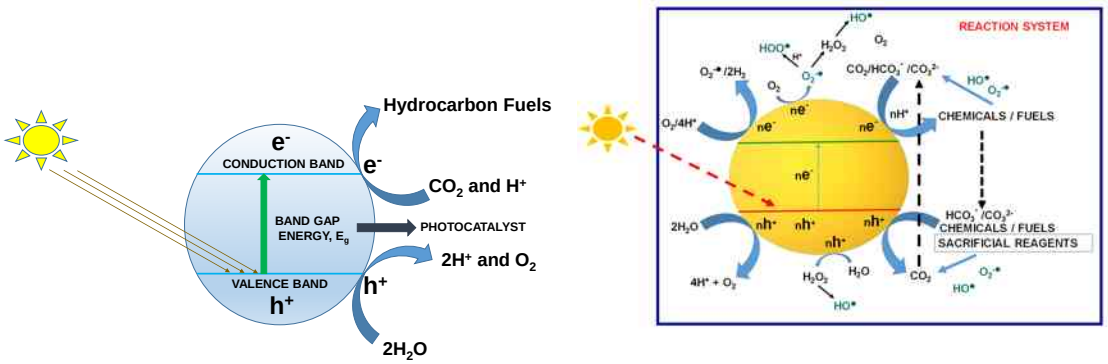

Figure 2.3: Illustrate the mechanisms of gaseous phase CO_2 reduction and the possible reactions involved in the CO_2 reduction process, respectively [11]. *Reproduced from Indian J. Chem. Sec. A 56 (2017) 251–269. ©2017 Council of Scientific and Industrial Research–National Institute of Science Communication and Policy Research, India.*

2.2.1 Thermodynamics: The Defining Difference

The primary distinction between photocatalysis and photosynthesis lies in the thermodynamics of the coupled chemical reactions. Photocatalytic processes are thermodynamically downhill, with a negative change in Gibbs free energy ($\Delta G < 0$). In these systems, light absorption serves to accelerate the reaction kinetics, but the catalyst does not provide additional energy input. In contrast, photosynthetic processes are thermodynamically uphill ($\Delta G > 0$) and require photochemical energy input from the absorbed light to proceed. This additional energy is harnessed to drive the synthesis of higher-energy products, such as hydrogen fuel from water or reduced carbon compounds from CO_2.

2.2.2 Suppressing the Back Reaction: The Challenge of Photosynthesis

The thermodynamic favorability of the reverse reaction poses a significant challenge in the design of photosynthetic systems. To achieve net production of the desired high-energy products, the reverse reaction must be effectively suppressed. This crucial function distinguishes photosynthetic devices from photocatalysts and traditional catalysts. Two primary strategies have been employed to address this issue: spatial separation of the half-reactions (type 1) and selective charge transfer (type 2).

2.2.3 Classification of Excitonic Chemical Conversion Devices

Excitonic chemical conversion devices, which rely on the generation and transfer of photogenerated charge carriers, can be broadly categorized into three types:

1. Photocatalytic (PC) devices: These systems drive thermodynamically downhill reactions ($\Delta G < 0$) without the need for additional energy input.

2. Type 1 Photosynthetic (PS) devices: These systems achieve uphill reactions ($\Delta G > 0$) by spatially separating the oxidation and reduction half-reactions, typically using a semi-permeable membrane, to prevent the reverse reaction.

3. Type 2 Photosynthetic (PS) devices: These systems also drive uphill reactions but rely on selective charge transfer to prevent the back reaction. This selectivity is typically achieved through the use of co-catalysts or surface modifications that promote the desired half-reactions while suppressing the reverse processes.

2.2.4 Optimization Strategies and Limiting Factors

The classification of excitonic chemical conversion devices has important implications for their optimization and practical application. While all such devices benefit from improved light absorption, carrier lifetimes, and interfacial charge transfer kinetics, the limiting factors and optimization strategies differ between photocatalytic and photosynthetic systems. For photocatalytic devices, the primary limiting factor is the available surface area for the reaction. Optimization efforts should therefore focus on increasing the specific surface area, for example, by decreasing the size of the light-absorbing particles or using high-surface-area support materials. In type 1 photosynthetic devices, the key limiting factors are charge mobility and mass transport across the system. Optimization strategies include enhancing the electric field strength to improve charge separation, increasing the charge carrier mobility of the light-absorbing materials, and improving the mass transfer rates of reactants and intermediates. For type 2 photosynthetic devices, the primary limitation is the selectivity of the charge transfer processes at the surface. The development of highly selective co-catalysts and surface modifications that promote the desired half-reactions while suppressing the back reaction is crucial for their efficient operation.

2.2.5 Applications and Examples

Photocatalytic and photosynthetic systems have been applied to a wide range of chemical transformations, including water splitting, CO_2 reduction, nitrogen fixation, and environmental remediation. Some notable examples include:

1. Photocatalytic oxidation of organic pollutants using TiO_2 and other metal oxide nanoparticles.

2. Z-scheme type 1 photosynthetic water splitting using spatially separated photocatalysts, such as $SrTiO_3$:Rh and $BiVO_4$.

3. Type 2 photosynthetic water splitting using GaN:ZnO and Ta_3N_5 nanoparticles with selective co-catalysts for hydrogen and oxygen evolution.

4. Photosynthetic CO_2 reduction to fuels using hybrid inorganic-biological systems, such as silicon nanowires with immobilized enzymes.

Interestingly, natural photosynthesis in plants and cyanobacteria combines both type 1 and type 2 strategies, using spatial separation of the light-driven water

oxidation and carbon fixation reactions, as well as selective enzymes to promote the desired transformations and suppress the back reactions.

The distinction between photocatalysis and photosynthesis is rooted in the thermodynamics of the coupled chemical reactions, with photosynthetic processes requiring additional energy input to drive uphill transformations. This fundamental difference necessitates the suppression of the reverse reaction in photosynthetic systems, either through spatial separation of the half-reactions or selective charge transfer at the surface. The classification of excitonic chemical conversion devices into photocatalytic, type 1 photosynthetic, and type 2 photosynthetic systems provides a framework for understanding their operating principles and guides the development of optimization strategies. As research in this field continues to advance, it is crucial to recognize the unique challenges and opportunities associated with each approach, ultimately leading to the development of efficient and sustainable technologies for solar energy conversion and storage.

2.3 Basic Postulates and Principles

The design of photoelectrodes and photocatalysts is influenced by numerous factors, each of which plays a distinct role in the overall process. These factors include the nature of light irradiation, penetration of light into the semiconductor, absorption of photons, generation, separation, and transportation of charge carriers to the interface, thermodynamic and kinetic factors of the interface reactions, competing reactions, and the overall stability of the photocatalysts. Additionally, the characteristics of the materials, such as the particle size, surface area, pore size, active sites on the surface, and morphology, have a significant impact on the CO_2 reduction and water-splitting processes. Given the interrelated nature of these factors, their correlations are complex. Simply focusing on the inherent properties of a material is insufficient to achieve a viable process at a scale. Therefore, optimization of all physical, chemical, and electrochemical parameters in an efficient manner is necessary for the selection and design of new materials for solar fuel production.

2.3.1 Photon Management

The primary process in a photon-assisted catalytic system or photoelectrocatalytic cell is the excitation of charge carriers under irradiation with light of an appropriate wavelength and constant intensity. Any variation in light intensity would have a noticeable impact on the subsequent processes. To maximize light absorption, the surface morphology must be controlled. The absorption coefficient depends on both the intrinsic material properties and nature of the incident light[20].

$$\text{Photon Intensity} \propto e^{-\alpha x} \tag{2.1}$$

Photons with energies less than the bandgap energy (E_g) are not absorbed by the semiconductor. Photons with energies greater than E_g are absorbed; however, some photons travel a considerable distance before being absorbed. The light intensity decreases exponentially with the distance travelled (x) inside the semiconductor. α is the absorption coefficient or absorptivity, and is proportional to the extinction coefficient (κ), which is the square root of the complex part of the

dielectric constant. The inverse of the absorption coefficient, usually referred to as the penetration depth or skin depth (δ), is the distance over which the incident light intensity falls to 1/e of its original value in a semiconductor and is roughly proportional to the inverse of the square root of the dielectric constant[21, 22].

$$\text{Penetration Depth, } \delta = \frac{1}{\alpha} \text{ or } \alpha^{-1} \tag{2.2}$$

The skin depth value enables the prediction of the distance to which light penetrates a semiconductor, and the value of δ depends on the frequency (inverse of the wavelength) as well as the semiconductor properties. For example, in the case of Fe_2O_3, $\delta = 118\,\mathrm{nm}$ at $550\,\mathrm{nm}$; for Si, $\delta = 680\,\mathrm{nm}$ at $510\,\mathrm{nm}$; and for CdTe, $\delta = 106\,\mathrm{nm}$ at $550\,\mathrm{nm}$[23]. The penetration depth of the incident light in a photoelectrode should be in the range of the thickness of the space charge layer, such that the excitation in that region is uniform. If the bulk diffusion length is greater than the width of the space charge layer, recombination via surface states is negligible and no diffusion current flows towards the interface[24]. Controlling the penetration depth up to the space charge layer is highly significant because it reduces the charge carrier recombination and improves migration into the interface. Owing to the direct dependence of the wavelength on the penetration depth[21], the use of monochromatic radiation is encouraged for water splitting to achieve precise control over the penetration depth. This indicates that the selection of the incident radiation is not random, and the penetration depth must be factored into before selecting the appropriate wavelength of incident radiation for PEC water splitting.

2.3.2 Bandgap, Photovoltage and Band Edge Positions

The material must possess a sufficient bandgap to generate a photovoltage across the interface, which serves as the driving force for CO_2 and water splitting. To achieve an effective CO_2 reduction and water splitting, the generated photovoltage must overcome the overvoltage associated with the process. For example, in the case of water splitting, the thermodynamic voltage required to split water is $1.23\,\mathrm{V}$, and the additional overpotential increases this value to $1.8\,\mathrm{V}$, depending on the photoelectrode used. Hence, a material with a band gap of more than $2.2\,\mathrm{eV}$ to $2.4\,\mathrm{eV}$ is necessary to produce $1.8\,\mathrm{V}$ to $2\,\mathrm{V}$ of photovoltage, as the quasi-Fermi level lies above and below the respective bands owing to nonradiative recombination, incomplete light trapping, and spontaneous emission[25]. The nonideal alignment of the band structure can further reduce the photovoltage. Photophysical processes that occur under illumination also affect the photovoltage stability. Additionally, the photovoltage and bandgap of the photoelectrode must have sufficient potential compared with the water redox potential, or the water redox potential must be within the bandgap of the material at any pH value. The selection of materials with significant band gaps and band edge positions does not guarantee full-fledged water-splitting. To achieve efficient CO_2 reduction and water splitting, the photovoltage generated under illumination must be uniform throughout the reaction process. Sustaining the photovoltage throughout the reaction is a significant challenge, and stable photovoltage generation depends on several factors, such as the presence of additional states between the bandgap and the morphology of the material surface. These aspects are explored in subsequent sections.

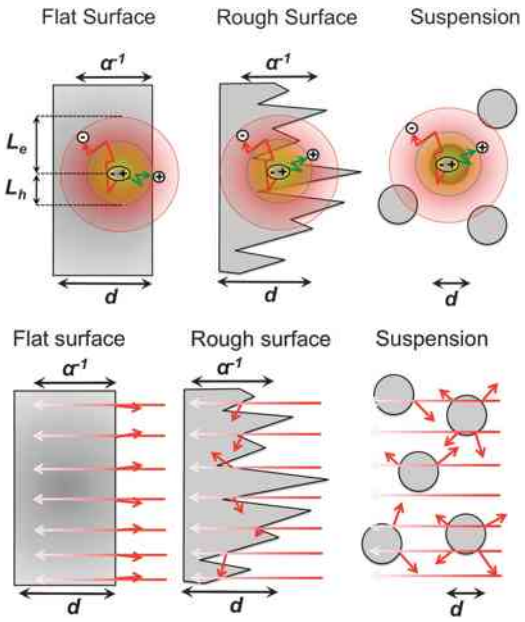

Figure 2.4: Charge collection on different surfaces: (a) flat surface, (b) nanostructured surface, and (c) particle suspension. Here, d is the thickness of the particle, L_e and L_h are the electron and hole diffusion lengths, respectively. The figure also illustrates the diffusion of light on flat and rough surfaces and in suspension; α^{-1} is the optical penetration depth [23]. *Reproduced from Chem. Soc. Rev. 42 (2013) 2294–2320. ©2015 Royal Society of Chemistry.*

2.3.3 Morphology and Textural Parameters

The morphology of the photoelectrode was designed to maximize the amount of incident light captured. Roughening the surface of the photoelectrode allows light to be trapped by increasing the degree of horizontal light distribution through light scattering (as shown in Figure 2.4). In contrast, a flat surface is typically less desirable, owing to an increase in direct reflection[26].

The particle size plays a significant role in the solar fuel generation process. Materials with smaller particle sizes have higher surface-to-volume ratios, which is advantageous for surface reactions. A higher surface area containing suitable active sites is necessary for any surface reaction, and it promotes the reaction more effectively than larger particles do. In nanoscale particles, the potential drop and electric field across the space-charge region are significantly lower, which hinders carrier transport to the surface interface owing to the rapid recombination of excitons[24]. Additionally, the increase in electron-hole recombination in nanoscale particles retards the advantage gained from the higher interfacial surface area. However, the surface and interfacial electron-hole recombination in smaller particles can be reduced by appropriate surface treatments to remove any surface defects. Moreover, a decrease in the particle size also increases the bandgap of the material owing to the modification of the band-edge positions caused by quantum confinement[23, 27]. Consequently, nanoscale particles are better reducing/oxidising agents than bulk semiconductors. Finally, the increased bandgap shifts the absorption properties to the blue region of the spectrum, thereby reducing the absorption of the visible light.

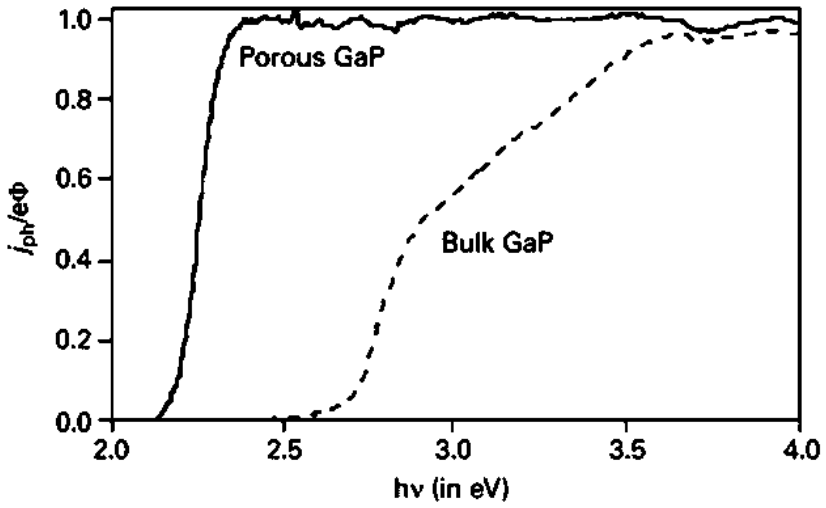

Figure 2.5: Relationship between the photocurrent quantum yield and photon energy for a polished n-GaP electrode (represented by the dashed curve) and the same electrode after undergoing porous etching (represented by the solid curve). The measurements were taken at a photocurrent density of $16\,\mathrm{C\ cm^{-2}}$ and a potential of $10\,\mathrm{V}$ vs. SCE in a $0.5\,\mathrm{M}$ H_2SO_4 solution at $+1\,\mathrm{V}$ vs. SCE [29]. *Reproduced from Electrochim. Acta 43 (1998) 2773–2780. ©1998 Elsevier B.V.*

Elevating the surface area of either the material or the cocatalyst has a profound influence on the reaction rate because it facilitates the transfer of charges across interfaces, allowing CO_2 and water-splitting reactions to occur at significantly lower current densities. Moreover, the material or co-catalyst must possess active sites that are responsible for capturing water from their surface lattices.

The scattering and internal reflection within the porous layer of the photoelectrode enhanced the light-absorption cross-section. As a result, the penetration depth in the porous photoelectrode decreases and therefore produces minority charge carriers near the semiconductor-electrolyte interface, thus reducing the light-induced recombination of excitons. However, the use of porous GaP (Figure 2.5) enables the absorption of light within the porous layer, which produces minority charge carriers near the interface, thus enhancing the quantum efficiency to unity in the presence of the bandgap photon energy[28, 29].

2.3.4 Stability

The primary challenge in photon-assisted catalytic systems is the susceptibility of the catalytic material to decomposition under reaction conditions. A deeper understanding of the photocorrosion mechanism is essential to determine the optimal material under these conditions. Therefore, material selection requires particular attention, and independent analysis is necessary to identify the actions required to stabilize the material[30].

Most photocorrosion studies have been conducted using photoelectrodes in the photoelectrochemical systems[†]. The photoelectrochemical decomposition of the

[†]The feasibility of extending the stability criteria for the photoelectrode to suspended photocat-

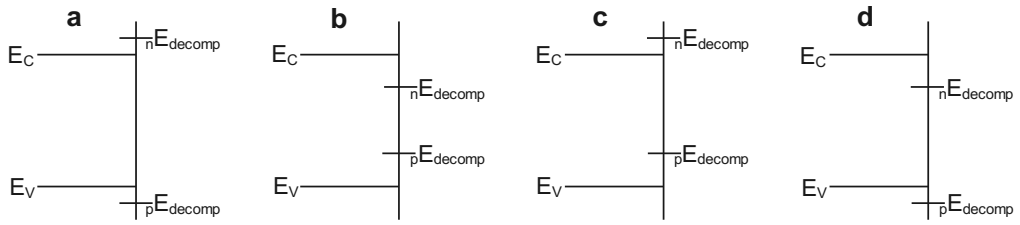

Figure 2.6: Shows three possible positions of the decomposition energy levels relative to the band edges in various scenarios. The energy levels of a relatively stable semiconductor are shown in (a). In (b), the energy levels imply instability if either the electrons or holes reach the surface. In (c) and (d), the energy levels imply instability of the holes and electrons, respectively. This information is taken from the work of Gerischer[31]. *Reproduced from J. Vac. Sci. Technol. 15 (1978) 1422–1428. ©1978 American Vacuum Society.*

photocathode and photoanode was primarily influenced by the conduction band electrons and valence band holes, respectively. The specific quasi-Fermi level of the photoelectrode under illumination determines the energetics of electrons and holes. Thus, the position of the decomposed Fermi levels relative to the quasi-Fermi levels determines the thermodynamic stability of a photoelectrode. The stability of a photoelectrode can be classified in four ways[31].

The classification of photoelectrodes based on the position of the Fermi level with respect to the bandgap is as follows: if the Fermi level lies outside the bandgap, the photoelectrode is considered stable; if it lies inside the bandgap, it is considered unstable. The free energy difference between the band edges and the Fermi level at the decomposition site determines the extent of anodic and cathodic decomposition. Ideally, the first case is preferred; however, in reality, there is no semiconductor that is completely stable against photodecomposition. Most photoelectrodes belong to the latter two categories. For the semiconductor depicted in figure 2.6b, complete decomposition occurs under light irradiation.

According to Geirscher[32], the decomposition of photoelectrodes (MX) can be expressed as

$$\text{Photocathodic reaction:} \quad \mathrm{MX} + \mathrm{Z_e^-} + \mathrm{solv} \rightarrow \mathrm{M} + \mathrm{X_{solv}^{Z^-}} \tag{2.3}$$

$$\text{Photoanodic reaction:} \quad \mathrm{MX} + \mathrm{Z_h^+} + \mathrm{solv} \rightarrow \mathrm{M_{solv}^{Z^+}} + \mathrm{X} \tag{2.4}$$

where M and X represent the elements present in the photoelectrode, and solv denotes the solvent. The superscripts Z, Z^+, and Z^- indicate the charges on the species during the reaction.

The presence of holes on the surface can be viewed as a lack of electrons in the bonding states of the valence band. This deficiency in bonding between adjacent

alysts remains an open question. Unlike photocatalysts, which are subject only to a photon field, photoelectrodes in a photoelectrochemical system are influenced by both electric and photon fields. This may result in a more rapid decomposition of the photoelectrode compared to the same material in a suspension.

atoms in the surface lattice creates a greater susceptibility to the electrons present in the nucleophilic reactants in the electrolyte. The degree of this susceptibility depends on the localization of the wave functions, with kink sites, lattice defects, and dislocations on the surface playing a significant role in the "transient hole-capturing process." The interaction of these sites with electron-donating atoms or molecules from the electrolyte results in the further localization of the holes through the formation of a new bond. In the case of electrons in the conduction band, the localization of electrons in the antibonding states weakens the bond and renders it vulnerable to the electrophilic reactants in the electrolyte. The formation of new bonds with electrophiles stabilizes the reduced state, allowing spontaneous decomposition[32]. Photodecomposition is primarily determined by reaction kinetics, as illustrated by the thermodynamic aspects of photocorrosion in figure 2.6. The photodecomposition of the photoelectrode is significantly influenced by the surface kinetics of the surface redox reaction of interest, and the photoelectrode may be stable under harsh conditions despite thermodynamic predictions of instability. Thus, kinetics can prevent photodecomposition to some extent. The kink sites present on the surface step site are responsible for the formation and decomposition of any crystal, where an atom possesses nearly half the binding energy compared with the same atom situated in the bulk of the crystal. Inhibitors can be used to shield kink sites and reduce the photodecomposition rate. Photodecomposition involves a series of reactions, and there is a rate-determining step that favors the formation of the most active intermediates. The activation energy of the rate-determining step controlled the overall photodecomposition rate. The thermodynamic decomposition potential derived for the overall reaction does not provide any details regarding the energetics of the reaction steps, and the generation of high-energy intermediates is regarded as the rate-determining step. Under such conditions, the redox potential, which corresponds to the rate-determining step, is a better indicator of the photodecomposition reaction. From the above discussion, it is evident that the intermediate steps involved in the photodecomposition process depend on the surface composition and nature of the redox reactions at the interface, and vary significantly with each photoelectrode. Consequently, how photodecomposition begins and how fast it proceeds depend on many factors and cannot be predicted using general principles. The following equations show the generalized indication of a compound with kink sites (MX) and the successive association of the surface with holes and ligands[31]:

$$\mathrm{MX} + \mathrm{h}^+ + \mathrm{L} \rightarrow \mathrm{M}^+_{\mathrm{ad}}\mathrm{L}^{\pm} \tag{2.5}$$

$$\mathrm{M}^+_{\mathrm{ad}}\mathrm{L} + \mathrm{h}^+ + \mathrm{L} \rightarrow [\mathrm{ML}_2]^{(2+)} \tag{2.6}$$

$$\mathrm{X}_{\mathrm{ad}} + \mathrm{X}_{\mathrm{ad}} \rightarrow \mathrm{X}_2 \tag{2.7}$$

$$2\mathrm{MX} + 4\mathrm{h}^+ + 4\mathrm{L} \rightarrow 2[\mathrm{ML}_2]^{(2+)} + \mathrm{X}_2 \tag{2.8}$$

Photodecomposition can be prevented by employing photogenerated minority scavengers, which involve one-electron reactions with no kinetic complications that proceed more rapidly than the photodecomposition reactions. However, this approach cannot be applied to water-splitting reactions, because the solvent itself is oxidized or reduced. The water-splitting reaction is complex and involves a series of intermediate steps similar to the photodecomposition reaction. The kinetics of water splitting is subject to certain kinetic limitations that impede its progress;

thus, it will only protect the photoelectrode when the thermodynamic potential is significantly lower than the potential required for photodecomposition[32].

2.4 Photophysics and Photochemistry of the Semiconductor Surface and Interface

2.4.1 Semiconductor in Equilibrium

Knowledge of the system under equilibrium is indispensable for gaining a comprehensive understanding of any energy-conversion process. In this section, we examine semiconductors in the absence of an electric field, magnetic field, voltage, or irradiation. Notably, under equilibrium conditions, semiconductor properties remain constant over time[33–35]. First discuss about Intrinsic semiconductors, followed by extrinsic semiconductors, are commonly utilized as materials in semiconductor-based photon-assisted CO_2 reduction systems.

Charge Carriers in Semiconductors

The behavior of semiconductors is largely determined by the distribution of charge carriers such as electrons in the conduction band and holes in the valence band. The total density of electrons and holes in a semiconductor is closely related to the density of states and Fermi distribution functions. The relationship between the allowed quantum states and probability of an electron occupying a particular state gives rise to the distribution of electrons in the conduction band, as expressed by the following equation:

$$n(E) = g_c(E) f_F(E) \tag{2.9}$$

The density of quantum states in the conduction band, denoted by g_c, and the Fermi-Dirac probability function, denoted by f_F, can be used to express the total concentration of conduction band electrons through the integration of equation 2.9. Similarly, the hole distribution in the valence band of a semiconductor can be represented in a comparable manner [36, 37].

$$p(E) = g_V(E)[1 - f_F(E)] \tag{2.10}$$

The concentration of holes in the valence band arises from the products of the allowed quantum states in the valence band and probability that the state is not occupied by an electron. These factors determine the distribution of the holes in the valence band. The integration of (Equation 2.10) provides the total concentration of the holes in the valence band. To determine the concentrations of electrons and holes in a semiconductor, it is necessary to establish the precise position of the Fermi energy level (E_F) relative to the conduction band minimum (E_C) and valence band maximum (E_V). The Fermi level represents the electrochemical potential of an electron, and under equilibrium conditions, it is occupied by electrons with a 50% probability. In intrinsic semiconductors, the valence band is completely filled with electrons at absolute zero temperature (T= $0\,\mathrm{K}$), and the Fermi level is situated in the middle of the bandgap if the effective masses of the electrons and holes are equal. As the temperature increases, more electrons are promoted

to the conduction band, leaving electron vacancies in the valence band, which are typically referred to as holes. The occupation of these holes in bonding with electrons from adjacent covalent bonds creates holes in the bond, enabling the holes to move throughout the semiconductor. In intrinsic semiconductors with high purity and no lattice defects, electron and hole concentrations are equal.

The thermal equilibrium concentrations of electrons (n_0) and holes (p_0) can be calculated by integrating equations 2.9, and 2.10 over the ranges of E_C to ∞ and ∞ to E_V [36–39].

$$n_0 = \int_{E_c}^{\infty} g_c(E) f_F(E) dE \tag{2.11}$$

Similarly,

$$p_0 = \int_{-\infty}^{E_v} g_v(E)[1 - f_F(E)] dE \tag{2.12}$$

The solutions to equation 2.11 and 2.12 represent the thermal equilibrium concentrations of electrons and holes, respectively.

$$n_0 = N_C \exp\left[\frac{-(E_C - E_F)}{kT}\right] \tag{2.13}$$

$$p_0 = N_V \exp\left[\frac{-(E_F - E_V)}{kT}\right] \tag{2.14}$$

The terms N_C and N_V represent the effective density of states of the conduction and valence bands, respectively, and are constant at any given temperature for a specific semiconductor material. The Boltzmann constant k at temperature T indicates that a significant change in temperature increases the charge carrier concentration by several orders of magnitude.

$$N_C = 2\left(\frac{2\pi m_n^* kT}{h^2}\right)^{\frac{3}{2}} \tag{2.15}$$

$$N_V = 2\left(\frac{2\pi m_p^* kT}{h^2}\right)^{\frac{3}{2}} \tag{2.16}$$

Here, m_n^* and m_p^* are the effective masses of electrons and holes in the semiconductor lattice, respectively. For an intrinsic semiconductor, the carrier concentrations are equal, meaning that n_i=p_i=p_0. Thus, the product of equations 2.13, and 2.14 provides the carrier concentration of the intrinsic semiconductor.

$${n_i}^2 = N_C N_V \exp\left[\frac{-(E_C - E_V)}{kT}\right] = N_C N_V \exp\left[\frac{-E_g}{kT}\right] \tag{2.17}$$

E_g represents the bandgap energy. This equation demonstrates that the carrier concentration of an intrinsic semiconductor remains constant at a fixed temperature, and is independent of the Fermi level energy. The Fermi level position of an intrinsic semiconductor can be easily obtained from equations 2.13 and 2.14.

$$N_C \exp\left[\frac{-(E_C - E_{Fi})}{kT}\right] = N_V \exp\left[\frac{-(E_{Fi} - E_V)}{kT}\right] \tag{2.18}$$

To solve for E_{Fi}, the Fermi level position of an intrinsic semiconductor, the Fermi level equation is considered as the logarithm of both sides of the equation.

$$E_{Fi} = \frac{1}{2}(E_C + E_V) + \frac{1}{2}kT \ln\left(\frac{N_V}{N_C}\right) \tag{2.19}$$

Equation 2.17 redefines the Fermi level equation in terms of the effective masses of electrons and holes using the definitions of N_V and N_C in.

$$E_{Fi} = E_{midgap} + \frac{3}{4}kT \ln\left(\frac{m_p^*}{m_n^*}\right) \tag{2.20}$$

$$E_{Fi} - E_{midgap} = \frac{3}{4}kT \ln\left(\frac{m_p^*}{m_n^*}\right) \tag{2.21}$$

Equation 2.21 indicates that the relative position of the Fermi level in an intrinsic semiconductor depends on the effective masses of the charge carriers, which are directly related to the density of states. If the effective masses are the same, the Fermi level should be at the bandgap center. In n-type semiconductors, the majority of charge carriers are electrons, and the effective masses of electrons are much greater than those of holes. Therefore, the Fermi level position is above the intrinsic Fermi level $E_F > E_{Fi}$. When the majority charge carrier is a hole, the p-type semiconductor and Fermi level are below the intrinsic Fermi level $E_F < E_{Fi}$.

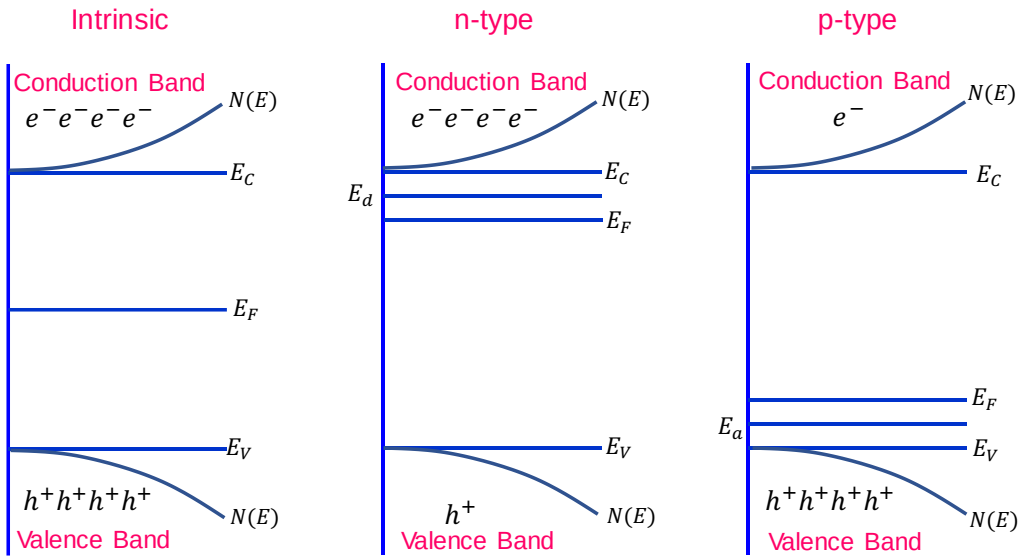

Figure 2.7: Illustrate the depiction of semiconductors in a state of thermal equilibrium, including (a) intrinsic, (b) n-type, and (c) p-type semiconductors. This information is taken from the work of Narayanan et al. [40]. *Reproduced from Narayanan, H.; Viswanathan, B.; Krishnamurthy, K. R.; Nair, H., in Photocatalytic Nanomaterials for Environmental Applications; Material Research Forum: 2018, pp 175–210. ©2018 by the authors.*

In n-type semiconductors, an additional donor energy level, E_d, is present near the conduction-band minimum. The energy required to excite an electron

from the donor level to the conduction band, referred to as the donor energy, was significantly lower than the bandgap excitation energy. The excitation of electrons from the donor level results in the formation of positively charged species at the donor sites, which are known as donor impurity atoms. These impurity atoms produced electrons in the conduction band without creating holes in the valence band.

In contrast, p-type semiconductors contain additional impurity atoms that create energy levels that are close to the valence band. A small amount of thermal energy is required to excite the valence electrons to the acceptor energy level E_a. The electrons in the acceptor energy level do not possess sufficient energy to move into the conduction band; instead, they occupy the unoccupied orbitals of acceptor impurity atoms. Consequently, the impurity atom becomes a negatively charged species fixed in the crystal and generates holes in the valence band without producing electrons in the conduction band.

Intrinsic semiconductors can be converted into n- or p-type semiconductors by introducing small amounts of donor or acceptor impurity atoms; these are collectively referred to as extrinsic semiconductors.

For an n-type semiconductor, equation 2.13 can be rewritten as [36–39],

$$n_0 = N_C \; exp \left[\frac{-(E_C - E_{Fi}) + (E_F - E_{Fi})}{kT}\right] \tag{2.22}$$

$$n_0 = N_C \exp\left[\frac{-(E_C - E_{Fi})}{kT}\right] \exp\left[\frac{(E_F - E_{Fi})}{kT}\right] \tag{2.23}$$

It is apparent from equations 2.13 and 2.15 that,

$$n_i = N_C \exp\left[\frac{-(E_C - E_{Fi})}{kT}\right] \tag{2.24}$$

By substituting the value of "n_i" in equation 2.23,

$$n_0 = n_i exp\left[\frac{(E_F - E_{Fi})}{kT}\right] \tag{2.25}$$

Likewise, we can express,

$$p_0 = p_i \exp\left[\frac{(E_F - E_{Fi})}{kT}\right] \tag{2.26}$$

The product of the n_0 and p_0 concentrations of the extrinsic semiconductor is comparable to that of the intrinsic semiconductor, as discussed in equation 2.15. At thermal equilibrium, as in previous instances, the product of the charge-carrier concentration remained constant at a specific temperature.

$$n_0 p_0 = n_i^2 \tag{2.27}$$

Although this equation appears straightforward, it is one of the fundamental principles in semiconductor physics at thermal equilibrium and is derived using the Boltzmann approximation. If the Boltzmann approximation is not applicable, the

equilibrium concentrations of electrons and holes can be determined by considering the Fermi-Dirac integral[36–39].

$$n_o = \frac{4\pi}{h^2}\left(2m_n^* kT\right)^{\frac{3}{2}} \int_0^\infty \frac{\eta^{\frac{1}{2}} d\eta}{1+\exp\left(\eta-\eta_F\right)}. \tag{2.28}$$

$$p_o = \frac{4\pi}{h^2}\left(2m_p^* kT\right)^{\frac{3}{2}} \int_0^\infty \frac{\eta'^{\frac{1}{2}} d\eta'}{1+\exp\left(\eta'-\eta'_F\right)} \tag{2.29}$$

This equation pertains to the Fermi-Dirac integral, which is an integral function of great significance in semiconductor physics at thermal equilibrium. In this equation, η_F and η'_F are defined as $\frac{(E_F-E_C)}{kT}$ and $\frac{(E_V-E_F)}{kT}$, respectively, and η and η' are represented by $\frac{(E-E_C)}{kT}$ and $\frac{(E_V-E)}{kT}$, respectively. It is important to note that if the values of η_F or η'_F are positive, the Fermi level is situated in the conduction or valence band, respectively, and such semiconductors are referred to as degenerate semiconductors.

The degeneracy factor, which is related to the probability density of electrons and holes in the donor and acceptor levels, is a concept described by the Pauli exclusion principle[36–39]. The degeneracy factor is represented mathematically by Equation 2.30, and 2.31.

$$n_d = \frac{N_d}{1+\frac{1}{g}\exp\left(\frac{E_d-E_F}{kT}\right)} \tag{2.30}$$

$$p_a = \frac{N_a}{1+\frac{1}{g}\exp\left(\frac{E_F-E_a}{kT}\right)} \tag{2.31}$$

The degeneracy factor g is directly related to the probability density of electrons and holes in the donor and acceptor levels. This relationship can be effectively represented by $n_d = N_d - N_d^+$ and $p_a = N_a - N_a^+$. Electrons and holes are present in the conduction and valence bands at room temperature in materials containing donor or acceptor levels, such as n- or p-type semiconductors, resulting in complete ionization of charge carriers. However, at 0 K, the electrons and holes are frozen at their respective energy levels, a phenomenon known as complete freeze-out.

Under conditions of thermal equilibrium, the semiconductor is electrically neutral, which is the principle used to derive the thermal equilibrium concentration of the charge carriers as a function of the impurity doping concentration. Compensated semiconductors contain both donor and acceptor impurities, which can spill into n- or p-type materials, resulting in the formation of n-($N_d > N_a$) or p-type ($N_d < N_a$)compensated semiconductors. If the carrier concentrations are equal, then the compensated semiconductor behaves as an intrinsic semiconductor.

The equilibrium concentration of charge carriers in a compensated semiconductor can be expressed using the following quadratic equation:

$$n_0 = \frac{(N_d-N_a)}{2} + \sqrt{\left(\frac{(N_d-N_a)}{2}\right)^2 + n_i^2} \tag{2.32}$$

$$p_0 = \frac{(N_a-N_d)}{2} + \sqrt{\left(\frac{(N_a-N_d)}{2}\right)^2 + n_i^2} \tag{2.33}$$

2.4.2 Importance of the Fermi Level

The equilibrium concentration of charge carriers in a semiconductor is described by equation 2.13 and 2.14, which can be expressed as logarithmic functions, as follows:

$$E_c - E_F = kT \ln\left(\frac{N_c}{n_0}\right) \tag{2.34}$$

$$E_F - E_V = kTln\left(\frac{N_V}{p_0}\right) \tag{2.35}$$

For n- and p-type semiconductors, $n_0 = N_d$ and $p_0 = N_a$ respectively. So that,

$$E_C - E_F = kT \ln\left(\frac{N_C}{N_d}\right) \tag{2.36}$$

$$E_F - E_V = kTln\left(\frac{N_V}{N_a}\right) \tag{2.37}$$

For n-type semiconductors, the equilibrium concentration of electrons (n_0) is equal to that of the donor impurities (N_d), whereas for p-type semiconductors, the equilibrium concentration of holes (p_0)) is equal to that of the acceptor impurities (N_a). The above equations illustrate the logarithmic relationship between the distances of the band-edge positions, Fermi level, and charge-carrier concentration. Increasing the concentration of donors or acceptors causes the Fermi level to move toward the band edges, thereby increasing the concentration of carriers in the respective bands.

For compensated semiconductors, the values of N_d and N_a in equation 2.34 can be replaced by N_d - N_a and N_a - N_d. For intrinsic semiconductors, slight modifications are required in equation 2.36, and 2.37 and can be expressed as

$$E_F - E_{Fi} = kT\ ln\left(\frac{n_0}{n_i}\right) \tag{2.38}$$

$$E_{Fi} - E_F = kTln\left(\frac{p_0}{n_i}\right) \tag{2.39}$$

It is important to note that the Fermi level (E_F) is above the intrinsic Fermi level (E_{Fi}) for n-type semiconductors and below it for p-type semiconductors. The concentration of charge carriers in any semiconductor material is temperature dependent, and temperature changes affect the position of the Fermi level. As the temperature increased, the carrier concentration increased and the Fermi level shifted towards the intrinsic Fermi level. In other words, extrinsic semiconductors exhibit behavior at higher temperatures, similar to that of intrinsic semiconductors.

When two electronic systems come in contact, the Fermi levels of both systems tend to equilibrate. For instance, in the p-n junction shown in Figure 2.8, the energy states are filled with E_{F1} and E_{F2} in the first and second semiconductors, respectively. When these two materials come in contact, the electrons in the system occupy the lowest energy level, resulting in electron transfer from the system with a higher electrochemical potential to that with a lower potential (or from that with a lower work function to that with a higher work function). This process creates a space-charge layer, which is known as Fermi-level equilibration.

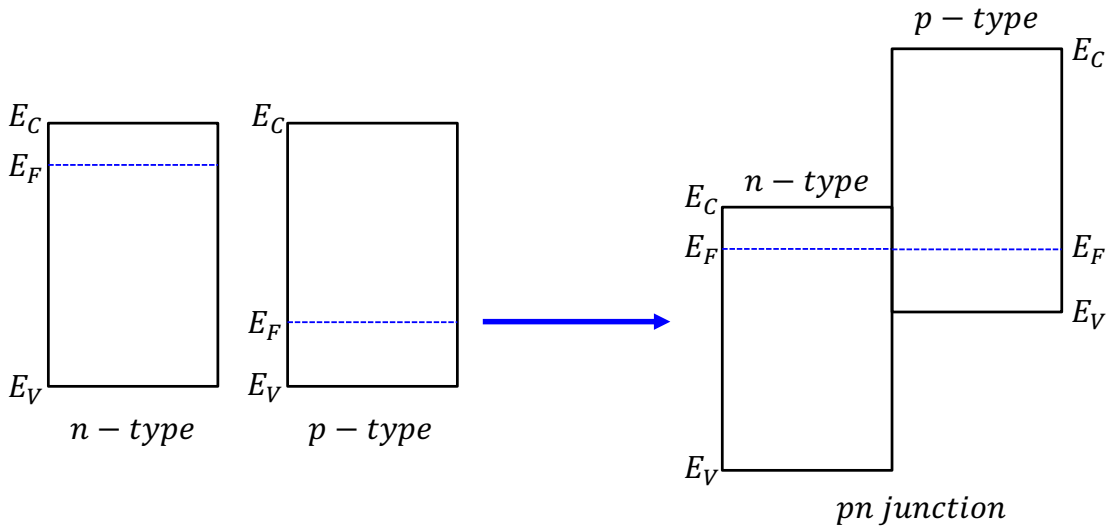

Figure 2.8: Graphical representation of the energy band structure at the p-n junction before and after contact [40]. *Reproduced from Narayanan, H.; Viswanathan, B.; Krishnamurthy, K. R.; Nair, H., in Photocatalytic Nanomaterials for Environmental Applications; Material Research Forum: 2018, pp 175–210. ©2018 by the authors.*

However, not all electron transfers across semiconductor heterojunctions are smooth, as shown in figure 2.8. Various heterojunction formulations exist, and the nature of the electron transfer across each is different. If we irradiate the heterojunction in figure 2.8 with light energy greater than the bandgap, electrons are transferred from the second system to the first (from the one with a higher work function to the one with a lower work function) and holes move in the opposite direction[41]. It is worth noting that the charge carrier transfer across the heterojunction was not smooth, as described in the situation mentioned earlier. There are more than 20 heterojunction formulations, and the nature of the electron transfer differs for each formulation[42].

Furthermore, the Fermi level reaches equilibrium when a semiconductor is in direct contact with a metal[43]. Similarly, it is important to note that when a semiconductor material comes into contact with an electrolyte, the Fermi levels of both equilibrate, resulting in the formation of a space charge layer at the interface. This equilibration causes a change in the energy levels within the semiconductor, leading to an energy difference between the surface interface and bulk semiconductor[44]. This energy difference is referred to as band bending and is dependent on the type of semiconductor and the electrolyte used. It is crucial to understand that the term 'band bending' refers to the interface being at a higher or lower energy level than the bulk and not an actual bending of the energy levels between the surface and bulk[45, 46]. Further details on this topic are discussed in the subsequent sections.

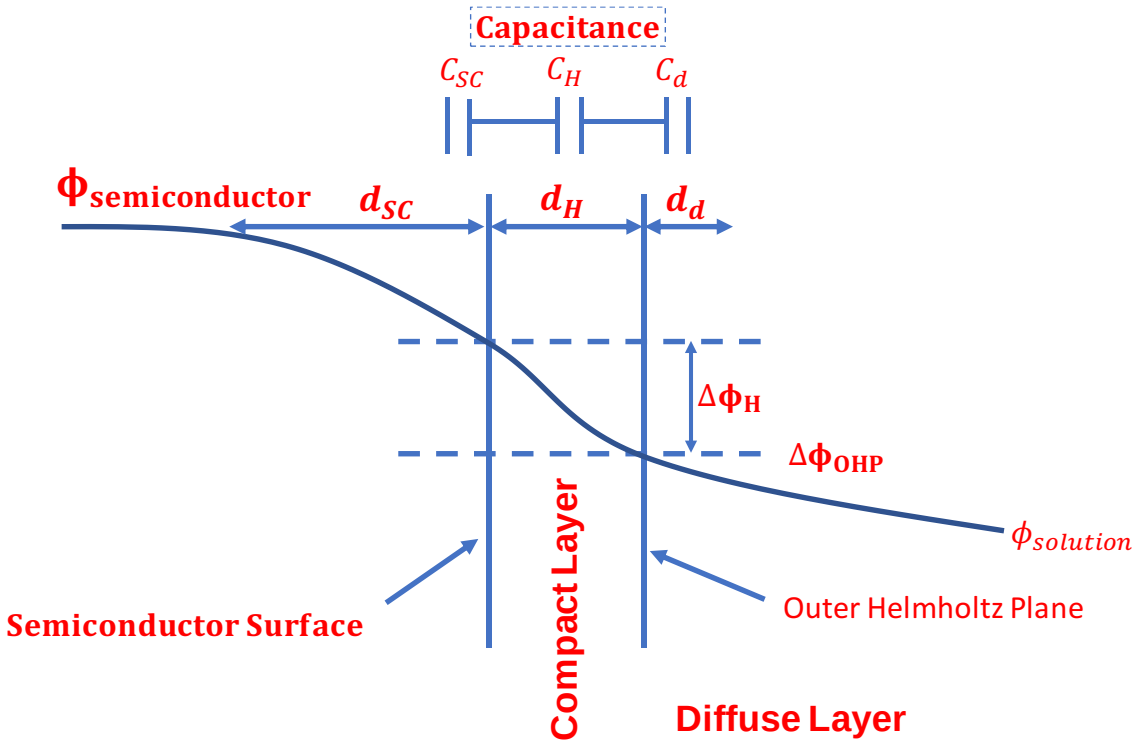

Figure 2.9: Electrical double layer at the semiconductor-electrolyte interface [40]. *Reproduced from Narayanan, H.; Viswanathan, B.; Krishnamurthy, K. R.; Nair, H., in Photocatalytic Nanomaterials for Environmental Applications; Material Research Forum: 2018, pp 175–210. ©2018 by the authors.*

2.4.3 Electrical Double Layer at Semiconductor-Electrolyte Interfaces

Extensive literature and books that have explored the semiconductor/electrolyte interface have provided the following discussion[47–53], which has adopted the concepts presented in Sato's book[54]. The interface between the semiconductor and electrolyte comprises three layers, as depicted in figure 2.9: (a) a space-charge layer on the semiconductor side, with a thickness ranging from $10\,\mathrm{nm}$ to $100\,\mathrm{nm}$; (b) a compact layer at the interface, measuring $0.4\,\mathrm{nm}$ to $0.6\,\mathrm{nm}$ in thickness; and (c) a diffuse layer on the solution side, with a thickness of $1\,\mathrm{nm}$ to $10\,\mathrm{nm}$.

To represent the electroneutrality across the semiconductor/electrolyte interface, the following charges can be considered: the charge of the space charge layer, denoted as σ_{SC}; the charge of the surface states, represented by σ_{SS}; the charge of the adsorbed layers present in the compact layer, denoted as σ_{ad}; and the excess ionic charge of hydrated ions in the diffuse layer, represented by σ_S. This can be mathematically expressed as:

$$\sigma_{SC} + \sigma_{SS} + \sigma_{ad} + \sigma_S = 0 \tag{2.40}$$

The following equation demonstrates that the total charge at the interface must be zero to preserve the electroneutrality:

The total potential across the semiconductor interface, denoted by $\Delta\phi$, can be represented by the combined effect of the potentials generated by individual layers at the interface. These layers include the diffuse layer situated within the solution

($\Delta\phi_d$), the potential across the compact layer situated in the outer Helmholtz plane ($\Delta\phi_H$), and the potential across the interior space charge layer of the semiconductor ($\Delta\phi_{SC}$).

$$\Delta\phi = \Delta\phi_d + \Delta\phi_H + \Delta\phi_{SC} \tag{2.41}$$

The relationship between the thickness of the space charge and diffuse layers in a semiconductor, total concentration of mobile charge carriers (denoted as n_i), and concentration of ions in the aqueous solution is directly proportional to the Debye length (L_D).

$$L_D = \sqrt{\frac{\varepsilon kT}{e^2 \sum n_i z_i^2}} \tag{2.42}$$

The relationship between the thickness of the space charge and diffuse layers and the total concentration of mobile charge carriers in a semiconductor n_i, as well as the ions in an aqueous solution, can be calculated using the Debye length (L_D). The Debye length is typically approximately 100 nm for semiconductors with an impurity concentration of 10^{-15} cm^{-3} and $10\,\mathrm{nm}$ in a $0.1\,\mathrm{M}$ ionic solution. Memming derived a quantitative relationship between the thickness of the space-charge layer and the Debye length in 1983, as shown in equation 2.43 [48].

$$d_{SC} = 2 \times L_D \sqrt{\left(\frac{e\Delta\phi_{SC}}{kT}\right) - 1} \tag{2.43}$$

The overall differential capacitance C at the semiconductor-electrolyte interface can be calculated using the equation for a series plate capacitor, which includes C_{SC}, C_H, and C_d, representing the capacitance of the space charge and the compact and diffuse layers, respectively. Given that the total capacitance of a series-connected system is determined by the smallest capacitance value, the capacitance of the semiconductor interface is approximately equal to that of the space charge layer.

$$\frac{1}{C} = \frac{1}{C_{SC}} + \frac{1}{C_H} + \frac{1}{C_d} \tag{2.44}$$

The expression for the total potential across the semiconductor interface with respect to the Debye length is represented by equation 2.45 as follows:

$$\Delta\phi = E_{SC}\dot{L}_{D,SC} + E_H\dot{d}_H + E_S\dot{L}_{D,S} \tag{2.45}$$

If the surface states and adsorbed layers are devoid of charge (σ_{SS} and σ_{ad}), then the electrostatic equation can be expressed as follows:

$$E_{SC}\varepsilon_{SC} = E_H\varepsilon_H = E_S\varepsilon_S \tag{2.46}$$

Therefore, the potential distribution across the semiconductor/electrolyte interface can be expressed as total potential distribution.

$$\frac{\delta\Delta\phi_H}{\delta\Delta\phi_{SC}} = \frac{E_H d_H}{E_{SC} L_{D,SC}} \tag{2.47}$$

By substituting $E_H = {}^{E_{SC}\varepsilon_{SC}}/_{\varepsilon_H}$ into equation 2.47, the equation can be modified as follows:

$$\frac{\delta\Delta\phi_H}{\delta\Delta\phi_{SC}} = \frac{\varepsilon_{SC} d_H}{L_{D,SC}\ \varepsilon_H} \tag{2.48}$$

Similarly, it is possible to calculate the total potential across both the space charge and diffuse layers.

$$\frac{\delta\Delta\phi_d}{\delta\Delta\phi_{SC}} = \frac{L_{D,S}\,\varepsilon_{SC}}{L_{D,SC}\,\varepsilon_S} \tag{2.49}$$

The equations reveal that the primary site of potential change is the space charge layer, whereas the potentials of the other two layers remain constant. This semiconductor property is referred to as *band-edge pinning*, where the band-edge potentials of the semiconductor at the interface are fixed, resulting in a fixed potential across the compact layer. However, the aforementioned equations assume the absence of surface-state charge. If a surface state charge is present, the electrostatic equation can be expressed as in equation 2.50.

$$E_H\varepsilon_H = E_{SC}\varepsilon_{SC} + \sigma_{SS} \cong \sigma_{SS} \tag{2.50}$$

If the surface state charge value, that is, σ_{SS}, is relatively elevated, then the potential difference across the compact layer, that is, $\Delta\phi\_H$, can be approximated as

$$\Delta\phi_H = E_H d_H = \frac{\sigma_{SS} d_H}{\varepsilon_H} \tag{2.51}$$

Band Edge Pinning and Fermi Level Pinning

Band-edge pinning can be observed at the junction of a semiconductor when the Fermi level lies between the bandgap and away from the surface states and higher-density band-edge positions. During this phenomenon, the potential across the space charge and compact layers remains constant. In contrast, Fermi-level pinning occurs when the Fermi level of the semiconductor approaches the surface states or higher-density band-edge positions at the interface. In this case, the potential across the space-charge layer remains unchanged, but a significant change occurs in the compact layer[55, 56]. When Fermi-level pinning occurs, the semiconductor interface exhibits metallic behavior, a phenomenon referred to as quasi-metallization. Figures 2.10 and 2.11 show schematic representations of both the phenomena.

Space Charge Layers

When in contact with an electrolyte solution, semiconductors undergo an interfacial acid-base reaction that generates a surface charge, which significantly influences the energy levels near the semiconductor-electrolyte interface, resulting in band bending. The point at which the charges of the acidic and basic sites at the interface are equal is referred to as the Isoelectric Point (IEP) or Point of Zero Charge (PZC). At this point, the semiconductor exhibits flat-band conditions. When the pH is above the isoelectric point, the interface becomes negatively charged, causing an excess negative charge that repels electrons from the bulk of the semiconductor and the interface to be at a higher energy level than that of the bulk, leading to upward band bending. Conversely, a positive surface charge leads to a downward band bending. The maximum energy difference between the interface and bulk of the semiconductor is approximately $0.5\,\mathrm{V}$, which transports electrons and holes in opposite directions within the interfacial zone and reduces recombination. The

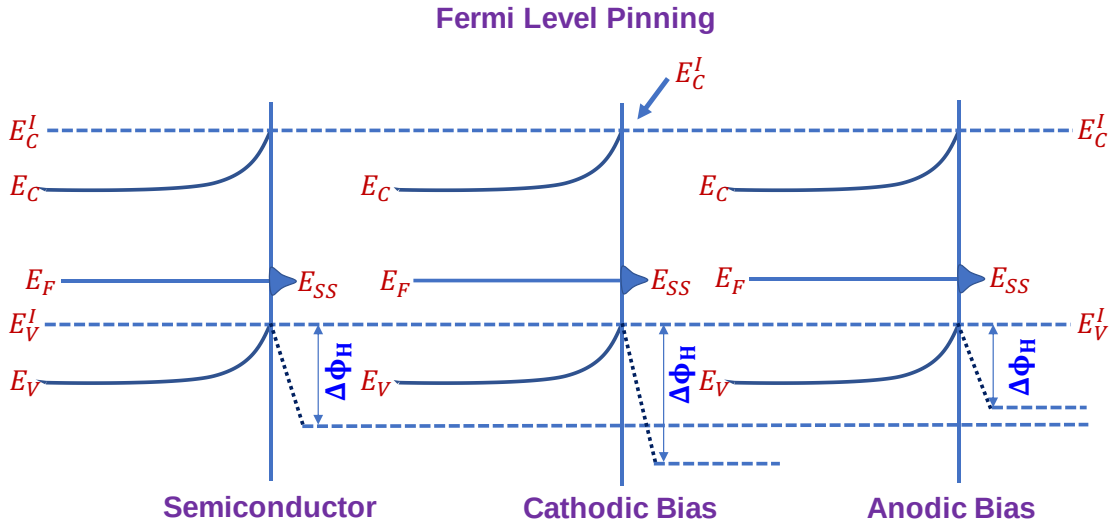

Figure 2.10: Fermi level pinning at the semiconductor interface under different conditions [40]. *Reproduced from Narayanan, H.; Viswanathan, B.; Krishnamurthy, K. R.; Nair, H., in Photocatalytic Nanomaterials for Environmental Applications; Material Research Forum: 2018, pp 175–210. ©2018 by the authors.*

region where band bending occurs is collectively referred to as the space charge layer.

The thickness of the space charge layer is affected by the magnitude of the interfacial charges, dielectric constant of the materials, and charge carrier concentration, and is typically on the order of $100\,\mathrm{nm}$ to $1\,\mu\mathrm{m}$. Four different types of space-charge layers exist: (a) accumulation layer, (b) depletion layer, (c) inversion layer, and (d) deep depletion layer (Figure 2.12).

The differential capacitance of the space charge region in an intrinsic semiconductor, denoted C_{SC}, can be expressed as follows:

$$C_{SC} = \frac{\varepsilon}{L_D} \cosh\left(\frac{e\Delta\phi_{SC}}{2kT}\right) \tag{2.52}$$

where L_D is the Debye length (Equation 2.42), n_i is the concentration of the charge carrier, and $\Delta\phi_{SC}$ is the potential across the space-charge layer. The capacitance of the space charge layer in an n- or p-type semiconductor can be expressed in the general form as follows:

$$C_{SC} = \frac{\varepsilon}{L_{D_{eff}}} \left(\frac{1 - \exp\left(\frac{\pm e\Delta\phi_{SC}}{kT}\right)}{\sqrt{\left|1 + \frac{\pm e\Delta\phi_{SC}}{kT} - \exp\left(\frac{\pm e\Delta\phi_{SC}}{kT}\right)\right|}} \right) \tag{2.53}$$

The effective Debye length, denoted by $L_{D_{eff}}$, is defined as $\sqrt{\frac{\varepsilon kT}{2Ne^2}}$, where N represents the concentration of the donor or acceptor, and the sign $\pm$ is considered positive for a p-type semiconductor and negative for an n-type semiconductor. This equation represents a general expression for the capacitance of the space charge layer in a semiconductor, and can be utilized to derive the specific capacitances for all four types of space charge layer classifications.

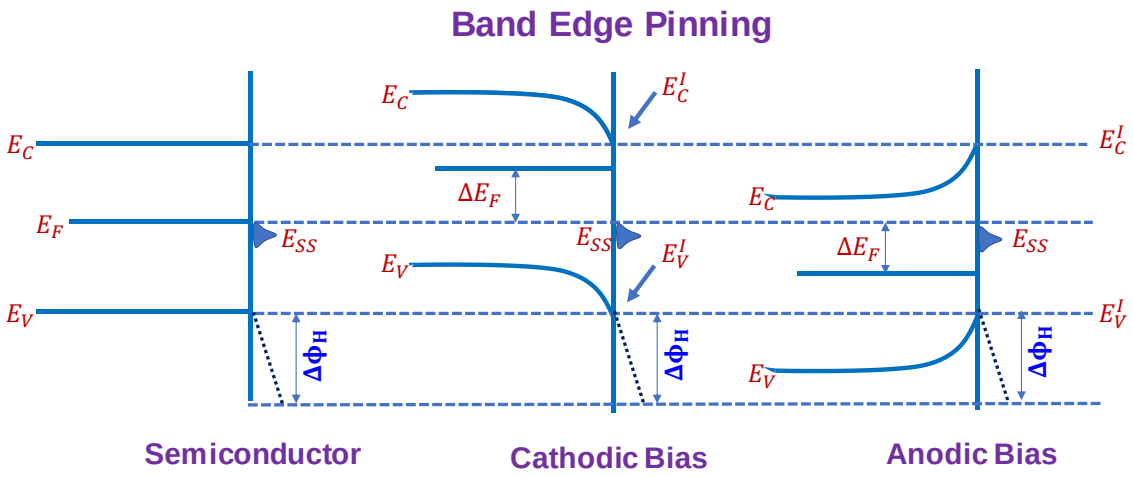

Figure 2.11: Band-edge pinning of semiconductors under different conditions [40]. *Reproduced from Narayanan, H.; Viswanathan, B.; Krishnamurthy, K. R.; Nair, H., in Photocatalytic Nanomaterials for Environmental Applications; Material Research Forum: 2018, pp 175–210. ©2018 by the authors.*

Accumulation Layer

The role of the accumulation layer is to convey the charge carriers predominantly to the interface. The capacitance associated with the accumulation layer can be determined using Boltzmann distribution, as shown in the preceding equation. It is presumed that the Fermi level is distant from the band edge positions. Nonetheless, when the Fermi level is in close proximity to the band edge position, a phenomenon referred to as Fermi level pinning occurs, leading to insensitivity of the capacitance C_{SC} to the potential of the space charge layer.

$$C_{SC} = \frac{\varepsilon}{L_{D_{eff}}} \exp\left(\frac{|e\Delta\phi_{SC}|}{kT} - 1\right) \approx \frac{\varepsilon}{2L_{D_{eff}}} \exp\left(\frac{|e\Delta\phi_{SC}|}{kT}\right) \tag{2.54}$$

The criteria for the potential difference across the space charge layer ($\Delta\phi_{SC}$) in n-type semiconductors are as follows: the absolute value of $e\Delta\phi_{SC}$ must be greater than three times the thermal energy (kT) and $\Delta\phi_{SC}$ must be negative. For p-type semiconductors, the conditions are opposite: $\Delta\phi_{SC}$ must be positive.

Depletion Layer

The formation of a depletion region occurs when the majority charge carriers are depleted from the semiconductor/electrolyte interface and the minority charge carriers are transported to the interface[57]. In the context of the capacitance equation, for an n-type semiconductor, the condition $|e\Delta\phi_{SC}| > 3kT$ and $\Delta\phi_{SC}$>0 must be satisfied, whereas for a p-type semiconductor, $\Delta\phi_{SC}$<0 and $|e\Delta\phi_{SC}| > 3kT$ hold true.

$$C_{SC} = \frac{\varepsilon}{2L_{D_{eff}}} \frac{1}{\sqrt{\left|\frac{e\Delta\phi_{SC}}{kT}\right| - 1}} \tag{2.55}$$

$$\frac{1}{C_{SC}^2} = \left(\frac{2L_{D,eff}}{\varepsilon}\right)^2 \left(\frac{\Delta\phi_{SC}}{kT} - 1\right) = \left(\frac{2L_{D,eff}}{\varepsilon}\right)^2 \frac{e}{kT}\left(E - E_{fb} - \frac{kT}{e}\right) \tag{2.56}$$

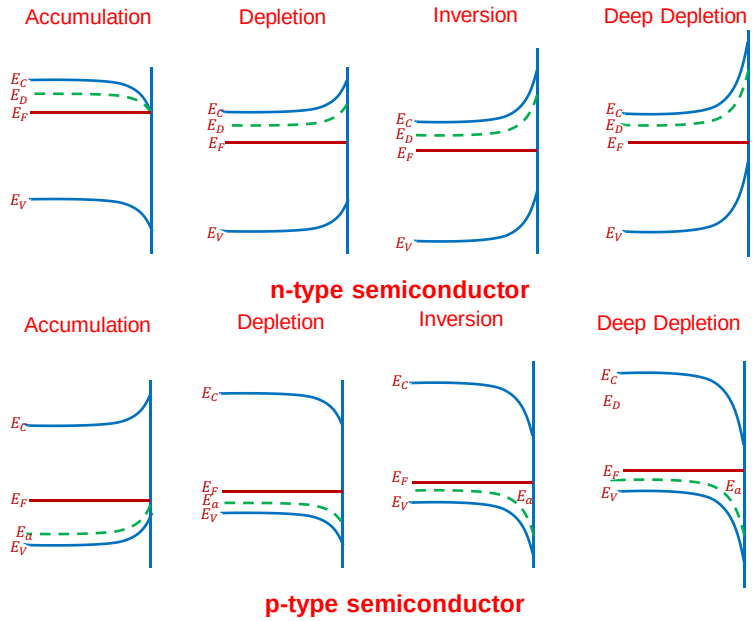

Figure 2.12: Different types of space charge layers in n- and p-type semiconductors [40]. *Reproduced from Narayanan, H.; Viswanathan, B.; Krishnamurthy, K. R.; Nair, H., in Photocatalytic Nanomaterials for Environmental Applications; Material Research Forum: 2018, pp 175–210. ©2018 by the authors.*

The Mott-Schottky equation describes the fundamental relationship between the capacitance of the space-charge region and the applied potential in a semiconductor. In this equation, E represents the potential of the semiconductor at the interface and E_{fb} signifies the flat-band potential. By plotting $\frac{1}{C_{SC}^2}$ against E, the Mott-Schottky plot can be used to determine the flat-band potential of the semiconductor and the effective Debye length. In the Mott-Schottky plot, the valence band edge position is obtained for n-type semiconductors, whereas the conduction band edge position is obtained for p-type semiconductors. The energy barrier associated with the depletion region is known as Schottky barrier[58].

Inversion Layer

When the Fermi level at the interface approaches the band-edge position associated with minority charge carriers, it leads to the formation of an inversion layer, which increases the potential change in the depletion region. This inversion layer results in the accumulation of minority charge carriers at the interface and can cause a reversal of the interfacial properties from n-type to p-type or p-type to n-type. Consequently, this type of space-charge layer is referred to as an inversion layer. The capacitance equation for the inversion layer was comparable to that of the accumulation layers.

$$C_{SC} = \frac{\varepsilon}{2L_{D_{min}}} \exp\left(\frac{|e\Delta\phi_{SC}|}{2kT}\right) \tag{2.57}$$

The Debye length of the minority charge carriers is represented by the formula $L_{D_{min}} = \sqrt{\frac{\varepsilon k_B T}{2n_{min}e^2}}$, where n_{min} denotes the concentration of minority charge carriers. In n- and p-type semiconductors, $\Delta\phi_{SC} > 0$ and $\Delta\phi_{SC} < 0$, respectively. As

the potential $\Delta\phi_{SC}$ increased, Fermi-level pinning occurred in the inversion layer, resulting in a constant band-edge position and capacitance.

Deep Depletion Layer

Deep depletion is a characteristic of large-bandgap semiconductors in which a space charge layer is formed that extends beyond the depletion layer. This layer is characterized by the consumption of minority charge carriers at a faster rate than their generation, resulting in the formation of an insulating layer at the interface. The capacitance of the deep depletion layer can be determined using the Mott-Schottky relationship.

Compact Layer

The hydroxylation process of the semiconductor results in the formation of acid and base sites on its surface, which attract other ions to form a compact layer at the interface of the semiconductor. This process creates a positive charge on the semiconductor surface in acidic solutions and negative charge in basic solutions. The potential difference across the compact layer is denoted as $\Delta\phi_H$.

$$\Delta\phi_H = Constant + \frac{kT}{e}\ln\left[H^+_{aq}\right] = Constant - 2.3\frac{kT}{e}(\mathrm{pH}) \tag{2.58}$$

The present equation expresses the linear correlation between the pH of the solution and the potential across the compact layer. The potential of the compact layer, denoted by $\Delta\phi_H$, comprises the interfacial potential, $\Delta\phi_\sigma$, which is derived from the interfacial charge, (σ_H), and the dipole potential, $\Delta\phi_{dipole}$, produced by the interfacial dipole.

$$\Delta\phi_H = \Delta\phi_\sigma + \Delta\phi_{dipole} \tag{2.59}$$

The point at which the interfacial charge, denoted by σ_H, becomes zero is referred to as the point of zero charge (PZC) or isoelectric point (IEP) of the semiconductor. This concept can be mathematically represented using equation 2.58, as expressed below.

$$\Delta\phi_H = \Delta\phi_{dipole} - 2.3\frac{kT}{e}(\mathrm{pH} - \mathrm{pH_{IEP}}) \tag{2.60}$$

$$\Delta\phi_H = d\mathrm{pH} \times 59\ \mathrm{mV/pH} \tag{2.61}$$

The alteration of one pH unit was accompanied by a modification of 59 mV across the compact layer. By reorganizing the electroneutrality equation at the interface involving the interfacial hydroxyl charge (σ_H), the following equation was obtained:

$$\sigma_{SC} + \sigma_{SS} + \sigma_H + \sigma_{ad} + \sigma_S = 0 \tag{2.62}$$

When the semiconductor is in its flat-band condition, with σ_{SC} equal to zero, the equation is reduced to the following simplified form:

$$\sigma_{SS} + \sigma_H + \sigma_{ad} + \sigma_S = 0 \tag{2.63}$$

In conventional semiconductors, it is often assumed that the surface state charges (σ_{SS}) and adsorption charges (σ_{ad}) are either negligible or constant. Under these conditions, the flat-band potential was determined using the following equation:

$$E_{FB} = E_{FB,IEP} - 2.3\frac{kT}{e}(pH - pH_{IEP}) \tag{2.64}$$

The aforementioned equation establishes that the flat-band potential at the point of zero charge (PZC) or isoelectric point (IEP) is represented by $E_{FB,IEP}$. This finding also signifies that the conduction band position shifts towards more negative values at the rate of $59\,\mathrm{mV}$/pH as the solution pH increases. In many simple and compound semiconductors, the flat-band potential has a linear relationship with solution pH. However, there are exceptions, such as in the case of WSe_2, where the flat-band potential is not influenced by pH, but rather depends on the concentration of hydrated selenide ions, known as the potential-determining ion. Commonly, adsorbed hydroxylated groups (hydrated protons and hydroxyl groups) serve as potential-determining ions, giving the flat-band potential a linear dependence on the pH. Nevertheless, in metal chalcogenides, including metal sulfides, selenides, and tellurides, the flat-band potential remains constant with a change in the pH of the solution because the concentration of hydrated chalcogenides acts as a potential-determining ion.

2.4.4 Semiconductor in Non-Equilibrium

G. N. Lewis and M. Randall postulated that the operation of a steam engine is not attributed to coal itself, but rather to its combustion[59]. The fundamental principle is that alterations within a system can affect other interconnected systems. A system that is significantly distant from its equilibrium state is typically selected to utilize its processes to perform productive work. Consequently, by leveraging the processes of a perturbed semiconductor at equilibrium, it is possible to generate useful energy, carry out redox reactions, and produce electricity in solar cells.

Charge Carrier Recombination Mechanisms

When a semiconductor is exposed to threshold light, it generates electrons and holes in the conduction and valence bands, respectively, and disrupts thermal equilibrium. Consequently, there is an excess of charge carriers in the respective bands, which contradicts equation 2.27.

$$np > n_i^2 \tag{2.65}$$

Here, n and p represent the non-equilibrium excess concentrations of the electrons and holes, respectively. Upon recombination, the electrons and holes return to a state of thermal equilibrium. The recombination of charge carriers is advantageous for photocatalysts because it prevents the buildup of charges in a particular band. In materials with direct bandgaps, the valence and conduction bands are vertically aligned, resulting in a high absorption coefficient, because only the threshold photon energy is required to excite an electron from the valence band to the conduction band. In contrast, in materials with indirect bandgaps, extra energy from phonons is required in addition to the photon energy for excitation, because the bands are not vertically aligned. Similarly, direct recombination is spontaneous in materials with direct bandgaps but not in materials with indirect bandgaps, such as crystalline silicon. The Auger recombination mechanism is more prevalent than the radiative recombination mechanism in these materials. Various recombination processes depend on the semiconductor properties, as discussed in this section[37, 60].

Direct Recombination

Radiative generation and recombination mechanisms are primarily observed in direct-bandgap materials. This mechanism requires bandgap energy to produce excitons that subsequently recombine and emit equal amounts of energy. At the equilibrium temperature, the product of the excess carrier concentrations of electrons (n) and holes (p) is equivalent to the squared intrinsic carrier concentration (n_i^2). Some bonds break at temperatures above absolute zero, and electron-hole pairs are generated at a rate of $G_{thermal}$ or G_{th}. In other words, the rates of recombination ($R_{thermal}$ or R_{th}) and generation are equal at the thermal equilibrium. Consequently, at thermal equilibrium, the recombination rate was directly proportional to the charge-carrier concentration.

$$R_{th} = G_{th} \tag{2.66}$$

$$R_{th} = \beta n_0 p_0 \tag{2.67}$$

Under nonequilibrium conditions, the equivalent equation can be expressed as follows: β represents the proportionality constant.

$$R* = \beta np \tag{2.68}$$

The total recombination rate can be expressed as a function of the equilibrium concentration (n_0, p_0) and excess carrier concentration $(\Delta n = n - n_0, \Delta p = p - p_0)$.

$$R^* = \beta np = \beta(n_0 + \Delta n)(p_0 + \Delta p) \tag{2.69}$$

The production rate of excitons can be represented as the aggregate of the generation rate that occurs at thermal equilibrium (G_{th}) and the generation rate that arises in non-equilibrium settings (G_L).

$$G = G_{th} + G_L \tag{2.70}$$

Under steady-state conditions, the rates of synthesis and reorganization were balanced.

$$G_L = R^* - G_{th} = \beta\left(np - n_0 p_0\right) = R_d \tag{2.71}$$

The net radiative recombination rate, denoted by R_d, for n-type semiconductors can be expressed as follows when the conditions Δn « n and p « n are satisfied:

$$R_d = \beta n_0 (p - p_0) = \frac{p - p_0}{\tau_p} \tag{2.72}$$

The symbol τ_p denotes the lifespan of minority charge carriers, specifically, holes. The excess charge carrier concentration can be expressed as the product of the generation rate and the lifespan of the minority charge carriers.

$$p - p_0 = G_L \tau_p \tag{2.73}$$

If no excess charge carriers are present in the semiconductor, then the net recombination rate, denoted by R_d, is equal to zero. When the irradiation process is

discontinued, the rate of charge-carrier generation is no longer present, and the concentration of excess charge carriers can be represented as follows:

$$\frac{dp}{dt} = -\frac{p(t) - p_0}{\tau_p} \tag{2.74}$$

The above equation can be solved to obtain the following:

$$p(t) = p_0 + G_L \tau_p exp(-1/\tau_p) \tag{2.75}$$

The lifetime of the minority charge carriers is defined as a time constant that represents the exponential decay of the excess carrier concentration when the generation rate of charge carriers is zero. This definition provides a clear understanding of the lifetime of minority charge carriers. For p-type semiconductors, where Δp $\ll$ p and n $\ll$ p, the recombination rate can be expressed as

$$R_d = \beta p_0 \left(n - n_0\right) = \frac{n - n_0}{\tau_n} \tag{2.76}$$

The symbol τ_n represents the lifetime of the electrons in a semiconductor. The diffusion length of any minority carrier can be expressed in terms of the lifetime, as follows:

$$L_n = \sqrt{D_n \tau_n} \quad \text{for electrons in p-type semiconductors} \tag{2.77}$$

$$L_p = \sqrt{D_p \tau_n} \quad \text{for holes in n-type semiconductors} \tag{2.78}$$

The terms D_n and D_p pertain to the diffusion coefficients, while L_n and L_p are referred to as the minority carrier diffusion lengths.

In this context, the recombination process involves the utilization of trap states (E_T) generated by lattice defects or impurity atoms. The electrons trapped in these states attract holes, resulting in recombination and dissipation of heat into the lattice. There are two distinct types of trap states, classified based on the nature of the impurities or defects: donor- and acceptor-type traps.

Shockley-Read-Hall (SRH) Recombination

In this context, the recombination process involves the utilization of trap states (E_T) generated by lattice defects or impurity atoms. The electrons trapped in these states attract holes, resulting in recombination and dissipation of heat into the lattice. There are two distinct types of trap states, classified based on the nature of the impurities or defects: donor- and acceptor-type traps.

The SRH recombination rate of an intrinsic semiconductor can be represented mathematically.

$$R_{SRH} = \upsilon_{th} \sigma N_T \frac{np - n_i^2}{n + p + 2n_i cosh\left(\frac{E_T - E_{Fi}}{k_B T}\right)} \tag{2.79}$$

With regard to n-type semiconductors, it can be stated that the excess electron concentration is approximately equal to the thermal equilibrium electron concentration, i.e., n $\approx$ n_0, and is significantly higher than the concentration of holes, i.e.,

n $\gg$ p.

$$R_{SRH} = \upsilon_{th}\sigma N_T \frac{p - p_0}{1 + 2\frac{n_i}{n_0}\cosh\left(\frac{E_T - E_{Fi}}{k_B T}\right)} = c_p N_T (p - p_0) = \frac{p - p_0}{\tau_{p,SRH}} \tag{2.80}$$

The hole capture coefficient and hole lifetime in an n-type semiconductor are represented by c_{p} and $\tau_{\mathrm{p,SRH}}$, respectively, where ν_{th} represents the thermal velocity. Correspondingly, the recombination rate in a p-type semiconductor can be characterized by its electron-capture coefficient (c_{n}) and electron lifetime ($\tau_{\mathrm{n,SRH}}$).

$$R_{SRH} = \upsilon_{th}\sigma N_T \frac{p - p_0}{1 + 2\frac{n_i}{p_0}\cosh\left(\frac{E_T - E_{Fi}}{k_B T}\right)} = c_n N_T (n - n_0) = \frac{n - n_0}{\tau_{p,SRH}} \tag{2.81}$$

All the aforementioned situations exhibit an inverse relationship between the density of trap states and the lifetime of minority charge carriers.

$$\tau_{p,SRH} = \frac{1}{c_p N_T} \; ; \; \tau_{n,SRH} = \frac{1}{c_n N_T} \tag{2.82}$$

More comprehensive information on the statistics of charge carrier recombination in Shockley-Read-Hall recombination can be found in cited references[60–62].

Auger Recombination

Auger recombination is a three-particle process involving the interaction of electrons, holes, and neighboring electrons or holes. This process has a significant impact on the carrier concentration. In Auger recombination, the energy and momentum of the recombining particles are transferred to a third carrier that is excited to a higher energy level. The energy is then dissipated in the form of lattice vibrational energy during relaxation of the third carrier. The Auger recombination rate can be mathematically expressed as

$$\mathbf{R}\mathrm{eeh} = C\mathrm{n}n^2 p = C_{\mathrm{n}} N_{\mathrm{D}}^2 p \tag{2.83}$$

$$\mathbf{R}\mathrm{ehh} = C\mathrm{p}np^2 = C_{\mathrm{p}} N_A^2 n \tag{2.84}$$

where C_n and C_p are temperature-dependent proportionality constants, and R_{eeh} and R_{ehh} are the Auger recombination rates for n-type and p-type semiconductors, respectively. The Auger lifetimes of n- and p-type semiconductors can be expressed as

$$R_{eeh} = \frac{1}{C_n N_d^2} \; ; R_{ehh} = \frac{1}{C_p N_A^2} \tag{2.85}$$

The rate of Auger recombination is proportional to the square of the density of either the donor or acceptor. Consequently, Auger recombination become the predominant recombination process at higher doping levels.

Surface Recombination

The previously discussed recombination mechanisms occur within the semiconductor volume. However, in high-purity semiconductors, surface recombination is more

prevalent than bulk recombination. This is because surface trap states are created within the bandgap because of dangling bonds at the surface of the semiconductor. The rate of surface recombination for both n- and p-type semiconductors can be described by the following equation:

$$R_{sn} = \upsilon_{th}\sigma_p N_{ST}(p_s - p_0) \tag{2.86}$$

$$R_{sp} = \upsilon_{th}\sigma_n N_{ST}\,(n_s - n_0) \tag{2.87}$$

The cross sections of the holes and electrons are represented by σ_p and σ_n, respectively. N_{ST} denotes the surface trap density. The concentrations of holes and electrons at the surface are denoted by p_s and n_s, while p_0 and n_0 represent the thermal equilibrium concentrations of holes and electrons, respectively.

2.4.5 Concept of Quasi-Fermi Level

When a semiconductor is under thermal equilibrium and is exposed to light with energy greater than its bandgap, electrons are excited from the valence band to the conduction band, resulting in the formation of excitons in both the bands. In n-type semiconductors, this irradiation has little effect on the concentration of conduction-band electrons, which serve as the majority charge carriers, but it increases the concentration of holes, which act as minority charge carriers in the valence band. Similarly, in p-type semiconductors, irradiation enhances the concentration of electrons, which act as minority charge carriers, and has a minimal impact on the concentration of holes, which serve as majority charge carriers. Therefore, irradiating a semiconductor generally increases the concentration of minority charge carriers.

$$n^* = n + \Delta n \tag{2.88}$$

$$p^* = p + \Delta p \tag{2.89}$$

The electron and hole concentrations in the dark and under irradiation are denoted as n, p, n*, and p*, respectively. The increase in the concentration of charge carriers after irradiation is represented by the deltas $\Delta n*$ and $\Delta p*$. During photoexcitation, charge carriers equilibrate with the phonons in their respective bands. Irradiation splits the Fermi level into two: the quasi-Fermi level of electrons and the quasi-Fermi level of holes. The electrochemical potentials of electrons and holes in the photostationary state are referred to as the quasi-Fermi level of electrons (E_F^{n*}) and quasi-Fermi level of holes (E_F^{p*}), respectively. In the absence of irradiation, the quasi-Fermi and Fermi levels of the semiconductor were the same under thermal equilibrium. However, under photoexcitation conditions, the quasi-Fermi level of electrons is situated above the Fermi level, while the quasi-Fermi level of holes is below the Fermi level (2.13).

$$E_F^* = E_C - kT\ ln\left(\frac{N_C}{n^*}\right) = E_F + kT\ ln(n) + \Delta n \cdot n \tag{2.90}$$

$$E_F^{p^*} = E_V + kT \ln\left(\frac{N_V}{p^*}\right) = E_F - kT \ln p + \Delta p p^* \tag{2.91}$$

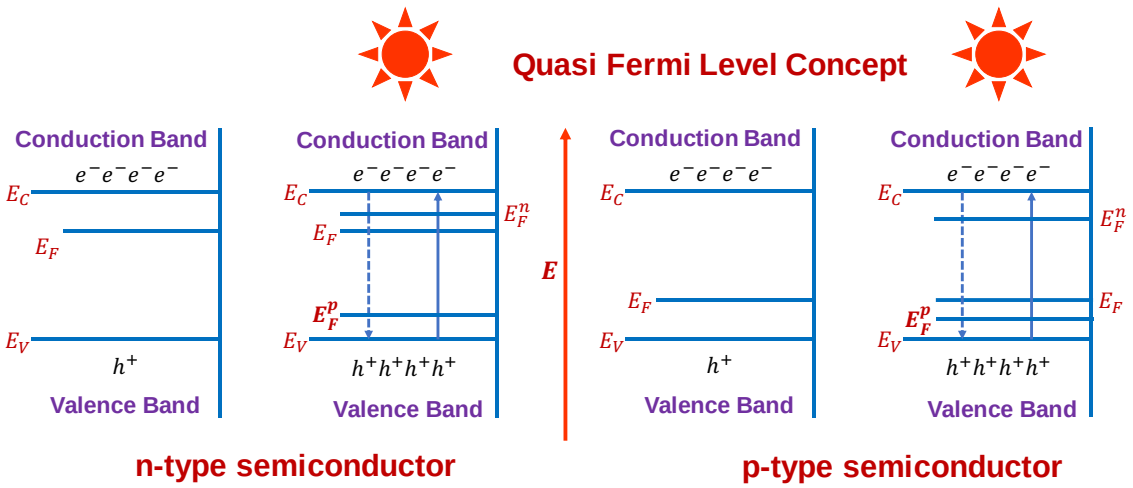

Figure 2.13: Illustrates the separation of the Fermi level into quasi-Fermi levels in the presence of radiation and the formation of quasi-Fermi levels in n- and p-type semiconductors [40]. *Reproduced from Narayanan, H.; Viswanathan, B.; Krishnamurthy, K. R.; Nair, H., in Photocatalytic Nanomaterials for Environmental Applications; Material Research Forum: 2018, pp 175–210. ©2018 by the authors.*

In an n-type semiconductor where the electron concentration is significantly higher than the hole concentration and the fluctuation in electron concentration, the quasi-Fermi level of electrons is almost equal to the Fermi level, while the quasi-Fermi level of holes is situated much lower than the Fermi level. Typically, under photoexcitation, the quasi-Fermi level of the dominant charge carrier is either very close to or equal to the Fermi level.

At equilibrium, the Fermi levels of the redox species and the semiconductor are balanced, resulting in no electron transfer or reaction in the absence of irradiation. When electron transfer occurs between a semiconductor and redox species, the Fermi level of the semiconductor should be higher than that of the redox species. This condition is fulfilled when the semiconductor is subjected to a threshold light. To initiate the reduction reaction, the quasi-Fermi level of electrons must be higher than that of the redox species, allowing electrons from the conduction band to flow to the oxidant species. Similarly, the quasi-Fermi level position of the hole must be lower than that of the reductant species for a reduction reaction to occur.

$$E_F^* n > E_{F_{redox}} \tag{2.92}$$

$$E_F^{p^*} < E_{F_{redox}} \tag{2.93}$$

The water-splitting reaction was used as an example to illustrate the above concepts. When an n-type semiconductor is immersed in water, the Fermi levels of both the species reach equilibrium. Consequently, the semiconductor does not possess sufficient potential to either reduce or oxidize the redox species, making the reaction thermodynamically infeasible under dark conditions. However, in the presence of irradiation, the Fermi level splits into two quasi-Fermi levels and aligns above and below the redox potential of the water. Consequently, the necessary prerequisites for reduction and oxidation are satisfied, and water undergoes a redox reaction under these circumstances (Figure 2.14).

$$E_F^{n^*} > E_{F_{(\frac{H_2O}{H_2})}} \tag{2.94}$$

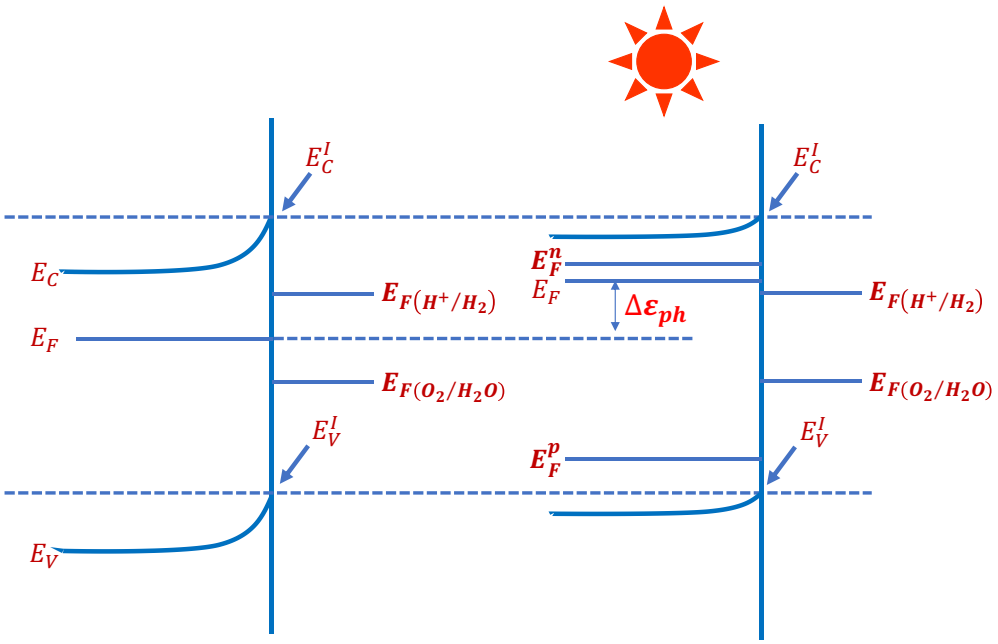

Figure 2.14: Splitting of Fermi level to quasi-Fermi levels in the presence of irradiation and quasi-Fermi level formation in n- and p-type semiconductors [40]. *Reproduced from Narayanan, H.; Viswanathan, B.; Krishnamurthy, K. R.; Nair, H., in Photocatalytic Nanomaterials for Environmental Applications; Material Research Forum: 2018, pp 175–210. ©2018 by the authors.*

$$E_F^{p^*} < E_{F_{\left(\frac{O_2}{H_2O}\right)}} \tag{2.95}$$

The water-splitting reaction, or any other photocatalytically or photosynthetically driven reaction, cannot occur without irradiation, or a field is due to the laws of thermodynamics.

2.4.6 Photo-potential

As previously mentioned, the flat-band condition of a semiconductor leads to the recombination of charge carriers, whereas the space charge layer formed at the interface divides the charge carriers by directing them in opposite directions. This separation of charge carriers causes an inverse potential in the semiconductor, which diminishes the potential across the space charge layer. This reduction in potential slows the movement of charges in the opposite direction. The photoexcitation-induced inverse potential in the space-charge layer corresponded to the photopotential.

$$\Delta E_{ph} = -\Delta\epsilon_{ph} \tag{2.96}$$

During photoexcitation, when the energy band exhibits an upward bend, the Fermi level of the semiconductor increases by $\Delta\varepsilon_{ph}$. However, when the energy band was bent downward, the Fermi level decreased. The maximum photopotential (ΔE_{ph}^0) of the semiconductor can be determined as the difference between the semiconductor's potential in the dark (E) and its flat-band potential (E_{fb}) when

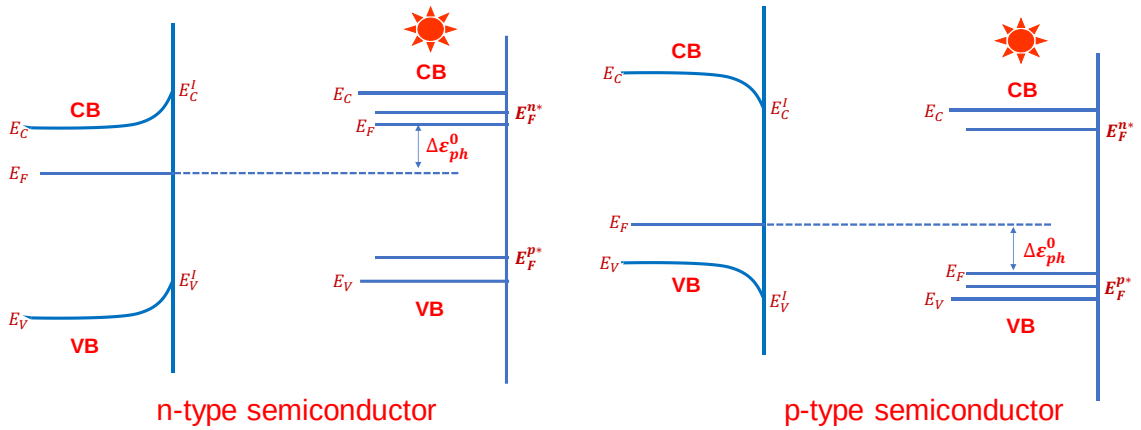

Figure 2.15: Band characteristics of the semiconductor in the presence and absence of illumination with respect to the water redox potential [40]. *Reproduced from Narayanan, H.; Viswanathan, B.; Krishnamurthy, K. R.; Nair, H., in Photocatalytic Nanomaterials for Environmental Applications; Material Research Forum: 2018, pp 175–210. ©2018 by the authors.*

exposed to light, at which point band bending is eliminated.

$$|\Delta E_{ph}| \leq \Delta E_{ph}^{0} = |E - E_{fb}| \tag{2.97}$$

If there is no interfacial chemical reaction, the photopotential of a semiconductor with a high impurity concentration can be estimated using the charge-carrier concentration (as shown in figure 2.15).

2.4.7 Band Edge Positions and Its Calculation

The position of the Fermi level under flat-band conditions determines the flat-band potential of the semiconductor. It is essential to clarify that the flat-band potential of a semiconductor is distinct from its band-edge potential[63, 64]. Although the flat-band potential depends on the impurity concentration, the band-edge potential is an inherent property of semiconductors and is not affected by the impurity concentration. The relationship between the band-edge potential and flat-band potential is as follows: In typical semiconductors, the values $E_C - E_F^n = 0.1\,\mathrm{eV}$ and $E_V - E_F^p = -0.1\,\mathrm{eV}$ [63, 64].

$$E_C = E_{FB}^n - \frac{E_C - E_F^n}{e} \quad \text{for n-type} \tag{2.98}$$

$$E_V = E_{FB}^p - \frac{E_V - E_F^p}{e} \quad \text{for p-type} \tag{2.99}$$

In any photon-assisted catalytic process, the position of the band edges is a crucial factor in determining the redox behavior of the charge carriers. Calculation of the band-edge position plays a significant role in determining the extent and feasibility of a particular photon-assisted catalytic reaction. In this section, we outline conventional methods for determining the band positions of semiconductor materials. The flat band potentials of semiconductors can be calculated manually using an equation that connects the electronegativity of the semiconductor (χ),

energy of a free electron on the hydrogen scale ($E^e = 4.5\,\mathrm{eV}$), conduction band position (E_{CB}), and bandgap (E_g)[65].

$$E_{CB} = \chi - E^e - 0.5E_g \tag{2.100}$$

The electronegativity of a semiconductor can be determined by calculating the geometric mean of the electronegativity of its constituent atoms. The bandgap of TiO_2, a semiconductor material composed of titanium (Ti) and oxygen (O), was determined to be $3.2\,\mathrm{eV}$. The electron affinities of Ti and O were measured at $0.08\,\mathrm{eV}$ and $1.46\,\mathrm{eV}$, respectively, while their ionization energies were $1.46\,\mathrm{eV}$ (Ti) and $6.81\,\mathrm{eV}$ (O). Using these values, the electronegativity of Ti was calculated as the arithmetic mean of its electron affinity and ionization energy, resulting in $3.44\,\mathrm{eV}$. Similarly, for oxygen, the electronegativity is computed as $(1.46 + 6.81)/2$, yielding $7.53\,\mathrm{eV}$. The semiconductor electronegativity of TiO_2, which is determined by the geometric mean of the electronegativities of the constituent elements, is approximately $5.79\,\mathrm{eV}$. The formula $\chi - E^e - 0.5E_g$ was employed to determine the conduction band position (E_{CB}) of TiO_2, and the formula $\chi - E^e - 0.5E_g$ was employed. By substituting these values, we obtain $5.79 - 4.5 - 0.5 \times 3.2$, which results in $-0.31\,\mathrm{V}$. Conversely, for valence band calculation, the valence band position (E_{VB}) was determined by adding E_{CB} to the bandgap, yielding $-0.31\,\mathrm{V}$ + $3.2\,\mathrm{V}$, which is equal to $2.89\,\mathrm{V}$.

The calculation of the band-edge positions in the experiments involved the integration of various instrumental methods. Valence band XPS and UPS offer direct insight into the valence and conduction band positions of the material. By adding the bandgap of the semiconductor, as determined through diffuse reflectance spectrometry (DRS) measurements or Tauc extrapolation, the valence or conduction band position can be obtained [66]. These positions are essential for understanding the mechanism of the gaseous photon-assisted catalytic reactions. However, in liquid-phase reactions, the band edge position changes because of the Fermi level equilibration with the solvent. In such cases, electrochemical techniques such as impedance or cyclic voltammetry can be employed to determine band positions[67–72]. The Mott-Schottky plot obtained through impedance measurements provides the flat-band potential of a semiconductor[73–77]. For n-type semiconductors, the flat-band potential is closer to the conduction-band edge and offers an approximate position of the conduction band, whereas for p-type semiconductors, the flat-band potential is just above the valence band, providing a rough position of the valence band. Adding the bandgap value to the flat-band potential yields the corresponding approximate valence or conduction band position.

2.5 Underlying Theories of CO_2 Reduction

The principle of the photon-assisted catalytic carbon dioxide reduction is based on electrochemical methods. Typically, the electrochemical reactions are performed under ideal conditions. Consequently, the application of these principles to photocatalytic or photosynthetic contexts has been a topic of discussion and has been analyzed from various perspectives[78–85]. The primary objective of the photon-assisted catalytic or electrocatalytic reduction is to bypass the initial

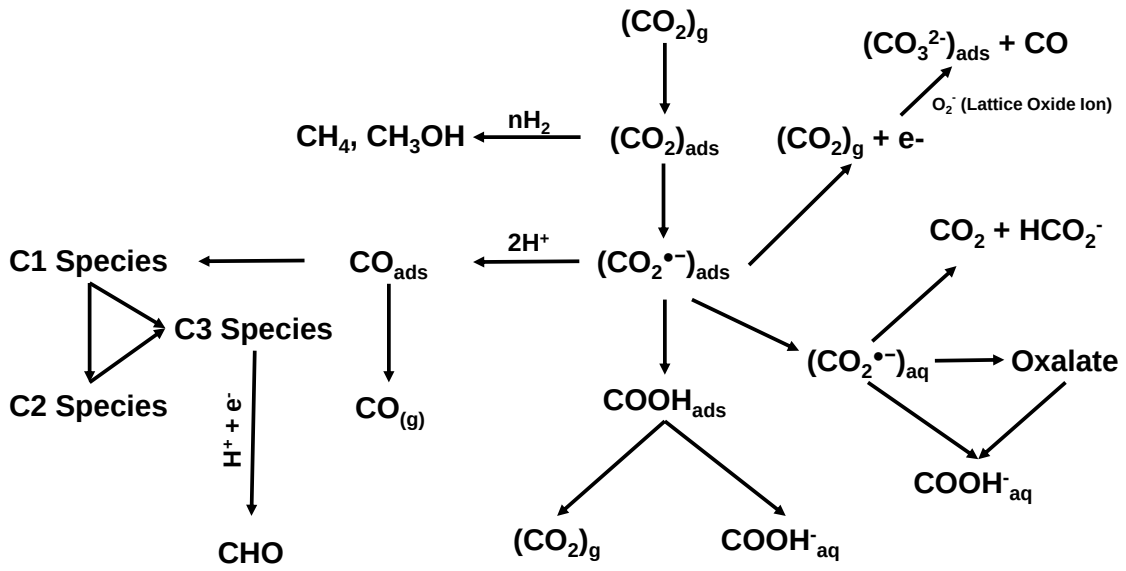

Figure 2.16: The reaction network for the reduction of carbon dioxide in an aqueous environment is illustrated. The central point of this network is the formation of the CO_2 anion radical [86]. *Reproduced from Viswanathan, B., in New and Future Developments in Catalysis, Suib, S. L., Ed.; Elsevier: Amsterdam, 2013, pp 275–295. ©2013 Elsevier B.V.*

activation step of CO_2 by creating intermediates with lower potential energies that are thermodynamically more favorable.

The initial stage of the direct reduction of CO_2 is believed to be the formation of a carbon dioxide anion radical ($^{-\bullet}CO_2$). The subsequent hydrogenation of $^{-\bullet}CO_2$ radicals leads to a variety of reduction products, depending on the catalyst surface (Figure 2.16)[86].

$$CO_{2(g)} + e^- \longrightarrow {}^{-\bullet}CO_2 \quad E^\circ = -1.9\,\text{V vs NHE} \tag{2.101}$$

The E° for the process is considerably higher or more negative than that of any of the individual hydrogenation reactions of carbon dioxide and requires an enormous amount of energy. This reaction is applicable to non-protic solvents. Regarding protic solvents, the measurement of the thermodynamic potential highly depends on the type of electrode used, owing to the participation of adsorbed hydrogen ($H^\star$) in the reduction process. Any of the CO_2 utilization techniques involving this initiation step would require the application of a high negative potential to the cathode. If the anode reaction is water oxidation, then a total potential of $3.129\,\text{V}$ across the cell is needed to drive the complete reaction. In the case of the photon-assisted catalytic reduction of CO_2, the oxidation and reduction reactions are carried out by the charge carriers produced as a result of the light-induced initiation of the photocatalyst. The energy required for photon-assisted catalytic conversion of CO_2 is lower than that required for the corresponding electrocatalytic reduction[15].

Semiconductors exhibit distinct reduction and oxidation potentials, the values of which depend on the positioning of the conduction and valence bands relative to the standard hydrogen electrode or vacuum (Figure 2.17).

Among the currently known semiconductors, there is no known material that possesses the necessary reduction potential for the reduction of carbon dioxide

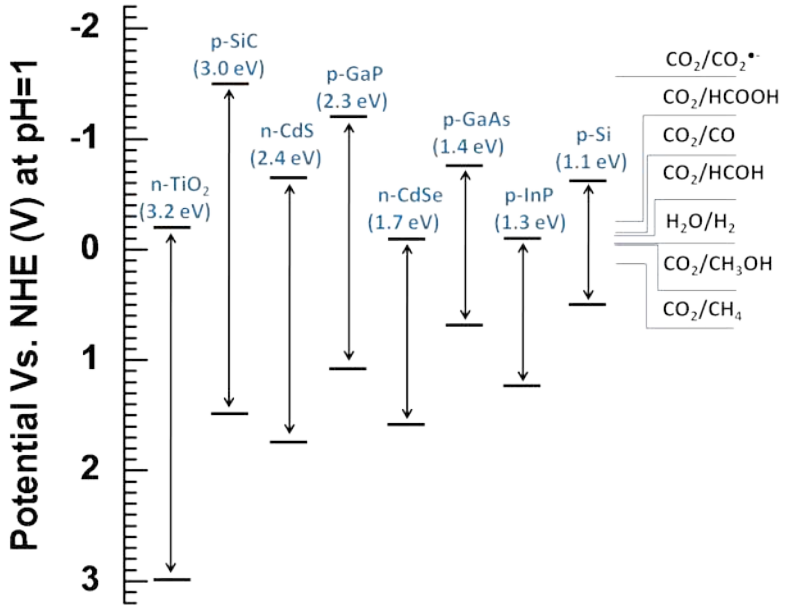

Figure 2.17: The positions of the conduction and valence bands for several semiconductors at pH = 1 and NHE are displayed along with the thermodynamic potentials for CO_2 reduction to various products under the same pH and NHE conditions. In addition, the band edge positions of the semiconductors are included in the representation [87]. This figure is made available under the Creative Commons CC0 1.0 Universal Public Domain Dedication.

into its corresponding carbon dioxide radical anion. Upon approaching the surface of the photocatalyst, the geometry of the carbon dioxide molecule changes from linear to bent, which in turn reduces the energy of the LUMO level[88]. The activation energy required for the activation of $CO_{2(ads)}$ is lower than that of $CO_{2(g)}$. The addition of electrons to the CO_2 molecule is influenced by its interaction with surface catalytic species[88, 89]. The modification of the surface properties of photocatalysts can facilitate the production of specific reduction products.

The interaction of carbon dioxide with the photocatalyst surface can occur through either carbon or oxygen attachment (Figure 2.18), which is determined by the presence of active sites on the photocatalytic surface[90]. Each photocatalytic material exhibited a unique adsorption mechanism and electron transfer type. The adsorption of carbon dioxide on various metal oxide surfaces has been thoroughly explained in the book "Surface Science of Metal Oxide" by Victor E. Henrich[91]. In aqueous phase reduction, particularly at an alkaline pH, carbonate or bicarbonate ions are the dominant species. The interaction of these ions with the photocatalytic surface occurs primarily through hydrogen or oxygen as they exist as ions. Therefore, the reaction mechanism associated with the aqueous phase differs from that associated with the gaseous CO_2 reduction. To the best of our knowledge, there are no detailed studies available on the interaction of carbonate and bicarbonate structures with metal oxides or any other photocatalyst[92, 93]. Elucidating the mechanism of aqueous-phase photocatalytic reduction of carbon dioxide requires further detailed studies. Carbonate and bicarbonate are commonly used as hole scavengers in water splitting and photooxidation reactions. Therefore, the carbon dioxide radical ion observed in the aqueous medium may be due to the direct

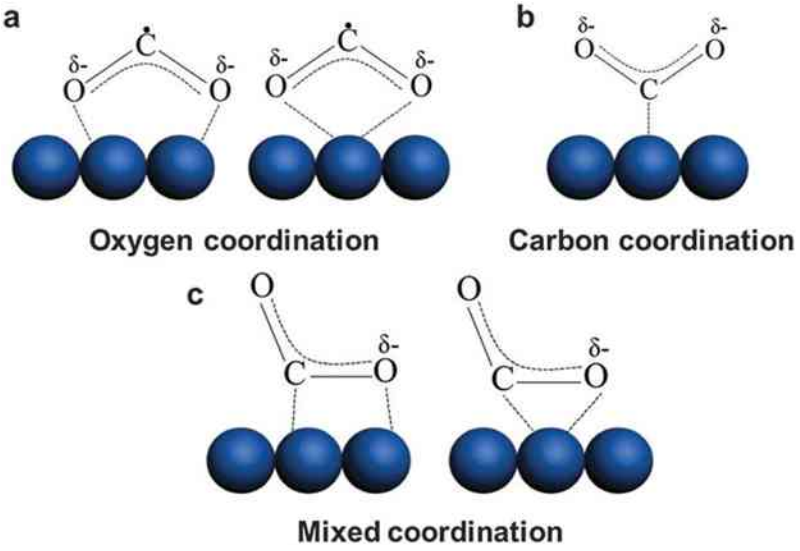

Figure 2.18: Possible binding modes of CO_2 on the surface through (a) oxygen, (b) carbon, and (c) mixed coordination [90]. Reproduced from *J. Electroanal. Chem. 594 (2006) 1–19. ©2006 Elsevier B.V.*

oxidation of carbonate or bicarbonate with holes.

The primary objective of photocatalytic and electrocatalytic conversion reactions is to bypass the initial activation of CO_2, generate intermediates with lower potential energies, and direct the reaction toward a favorable pathway. The formation of intermediates depends on the interaction of CO_2 with catalyst surfaces or electron-rich entities. The challenge of executing multiple proton-coupled electron transfers creates an additional thermodynamic barrier for the photocatalytic and electrocatalytic reduction of CO_2. The following are the most commonly occurring proton-coupled electron transfer reactions of carbon dioxide (CO_2(g)) at pH seven, as reported in the literature[94].

Carbon Monoxide

$$\begin{aligned} \mathrm{CO_2(g) + H_2(g)} &\longrightarrow \mathrm{CO\,(g) + 2\,H_2O\,(l)} \qquad E^\circ = -0.51\,\mathrm{V} \\ \mathrm{2\,H^+\,(aq) + 2\,e^-} &\longrightarrow \mathrm{H_2(g)} \qquad E^\circ = -0.41\,\mathrm{V} \\ \mathrm{CO_2\,(g) + 2\,H^+\,(aq) + 2\,e^-} &\longrightarrow \mathrm{CO\,(g) + 2\,H_2O\,(l)} \qquad \mathrm{E^\circ = -0.92\,V} \end{aligned} \tag{2.102}$$

Formic Acid

$$\begin{aligned} \mathrm{CO_2(g) + H_2(g)} &\longrightarrow \mathrm{HCOOH\,(l) + H_2O\,(l)} \qquad E^\circ = -0.58\,\mathrm{V} \\ \mathrm{2\,H^+\,(aq) + 2\,e^-} &\longrightarrow \mathrm{H_2(g)} \qquad E^\circ = -0.41\,\mathrm{V} \\ \mathrm{CO_2\,(g) + 2\,H^+\,(aq) + 2\,e^-} &\longrightarrow \mathrm{HCOOH\,(l) + H_2O\,(l)} \qquad \mathrm{E^\circ = -0.99\,V} \end{aligned} \tag{2.103}$$

Formaldehyde

$$\begin{aligned} \mathrm{CO_2(g) + 2\,H_2(g) &\longrightarrow HCHO\,(g) + H_2O\,(l)} & E^\circ &= -0.55\,\mathrm{V} \\ \mathrm{4\,H^+\,(aq) + 4\,e^- &\longrightarrow 2\,H_2(g)} & E^\circ &= -0.41\,\mathrm{V} \\ \mathrm{CO_2\,(g) + 4\,H^+\,(aq) + 4\,e^- &\longrightarrow HCHO\,(g) + H_2O\,(l)} & \mathrm{E^\circ} &= -0.96\,\mathrm{V} \end{aligned} \tag{2.104}$$

Methanol

$$\begin{aligned} \mathrm{CO_2(g) + 3\,H_2(g) &\longrightarrow CH_3OH\,(l) + H_2O\,(l)} & E^\circ &= -0.39\,\mathrm{V} \\ \mathrm{6\,H^+\,(aq) + 6\,e^- &\longrightarrow 3\,H_2(g)} & E^\circ &= -0.41\,\mathrm{V} \\ \mathrm{CO_2\,(g) + 6\,H^+\,(aq) + 6\,e^- &\longrightarrow CH_3OH\,(l) + H_2O\,(l)} & \mathrm{E^\circ} &= -0.80\,\mathrm{V} \end{aligned} \tag{2.105}$$

Acetic Acid

$$\begin{aligned} \mathrm{2\,CO_2(g) + 4\,H_2(g) &\longrightarrow CH_3COOH\,(l) + 2\,H_2O\,(l)} & E^\circ &= -0.31\,\mathrm{V} \\ \mathrm{8\,H^+\,(aq) + 8\,e^- &\longrightarrow 4\,H_2(g)} & E^\circ &= -0.41\,\mathrm{V} \\ \mathrm{2\,CO_2\,(g) + 8\,H^+\,(aq) + 8\,e^- &\longrightarrow CH_3COOH\,(l) + 2\,H_2O\,(l)} & \mathrm{E^\circ} &= -0.72\,\mathrm{V} \end{aligned} \tag{2.106}$$

Methane

$$\begin{aligned} \mathrm{CO_2(g) + 4\,H_2(g) &\longrightarrow CH_4(g) + 2\,H_2O\,(l)} & E^\circ &= -0.24\,\mathrm{V} \\ \mathrm{8\,H^+\,(aq) + 8\,e^- &\longrightarrow 4\,H_2(g)} & E^\circ &= -0.41\,\mathrm{V} \\ \mathrm{CO_2\,(g) + 8\,H^+\,(aq) + 8\,e^- &\longrightarrow CH_4(g) + 2\,H_2O\,(l)} & \mathrm{E^\circ} &= -0.65\,\mathrm{V} \end{aligned} \tag{2.107}$$

Acetaldehyde

$$\begin{aligned} \mathrm{2\,CO_2(g) + 5\,H_2(g) &\longrightarrow CH_3CHO\,(g) + 3\,H_2O\,(l)} & E^\circ &= -0.36\,\mathrm{V} \\ \mathrm{10\,H^+\,(aq) + 10\,e^- &\longrightarrow 5\,H_2(g)} & E^\circ &= -0.41\,\mathrm{V} \\ \mathrm{CO_2\,(g) + 10\,H^+\,(aq) + 10\,e^- &\longrightarrow CH_3CHO\,(g) + 3\,H_2O\,(l)} & \mathrm{E^\circ} &= -0.77\,\mathrm{V} \end{aligned} \tag{2.108}$$

Ethanol

$$\begin{aligned} \mathrm{2\,CO_2(g) + 6\,H_2(g) &\longrightarrow CH_3CH_2OH\,(g) + 3\,H_2O\,(l)} & E^\circ &= -0.33\,\mathrm{V} \\ \mathrm{12\,H^+\,(aq) + 12\,e^- &\longrightarrow 6\,H_2(g)} & E^\circ &= -0.41\,\mathrm{V} \\ \mathrm{CO_2\,(g) + 12\,H^+\,(aq) + 12\,e^- &\longrightarrow CH_3CH_2OH\,(g) + 3\,H_2O\,(l)} & \mathrm{E^\circ} &= -0.74\,\mathrm{V} \end{aligned} \tag{2.109}$$

Ethane

$$\begin{aligned} 2\,CO_2(g) + 7\,H_2(g) &\longrightarrow CH_3CH_3(g) + 4\,H_2O\,(l) && E^\circ = -0.27\,V \\ 14\,H^+\,(aq) + 14\,e^- &\longrightarrow 7\,H_2(g) && E^\circ = -0.41\,V \\ CO_2\,(g) + 14\,H^+\,(aq) + 14\,e^- &\longrightarrow CH_3CH_3(g) + 4\,H_2O\,(l) && E^\circ = -0.68\,V \end{aligned} \tag{2.110}$$

Propanal

$$\begin{aligned} 3\,CO_2(g) + 8\,H_2(g) &\longrightarrow CH_3CH_2CHO\,(g) + 5\,H_2O\,(l) && E^\circ = -0.32\,V \\ 16\,H^+\,(aq) + 16\,e^- &\longrightarrow 8\,H_2(g) && E^\circ = -0.41\,V \\ 3\,CO_2\,(g) + 16\,H^+\,(aq) + 16\,e^- &\longrightarrow CH_3CH_2CHO\,(g) + 5\,H_2O\,(l) && E^\circ = -0.73\,V \end{aligned} \tag{2.111}$$

Acetone

$$\begin{aligned} 3\,CO_2(g) + 8\,H_2(g) &\longrightarrow CH_3COCH_3(g) + 5\,H_2O\,(l) && E^\circ = -0.31\,V \\ 16\,H^+\,(aq) + 16\,e^- &\longrightarrow 8\,H_2(g) && E^\circ = -0.41\,V \\ 3\,CO_2\,(g) + 16\,H^+\,(aq) + 16\,e^- &\longrightarrow CH_3COCH_3(g) + 5\,H_2O\,(l) && E^\circ = -0.72\,V \end{aligned} \tag{2.112}$$

Propanol

$$\begin{aligned} 3\,CO_2(g) + 9\,H_2(g) &\longrightarrow CH_3CH_2CH_2OH\,(aq) + 5\,H_2O\,(l) && E^\circ = -0.31\,V \\ 18\,H^+\,(aq) + 18\,e^- &\longrightarrow 9\,H_2(g) && E^\circ = -0.41\,V \\ 3\,CO_2\,(g) + 18\,H^+\,(aq) + 18\,e^- &\longrightarrow CH_3CH_2CH_2OH\,(aq) + 5\,H_2O\,(l) && E^\circ = -0.72\,V \end{aligned} \tag{2.113}$$

2-Propanol

$$\begin{aligned} 3\,CO_2(g) + 9\,H_2(g) &\longrightarrow CH_3CH(OH)CH_3(aq) + 5\,H_2O\,(l) && E^\circ = -0.30\,V \\ 18\,H^+\,(aq) + 18\,e^- &\longrightarrow 9\,H_2(g) && E^\circ = -0.41\,V \\ 3\,CO_2\,(g) + 18\,H^+\,(aq) + 18\,e^- &\longrightarrow CH_3CH(OH)CH_3(aq) + 5\,H_2O\,(l) && E^\circ = -0.71\,V \end{aligned} \tag{2.114}$$

To elucidate the overall potential associated with the complete reduction reaction, the potential required for water oxidation should be considered.

$$H_2O\,(l) \longrightarrow 2\,H^+\,(aq) + \frac{1}{2}\,O_2(g) + 2\,e^- \qquad E^\circ = -0.815\,V \tag{2.115}$$

When interpreting these potentials, it is crucial to consider that they are referenced to H^+/H_2 potential. The negative potentials signify the voltages required to facilitate the reduction of CO_2 at the cathode when 1 atm of hydrogen is oxidized at the anode. However, when a more practical anode reaction was assumed, there was a significant increase in the cell potential. For example, when water is oxidized at the anode, an additional $-1.229\,V$ must be added to the half-cell potential to

Table 2.1: Required reduction potentials for CO_2 at different pH values. The pH 7 values are extracted from [94]. Reproduced from *Anal. Methods 5 (2013) 1086. ©2013 Royal Society of Chemistry*. To elucidate the overall potential associated with a complete reduction reaction, the potential required for water oxidation should be considered.

Product (Equation Number)	pH 0	pH 7	pH 14
	E°	(V vs. NHE)	
Carbon Monoxide(2.102)	-0.1	-0.51	-0.92
Formic Acid(2.103)	-0.17	-0.58	-0.99
Formaldehyde(2.104)	-0.14	-0.55	-0.96
Methanol(2.105)	+0.02	-0.39	-0.8
Acetic Acid(2.106)	+0.1	-0.31	-0.72
Methane(2.107)	+0.17	-0.24	-0.65
Acetaldehyde(2.108)	+0.05	-0.36	-0.77
Ethanol(2.109)	-0.08	-0.33	-0.74
Ethane(2.110)	+0.14	-0.27	-0.68
Propanal(2.111)	+0.09	-0.32	-0.73
Acetone(2.112)	+0.1	-0.31	-0.72
Propanol(2.113)	+0.1	-0.31	-0.72
Isopropanol(2.114)	+0.11	-0.3	-0.71

determine the overall cell potential. Accordingly, a potential of $-1.735\,\mathrm{V}$ is necessary to convert CO_2 (g) into CO (g) at pH 7. It may be more suitable to utilize a 1 M aqueous solution of methanol or formic acid as the standard state for an electrochemical reaction rather than employing a pure liquid form.

The production of reduced carbon products from CO_2 through electrolysis involves a voltage range of -1.805 to -1.465 V, with formic acid requiring a higher voltage and methane requiring a lower voltage at pH 7. It is important to note that the electrochemical reactions in such a cell are thermodynamically equivalent to the corresponding chemical reactions. Therefore, the voltage required for the reduction of CO_2 to methane and the oxidation of water to oxygen correspond to the free-energy change, which is opposite to the free-energy change for the combustion of methane. In other words, it is more efficient to use solar electricity to replace the energy obtained by burning CH_4 as fuel, instead of using electricity to synthesize CH_4 from CO_2.

For photocatalytic conversion reactions, it is necessary to decrease the required potential because of the adsorptive interactions between CO_2/water and the photocatalyst surface. The reduction potential corresponding to the formation of fuel products with respect to NHE at pH 7 cannot be applied to reactions carried out under other pH conditions. The standard reduction potential varies significantly at different pH values (Table 2.1) and temperatures (Table 2.2). According to recent advancements, the conduction band becomes more negative by 1mv per unit change in the pH[95–97]. Hence, a pH correction should be performed while utilizing the reduction potential to interpret the results.

Table 2.2: The figure shows the variation in reduction potential at different temperatures for the reaction between CO_2, H_2O, and electrons, resulting in the formation of $HCOO^-$ and OH^- ions. This table is reproduced from Bard et al.[98]. *Bard, A. J.; Parsons, R.; Jordan, J., Standard Potentials in Aqueous Solution; Marcel Decker: New York, Basel, 1985. ©1985 International Union of Pure and Applied Chemistry*.

T (°C)	$E°$ (V)
2	-0.699
10	-0.708
25	-0.723
40	-0.739
50	-0.750
60	-0.760

These potentials pertain specifically to CO_2 in its gaseous state. Regrettably, numerous reports have erroneously employed these data to interpret reactions in the liquid phase of CO_2 reduction. In liquid-phase CO_2 reduction, the CO_2molecules exist in the form of H_2CO_3, HCO_3^-, or HCO_3^{2-}, depending on the pH of the reaction medium. Notably, the reduction potential required to reduce H_2CO_3, HCO_3^-, or HCO_3^{2-} differs from that of gaseous CO_2 at any given pH[98–102].

$$\begin{aligned}
2\,H_2CO_3 + 2\,H^+ + 2\,e^- &\longrightarrow H_2C_2O_4 + 2\,H_2O && E° = -0.391\,V \\
H_2CO_3 + 2\,H^+ + 2\,e^- &\longrightarrow HCOOH + H_2O && E° = -0.166\,V \\
H_2CO_3 + 4\,H^+ + 4\,e^- &\longrightarrow HCHO + 2\,H_2O && E° = -0.05\,V \\
H_2CO_3 + 6\,H^+ + 6\,e^- &\longrightarrow CH_3OH + 2\,H_2O && E° = 0.044\,V \\
H_2CO_3 + 4\,H^+ + 4\,e^- &\longrightarrow C + 3\,H_2O && E° = 0.228\,V
\end{aligned} \tag{2.116}$$

The corresponding reactions of the carbonates are as follows:

$$\begin{aligned}
2\,CO_3^{2-} + 4\,H^+ + 2\,e^- &\longrightarrow C_2O_4^{2-} + 2\,H_2O && E° = 0.478\,V \\
CO_3^{2-} + 3\,H^+ + 2\,e^- &\longrightarrow HCOO^- + H_2O && E° = 0.311\,V \\
CO_3^{2-} + 6\,H^+ + 4\,e^- &\longrightarrow HCHO + 2\,H_2O && E° = 0.197\,V \\
CO_3^{2-} + 8\,H^+ + 6\,e^- &\longrightarrow CH_3OH + H_2O && E° = 0.209\,V \\
CO_3^{2-} + 6\,H^+ + 4\,e^- &\longrightarrow C + 3\,H_2O && E° = 0.475\,V
\end{aligned} \tag{2.117}$$

All reduction reactions involving CO_2, H_2CO_3, HCO_3^-, and HCO_3^{2-} are characterized by a thermodynamic potential close to zero (Figure 2.19). Nevertheless, owing to the significant overpotentials associated with each reaction, they are rarely observed in aqueous solutions under normal conditions. Further information and examples related to these aspects can be found in the well-known textbook standard potential for aqueous solutions by Bard et al.[98].

2.6 The Carbon Dioxide Radical Anion ($^{-\bullet}CO_2$)

The stable oxidation product of carbon, Carbon Dioxide, exhibits a formal tone. As a linear and non-polar molecule, it possesses a C-O bond length of $1.16\,Å$ and bond

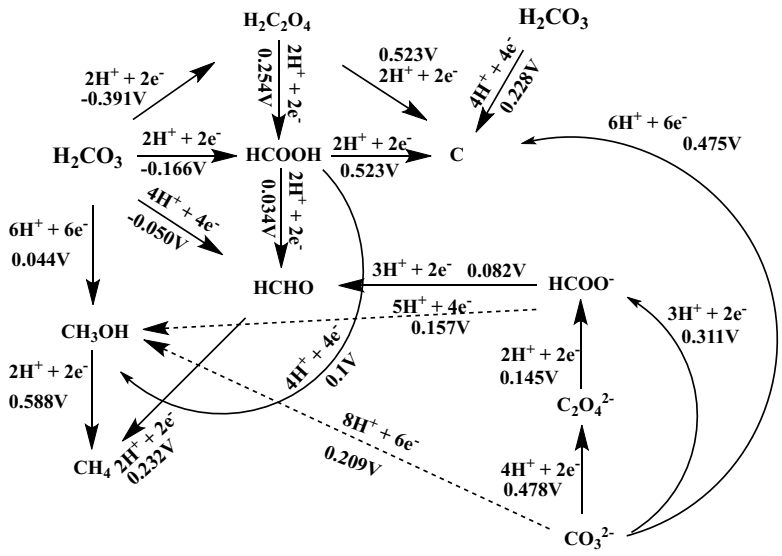

Figure 2.19: Possible reactions of carbon dioxide in aqueous solutions [98]. Reproduced from *Bard, A. J.; Parsons, R.; Jordan, J., Standard Potentials in Aqueous Solution; Marcel Decker: New York, Basel, 1985. ©1985 International Union of Pure and Applied Chemistry*

strength D = $532\,\mathrm{kJ\,mol^{-1}}$. Despite being nonpolar, it contains polar bonds owing to the electronegativity difference between carbon and oxygen.

Owing to its molecular structure, carbon dioxide is prone to nucleophilic and electrophilic attacks at its carbon and oxygen centers, respectively. The first ionization potential of carbon dioxide ($13\,\mathrm{eV}$) is greater than that of water ($12.6\,\mathrm{eV}$) and ammonia ($10\,\mathrm{eV}$), suggesting notable electrophilicity of the central carbon atom [103]. The molecular orbital energy level diagram of carbon dioxide is depicted in Figure 2.20.

In keeping with Molecular Orbital Theory (MOT), the energy of the lowest unoccupied antibonding orbital (LUMO) was calculated to be approximately $3.8\,\mathrm{eV}$, which suggests a considerable electron affinity for the central carbon atom. Therefore, it is prone to attack by nucleophiles and reduction, while the energy of the highest occupied molecular orbital (HOMO) makes it susceptible to assault by electrophiles owing to its elevated localized electron density in the oxygen in-plane lone pairs. Moreover, the HOMO exhibits relatively weak interactions with both Lewis and Brønsted acids[103, 105].

Carbon dioxide possesses two degenerate HOMO and LUMO energy levels. The degenerate frontier orbitals of this molecule resemble the d- and f-orbitals of the transition metals and lanthanides, respectively. The HOMO of CO_2 contains four electrons with the same energy available for release. In addition, the molecule has four unoccupied states that can accept four electrons through transfer (Figure 2.20). However, the degeneracy is broken when one of the four electrons is transferred or released[104]. It is important to note that the simultaneous addition or transfer of electrons does not occur in the case of carbon dioxide, making the activation process a Holy Grail.

The activation of a molecule or substrate plays a crucial role in catalytic reactions by enhancing its reactivity through surface reactions. Activation is a critical factor in

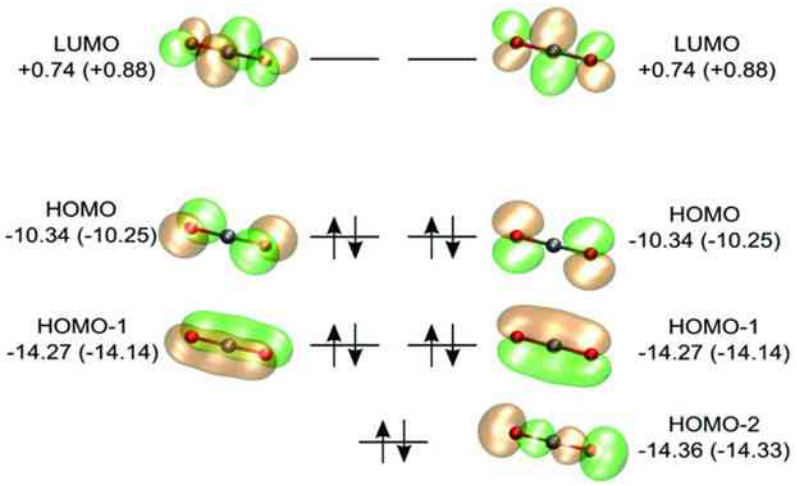

Figure 2.20: Investigation of the molecular orbitals of ground state CO_2 at the frontier level. Orbital energies are expressed in electron volts (eV) in a vacuum environment, and in water or PCM, the unit remains eV. Calculations were performed using the B3LYP/cc-pVTZ method [104]. Reproduced from *Nakamura, S.; Hatakeyama, M.; Wang, Y.; Ogata, K.; Fujii, K. ACS Symposium Series 2015, 123–134. ©2015 American Chemical Society.*

determining the overall catalytic reaction rate. In many cases, substrate activation is the rate-determining step in catalytic reactions. The activation of carbon dioxide is a significant step in several catalytic reactions. This process involves three main pathways: (i) bending of the $\mathrm{O}{=}\mathrm{C}{=}\mathrm{O}$ bond, (ii) elongation of two or more $\mathrm{C}{=}\mathrm{O}$ bonds in CO_2, and (iii) polarization of the CO_2 molecule. These pathways were not separated and occurred simultaneously, as shown in Figure 2.21.

The stability of CO_2 in its linear form necessitates the provision of additional energy to convert it into its bent form, that is, CO_2 to $^{-\bullet}CO_2$. The high LUMO level of carbon dioxide makes it thermodynamically unfavorable to transfer one electron to free CO_2, requiring a very negative redox potential of approximately $-1.9\,\mathrm{V}$ vs. a Normal Hydrogen Electrode (NHE). In the photocatalytic route, no semiconductor possesses the conduction-band potential required for CO_2 activation, resulting in the need to supply an additional overvoltage, which presents another

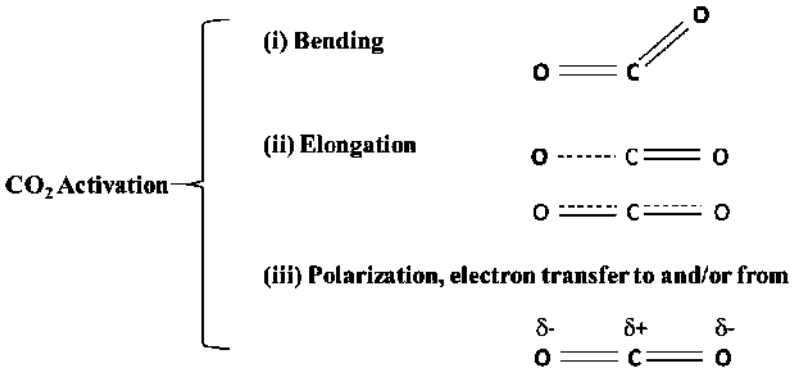

Figure 2.21: Type of CO_2 activation [104]. Reproduced from *Nakamura, S.; Hatakeyama, M.; Wang, Y.; Ogata, K.; Fujii, K. ACS Symposium Series 2015, 123–134. ©2015 American Chemical Society.*

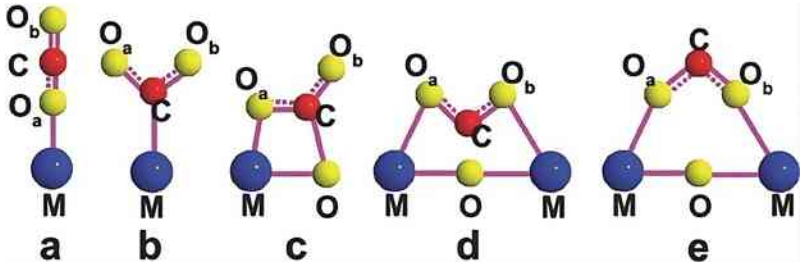

Figure 2.22: Possible adsorption configurations of carbon dioxide on metal-oxide surfaces [107]. Reproduced from *Adv. Mater. 26 (2014) 4607-4626. ©2014 WILEY-VCH Verlag GmbH & Co. KGaA, Weinheim*

energy dilemma.

One notable strategy to overcome these obstacles is to immobilize the substrate on the catalytic surface. This process alters the molecular structure of CO_2, transforming it from a linear to a bent shape. The extent to which CO_2 bends depends on the catalytic surface properties. Carbon adsorption onto metal surfaces occurs in multiple ways and nine distinct modes have been identified[106]. However, the specific interactions between CO_2 and the metal surfaces were not the focus of this study. Instead, the focus was on the diverse ways in which CO_2 interacted with semiconductor surfaces, as illustrated in Figure 2.22.

Interaction between CO_2 and the semiconductor surface can occur with either oxygen or carbon. The production of photoelectrons on the catalyst surface leads to the formation of $^{-\bullet}CO_2$, which is added to the LUMO level of chemically stable carbon dioxide. The first electron transfer changes the geometry of CO_2 from linear to bent $^{-\bullet}CO_2$. The structural arrangement of linear CO_2 into a bent shape involves a change in hybridization from sp to sp^2 at carbon, which is characterized by a high overpotential, signifying a substantial kinetic barrier to the reaction. Once formed, the bent $^{-\bullet}CO_2$ undergoes two-electron reduction rather than one-electron reduction. The formation of $^{-\bullet}CO_2$ plays a significant role in the reduction of carbon dioxide. The decrease in the $O{=}{=}C{=}{=}O$ bond angle via surface interactions facilitated the charge transfer to CO_2 by lowering its LUMO. Theoretical studies provide a clear picture of the energy-level variation of molecular orbitals as a function of the $O{=}{=}C{=}{=}O$ angle, known as the Walsh diagram[104, 108]. The change in LUMO energy of the OCO bond angle is shown in Figure 2.23.

The linear carbon dioxide molecule is the most stable state, with a bond angle of $180°$. The energies of the frontier orbitals fluctuated with a decrease in the bond angle. The anionic $^{-\bullet}CO_2$ radical has a bent geometry with a bond angle of $134°$, whereas neutral and cationic molecules exhibit a linear geometry. The reduction in the bond angle was investigated using infrared spectroscopy.

It has been established that rutile (100) crystal faces are active for the photocatalytic reduction of CO_2, whereas the (110) crystal lattice was found to be inactive towards the reaction[109–111]. The interaction between TiO_2 and CO_2 has been studied using a range of spectroscopic techniques and quantum mechanical modelling. For convenience, all mechanisms related to semiconductors are expressed using TiO_2 as a representative. Carbon dioxide can attach to the TiO_2 surface via oxygen or carbon atoms. It is believed that the attachment via two oxygen atoms is more stable because of the bidentate nature of the CO_2 ligand. The $Ti3+$ formed

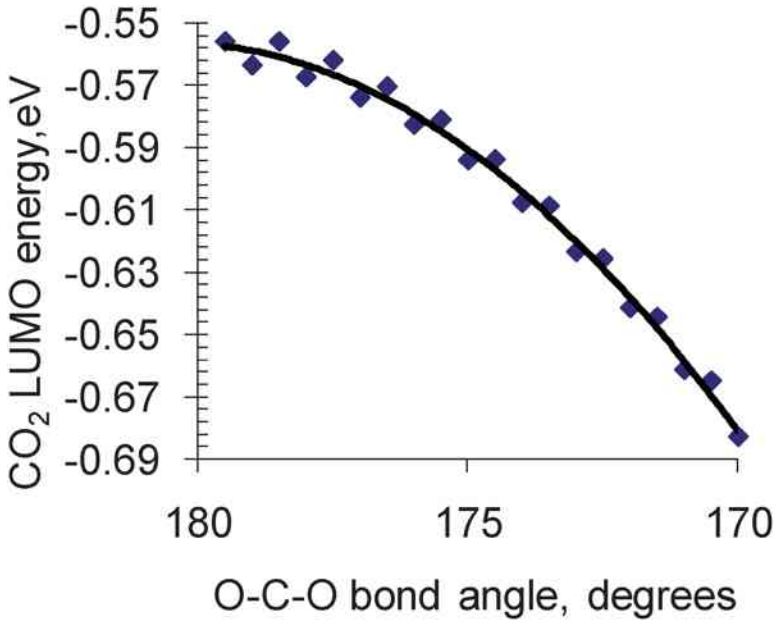

Figure 2.23: The variation in the LUMO energy of gaseous CO_2 relative to the O–C–O bond angle is of interest. By decreasing the O–C–O bond angle through surface interactions, it may be possible to facilitate charge transfer to CO_2 by reducing its LUMO energy [104]. Reproduced from *Nakamura, S.; Hatakeyama, M.; Wang, Y.; Ogata, K.; Fujii, K. ACS Symposium Series 2015, 123–134. ©2015 American Chemical Society.*

on the surface reduced CO_2 to the corresponding radical. Oxygen vacancies can also reduce CO_2 to CO, and one of the oxygen atoms in carbon dioxide heals the vacancy. The hydrogen atoms adsorbed on the TiO_2 surface reduced the amount of bound $^{-\bullet}CO_2$. Figure 2.24 illustrates the activation of carbon dioxide on titanium dioxide surfaces.

2.7 Identity Crisis of Carbon Dioxide Radical Anion

According to the prevailing theory in the field of gaseous CO_2 reduction mechanisms, the formation of carbon dioxide anion radical intermediates is considered the rate-limiting step in the overall process. Electron spin resonance studies revealed the presence of radical anions in the CO_2 reduction system, and it was determined that the CO_2 radical anion possesses a bent structure with a bond angle of approximately $134°$[112–114]. However, there is an ongoing debate regarding the source of these carbon dioxide anion radicals, with some suggesting that they may originate directly from CO_2 molecules, while others propose that they may come from bicarbonate or other sources[11, 115, 116]. It is also worth noting that intermediate reactions may play a role in the formation of these intermediates, which are the primary chemical products of the CO_2 reduction.

Carbonate ions serve as precursors for CO_2 radical anions (Equation 2.118), which can also be generated through the reaction of formate ions in a specific manner (Equation 2.119-2.123) or through the action of hydroxyl radicals (Equation 2.124-2.127).

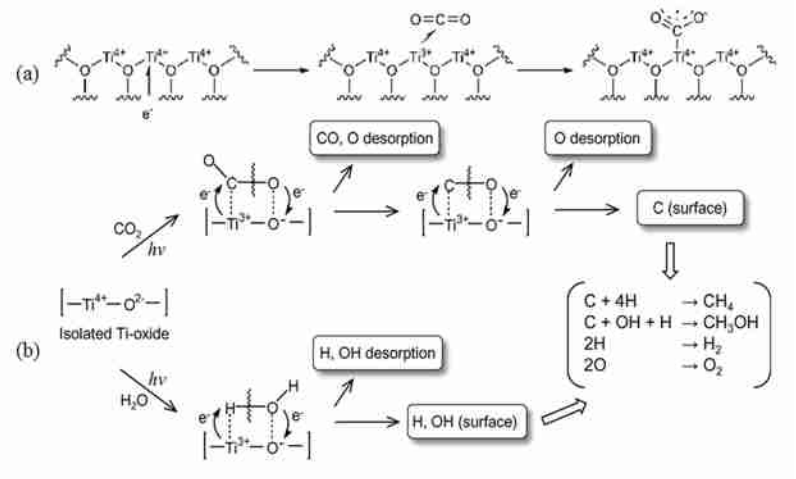

Figure 2.24: (a) The process by which CO_2 molecules are adsorbed and subsequently converted into $^{-\bullet}CO_2$ species on TiO_2 surfaces, as well as the concurrent formation of these species [110]. Reproduced from *Chem. Rev. 115 (2015) 12888–12935. ©2015 Americal Chemical Society* (b) Photoreduction of CO_2 to the reduced forms of anchored TiO_2 species [111]. Reproduced from *RSC Adv. 2 (2012) 3165. ©2012 Royal Society of Chemistry.*

$$CO_3{}^{2-} + e^- \longrightarrow CO_3{}^{3-} \longrightarrow {}^{-\bullet}CO_2 \tag{2.118}$$

$$HCOO^- \longrightarrow HCOO + e^- \tag{2.119}$$

$$HCOO \longrightarrow H + CO_2 \tag{2.120}$$

$$H + HCOO^- \longrightarrow H_2 + {}^{-\bullet}CO_2 \tag{2.121}$$

$$HCOO^- + e^- \longrightarrow HCOO_2{}^{2-} \tag{2.122}$$

$$HCOO^- + h^+ \longrightarrow {}^{-\bullet}CO_2 + H^+ \tag{2.123}$$

$$OH + HCO_2/HCO_2{}^- \longrightarrow H_2O + OCOH/{}^{-\bullet}CO_2 \tag{2.124}$$

$$H + HCO_2H/HCO_2{}^- \longrightarrow H_2 + OCOH/{}^{-\bullet}CO_2 \tag{2.125}$$

$$CO + OH \longrightarrow OCOH \tag{2.126}$$

$$OCOH \rightleftharpoons {}^{-\bullet}CO_2 + H^+ \tag{2.127}$$

Considering the aforementioned possibilities, it is plausible that the detected CO_2 anion radical is derived from the reactions outlined above (Equation 2.118-2.127) rather than from the addition of a single electron to CO_2(g). Carbon dioxide anion radicals are known to be short-lived and are prone to undergo transformation into oxalate in neutral and alkaline environments, or into CO_2 in the presence of a formic acid solution with a pH below 4. The formation of oxalate from the head-to-head recombination of CO_2 radicals occurs in the former scenario, whereas in the latter scenario, it results from the disproportionation of two OCOH radicals.

$$2\,OCOH \longrightarrow CO_2 + HCO_2H \tag{2.128}$$

$$OCOH + CO_2{}^- \longrightarrow HCO_2{}^- + CO_2 \tag{2.129}$$

$$2\,{}^{-\bullet}CO_2 \longrightarrow CO_3{}^{2-} + CO \tag{2.130}$$

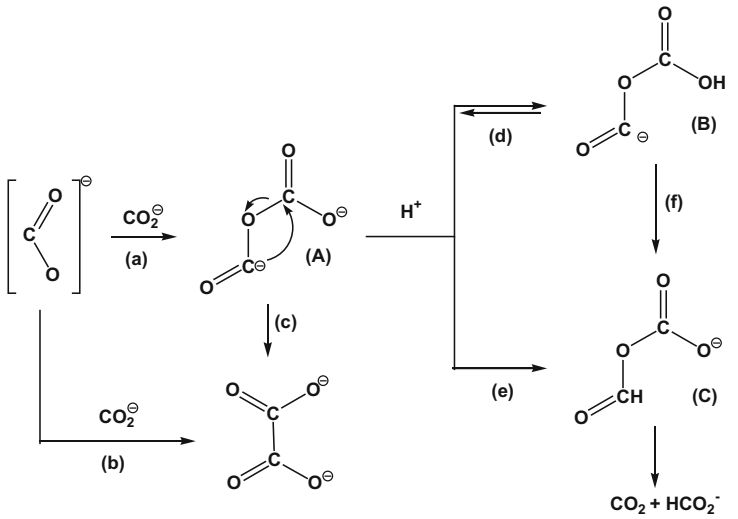

Figure 2.25: Depicts the bimolecular decay of the carbon dioxide radical anion [115]. Reproduced from *M. Aresta, A. Dibenedetto, E. Quaranta, Reaction Mechanisms in Carbon Dioxide Conversion, Springer-Verlag, Berlin Heidelberg, 2016. ©2016 Springer-Verlag.*

$$2\ {}^{-\bullet}\mathrm{CO_2} \longrightarrow {\mathrm{C_2O_4}}^{2-} \tag{2.131}$$

The bimolecular decay constant of CO_2 anion radicals was found to be approximately $1.0 \times 10^9\,\mathrm{dm^3 mol^{-1} s^{-1}}$ and independent of the pH in the range of 3-8 at a constant ionic strength[117]. Anion radicals can be stabilized using radical traps or solvents. More than 90% of carbon dioxide anions undergo head-to-tail recombination through hetero-C coupling, which forms a carbanion (A) as an intermediate. This intermediate can either rearrange into oxalate ions, which can be a source of CO and carbonate, or undergo a proton-catalyzed disproportionation reaction, resulting in CO_2, $HCO_2{}^-$, CO, or $HCO_3{}^-$ as the final products. Similarly, the homo-C-C coupling of two ${}^{-\bullet}\mathrm{CO_2}$ molecules with antiparallel spin leads to the formation of an oxalate anion (B). ${}^{-\bullet}\mathrm{CO_2}$ can react with ions present in the solution and is easily converted into CO_2 molecules[118, 119]. The nature of ${}^{-\bullet}\mathrm{CO_2}$ in water has been discussed in detail elsewhere[120]. Further research is needed to confirm the identity of the carbon dioxide radical anion in the CO_2 reduction system.

2.8 Role of Material Modifications

Surface engineering is a powerful technique for tuning the transport properties of charge carriers, and therefore, for the design of new semiconductor materials. This section analyzes the problems with surface engineering techniques and does not cover the state-of-the-art development. Significant studies have been conducted on these aspects, and it is recommended that readers follow the following references[121–127]. The application of doped semiconductors in the field of solar energy conversion started with the primary intention of enhancing the photon absorption cross-section of the photoactive materials, as well as the photoactivity. It is understandable that surface engineering techniques help to enhance the photoactivity towards thermodynamically favorable reactions, such as pollutant

degradation, which does not mean that the same can be true for all other solar energy utilization processes. It is also worth noting that the surface techniques used to date do not solve the problems existing in water splitting or other thermodynamically unfavorable reactions, such as the photoreduction of carbon dioxide[11, 12, 40].

Furthermore, the aforementioned statement regarding the increase in photoactivity remains marginal. The majority of studies in this area primarily focus on addressing the thermodynamic aspects of the reaction while neglecting the kinetic factors. It is important to recognize that a reaction with favorable thermodynamics may not progress efficiently if its kinetics are slow. This is particularly relevant for carbon dioxide reduction and water splitting, where both thermodynamic and kinetic factors must be controlled to achieve significant improvements in the process[128]. A reevaluation of this concept may shift the prevailing paradigm.

To date, a wide range of materials have been investigated, including oxides, sulfides, chalcogenides, oxynitrides, perovskites, carbon and carbon nitride-based materials, graphene analogs, and traditional semiconductors (III-V and, more recently, III-V nitrides)[129, 130]. However, no material satisfies all of the necessary conditions for the activation and conversion of carbon dioxide. The champion material must have an appropriate bandgap to absorb visible light and the band edge positions to provide energetic electrons for the reduction reaction. Additionally, the material must be able to execute proton-coupled electron transfer in a facile manner, possess good charge-transport properties and stability, and be composed of inexpensive and non-toxic earth-abundant elements. To address these challenges, various efforts have been made to engineer better materials for solar-fuel production.

1. Design of surface sites for successive CO_2 adsorption and subsequent activation
    - Design of step sites on the surface [131, 132]
    - Design of porous structures with large surface areas[133]
    - Design of high-energy facets[134, 135]
    - Surface modifications[136, 137]
    - Inducing surface oxygen vacancies[138]
2. Design of visible light active photocatalyst:
    - Heteroatom doping[139]
    - Solid solutions modified with nanoparticles[140]
    - Sensitization[141]
3. Design of photocatalyst with better charge separation and transportation:
    - Addition of co-catalysts[142, 143]
    - Construction of Heterojunctions[144–146]
    - Use of one-dimensional nanomaterials[147–149]
    - Incorporation of the Z-scheme system[150, 151]

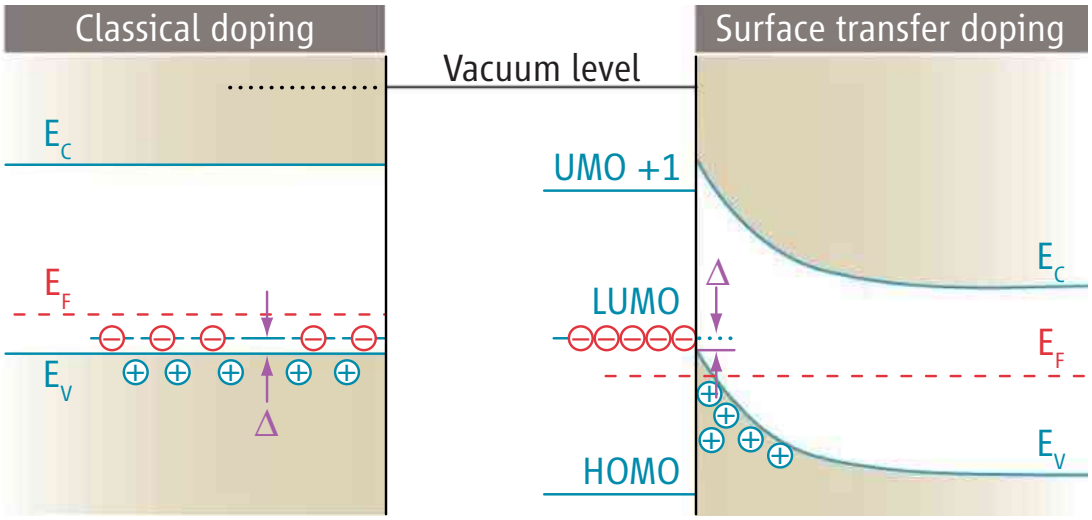

Figure 2.26: This band diagram depicts the process of classical p-type doping on the left-hand side and p-type surface-transfer doping on the right-hand side. The energy level of an electron in free space is used as a reference point; otherwise, it is known as the vacuum level. E_c represents the energy of the conduction band minimum and E_v signifies the energy of the valence band maximum [161]. Reproduced from *Science 313 (2006) 1057–1058. ©2006 American Association for the Advancement of Science.*

The bottleneck of carbon dioxide activation often results in only modest improvements in product yield through the design strategies employed. Therefore, discovering a photocatalyst with a high capacity to harness visible light may not be sufficient for carbon dioxide reduction unless it also possesses an appropriate band edge position to provide energetic electrons for the activation of carbon dioxide. A plethora of literature reviews is available on the design of catalysts for carbon dioxide reduction[152–159]. This discussion focuses on specific aspects of the development of efficient materials for carbon dioxide reduction.

2.8.1 Doped Semiconductors

Doping, which is achieved by adding impurities to a semiconductor matrix to modify its electrical characteristics, has frequently been employed in the electronics industry to control carrier generation and transport[160, 161]. Additionally, this technique has led to the emergence of cutting-edge electronic materials, including solid-state photomultipliers and resonant tunnelling transistors, in which impurities are introduced directly into the bulk of the semiconductor[161]. Moreover, dopant atoms can adsorb onto the surface lattice of a semiconductor, causing electronic interactions between the two, resulting in doping. This method also enables fine-tuning of the light-absorption properties of semiconductors (Figure 2.26). The incorporation of heteroatoms in semiconductors does not alter the reduction potential but rather creates intermediate states above the valence band[162–165]. The presence of heteroatoms enhanced the adsorption of CO_2 on the photocatalytic surface, facilitating more efficient electron transfer. Although catalyst modification increases the rate of competing reactions involved in CO_2 reduction, it also restricts

the increase in the product yield to a certain extent. Many previous studies have failed to consider the interaction of CO_2 with heteroatoms and have attributed the increase in product yield solely to the increased visible-light activity of the photocatalyst.

Let us consider semiconductors, such as titanium dioxide, which possess the ability to split water. To achieve efficient water splitting, a photovoltage of approximately $1.8\,\mathrm{eV}$, and as such, the band gap should be greater than $2\,\mathrm{eV}$. Photovoltage refers to the potential difference between two quasi-Fermi levels positioned closer to the conduction and valence bands. The introduction of a dopant into the surface layer creates an intermediate state above the valence band, which acts as the highest occupied molecular orbital (HOMO) level from which electrons are excited to the conduction band. As a result, the energy required to excite an electron in a doped system is less than that in an undoped system, but the oxidation potential of the latter is more pronounced than that of the former. Consequently, the photovoltage generated in the doped system was less than that in the undoped system because of the shift in the valence band quasi-Fermi level to a less positive value. The changes in the Fermi level that occur in the semiconductor alter the dark Fermi level equilibrium with the electrolyte, leading to a difference in band bending at the interface compared with the undoped system[58].

The effect of the surface space-charge layer on the semiconductor doping can be explained by these interfacial changes. By adding an optimal dopant concentration, the depletion region decreases to the photon penetration depth of the semiconductor (Figure 2.27). This resulted in the uniform generation of charge carriers in the space charge layer, reduction in the recombination rate, and enhanced charge transfer to the interface. At dopant concentrations higher than the optimal level, the depletion layer width decreases beyond the photon penetration depth, which reduces the number of charge carriers produced in that region and at the interface. Additionally, excess dopant concentration increases the recombination of charge carriers in the bulk region within the photon penetration depth or acts as a recombination center[58].

The charge density in the doped semiconductor cannot be overstated as it plays a crucial role in determining its interactions with the electrolyte. Alterations in the potential of the doped semiconductor in the electrolyte can significantly affect the kinetic stability of a material. As doping increases, the electrostatic repulsion between particles decreases, resulting in a decreased stability of the doped semiconductor colloids suspended in the electrolyte solution when the surface chemical groups are the same. This condition is particularly critical because doping affects surface chemistry, thereby exerting a significant influence on the stability of the material. The decrease in electrostatic potential with doping suggests the dominance of van der Waals forces, ultimately leading to particle precipitation or coagulation[166, 167].

The distribution of the electrostatic potential in an n-doped semiconductor-oxide-electrolyte system is illustrated in Figure 2.28, which demonstrates the relationship between the dopant concentration and potential distribution[167]. The oxide layer on the surface was uncharged and functioned as a capacitor. This figure depicts the alteration in the surface potential at the oxide-electrolyte interface resulting from doping. Doping has a significant impact on the potential distribution within the semiconductor because of screening, whereas its impact on

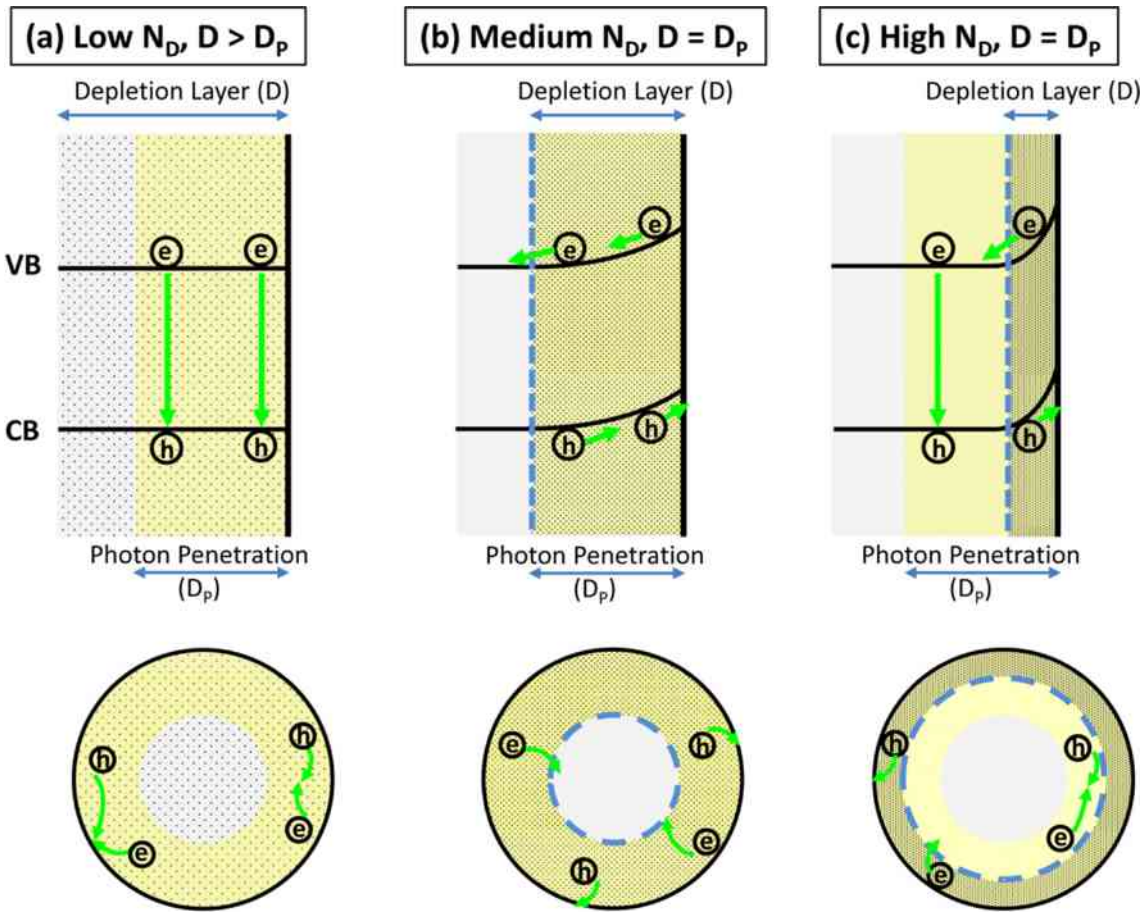

Figure 2.27: The impact of the dopant concentration on band bending and photogenerated carrier behavior in semiconductor nanoparticles can be observed in three distinct scenarios. At low dopant concentrations, the depletion layer length (D) exceeded photon penetration (D_P). At medium dopant concentrations, the depletion layer length (D) is equal to photon penetration (D_P). However, at high dopant concentrations, the depletion layer length (D) is less than the photon penetration length (D_P). In the latter scenario, the extreme upward band bending that results from the high N_D facilitates the efficient transfer of holes to the particle surface [58]. Reproduced from *Chem. Rev. 112 (2012) 5520–5551. ©2012 American Chemical Society.*

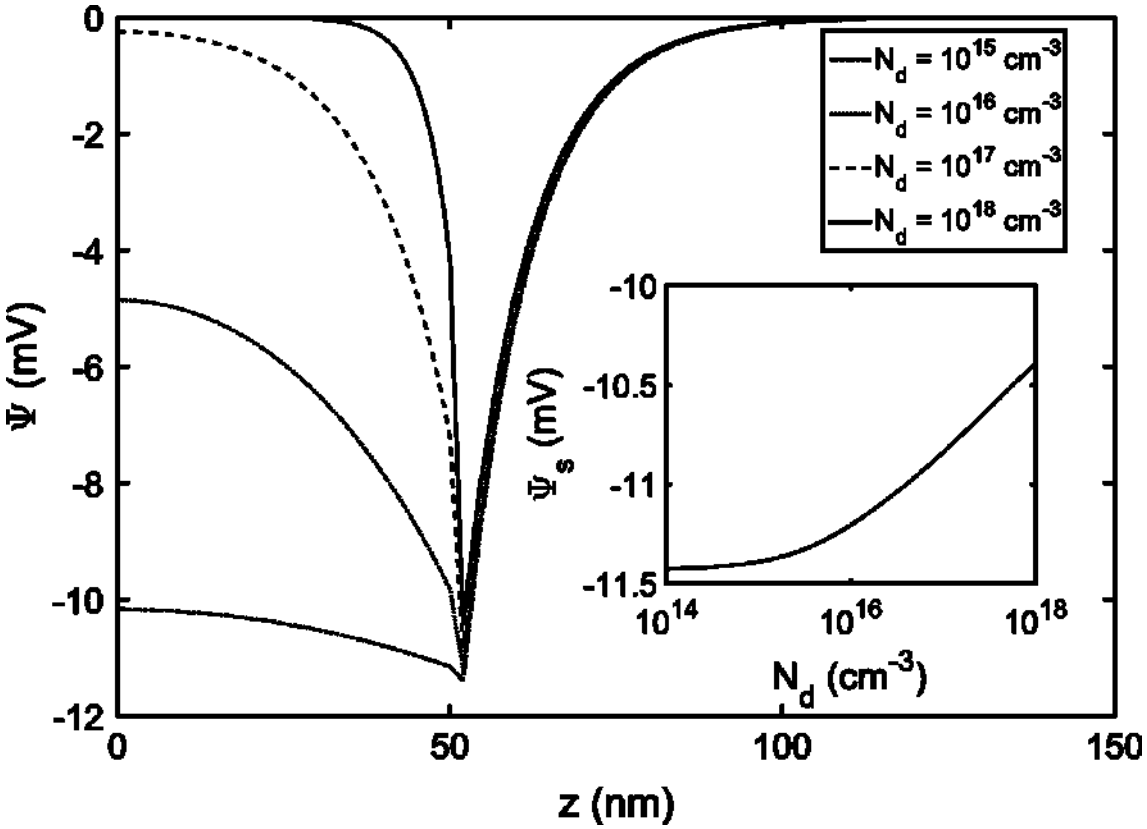

Figure 2.28: The potential distributions were graphed in relation to the distance z. The semiconductor/oxide interface was located at z = $50\,\mathrm{nm}$, whereas the oxide/-electrolyte interface was located at z = $52\,\mathrm{nm}$. The pH of the electrolyte solution was adjusted to 3. The different lines indicate the varying doping concentrations. The inset shows a plot of the surface potential Ψ_s versus N_d doping. The potential distributions are plotted for a constant N_d doping level of 10^{18} cm^{-3}. Additionally, the inset shows a plot of the surface potential Ψ_s in relation to the Debye length κ^{-1} [167]. Reproduced from *J. Colloid Interface Sci. 449 (2015) 409–415. ©2015 Elsevier B.V.*

the potential distribution in the electrolyte is relatively minor because the surface groups involved in charge regulation interact directly with the electrolyte[168].

The enhancement of CO_2 reduction, water splitting reaction, and hydrogen output was solely due to the increase in carrier concentration at the interface and the decrease in electron-hole recombination. However, this advancement was restricted, mainly because the influence of dynamic interactions at the interface was not considered. Additional experimental research is required to examine the stability of doped semiconductors and their effects on interfacial band energies.

2.8.2 Semiconductor Heterojunction

The use of semiconductor heterojunctions in photocatalytic water splitting relies on the formation of a photovoltage necessary for the process. Additionally, it allows the utilization of a broader range of semiconductors that do not possess band positions that overlap with the CO_2 and water redox potentials. The use of a heterojunction offers the advantage that the electric field formed at the interface

of the two semiconductors facilitates the movement of charge carriers in opposite directions. The literature provides details on various aspects and applications of heterojunction semiconductors as photocatalysts[169–175]. To be considered a champion for CO_2 reduction, a material must possess several qualities, including significant absorption characteristics, appropriate band alignment with respect to water redox potentials, rapid reaction kinetics, and long-term stability. Although the heterojunction assists in fulfilling the thermodynamic requirements of CO_2 reduction or water splitting, the marginal improvement in the reaction rate is attributed to a decrease in the recombination rate of the charge carriers rather than an increase in the reaction rate.

Let us now examine the four key characteristics of champion materials in the context of heterojunctions. It is well known that heterojunctions significantly enhance the absorption of light radiation depending on the type of semiconductor used. However, the transport of charge carriers between semiconductors can reduce their inherent potential of the charge carriers. Electrons and holes move towards semiconductors with lower oxidation/reduction potentials. Consequently, water oxidation occurs in a semiconductor with a lower oxidation potential and the reduction of CO_2 or water by electrons occurs at the semiconductor surface with a lower reduction potential. Under these circumstances, the full advantage of the increased light absorption may not be realized in the heterostructure.

The manner in which heterojunctions function in photon-assisted catalytic or photoelectrocatalytic processes is important for understanding the band alignment of individual semiconductors. There are four types of heterojunctions: Type I (straddling gap), Type 2 (staggered gap), Type 3 (broken gap), and conventional p-n junctions. However, the use of these theories to interpret the nature of electron transfer across semiconductor heterojunctions is not entirely accurate, necessitating a more reasonable approach based on the electron affinity and work function of individual semiconductors[176, 177]. Ag_2O/TiO_2 is an example of a Type 2 heterojunction (Figure 2.29), with the respective band positions of Ag_2O lying above those of TiO_2[178]. Therefore, electron transfer from Ag_2O to TiO_2 and hole transfer from TiO_2 to Ag_2O were expected. However, this was not the case because the built-in electric field was not continuous in the case of Ag_2O/TiO_2 (Figure 2.29). The use of heterojunctions to illuminate such interfaces can lead to a reduction in the efficiency of charge-carrier recombination at the interface, resulting in a system that becomes active under visible light but not under UV light. Further information on the construction of heterojunction interfaces has been discussed previously by researchers[179–182].

Furthermore, the heterojunction photoelectrode does not address kinetic factors, such as charge carrier mobility in two semiconductor systems or surface kinetics. As a result, a heterojunction photoelectrode cannot respond to significant CO_2 or water-splitting reactions until it effectively addresses these kinetic issues. Additionally, stability of both the material and the interface is another critical aspect that has not been considered in the literature. When designing the electrode, in addition to considering the electron affinity and work function characteristics, one must also examine the interactions at the three interfaces formed in the PEC cell, namely,

- The semiconductor/metal contact interface
- The heterojunction interface between the two semiconductors

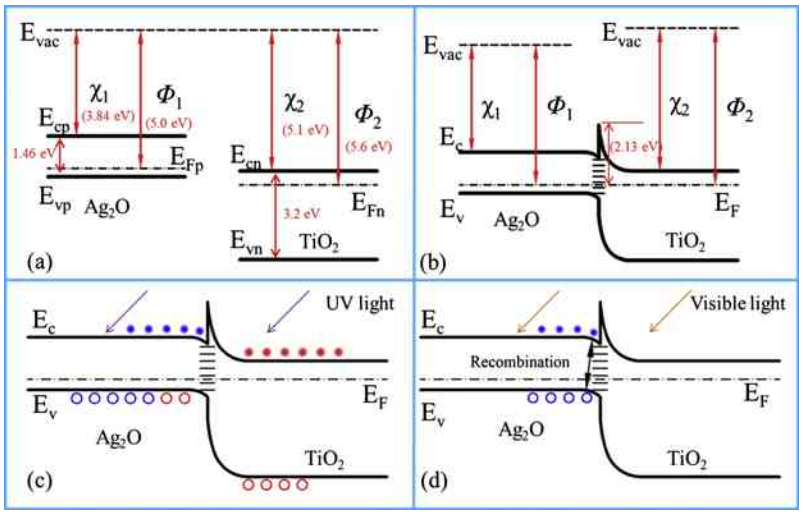

Figure 2.29: (a) Energy band structures of Ag_2O and TiO_2 before the formation of the nanoheterojunction. (b) Energy band structures of the p-Ag_2O/n-TiO_2 nano-heterojunction at the equilibrium state. (c) Energy band structures of the p-Ag_2O/n-TiO_2 nano-heterojunction upon UV irradiation. (d) Energy band structures of the p-Ag_2O/n-TiO_2 nano-heterojunction upon visible light irradiation [178]. Reproduced from *J. Colloid Interface Sci. 492 (2017) 167–175. ©2017 Elsevier B.V.*

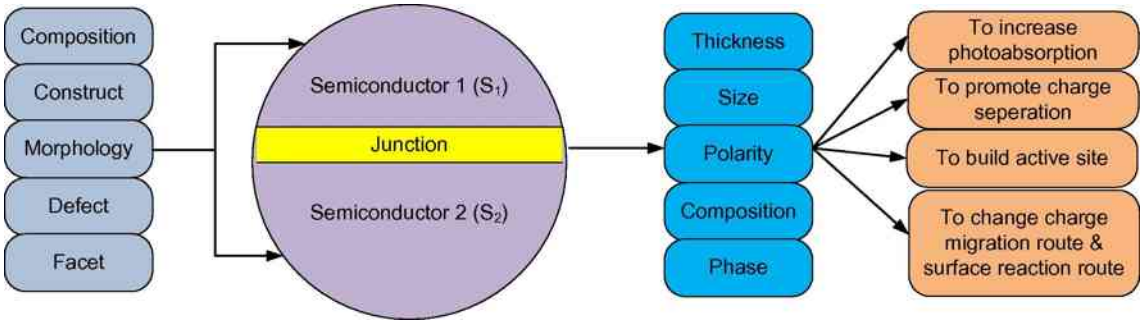

Figure 2.30: Adjusting and controlling factors of the heterojunction [183]. Reproduced from *Sci. Bull. 62 (2017) 599–601. ©2017 Science China Press.*

- The heterojunction semiconductor/electrolyte interface

Individual studies on each interface are required to interpret the nature of carrier transfer within heterojunction photocatalysts. To the best of our knowledge, there are no reports on the behavior of these three interfaces in the presence of simultaneous electric and photon fields or photoelectric fields. Additionally, a variety of other issues must be considered (Figure 2.30), including

- The optical and electrical properties of individual semiconductors and whether they meet the necessary criteria for the desired application of water splitting
- The nature of the electrostatic fields developed at the heterojunction interfaces and how defects in the parent semiconductors would affect this
- The thermodynamic stability of the interface formed during heterojunction formation

- Controlling the lattice mismatch at the interface

It should be emphasized that the built-in electric field and band bending at the heterojunction are symmetric only when the doping levels in the individual semiconductors are nearly equal[182]. This indicates that a significant amount of effort is required to develop highly efficient heterojunction photocatalysts. Without this, the interface may hinder the carrier flow and lead to instability. These challenges indicate that there is ample scope for advancement in the design of heterojunction photocatalysts for CO_2 reduction and overall water splitting[183].

2.8.3 Plasmon Semiconductor

The incorporation of plasmonic metals in photocatalysts aims to improve their optical absorption properties in the visible range and reduce the activation barrier for the desired reactions[184–186]. Among plasmonic metals, AuNPs have not been extensively studied, but they have shown the most promise owing to their resistance to oxidation[187]. Despite this, the mechanism of plasmon-enhanced water splitting remains unclear, and there is disagreement regarding the mode of oxygen evolution on plasmonic metal surfaces[188–190]. The proposed mechanisms based on direct electron transfer (DET) and plasmonic resonant energy transfer (PRET) do not provide a detailed explanation of the phenomena occurring at plasmonic interfaces[188–190]. A deeper understanding of these aspects is necessary to design more effective plasmonic-semiconductor interfaces. Recent research (Figure 2.31) has suggested that plasmon-generated holes at the semiconductor/plasmonic metal interface are responsible for water oxidation and have been identified as reaction sites[191].

In numerous studies, the function of plasmonic semiconductors has been compared with the dye sensitization mechanism, although this comparison was deemed irrelevant[187]. In a dye-sensitized photocatalyst, the potential dependence of the photocurrent is similar to that of a bare dye molecule. Conversely, the potential dependence of the plasmonic photocurrent in plasmonic semiconductors is similar to that of bare photoelectrodes[192]. This suggests that local surface plasmon resonance (LSPR) decay is triggered by UV light rather than by hot electrons, and the overall efficiency of the process depends on the distribution of electric and potential fields across the space charge layer. Additionally, there is the possibility of an upconversion mechanism at the plasmonic interface owing to energy pooling. The occurrence of energy-pooling-like phenomena between particles with identical physical properties such as shape, size, and separation distance must be below the plasmon wavelength. This underscores the significant impact of the shape, size, and concentration of the plasmonic metal on the photoelectrode surface on hot electron injection efficiency (HEIE)[193].

The hot electron injection efficiency (HEIE) performance of photocatalysts is influenced by the semiconductor support and the interface formed. The presence of surface defects can increase the Schottky barrier height of the plasmonic metal, thereby reducing HEIE. Therefore, it is essential to conduct a comprehensive surface treatment before depositing plasmonic metal on the photocatalyst surface to ensure optimal HEIE performance.

The real-time assessment of plasmon-mediated PEC water-splitting mechanisms is indispensable. The theoretical design of the interface only considers the work

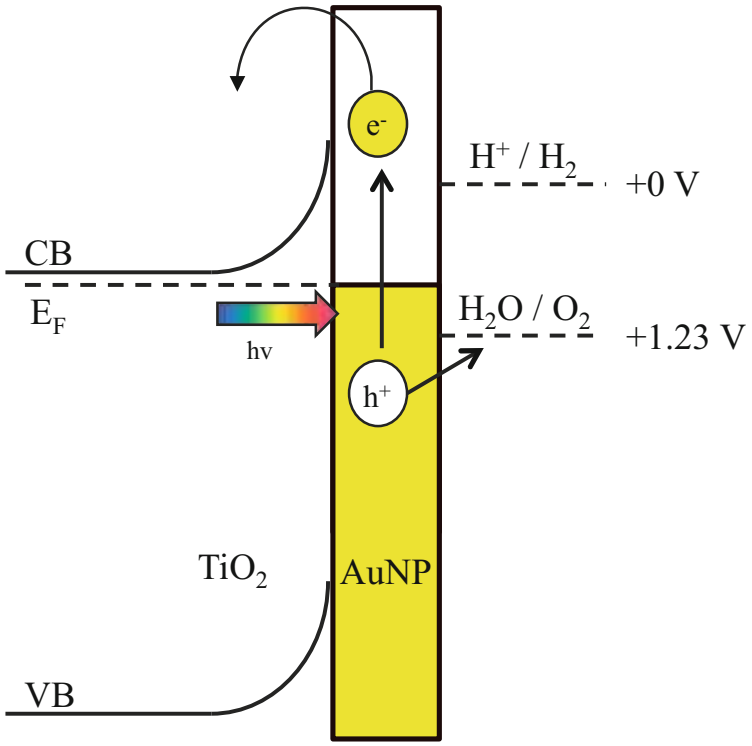

Figure 2.31: Schematic illustrating the process of electron injection from a metal nanoparticle into the conduction band of TiO_2 [188]. Reproduced from *Literature Review, In Surface Modifications and Growth of Titanium Dioxide for Photo-Electrochemical Water Splitting; Springer International Publishing: 2016, pp 5–45.* *©2016 Springer International Publishing Switzerland.*

functions of the photocatalyst and plasmonic metal, whereas the presence of water in the solution alters the work functions of both components[194]. These factors must be considered when examining the mechanisms of water oxidation in plasmonic photocatalysts. It is crucial to acknowledge that the interface may exhibit behavior distinct from that predicted by the theoretical photocatalyst/plasmonic interfaces.

The deposition of metal on surfaces facilitates electron transfer from the metal's d-state to the pi* state of a carbon dioxide molecule, leading to a change in the molecule's shape from linear to bent. Deposited metal typically serves as a reduction site. The presence of a co-catalyst aids in charge carrier separation and migration by creating an internal electric field between the semiconductor and the co-catalyst. The particle size, shape, and surface characteristics of the deposited metal atoms as well as their affinity for CO_2 are crucial for determining the final product yield. Smaller metal particles possess a higher Fermi level energy, which impedes semiconductor-to-metal electron transfer. In contrast, metals with larger particle sizes act as electron-hole recombination centers.

To achieve significant reductions in carbon dioxide emissions, the metal component must possess a strong affinity for adsorbing CO_2, which facilitates electron transfer to the adsorbed carbon precursors without altering the reduction potential of the photocatalyst. Instead, it decreased the barriers associated with CO_2 activation. The increased photoresponse can be attributed to surface plasmon

resonance, and the improved separation of charge carriers contributes to a higher photocatalytic activity and a faster rate of competing reactions. The incorporation of metal does not modify the energy of the electrons in the conduction band or alter the reduction potential, but it does enhance the efficient utilization of available electrons. These modifications are essential for the development of unexplored champion materials for CO_2 reduction, in which the efficient use of energetic electrons is critical.

2.8.4 Selection of Metal Surfaces

When selecting a metal for catalyst modification to facilitate CO_2 reduction, certain criteria must be considered. The selected metal must exhibit a high hydrogen evolution overpotential as hydrogen evolution becomes the dominant reaction. The type of reduction product formed depends on the overpotential of the metal surface for hydrogen evolution. Metals can be categorized into four groups based on their hydrogen evolution overpotentials (Figure 2.32)[195–197].

1. Pb, Hg, In, Sn, Cd, Tl, and Bi exhibit high hydrogen evolution overvoltages and minimal CO adsorption strengths. Consequently, the adsorbed carbon precursors participated in proton-coupled electron transfer, leading to the formation of formates through the following reactions:

$$^{-\bullet}\mathrm{CO_{2\ ads}} + \mathrm{H_2O} \longrightarrow \mathrm{HCOO^{\bullet}_{ads}} + \mathrm{OH^-} \tag{2.132}$$

$$\mathrm{HCOO^{\bullet}_{ads}} + \mathrm{e} \longrightarrow \mathrm{HCOO^-} \tag{2.133}$$

   Formate ions are also produced as a result of the reaction with adsorbed hydrogen.

$$^{-\bullet}\mathrm{CO_{2ads}} + \mathrm{H_{ads}} \longrightarrow \mathrm{HCOO^-} \tag{2.134}$$

   Except for mercury (Hg), which activates the CO_2 molecule at a potential of $1.6\,\mathrm{V}$ versus the normal hydrogen electrode (NHE), all other metals exhibit higher overvoltages for the reduction of CO_2.

2. The utilization of Au, Ag, Pd, Ga, and Zn in the presence of a medium hydrogen evolution overvoltage and weak CO adsorption promotes the formation of fuel precursor CO from the reduction of CO_2. The carbon atom of the CO_2 molecule coordinates with the metal surface, facilitating the formation of $^{\bullet}\mathrm{COOH}$ instead of $\mathrm{HCOO^{\bullet}}$. It is evident that CO is the predominant product of metals, as it stabilizes $^{-\bullet}\mathrm{CO_2}$ more efficiently and exhibits weak CO adsorption.

$$^{-\bullet}\mathrm{CO_2\ \ ads} + \mathrm{H_2O} \longrightarrow {}^{\bullet}\mathrm{COOH_{ads}} + \mathrm{OH^-} \tag{2.135}$$

$${}^{\bullet}\mathrm{COOH_{ads}} + \mathrm{e} \longrightarrow \mathrm{CO_{ads}} + \mathrm{OH^-} \tag{2.136}$$

   Additionally, CO_{ads} are generated through the direct reaction of the adsorbed hydrogen.

$$^{-\bullet}\mathrm{CO_2\,ads} + \mathrm{H_{ads}} \longrightarrow \mathrm{CO_{ads}} + \mathrm{OH^-} \tag{2.137}$$

3. Pt, Fe, Ni, and Ti exhibit a low overpotential for hydrogen evolution and demonstrate efficient adsorption of CO molecules on their surfaces. Consequently, the predominant reaction is hydrogen production, which reduces the availability of electrons for adsorbed CO_2 molecules. In this context, the adsorption of CO_2 onto a metal surface is fragile.

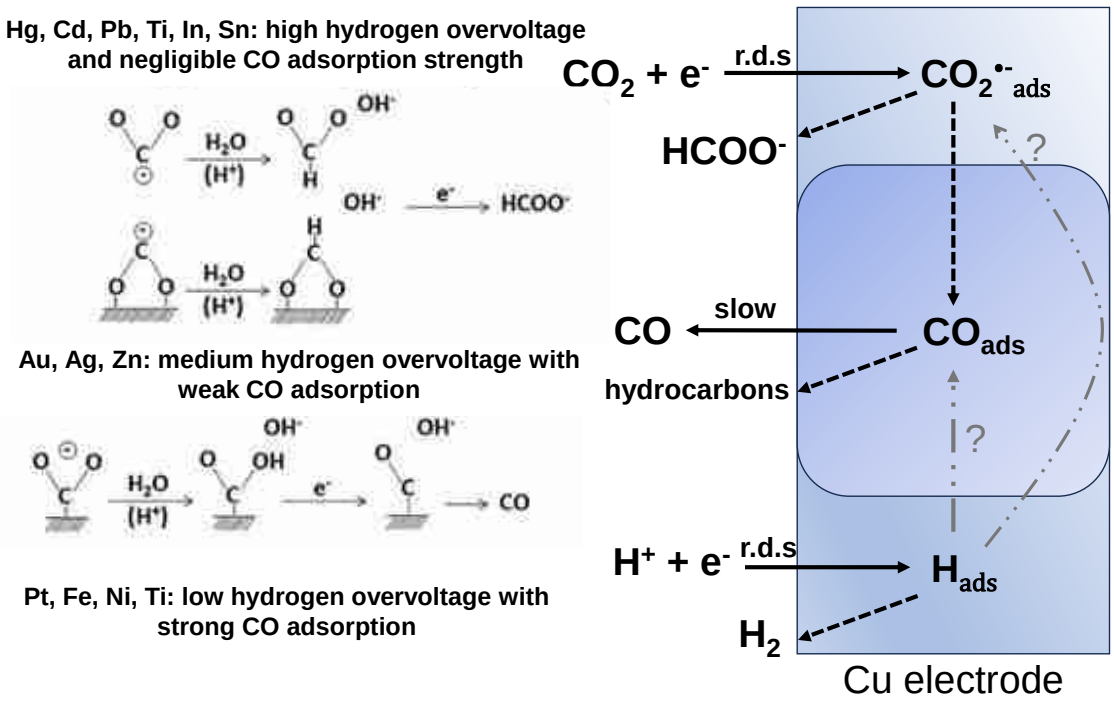

Figure 2.32: Reaction pathways for CO_2 reduction on different metal surfaces [195–197]. Reproduced from *Electrochim. Acta, 1994, 39, 1833-1839 - ©1994 Elsevier & ACS Symposium Series 2010, 55–76 - ©2010 American Chemical Society.*

4. CO_2 adsorption and subsequent hydrocarbon and alcohol formation in Cu, La, Ce, and Mg involve the intermediate formation of CO, which suppresses the hydrogen evolution reaction through surface adsorption. The interaction between CO and the metal surface facilitated the simultaneous reduction of CO, leading to the formation of hydrocarbons and alcohols.

An efficient catalyst for the reduction of CO_2 must be capable of initiating the protonation of adsorbed CO to form either COH or CHO surface species while simultaneously demonstrating limited activity towards competing hydrogen evolution reactions. Peterson and Norskov[198] have theoretically proposed strategies for the identification of champion catalysts for CO_2 reduction with reduced overpotential (Figure 2.33), which may also be applicable to photocatalyst surfaces.

- Alloying: The alloying process can have a significant impact on the binding of CO and CHO to the catalyst surface. Carbon atoms tend to form an upright and planar geometry on the surface, whereas the binding of CHO* is influenced by the affinity of the catalyst material for carbon and oxygen. To stabilize CHO* without disrupting CO*, it may be necessary to introduce an element with high affinity for oxygen into the catalyst matrix. However, care must be taken to maintain a balance in the introduction of this element, as an imbalance could alter the potential-determining step of the reaction.

- Ligand Stabilization: The stabilization of ligands in close proximity to CHO* can be achieved through geometrically compatible interactions. This arrangement leads to stabilization of the planar complex while simultaneously preserving the integrity of CO*.

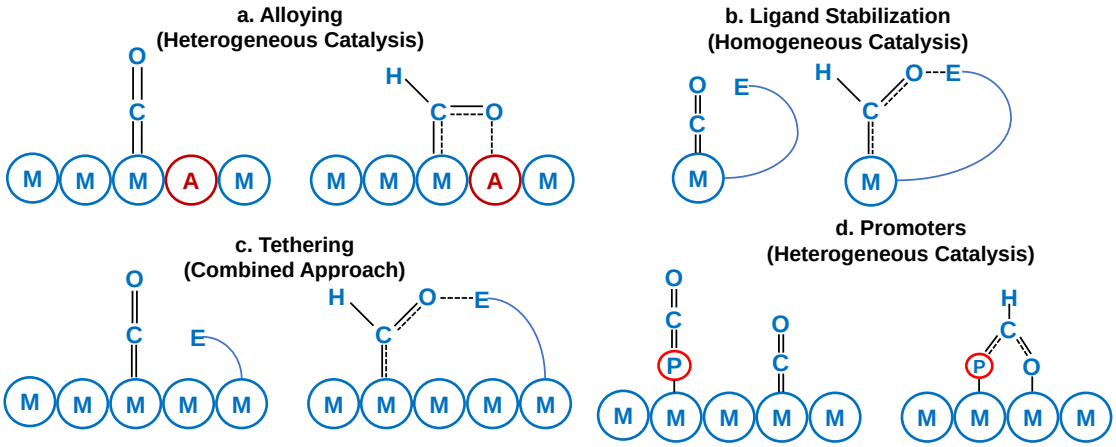

Figure 2.33: The strategies that have been suggested for the design of champion catalysts for CO_2 reduction encompass a range of approaches, including (a) the use of alloys, (b) the stabilization of ligands, (c) the implementation of tethering, and (d) the incorporation of promoters [198]. Reproduced from *J. Phys. Chem. Lett. 3 (2012) 251–258. ©2012 American Chemical Society.*

- Tethering: The tethering process involves interaction of a ligand with the surface, specifically with adsorbed CHO molecules.
- Promoters: The incorporation of promoters can influence the binding affinity of the adsorbates. In this context, the promoter serves to enhance the stability of the adsorbate complex through bidentate binding while simultaneously facilitating CO adsorption.
- Hydrogen Bond Stabilization: Stabilization of hydrogen bonds is a crucial aspect of surface chemistry. In particular, the hydrogen bond donors present near the surface may interact with adsorbed species, such as CO* and CHO*, in various ways because of differences in their binding geometries. The presence of a strong hydrogen bonding group results in the preferential stabilization of COH* on the surface compared to that of CO*. This phenomenon is known as hydrogen-bond stabilization.

Owing to the highly site-specific nature of CO_2 reduction, even minor variations in the material properties can significantly impact the overall reaction. The incorporation of heteroatoms or the deposition of metal on the surface of the catalyst can block the active sites, thereby hindering the reaction. In this regard, the development of metal-free materials, such as carbon nitride, offers a promising alternative for CO_2 transformation[81, 199–201]. However, the limited depth of research on this material currently restricts its full potential. Therefore, a comprehensive investigation of the fundamental mechanistic aspects of CO_2 reduction is necessary to elucidate the design of active materials.

2.9 The Interface Challenge: Competing Chemical Reactions in CO_2 Reduction

2.9.1 Hydrogen Evolution Reaction

The primary factor influencing hydrogen evolution from a photoelectrode is the nature of the active sites on the surface, which significantly reduces the required overpotentials. This suggests that a photoelectrode that generates sufficient photovoltage and possesses the desired band-edge positions will not evolve appreciable amounts of hydrogen if the surface is inactive. The mechanism for hydrogen evolution on a catalyst surface proceeds through either the Volmer-Heyrovsky or the Volmer-Tafel mechanism [202–204].

$$\text{Volmer Step} : \mathrm{H^+ + e^- + {}^* \longrightarrow H^*} \tag{2.138}$$

$$\text{Heyrovsky Step} : \mathrm{H^+ + H^* + e^- \longrightarrow H_2 + {}^*} \tag{2.139}$$

$$\text{Tafel Step} : \mathrm{2H^* \longrightarrow H_2 + 2^*} \tag{2.140}$$

The development of an active photoelectrode for hydrogen evolution requires adherence to the Sabatier principle, which involves binding reaction intermediates to the surface in a manner that is neither too weak nor firm. Weak adsorption to the surface can limit the overall reaction rate by restricting the Volmer step, whereas strong adsorption can hinder the desorption of intermediates and reduce the overall reaction rate. Therefore, an active hydrogen evolution catalyst must meet the necessary but insufficient condition of $\Delta G_{H^*} \approx 0$[205, 206]. Experimental data on the current density versus ΔG_H for various catalyst materials reveal a volcano-type relationship[207–209](Figure 2.34).

The key to designing a catalyst material is the ability to control the binding energies of the active intermediate species involved in a specific process and direct them to the active surface sites. Although volcano plots provide valuable information for catalyst design in the HER, a quantitative measurement of the absolute reaction rate is necessary for each class of materials. This is because the kinetic barrier associated with a process can vary depending on the material used and pH of the electrolyte[210]. It is noteworthy that the catalytic activity in the volcano curve changes with pH or kinetic barrier and not from left to right, suggesting the suitability of the descriptor in designing materials for the HER under a variety of conditions[211].

The most effective catalyst for the hydrogen evolution reaction (HER) is platinum, which sits at the peak of the volcano curve and requires negligible overpotential in an acidic medium[202]. However, owing to its high cost and low abundance, the widespread use of Pt is limited. To find new, earth-abundant materials, scientists have studied MoS_2 edge sites and discovered that they have a relatively low activation energy of $\Delta G_H \approx 0.08\,\mathrm{eV}$ at 50% hydrogen coverage, close to the thermo-neutral value[212]. Further research has shown that the hydrogen evolution activity of MoS_2-based systems depends on the length of the perimeter of the edge sites rather than the increased surface area[213, 214]. By nanostructuring MoS_2 into a three-dimensional porous structure with a double-gyroid morphology, researchers have observed a marginal but 2 to 4 fold increase in turnover

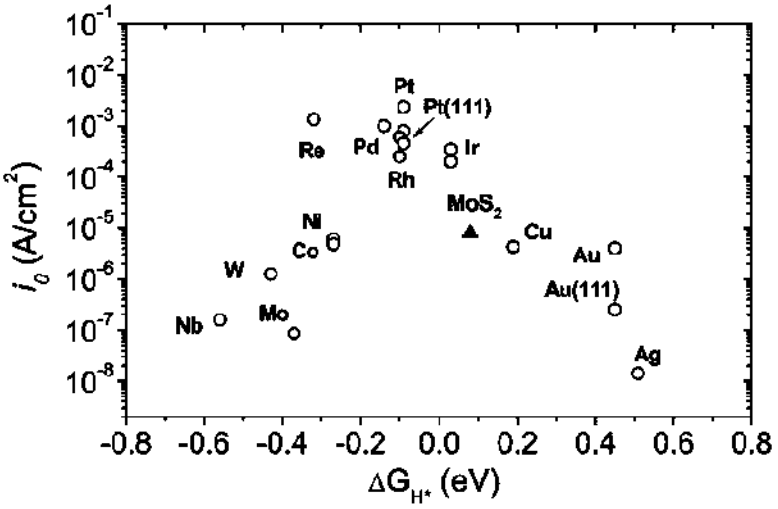

Figure 2.34: The plots depict the measured exchange currents for hydrogen evolution across various metal surfaces in relation to the calculated hydrogen chemisorption energy per atom. Additionally, the results of the simple kinetic model were plotted in relation to the free energy associated with hydrogen adsorption [205]. Reproduced from *J. Electrochem. Soc. 152 (2005) J23–J26. ©2005 ECS-The Electrochemical Society*.

frequency[215]. However, this approach has drawbacks, such as longer transport distances to the active sites, which increase the resistance to electron flow, making well-designed lower-dimensional materials preferable for vectorial electron transfer reactions, such as water splitting.

There have been studies on increasing the number of active edge sites on the molybdenum disulfide surface to improve the overall activity of the electrode; however, the reaction rate is still limited owing to the small fraction of edge sites responsible for the activity. To overcome the limitations of Pt-based catalysts, it is necessary to study alternative systems with higher intrinsic activities. Metal nitrides[216], carbides[217, 218], borides[219], phosphides[219, 220], and selenides[221] are examples of catalysts that exhibit higher hydrogen evolution reaction activity, comparable to that of Pt, in terms of the overpotential required to reach a current density of $10\ mA\ cm^{-2}$. However, these systems require high catalyst loading and surface area, which limit their potential, especially when considering the turnover frequency (TOF$_{avg}$) under acidic conditions. In a basic medium, the Ni-Mo system demonstrated a lower overpotential to reach $10\ mA\ cm^{-2}$, but its TOF was significantly lower than that of Pt[222]. Developing a catalyst system for the hydrogen evolution reaction remains a critical challenge that requires further effort, and the design of such a system should consider both long-term stability and activity to be technologically viable.

2.9.2 Oxygen Evolution Reaction

The oxygen evolution reaction (OER) is an essential process that entails the transfer of four excitons and accounts for the sluggish kinetics of photoelectrochemical (PEC) water splitting. The main intermediates in OER include O*, HO*, and HOO*[202]. The M-O bonding interactions significantly contributed to the stabilization of the

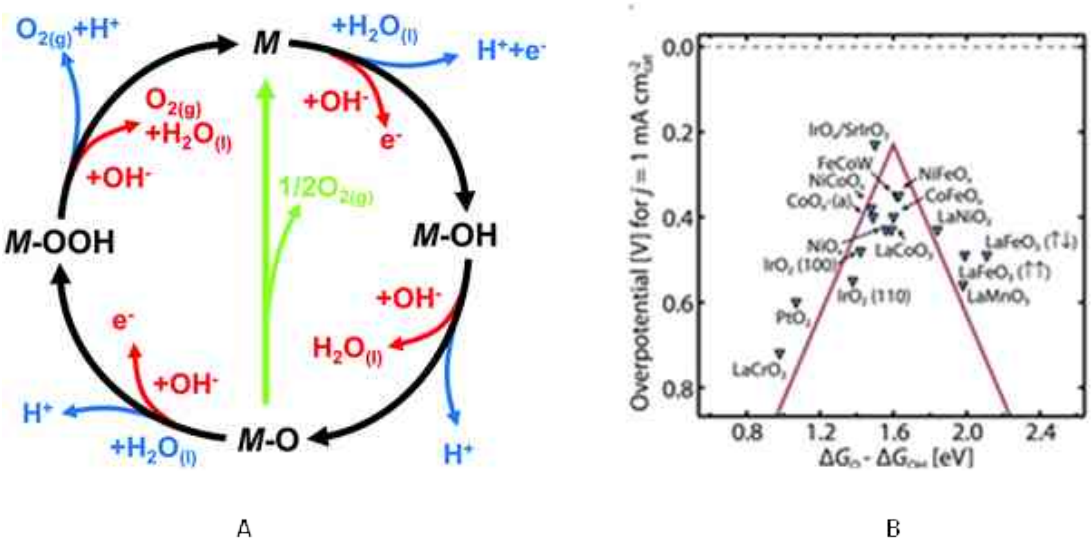

Figure 2.35: (A) The mechanism by which oxygen evolves under acidic conditions (represented by blue lines) differs from that under alkaline conditions (represented by red lines) [223]. (B) Activity trends towards the oxygen evolution reaction across metal oxide surfaces [224]. ((A) Reproduced from *Chem. Soc. Rev. 46 (2017) 337–365. ©2017 The Royal Society of Chemistry*. (B) Reproduced from *ChemCatChem 3 (2011) 1159–1165. ©2011 John Wiley & Sons, Inc.*)

reaction intermediates on the surface and exerted a considerable influence on the overall water-splitting efficiency. Under acidic conditions, OER (Figure 2.35) can be represented as[223]:

$$\begin{aligned} \text{Cathode Reaction} &: 4\,H^+ + 4\,e^- \longrightarrow 2\,H_2 \\ \text{Anode Reaction} &: 2\,H_2O \longrightarrow O_2 + 4\,H^+ + 4\,e^- \\ \text{Overall Reaction} &: 2\,H_2O \longrightarrow 2\,H_2 + O_2 \end{aligned} \tag{2.141}$$

$$\begin{aligned} {}^* + H_2O &\longrightarrow HO^* + H^+ + e^- \\ HO^* + OH^- &\longrightarrow O^* + H_2O + e^- \\ 2\,O^* &\longrightarrow 2\,{}^* + O_2 \\ O^* + H_2O &\longrightarrow HOO^* + H^+ + e^- \\ HOO^* + H_2O &\longrightarrow {}^* + O_2 + H^+ + e^- \end{aligned} \tag{2.142}$$

In akaline medium,

$$\begin{aligned} \text{Cathode Reaction} &: 4\,H_2O + 4\,e^- \longrightarrow 2\,H_2 + 4\,OH^- \\ \text{Anode Reaction} &: 4\,OH^- \longrightarrow 2\,H_2 + 2\,H_2O + 4\,e^- \end{aligned} \tag{2.143}$$

$$\begin{aligned} OH^- + {}^* &\longrightarrow HO^* \\ HO^* + OH^- &\longrightarrow O^* + H_2O \\ 2\,O^* &\longrightarrow 2\,{}^* + O_2 \\ O^* + OH^- &\longrightarrow HOO^* + e^- \\ HOO^* + HO^- &\longrightarrow {}^* + O_2 + H_2O \end{aligned} \tag{2.144}$$

Metal oxide catalysts, including perovskites, RuO_2, IrO_2, IrOx/$SrIrO_3$, Ni-oxides, Co-oxides, Mn-oxides, and tertiary oxyhydroxides, are widely recognized as efficient electrocatalysts for OER[223]. In analogy to the HER, a volcano-type relationship (Figure 2.35b) can be established for the OER by using ($\Delta G^\circ_{\mathrm{OER}} - \Delta G^\circ_{\mathrm{H}}$) as a descriptive parameter[224]. By stabilizing HOO^* relative to the HO^* intermediate on the catalyst surface, the fundamental overpotential of the reaction can be bypassed.

2.9.3 Sacrificial Reagent and Reactive Oxygen Species

The main advantage of photocatalysts is the presence of redox sites on the same surface, which is a disadvantage in many cases, as discussed in subsequent sections. Numerous studies have comprehensively reviewed the role of sacrificial reagents in photocatalytic reactions[225–230]. The introduction of sacrificial reagents into the reaction system complicates the overall reduction process and absorbs some of the irradiated light. The production of chemicals via sacrificial moieties is not economically viable, as the sacrificial reagents initially increase the product yield, but then disintegrate into various products. Commonly used sacrificial reagents include organic electron donors such as methanol, organic acids, and hydrocarbons, which are the primary products of CO_2 reduction. Therefore, the use of such sacrificial agents is not suitable for CO_2 reduction.

Inorganic electron donors, including sulfide (S^{2-}) and sulfite ($SO_3{}^{2-}$), are another set of sacrificial reagents that primarily capture holes from the valence band and convert them into the corresponding ions.

$$\begin{aligned}
2\,H_2O + 2\,e^- &\longrightarrow H_2 + 2\,OH^- \\
SO_3{}^{2-} + 2\,OH^- + 2\,h^+ &\longrightarrow SO_4{}^{2-} + H_2O \\
2\,SO_3{}^{2-} + 2\,h^+ &\longrightarrow S_2O_6{}^{2-} \\
2\,S_2{}^- + 2\,h^+ &\longrightarrow S_2{}^{2-} \\
SO_3{}^{2-} + S^{2-} + 2\,h^+ &\longrightarrow S_2O_3{}^{2-} \\
SO_3{}^{2-} + S^{2-} + 2\,h^+ &\longrightarrow S_2O_3{}^{2-} \\
S_2{}^{2-} + SO_3{}^{2-} &\longrightarrow S_2O_3{}^{2-} + S^{2-}
\end{aligned} \tag{2.145}$$

Although much of the current literature focuses on direct hole oxidation reactions, inorganic electron donors can undergo a series of electron-coupled proton transfer reactions within the potential range of CO_2 reduction.

$$\begin{aligned}
2\,SO_3{}^{2-} + 2\,e^- + H^+ &\longrightarrow S_2O_4{}^{2-} + 2\,H_2O_4{}^{2-} + 2\,H_2O && E^\circ = 0.256\,\mathrm{V} \\
2\,SO_3{}^{2-} + 2\,e^- + 2\,H_2O &\longrightarrow S_2O_4{}^{2-} + 4\,OH^- && E^\circ = -1.13\,\mathrm{V} \\
S_2O_6{}^{2-} + 2\,e^- + 2\,H_2O &\longrightarrow 2\,H_2SO_3 && E^\circ = 0.569\,\mathrm{V} \\
S_2O_6{}^{2-} + 2\,e^- + 4\,H^+ &\longrightarrow 2\,HSO_3{}^- && E^\circ = 0.464\,\mathrm{V} \\
S_2O_6{}^{2-} + 2\,e^- &\longrightarrow 2\,SO_3{}^{2-} && E^\circ = 0.037\,\mathrm{V} \\
SO_4{}^{2-} + 2\,e^- + 4\,H^+ &\longrightarrow S_2O_6{}^{2-} + 2\,H_2O && E^\circ = -0.253\,\mathrm{V} \\
S_2O_6{}^{2-} + H_2O &\longrightarrow H_2SO_3 + SO_4{}^{2-} && E^\circ = 0.41\,\mathrm{V} \\
S_2O_2{}^{2-} + 6\,H^+ &\longrightarrow 2\,S_5O_6{}^{2-} + 3\,H_2O && \Delta G^\circ = -29.6\,\mathrm{kJ\,mol^{-1}}
\end{aligned} \tag{2.146}$$

The incorporation of carbonate or bicarbonate ions results in increased stoichiometric hydrogen and oxygen evolution from water[231–237] and suppresses the reverse reaction of H_2 and O_2 with water on the deposited metallic surfaces. This promoted the splitting of water into H_2 and O_2. Surprisingly, many current studies do not consider these possibilities in the context of aqueous-phase CO_2 reduction, despite these facts being well-established. It is more thermodynamically feasible to undergo direct hole oxidation of HCO_3^-/CO_3^{2-} than proton-coupled electron reduction. In aqueous-phase reduction, the CO_2 precursors enhance the rate of competing hydrogen and oxygen evolution reactions.

$$\begin{aligned} \mathrm{Na_2CO_3} &\longrightarrow 2\,\mathrm{Na^+} + \mathrm{CO_3^{2-}} \\ \mathrm{CO_3^{2-}} + \mathrm{h^+} &\longrightarrow \mathrm{HCO_3^-} \\ \mathrm{HCO_3^-} + \mathrm{h^+} &\longrightarrow \mathrm{HCO_3^\bullet} \\ \mathrm{HCO_3^\bullet} &\longrightarrow \mathrm{H^+} + \mathrm{CO_3^{\bullet -}} \\ 2\,\mathrm{CO_3^{\bullet -}} &\longrightarrow \mathrm{C_2O_6^{2-}} \\ \mathrm{C_2O_6^{2-}} + 2\,\mathrm{h^+} &\longrightarrow \mathrm{O_2} + 2\,\mathrm{CO_2} \end{aligned} \tag{2.147}$$

Recent studies have shown that the presence of carbonate ions in solution significantly increases the efficiency of the water-splitting reaction on metal-supported photocatalysts[238–240]. Detailed investigations revealed that the impact of carbonate on hydrogen evolution is more pronounced in TiO_2 than in other materials. Based on the effects of carbonate addition, photocatalysts can be grouped into four categories[241].

1. The first group comprises various photocatalysts including Pt/TiO_2, RuO_2/TiO_2, $NiOx/TiO_2$, Rh/TiO_2, Cu/TiO_2, Pt/ZrO_2, $Pt/K_4Nb_6O_7$, $Pt/K_2Ti_6O_{13}$, and $Pr/Na_2Ti_6O_{13}$. These photocatalysts can split water in the presence of carbonates.

2. The second category encompasses several photocatalysts, such as RuO_5/Ta_2O_5, $Rh/SrTiO_3$, $NiOx/SrTiO_3$, $RuO_2/Na_2Ti_6O_{13}$, $RuO_2/K_2Ti_6O_{13}$, and $RuO_2/BaTi_4O_6$, which demonstrate increased activity upon incorporation of carbonates.

3. The third category consists of photocatalysts such as RuO_2/ZrO_2 and $Pt/SrTiO_3$, which exhibit stable activity levels in the presence of carbonates.

4. The presence of carbonate ions causes a decrease in the activity of certain compounds, such as sodium tantalate ($NaTaO_3$), lithium tantalate ($LiTaO_3$), potassium tantalate ($KTaO_3$), barium tantalate ($Ba_2Ta_2O_6$), strontium tantalate ($Sr_2Ta_2O_6$), strontium tantalate ($Sr_2Ta_2O_7$), and strontium niobate ($Sr_2Nb_2O_7$).

Reactive oxygen species (ROS) are critical components of the photocatalytic reduction of CO_2. During the process, in situ oxygen generated through water oxidation captures an electron from the conduction band and transforms it into a superoxide radical with a higher oxidation potential. The products formed during the reduction of CO_2 are highly susceptible to oxidative attacks by ROS. Hydrocarbon oxidation produces CO_2 in the reaction system, and it is possible that the carbon atoms undergo multiple reduction reactions in a cyclic manner. The primary challenge

is to control the activity of the in situ-produced oxygen and ROS in the reaction system. Further information on the production and reactions of ROS is presented in Table 2.3[242].

Table 2.3: Common reactions of reactive oxygen species in aqueous solution [242]. Reproduced from *J. Phys. Chem. Ref. Data 14 (1985) 1041–1100. ©1985 AIP Publishing*.

Reactions	Rate Constant, k ($L\,\mathrm{mol}^{-1}\,\mathrm{s}^{-1}$)
$HO_2^\bullet/O_2^\bullet + H_2CO_3/HCO_3^-/CO_3^{2-} \longrightarrow HO_2^- + CO_3^-$	0.04 at pH 10.1
$O_2^\bullet + {}^\bullet CO_3^- \longrightarrow CO_3^{2-} + O_2$	$4 \pm 1 \times 10^8$
$HO_2^\bullet + Cu^+ \longrightarrow Cu^{2+} + H_2O_2$	2.3×10^9
$HO_2^\bullet + Cu^{2+} + H^+ + Cu^+ + O_2$	1×10^9
$O_2^\bullet + Cu^+ \longrightarrow Cu^+ + O_2$	4.81×10^9
$O_2^\bullet + Cu(HCO_2)^+ \longrightarrow O_2 + Cu(HCO_2)$	1.7×10^8
$HO_2^\bullet/O_2^\bullet + H_2 \longrightarrow H + H_2O_2$	< 1
$O_2^\bullet + H^+ \longrightarrow HO_2^\bullet$	$5 \pm 1 \times 10^{10}$
$HO_2^\bullet + OH^\bullet \longrightarrow H_2O_3$	0.71×10^{10}
$O_2^\bullet + OH^\bullet \longrightarrow OH^- + O_2$	1.1×10^{10}
$HO_2^\bullet + H_2O_2 \longrightarrow OH + H_2O + O_2$	0.5
$O_2^\bullet + H_2O_2 \longrightarrow OH^- + OH + O_2$	0.13
$O_2^\bullet + HO_2^- \longrightarrow H_2O_2 + O_2$	< 2
$HO_2^\bullet / O_2^\bullet + SO_3^{2-} \longrightarrow SO_3^- + OH^- + H_2O_2$	82
$HO_2^\bullet/O_2^\bullet + I_2 \longrightarrow I_2^- + H^+ + O_2$	1×10^8
$O_2^\bullet + I_2 \longrightarrow I_2^- + O_2$	5.5×10^9
$O_2^\bullet + I_3^- \longrightarrow I_2^- + I^- + O_2$	8×10^8

Observations have revealed the occurrence of carbonate anion radicals, resulting from the interaction of hydroxyl radicals with carbonate species in the system. Furthermore, it has been noted that hydroxyl radicals engage in a series of reactions with other inorganic species present in the system (as detailed in Table 2.4)[119].

$$\begin{aligned} \mathrm{CO_3^{2-} + HO^\bullet} &\longrightarrow \mathrm{CO_3^{-\bullet} + HO^-} \\ \mathrm{CO_3^{2-} + h\nu} &\longrightarrow \mathrm{CO_3^{-\bullet} + e_{aq}^-} \end{aligned} \tag{2.148}$$

The photooxidation of methanol has been proposed to occur via two distinct mechanisms: direct hole oxidation and oxidation mediated by $^\bullet$OH radicals, which are formed through the oxidation of surface-adsorbed water[243]. According to previous studies, the oxidation of methanol is favored by hydroxyl radicals when water is the dominant surface species. Conversely, direct hole oxidation was the preferred method in all other cases[243].

$$\begin{aligned} \mathrm{CH_3OH + {}^\bullet OH} &\longrightarrow \mathrm{{}^\bullet CH_2OH + H_2O\,(93\,\%)} \\ \mathrm{CH_3OH + {}^\bullet OH} &\longrightarrow \mathrm{CH_3O^\bullet + H_2O\,(7\,\%)} \\ \mathrm{{}^\bullet CH_2OH + O_2} &\longrightarrow \mathrm{HCHO + HO_2^\bullet} \\ \mathrm{CH_3OH + h^+} &\longrightarrow \mathrm{{}^\bullet CH_2OH + H^+} \\ \text{Current Doubling Effect}: \mathrm{{}^\bullet CH_2OH} &\longrightarrow \mathrm{HCHO + H^+ + 2\,e_{CB}^-} \end{aligned} \tag{2.149}$$

Table 2.4: Common reactions involving carbonate radicals in aqueous solution. Extracted from [119]. Reproduced from *J. Phys. Chem. Ref. Data 19 (1990) 413–513. ©1990 AIP Publishing*

Reactions	Rate Constant, k ($M^{-1}\,s^{-1}$)
$^{\bullet}CO_3^- + {}^{\bullet}CO_3^- \longrightarrow CO_2 + CO_4^{2-}$	$2k = 1.2 \times 10^7$ at pH 8.4-13.5
$^{\bullet}CO_3^- + O_2^- \longrightarrow CO_3^{2-} + O_2$	1.5×10^9 at pH 11.6
$^{\bullet}CO_3^- + H_2O_2$	8×10^5 at pH 8-9
$^{\bullet}CO_3^- + HO_2^-$	5.6×10^7 at pH 13-14
$^{\bullet}CO_3^- + CH_3CH_2OH + OH^- \longrightarrow CO_3^{2-} + CH_3CHOH + H_2O$	$1.5 - 1.7 \times 10^4$ at pH 12.5
$^{\bullet}CO_3^- + {}^{\bullet}CH_3 \longrightarrow CH_3OCO_2^-$	$3 \pm 1 \times 10^9$

The same process applies to all alcohols that contain hydrogen-bearing hydroxyl groups attached to the alpha carbon atom, as well as formate ions. These compounds produce $^{-\bullet}CO_2$ as the reducing intermediate, which is thought to be the primary product of CO_2 reduction. This reaction favors a formate-based CO_2 reduction mechanism. According to this mechanism, CO_2 is directly hydrogenated by a hydrogen atom produced through a water-splitting process, forming HCOO species that may undergo further protonation or C—O bond cleavage[244–247]. ESR detected $^{-\bullet}CO_2$ on the surface of the photocatalyst, which may have been produced directly from the adsorbed formate rather than the first electron addition to the CO_2 molecule.

$$\begin{aligned} HCOO^- + h^+ &\longrightarrow {CO_2}^{-\bullet} + H^+ \\ \textbf{Current Doubling Effect}: {CO_2}^{-\bullet} &\longrightarrow {CO_2}^{\bullet} + 2\,{e_{CB}}^- \end{aligned} \tag{2.150}$$

It is crucial to separate the oxidation and reduction sites to obtain optimal results. Recent research has shown that photochemical conversion of carbon dioxide (CO_2) into hydrocarbons is possible using palladium (Pd) and titanium dioxide (TiO_2) in conjunction with Nafion[13]. The purpose of the Nafion layer is to increase the local proton activity to facilitate PCET reactions, stabilize intermediates, and prevent the re-oxidation of CO_2 reduction products. The Nafion/Pd-TiO_2 catalyst demonstrated greater activity in the photoproduction of hydrocarbons than Pd-TiO_2 alone. Additionally, the Nafion/Pd-TiO_2 catalyst maintained its photosynthetic activity after multiple photoreaction cycles, indicating the stability of the Nafion layer. This catalytic system represents a promising model for the development of highly efficient artificial photosynthetic catalysts. However, the low photoconversion efficiency of this process can be attributed to the need for highly energetic electrons to activate the stable CO_2. Figure 2.36 illustrates the conceptual design of the catalyst system used in this study.

In light of the aforementioned factors, a conceptual analysis and potential adaptations were proposed. The primary objectives were to explore the feasibility of using a direct proton source other than water for carbon dioxide reduction and to identify the optimal species for use as the proton source. It is crucial that the proton source species does not undergo any electrochemical reactions within

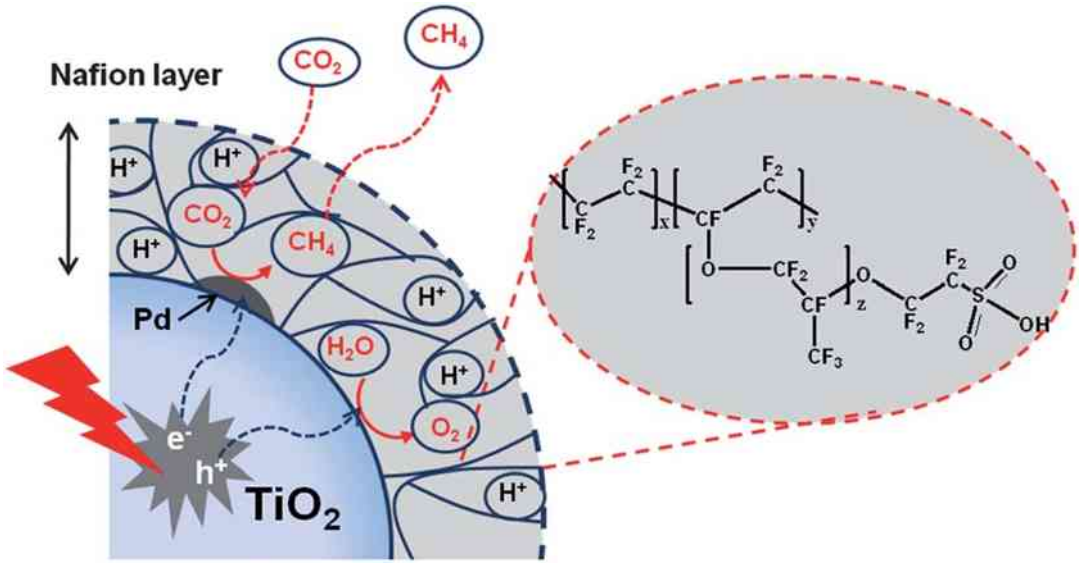

Figure 2.36: Nafion-decorated Pd/TiO_2 catalyst system for photoreduction of CO_2 [13]. Reproduced from *Energy Environ. Sci. 5 (2012) 6066–6070. ©2012 Royal Society of Chemistry*.

the potential range of the CO_2 reduction reaction. Moreover, the reactivity of the proton should be comparable to that of Nafion, where the proton is in a highly electronegative environment with fluorine atoms. The available protons should be able to react directly with carbon dioxide, promoted by the absorption of light in TiO_2, and undergo a reduction reaction on some reactive metal sites. To address the low solubility of CO_2, the source was carbonate, which can generate and sustain CO_2 in situ. Overall, these findings suggest that the use of a direct proton source other than water and the identification of optimal proton source species could have significant implications for the development of efficient and sustainable carbon dioxide reduction processes.

Considering the aforementioned factors and employing argumentative foundations, alternative PCET catalyst-support systems should be explored. These systems should possess the capacity to sustain more acidic protons, such as heteropoly acids, or superacids, such as sulfated zirconia.

2.10 Proposed Reaction Pathways

Currently, there are no established mechanistic pathways for the aqueous-phase reduction of carbon dioxide. While numerous studies have explored the reactions of carbon dioxide in its gaseous form, there has been limited research on its reduction in aqueous solutions. However, some researchers have proposed plausible reaction pathways based on the binding mode of carbon dioxide anion radicals on the surface of semiconductors. These pathways include the formaldehyde, carbene, and glyoxal pathways (Figure 2.37)[248].

The production of CH_4 or CH_3OH results from a series of electron-coupled protonation reactions involving adsorbed CO_2. In the initial two scenarios (a) and

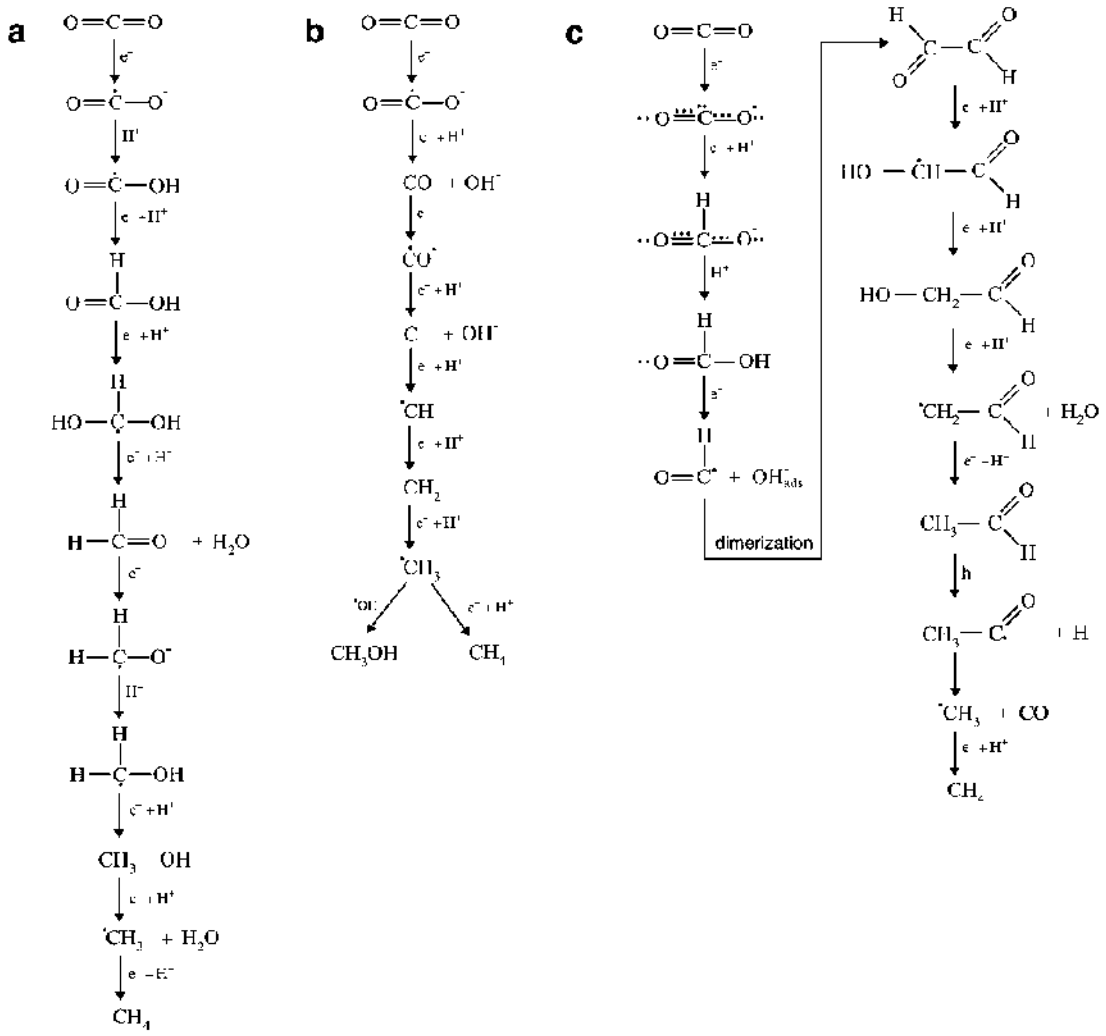

Figure 2.37: There are three proposed reaction pathways for the reduction of CO_2(g): (a) the formaldehyde pathway, (b) carbene pathway, and (c) glyoxal pathway [248]. Reproduced from *Angew. Chemie - Int. Ed. 52 (2013) 7372–7408. ©2013 WILEY-VCH Verlag GmbH & Co. KGaA, Weinheim*.

(b), the proponents only considered the reduction pathway. However, photocatalytic systems require both reduction and oxidation; hence, a more precise proposal is scenario (c), which considers the role of oxidation in the reaction mechanism. Dimerization of the formyl radical leads to the formation of glyoxal, which is further transformed into acetaldehyde via the reduction of vinoxyl radicals. The acetaldehyde produced is highly susceptible to hole attack and is transformed into an unstable acetyl group. The decarbonylation of the acetyl radical yields a methyl radical, which serves as a direct precursor for methane. However, the reaction pathways are primarily influenced by the surface structure of the semiconductor and the interaction between the CO_2(g)/HCO_3^- structures and surface. Therefore, it is challenging to propose a universal mechanism for CO_2 reduction because the mechanism is highly dependent on the nature of the catalyst and active sites and varies with the semiconductor surface.

It is worth entertaining the notion that alternative reaction pathways for the hydrogenation of CO_2 molecules may exist, as suggested by researchers[249].

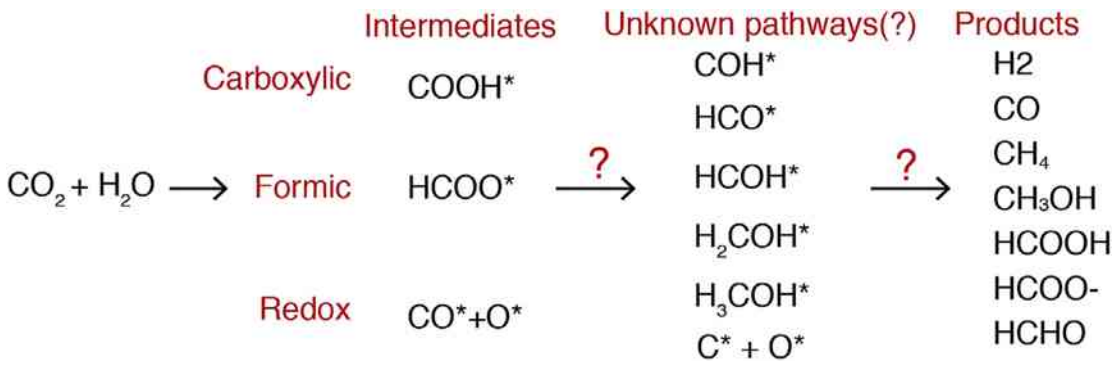

Figure 2.38: Potential mechanisms involved in the photon-assisted catalytic reduction of CO_2 and hypothetical intermediates may be present during this process [249]. Reproduced from *S. Laursen, S. Poudyal, Photo- and Electro-Catalysis: CO_2 Mitigation Technologies, in: B. Morreale, F. Shi (Eds.), Novel Materials for Carbon Dioxide Mitigation Technology, Elsevier B. V. 2015, 233-268.©2013 Elsevier B.V.*

These scientists have proposed three possible pathways: (a) a redox mechanism that involves a CO intermediate, (b) a formate mechanism that involves a formate intermediate [HCOO], and (c) a carboxyl mechanism involving a carboxylic acid [COOH] intermediate (Figure 2.38).

- Redox mechanism: The redox mechanism is characterized by the ongoing hydrogenation of the primary intermediate CO, which results in the formation of either methane or methanol.
- Formate mechanism: This mechanism involves the direct hydrogenation of CO_2 by an H atom produced from water splitting, without prior dissociation of CO_2. The resulting [HCOO] species can either be protonated or undergo C-O dissociation, which ultimately leads to the formation of methanol or methane.
- Carboxyl mechanism: Similar to the mechanism of formate, carbon dioxide was subjected to direct hydrogenation without the need for dissociation. The intermediate formaldehyde underwent a subsequent hydrogenation and dissociation process to produce the final product.

In the liquid-phase CO_2reduction process, the carbonate ion undergoes oxidation in the presence of a hole, leading to the formation of a carbonate neutral radical, which then yields carbon monoxide and oxygen. This carbon monoxide is subsequently hydrogenated, resulting in the production of formaldehyde. Experimental evidence from flash photolysis[250] and EPR [93, 251] support the direct oxidation of CO_3^{2-} to CO_3^{-}.

$$\begin{aligned} TiO_2 &\longrightarrow e^- + h^+ \\ CO_3^{2-} + h^+ &\longrightarrow CO_3^- \\ CO_3^- + e^- &\longrightarrow CO_2^{2-} \\ CO_3^- + O_2 &\longrightarrow CO_3 + O_2^- \\ CO_3CO^+ &\longrightarrow O_2 \end{aligned} \tag{2.151}$$

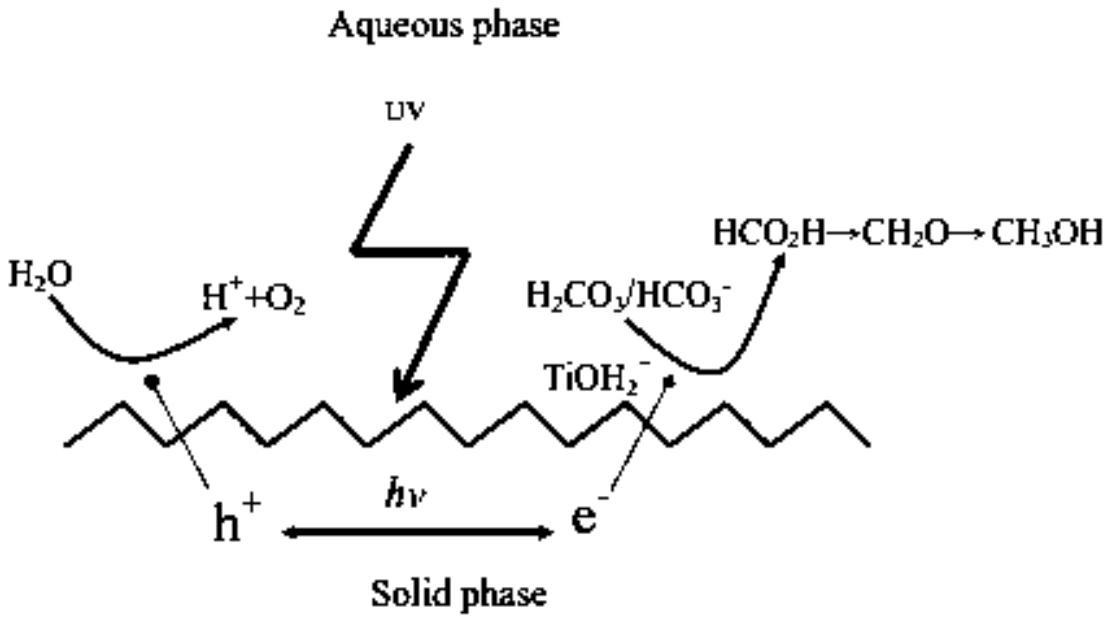

Figure 2.39: Photoreduction of bicarbonate solutions in the presence of TiO_2 [252]. Reproduced from *J. Mol. Catal. A Chem. 212 (2004) 191–196. ©2003 Elsevier B.V.*

Another pathway involves the direct reduction of carbonate to formate, which is then converted to formaldehyde and methanol[252, 253] (Figure 2.39). In accordance with the hypothesis that hydrogen carbonate serves as a source of molecular carbon dioxide and that the reaction mechanism proposed by Chandrasekaran and Thomas. constitutes a more favorable pathway under specific conditions, Yang conducted experiments in the presence of carbonates over Cu/TiO_2 and concluded that this mechanism exhibits higher reactivity under their reaction conditions[254]. More recently, Nakanishi et al. proposed that hydrogen carbonate may function as a source of molecular carbon dioxide rather than directly reacting with electrons in an aqueous medium[255]. Their experiment, which involved aqueous solutions of Na_2CO_3 and $NaHCO_3$ under continuous argon bubbling, revealed that the evolution of CO_2 was not observed in the presence of Na_2CO_3, whereas it was released concurrently with CO in the $NaHCO_3$ solution. The rate of CO production decreased as the rate of CO_2 evolution from the solution decreased. These findings suggest that hydrogen carbonate can be transformed into molecular carbon dioxide at the interface, although further experimental and computational studies are necessary to propose a widely accepted reaction pathway for CO_2 reduction in aqueous media (Figure 2.40)[256].

2.10.1 Additional Notes

The development of an internal electric field at the interface between semiconductors and electrolytes owing to charge redistribution is referred to as Fermi-level equilibration. This results in band bending, which affects the transfer of charge carriers through the interface and modifies the redox properties of the semiconductor surface by altering the density of states. It is crucial to determine the interfacial band alignment, which differs from that in the free state, using in-situ

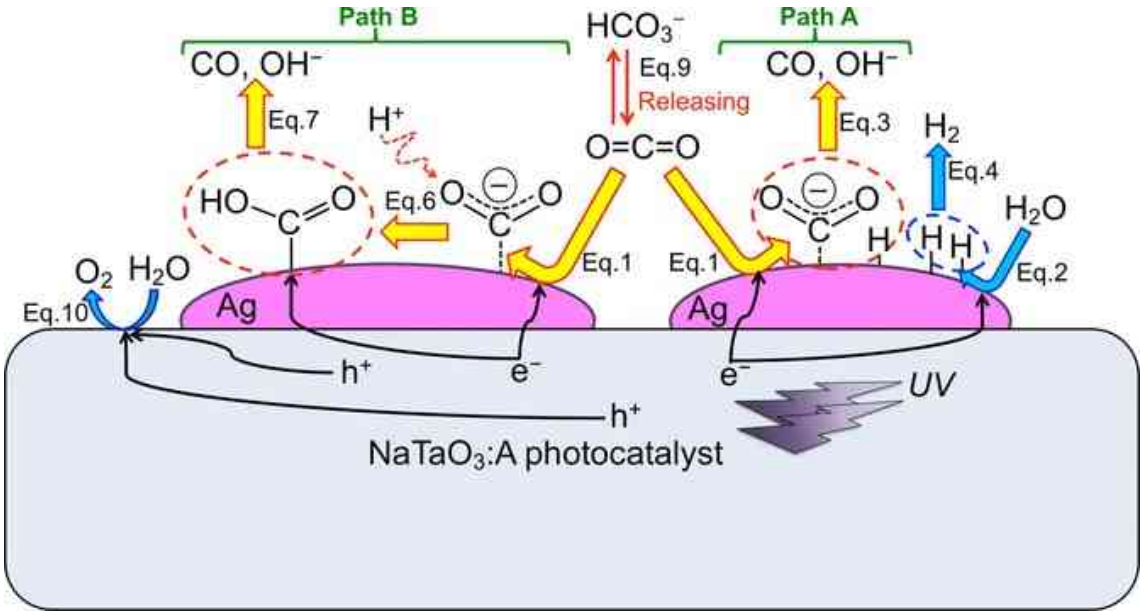

Figure 2.40: The proposed mechanism for CO_2 reduction to form CO over Ag/$NaTaO_3$ photocatalysts involving Path A [hydrogenation of $^{-\bullet}CO_2$] and Path B [reduction of $COOH_{(ad)}$] is discussed. The photocatalysts used were A=Mg, Ca, Sr, Ba, and La [255]. Reproduced from *ChemSusChem. 10 (2017) 112–118. ©2017 Wiley-VCH Verlag GmbH & Co. KGaA, Weinheim*.

techniques. The band position used to interpret the results was in the free state of the semiconductor and not at the interface.

The primary issue in the water decomposition process is the lack of understanding of the semiconductor/electrolyte interface in real-time, particularly when an optoelectrical field is present[257]. The application of light with an appropriate wavelength that matches the bandgap of the photoelectrode causes the transition of charge carriers from the valence band to the conduction band states, resulting in a change in the net charge density during the illumination process. This change in the charge density leads to a corresponding change in the field gradient at the interface. Specifically, in the case of an oxide photoelectrode system, photoexcitation modifies the conduction band wave functions contributed by the d orbital of the metal ions and the valence band wave functions contributed by the p orbital of the oxide ions. The loss of an electron from the valence band may result in a change in its binding energy and the expansion of the valence band states to a more negative or less positive value. However, the addition of electrons to the conduction band may shift its position to more negative values. These assumptions suggest that the interface behaves differently in the presence and absence of a photon field, which could alter surface interactions with water. Therefore, it is crucial to consider the effect of applied bias on photon-induced changes. The externally applied bias also changes the net charge density of the photoelectrode, which has a significant impact on the field gradient in the Garrett–Bratté space-charge region on both the electrolyte and semiconductor sides[257].

The accumulation of species, including charge carriers, at the interface alters the wave function overlap between the water molecule and photocatalyst under equilibrium conditions. This may vary because of the introduction of an optoelectri-

cal field, which can modify the density of states (DOS), photoadsorption capacity, and surface states. These changes can also affect other factors such as the refractive index, dielectric constant, and capacity of the double layer formed across the interface. The density of states at the interface may be altered by the optoelectrical field, which can affect the photoadsorption behavior. Simultaneously, both the displacement at the Fermi level and the natural band curvature may be modified, resulting in the reversal of the photoabsorption effect at the interface[258].

The theoretical challenge of mapping the interaction between defect sites and substrate (water) wave functions is complicated by the difficulty in tracing the wave function overlap in contour maps. Furthermore, the nature of the frontier wavefunction of defect states is distinct from that of the semiconductor surface. As a result, the theoretical treatment provides only a rough estimate of the eigenvalues and eigenfunctions of the frontier orbitals. This lack of knowledge can potentially hinder the theoretical design of suitable materials to a significant extent.

Although the primary focus of our research was on the thermodynamics of water splitting, we did not consider the kinetic factors associated with this process. Specifically, the changes in band alignment only reflect the free energy changes and do not consider the kinetics of the gas evolution at the interface. The evolution of gas from the surface involves a series of steps, such as the formation of molecules from atomic species, bubble formation, and desorption of gas from the surface, all of which may be the rate-determining step and beyond the control of electron transfer. Therefore, it is essential to determine whether bandgap engineering alone is sufficient for photocatalyst development. In addition, material design should consider environmental factors such as the ionic strength, composition, and pH of the electrolyte, which can affect the CO_2 reaction or water-splitting reaction.

The field of photon-assisted catalysis for CO_2 reduction or water decomposition has been a major research focus over the past five decades, and significant progress has been made. However, the efficiency of this process is inadequate for commercial application. Currently, an understanding of the nature of the interface formed under optoelectrical conditions at the semiconductor/electrolyte junction is in its infancy, and a more detailed understanding of the dynamic nature of the interface is necessary for the successful treatment of the overall water-splitting process. In addition to the conventional bandgap engineering approach for increasing the photoresponse of the process, the thermodynamic and kinetic aspects of the process must be carefully considered. There is an urgent need for the development of in-situ techniques that can visualize changes at the interface under photon and electric fields. It is also necessary to reconsider the role of G. N. Lewis, as the process is not solely dependent on the semiconductor itself, but rather on the semiconductor in the excited state or at the interface, which causes the photon-assisted catalysis system to operate[59]. The field of photon-assisted catalysis cannot be improved without a better understanding of the dynamic nature of interfaces.

2.11 Conclusion and Perspectives

It is suggested that future research into the photocatalytic reduction of CO_2 should focus on critical mechanistic aspects and experimental methodologies. Currently, there have been no comprehensive studies on anion radicals and their responsive-

ness, leading to uncertainty regarding their relevance and participation in the CO_2 reduction process. Furthermore, the examination of CO_2 reduction products and the established methods for analyzing these products have not been thoroughly investigated. For instance, it is uncertain whether the analysis should be conducted in the gas or aqueous phase, or both, and which sampling techniques should be used. Additionally, a standardized reactor design is lacking in experimental studies, which impedes the comparison of results from different research laboratories. A standardized reactor design is necessary for meaningful comparisons, because the products formed can be simultaneously present in multiple phases.

The impact of carbon artifacts on CO_2 reduction remains largely unknown, although some studies have been conducted on this topic. However, a comprehensive understanding of this phenomenon has not yet been achieved. Instead of ^{13}C labeling, a new methodology that is not universally available in laboratories must be developed.

The precise role of competitive reactions in the photocatalytic CO_2 reduction has not yet been thoroughly examined. Reactive oxygen species can hinder CO_2 reduction efficiency, and researchers have recently used ROS-resistant cobalt-phosphorus alloys to mitigate these negative effects. Another challenge in CO_2 reduction is hydrogen evolution because most semiconductors are thermodynamically favorable for hydrogen production. Therefore, controlling hydrogen evolution is essential for studies on CO_2 photocatalytic conversion, and further investigation into competitive reactions in CO_2 reduction is necessary. Pursuing innovative photocatalytic materials necessitates a departure from the conventional use of titanium dioxide. The redox capacity of TiO_2 is inferior to that of other semiconductor oxides in the same group. To develop new materials for the reduction of CO_2, collective efforts are imperative. The ideal material should possess an appropriate redox potential and a considerable bandgap to harness light energy. It would be even more advantageous if the material exhibited a valence band edge that was more negative than the oxygen evolution potential.

In-depth studies are crucial for metal-free photocatalysts such as carbon nitride, boron nitride, and their derivatives. The compositions of these materials can be selectively controlled by modifying the preparation method. The lack of independent research on these materials highlights their potential. Notably, carbon nitride can be synthesized from carbon dioxide as a raw material (the reaction of CO_2 with ammonia produces urea); however, this route is not cost effective. The necessity for extensive research is paramount in the pursuit of understanding the function of hydrogen carbonate in the reduction of CO_2 in water and the underlying mechanism of the reaction. As Schmidt noted, " the potential for further advancements in CO_2 catalysis extends beyond the elimination of the $^{-\bullet}CO_2$ intermediate to include the reduction of more stable species such as CO and formaldehyde, ultimately leading to the production of valuable methanol and methane fuels. However, it is crucial to recognize that the fundamental thermodynamics of the overall process will remain unchanged, and a substantial input of energy will be necessary for the conversion of CO_2 into more reduced carbon compounds[259]."

References

[1] Aresta, M. My journey in the CO_2-chemistry wonderland. *Coordination Chemistry Reviews* **2017**, *334*, 150–183.

[2] Corma, A.; Garcia, H. Photocatalytic reduction of CO_2 for fuel production: Possibilities and challenges. *Journal of Catalysis* **2013**, *308*, 50th Anniversary Special Issue, 168–175.

[3] Wu, J.; Zhou, X.-D. Catalytic conversion of CO_2 to value added fuels: Current status, challenges, and future directions. *Chinese Journal of Catalysis* **2016**, *37*, 999–1015.

[4] Zaera, F. New Challenges in Heterogeneous Catalysis for the 21^{st} Century. *Catalysis Letters* **2012**, *142*, 501–516.

[5] Bell, A. T.; Gates, B. C.; Ray, D.; Thompson, M. R. *Basic Research Needs: Catalysis for Energy*; tech. rep.; United States, 2008.

[6] Schneider, J.; Jia, H.; Muckerman, J. T.; Fujita, E. Thermodynamics and kinetics of CO_2, CO, and H^+ binding to the metal centre of CO_2 reduction catalysts. *Chem. Soc. Rev.* **2012**, *41*, 2036–2051.

[7] Ciamician, G. The Photochemistry of the Future. *Science* **1912**, *36*, 385–394.

[8] Ozin, G. A. You cant have an energy revolution without transforming advances in materials, chemistry and catalysis into policy change and action. *Energy & Environmental Science* **2015**, *8*, 1682–1684.

[9] Thomas, J. M.; Harris, K. D. M. Some of tomorrow's catalysts for processing renewable and non-renewable feedstocks, diminishing anthropogenic carbon dioxide and increasing the production of energy. *Energy Environ. Sci.* **2016**, *9*, 687–708.

[10] Ozin, G. A. Throwing New Light on the Reduction of CO_2. *Advanced Materials* **2015**, *27*, 1957–1963.

[11] Narayanan, H.; Viswanathan, B.; Nair, H. On the current status of the mechanistic aspects of photocatalytic reduction of carbon dioxide. *Indian Journal of Chemistry-Section A (IJCA)* **2017**, *56*, 251–269.

[12] Narayanan, H.; Viswanathan, B.; Yesodharan, S. Photocatalytic reduction of carbon dioxide: Issues and prospects. *Current Catalysis* **2016**, *5*, 79–107.

[13] Kim, W.; Seok, T.; Choi, W. Nafion layer-enhanced photosynthetic conversion of CO_2 into hydrocarbons on TiO_2 nanoparticles. *Energy Environ. Sci.* **2012**, *5*, 6066–6070.

[14] Aresta, M., Carbon Dioxide: Utilization Options to Reduce its Accumulation in the Atmosphere In *Carbon Dioxide as Chemical Feedstock*; John Wiley & Sons, Ltd: 2010; Chapter 1, pp 1–13.

[15] Herron, J. A.; Kim, J.; Upadhye, A. A.; Huber, G. W.; Maravelias, C. T. A general framework for the assessment of solar fuel technologies. *Energy & Environmental Science* **2015**, *8*, 126–157.

[16] Armor, J. N. Addressing the CO_2 dilemma. *Catalysis Letters* **2007**, *114*, 115–121.

[17] Karamian, E.; Sharifnia, S. On the general mechanism of photocatalytic reduction of CO_2. *Journal of CO_2 Utilization* **2016**, *16*, 194–203.

[18] Lewis, N. S. Research opportunities to advance solar energy utilization. *Science* **2016**, *351*, aad1920.

[19] Osterloh, F. E. Photocatalysis versus Photosynthesis: A Sensitivity Analysis of Devices for Solar Energy Conversion and Chemical Transformations. *ACS Energy Letters* **2017**, *2*, 445–453.

[20] Milnes, A. G., *Heterojunctions and metal semiconductor junctions*; Elsevier: 2012.

[21] Perkowitz, S., 1 - Introduction In *Optical Characterization of Semiconductors*, Perkowitz, S., Ed.; Techniques of Physics, ISSN: 18746012; Academic Press: Boston, 1993, pp 1–6.

[22] PERKOWITZ, S., 2 - Optical Theory for Semiconductor Characterization In *Optical Characterization of Semiconductors*, PERKOWITZ, S., Ed.; Techniques of Physics, ISSN: 18746012; Academic Press: Boston, 1993, pp 7–16.

[23] Osterloh, F. E. Inorganic Nanostructures for Photoelectrochemical and Photocatalytic Water Splitting. *Chem. Soc. Rev.* **2013**, *42*, 2294–2320.

[24] Li, L.; Salvador, P. A.; Rohrer, G. S. Photocatalysts with internal electric fields. *Nanoscale* **2014**, *6*, 24–42.

[25] Chen, Z.; Deutsch, T. G.; Dinh, H. N.; Domen, K.; Emery, K.; Forman, A. J.; Gaillard, N.; Garland, R.; Heske, C.; Jaramillo, T. F.; Kleiman-Shwarsctein, A.; Miller, E.; Takanabe, K.; Turner, J., Introduction In *Photoelectrochemical Water Splitting: Standards, Experimental Methods, and Protocols*, Chen, Z., Dinh, H. N., Miller, E., Eds.; Springer New York: New York, NY, 2013, pp 1–5.

[26] Polman, A.; Atwater, H. A. Photonic design principles for ultrahigh-efficiency photovoltaics. *Nature Materials* **2012**, *11*, 174–177.

[27] Holmes, M. A.; Townsend, T. K.; Osterloh, F. E. Quantum confinement controlled photocatalytic water splitting by suspended CdSe nanocrystals. *Chem. Commun.* **2012**, *48*, 371–373.

[28] Memming, R., Electrochemical Decomposition of Semiconductors In *Semiconductor Electrochemistry*; John Wiley & Sons, Ltd: 2015; Chapter 8, pp 267–294.

[29] Kelly, J. J.; Vanmaekelbergh, D. Charge carrier dynamics in nanoporous photoelectrodes. *Electrochimica Acta* **1998**, *43*, 2773–2780.

[30] Su, J.; Wei, Y.; Vayssieres, L. Stability and Performance of Sulfide-, Nitride-, and Phosphide-Based Electrodes for Photocatalytic Solar Water Splitting. *The Journal of Physical Chemistry Letters* **2017**, *8*, 5228–5238.

[31] Gerischer, H. Electrolytic decomposition and photodecomposition of compound semiconductors in contact with electrolytes. *Journal of Vacuum Science and Technology* **1978**, *15*, 1422–1428.

[32] Gerischer, H. Solar photoelectrolysis with semiconductor electrodes. *Topics in Applied Physics* **1979**, 115–172.

[33] Böer, K. W., *Introduction to Space Charge Effects in Semiconductors*; Springer-Verlag: Berlin Heidelberg, 2010.

[34] Kokorin, A. I.; Bahnemann, D. W., *Chemical Physics of Nanostructured Semiconductors*; CRC Press: The Netherlands, 2003.

[35] Shockley, W., *Electrons and Holes in Semiconductors with Application to Transistor Electronics*; Van Nostrand Reinhold Inc.: U.S, 1950.

[36] Neamen, D. A., *Semiconductor Physics and Devices: Basic Principles*, Fourth; McGraw-Hill Education: New York, 2011.

[37] Sze, S. M.; Ng, K. K., *Physics of Semiconductor Devices*, Third; John Wiley & Sons: New Jersey, 2007.

[38] Peter, Y. Y.; Cardona, M., *Fundamentals of Semiconductors: Physics and Materials Properties*, Fourth; Springer-Verlag: Berlin-Heidelberg, 2010.

[39] Pierret, R. F., *Advanced Semiconductor Fundamentals*; Modular Series on Solid State Devices, Vol. 6; Pearson Prentice Hall: New Jersey, 2002.

[40] Narayanan, H.; Viswanathan, B.; Krishnamurthy, K. R.; Nair, H., Understanding reaction mechanism in photon-assisted reduction of carbon dioxide In *Photocatalytic Nanomaterials for Environmental Applications*; Material Research Forum: 2018, pp 175–210.

[41] Bisquert, J., *Nanostructured Energy Devices: Equilibrium Concepts and Kinetics*; CRC Press: Boca Raton, 2015.

[42] Milnes, A. G.; Feucht, D. L., *Heterojunction and Metal Semiconductor Junctions*; Academic Press: New York, 1972.

[43] Sharma, B. L., *Metal-Semiconductor Schottky Barrier Junctions and Their Applications*; Plenum Press: New York, 1984.

[44] Yang, X.; Wang, D. Photophysics and photochemistry at the semiconductor/-electrolyte interface for solar water splitting. *Semiconductors and Semimetals* **2017**, 47–80.

[45] Tan, M. X.; Laibinis, P. E.; Nguyen, S. T.; Kesselman, J. M.; Stanton, C. E.; Lewis, N. E., Principles and Applications of Semiconductor Photoelectrochemistry In *Progress in Inorganic Chemistry*, Karlin, K. D., Ed.; John Wiley & Sons, Inc.: Hoboken, NJ, USA, 1994; Vol. 41, pp 21–144.

[46] Grätzel, M. Photoelectrochemical cells. *Nature* **2001**, *414*, 338–344.

[47] Bockris, J. O.; Reddy, A. K. N.; Gamboa-Aldeco, M. E., *Modern Electrochemistry 2A: Fundamentals of Electrodics*; Springer-Verlag US: 2000.

[48] Memming, R., *Semiconductor Photoelectrochemistry*; Wiley VCH: Weinheim, 2015.

[49] Bard, A. J.; Stratmann, M.; Licht, S., *Encyclopedia of Electrochemistry, Semiconductor Electrodes and Photoelectrochemistry, Volume 6*; Wiley-VCH: 2002.

[50] Plieth, W., *Electrochemistry of Material Science*; Elsevier B.V.: UK, 2008.

[51] Bisquert, J., *Nanostructured Energy Devices: Foundations of Carrier Transport*, 1st; CRC Press: 2017.

[52] Bisquert, J., *The Physics of Solar Cells: Perovskites, Organics, and Photovoltaic Fundamentals*, 1st; CRC Press: 2017.

[53] Bisquert, J., *The Physics of Solar Energy Conversion*, 1st; CRC Press: 2020.

[54] Sato, N., *Electrochemistry at Metal and Semiconductor Electrodes*; Elsevier B.V.: The Netherlands, 1998.

[55] Bard, A. J.; Bocarsly, A. B.; Fan, F. R. F.; Walton, E. G.; Wrighton, M. S. The concept of fermi level pinning at semiconductor/liquid junctions. consequences for energy conversion efficiency and selection of useful solution redox couples in solar devices. *Journal of the American Chemical Society* **1980**, *102*, 3671–3677.

[56] Thorne, J. E.; Li, S.; Du, C.; Qin, G.; Wang, D. Energetics at the surface of photoelectrodes and its influence on the photoelectrochemical properties. *The Journal of Physical Chemistry Letters* **2015**, *6*, 4083–4088.

[57] Gärtner, W. W. Depletion-layer photoeffects in semiconductors. *Physical Review* **1959**, *116*, 84–87.

[58] Zhang, Z.; Yates, J. T. Band bending in semiconductors: chemical and physical consequences at surfaces and interfaces. *Chemical Reviews* **2012**, *112*, 5520–5551.

[59] Lewis, G. N.; Randall, M., *Thermodynamics and the Free Energy of Chemical Substances*; McGraw-Hill: United States, 1923.

[60] Smets, A.; Jäger, K.; Isabella, O.; van Swaaij, R.; Zeman, M., *Solar Energy: The Physics and Engineering of Photovoltaic Conversion, Technologies and Systems*; UIT Cambridge Limited: 2016.

[61] Shockley, W.; Read, W. T. Statistics of the Recombinations of Holes and Electrons. *Phys. Rev.* **1952**, *87*, 835–842.

[62] Hall, R. N. Electron-hole recombination in germanium. *Physical Review* **1952**, *87*, 387–387.

[63] Bisquert, J.; Cendula, P.; Bertoluzzi, L.; Gimenez, S. Energy diagram of semiconductor/electrolyte junctions. *The Journal of Physical Chemistry Letters* **2013**, *5*, 205–207.

[64] Smith, W. A.; Sharp, I. D.; Strandwitz, N. C.; Bisquert, J. Interfacial band-edge energetics for solar fuels production. *Energy & Environmental Science* **2015**, *8*, 2851–2862.

[65] Chai, B.; Peng, T.; Zeng, P.; Mao, J. Synthesis of floriated In_2S_3 decorated with TiO_2 nanoparticles for efficient photocatalytic hydrogen production under visible light. *Journal of Materials Chemistry* **2011**, *21*, 14587.

[66] He, Z.; Wang, D.; Tang, J.; Song, S.; Chen, J.; Tao, X. A quasi-hexagonal prism-shaped carbon nitride for photoreduction of carbon dioxide under visible light. *Environmental Science and Pollution Research* **2017**, *24*, 8219–8229.

[67] Chun, W.; Ishikawa, A.; Fujisawa, H.; Takata, T.; Kondo, J. N.; Hara, M.; Kawai, M.; Matsumoto, Y.; Domen, K. Conduction and valence band positions of Ta_2O_5, TaON, and Ta_3N_5 by UPS and electrochemical methods. *The Journal of Physical Chemistry B* **2003**, *107*, 1798–1803.

[68] Giménez, S.; Dunn, H. K.; Rodenas, P.; Fabregat-Santiago, F.; Miralles, S. G.; Barea, E. M.; Trevisan, R.; Guerrero, A.; Bisquert, J. Carrier density and interfacial kinetics of mesoporous TiO_2 in aqueous electrolyte determined by impedance spectroscopy. *Journal of Electroanalytical Chemistry* **2012**, *668*, 119–125.

[69] Bertoluzzi, L.; Lopez-Varo, P.; Jimenez-Tejada, J.; Bisquert, J. Charge transfer processes at the semiconductor/electrolyte interface for solar fuel production: insight from impedance spectroscopy. *Journal of Materials Chemistry A* **2016**, *4*, 2873–2879.

[70] Bonham, D. B.; Orazem, M. E. A mathematical model for the influence of deep-level electronic states on photoelectrochemical impedance spectroscopy: i . theoretical development. *Journal of the Electrochemical Society* **1992**, *139*, 118–126.

[71] Haram, S. K.; Kshirsagar, A.; Gujarathi, Y. D.; Ingole, P. P.; Nene, O. A.; Markad, G. B.; Nanavati, S. P. Quantum confinement in CdTe quantum dots: investigation through cyclic voltammetry supported by density functional theory (DFT). *The Journal of Physical Chemistry C* **2011**, *115*, 6243–6249.

[72] Bertoluzzi, L.; Badia-Bou, L.; Fabregat-Santiago, F.; Gimenez, S.; Bisquert, J. Interpretation of cyclic voltammetry measurements of thin semiconductor films for solar fuel applications. *The Journal of Physical Chemistry Letters* **2013**, *4*, 1334–1339.

[73] Gelderman, K.; Lee, L.; Donne, S. W. Flat-band potential of a semiconductor: using the mott-schottky equation. *Journal of Chemical Education* **2007**, *84*, 685.

[74] Albery, W. J.; O'Shea, G. J.; Smith, A. Interpretation and use of mott-schottky plots at the semiconductor/electrolyte interface. *J. Chem. Soc., Faraday Trans.* **1996**, *92*, 4083–4085.

[75] Mani, A.; Huisman, C. L.; Goossens, A.; Schoonman, J. Mott-schottky analysis and impedance spectroscopy of TiO_2/6T and ZnO/6T devices. *The Journal of Physical Chemistry B* **2008**, *112*, 10086–10091.

[76] Almora, O.; Aranda, C.; Mas-Marzá, E.; García-Belmonte, G. On mott-schottky analysis interpretation of capacitance measurements in organometal perovskite solar cells. *Applied Physics Letters* **2016**, *109*, 173903-1 - 173903–5.

[77] Lasia, A., *Semiconductors and Mott-Schottky Plots*; Lasia, A., Ed.; Springer New York: New York, NY, 2014, pp 251–255.

[78] Childs, L. P.; Ollis, D. F. Is photocatalysis catalytic? *Journal of Catalysis* **1980**, *66*, 383–390.

[79] Ohtani, B. Preparing articles on photocatalysis-beyond the illusions, misconceptions, and speculation. *Chemistry Letters* **2008**, *37*, 216–229.

[80] Ohtani, B. Photocatalysis a to z-what we know and what we do not know in a scientific sense. *Journal of Photochemistry and Photobiology C: Photochemistry Reviews* **2010**, *11*, 157–178.

[81] Yang, N.; Waldvogel, S. R.; Jiang, X. Electrochemistry of carbon dioxide on carbon electrodes. *ACS Applied Materials & Interfaces* **2016**, *8*, 28357–28371.

[82] Gao, D.; Fan, C.; Wang, Q.; Bao, X. Nanostructured heterogeneous catalysts for electrochemical reduction of CO_2. *Current Opinion in Green and Sustainable Chemistry* **2017**, *3*, 39–44.

[83] Ohtani, B. Photocatalysis by inorganic solid materials. *Inorganic Photochemistry* **2011**, 395–430.

[84] Ohtani, B. Revisiting the fundamental physical chemistry in heterogeneous photocatalysis: its thermodynamics and kinetics. *Physical Chemistry Chemical Physics* **2014**, *16*, 1788–1797.

[85] Emeline, A. V.; Ryabchuk, V. K.; Serpone, N. Dogmas and misconceptions in heterogeneous photocatalysis. some enlightened reflections. *The Journal of Physical Chemistry B* **2005**, *109*, 18515–18521.

[86] Viswanathan, B., Chapter 10 - Electro-Catalytic Reduction of Carbon Dioxide In *New and Future Developments in Catalysis*, Suib, S. L., Ed.; Elsevier: Amsterdam, 2013, pp 275–295.

[87] Wikipedia Semiconductor band edge positions diagram, Accessed on 2024-01-26, `https://en.wikipedia.org/wiki/File:Semiconductor_Band_edge_positions.png`.

[88] Freund, H.; Messmer, R. P. On the bonding and reactivity of CO_2 on metal surfaces. *Surface Science* **1986**, *172*, 1–30.

[89] Taifan, W.; Boily, J.; Baltrušaitis, J. Surface chemistry of carbon dioxide revisited. *Surface Science Reports* **2016**, *71*, 595–671.

[90] Gattrell, M.; Gupta, N.; Co, A. C. A review of the aqueous electrochemical reduction of CO_2 to hydrocarbons at copper. *Journal of Electroanalytical Chemistry* **2006**, *594*, 1–19.

[91] Henrich, V. E.; Cox, P. A., *Surface Science of Metal Oxide*; Cambridge University Press: 1996.

[92] Ku, Y.; Lee, W.; Wang, W. Photocatalytic reduction of carbonate in aqueous solution by UV/TiO_2 process. *Journal of Molecular Catalysis A: Chemical* **2004**, *212*, 191–196.

[93] Dimitrijevic, N. M.; Vijayan, B. K.; Poluektov, O. G.; Rajh, T.; Gray, K. A.; He, H.; Zapol, P. Role of water and carbonates in photocatalytic transformation of CO_2 to CH_4 on titania. *Journal of the American Chemical Society* **2011**, *133*, 3964–3971.

[94] Hong, J.; Zhang, W.; Ren, J.; Xu, R. Photocatalytic reduction of CO_2: a brief review on product analysis and systematic methods. *Analytical Methods* **2013**, *5*, 1086.

[95] Chen, S.; Wang, L. Thermodynamic oxidation and reduction potentials of photocatalytic semiconductors in aqueous solution. *Chemistry of Materials* **2012**, *24*, 3659–3666.

[96] Ping, Y.; Sundararaman, R.; Goddard, W. A. Solvation effects on the band edge positions of photocatalysts from first principles. *Physical Chemistry Chemical Physics* **2015**, *17*, 30499–30509.

[97] Gratzel, M., Molecular Engineering in Photoconversion Systems In *Energy Resources Through Photochemistry and Catalysis*, Gratzel, M., Ed.; Academic Press: 1983, pp 71–98.

[98] Bard, A. J.; Parsons, R.; Jordan, J., *Standard Potentials in Aqueous Solution*; Marcel Decker: New York, Basel, 1985.

[99] Pegis, M. L.; Roberts, J. A.; Wasylenko, D. J.; Mader, E. A.; Appel, A. M.; Mayer, J. M. Standard reduction potentials for oxygen and carbon dioxide couples in acetonitrile and n,n-dimethylformamide. *Inorganic Chemistry* **2015**, *54*, 11883–11888.

[100] Daschakraborty, S.; Kiefer, P. M.; Miller, Y.; Motro, Y.; Pines, D.; Pines, E.; Hynes, J. T. Reaction mechanism for direct proton transfer from carbonic acid to a strong base in aqueous solution I: acid and base coordinate and charge dynamics. *The Journal of Physical Chemistry B* **2016**, *120*, 2271–2280.

[101] Daschakraborty, S.; Kiefer, P. M.; Miller, Y.; Motro, Y.; Pines, D.; Pines, E.; Hynes, J. T. Reaction mechanism for direct proton transfer from carbonic acid to a strong base in aqueous solution II: solvent coordinate-dependent reaction path. *The Journal of Physical Chemistry B* **2016**, *120*, 2281–2290.

[102] Stumm, W.; Morgan, J. J., *Aquatic Chemistry: Chemical Equilibria and Rates in Natural Waters*, 3rd; Wiley-Interscience: 1996.

[103] Appel, A. M. et al. Frontiers, opportunities, and challenges in biochemical and chemical catalysis of CO_2 fixation. *Chemical Reviews* **2013**, *113*, 6621–6658.

[104] Nakamura, S.; Hatakeyama, M.; Wang, Y.; Ogata, K.; Fujii, K. A basic quantum chemical review on the activation of CO_2. *ACS Symposium Series* **2015**, 123–134.

[105] Sullivan, B. P.; Krist, K.; Guard, H., *Electrochemical and electrocatalytic reactions of carbon dioxide*; Elsevier: 2012.

[106] Lu, X.-B., *Carbon dioxide and organometallics*; Springer: 2016.

[107] Tu, W.; Zhou, Y.; Zou, Z. Photocatalytic Conversion of CO_2 into Renewable Hydrocarbon Fuels: State-of-the-Art Accomplishment, Challenges, and Prospects. *Advanced Materials* **2014**, *26*, 4607–4626.

[108] Indrakanti, V. P.; Kubicki, J. D.; Schobert, H. H. Photoinduced activation of CO_2 on Ti-based heterogeneous catalysts: current state, chemical physics-based insights and outlook. *Energy & Environmental Science* **2009**, *2*, 745.

[109] Anpo, M.; Yamashita, H.; Ichihashi, Y.; Ehara, S. Photocatalytic reduction of CO_2 with H_2O on various titanium oxide catalysts. *Journal of Electroanalytical Chemistry* **1995**, *396*, 21–26.

[110] White, J. L.; Baruch, M. F.; Pander, J. E.; Hu, Y.; Fortmeyer, I. C.; Park, J. E.; Zhang, T.; Liao, K.; Gu, J.; Yan, Y.; Shaw, T. W.; Abelev, E.; Bocarsly, A. B. Light-driven heterogeneous reduction of carbon dioxide: photocatalysts and photoelectrodes. *Chemical Reviews* **2015**, *115*, 12888–12935.

[111] Mori, K.; Yamashita, H.; Anpo, M. Photocatalytic reduction of CO_2 with H_2O on various titanium oxide photocatalysts. *RSC Advances* **2012**, *2*, 3165.

[112] Chiesa, M.; Giamello, E.; Che, M. EPR characterization and reactivity of surface-localized inorganic radicals and radical ions. *Chemical Reviews* **2009**, *110*, 1320–1347.

[113] Preda, G.; Pacchioni, G.; Chiesa, M.; Giamello, E. Formation of CO_2-radical anions from CO_2 adsorption on an electron-rich MgO surface: a combined ab initio and pulse epr study. *The Journal of Physical Chemistry C* **2008**, *112*, 19568–19576.

[114] Flyunt, R.; Schuchmann, M. N.; Sonntag, C. v. A common carbanion intermediate in the recombination and proton-catalysed disproportionation of the carboxyl radical anion, $^{-\bullet}CO_2$, in aqueous solution. *Chemistry* **2001**, *7*, 796–799.

[115] Aresta, M.; Dibenedetto, A.; Quaranta, E., The Carbon Dioxide Molecule In *Reaction Mechanisms in Carbon Dioxide Conversion*; Springer Berlin Heidelberg: Berlin, Heidelberg, 2016, pp 1–34.

[116] Shah, A. H.; Wang, Y.; Woldu, A. R.; Lin, L.; Iqbal, M.; He, T. Revisiting electrochemical reduction of CO_2 on cu electrode: where do we stand about the intermediates? *The Journal of Physical Chemistry C* **2018**, *122*, 18528–18536.

[117] Aresta, M.; Angelini, A. The carbon dioxide molecule and the effects of its interaction with electrophiles and nucleophiles. *Topics in Organometallic Chemistry* **2015**, 1–38.

[118] Yamazaki, Y.; Takeda, H.; Ishitani, O. Photocatalytic reduction of CO_2 using metal complexes. *Journal of Photochemistry and Photobiology C: Photochemistry Reviews* **2015**, *25*, 106–137.

[119] Neta, P.; Huie, R. E.; Ross, A. B. Rate constants for reactions of peroxyl radicals in fluid solutions. *Journal of Physical and Chemical Reference Data* **1990**, *19*, 413–513.

[120] Janik, I.; Tripathi, G. N. R. The nature of the CO_2- radical anion in water. *The Journal of Chemical Physics* **2016**, *144*, DOI: 10.1063/1.4946868.

[121] Capasso, F. Band-gap engineering: from physics and materials to new semiconductor devices. *Science* **1987**, *235*, 172–176.

[122] Gongming, W.; Yang, Y.; Li, Y. Surface engineering of semiconductors for photoelectrochemical water splitting. *Nanomaterials for Energy Conversion and Storage* **2017**, 223–249.

[123] Kaneko, H.; Minegishi, T.; Domen, K. Recent progress in the surface modification of photoelectrodes toward efficient and stable overall water splitting. *Chemistry - A European Journal* **2017**, *24*, 5697–5706.

[124] Kuang, Y.; Yamada, T.; Domen, K. Surface and interface engineering for photoelectrochemical water oxidation. *Joule* **2017**, *1*, 290–305.

[125] Nellist, M. R.; Laskowski, F. A. L.; Lin, F.; Mills, T. J.; Boettcher, S. W. Semiconductor-electrocatalyst interfaces: theory, experiment, and applications in photoelectrochemical water splitting. *Accounts of Chemical Research* **2016**, *49*, 733–740.

[126] Wang, A.; Bozal-Ginesta, C.; Kumar, S. G. H.; Aspuru-Guzik, A.; Ozin, G. A. Designing materials acceleration platforms for heterogeneous CO_2 photothermalcatalysis. *Matter* **2023**, *6*, 1334–1347.

[127] Narayanan, H.; Viswanathan, B.; Krishnamurthy, K. R.; Nair, H., Chapter 12 - Hydrogen from photo-electrocatalytic water splitting In *Solar Hydrogen Production*, Calise, F., D'Accadia, M. D., Santarelli, M., Lanzini, A., Ferrero, D., Eds.; Academic Press: 2019, pp 419–486.

[128] Peter, L. M.; Wijayantha, K. G. U. Photoelectrochemical water splitting at semiconductor electrodes: fundamental problems and new perspectives. *ChemPhysChem* **2014**, *15*, 1983–1995.

[129] Montoya, J. H.; Seitz, L. C.; Chakthranont, P.; Vojvodić, A.; Jaramillo, T. F.; Nørskov, J. K. Materials for solar fuels and chemicals. *Nature Materials* **2016**, *16*, 70–81.

[130] Nørskov, J. K.; Bligaard, T.; Rossmeisl, J.; Christensen, C. H. Towards the computational design of solid catalysts. *Nature Chemistry* **2009**, *1*, 37–46.

[131] Pelletier, J. D. A.; Basset, J. Catalysis by design: well-defined single-site heterogeneous catalysts. *Accounts of Chemical Research* **2016**, *49*, 664–677.

[132] Suárez, S., Single-Site Photocatalysts: Photoactive Species Dispersed on Porous Matrixes In *Design of Advanced Photocatalytic Materials for Energy and Environmental Applications*, Coronado, J. M., Fresno, F., Hernández-Alonso, M. D., Portela, R., Eds.; Springer London: London, 2013, pp 171–194.

[133] Bai, S.; Wang, L.; Li, Z.; Xiong, Y. Facet-engineered surface and interface design of photocatalytic materials. *Advanced Science* **2016**, *4*, DOI: 10.1002/advs.201600216.

[134] Chen, W.; Kuang, Q.; Wang, Q.; Xie, Z. Engineering a high energy surface of anatase TiO_2 crystals towards enhanced performance for energy conversion and environmental applications. *RSC Advances* **2015**, *5*, 20396–20409.

[135] Kumar, S. G.; Devi, L. G. Review on modified TiO_2 photocatalysis under uv/visible light: selected results and related mechanisms on interfacial charge carrier transfer dynamics. *The Journal of Physical Chemistry A* **2011**, *115*, 13211–13241.

[136] Wen, J. Z.; Li, X.; Liu, W.; Fang, Y.; Xie, J.; Xu, Y. Photocatalysis fundamentals and surface modification of TiO_2 nanomaterials. *Chinese Journal of Catalysis* **2015**, *36*, 2049–2070.

[137] Nowotny, J.; Alim, M. A.; Bak, T.; Idris, M. A.; Ionescu, M.; Prince, K.; Sahdan, M. Z.; Sopian, K.; Mat Teridi, M. A.; Sigmund, W. Defect chemistry and defect engineering of TiO_2-based semiconductors for solar energy conversion. *Chem. Soc. Rev.* **2015**, *44*, 8424–8442.

[138] Portela, R., Non-metal Doping for Band-Gap Engineering In *Design of Advanced Photocatalytic Materials for Energy and Environmental Applications*, Coronado, J. M., Fresno, F., Hernandez-Alonso, M. D., Portela, R., Eds.; Springer London: London, 2013, pp 287–309.

[139] Maeda, K.; Domen, K. Solid solution of GaN and ZnO as a stable photocatalyst for overall water splitting under visible light. *Chemistry of Materials* **2009**, *22*, 612–623.

[140] Fresno, F.; Hernandez-Alonso, M. D., Sensitizers: Dyes and Quantum Dots In *Design of Advanced Photocatalytic Materials for Energy and Environmental Applications*, Coronado, J. M., Fresno, F., Hernandez-Alonso, M. D., Portela, R., Eds.; Springer London: London, 2013, pp 329–343.

[141] Bai, S.; Yin, W.; Wang, L.; Li, Z.; Xiong, Y. Surface and interface design in cocatalysts for photocatalytic water splitting and CO_2 reduction. *RSC Advances* **2016**, *6*, 57446–57463.

[142] De la Pena O'Shea, V. A., The Role of Co-catalysts: Interaction and Synergies with Semiconductors In *Design of Advanced Photocatalytic Materials for Energy and Environmental Applications*, Coronado, J. M., Fresno, F., Hernandez-Alonso, M. D., Portela, R., Eds.; Springer London: London, 2013, pp 195–216.

[143] Wang, H.; Zhang, L.; Chen, Z.; Hu, J.; Li, S.; Wang, Z.; Liu, J.; Wang, X. Semiconductor heterojunction photocatalysts: design, construction, and photocatalytic performances. *Chemical Society Reviews* **2014**, *43*, 5234.

[144] Ding, C.; Shi, J.; Wang, Z.; Li, C. Photoelectrocatalytic water splitting: significance of cocatalysts, electrolyte, and interfaces. *ACS Catalysis* **2016**, *7*, 675–688.

[145] Marschall, R. Semiconductor composites: strategies for enhancing charge carrier separation to improve photocatalytic activity. *Advanced Functional Materials* **2013**, *24*, 2421–2440.

[146] Fresno, F., Heterojunctions: Joining Different Semiconductors In *Design of Advanced Photocatalytic Materials for Energy and Environmental Applications*, Coronado, J. M., Fresno, F., Hernandez-Alonso, M. D., Portela, R., Eds.; Springer London: London, 2013, pp 311–327.

[147] Xiao, F.; Miao, J.; Tao, H. B.; Hung, S.; Wang, H.; Yang, H. B.; Chen, J.; Chen, R.; Liu, B. One-dimensional hybrid nanostructures for heterogeneous photocatalysis and photoelectrocatalysis. *Small* **2015**, *11*, 2115–2131.

[148] Weng, B.; Liu, S.; Tang, Z.; Xu, Y. One-dimensional nanostructure based materials for versatile photocatalytic applications. *RSC Advances* **2014**, *4*, 12685.

[149] Lee, K.; Mazare, A.; Schmuki, P. One-dimensional titanium dioxide nanomaterials: nanotubes. *Chemical Reviews* **2014**, *114*, 9385–9454.

[150] Zhou, P.; Wang, Y.; Jaroniec, M. All-solid-state z-scheme photocatalytic systems. *Advanced Materials* **2014**, *26*, 4920–4935.

[151] Kudo, A. Z-scheme photocatalyst systems for water splitting under visible light irradiation. *MRS Bulletin* **2011**, *36*, 32–38.

[152] Wang, H.; Zhang, L.; Chen, Z.; Hu, J.; Li, S.; Wang, Z.; Liu, J.; Wang, X. Semiconductor heterojunction photocatalysts: design, construction, and photocatalytic performances. *Chemical Society Reviews* **2014**, *43*, 5234.

[153] Li, X.; Wen, J. Z.; Low, J.; Fang, Y.; Yu, J. Design and fabrication of semiconductor photocatalyst for photocatalytic reduction of CO_2 to solar fuel. *Science China Materials* **2014**, *57*, 70–100.

[154] Li, G.; Du, K.; Haussener, S. Charge transport in two-photon semiconducting structures for solar fuels. *ChemSusChem* **2016**, *9*, 2878–2904.

[155] Zhou, Y.; Tu, W.; Zou, Z., New Materials for CO_2 Photoreduction In *Photocatalysis: Fundamentals and Perspectives*; The Royal Society of Chemistry: 2016.

[156] Gao, D.; Fan, C.; Wang, Q.; Bao, X. Nanostructured heterogeneous catalysts for electrochemical reduction of CO_2. *Current Opinion in Green and Sustainable Chemistry* **2017**, *3*, 39–44.

[157] Liu, S.; Han, C.; Tang, Z.; Xu, Y. Heterostructured semiconductor nanowire arrays for artificial photosynthesis. *Materials Horizons* **2016**, *3*, 270–282.

[158] Liu, X.; Iocozzia, J.; Wang, Y.; Cui, X.; Chen, Y.; Zhao, S.; Li, Z.; Lin, Z. Noble metal-metal oxide nanohybrids with tailored nanostructures for efficient solar energy conversion, photocatalysis and environmental remediation. *Energy & Environmental Science* **2017**, *10*, 402–434.

[159] Low, J.; Cheng, B.; Wang, Y. Surface modification and enhanced photocatalytic CO_2 reduction performance of TiO_2: a review. *Applied Surface Science* **2017**, *392*, 658–686.

[160] Chen, W.; Qi, D.; Gao, X.; Wee, A. T. S. Surface transfer doping of semiconductors. *Progress in Surface Science* **2009**, *84*, 279–321.

[161] Ristein, J. Surface transfer doping of semiconductors. *Science* **2006**, *313*, 1057–1058.

[162] Viswanathan, B.; Krishanmurthy, K. R. Nitrogen incorporation in TiO_2: does it make a visible light photo-active material? *International Journal of Photoenergy* **2012**, *2012*, 1–10.

[163] Banerjee, S.; Pillai, S. C.; Falaras, P.; O'Shea, K. E.; Byrne, J.; Dionysiou, D. D. New insights into the mechanism of visible light photocatalysis. *The Journal of Physical Chemistry Letters* **2014**, *5*, 2543–2554.

[164] Viswanathan, B., Chapter 11 - Photo-Catalytic Routes for Fuel Production In *Energy Sources*, Viswanathan, B., Ed.; Elsevier: Amsterdam, 2017, pp 213–261.

[165] Lee, W.; Lim, J.; Kim, S. O. Nitrogen dopants in carbon nanomaterials: defects or a new opportunity? *Small Methods* **2016**, *1*.

[166] Trefalt, G.; Behrens, S. H.; Borkovec, M. Charge regulation in the electrical double layer: ion adsorption and surface interactions. *Langmuir* **2015**, *32*, 380–400.

[167] Fleharty, M.; Swol, F. v.; Petsev, D. N. Charge regulation at semiconductor-electrolyte interfaces. *Journal of Colloid and Interface Science* **2015**, *449*, 409–415.

[168] Fleharty, M.; Swol, F. v.; Petsev, D. N. Manipulating semiconductor colloidal stability through doping. *Physical Review Letters* **2014**, *113*, DOI: 10.1103/physrevlett.113.158302.

[169] Kim, J. H.; Lee, J. S. $BiVO_4$-based heterostructured photocatalysts for solar water splitting: a review. *Energy and Environment Focus* **2014**, *3*, 339–353.

[170] Wang, S.; Yun, J.; Luo, B.; Butburee, T.; Peerakiatkhajohn, P.; Thaweesak, S.; Xiao, M.; Wang, L. Recent progress on visible light responsive heterojunctions for photocatalytic applications. *Journal of Materials Science & Technology* **2017**, *33*, 1–22.

[171] Nozik, A. J., Novel Approaches to Water Splitting by Solar Photons In *Photoelectrochemical Water Splitting: Materials, Processes and Architectures*; The Royal Society of Chemistry: 2013.

[172] Chen, X.; Li, Y.; Shen, S. Surface- and interface-engineered heterostructures for solar hydrogen generation. *Journal of Physics D: Applied Physics* **2018**, *51*, 163002.

[173] Peerakiatkhajohn, P.; Yun, J.; Wang, S.; Wang, L. Review of recent progress in unassisted photoelectrochemical water splitting: from material modification to configuration design. *Journal of Photonics for Energy* **2016**, *7*, 012006.

[174] Mayer, M. T.; Lin, Y.; Yuan, G.; Wang, D. Forming heterojunctions at the nanoscale for improved photoelectrochemical water splitting by semiconductor materials: case studies on hematite. *Accounts of Chemical Research* **2013**, *46*, 1558–1566.

[175] Moniz, S. J. A.; Shevlin, S. A.; Martin, D.; Guo, Z.; Tang, J. Visible-light driven heterojunction photocatalysts for water splitting – a critical review. *Energy & Environmental Science* **2015**, *8*, 731–759.

[176] Oldham, W.; Milnes, A. G. Interface states in abrupt semiconductor heterojunctions. *Solid-State Electronics* **1964**, *7*, 153–165.

[177] Dale, J. Alloyed semiconductor heterojunctions. *Physica Status Solidi (B)* **1966**, *16*, 351–387.

[178] Lei, Y.; Lu, X. The decisive effect of interface states on the photocatalytic activity of the silver(I) oxide/titanium dioxide heterojunction. *Journal of Colloid and Interface Science* **2017**, *492*, 167–175.

[179] *Electronic Structure of Semiconductor Heterojunctions*; Margaritondo, G., Ed.; Perspectives in Condensed Matter Physics; Springer Dordrecht: 1988, pp XIII, 338.

[180] SHARMA, B.; PUROHIT, R.; SHARMA, B., PUROHIT, R., Eds.; International Series in the Science of the Solid State, Vol. 5; Pergamon: 1974, pp 1–23.

[181] Ferry, D. K., *Semiconductor Transport*, 1st; CRC Press: 2000.

[182] Overview of Electronic Devices In *The Materials Science of Semiconductors*; Springer US: Boston, MA, 2008, pp 73–139.

[183] An, X.; Wang, Y.; Lin, J.; Shen, J.; Zhang, Z.; Wang, X. Heterojunction: important strategy for constructing composite photocatalysts. *Science Bulletin* **2017**, *62*, Solar Photocatalytic Energy Conversion, 599–601.

[184] Valenti, M.; Jonsson, M. P.; Biskos, G.; Schmidt-Ott, A.; Smith, W. A. Plasmonic nanoparticle-semiconductor composites for efficient solar water splitting. *J. Mater. Chem. A* **2016**, *4*, 17891–17912.

[185] Kriegel, I.; Scotognella, F.; Manna, L. Plasmonic doped semiconductor nanocrystals: Properties, fabrication, applications and perspectives. *Physics Reports* **2017**, *674*, Plasmonic Doped Semiconductor Nanocrystals: Properties, Fabrication, Applications and Perspectives, 1–52.

[186] Jiang, R.; Li, B.; Fang, C.; Wang, J. Metal/Semiconductor Hybrid Nanostructures for Plasmon-Enhanced Applications. *Advanced Materials* **2014**, *26*, 5274–5309.

[187] Ghobadi, T. G. U.; Ghobadi, A.; Ozbay, E.; Karadas, F. Strategies for Plasmonic Hot-Electron-Driven Photoelectrochemical Water Splitting. *ChemPhotoChem* **2018**, *2*, 161–182.

[188] Alexander, J. C., Literature Review In *Surface Modifications and Growth of Titanium Dioxide for Photo-Electrochemical Water Splitting*; Springer International Publishing: Cham, 2016, pp 5–45.

[189] Ma, X.; Dai, Y.; Lin, Y.; Huang, B. Energy transfer in plasmonic photocatalytic composites. *Light: Science & Applications* **2016**, *5*, e16017–e16017.

[190] Achermann, M. Exciton-plasmon interactions in metal-semiconductor nanostructures. *The Journal of Physical Chemistry Letters* **2010**, *1*, 2837–2843.

[191] Wang, S.; Gao, Y.; Miao, S.; Liu, T.; Mu, L.; Li, R.; Fan, F.; Li, C. Positioning the water oxidation reaction sites in plasmonic photocatalysts. *Journal of the American Chemical Society* **2017**, *139*, 11771–11778.

[192] Alexander, J. C., Results: Plasmonic Photocurrent with AuNP-TiO_2 In *Surface Modifications and Growth of Titanium Dioxide for Photo-Electrochemical Water Splitting*; Springer International Publishing: Cham, 2016, pp 131–177.

[193] Burda, C.; Chen, X.; Narayanan, R.; El-Sayed, M. A. Chemistry and properties of nanocrystals of different shapes. *Chemical Reviews* **2005**, *105*, 1025–1102.

[194] Musumeci, F.; Pollack, G. H. Influence of water on the work function of certain metals. *Chemical Physics Letters* **2012**, *536*, 65–67.

[195] Hori, Y.; Wakebe, H.; Tsukamoto, T.; Koga, O. Electrocatalytic process of CO selectivity in electrochemical reduction of CO_2 at metal electrodes in aqueous media. *Electrochimica Acta* **1994**, *39*, 1833–1839.

[196] Hori, Y., Electrochemical CO_2 Reduction on Metal Electrodes In *Modern Aspects of Electrochemistry*, Vayenas, C. G., White, R. E., Gamboa-Aldeco, M. E., Eds.; Springer New York: New York, NY, 2008, pp 89–189.

[197] Li, W. Electrocatalytic reduction of CO_2 to small organic molecule fuels on metal catalysts. *ACS Symposium Series* **2010**, 55–76.

[198] Peterson, A. A.; Nørskov, J. K. Activity descriptors for CO_2 electroreduction to methane on transition-metal catalysts. *The Journal of Physical Chemistry Letters* **2012**, *3*, 251–258.

[199] Ye, S.; Wang, R.; Wu, M.; Yuan, Y. A review on g-c3n4 for photocatalytic water splitting and CO_2 reduction. *Applied Surface Science* **2015**, *358*, 15–27.

[200] Ong, W.; Tan, L.; Ng, Y. H.; Yong, S. T.; Chai, S. Graphitic carbon nitride (g-c3n4)-based photocatalysts for artificial photosynthesis and environmental remediation: are we a step closer to achieving sustainability? *Chemical Reviews* **2016**, *116*, 7159–7329.

[201] Chiang, Y.; Juang, R. Surface modifications of carbonaceous materials for carbon dioxide adsorption: a review. *Journal of the Taiwan Institute of Chemical Engineers* **2017**, *71*, 214–234.

[202] Seh, Z. W.; Kibsgaard, J.; Dickens, C. F.; Chorkendorff, I.; Nørskov, J. K.; Jaramillo, T. F. Combining theory and experiment in electrocatalysis: insights into materials design. *Science* **2017**, *355*, DOI: 10.1126/science.aad4998.

[203] Jiao, Y.; Zheng, Y.; Jaroniec, M.; Qiao, S. Z. Design of electrocatalysts for oxygen- and hydrogen-involving energy conversion reactions. *Chemical Society Reviews* **2015**, *44*, 2060–2086.

[204] Benck, J. D.; Hellstern, T. R.; Kibsgaard, J.; Chakthranont, P.; Jaramillo, T. F. Catalyzing the hydrogen evolution reaction (HER) with molybdenum sulfide nanomaterials. *ACS Catalysis* **2014**, *4*, 3957–3971.

[205] Norskov, J. K.; Bligaard, T.; Logadottir, A.; Kitchin, J. R.; Chen, J.; Pandelov, S.; Stimming, U. Trends in the exchange current for hydrogen evolution. *Journal of the Electrochemical Society* **2005**, *152*, J23.

[206] Parsons, R. The rate of electrolytic hydrogen evolution and the heat of adsorption of hydrogen. *Transactions of the Faraday Society* **1958**, *54*, 1053.

[207] Skulason, E.; Tripkovic, V.; Bjorketun, M. E.; Guomundsdottir, S.; Karlberg, G.; Rossmeisl, J.; Bligaard, T.; Jonsson, H.; Norskov, J. K. Modeling the electrochemical hydrogen oxidation and evolution reactions on the basis of density functional theory calculations. *The Journal of Physical Chemistry C* **2010**, *114*, 18182–18197.

[208] Greeley, J.; Jaramillo, T. F.; Bonde, J. L.; Chorkendorff, I.; Norskov, J. K. Computational high-throughput screening of electrocatalytic materials for hydrogen evolution. *Nature Materials* **2006**, *5*, 909–913.

[209] Greeley, J.; Mavrikakis, M. Alloy catalysts designed from first principles. *Nature Materials* **2004**, *3*, 810–815.

[210] Strmcnik, D.; Uchimura, M.; Wang, C.; Subbaraman, R.; Danilovic, N.; Vliet, D. V.; Paulikas, A. P.; Stamenkovic, V. R.; Markovic, N. M. Improving the hydrogen oxidation reaction rate by promotion of hydroxyl adsorption. *Nature Chemistry* **2013**, *5*, 300–306.

[211] Danilovic, N.; Subbaraman, R.; Strmcnik, D.; Stamenkovic, V. R.; Markovic, N. M. Electrocatalysis of the HER in acid and alkaline media. *Journal of the Serbian Chemical Society* **2013**, *78*, 2007–2015.

[212] Hinnemann, B.; Moses, P. G.; Bonde, J. L.; Jørgensen, K. P.; Nielsen, L.; Horch, S.; Chorkendorff, I.; Nørskov, J. K. Biomimetic hydrogen evolution: MoS_2 nanoparticles as catalyst for hydrogen evolution. *Journal of the American Chemical Society* **2005**, *127*, 5308–5309.

[213] Jaramillo, T. F.; Jorgensen, K. P.; Bonde, J. L.; Nielsen, L.; Horch, S.; Chorkendorff, I. Identification of active edge sites for electrochemical H_2 evolution from MoS_2 nanocatalysts. *Science* **2007**, *317*, 100–102.

[214] Tsai, C.; Chan, K.; Nørskov, J. K.; Abild-Pedersen, F. Theoretical insights into the hydrogen evolution activity of layered transition metal dichalcogenides. *Surface Science* **2015**, *640*, 133–140.

[215] Kibsgaard, J.; Chen, Z.; Reinecke, B. N.; Jaramillo, T. F. Engineering the surface structure of MoS_2 to preferentially expose active edge sites for electrocatalysis. *Nature Materials* **2012**, *11*, 963–969.

[216] Chen, W.; Sasaki, K.; Ma, C.; Frenkel, A. I.; Marinkovic, N.; Muckerman, J. T.; Zhu, Y.; Adžić, R. R. Hydrogen-evolution catalysts based on non-noble metal nickel–molybdenum nitride nanosheets. *Angewandte Chemie International Edition* **2012**, *51*, 6131–6135.

[217] Vrubel, H.; Hu, X. Molybdenum boride and carbide catalyze hydrogen evolution in both acidic and basic solutions. *Angewandte Chemie International Edition* **2012**, *51*, 12703–12706.

[218] Seh, Z. W.; Fredrickson, K. D.; Anasori, B.; Kibsgaard, J.; Strickler, A. L.; Lukatskaya, M. R.; Gogotsi, Y.; Jaramillo, T. F.; Vojvodić, A. Two-dimensional molybdenum carbide (MXene) as an efficient electrocatalyst for hydrogen evolution. *ACS Energy Letters* **2016**, *1*, 589–594.

[219] Laursen, A. B.; Patraju, K. R.; Whitaker, M. J.; Retuerto, M.; Sarkar, T.; Yao, N.; Ramanujachary, K. V.; Greenblatt, M.; Dismukes, G. C. Nanocrystalline Ni_5P_4: a hydrogen evolution electrocatalyst of exceptional efficiency in both alkaline and acidic media. *Energy & Environmental Science* **2015**, *8*, 1027–1034.

[220] Popczun, E. J.; McKone, J. R.; Read, C. G.; Biacchi, A. J.; Wiltrout, A. M.; Lewis, N. S.; Schaak, R. E. Nanostructured nickel phosphide as an electrocatalyst for the hydrogen evolution reaction. *Journal of the American Chemical Society* **2013**, *135*, 9267–9270.

[221] Saadi, F. H.; Carim, A. I.; Velazquez, J. M.; Baricuatro, J. H.; McCrory, C. C. L.; Soriaga, M. P.; Lewis, N. S. Operando synthesis of macroporous molybdenum diselenide films for electrocatalysis of the hydrogen-evolution reaction. *ACS Catalysis* **2014**, *4*, 2866–2873.

[222] McKone, J. R.; Sadtler, B.; Werlang, C. A.; Lewis, N. S.; Gray, H. B. Ni–Mo nanopowders for efficient electrochemical hydrogen evolution. *ACS Catalysis* **2013**, *3*, 166–169.

[223] Suen, N. T.; Hung, S.; Quan, Q.; Zhang, N.; Xu, Y.; Chen, H. M. Electrocatalysis for the oxygen evolution reaction: recent development and future perspectives. *Chemical Society Reviews* **2017**, *46*, 337–365.

[224] Man, I. C.; Su, H.; Calle-Vallejo, F.; Hansen, H. A.; Martínez, J. I.; İnoglu, N.; Kitchin, J. R.; Jaramillo, T. F.; Nørskov, J. K.; Rossmeisl, J. Universality in oxygen evolution electrocatalysis on oxide surfaces. *ChemCatChem* **2011**, *3*, 1159–1165.

[225] Nosaka, Y.; Nosaka, A. Y. Understanding hydroxyl radical (.OH) generation processes in photocatalysis. *ACS Energy Letters* **2016**, *1*, 356–359.

[226] Nosaka, Y.; Nosaka, A. Y., Kinetic Processes in the Presence of Photogenerated Charge Carriers In *Photocatalysis: Fundamentals and Perspectives*; The Royal Society of Chemistry: 2016.

[227] Hayyan, M.; Hashim, M. A.; AlNashef, I. M. Superoxide ion: generation and chemical implications. *Chemical Reviews* **2016**, *116*, 3029–3085.

[228] Gligorovski, S.; Strekowski, R.; Barbati, S.; Vione, D. Environmental implications of hydroxyl radicals (.OH). *Chemical Reviews* **2015**, *115*, 13051–13092.

[229] Chen, X.; Wang, F.; Hyun, J. Y.; Wei, T.; Jin, Q.; Ren, X.; Shin, I.; Yoon, J. Recent progress in the development of fluorescent, luminescent and colorimetric probes for detection of reactive oxygen and nitrogen species. *Chem. Soc. Rev.* **2016**, *45*, 2976–3016.

[230] Nosaka, Y.; Nishikawa, M.; Nosaka, A. Y. Spectroscopic investigation of the mechanism of photocatalysis. *Molecules* **2014**, *19*, 18248–18267.

[231] Sayama, K.; Arakawa, H. Effect of Na_2CO_3 addition on photocatalytic decomposition of liquid water over various semiconductor catalysis. *Journal of Photochemistry and Photobiology A: Chemistry* **1994**, *77*, 243–247.

[232] Sayama, K.; Arakawa, H. Effect of carbonate addition on the photocatalytic decomposition of liquid water over a ZrO_2 catalyst. *Journal of Photochemistry and Photobiology A: Chemistry* **1996**, *94*, 67–76.

[233] Sayama, K.; Yase, K.; Arakawa, H.; Asakura, K.; Tanaka, A.; Domen, K.; Onishi, T. Photocatalytic activity and reaction mechanism of Pt-intercalated $K_4Nb_6O_{17}$ catalyst on the water splitting in carbonate salt aqueous solution. *Journal of Photochemistry and Photobiology A: Chemistry* **1998**, *114*, 125–135.

[234] Mills, A.; Porter, G. Photosensitised dissociation of water using dispersed suspensions of n-type semiconductors. *Journal of the Chemical Society, Faraday Transactions 1: Physical Chemistry in Condensed Phases* **1982**, *78*, 3659.

[235] Parida, K.; Mohapatra, L. Recent progress in the development of carbonate-intercalated Zn/Cr LDH as a novel photocatalyst for hydrogen evolution aimed at the utilization of solar light. *Dalton Trans.* **2012**, *41*, 1173–1178.

[236] Arakawa, H.; Sayama, K. Solar hydrogen production. Significant effect of Na_2CO_3 addition on water splitting using simple oxide semiconductor photocatalysts. *Catalysis Surveys From Japan* **2000**, *4*, 75–80.

[237] Sayama, K.; Arakawa, H. Effect of carbonate salt addition on the photocatalytic decomposition of liquid water over Pt–TiO_2 catalyst. *Journal of the Chemical Society, Faraday Transactions* **1997**, *93*, 1647–1654.

[238] Ni, M.; Leung, M. K.; Leung, D. Y.; Sumathy, K. A review and recent developments in photocatalytic water-splitting using TiO_2 for hydrogen production. *Renewable and Sustainable Energy Reviews* **2007**, *11*, 401–425.

[239] Dhere, N. G.; Bennur, R. S., Use of Solar Energy to Produce Hydrogen In *Hydrogen Fuel*, 1st; CRC Press: 2008, p 56.

[240] Grimes, C. A.; Varghese, O. K.; Ranjan, S., Oxide Semiconductors: Suspended Nanoparticle Systems In *Light, Water, Hydrogen: The Solar Generation of Hydrogen by Water Photoelectrolysis*, Grimes, C. A., Varghese, O. K., Ranjan, S., Eds.; Springer US: Boston, MA, 2008, pp 371–426.

[241] Arakawa, H., Water Photolysis by TiO_2 Particle – Significant Effect of Na_2CO_3 Addition on Water Splitting In *Photocatalysis: Science and Technology*, Kaneko, M., Okura, I., Eds.; Springer Berlin Heidelberg: 2002, pp 235–248.

[242] Bielski, B. H. J.; Cabelli, D. E.; Arudi, R. L.; Ross, A. B. Reactivity of HO_2/O_2^- radicals in aqueous solution. *Journal of Physical and Chemical Reference Data* **1985**, *14*, 1041–1100.

[243] Schneider, J.; Bahnemann, D. W. Undesired role of sacrificial reagents in photocatalysis. *The Journal of Physical Chemistry Letters* **2013**, *4*, 3479–3483.

[244] Hykaway, N.; Sears, W.; Morisaki, H.; Morrison, S. Current-doubling reactions on titanium dioxide photoanodes. *The Journal of Physical Chemistry* **1986**, *90*, 6663–6667.

[245] Memming, R. In *Electron Transfer I*, ed. by Mattay, J., Springer Berlin Heidelberg: Berlin, Heidelberg, 1994, pp 105–181.

[246] Nogami, G.; Kennedy, J. H. Investigation of "Current Doubling" Mechanism of Organic Compounds by the Rotating Ring Disk Electrode Technique. *J. Electrochem. Soc.* **1989**, *136*, 2583–2588.

[247] Lana–Villarreal, T.; Gomez, R.; Neumann-Spallart, M.; Alonso-Vante, N.; Salvador, P. Semiconductor photooxidation of pollutants dissolved in water: a kinetic model for distinguishing between direct and indirect interfacial hole transfer. i. photoelectrochemical experiments with polycrystalline anatase electrodes under current doubling and absence of recombination. *The Journal of Physical Chemistry B* **2004**, *108*, 15172–15181.

[248] Habisreutinger, S. N.; Schmidt-Mende, L.; Stolarczyk, J. K. Photocatalytic reduction of CO_2 on TiO_2 and other semiconductors. *Angewandte Chemie International Edition* **2013**, *52*, 7372–7408.

[249] Laursen, S.; Poudyal, S., Chapter 8 - Photo- and Electro-Catalysis: CO_2 Mitigation Technologies In *Novel Materials for Carbon Dioxide Mitigation Technology*, Shi, F., Morreale, B., Eds.; Elsevier: Amsterdam, 2015, pp 233–268.

[250] Chandrasekaran, K.; Thomas, J. K. Photochemical reduction of carbonate to formaldehyde on TiO_2 powder. *Chemical Physics Letters* **1983**, *99*, 7–10.

[251] Yui, T.; Kan, A.; Saitoh, C.; Koike, K.; Ibusuki, T.; Ishitani, O. Photochemical reduction of CO_2 using TiO_2: effects of organic adsorbates on TiO_2 and deposition of Pd onto TiO_2. *ACS Applied Materials &; Interfaces* **2011**, *3*, 2594–2600.

[252] Ku, Y.; Lee, W.; Wang, W. Photocatalytic reduction of carbonate in aqueous solution by UV/TiO_2 process. *Journal of Molecular Catalysis A: Chemical* **2004**, *212*, 191–196.

[253] Raphael, M. W.; Malati, M. A. The photocatalysed reduction of aqueous sodium carbonate using platinized titania. *Journal of Photochemistry and Photobiology A: Chemistry* **1989**, *46*, 367–377.

[254] Yang, C.-C. Photocatalytic CO_2 Activation by Water, English, Ph.D. Thesis, University of Twente.

[255] Nakanishi, H.; Iizuka, K.; Takayama, T.; Iwase, A.; Kudo, A. Highly active $natao_3$-based photocatalysts for CO_2 reduction to form CO using water as the electron donor. *ChemSusChem* **2016**, *10*, 112–118.

[256] Wang, H.; Schneider, W. F. Nature and role of surface carbonates and bicarbonates in CO oxidation over RuO_2. *Physical Chemistry Chemical Physics* **2010**, *12*, 6367.

[257] Viswanathan, B., Material Selection for Photoelectrochemical or Photocatalytic Processes In *Solar Fuel Generation*, 2017, pp 61–76.

[258] Frumkin, A. N., Ed., Surface Properties of Semiconductors: Conference, Moscow, 1961: Papers, Consultants Bureau: 1964.

[259] Schmidt, M., The Thermodynamics of CO_2 Conversion In *Carbon Dioxide Chemistry*, Paul, J., Pradier, C.-M., Eds.; Woodhead Publishing: 1994, pp 23–30.

Chapter 3

Experimental Methods

Abstract

The methodology employed in this study is comprehensively described in this chapter, encompassing the selection and characterization of the materials, reaction conditions, and sample preparation procedures. Additionally, a detailed protocol outlining the steps involved in CO_2 activation, reduction, data collection, and analysis is provided. Ethical considerations, quality control measures, potential pitfalls of the experimental methodology, and recommendations for future research were also discussed.

3.1 Preparative Methods

This thesis outlines the experiments carried out at the National Centre for Catalysis Research, Department of Chemistry, Indian Institute of Technology, Madras. These experiments were conducted in compliance with established safety protocols and guidelines. It is imperative to emphasize that these protocols were strictly adhered to in order to safeguard the well-being of the personnel and maintain a secure working environment in the chemical laboratory.

3.1.1 Glass wares

In this study, we utilized borosilicate glassware manufactured by the esteemed company Borosil for all the experimental procedures. Prior to using the glassware, a calibration process was conducted, as described in a separate report. In addition, we incorporated in-house manufactured glassware and its components into the photoreactor and related equipment. To maintain the required level of cleanliness, we subjected the glassware to a comprehensive cleaning regimen that involved the use of a soap solution, manual scrubbing with nylon bristle brushes, rinsing with distilled water, and drying at a temperature of $60\,^{\circ}\mathrm{C}$.

3.1.2 Spatula

The stainless steel lab spatula and micro scoop reagent laboratory mixing spatula were comprehensively cleaned using methanol and subsequently dried in an air

(a) Alumina crucible

(b) Silica crucible

(c) Graphite crucible

(d) Platinum crucible

(e) Nickel crucible

(f) Zirconia crucible

(g) Quartz crucible

(h) Quartz boat

Figure 3.1: Various crucibles used for material synthesis

oven at a temperature of $80\,^{\circ}\mathrm{C}$. These instruments were then employed for sampling and mixing all solid materials.

3.1.3 Weighing Balance

The Sartorius TE64 analytical balance, which operates at a voltage of $115\,\mathrm{V}$ AC and has a capacity of $60\,\mathrm{g}$, was employed for weighing in all experiments. A LabExact 1200159 W44 cellulose weighing paper sheet, with its nitrogen-free, non-absorbing, and high-gloss surface, was utilized to ensure accurate measurements and prevent potential contamination. Each sheet measured 4×4 in and provided a suitable platform for weighing the samples in a precise and controlled manner.

3.1.4 Crucibles and Boats

In this study, several crucibles were used to synthesize these materials. These crucibles were comprised of alumina, boats, silica, graphite, platinum, nickel, zirconia, and quartz.

3.1.5 Chemicals

In this study, a range of chemicals were used to perform the experiments. These chemicals were obtained from reputable suppliers or manufacturers and were of analytical grade to guarantee high purity and reliability. The chemicals listed in Table 3.1 were chosen based on their relevance to the research objectives and compatibility with the experimental procedures. The experimental protocols specify the quantity and concentration of each chemical. All chemicals were handled and stored in accordance with established safety guidelines and standard laboratory practices.

Table 3.1: List of Chemicals Used in the Experiment

Chemical Name	Manufacturer	Grade	CAS Number	Formula
Melamine	Sigma Aldrich	99%	108-78-1	$C_3H_6N_6$
Ammonium Thiocyanate	Sigma Aldrich	99%	1762-95-4	NH_4CNS
Cyanamide	Sigma Aldrich	99%	420-04-2	CH_2N_2
Dicyandiamide	Sigma Aldrich	99%	461-58-5	$C_2H_4N_4$
Urea	Sigma Aldrich	99%	57-13-6	CH_4N_2O
Thiourea	Sigma Aldrich	99%	62-56-6	CH_4N_2S
Sodium Hydroxide	SRL	98%	1310-73-2	NaOH
Lithium Chloride	Sigma Aldrich	99%	7447-41-8	LiCl
Potassium Chloride	Merck	99.5%	7447-40-7	KCl
Cesium Chloride	Sigma Aldrich	99%	7647-17-8	CsCl
Nickel Chloride	SRL	99%	7791-20-0	$NiCl_2$
Cyanuric Acid	Sigma Aldrich	98%	108-80-5	$C_3H_3N_3O_3$
Hydrochloride Acid	Merck	37%	7647-01-0	HCl
Phenolphthalein	Merck	99%	77-09-8	$C_{20}H_{14}O_4$
Methanol	SRL	99.8%5	67-56-1	CH_3OH
Absolute Ethanol	SRL	99%	64-17-5	C_2H_5OH

3.1.6 Ultrapure Water System

In each experiment, a Milli-Q® EQ 7000 ultrapure water system was used to maintain a consistently high level of water purity. This system ensured that the water used in the experiments had a resistivity of $18.2\,\mathrm{M\Omega\,cm}$ at 25 °C and a total organic carbon (TOC) level of $\leq 5\,\mathrm{ppb}$.

3.1.7 Furnaces

The experimental setup utilized equipment that played a vital role in creating the desired conditions for the synthesis and processing of the investigated materials. This section highlights the features and functionalities of these tools.

1. Sigma1400 tubular furnace: A tubular furnace, specifically a Sigma1400 model, was utilized for experiments involving material synthesis. This furnace boasted a high-quality recrystallized alumina tube with a purity level of 99.85%, and it was capable of withstanding temperatures up to $1600\,^{\circ}\mathrm{C}$. A controlled heating environment was ensured using this furnace, which was optimal for the synthesis process.

2. Sigma electric muffle furnace: The Sigma electric muffle furnace was used for precise experiments in low-temperature environments. This furnace can reach temperatures up to $1200\,^{\circ}\mathrm{C}$. Its stable and reliable heat source facilitates precise temperature control during critical stages of the synthesis process.

3. $1\,\mathrm{L}$ Borosil filtration assembly: The filtering of synthesized materials was accomplished utilizing a filtration assembly from Borosil, which boasted a capacity of one liter. This assembly, designed for maximum filtration efficiency, included a borosilicate glass vessel with a volume of one liter and suitable

filter medium. Furthermore, the assembly was connected to a single-stage vacuum pump to create the suction required for filtration.

4. Sigma electric oven: The synthesized materials were subsequently dried and filtered, and the drying process was carried out using a Sigma electric oven. The oven was chosen for its ability to provide controlled and uniform heat distribution, which ensured efficient drying of the synthesized materials. The oven temperature range was also found to be dependable, making it suitable for drying.

5. Sigma electric vacuum oven: The efficient drying of materials with sensitive properties or volatile components often requires a vacuum environment. To meet these requirements, an electric vacuum oven (Sigma) was used. This oven integrates the advantages of vacuum technology with controlled heating, enabling the effective drying of the materials while preserving the desired vacuum conditions.

3.1.8 Miscellaneous Items

Teflon tape PTFE for water pipe sealing, parafilm M roll, silicone rubber septum, silicone tubes, water recirculation system, beakers, volumetric flasks, Erlenmeyer flasks, test tubes, pipettes (various sizes), burettes, graduated cylinders, petri dishes, watch glasses, gas sampling tubes with glass stopcocks, gas washing Dreschel bottle, glass filter funnel, glass adapter and stoppers.

3.2 Synthesis of Photocatalyts (g-C_3N_4) System

This section discusses the various synthesis methods of carbon nitride adopted for this study in detail, along with the rationale behind each method employed.

3.2.1 One Pot Synthesis of g-C_3N_4

The methodology employed in Chapter 4 investigates the importance of surface functionalities in the photon-mediated reduction of carbon dioxide using C_3N_4 as a potential photocatalyst. The selection of the precursor is essential for determining the surface and electronic properties of g-C_3N_4, as different precursors can result in various morphological, structural, optical, and chemical properties. In this study, g-C_3N_4 was prepared using a range of precursors including ammonium thiocyanate (NH_4SCN), melamine ($C_3H_6N_6$), urea ($CO(NH_2)_2$), thiourea ($SC(NH_2)_2$), cyanamide (CN_2H_2), and dicyandiamide ($(CNH_2)_2(CR)N_3$). The structures of the precursors were analyzed and their chemical compositions and morphologies were studied. The electronic structure and bandgap of g-C_3N_4 are influenced by its chemical composition, whereas its surface area and surface defects are affected by its morphology and crystallinity, which can impact its activity towards the desired chemical reaction. The general preparation of graphitic carbon nitride from the precursors involves the following steps.

1. Analysis of the Precursor: The X-ray Diffraction (XRD) analysis was performed to verify the presence of the desired compound in the precursor.

2. Mixing and Sonication: The mixture of the precursor and acetone was thoroughly combined in a $250\,\mathrm{mL}$ beaker, with $10\,\mathrm{g}$ of the precursor and $100\,\mathrm{mL}$ of acetone being used for the process. The resulting mixture was sonicated for $15\,\mathrm{min}$.

3. Recrystallization: A method for the recrystallization of melamine, cyanamide, dicyandiamide, urea, thiourea, and ammonium thiocyanate in acetone was carried out. The substances were dissolved in acetone to a level approximately ten times the volume of acetone relative to the recrystallized compound. The solution was then heated until the compound was fully dissolved, and cooled slowly in a water bath at a decreasing temperature. As the solution cooled, the compounds crystallized. The resulting crystals were filtered to remove impurities and gently washed with cold acetone. The crystals were air-dried in a clean, dry environment. This procedure yielded purified compounds with the desired physical properties. The purity and crystal structure of the recrystallized precursor were characterized by X-ray diffraction (XRD). This method provides a means of obtaining purified precursor crystals for further analysis and application.

4. Heating: An alumina crucible containing the appropriate amount of precursor was placed in a Sigma laboratory muffle furnace at a temperature of $550\,^{\circ}\mathrm{C}$ with a ramping rate of $2\,^{\circ}\mathrm{C\,min^{-1}}$. After reaching $550\,^{\circ}\mathrm{C}$, the temperature is maintained at $4\,\mathrm{h}$. The samples were removed once the oven cooled to room temperature.

5. Grinding: The graphitic carbon nitride, which had been transformed into a hard yellow block, was subsequently placed into a mortar and subjected to thorough grinding using a pestle.

6. Storage: The transfer of the delicate yellow powder was executed into a $25\,\mathrm{mL}$ storage amber glass vial, complete with an air-tight cap.

The investigation utilized containers designated AT-gCN, CY-gCN, DC-gCN, MEL-gCN, TU-gCN, and U-gCN. The prefix for each label was derived from the names of the precursors, including ammonium thiocyanate (AT), cyanamide (CY), dicyandiamide (DC), melamine (MEL), thiourea (TU), and urea (U).

3.2.2 Crucible Based Synthesis

The identity of the compound was confirmed by the x-ray diffraction (XRD) analysis of melamine. The compound was recrystallized in acetone, and $20\,\mathrm{g}$ of melamine was mixed well with 200mL of acetone and sonicated for $15\,\mathrm{min}$ to ensure complete mixing. The detailed procedure for the recrystallization of melamine in acetone is described in Section 3.2.1. The recrystallized precursors were collected, ground well in a mortar, and transferred into different crucibles, such as alumina, silica, platinum, graphite, nickel, zirconia, and quartz, using a spatula. The samples were then placed in a Sigma laboratory muffle furnace for $4\,\mathrm{h}$ at $550\,^{\circ}\mathrm{C}$ at a ramping rate

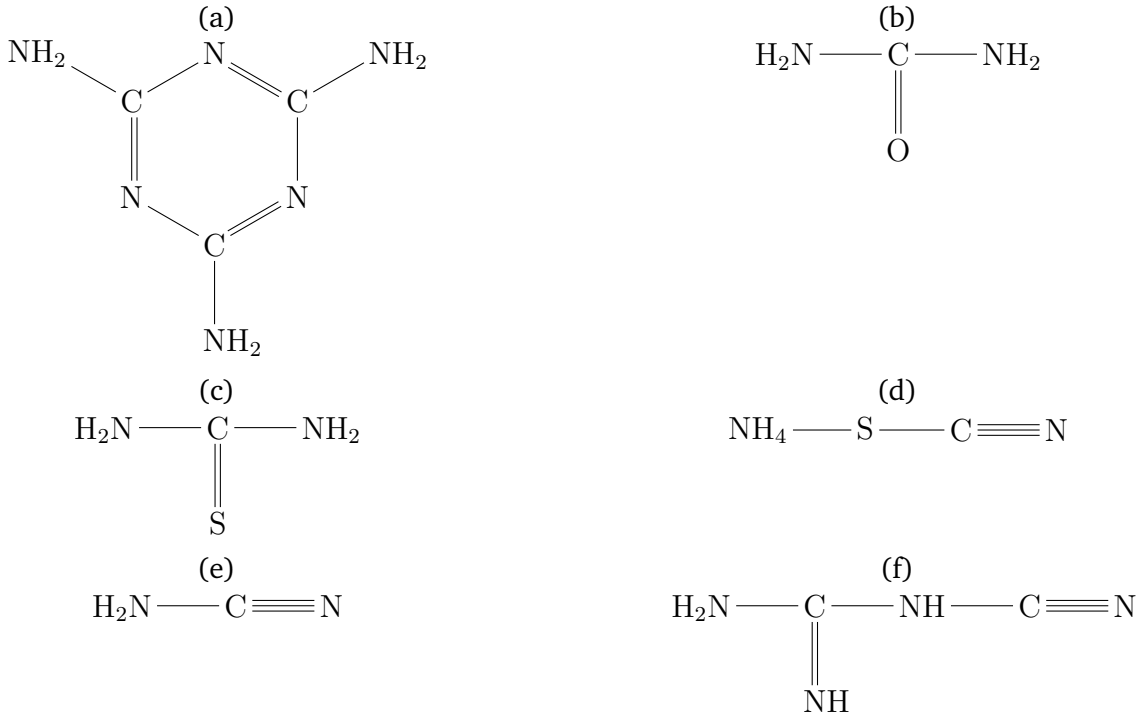

Figure 3.2: Chemical structures of compounds (a) Melamine and (b) Urea (c) Thiourea (d) Ammonium Thiocyanate (e) Cyanamide (f) Dicyandiamide

of $5\,^{\circ}\mathrm{C\,min^{-1}}$. Once the oven reached room temperature, the resulting hard yellow block of graphitic carbon nitride was transferred to a mortar and observed using a pestle. The delicate yellow powder was then transferred to a $25\,\mathrm{mL}$ storage amber glass vial with an airtight cap. The experiment utilized bottles labeled as Al-gCN, Si-gCN, Pt-gCN, Gr-gCN, Ni-gCN, Zr-gCN, and Q-gCN, with each label designating a specific type of crucible that was employed in the synthesis process: alumina crucible (Al), silica crucible (Si), platinum crucible (Pt), graphite crucible (Gr), nickel crucible (Ni), zirconia crucible (Zr), and quartz crucible (Q).

3.2.3 Ionothermal Synthesis

Synthesis of Li-PTI-AIR

In a glove box under inert atmosphere, $4\,\mathrm{g}$ ($15.58\,\mathrm{mmol}$) of recrystallized melamine ($C_3H_6N_6$) was thoroughly mixed with lithium chloride. The resulting mixture was then transferred to a flat-bottomed cylindrical alumina crucible with a lid. The reaction mixture was placed in a muffle furnace and heated at a ramping rate of $5\,^{\circ}\mathrm{C\,min^{-1}}$ to a terminal temperature of $550\,^{\circ}\mathrm{C}$. After $4\,\mathrm{h}$, the salt block was removed from the reaction mixture by washing with boiling distilled water and centrifuging at $7000\,\mathrm{rpm}$ for $15\,\mathrm{min}$. The obtained material was subsequently dried overnight in a vacuum oven at $110\,^{\circ}\mathrm{C}$ at a pressure of $1 \times 10^{-5}\,\mathrm{Torr}$. After thorough grinding with a mortar and pestle, the resulting compound was transferred to a $25\,\mathrm{mL}$ amber glass vial for storage. The sample was subsequently designated as Li-PTI-AIR, with "PTI" referring to "Poly Triazine Imide."

Synthesis of Li-PTI-N_2

In a glove box under inert conditions, $4\,\mathrm{g}$ ($15.58\,\mathrm{mmol}$) of recrystallized melamine ($C_3H_6N_6$) was thoroughly mixed with lithium chloride. The resulting mixture was then transferred to an alumina boat with a lid and placed under nitrogen atmosphere. The reaction mixture was introduced into a tubular furnace and heated at a ramping rate of $5\,^{\circ}\mathrm{C\,min^{-1}}$ until it reached a terminal temperature of $550\,^{\circ}\mathrm{C}$. After a period of $4\,\mathrm{h}$, the salt block was removed from the reaction mixture by washing with boiling distilled water and centrifugation at $7000\,\mathrm{rpm}$ for $15\ \mathrm{min}$. The obtained material was subsequently dried overnight in a vacuum oven at $110\,^{\circ}\mathrm{C}$ at a pressure of $1 \times 10^{-5}\,\mathrm{Torr}$. After thorough grinding using a mortar and pestle, the resulting compound was transferred to a $25\,\mathrm{mL}$ amber glass vial for storage and labeled as Li-PTI-N_2.

3.2.4 Eutectic Synthesis

Synthesis of Melamine Cyanurate (CAM)

Melamine cyanurate was used as the precursor for the eutectic synthesis process. A mixture of melamine and cyanuric acid in a 1:1 ratio was prepared using Millipore water, and the solution was refluxed and stirred at $90\,^{\circ}\mathrm{C}$ for $6\,\mathrm{h}$. After cooling, the mixture was filtered to obtain melamine cyanurate crystals, which were then washed with water and dried in a vacuum furnace under 10^{-5} torr pressure at $110\,^{\circ}\mathrm{C}$ overnight. The resulting melamine-cyanurate crystals were ground into a powder using a mortar and pestle. Melamine cyanurate was recrystallized from ethanol by weighing the powder ($0.5\,\mathrm{g}$), transferring it to a beaker, adding $50\,\mathrm{mL}$ of ethanol, and heating the solution until the melamine cyanurate dissolved. The solution was then cooled and filtered through filter paper, and the crystals were transferred to a petri dish to dry completely. The resulting crystals were pure and free of contaminants, and the powder was stored in an amber bottle (CAM).

Synthesis of CAM-gCN

The synthesized melamine cyanurate was subjected to powder x-ray diffraction (XRD) analysis to confirm its presence. To prepare the sample, $10\,\mathrm{g}$ of CAM was thoroughly mixed with $20\,\mathrm{mL}$ of methanol in a $250\,\mathrm{mL}$ beaker. The mixture was then sonicated for $15\,\mathrm{min}$ to ensure complete mixing. The resulting mixture was placed in a hot-air oven at $60\,^{\circ}\mathrm{C}$ overnight to promote crystallization. After cooling to room temperature, the recrystallized precursors were collected, ground in a mortar, and transferred to an alumina boat with a lid using a spatula. The alumina crucible was then placed in a Sigma laboratory tubular furnace and subjected to a ramping rate of $5\,^{\circ}\mathrm{C\,min^{-1}}$ and terminal temperature of $450\,^{\circ}\mathrm{C}$ for $4\,\mathrm{h}$. After cooling to room temperature, the resulting fine yellow block of graphitic carbon nitride was thoroughly ground using a pestle. The delicate yellow powder was then transferred into a $25\,\mathrm{mL}$ storage amber glass vial with an airtight cap and labeled as CAM-gCN.

Synthesis of CAM-gCN-$NiCl_2$-KCl

Under an inert atmosphere in a glove box, $4\,\mathrm{g}$ ($10.9\,\mathrm{mmol}$) of melamine cyanurate ($C_6H_9N_9O_3$), recrystallized from methanol, was ground thoroughly. This mixture was then combined with $10\,\mathrm{g}$ of a eutectic mixture of nickel chloride and potassium chloride (39.4:60.6 wt%). The mixture was transferred to an alumina boat with a lid. The reaction mixture was placed in a tubular furnace under a nitrogen atmosphere and heated for $4\,\mathrm{h}$ at a ramping rate of $5\,^{\circ}\mathrm{C\,min^{-1}}$ until it reached a terminal temperature of $450\,^{\circ}\mathrm{C}$. The salt block was removed from the reaction mixture by washing with boiling distilled water and centrifuging at $7000\,\mathrm{rpm}$ for $15\,\mathrm{min}$. The resulting material was then dried overnight in a vacuum oven at $110\,^{\circ}\mathrm{C}$ under a pressure of $1 \times 10^{-5}\,\mathrm{Torr}$ and stored in a $25\,\mathrm{mL}$ amber bottle labelled as CAM-gCN-$NiCl_2$-KCl.

Synthesis of CAM-gCN-$NiCl_2$-CsCl

In the glove box under an inert atmosphere, we thoroughly ground $4\,\mathrm{g}$ ($10.9\,\mathrm{mmol}$) melamine cyanurate ($C_6H_9N_9O_3$), which was recrystallized from methanol, along with $10\,\mathrm{g}$ a eutectic mixture of nickel chloride and cesium chloride (50:50 wt%). The resulting mixture was then transferred to an alumina boat with a lid. Under nitrogen atmosphere, the reaction mixture was introduced into a tubular furnace and heated for $4\,\mathrm{h}$ at a ramping rate of $5\,^{\circ}\mathrm{C\,min^{-1}}$ until it reached a terminal temperature of $450\,^{\circ}\mathrm{C}$. To remove the salt block from the reaction mixture, it was washed with boiling distilled water and centrifuged at $7000\,\mathrm{rpm}$ for $15\,\mathrm{min}$. The obtained material was subsequently dried in a vacuum oven at $110\,^{\circ}\mathrm{C}$ overnight under a pressure of $1 \times 10^{-5}\,\mathrm{Torr}$, and then stored in a $25\,\mathrm{mL}$ amber bottle labelled as CAM-gCN-$NiCl_2$-CsCl.

3.3 Analytical Methods

3.3.1 Powder X-ray Diffraction (XRD)

Powder X-ray Diffraction (XRD) is a scientific method used to examine the crystal structures of materials. This technique is based on constructive interference of monochromatic X-rays with crystalline samples. When X-rays are directed to a crystal, they diffract in a distinct pattern that is unique to the crystal structure. In powder X-ray diffraction, the diffraction pattern is obtained from the powdered form of the material, instead of a single crystal. This form of diffraction is often more convenient and accessible than single-crystal diffraction, because it eliminates the need for the formation of individual crystals. Furthermore, powder X-ray diffraction provides a diffraction pattern for the bulk material of a crystalline solid rather than just a single crystal, which may not represent the entire material.

Powder X-ray diffraction (XRD) is typically performed using a powder diffractometer. In this procedure, X-rays are generated inside a sealed tube under vacuum, and an electric current is applied to heat the filament within the tube. The greater the current, the more X-rays are emitted. These X-rays are then directed onto a sample comprising a crystalline material, and the resulting diffraction pattern is detected by a detector.

XRD experiments were used to determine the mineral phases present in the samples using the diffraction patterns obtained from the experiments. In the diffraction pattern, equation $\sin\theta = \frac{n\lambda}{2d}$ is plotted, where θ is the angle of incidence of the X-ray, n is an integer, λ is the wavelength, and d is the spacing between the atomic layers. It is important to note that only crystalline solids can produce the highly regular structure necessary for diffraction. Consequently, only crystalline solids produce a diffraction pattern, whereas amorphous materials will not be present in the pattern [1, 2].

X-ray diffraction (XRD) is a non-destructive method that enables the detection of crystalline phases, as well as the assessment of structural characteristics and identification of any deviations from the ideal structure resulting from internal stresses and defects.

Debye-Scherrer equation

The Debye-Scherrer equation is a mathematical relationship between the diffraction angle, interatomic spacing, and X-ray wavelength, which is employed to determine the crystalline size of nanoparticles [3]. The equation is expressed as follows:

$$D = \frac{K\lambda}{\beta\cos\theta} \tag{3.1}$$

where D is the crystal size of the nanoparticle, K is a constant, λ is the X-ray wavelength, β is the full-width-at-half-maximum of the diffraction peak, and θ is the diffraction angle.

The Debye-Scherrer equation is derived from Bragg's Law of X-ray Diffraction, which posits that the path difference between two waves diffracted from separate crystal planes must be a whole-number multiple of the X-ray wavelength in order to produce constructive interference and form a diffraction peak. The Debye-Scherrer equation calculates the interatomic spacing of the crystal planes based on the diffraction angle[4].

Microstrain

Microstrain refers to localized elastic deformation that occurs within a crystal lattice owing to factors such as dislocations, point defects, and grain boundaries[5]. It can be measured using X-ray diffraction (XRD) data and the Williamson-Hall equation, which is a fundamental tool in materials science. The Williamson-Hall equation relates the full width at half maximum (FWHM) of a diffraction peak, known as 'β,' to the microstrain, 'ε,' and the Bragg angle, 'θ':

$$\varepsilon = \frac{\beta}{4\tan(\theta)} \tag{3.2}$$

In this context, 'β' refers to the width of the peak measured at half of its maximum intensity, usually in radians or degrees. A broader peak indicates a higher degree of strain or a smaller crystallite size. The 'θ' is the angle at which the X-rays are diffracted by crystal planes, and 'ε' is a dimensionless measure of the elastic deformation within the crystal lattice. Positive values indicate stretching, while negative values indicate compression.

The assumptions and limitations of this equation are acknowledged. It is assumed that the broadening of the XRD peaks is primarily attributed to microstrain and crystallite size effects, while excluding other factors, such as instrumental broadening and preferred orientation, which may introduce errors. Additionally, this equation is applicable only under small-strain conditions (typically less than 0.1), as its relationship with larger strains becomes more intricate.

3.3.2 Rietveld refinement

Rietveld refinement is a highly regarded technique for determining the crystal structure of a substance by comparing observed X-ray or neutron diffraction patterns with calculated patterns based on the proposed crystal structure [6, 7]. The foundational principles of the Rietveld refinement can be elucidated using the following primary equations:

1. The diffraction pattern obtained through observation, referred to as $I_{obs}(2\theta)$, is modeled as a combination of the calculated diffraction pattern, denoted as $I_{calc}(2\theta)$, and a background function, denoted as $B(2\theta)$. The background function is intended to account for any noncrystalline or amorphous scattering.
$$I_{\text{obs}}(2\theta) = I_{\text{calc}}(2\theta) + B(2\theta) \tag{3.3}$$

2. The diffraction pattern that is determined by the crystal structure is characterized by structural parameters, such as atomic positions, thermal vibrations, and isotropic or anisotropic temperature factors. These structural parameters were optimized using the least-squares method to minimize the difference between the observed and calculated diffraction patterns.

3. The degree of agreement between the observed and calculated patterns is assessed by the R-factor, which is defined as:
$$R = \frac{\sum |I_{\text{obs}}(2\theta) - I_{\text{calc}}(2\theta)|}{\sum I_{\text{obs}}(2\theta)} \tag{3.4}$$
In crystallography, the R-factor is a crucial parameter that assesses the quality of crystal structure refinement. It measures the deviation between the observed and calculated diffraction patterns across all the peaks and provides a quantitative estimate of the accuracy of the refinement process.

4. The reliability of the refinement process is assessed by the goodness of fit (GoF) parameter, also known as the reduced chi-square. This parameter is defined as:
$$\chi^2 = \frac{\sum (I_{\text{obs}}(2\theta) - I_{\text{calc}}(2\theta))^2}{\sigma^2} \tag{3.5}$$
The use of a reduced chi-square test allowed for the assessment of the quality of fit between the observed and computed patterns, considering the experimental error associated with the data and summing the error across all detected diffraction peaks.

3.3.3 B.E.T Analysis

Brunauer–Emmett–Teller (B.E.T) analysis is a widely used method for determining the specific surface area of porous materials[8, 9]. It is named after its developers, Stephen Brunauer, Paul Hugh Emmett, and Edward Teller.

The basic principle of the B.E.T analysis is the adsorption of gas molecules onto the surface of a solid material. The analysis assumes that adsorption occurs during monolayer formation, meaning that gas molecules form a single layer on the surface of the material. The B.E.T method uses the relationship between the amount of gas adsorbed at a given pressure and relative pressure to calculate the specific surface area.

The analysis began by exposing the material to a gas, typically nitrogen, at different pressures. As the gas molecules adsorbed onto the surface of the material, the amount of gas adsorbed was measured. The data obtained from these measurements were then used to construct an adsorption isotherm, which is a plot of the amount of gas adsorbed as a function of relative pressure.

The B.E.T theory posits that adsorption occurs in multiple layers, with the initial layer forming a monolayer on the surface. The subsequent layers may have formed into multiple layers. This study focused on the low relative pressure adsorption behavior, which predominantly occurs in the monolayer regime.

The surface area of a substance can be determined using Equation 3.6, where S denotes the surface area of the substance, q_m is the amount of adsorbate required to form a monolayer per unit mass of the substance, N is Avogadro's constant, and A_m is the area occupied by a single adsorbate molecule in the monolayer[10].

$$S = q_m \cdot N \cdot A_m \tag{3.6}$$

The Brunauer–Emmett–Teller (B.E.T) equation (Equation 3.7) is derived from the isotherm and incorporates variables such as vapor pressure (p), saturation vapor pressure (p_0), adsorbate loading (q), and B.E.T constant (C).

$$\frac{\frac{p}{p_0}}{q(1-\frac{p}{p_0})} = \frac{1}{q_m.C} + \frac{(c-1)}{q_m C}\frac{p}{p_0} \tag{3.7}$$

In the context of monolayer loading, a linear relationship exists between $\frac{\frac{p}{p_0}}{q(1-\frac{p}{p_0})}$ and $\frac{p}{p_0}$: To determine the linear region, B.E.T analysis typically employs the criteria proposed by Rouquerol et al[11, 12]. These criteria are based on consistency and are used to select an appropriate linear region for the analysis.

1. The linear region must be confined to the range of $\frac{p}{p_0}$ values for which the function $q(1-\frac{p}{p_0})$ demonstrates a consistent rise without interruption.

2. Parameter C should be a positive value.

3. The monolayer loading capacity, denoted by q_m, ought to be equivalent to a value of $\frac{p}{p_0}$ that is situated within the previously mentioned linear range.

4. The equality between the values of $\frac{p}{p_0}$ derived from BET theory, $\frac{1}{\sqrt{C}+1}$, and the value obtained from the third consistency rule must be ensured, with a permissible margin of error of $\pm$10%.

5. The linear portion of the isotherm extended to the knee.

Selecting a linear region, the identified uptake value was multiplied by the molecular cross-sectional area of the adsorbate, typically derived from the bulk liquid density (16.2 $Å^2$/molecule for N_2; 14.2 $Å^2$/molecule for Ar), to obtain the surface area of the material, assuming that the adsorbate molecules only formed a monolayer (Equation 3.6). The surface area obtained in this manner was referred to as the B.E.T area.

It is vital to recognize that B.E.T analysis is predicated on specific ideal conditions, such as a uniform surface and the formation of a complete monolayer. Any deviation from these assumptions may lead to inaccuracies in the calculated specific surface area. Consequently, caution should be exercised when interpreting the outcomes of B.E.T analysis and taking into account the limitations of the method.

B.E.T Surface Identification (BETSI) Analysis

The Brunauer–Emmett–Teller Surface Identification (BETSI) analysis is a method that is employed to determine the specific surface area and pore size distribution of solid materials by utilizing the principles of the B.E.T theory[13]. This method represents an expansion of the B.E.T method, which involves the physical adsorption of an inert gas such as nitrogen, argon, or krypton onto the surface of the sample. The BETSI algorithm is based on adsorption isotherm analysis, which is a plot that illustrates the amount of gas adsorbed as a function of relative pressure. BETSI analysis is widely used in various fields such as catalysis, chemical engineering, and materials science to characterize the surface properties of materials (`https://github.com/fairen-group/betsi-gui/releases/tag/v2.0`).

SESAMI (Script to Estimate the Surface Area of Materials from their Isotherms) Analysis

The SESAMI (Script to Estimate the Surface Area of Materials from their Isotherms) Analysis is a computational tool employed in this study for the comprehensive assessment of surface area and porosity characteristics of the synthesized materials[14, 15]. This script-based approach utilizes advanced algorithms to process adsorption isotherm data, thereby providing valuable insights into the porosity, pore size distribution, and surface area of materials. In our experimental methodology, the SESAMI system played a crucial role in interpreting the adsorption isotherm data acquired during nitrogen (N_2) adsorption-desorption experiments. These data were subsequently processed to determine parameters such as the surface area, micropore volume, and other essential characteristics that contribute to the adsorption properties of the material. The SESAMI method offers a precise understanding of the porosity and surface characteristics of the material, thereby enabling correlations with the observed carbon dioxide reduction activities. The outcomes derived from SESAMI analysis significantly add to the extensive characterization of the synthesized materials, thereby enhancing the overall understanding of their catalytic performance. The SESAMI web interface is publicly accessible at `https://sesami-web.org/`, and the source code can be obtained at `https://github.com/hjkgrp/SESAMI_web`.

Derivative Isotherm Summation

The Derivative Isotherm Summation (DIS) approach is a highly valuable method for characterizing the adsorption on heterogeneous surfaces. This technique provides crucial information regarding the distribution of adsorption energies and surface heterogeneity, which is essential for understanding the properties of various materials. The DIS technique is particularly effective for analyzing and interpreting gas adsorption isotherms on heterogeneous surfaces.

DIS methodology is based on the idea that the overall adsorption isotherm for a heterogeneous surface can be partitioned into separate isotherms, each corresponding to a distinct energetically homogeneous surface area[16–18]. These subregions were identified based on the unique distribution of their adsorption energies.

Theoretically, this concept can be represented as

$$Q(p) = \sum n(\varepsilon) q_n(p) \tag{3.8}$$

where:

$Q(p)$ is the total amount of adsorbate adsorbed at pressure p
$n(\varepsilon)$ is the density of surface sites with adsorption energy ε
$q_n(p)$ is the isotherm for a sub-region with energy ε

The primary objective of the DIS method is to determine the individual isotherms $q_n(p)$. To achieve this, the method involves taking the derivative of the overall isotherm $Q(p)$ with respect to the logarithm of pressure $\ln(p)$, and applying mathematical techniques to separate the resulting curve into its individual components.

The DIS method has broad applications in diverse fields including

- **Material Characterization:** The DIS method offers valuable insights into the adsorption properties and performance of catalysts, zeolites, porous materials, and carbons by examining their surface heterogeneity.
- **Adsorption Mechanisms:** The DIS method is a valuable tool for distinguishing between adsorption types, including physisorption and chemisorption, and for investigating the interplay between the adsorbate and adsorbent.
- **Isotherm Prediction:** By deconvoluting complex isotherms into simpler components, the DIS method facilitates the modeling and prediction of adsorption behavior under different conditions.
- **Material Optimization:** The DIS method can be useful for identifying materials with the desired adsorption properties for applications such as gas storage and separation by analyzing their surface energy distributions, thereby simplifying the selection process for optimal materials.

Although the DIS method is powerful, it presents certain challenges and limitations. One of the main difficulties of this approach is obtaining accurate individual isotherms from the derivative curve, particularly when dealing with complex isotherms with overlapping energy distributions. Another challenge is choosing appropriate isotherm models to represent individual subregions, which can be

subjective and affect the deconvolution results. Additionally, the DIS method may not be able to resolve very closely spaced energy distributions or subtle variations in surface heterogeneity with a limited resolution.

3.3.4 Solid State Ultraviolet-Visible Spectroscopy

Solid-state ultraviolet-visible spectroscopy is a specific type of absorption spectroscopy that involves the examination of the reflectance or backscattering of light from a material. This technique was used to investigate the optical properties of the materials. This method is noninvasive and rapid. To obtain the diffuse reflectance spectrum of the sample, the reflectance of the light scattered by the sample at various wavelengths was measured. By analyzing the spectrum, it is possible to obtain information about the optical properties of the sample, including the absorption and scattering coefficients.

Kubelka-Munk Theory

The Kubelka-Munk equation was employed to elucidate the relationship between the diffuse reflectance and absorption spectra of the sample. This equation is a mathematical model used to describe the optical properties of thin, highly scattered materials. It was formulated by Munk and Kubelka in the 1930s to explain the reflection and transmission of light in painted films[19]. This theory is rooted in the concept that light is scattered several times within a material, and the amount of light absorbed and transmitted is contingent upon the thickness and optical properties of the material[20, 21]. The Kubelka-Munk equation is expressed as follows:

The Kubelka-Munk equation was used to calculate the absorption and scattering coefficients of the samples[22]. The mathematical relationship among the absorption coefficient (K), scattering coefficient (S), and sample reflectance (R) is expressed as follows:

$$K/S = \frac{(1-R)^2}{2R} \tag{3.9}$$

Kubelka-Munk constants, which are proportional to the absorption coefficient (α) and scattering coefficient (β) of the material, were employed to determine the optical properties of the material, including its transmittance (T) and absorbance (A).

The widely accepted custom of employing a well-defined diffuse-reflectance sample for calibration is frequently used in the acquisition of optical properties via diffuse reflectance spectroscopy. In this process, the spectrum of the sample was assessed against that of the standard, thereby allowing the determination of the optical properties of the sample. Despite its extensive application, this method has certain limitations and potential sources of error, including the effects of higher-order diffraction, sample positioning, and monochromator settings, all of which can jeopardize the precision of the outcomes obtained[23].

Tauc plot theory

The Tauc plot is a widely used method for determining the optical bandgap of disordered or amorphous semiconductors such as amorphous germanium or sili-

con[24–26]. This method is based on the principle that the absorption coefficient of a material correlates with its photon energy, as described by the Tauc plot equation. This equation involves plotting hν (photon energy) against the absorption coefficient and extrapolating the linear region to establish the optical bandgap. The use of a Tauc plot is a reliable method for determining the optical bandgaps of crystalline semiconductors. The ordinate in this plot is represented by $(\alpha)^{1/r}$, where the exponent 1/r indicates the nature of the transition. The value of r is significant in determining the type of transition, whether direct or indirect. Direct transitions have a value of r = 1/2, whereas forbidden transitions have r = 3/2. Indirect allowed transitions have a value of r = 2 and indirect forbidden transitions have r = 3 [27–31]. The Tauc plot offers a valuable means for unraveling the complexities of electronic transitions in crystalline semiconductors, and has numerous applications in various fields. However, it also has limitations such as the lack of a definitive assessment of the bandgap.

3.3.5 Derivative Spectroscopy

Derivative spectroscopy improves the information obtained from spectroscopic measurements by calculating the derivative of a spectrum. The main goal of this technique is to increase the sensitivity and resolution of spectroscopic measurements by emphasizing changes in the spectrum. Derivative spectroscopy has been extensively used in various fields, including analytical chemistry, pharmaceuticals, and biochemistry, to examine absorption, fluorescence, and Raman spectra.

The essential tenet of derivative spectroscopy is the acquisition of the first or second derivative of a spectrum, which yields a signal that can be used to recognize peaks. This approach was implemented to determine the concentration of the absorbing species and examine the intricate spectra. There are diverse forms of derivative spectroscopy, including first- and second-order derivatives, as well as higher-order derivatives, such as third- and fourth-order derivatives. Each type of derivative spectroscopy has distinct advantages and applications across various disciplines[32–34].

- First-derivative spectroscopy: The process of differentiating the first derivative of a spectrum is utilized to accentuate variations in slope, and this is especially beneficial for recognizing peaks and pinpointing their locations and widths.

- Second-derivative spectroscopy: The extraction of the second derivative of a spectrum is a valuable technique that increases the amount of information that can be obtained from it. By emphasizing the differences between the baseline and peaks, this method is particularly useful for determining the concentration of absorbing species.

- Zero-crossing spectroscopy: Zero-crossing spectroscopy is a technique that involves determining the wavelengths where the first derivative of the spectrum intersects zero. This approach aids in identifying the locations of the peaks and estimating the absorbance intensity.

- Hilbert transform spectroscopy:The application of the Hilbert transform in spectroscopy aims to enhance the analytical signal of a spectrum, thereby improving the information that can be derived from it. This approach enables

the analysis of complex spectra by identifying peaks and their intensities, making it a useful tool in the field of spectroscopy.

3.3.6 X-ray Photoelectron Spectroscopy

X-ray photoelectron spectroscopy (XPS) is a surface analysis method that utilizes X-ray radiation to excite photoelectrons from the surface of a material. The elemental composition, chemical state, and electronic state of the sample surface were determined by measuring the kinetic energy of the emitted photoelectrons. XPS is an invaluable tool for studying the surface properties up to a depth of approximately $< 10\,\mathrm{nm}$ [35].

Ultraviolet photoelectron spectroscopy (UPS) is a technique that utilizes ultraviolet radiation to eject photoelectrons from a material. This method is surface-sensitive and provides valuable information regarding the valence band electronic structure of a material. This is particularly useful for investigating the electronic properties of surfaces, including the band structure, work function, and energy levels of the surface states.

The kinetic energy of the photoelectrons emitted by XPS is represented by the following equation:

$$KE = h\nu - BE - \phi \tag{3.10}$$

The quantity KE represents the kinetic energy of the photoelectrons emitted, whereas hν refers to the energy of the incident X-ray radiation. In addition, BE represents the binding energy of the photoelectrons, and ϕ denotes the work function of the material of the instrument.

The intensity of the emitted photoelectrons and the number of atoms in the surface region are proportional. Furthermore, the sensitivity factor, which is influenced by the cross-section of the photoionization process and escape depth of the photoelectrons, also plays a role.

Valence-band X-ray photoelectron spectroscopy (XPS) is a highly valuable analytical technique that is widely used to investigate the electronic structure of materials. This technique is particularly useful for providing insights into the valence band of a material, which is the range of energy levels occupied by the outermost electrons in a solid. By analyzing the valence band, researchers can gain a deeper understanding of the chemical bonding and electronic properties of the materials.

Valence-band XPS is typically performed using an X-ray source, which emits high-energy X-rays that are absorbed by the material being studied. When X-rays are absorbed, they eject one or more electrons from the material, which are then analyzed using a spectrometer. The resulting spectrum provides information on the energy levels and chemical identities of the valence-band electrons.

One of the key advantages of valence-band XPS is its ability to provide high-resolution spectra that can be used to identify the specific chemical species present in a material. This makes it an invaluable tool for researchers to study the composition and structure of complex materials. Additionally, valence band XPS can be used to study a wide range of materials, including metals, semiconductors, and insulators, making it a versatile technique applicable to many different fields of study.

Ultraviolet photoelectron spectroscopy (UPS) was utilized to investigate the valence-band electronic structure of the material in question. This method involves measuring the kinetic energy of the photoelectrons emitted upon exposure to light, which is directly proportional to the energy levels of the valence band. The work function of the material, which represents the energy required to remove an electron from its surface, can be calculated by determining the energy difference between the Fermi level and vacuum level. The energy levels of the surface states were determined from the UPS spectrum.

3.3.7 HRSEM and EDAX

Field Emission Scanning Electron Microscopy (FESEM) is a type of electron microscopy that utilizes a focused electron beam to produce images of the sample surfaces. FESEM can obtain information regarding the surface topography and composition of the sample by scanning the surface with an electron beam. Electrons interact with atoms in the sample, generating signals that contain valuable information about the sample. FESEM employs electromagnetic lenses to focus the electron beam and scan the specimen surface, resulting in an image of the sample surface and topography. The column containing the lenses is designed to reduce the size of the electron beam, or "spot size," to a sufficiently small extent that it can produce high-resolution images when it reaches the specimen [36].

The resolution of the FESEM images was calculated using the following equation.

$$R = \frac{0.61\lambda}{\text{NA}} \tag{3.11}$$

The resolution R is influenced by the wavelength of the electron beam, denoted by λ, and the numerical aperture of the objective lens.

Field emission scanning electron microscopy (FESEM) is a highly versatile technique that can achieve a magnification of 500,000 $\times$ with a spatial resolution of up to 1.5 nanometers. This makes it an ideal choice for high-magnification, high-resolution imaging applications. FESEM is particularly useful for obtaining ultra-high-resolution images at low accelerating voltages and short working distances.

Energy-dispersive X-ray spectroscopy (EDS), also known as energy dispersive X-ray analysis (EDXA or EDAX) or energy dispersive X-ray microanalysis (EDXMA), is a technique used to identify the elements present in a sample by analyzing the energy of X-rays emitted or absorbed by the sample. This method involves the excitation of electrons near the atomic nucleus, resulting in a cascade of electrons filling the resulting energy holes. Each element possesses a unique set of energy levels, and thus the X-rays emitted by the sample bear a specific signature characteristic of the elements present. The X-rays were detected by an energy-dispersive detector, which is a solid-state detector that converts X-rays into electrical signals. Subsequently, a computer processes these signals to produce a spectrum that illustrates the energy and intensity of the X-rays emitted from the sample.

The present equation calculates the energy of X-rays emitted by a sample.

$$E = \frac{hc}{\lambda} \tag{3.12}$$

where the variable E represents the X-ray energy and h represents Planck's

constant. Additionally, c represents the speed of light and λ represents the X-ray wavelength.

The intensity of the X-rays emitted by the sample was directly proportional to the number of atoms present in the sample, as indicated by the equation that calculates the intensity of the X-rays.

$$I = KZ^2 \frac{C}{\lambda^2} \tag{3.13}$$

where I represents the X-ray intensity, K is a constant, Z is the atomic number of the element, C is the concentration of the element in the sample, and λ is the X-ray wavelength.

3.3.8 Solid State NMR

Solid-state nuclear magnetic resonance (NMR) spectroscopy is an analytical method used to examine the properties of solids, including their molecular structures, dynamics, and interactions. This method is based on the interaction between the nuclear magnetic moments in a solid and an external magnetic field, which results in the absorption or emission of radio frequency (RF) signals. The fundamental principles of NMR spectroscopy are rooted in the intrinsic spin of the nucleus, as described by the quantum number S. The nuclei with nonzero spin are always associated with a nonzero magnetic moment, which is expressed by the equation $\mu = \gamma S$, where μ represents the magnetic moment, γ denotes the gyromagnetic ratio, and S denotes the spin quantum number [37]. In a conventional solid-state NMR experiment, a sample is placed within a magnetic field and subjected to RF pulses. These RF pulses excite the nuclei, causing them to precess around the magnetic-field axis. Precessing nuclei generate an RF signal that is directly proportional to the magnetic field experienced by them. By examining this RF signal, researchers can obtain crucial information regarding the molecular structure, orientation, and dynamics of the solid-state systems under investigation.

The following equation represents the fundamental form of the solid-state Hamiltonian:

$$H = -\gamma B_0 I_z + \sum_j \gamma B_j I_j \tag{3.14}$$

where H is the Hamiltonian, γ is the gyromagnetic ratio, B_0 is the external magnetic field, I_z is the $z$component of the nuclear spin operator, B_j is the magnetic field generated by the jth nucleus, and I_j is the nuclear spin operator for the jth nucleus.

The process of analyzing solid-state NMR spectra typically involves a number of steps, including data acquisition, data processing, spectral analysis, and interpretation of spectral information. These methods can be combined with other spectroscopic techniques, including infrared spectroscopy and X-ray crystallography, to comprehensively study the molecular structures and interactions of the samples.

3.3.9 Photoluminescence Spectroscopy

Photoluminescence spectroscopy is a commonly used technique to explore the optical properties of materials. This method involves the absorption of photons

by a material, which subsequently excites electrons from the valence band to the conduction band. Upon the return of electrons to the valence band, they emit photons with characteristic energy that can be measured and analyzed, thereby providing information about the electronic structure, defects, and impurities of the material.

The foundation of the Photoelectric Effect is the interaction between photons and electrons in a material. The photon energy can be expressed as $E = h\nu$, where E denotes the photon energy, h represents Planck's constant, and ν is the photon frequency. When a material absorbs a photon, an electron in the valence band is excited to the conduction band, and the bandgap energy facilitates the energy required for excitation $E_g = E_c - E_v$. where E_c represents the energy of the conduction band and E_v denotes the energy of the valence band [38].

When the electron returns to the valence band, it emits a photon with a characteristic energy of $E = h\nu$. The energy of the emitted photon is related to the bandgap energy through the equation $E = E_g - \Delta E$, where ΔE represents the energy lost owing to nonradiative processes, such as thermalization and recombination.

The Photoluminescence (PL) spectra were obtained by measuring the intensity of the emitted photons as a function of their energy, providing valuable information about the electronic structure of a material, including bandgap energy, defect states, and impurities. PL spectra also enable the examination of charge carrier dynamics such as carrier lifetime and diffusion length.

3.4 Instrument Detail and Specifications

3.4.1 Adsorption and Porosity Analyzer

For the adsorption and porosity analyses, the following experimental conditions were implemented: Nitrogen (N_2) served as the adsorption gas. The analysis bath was maintained at an extremely low temperature of $-195.687\,^{\circ}\mathrm{C}$ to ensure precise measurement of the adsorption properties. No thermal correction was applied to the recorded data in this analysis, indicating that the measurements were not adjusted for temperature effects. The mass of the sample used for analysis was $0.8\,\mathrm{g}$ to $1.5\,\mathrm{g}$, according to the nature of the sample. An equilibration interval of $5\,\mathrm{s}$ was used for analysis. This interval allows the system to reach a stable state before each measurement, thereby ensuring consistent and reliable results. A low-pressure dose of $10.010\,\mathrm{cm^3\,g^{-1}}$ at standard temperature and pressure (STP) was applied to the sample. This dosage ensured sufficient adsorption for accurate measurements and a comprehensive sample porosity analysis.

3.4.2 X-ray Diffraction

The XRD data were collected using a Bruker D8 Advance diffractometer equipped with Cu Kα radiation (wavelength = $1.5418\,$Å) with a 2θ range of 10° to 70°. The step size was 0.034°, and each step was performed for $5\,\mathrm{s}$. The acquired data were processed using the X'Pert HighScore Plus software (version 3.0), which involved subtracting the background and normalizing the data.

3.4.3 HRSEM EDAX

The FESEM analysis in this study was carried out using a Quanta 3D FEG, a versatile and high-resolution Scanning Electron Microscope (SEM) that operates at low vacuum and features a field-emission gun (FEG) for improved imaging and Energy-Dispersive X-ray Spectroscopy (EDS). The following steps were used in this experiment.

The Quanta 3D FEG has a unique field-emission electron source that enables clear and precise electron imaging. By increasing the electron beam current, the accuracy of EDS analysis was significantly improved.

Pump-down Time:

- The time taken for pump-down in the high-vacuum mode was minimized to less than three minutes, thereby ensuring the optimal preparation of the sample for analysis in an efficient manner.

Experimental Procedure:

- *Sputtering:* Prior to conducting FESEM analysis, the samples were sputter-coated to improve the conductivity and minimize the impact of charging effects during imaging.

- *Instrument Calibration:* The settings were appropriately adjusted to guarantee the optimal conditions for both imaging and EDS analysis. The samples were firmly affixed to suitable mounts to ensure stability during analysis. The initial imaging was performed under high-vacuum conditions for precise surface analysis at a high resolution. Subsequent imaging was conducted in low-vacuum and ESEM modes to accommodate sensitive samples.

3.4.4 DRS UV Spectroscopy

The JASCO instrument is a highly advanced spectrometer and data system designed for ultraviolet diffuse reflectance spectroscopy (DRS) analysis. It was configured as follows: the X-unit parameter was set to nm to define the wavelength range, while the Y-unit parameter indicated that the measured data were expressed in absorbance units. The ΔX parameter, set to -1, signified that the wavelength increment between the data points was not constant. For UV DRS analysis, the experimental configuration specified the range of wavelengths to be measured, with the analysis commencing in the wavelength range of $800\,\mathrm{nm}$ to $200\,\mathrm{nm}$. During the analysis, 600 data points were acquired, resulting in a comprehensive dataset of absorbance values covering the defined wavelength range, providing detailed information for further analysis.

3.4.5 Photoluminescence Spectrometer

Photoluminescence analysis was performed using a JASCO spectrometer system. The experimental parameters included the resolution, ΔX $(0.5\,\mathrm{nm})$, X units (nm), and Y units (intensity). The spectral range extended from $410\,\mathrm{nm}$ to $600\,\mathrm{nm}$, with a total of 381 data points collected.

3.4.6 XPS

A Thermo Scientific K-Alpha+ device was used to collect the experimental data. The excitation was supplied by an Al Kα monochromatic source, which had an energy of $1486.6\,\mathrm{eV}$ and a power of $72\,\mathrm{W}$, with a measured source size of 0.004 × 0.006 mm^2. A double-focusing hemispherical analyzer was employed in the instrument. The angle of incidence was set at $30°$, whereas the angle of emission was fixed at $90°$. The analyzer pass energy was set at $40\,\mathrm{eV}$, allowing for the capture of emitted signals with a resolution of $0.6\,\mathrm{eV}$. The total time for signal accumulation and the duration of the experiment were $815\,\mathrm{s}$, and 50 scans were performed. The effective width of the detector was determined to be $5\,\mathrm{eV}$.

During the experimental phase of this research, the implementation of the peak shape and background methodologies was carried out with great rigor. Data analysis was conducted using CasaXPS v2.3.26rev 1.1P, and a three-parameter Tougaard (U3) background was systematically applied. Furthermore, this study considered the possibility of terminating with a Shirley-type background after the largest N1s peak. The use of Lorentzian asymmetric (LA) Voigt line shapes (LA(α, β, m)) also contributes to the accuracy of the analysis. The fitting parameters, specifically LA(1.3, 243), were consistently used for all the peaks, excluding C(1s) and N(1s), where LA(1.03, 1.24, 243) was deemed more appropriate.

The contributions of CasaXPS V2.3.24 rev 1.1 Z were instrumental in the development of the quantitation methodology. Throughout the quantitation process, the three-parameter Tougaard (U3) background was maintained at a constant level to ensure methodological consistency. In addition, the scofield sensitivity factors were used for precise quantification. Furthermore, a kinetic energy dependence of -0.6 was taken into account, which enhanced the robustness and dependability of the quantitation methodology employed in this experimental study.

3.4.7 Solid State NMR

Solid-state ^{13}C and ^{15}N cross-polarization magic-angle spinning (CP-MAS) NMR spectra were obtained using Bruker Avance $500\,\mathrm{MHz}$ and $800\,\mathrm{MHz}$ spectrometers, respectively. The experiments were performed at room temperature with a spinning frequency of $10\,\mathrm{kHz}$. Tetramethylsilane (TMS) was used as the reference for ^{13}C signals, while nitromethane was used as the reference for ^{15}N signals. The NMR technique was enhanced by the application of CP-MAS, and the spectrometers were adjusted with optimal parameters to attain high resolution and sensitivity. After acquiring the data, the obtained spectra were processed, including phase and baseline correction, using Topspin followed by Mestanova. The convolution of ^{13}C and ^{15}N spectra was performed using the Pseudo Voigt (PsdVoigt1) function. Other functions, such as PsdVoigt2 and Voigt, did not provide satisfactory convolution within the NMR dataset.

3.5 The Photosynthetic Reactor Setup

3.5.1 The Photoreactor

Custom-designed photoreactors were used in all CO_2 reduction experiments. These photoreactors were constructed with borosilicate glass and featured separate quartz windows designed specifically for light irradiation. The photoreactor had a total volume of $300\,\mathrm{mL}$, which was divided into a reaction volume of $225\,\mathrm{mL}$ and dead volume of $75\,\mathrm{mL}$. The reaction volume was determined based on the size of the quartz window.

The photoreactor was equipped with five plain-shank single-cone ports, each serving a specific purpose. Two ports were designated for sample withdrawal and were sealed with silicone septa. Two other ports were dedicated to gas bubbling and were connected to Teflon-lined stoppers for the gas-washing bottles. In addition, a port is allocated to the thermowell. Each port was securely sealed using a combination of silicone rubber septum, parafilm, and PTFE Teflon tape.

The reactor was equipped with a water recirculation system to regulate the temperature and enhance the reaction conditions. The system consists of a plastic bucket filled with water and a submersible water pump. Silicone tubes were used to connect the pump to the photoreactor recirculation outlet. Furthermore, two 1.5-ton window air conditioners were used to maintain a stable temperature of $25\,^{\circ}\mathrm{C}$ in the photoreactor room.

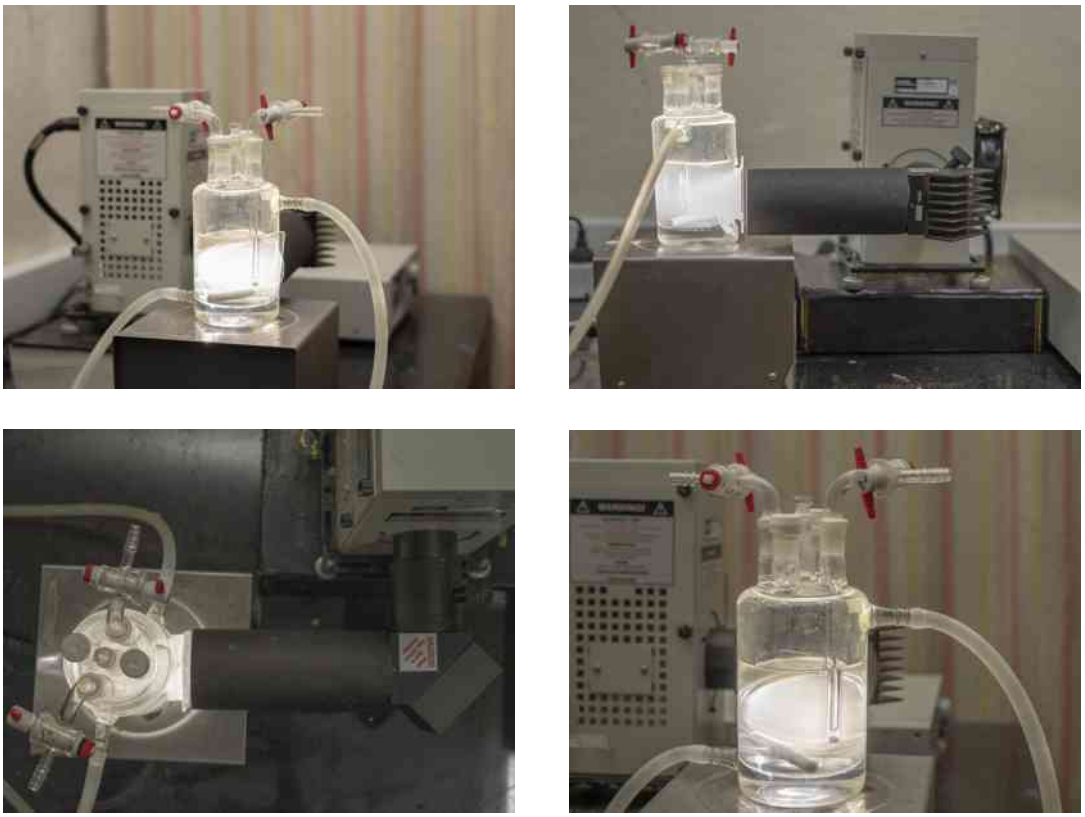

Figure 3.3: Photoreactor used for CO_2 reduction experiments

3.5.2 The Light Source and Filters

A xenon UV-enhanced lamp, with a powerful wattage of $300\,\mathrm{W}$, acted as the light source for the experiments. To guarantee extensive coverage, the output beam size was precisely set to $33\,\mathrm{mm}$, thereby providing a broad range of illumination. The use of a condenser with a refined two-element planoconvex design ensures the optimal quality of the light beam. This condenser effectively collimated the beam, resulting in a focused and directed illumination.

Fused silica was selected as the optimal lens material because of its remarkable optical characteristics and robustness. The lens demonstrated exceptional transmittance over the range of $200\,\mathrm{nm}$ to $2500\,\mathrm{nm}$, enabling the emission of a broad spectrum of wavelengths. In addition, the lens exhibited a multiplication factor of 0.11, which significantly enhanced the overall intensity of the emitted light. The xenon light source was securely attached to the experimental setup through a 1.5-inch flange series size to ensure stability and reliability. The carefully selected specifications of the light source provided consistent and versatile illumination for the experimental investigations conducted in this study.

Our experimental setup was further enhanced by the incorporation of Air Mass Filter-AM 1.5 Global, which was mounted on a multiple filter holder, specifically the 62020 model. The primary purpose of the 81094 air mass filter was to accurately correct the output of the xenon lamp, ensuring a closer match to the total spectrum, which encompasses both direct and diffuse components, particularly when the sun is at a zenith angle of $37°$. This 2-inch in x 2-inch square filter was meticulously designed to seamlessly fit into the integral filter holder of the solar simulator or could be conveniently mounted into an external filter holder that flanges to the Oriel® research arc lamp housings. This conforms to the AM 1.5 G standard defined by ASTM E 892, ensuring precise and standardized measurements.

The 62020 multiple-filter holder is a cost-effective solution for experiments that do not require an enclosed light path. Its open filter holder design facilitates easy access to the filters, allowing for the simultaneous insertion of various filters with a total thickness not exceeding 3/4 in ($38.1\,\mathrm{mm}$). It accommodates 2-inch ($50.8\,\mathrm{mm}$) circular or square filters and features a 1.5-inch clear aperture, ensuring optimal compatibility with the experimental setup. The filters were securely held in place using reliable thumbwheels to provide stability and accuracy during the experiments. Including the 1.5 inch series flanges, the multiple filter holder was seamlessly integrated into our experimental setup, offering enhanced functionality and flexibility. Together, these carefully selected components provide the necessary versatility and reliability for the experimental investigations conducted in this study.

3.6 The Gas Chromatography Setup

Gas chromatography, a widely utilized and highly efficient method for separating, identifying, and quantifying the components of a mixture, involves the conversion of the sample into a gaseous form that is then carried by a carrier gas, which flows through a temperature-controlled column. In this study, a Perkin Elmer Clarus 580 gas chromatograph was employed as the analytical instrument, and it was fitted with a PoraPlot column and molecular sieve column to ensure efficient separation and analysis. Furthermore, the GC system was equipped with a Flame Ionization

Detector and a Thermal Conductivity Detector to ensure comprehensive detection capabilities.

3.6.1 Gas Cylinders and Canisters

High-pressure (HP) cylinders of HP-Hydrogen, HP-Zero Air, and HP-Nitrogen were connected to the system to ensure a steady supply of gases suitable for gas chromatography (GC). Additionally, a gas purification system was connected to guarantee the gas purity. High-purity cylinders of HP-argon and HP-nitrogen were used for purging and calcination. These high-purity cylinders were obtained from the Indogas agencies located in Chennai. This gas supply configuration was essential for reliable and consistent operation of the GC system during the experimental studies.

3.6.2 Syringes

In the experimental design, a Hamilton 1700 gas-tight syringe was employed for gas-phase sampling. The syringe boasted a removable needle with a capacity of $500\,\mu\mathrm{L}$, enabling precise and accurate sampling of the gaseous phase during the experiments.

For liquid product sampling, Agilent gold-standard autosampler syringes with a capacity of $5\,\mu\mathrm{L}$ and bevel tips were used. The syringes were designed to ensure precise liquid sampling, resulting in accurate experimental results.

An ordinary glass syringe equipped with a long stainless-steel needle was used to extract liquid samples from the photoreactor. This syringe facilitated efficient collection of liquid samples for further analysis.

Syringe filters were used to filter the samples and ensure the purity of the liquid products. The filtered liquid samples were stored in amber glass vials, which provided protection against light-induced degradation or contamination.

The liquid products collected in the amber glass vials were transferred using Agilent gold standard syringes and injected into the GC system for analysis. This transfer method ensured consistent and reliable sample introduction into the GC, enabling the accurate analysis of the liquid products.

3.6.3 Septums

A PerkinElmer Green Injection Port Septa was used for gas chromatography (GC) analysis. This septa design presents a number of benefits, including an extended lifespan for injection, low-bleeding properties, and reliable adhesion to the injection port. In addition, the septa have a maximum temperature limit of $350\,^{\circ}\mathrm{C}$.

3.6.4 Gas Chromatograph Instrument Conditions

For Alcohol and Hydrocarbons

The following method was used for the PoraPlot Q capillary column in conjunction with a flame ionization detector (FID) and nitrogen as the carrier gas.

1. The temperature of the injector was set to $250\,^{\circ}\mathrm{C}$, which is higher than the boiling points of the components, which typically range around $120\,^{\circ}\mathrm{C}$.
2. The column temperature was set at $150\,^{\circ}\mathrm{C}$ and maintained isothermally for optimal separation of peaks in the shortest possible time. The temperature was adjusted for future runs using other compounds.
3. The FID detector temperature was set at $250\,^{\circ}\mathrm{C}$.
4. A volume of $1\,\mu\mathrm{L}$ of the liquid sample was drawn into a syringe with a capacity of $5\,\mu\mathrm{L}$, and the syringe needle was inserted into the hot injector port of the gas chromatograph. The samples were introduced into the columns for analysis.
5. For the purpose of gas phase sampling, a sample volume of $200\,\mu\mathrm{L}$ was collected into a $500\,\mu\mathrm{L}$ gas-tight syringe.

For Hydrogen and Oxygen

The following operational procedure was implemented using a Molecular Sieve column coupled with a Thermal Conductivity Detector (TCD) and nitrogen as the carrier gas.

1. The temperature of the injector was set to $150\,^{\circ}\mathrm{C}$.
2. The oven temperature was maintained at a constant $50\,^{\circ}\mathrm{C}$ and subsequently adjusted to optimize the separation of peaks in the shortest possible time for future runs using other compounds.
3. The temperature of the TCD detector was set to $110\,^{\circ}\mathrm{C}$.
4. A quantity of two hundred micro liters of the sample was extracted into a five-hundred micro liter gas-tight syringe, and the syringe's needle was inserted into the hot injector port of the gas chromatograph. The samples were then placed in a column.

3.6.5 GC Calibration

The Antoine equation is a widely used empirical model in the field of gas chromatography (GC) to determine the vapor pressure of compounds in the vapor phase [39]. This method offers a convenient means for estimating the vapor pressure of a substance at a specific temperature. The equation establishes a relationship between the logarithm of vapor pressure and temperature, incorporating parameters unique to each compound. The Antoine equation can provide precise vapor pressure values, thereby facilitating accurate calibration and quantification during GC analysis [40].

Calibration is a crucial step in gas chromatography (GC) for determining the relationship between the detector response and the concentration of the analyte of interest. Calibration curves are typically developed by plotting the detector response against the known analyte concentrations. However, in situations where

it is challenging to accurately prepare liquid solutions of the analyte at specific concentrations for calibration, the Antoine equation provides an alternative approach for indirectly estimating the concentration based on vapor pressure [41–43].

The Antoine equation can be mathematically represented as:

$$\log_{10} p = A - \frac{B}{T + C} \tag{3.15}$$

where p is the vapor pressure in mmHg and T is the temperature in $^{\circ}\mathrm{C}$.

The vapour pressure (VP) is an essential parameter for accurately measuring the concentration of analytes in gas chromatography (GC). With the appropriate equation rearranged, the vapor pressure can be determined when the temperature is known, allowing the calculation of the analyte concentration in the vapor phase. This information can be correlated to the detector response during the GC calibration process. The Antoine equation presents researchers with a method for estimating the concentration of analytes without the need for liquid standards, thereby offering greater flexibility in calibration procedures.

In this study, the Antoine equation was used to determine the vapor pressures of the compounds at various temperatures. Subsequently, these values were used to create calibration curves and quantify the analytes present in the vapor phase. The accuracy and dependability of the Antoine equation for GC calibration were assessed by comparing the calculated concentrations with those obtained using conventional liquid calibration standards. This technique enhances the analytical capabilities of GC systems and enables their precise quantification.

Methanol Vapour

Using the Antoine equation with the temperature expressed in degrees Celsius, it was possible to determine the vapor pressure of methanol at $25\,^{\circ}\mathrm{C}$ by employing the supplied values of A, B, and C. The values of A, B, and C are as follows: A = 8.07247, B = 1574.99, and C = 238.86 [44]. The Antoine equation for methanol at $25\,^{\circ}\mathrm{C}$ is expressed as follows:

$$\log_{10} p = 8.07247 - \frac{1574.99}{25 + 238.86}$$

$$\begin{aligned}
\log_{10} p &= 8.07247 - \frac{1574.99}{25 + 238.86} \\
\log_{10} p &= 8.07247 - 5.96903 \\
\log_{10} p &= 2.10344 \\
p &= 126.89\text{mmHg}
\end{aligned}$$

The application of Raoult's law enables the calculation of the mole fraction of methanol (CH_3OH).

$$\chi_{CH_3OH} = \frac{p_{CH_3OH}}{p_{\text{total}}}$$

Given that the vapor pressure of methanol (denoted as p_{CH_3OH}) at a temperature of 25°C is 126.89 mmHg, and the total vapor pressure of the mixture (denoted as p_{total}) is 760 mmHg, these values can be substituted into the equation.

$$\chi_{CH_3OH} = \frac{126.89\,\text{mmHg}}{760\,\text{mmHg}}$$

Calculating this expression:

$$\chi_{CH_3OH} \approx 0.167$$

$$\chi_{CH_3OH} \approx 16.7\%$$

The molar fraction of methanol in the mixture was ≈ 16.7%.

The gas chromatograph (GC) was calibrated to determine the mole fraction of methanol. To accomplish this, a calibration curve was constructed using samples with known mole fractions of methanol. These samples were prepared by purifying methanol with high-purity nitrogen gas in a gas washing system and collecting methanol vapor using a gas collection system. The collected samples were then analyzed by GC to determine their respective GC areas, which were plotted against known methanol mole fractions to construct a calibration curve. Using this calibration curve, the molar fraction of methanol in the unknown samples was determined based on the GC areas.

Based on the fact that the GC area corresponds to 16.7% methanol vapor, which is equivalent to 44,000,000, it is possible to calculate the unknown concentration of methanol vapor in parts per million (ppm) using the following mathematical equation:

$$\left(\frac{16.7}{44,000,00}\right) \times x \times 10^4 \text{ ppm} = \left(\frac{16.7}{440}\right) \times x \text{ ppm}$$

The concentration of methanol in the GC area was 16.7%, which can be mathematically represented as $\left(\frac{16.7}{44{,}000{,}00}\right) \times x \times 10^4$ ppm, where x is the GC area of the unknown sample. Simplifying this equation yields

$$CH_3OH_{\text{unknown}} = \left(\frac{16.7}{440}\right) \times x \text{ ppm}$$

The conversion of parts per million (ppm) to $\mu\text{mol}\,\text{g}^{-1}$ of catalyst was achieved using the following equation:

$$\text{umol/g of the catalyst} = \frac{\text{ppm}_{CH_3OH} \times \text{reactor volume} \times \rho_{CH_3OH}}{\text{catalyst loading} \times \text{M.W}_{CH_3OH}}$$

The volume of the reactor corresponded to its vapor phase volume, which was $75\,\text{mL}$. The catalyst loading was $25\,\text{mg}$ in $225\,\text{mL}$, resulting in a concentration of $0.1\,\text{g}\,\text{L}^{-1}$.

$$CH_3OH, \text{umol/g} = \frac{\text{ppm}_{CH_3OH} \times 75\text{ mL} \times 0.7918\text{ g/mL}}{0.1\text{ g} \times 32\text{ g}}$$

In accordance with the findings of this study, methanol vapor was predominantly detected in the gaseous phase, whereas no substantial amount of methanol was detected in the liquid phase. The rationale behind these observations is discussed comprehensively in the literature review section of this thesis.

Methane

Methane was evaluated using a calibration standard consisting of 10% methane. The gas chromatography (GC) area for the standard was 34,76,500. The conversion equation was determined accordingly.

$$\text{CH}_4, \text{unknown} = \left(\frac{10}{347.65}\right) \times x \text{ ppm}$$

$$\text{CH}_4, \text{umol/g} = \frac{\text{ppm}_{\text{CH}_4} \times \text{reactor volume} \times \rho_{\text{CH}_4}}{\text{catalyst loading} \times \text{M.W}_{\text{CH}_4} \times 1000}$$

where x is the GC area of the sample.

Hydrogen

$$\text{H}_2, \text{unknown} = \left(\frac{99.99}{152.3944}\right) \times x \text{ ppm}$$

$$\text{H}_2, \text{umol/g} = \frac{\text{ppm}_{\text{H}_2} \times \text{reactor volume} \times \rho_{\text{H}_2}}{\text{catalyst loading} \times \text{M.W}_{\text{H}_2} \times 1000}$$

Oxygen

$$\text{O}_2, \text{unknown} = \left(\frac{99.99}{4.8789}\right) \times x \text{ ppm}$$

$$\text{O}_2, \text{umol/g} = \frac{\text{ppm}_{\text{O}_2} \times \text{reactor volume} \times \rho_{\text{O}_2}}{\text{catalyst loading} \times \text{M.W}_{\text{O}_2} \times 1000}$$

Other Gaseous Standards

The present work shows the calibration of a gas chromatograph (GC) using standard gas samples, as outlined in Table 3.2. The introduction of each gas into the system was facilitated by its corresponding canister. However, the lack of identification of these gases as products of our reaction precludes the inclusion of extensive calculations or equations to determine their concentrations.

The calibration of the gas chromatograph (GC) utilizing standard gas samples is shown in Table 3.2. Each gas was introduced into the system using a corresponding canister. However, as these gases were not identified as the products of our reaction, comprehensive calculations or equations for determining their concentrations were not included in this thesis.

3.7 CO_2 Photoreduction Reaction Procedure

The following protocol was employed in the photoreduction experiment involving CO_2: all glassware and photoreactor were thoroughly cleaned with laboratory soap solution and water, followed by rinsing with Millipore water and drying in a hot-air oven at $60\,^{\circ}\text{C}$. Prior to each experiment, the graphitic carbon nitride material was

No. of Carbon	R.T	Component	%	Area
C1	1.96	Methane	10	34,76500
C2	2.07	Ethylene	4.3	8,19240
	2.12	Ethane	8.5	12,46953
C3	2.49	Propylene	6.5	12,86755
	2.54	Propane	12.9	23,30275
	2.6	Propadiene	2.1	3,56818
C4	3.48	Isobutane	10.8	30,03372
	3.66	Isobutene	2.2	15,87541
	3.74	1,3 butadiene	6.5	13,69683
	3.86	n-Butane	8.6	34,94979
	4.02	C-2-Butene	4.3	92,1027
C5	6.8	Iso-Pentane	2.2	5,49222
	7.1	1- Pentene	0.9	2,55510
	7.55	n- Pentane	4.3	11,53344
	7.7	2-Methyl-2-Butene	0.43	1,33281
C6	18.8	n- Hexane	0.21	1,719

Table 3.2: Standard Gases

degassed using an adsorption and porosity analyzer for a period of six hours to remove any carbon impurities that may have been present on its surface. Cleaning and degassing procedures were performed in accordance with the manufacturer's protocol.

1. Undertaking extensive examination of the gas chromatograph ensured its complete connection of all gases, as well as the loading of the specified GC method file.

2. In a boiling tube, $25\,\mathrm{mg}$ of carbon nitride material was uniformly distributed in $20\,\mathrm{mL}$ of Millipore water. The mixture was sonicated for $15\,\mathrm{min}$ to ensure a complete dispersion. The resulting solution was then transferred to the photoreactor using a glass filter funnel, and the boiling tube and funnel were subsequently rinsed with additional $20\,\mathrm{mL}$ of Millipore water.

3. Subsequently, $1.8\,\mathrm{mg}$ of sodium hydroxide were added to a photoreactor containing $185\,\mathrm{mL}$ of Millipore water, resulting in a total volume of $225\,\mathrm{mL}$. The solution concentration was 0.2N, with $1.8\,\mathrm{mg}$ of NaOH dissolved in $225\,\mathrm{mL}$ ($185\,\mathrm{mL} + 40\,\mathrm{mL}$). The pH of the 0.2N NaOH solution was approximately 13.3.

4. A suitable magnetic pellet is introduced into the photoreactor via the B14 port.

5. To prevent the contamination of carbon dioxide, a new sodium hydroxide solution was prepared within the photoreactor, and an existing solution was not utilized.

6. The photoreactor was promptly sealed using a silicone rubber septum and Teflon-lined stoppers, and secured with Parafilm and PTFE Teflon tape. The

initiation of water circulation was followed by placement of the photoreactor on a magnetic stirrer.

7. The photoreactor was initially flushed with nitrogen gas for thirty minutes to expel any dissolved oxygen present in the system, and its stirring speed was set at two hundred revolutions per minute. Thereafter, both liquid and gaseous samples were obtained from the photoreactor and subjected to gas chromatography analysis in both FID and TCD modes to evaluate the possibility of contamination.

8. The reaction system was subsequently subjected to high-purity CO_2 purging for a period of $30\,\mathrm{min}$, following which the liquid and gaseous products were examined to ensure the absence of contamination from the CO_2 source. The pH of the purged system was approximately 8.

9. The CO_2-deprived setup was subsequently left to attain adsorption equilibrium while continuously stirring for thirty minutes, followed by the collection and analysis of additional samples using gas chromatography (GC).

10. The experimental setup featured the reaction system placed at a distance of $15\,\mathrm{cm}$ from the light source, and exposure to irradiation was initiated. Following a duration of $4\,\mathrm{h}$, the reaction was discontinued, and both gaseous and liquid products were assessed using Gas Chromatography.

11. Upon completion of the reaction, the gas chromatograph (GC) was powered down, and the reactor was disassembled, cleaned with soap and water, and stored in a secure manner in the glassware cupboard.

3.8 Software's

Table 3.3 presents an exhaustive catalog of the software and web tools employed in this thesis.

References

[1] Kaduk, J. A.; Billinge, S. J. L.; Dinnebier, R. E.; Henderson, N.; Madsen, I.; Cerny, R.; Leoni, M.; Lutterotti, L.; Thakral, S.; Chateigner, D. Powder diffraction. *Nature Reviews Methods Primers* **2021**, *1*, 77.

[2] Dinnebier, R. E.; Billinge, S. J. L., Principles of Powder Diffraction In *Powder Diffraction: Theory and Practice*; The Royal Society of Chemistry: 2008.

[3] Muniz, F. T. L.; Miranda, M. A. R.; Morilla dos Santos, C.; Sasaki, J. M. The Scherrer equation and the dynamical theory of X-ray diffraction. *Acta Crystallographica Section A* **2016**, *72*, 385–390.

[4] Miranda, M. A. R.; Sasaki, J. M. The limit of application of the Scherrer equation. *Acta Crystallographica Section A* **2018**, *74*, 54–65.

Table 3.3: List of software and web utilities used in the thesis work.

Software/Web Utility	Purpose
TEX Live	Interface for TEX studio
TEX studio	Thesis writing & formatting
Origin Pro 2024	Scientific graphing and data analysis
PowDLL Converter 3.0	conversion between Powder X-Ray files
X'Pert HighScore Plus 3.0	Rietveld refinement
Mercury 2022.1.0	Visualization of crystal data
enCIFer 2022.1.0 (Build 343014)	Visualization of crystal data
VESTA 3.5.7	Visualization of crystal data
Crystal Maker 10.7.3	Visualization of the crystal data
Crystal Diffract 6.9.4	Analysis of Powder XRD
ChemDraw 22.2.0	Plotting chemical structures
CasaXPS 2.3.25PR1.0	XPS Analysis
ASAP 2020 Plus 2.0	Adsorption data analysis
ImageJ 1.53	SEM Image analysis
MestReNova 14.2.1-27684	NMR Analysis
Anaconda	Python script
Grammarly	Grammer check
`https://sesami-web.org/`	A web interface for SESAMI analysis
`https://tex.stackexchange.com/`	LATEX codes
`https://openai.com/`	LATEX codes

[5] Himabindu, B.; Latha Devi, N.; Rajini Kanth, B. Microstructural parameters from X-ray peak profile analysis by Williamson-Hall models; A review. *Materials Today: Proceedings* **2021**, *47*, FRESM'21, 4891–4896.

[6] Von Dreele, R. B., Rietveld Refinement In *Powder Diffraction: Theory and Practice*; The Royal Society of Chemistry: 2008.

[7] Caliandro, R.; Giacovazzo, C.; Rizzi, R., Crystal Structure Determination In *Powder Diffraction: Theory and Practice*; The Royal Society of Chemistry: 2008.

[8] Brunauer, S.; Emmett, P. H.; Teller, E. Adsorption of Gases in Multimolecular Layers. *Journal of the American Chemical Society* **1938**, *60*, 309–319.

[9] Brunauer, S., *The Adsorption of Gases and Vapors: Physical adsorption*; The Adsorption of Gases and Vapors; Princeton University Press: 1945.

[10] Terrones, G. G.; Chen, Y.; Datar, A.; Lin, L.-C.; Kulik, H. J.; Chung, Y. G. SESAMI APP: An Accessible Interface for Surface Area Calculation of Materials from Adsorption Isotherms. *Journal of Open Source Software* **2023**, *8*, 5429.

[11] Rouquerol, J.; Llewellyn, P.; Rouquerol, F., Is the bet equation applicable to microporous adsorbents? In *Characterization of Porous Solids VII*, Llewellyn, P., Rodriquez-Reinoso, F., Rouqerol, J., Seaton, N., Eds.; Studies in Surface Science and Catalysis, Vol. 160; Elsevier: 2007, pp 49–56.

[12] Rouquerol, J.; Rouquerol, F.; Llewellyn, P.; Maurin, G.; Sing, K., *Adsorption by Powders and Porous Solids: Principles, Methodology and Applications*; Elsevier Science: 2013.

[13] Osterrieth, J. W. M. et al. How Reproducible are Surface Areas Calculated from the BET Equation? *Advanced Materials* **2022**, *34*, 2201502.

[14] Datar, A.; Chung, Y. G.; Lin, L.-C. Beyond the BET Analysis: The Surface Area Prediction of Nanoporous Materials Using a Machine Learning Method. *The Journal of Physical Chemistry Letters* **2020**, *11*, 5412–5417.

[15] Sinha, P.; Datar, A.; Jeong, C.; Deng, X.; Chung, Y. G.; Lin, L.-C. Surface Area Determination of Porous Materials Using the Brunauer–Emmett–Teller (BET) Method: Limitations and Improvements. *The Journal of Physical Chemistry C* **2019**, *123*, 20195–20209.

[16] Mamleev, V. S.; Villiéras, F.; Cases, J.-M. Adsorption of Spherical Molecules in Probing the Surface Topography. 1. Patchwise Heterogeneity Model. *Langmuir* **2002**, *18*, 2075–2088.

[17] Villieras, F.; Michot, L. J.; Bardot, F.; Cases, J. M.; Francois, M.; Rudzinski, W. An Improved Derivative Isotherm Summation Method To Study Surface Heterogeneity of Clay Minerals. *Langmuir* **1997**, *13*, 1104–1117.

[18] Villieras, F.; Michot, L. J.; Gerard, G.; Cases, J. M.; Rudzinski, W. Application of Statistical Rate Theory of Interfacial Transport to Study Solid Surface Heterogeneity from Controlled-rate Thermal Desorption. *Journal of Thermal Analysis and Calorimetry* **1999**, *55*, 511–530.

[19] Kubelka, P.; Munk, F. An article on optics of paint layers. *Fuer Tekn. Physik* **1931**, *12*, 593–609.

[20] Kubelka, P. New Contributions to the Optics of Intensely Light-Scattering Materials. Part I. *Journal of the Optical Society of America* **1948**, *38*, 448–457.

[21] Kubelka, P. New Contributions to the Optics of Intensely Light-Scattering Materials. Part II: Nonhomogeneous Layers. *Journal of the Optical Society of America* **1954**, *44*, 330–335.

[22] Yang, L.; Kruse, B. Revised Kubelka–Munk theory. I. Theory and application. *J. Opt. Soc. Am. A* **2004**, *21*, 1933–1941.

[23] Kokhanovsky, A. A. Physical interpretation and accuracy of the Kubelka–Munk theory. *Journal of Physics D: Applied Physics* **2007**, *40*, 2210.

[24] Tauc, J. Optical properties and electronic structure of amorphous Ge and Si. *Materials Research Bulletin* **1968**, *3*, 37–46.

[25] Feng, Y.; Lin, S.; Huang, S.; Shrestha, S.; Conibeer, G. Can Tauc plot extrapolation be used for direct-band-gap semiconductor nanocrystals? *Journal of Applied Physics* **2015**, *117*, 125701.

[26] Zanatta, A. R. Revisiting the optical bandgap of semiconductors and the proposal of a unified methodology to its determination. *Scientific Reports* **2019**, *9*, 11225.

[27] Macfarlane, G. G.; Roberts, V. Infrared Absorption of Germanium near the Lattice Edge. *Phys. Rev.* **1955**, *97*, 1714–1716.

[28] Macfarlane, G. G.; McLean, T. P.; Quarrington, J. E.; Roberts, V. Fine Structure in the Absorption-Edge Spectrum of Si. *Phys. Rev.* **1958**, *111*, 1245–1254.

[29] Davis, E. A.; Mott, N. F. Conduction in non-crystalline systems V. Conductivity, optical absorption and photoconductivity in amorphous semiconductors. *The Philosophical Magazine: A Journal of Theoretical Experimental and Applied Physics* **1970**, *22*, 0903–0922.

[30] YU, P.; Cardona, M., *Fundamentals of Semiconductors: Physics and Materials Properties*; Graduate Texts in Physics; Springer Berlin Heidelberg: 2010.

[31] Mott, N.; Davis, E., *Electronic Processes in Non-Crystalline Materials*; Electronic Processes in Non-crystalline Materials; OUP Oxford: 2012.

[32] Dubrovkin, J., *Derivative Spectroscopy*; Cambridge Scholars Publishing: 2020.

[33] Dubrovkin, J., *Data Compression in Spectroscopy*; Cambridge Scholars Publishing: 2022.

[34] Dubrovkin, J., *Mathematical Processing of Spectral Data in Analytical Chemistry: A Guide to Error Analysis*; Cambridge Scholars Publishing: 2019.

[35] Greczynski, G.; Hultman, L. A step-by-step guide to perform x-ray photoelectron spectroscopy. *Journal of Applied Physics* **2022**, *132*, 011101.

[36] Ul-Hamid, A., *A Beginners Guide to Scanning Electron Microscopy*; Springer International Publishing: 2019.

[37] Reif, B.; Ashbrook, S. E.; Emsley, L.; Hong, M. Solid-state NMR spectroscopy. *Nature Reviews Methods Primers* **2021**, *1*, 2.

[38] Pelant, I.; Valenta, J., *Luminescence Spectroscopy of Semiconductors*; Oxford University Press: 2012.

[39] Littlewood, A., *Gas Chromatography: Principles, Techniques, and Applications*; Elsevier Science: 2013.

[40] McNair, H.; Miller, J.; Snow, N., *Basic Gas Chromatography*; Wiley: 2019.

[41] Dettmer-Wilde, K.; Engewald, W., *Practical Gas Chromatography: A Comprehensive Reference*; Springer Berlin Heidelberg: 2014.

[42] Swinley, J.; de Coning, P., *A Practical Guide to Gas Analysis by Gas Chromatography*; Elsevier Science: 2019.

[43] Kromidas, S.; Kuss, H., *Quantification in LC and GC: A Practical Guide to Good Chromatographic Data*; Wiley: 2009.

[44] Haynes, W., *CRC Handbook of Chemistry and Physics*; CRC Press: 2016.

Chapter 4

Understanding the Role of Surface Functionalities in the Photon-Assisted Reduction of Carbon Dioxide on Graphitic Carbon Nitride ($g\text{-}C_3N_4$) Surfaces

Abstract

Graphitic carbon nitride ($g\text{-}C_3N_4$) has emerged as a promising photocatalyst for CO_2 reduction, owing to its unique properties and tunable electronic and surface characteristics. However, the rational design of efficient $g\text{-}C_3N_4$-based photocatalysts remains a challenge because the photocatalytic performance is significantly influenced by the synthesis conditions and choice of precursors. In this comprehensive study, we investigated the impact of the precursor selection on the photocatalytic CO_2 reduction performance of $g\text{-}C_3N_4$. Six different precursors, namely ammonium thiocyanate (AT), cyanamide (CY), dicyandiamide (DC), melamine (M), thiourea (TU), and urea (U), were used to synthesize a series of $g\text{-}C_3N_4$ photocatalysts. The structural, optical, and surface properties of the synthesized materials were thoroughly characterized using various advanced techniques, including XRD, N_2 physisorption, DRS, PL, solid-state NMR, XPS, and valence band XPS. To enable a meaningful comparison of the photocatalytic capabilities, we introduced two key parameters: DP/SA, which represents the light absorption efficiency per unit surface area, and NSC%, which denotes the surface concentration of functional groups per unit area. CO_2 photoreduction experiments revealed that the product yield and selectivity were significantly influenced by the precursor choice, with TU-gCN exhibiting the highest methane yield and AT-gCN demonstrating the highest methanol yield. Extensive characterization results provide valuable insights into the structure-property-performance relationships, highlighting the importance of porosity, surface area, light absorption efficiency, and surface functionalities in determining CO_2 reduction performance. Plausible mechanistic pathways for the formation of methane and methanol on $g\text{-}C_3N_4$ surfaces were proposed based on the insights gained from this study. This study provides a comprehensive understanding of the influence of precursor selection on the photocatalytic CO_2 reduction

performance of g-C_3N_4, and offers valuable guidelines for the rational design of efficient g-C_3N_4-based photocatalysts for sustainable CO_2 utilization.

4.1 Introduction

To understand the effect of precursors on the properties of carbon nitride, it is crucial to consider the impact of different precursors on the structure, morphology, and performance of the resulting material. The choice of precursor has been shown to significantly influence the properties of carbon nitride, such as its catalytic activity, bandgap, electronic structure, and surface area [1]. For instance, the use of mesoporous carbon nitride as a precursor has been found to act as a confinement for particle growth and as a nitrogen source, allowing control over particle size and composition, which is typical in nanoreactors[1, 2]. In addition, the photon-assisted catalytic performance of carbon nitride prepared using supramolecular precursors is reported to be significantly higher than that of the original carbon nitride [3]. Furthermore, the type of precursor used was shown to exert an obvious influence on the structural defects of carbon nitride, thereby affecting its synergistic photocatalytic activity [4].

Moreover, the history of carbon nitride and its precursors has been traced back to the early days, emphasizing the importance of understanding the evolution of precursors that influences the properties of carbon nitride [5]. The synthesis of carbon nitride materials in the presence of inorganic salts has led to highly ordered carbon nitride-based materials with improved efficiency in the hydrogen evolution reaction [6]. Additionally, the synthesis of mesoporous carbon nitride using mixed material sources of carbon and nitrogen has been reported, highlighting the significance of the precursor selection in the synthesis process [7].

Precursor selection, which is a critical component in g-C_3N_4 synthesis, has a significant impact on photon-assisted catalytic performance [8–13]. This chapter explores the fascinating interplay between precursor choice and the subsequent CO_2 reduction and water splitting activities of g-C_3N_4. The effects of various precursors on the physicochemical and electronic properties of g-C_3N_4 were comprehensively examined.

The primary focus of this investigation pertains to studies evaluating the mechanisms by which precursor manipulation influences CO_2 photoreduction and water splitting. Specifically, this study seeks to elucidate the role of precursors in modulating the morphology, porosity, electronic structure, and defects of g-C_3N_4. Precursors play a crucial role in determining the surface area, texture, and dimensionality of g-C_3N_4, which in turn affects the availability of active sites, light absorption cross-section, and mass transfer of reactants. By selecting specific precursors, the bandgap, edge positions, and defect states can be optimized, thereby enhancing the light absorption, charge separation, and reactivity towards CO_2 and water.

This chapter discusses the complexities of optimizing g-C_3N_4 for the photon-assisted catalysis of CO_2 using Rietveld refinement, derivative spectroscopic techniques, and derivative isotherm summation. This highlights studies that have revealed the previously untapped potential of g-C_3N_4 in these applications. Through a comprehensive examination of the experimental findings and theoretical insights, this chapter provides groundwork for future design approaches aimed at enhanc-

ing the efficiency and selectivity of g-C_3N_4-based photon-assisted catalysis in the emerging energy landscape.

4.2 Results and Discussion

4.2.1 Discussion on CO_2 Photoreduction Results

In this study, the CO_2 photoreduction process for methane, methanol, and oxygen utilizing graphitic carbon nitride (gCN) materials, including TU-gCN, AT-gCN, CY-gCN, DC-gCN, M-gCN, and U-gCN, was investigated. Among these materials, TU-gCN and AT-gCN exhibited considerable methane yields, indicating their effectiveness for methane production. In contrast, CY-gCN, DC-gCN, M-gCN, and U-gCN produced lower amounts of methane (Figure 4.1).

In terms of methanol yield, AT-gCN demonstrated a rate of $164.5\,\mu\mathrm{mol\,g^{-1}\,h^{-1}}$, while CY-gCN and TU-gCN showed significant methanol yields of $87\,\mu\mathrm{mol\,g^{-1}\,h^{-1}}$ and $82\,\mu\mathrm{mol\,g^{-1}\,h^{-1}}$, respectively. Other materials, including DC-gCN, M-gCN, and U-gCN, displayed lower but noteworthy methanol yields.

CY-gCN was the most prominent performer in the oxygen evolution reaction, with a yield of $1188\,\mu\mathrm{mol\,g^{-1}\,h^{-1}}$, highlighting its exceptional effectiveness in oxygen generation. U-gCN and DC-gCN exhibited significant oxygen production with values of $839\,\mu\mathrm{mol\,g^{-1}\,h^{-1}}$ and $567\,\mu\mathrm{mol\,g^{-1}\,h^{-1}}$, respectively. AT-gCN, M-gCN, and TU-gCN displayed varying levels of oxygen production.

This is the conventional interpretation of product yield over any catalyst system. A problem that arises when comparing different catalyst systems in these methods is that the surface area of the material is not normalized. All six catalyst systems had different surface areas, and the yield did not show any correlation with the surface area of the materials. If the surface area is a factor, doubling the surface area doubles the yield [14]. However, no such observation were made. The figure shows the product yield with respect to the total surface area of the graphitic carbon nitride samples.

A more appropriate way to compare different catalyst systems is to express the product yield per unit surface area (Figure 4.2). Expressing the yield per unit surface area when comparing different catalytic systems has several advantages. First, this method normalizes the activity for variations in catalyst loading, as the amount of catalyst used in a reaction may differ across studies, making direct comparison challenging. By expressing the yield per unit surface area, the influence of different loadings was considered, enabling a more meaningful and standardized assessment of the catalyst performance, even with varying amounts of catalyst. Second, this method provides a more fundamental measure of the catalyst activity. The surface area of a catalyst reflects the number of active sites available for the reaction. Expressing the yield per unit surface area essentially measures the turnover rate of the catalyst, offering a more intrinsic gauge of activity than assessing only the total amount of the product produced. Expressing the yield per unit surface area allows for the comparison of catalysts with different morphologies, as the catalyst morphology, encompassing shape and size, can significantly affect activity. This normalization method helps address these differences, facilitating a fair comparison of catalysts with distinct shapes and sizes. This approach is

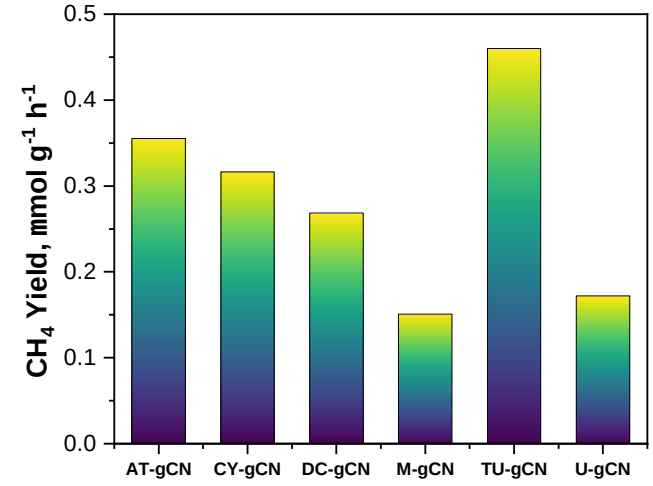

(a) Methane yield

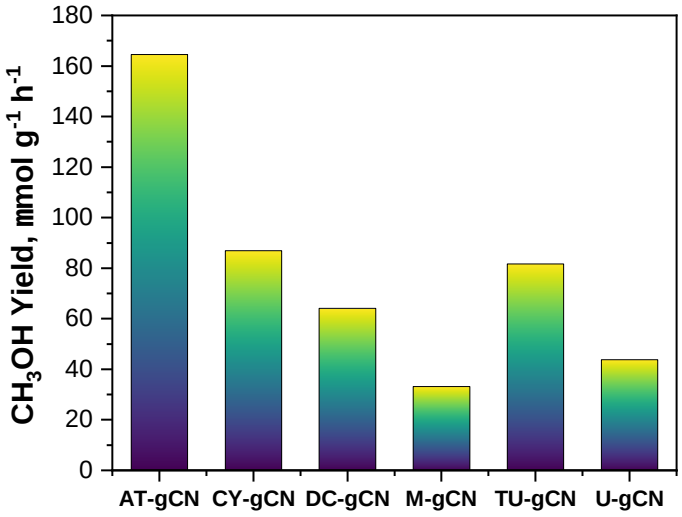

(b) Methanol yield

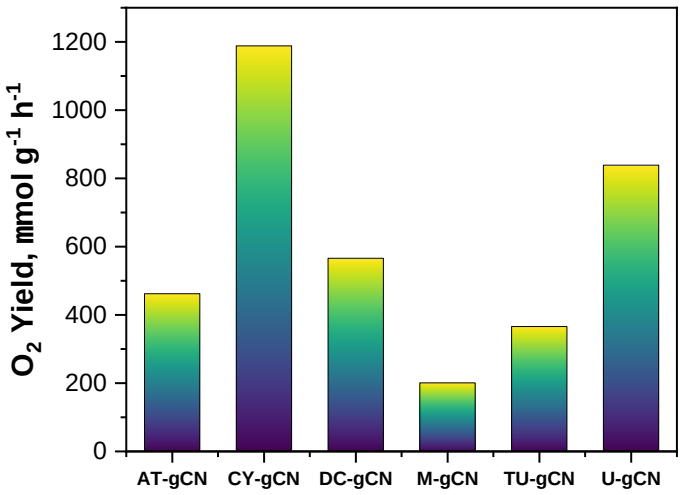

(c) Oxygen yield

Figure 4.1: The yield of CO_2 reduction products (a) methane (b) methanol (c) oxygen with respect to total surface area.

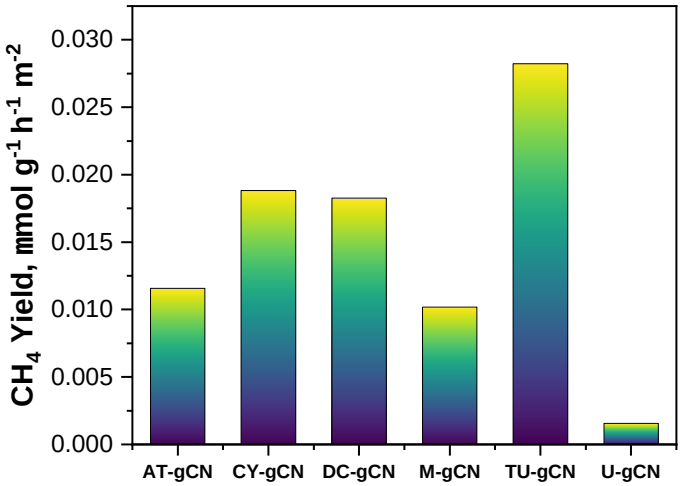

(a) Methane yield

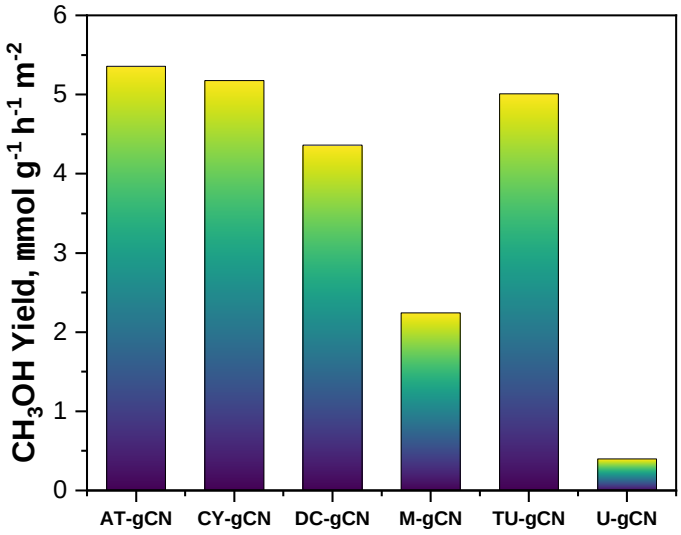

(b) Methanol yield

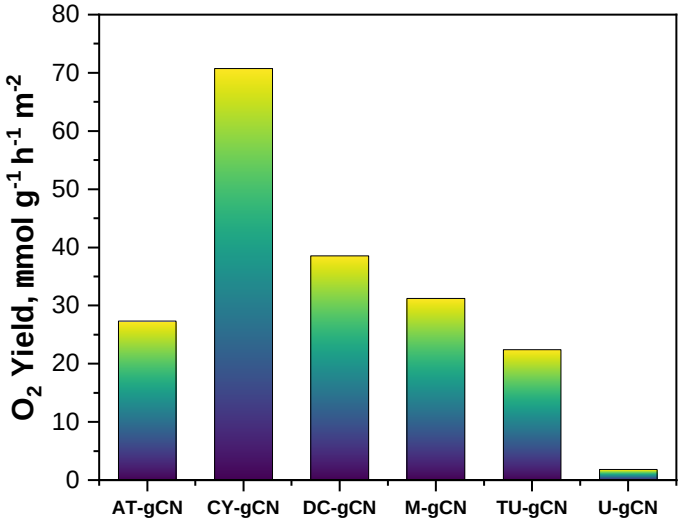

(c) Oxygen yield

Figure 4.2: CO_2 product yields of graphitic carbon nitride samples, consistently reported in units relative to their respective surface areas. (a) Methane Yield: TU-gCN > CY-gCN > DC-gCN > AT-gCN > M-gCN > U-gCN (b) Methanol Yield: AT-gCN > CY-gCN > TU-gCN > DC-gCN > M-gCN > U-gCN (c) Oxygen Yield: CY-gCN > DC-gCN > M-gCN > AT-gCN > TU-gCN > U-gCN

crucial for identifying the most efficient catalysts. By comparing the yield per unit surface area of different catalysts, it is possible to identify the catalyst that excels in producing the desired product most effectively.

In this investigation, the product yields of graphitic carbon nitride samples were consistently reported in units relative to their respective surface areas. This normalization approach provides a comprehensive and standardized basis for comparing the catalytic performances of various systems, considering differences in catalyst loading, surface area, and morphology.

In terms of the methane yield, the results revealed substantial variations among the different gCN materials. Among the studied catalysts, TU-gCN exhibited the highest methane yield, indicating an efficient methane production performance. CY-gCN and DC-gCN also exhibited relatively high methane yields, while U-gCN produced the lowest amount of methane. Switching the focus to the methanol yield, AT-gCN emerged as the top-performing catalyst, followed closely by CY-gCN and TU-gCN. DC-gCN and M-gCN also significantly contributed to methanol production, whereas U-gCN produced a relatively lower yield. Considering the oxygen yield, CY-gCN led to the highest oxygen production among the catalysts. DC-gCN and M-gCN also demonstrated notable oxygen yields, whereas AT-gCN, TU-gCN, and U-gCN displayed varying levels of oxygen production, with U-gCN showing the lowest yield.

In the subsequent sections, a detailed examination is presented to evaluate the role of surface functionalities in the photon-assisted reduction of carbon dioxide on graphitic carbon nitride surfaces.

4.2.2 X-ray Diffraction

The XRD data were collected using a Bruker D8 Advance diffractometer equipped with Cu Kα radiation (wavelength = 1.5418 Å) in the 2θ range of 10–70°. The step size was 0.034° and each step was performed for 5 s. The acquired data were processed using the X'Pert HighScore Plus software (version 3.0), which involved subtracting the background and normalizing the data [15].

X-ray diffraction (XRD) is a widely used technique for determining the structures of crystalline and polymeric materials. Graphene-based materials, known as gCN, often exhibit characteristics that suggest an amorphous-to-nanocrystalline nature. The primary reflection at 2θ=26-28°, which is typically associated with a "graphitic" structure and an interplanar spacing of 3.2-3.4 Å, is not a conclusive criterion for determining the presence of graphitic sheets in gCN [16].

To examine the structure of the gCN materials, Rietveld refinement was performed using the PANalytical X'Pert HighScore Plus software (version 3.0). The initial model was based on the reported crystal structure of C_{24} H_{12} N_{36} (ICSD 194747; Structure: Carbon Nitride Amide; Space Group: $P2_12_12$; Cell: a= 16.4 Å, b= 12.4 Å, c= 6.49 Å, α = 90°, β = 90°, γ = 90°)), which is an orthorhombic crystal system [17]. The refinement process resulted in all single-digit agreement indices, indicating excellent agreement between the calculated and observed data.

The LeBail graph for each precursor-derived carbon nitride is shown in Figure 4.3.

The XRD data presented in Figure 4.4 and Table 4.1 provide a thorough investigation of the influence of the precursor choice on the crystal structure of g-CN. The

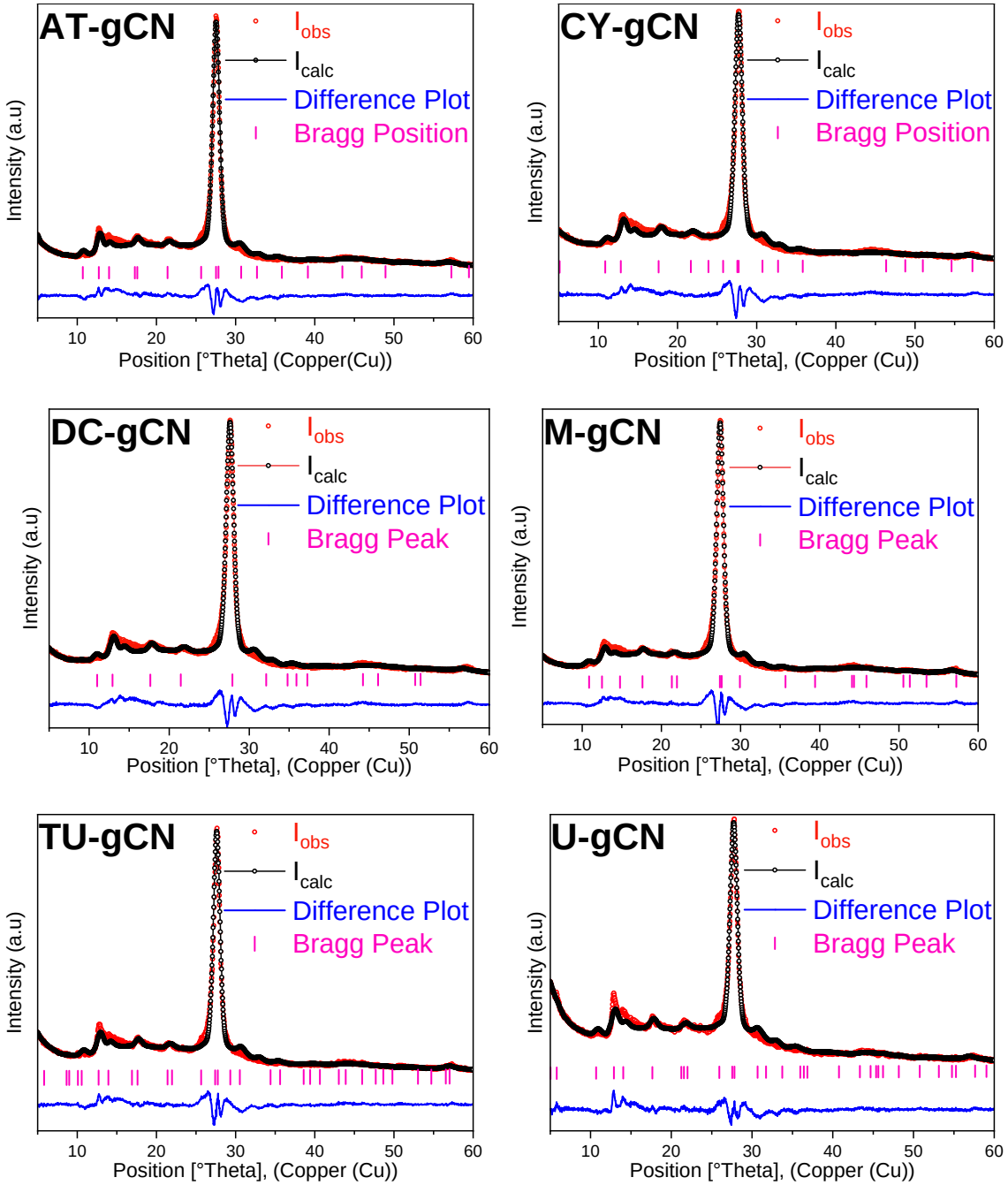

Figure 4.3: LeBail fits of graphitic carbon nitride derived from various precursors, including ammonium thiocyanate (AT-gCN), cyanamide (CY-gCN), dicyandiamide (DC-gCN), melamine (M-gCN), thiourea (TU-gCN), and urea (U-gCN).

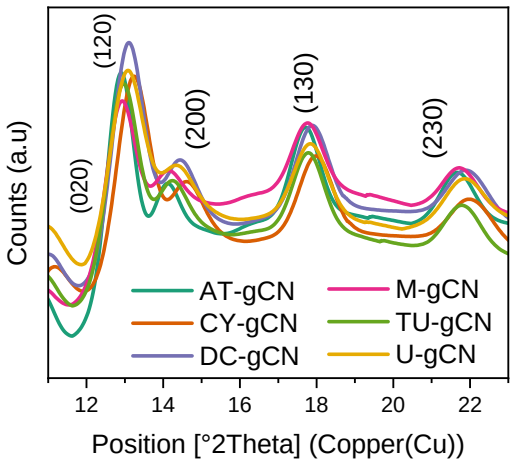

(a) X-ray Diffractogram 10-24°

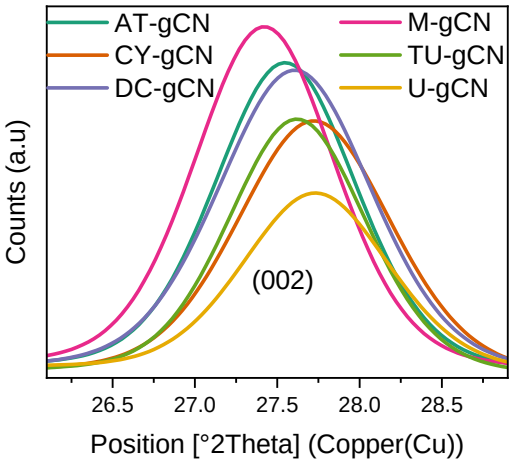

(b) X-ray Diffractogram 26-29°

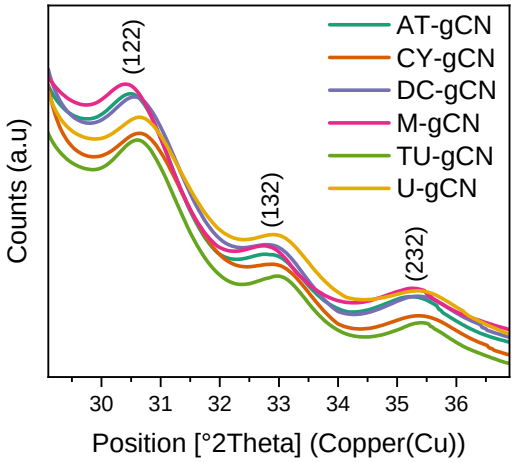

(c) X-ray Diffractogram 28-37°

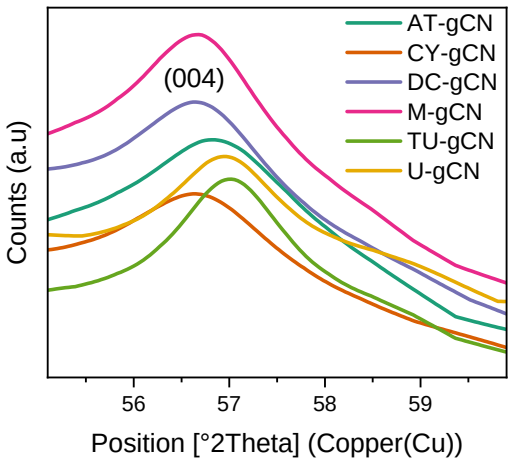

(d) X-ray Diffractogram 55-60°

Figure 4.4: The XRD diffractograms of the carbon nitrides were analyzed and separated into distinct angular ranges.

presence of reflections corresponding to the (120) and (002) planes in all samples indicates the characteristic layered g-C_3N_4 motif featuring distinct in-plane and interlayer spacings.

XRD analysis confirmed the layered structure of g-C_3N_4 in all samples, as evidenced by the presence of the (120) and (002) reflections. Notably, the peak positions varied across the samples, indicating that the choice of precursor influenced the stacking arrangement and lattice parameters of the g-CN layers. The AT-gCN and M-gCN samples displayed the highest crystallinity with the lowest FWHM values for the (120) and (002) peaks. CY-gCN, DC-gCN, and TU-gCN samples exhibited moderate crystallinity, whereas U-gCN displayed the lowest crystallinity.

The AT-gCN, DC-gCN, and M-gCN samples demonstrated exceptional peak areas, reflecting their high crystallinity and large fraction of crystalline material. The other samples exhibited smaller peak areas, suggesting a lower proportion of crystalline material in their structures.

All the samples exhibited consistent d-spacing values for the (002) plane, indi-

cating a precursor-independent interlayer distance of approximately $3.2\,\mathrm{nm}$. However, variations in the (120) reflection suggest that precursor choice primarily influences intralayer organization and packing. The intralayer spacing of bulk carbon nitride has been reported to be $6.71\,$Å[18]. However, deviations from this value are predominantly due to the presence of nitrogen defects or carbon doping.

AT-gCN, M-gCN, U-gCN, and TU-gCN possessed the largest crystallite sizes, whereas DC-gCN and CY-gCN had the smallest. U-gCN, TU-gCN, and M-gCN exhibited low microstrains compared with the other samples. This highlights the significant role of precursor choice in shaping the crystallite size and morphology.

The XRD results revealed a clear correlation between the precursor choice and structural properties of the g-CN samples. The observed variations in the peak positions, crystallinity, crystallite size, and microstrain can be attributed to the distinct chemical nature of the precursors, which influences the condensation and polymerization pathways during synthesis [19].

The consistent interlayer distances observed across all samples suggest that the fundamental building blocks of the g-CN layers remain largely unaffected by the precursor choice (Figure 4.5). However, the variations in the intralayer packing and stacking arrangements highlight the potential of tailoring the structure of g-CN materials by selecting appropriate precursors.

X-ray diffraction (XRD) analysis revealed notable features indicative of stacking disorder in the carbon nitride samples (Table 4.1). The appearance of doublet peaks across each reflection in various samples suggests the potential for stacking disorder in the crystal lattice [20, 21]. This finding is crucial for understanding detailed structural features and deviations from the anticipated well-ordered arrangement. The emergence of doublet peaks, characterized by closely spaced pairs, is a critical indicator of the stacking disorder. These peaks indicate variations in the stacking arrangement of the crystalline planes within the carbon nitride samples. In ideal and well-ordered crystal lattices, a single reflection is expected for each set of crystallographic planes. However, the presence of doublet peaks suggests deviations from this ideal scenario, indicating that the stacking disorder is a significant factor influencing the crystal structure. A detailed examination of the doublet peaks revealed subtle variations in the peak positions, indicating diverse stacking arrangements or orientations of the crystalline planes. This heterogeneity in the peak positions emphasizes the complexity introduced by the stacking disorder. Furthermore, the broader peaks observed, as indicated by the larger Full Width at Half Maximum (FWHM) values, support the presence of stacking disorders. This broadening is consistent with the expected behavior of the XRD patterns when the disorder disrupted the regular crystal lattice.

The crystallization of all samples in the orthorhombic $P2_12_12$ space group with similar cell parameters is noteworthy, because they indicate that despite variations in the peak positions and FWHM, the crystal structure motif remains consistent across the g-CN samples prepared from different precursors. However, minor differences were observed in the unit cell dimensions, particularly along the b and c axes (Table 4.2). These subtle variations may be attributed to slight alterations in the stacking arrangement or lattice parameters, which in turn emphasize the nuanced influence of the precursor choice on the intricate details of the g-CN crystal lattice.

XRD analysis provided valuable information about the structural properties

Table 4.1: XRD Data for Carbon Nitride Samples

Sample	Peak Position	FWHM	Area	h	k	l	D spacing	Height	R.I	Crystallite Size	Microstrain, ϵ
AT-gCN	12.87567	0.826853	482.6137	1	2	0	6.86999	531.865	7.92	7.595	2.172
	12.90781	0.827123	240.0897	1	2	0	6.86999	264.4624	3.94		
	27.52559	1.016705	8082.242	0	0	2	3.23787	6714.824	100		
	27.59535	1.017889	4019.466	0	0	2	3.23787	3334.284	49.66		
CY-gCN	13.21151	1.012406	528.5011	1	2	0	6.6961	474.8905	8.58	6.606	2.22
	13.24335	1.012439	262.9182	1	2	0	6.69667	236.2027	4.27		
	27.70031	1.106009	7255.64	0	0	2	3.21785	5536.131	100		
	27.76932	1.106818	3608.407	0	0	2	3.21798	2750.219	49.68		
DC-gCN	13.07677	0.96916	564.3341	1	2	0	6.76479	530.0726	8.06		
	13.10882	0.969385	280.744	1	2	0	6.76509	263.5963	4.01	7.003	2.098
	27.58369	1.105996	8614.822	0	0	2	3.23119	6577.408	100		
	27.65296	1.106809	4284.35	0	0	2	3.23126	3267.476	49.68		
M-gCN	12.88705	0.920132	394.8774	1	2	0	6.86395	391.0366	5.24		
	12.91945	0.920245	196.4426	1	2	0	6.86382	194.4767	2.61	7.569	1.855
	27.39891	1.009742	8906.91	0	0	2	3.25255	7456.067	100		
	27.46857	1.010357	4429.594	0	0	2	3.25253	3704.419	49.68		
TU-gCN	12.93683	0.93914	474.8256	1	2	0	6.83765	460.5764	8.26		
	12.96909	0.939221	236.2151	1	2	0	6.83766	229.0697	4.11		
	27.59702	0.990102	6540.685	0	0	2	3.22965	5577.941	100		
	27.66694	0.990413	3252.812	0	0	2	3.22966	2772.107	49.7	8.096	1.6
U-gCN	13.04636	1.027068	485.914	1	2	0	6.78049	430.7456	11.1		
	13.07828	1.0271	241.7318	1	2	0	6.78082	214.2458	5.52		
	27.70942	1.050725	4832.18	0	0	2	3.21681	3880.809	100		
	27.77899	1.05088	2403.147	0	0	2	3.21688	1929.001	49.71	7.797	1.59

of the g-CN samples; however, it is important to consider these findings along with data on the CO_2 reduction performance. Notably, TU-gCN, which had a crystallite size and d-spacing similar to those of other samples, exhibited the highest methane and methanol yields. Conversely, U-gCN, which had the smallest crystallite size and lowest peak area, showed the lowest methane yield. The trend in the oxygen yield was less clear. CY-gCN and DC-gCN, which had moderate crystallinity, showed the highest oxygen yield, whereas U-gCN, the least crystalline, had the lowest yield. This suggests that factors beyond the crystal structure, such as surface functional groups or electronic properties, can significantly impact CO_2 conversion efficiency. These findings emphasize the intricate relationship between the structural properties and catalytic activity of the g-CN materials.

	AT-gCN	CY-gCN	DC-gCN	M-gCN	TU-gCN	U-gCN
Space Group	$P2_12_12$					
Crystal System	Orthorhombic					
a	12.59	12.56	12.51	12.52	12.49	12.59
b	16.39	16.63	16.50	16.25	16.35	16.54
c	6.47	6.54	6.52	6.48	6.46	6.49
α	90	90	90	90	90	90
β	90	90	90	90	90	90
γ	90	90	90	90	90	90
R_{exp}	3.22	3.67	3.49	3.14	3.36	3.26
R_p	6.63	6.78	6.88	6.47	6.57	4.98
R_{wp}	8.95	8.96	9.04	8.66	8.85	6.86
GOF	7.72	5.95	6.69	7.63	6.93	4.43

Table 4.2: Pertinent crystallographic data for graphitic carbon nitride synthesized from different precursors. The table presents essential crystallographic parameters, including the space group, crystal system, unit cell parameters (a, b, c, α, β, γ), as well as R-factors (R_{exp}, R_p, R_{wp}) and the Goodness of Fit (GOF).

Refinement using the Rietveld method produced agreement indices, such as R_{exp}, R_p, and R_{wp}, with single-digit values (Table 4.2). However, the difference plot exhibits slight deviations from a straight line, and the overlap between the observed values (I_{obs}) and calculated values (I_{calc}) is not perfect. These variations may be due to inherent complexities in the sample, including sample heterogeneity, the presence of amorphous phases, or microstrain in the crystal lattice. Instrumental factors and data-processing considerations may have contributed to these differences.

The structural information obtained was reliable despite the observed differences. The limitations of the refinement process and the sensitivity of the technique to specific sample characteristics were acknowledged.

4.2.3 Adsorption Isotherm Analysis

The nitrogen adsorption-desorption isotherms of all carbon nitride samples were classified as type III, indicating weak adsorbate-adsorbent interactions, the presence of adsorbed N_2 in the interlayer, or the presence of porous structures in the samples (Figure 4.6)[22–24]. The isotherms displayed type H3 hysteresis loops at $0.45 <$

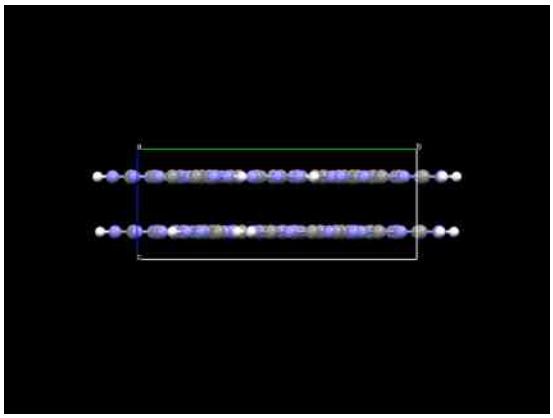

(a) 2D Layer Structure of AT-gCN

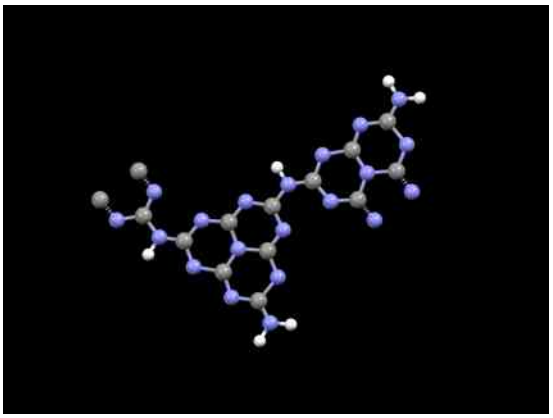

(b) Asymmetric Structure of AT-gCN

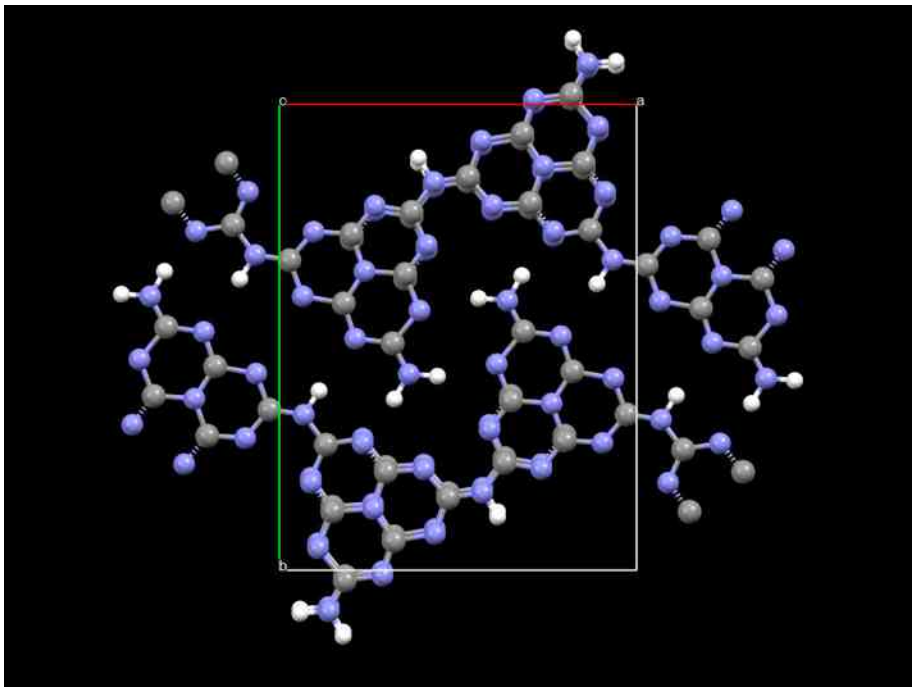

(c) Packing Structure of AT-gCN

Figure 4.5: Structural Features of AT-gCN: (a) 2D Layer Structure, (b) Asymmetric Structure, and (c) Packing Structure.

$\frac{P}{P_0} < 1.00$, a characteristic often observed in aggregates of plate-like particles, suggesting the existence of slit-shaped pores. The average pore sizes of all carbon nitride samples were in the mesoporous regime in the following order: DC-gCN > M-gCN ≈ TU-gCN ≈ AT-gCN > CY-gCN > U-gCN (Table 4.5). U-gCN exhibited the highest t-plot microporous area (U-gCN > AT-gCN > TU-gCN > DC-gCN > CY-gCN > M-gCN) and the lowest percentage of microporous area with respect to total surface area (TU-gCN > DC-gCN > AT-gCN > CY-gCN > M-gCN > U-gCN). As expected, the quantity of adsorbed gas was high in U-gCN, followed by the surface area trend. As the surface area increased, the quantity of the adsorbed gas also increased. The surface area of the sample was calculated using the B.E.T equation, as shown in Table 4.3.

The B.E.T equation is often rearranged to linearize the isotherm and determine the slope and intercept of a specific plot. If the resulting value of C is negative, the

linearized plot does not fit the assumed B.E.T model well [25]. This could be due to various reasons, such as the non-ideal behavior of the adsorbate or limitations in the applicability of the B.E.T model to a specific adsorption system. A negative C value suggests that the B.E.T model may not accurately describe the adsorption isotherm for a given material or condition [26]. It is essential to interpret such results cautiously and consider alternative models or factors that might affect adsorption behavior [27–30]. AT-gCN, DC-gCN, and TU-gCN show negative C values, indicating that they do not follow the B.E.T equation, or corrections in the B.E.T equation are recommended according to the Rouquerol equation [31]. The surface area data were fitted using BETSI and SESAMI techniques, and the results are presented in Table 4.4. Almost the same surface area was observed after the correction; however, as the microporosity increased, the deviation became too large. In addition, it is well known that the B.E.T equation is not suitable for microporous materials or materials containing large amounts of micropores.

	SA	C
AT-gCN	29.48	**-681.09**
CY-gCN	14.46	823.582
DC-gCN	14.1	**-585.807**
M-gCN	14.65	306.52
TU-gCN	15	**-239.13**
U-gCN	110.08	272.295

Table 4.3: Surface Area (SA) and B.E.T constant (C) for different precursors of graphitic carbon nitride from the raw data.

The study of the surface area and porosity data, primarily utilizing the SESAMI method yielded valuable insights into the relationship between these properties and the observed CO_2 reduction activity of the g-CN samples (Table 4.5). This comprehensive interpretation considers the previously presented crystallographic data. Although TU-gCN had lower crystallinity and surface area than AT-gCN and U-gCN, it exhibited the highest C value, as determined by the SESAMI method. The reason for this discrepancy is the increased presence of micropores, which can be seen in the substantially higher micropore volume and percentage compared to the other samples. The SESAMI method provides a measure of the interaction potential between the adsorbate and the adsorbent surface, which is denoted by the C value. A higher C value indicates stronger interactions, which can enhance CO_2 adsorption and activation. Notably, TU-gCN and AT-gCN displayed the highest C value among the samples, which likely played a crucial role in their exceptional CO_2 conversion performances. Enhanced micropore accessibility facilitates efficient CO_2 adsorption and interaction with the active sites, contributing to one of the reasons for the superior activity of TU-gCN and AT-gCN towards methane and methanol yields. The results of this study suggest that the Brunauer–Emmett–Teller (B.E.T) surface area is not a reliable indicator of catalytic performance. This was demonstrated by the fact that U-gCN, which had the highest B.E.T surface area, exhibited the lowest carbon dioxide (CO_2) conversion activity. It is hypothesized that the reduced micropore volume and percentage of U-gCN limits the availability of active sites for CO_2 adsorption, thereby hindering its overall activity. Although the pore sizes

of all the samples were within the mesoporous range ($16\,\mathrm{nm}$ to $27\,\mathrm{nm}$), variations in their pore size distribution could affect the diffusion of CO_2 and accessibility to active sites. Further research using advanced adsorption isotherms is necessary to fully understand the relationship between the pore size distribution and catalytic performance.

The relationship between crystallinity and surface area is complex and multi-faceted, suggesting that other factors, such as the formation of defects and surface chemistry significantly influence the overall surface properties of a material.

	Surface Area, m^2/g			
	B.E.T	**BETSI**	**SESAMI**	**C, SESAMI**
AT-gCN	29.48	31	30.7	547.6
CY-gCN	14.46	17	16.8	304.9
DC-gCN	14.1	15	14.7	452.3
M-gCN	14.65	15	14.8	231.3
TU-gCN	15	16	16.3	670.4
U-gCN	110.08	110	109.5	292.4

Table 4.4: Surface area analysis; B.E.T vs. BETSI vs. SESAMI Method

	q_m, mol/kg	**Pore Size, nm**	**t-plot MA**	**%micropore**
AT-gCN	0.31	26.67	10.41	33.92
CY-gCN	0.17	18.94	4.53	26.97
DC-gCN	0.15	33.89	5.54	37.67
M-gCN	0.15	27.79	3.29	22.29
TU-gCN	0.17	27.83	6.61	40.56
U-gCN	1.12	16.91	16.77	15.31

Table 4.5: Microporous properties of graphitic carbon nitride samples: q_m (quantity of gas adsorbed), pore size, t-plot surface area, and percentage of micropores.

4.2.4 Derivative Isotherm Summation

In gas adsorption analysis, assessing the surface heterogeneity typically entails acquiring a significant number of experimental data points at low relative pressures, usually less than 0.15, during which monolayer filling occurs. The free energy of adsorption on the kT scale can be accurately determined by calculating the derivatives of the adsorption amount relative to the logarithm of the relative pressure, $(\ln(p/p_0))$[32, 33].

Figure 4.7(a) shows the derivative curve obtained from the $77\,\mathrm{K}$ nitrogen adsorption isotherm, which illustrates the gas adsorption energy on the surface. The second derivative was used to distinguish between the peaks and shoulders in the derivative isotherm summation (DIS) plots. In the second-derivative isotherm summation (SDIS), noticeable peaks are observed as downward dips in the curve. This was because the DIS curve represented the second derivative of the adsorption isotherm. The minima in the second derivative correspond to the maxima in the original isotherm and represent the strongest binding sites.

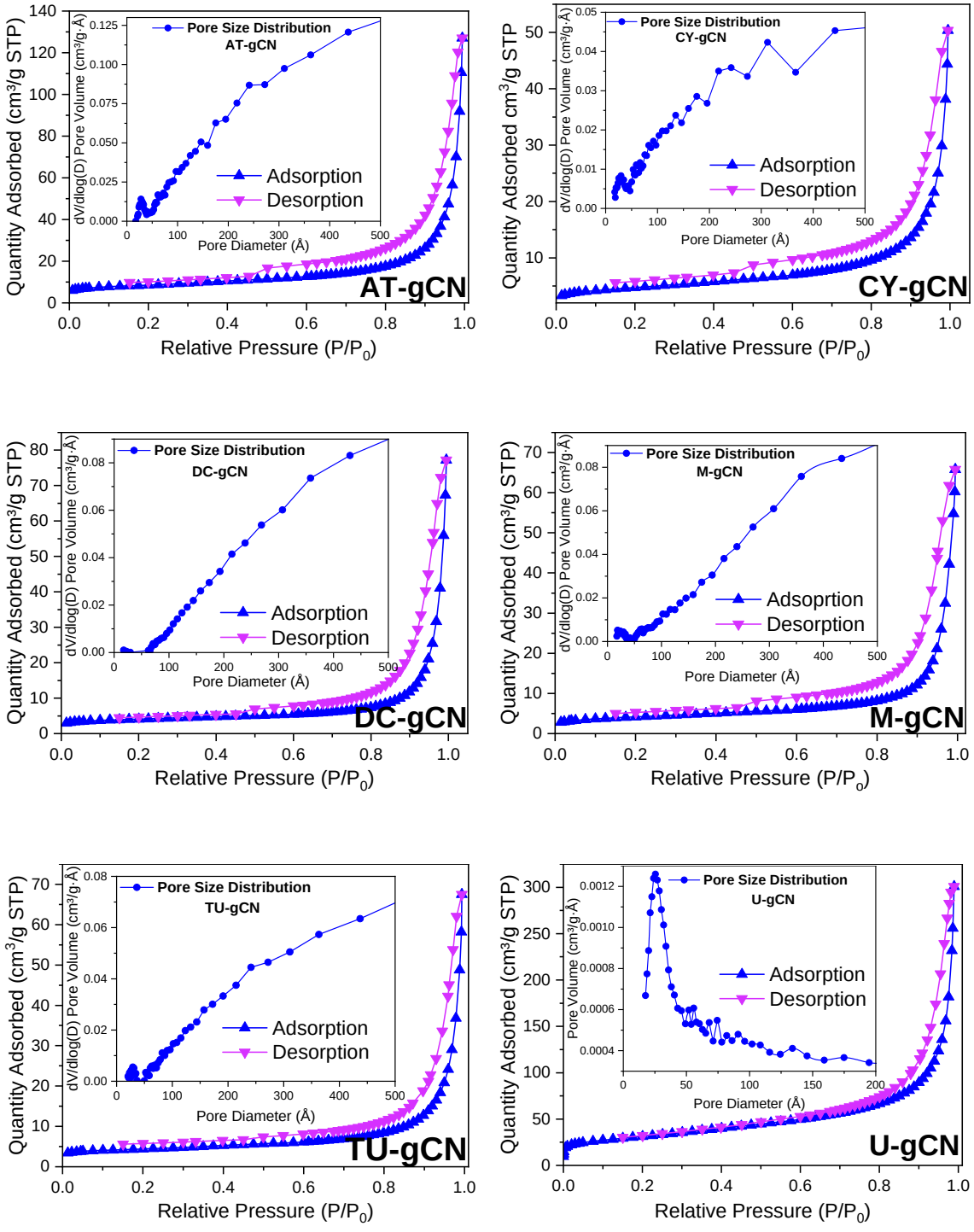

Figure 4.6: N_2 Adsorption isotherms of graphitic carbon nitride derived from ammonium thiocyanate (AT-gCN), cyanamide (CY-gCN), dicyandiamide (DC-gCN), melamine (M-gCN), thiourea (TU-gCN), urea (U-gCN)

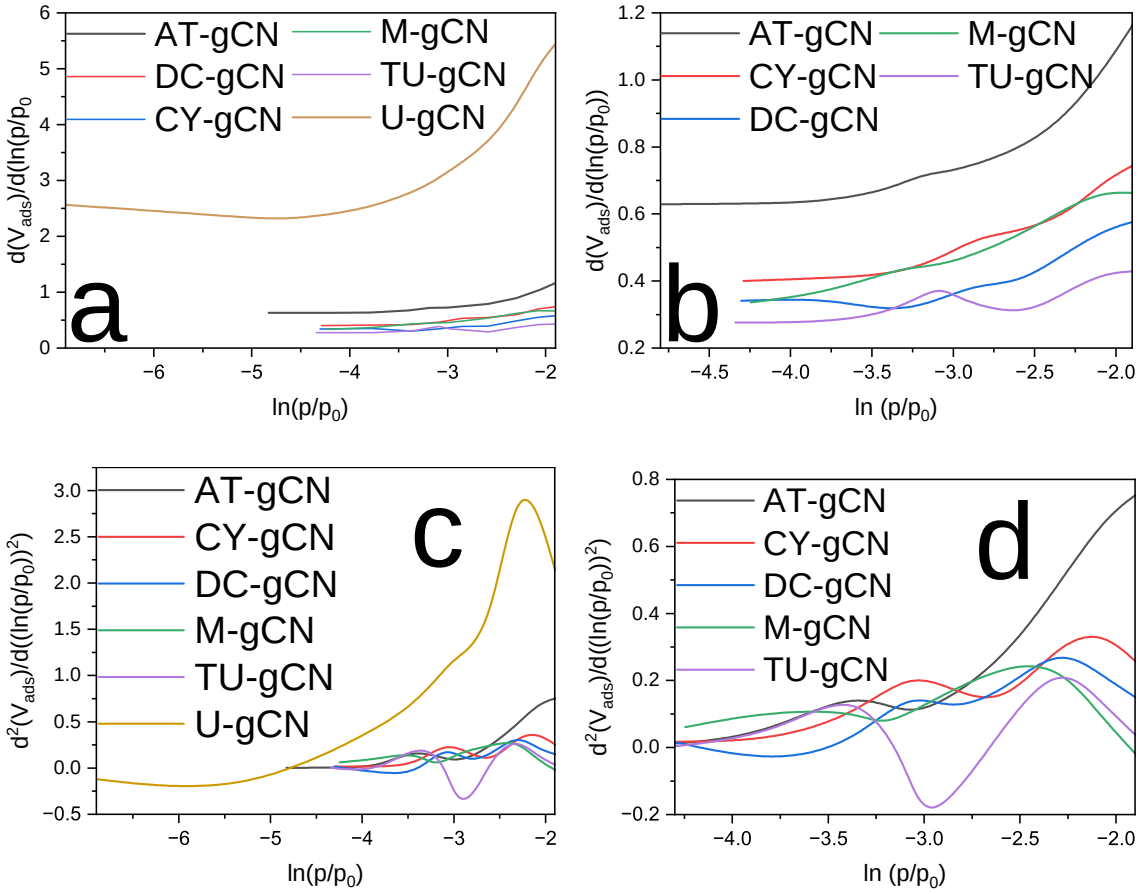

Figure 4.7: Derivative and second derivative isotherm summation analyses of graphitic carbon nitrides (gCN) exhibit unique surface characteristics. Figure (a) depicts the derivative isotherm summation of the gCN samples, while Figure (b) offers a detailed view by zooming in on the five selected samples, as shown in Figure (a). Figure (c) presents the second derivative isotherm summation of the same gCN samples, and Figure (d) provides a subset of samples from Figure (c) for closer examination.

According to existing research, two-dimensional materials are characterized by basal, edge, and high-energy adsorption surfaces, which correspond to low, medium, and high energies, respectively [32, 33].

The second derivative, as displayed in the DIS (Figure 4.7(c)), revealed that AT-gCN, CY-gCN, and DC-gCN exhibited prominent peaks, indicating strong and favorable interactions with the adsorbate at specific pore sizes. Conversely, M-gCN exhibited a weaker peak, whereas TU-gCN showed a broader peak, suggesting a weaker and more dynamic adsorption behavior. Notably, peaks of U-gCN were observed in the lower-energy regime, corresponding to basal sites. On a moderate-energy surface, that is, the edge-site regime, U-gCN displayed a weak peak. This observation may contribute to the lower activity of U-gCN towards CO_2 reduction and oxygen evolution.

The TU-gCN surface displayed a higher concentration of moderate-energy surfaces than AT-gCN, CY-gCN, DC-gCN, and M-gCN, resulting in higher methane and methanol yields. The methane and methanol yields of AT-gCN, CY-gCN, and

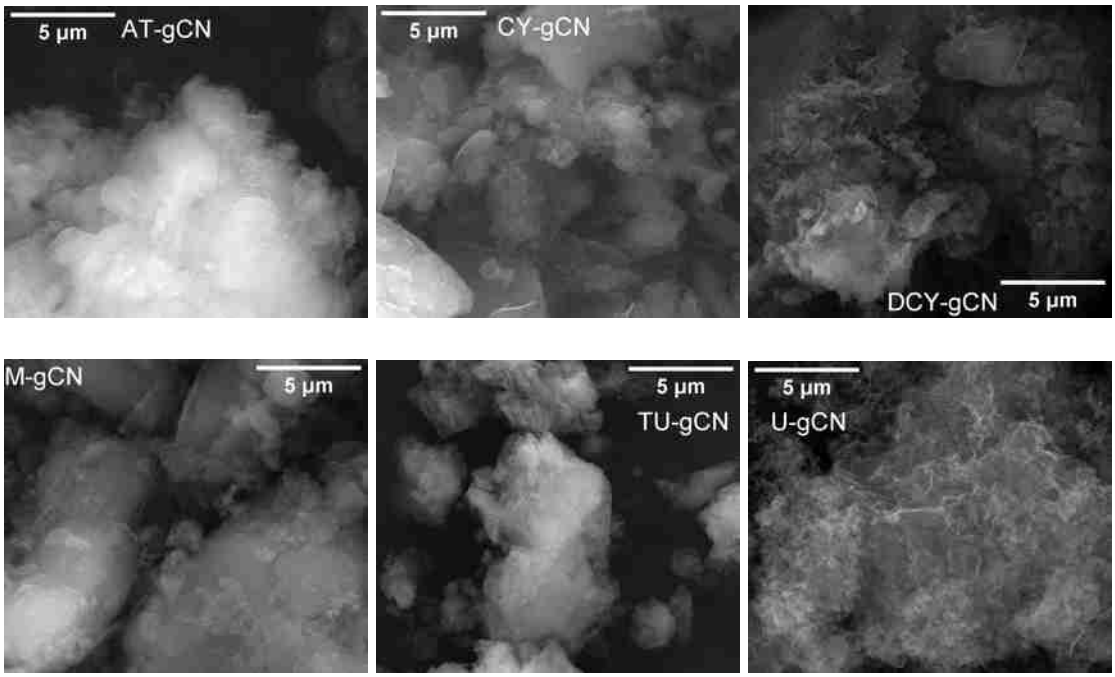

Figure 4.8: Field Emission Scanning Electron Microscopy (FESEM) images of the carbon nitride samples.

DC-gCN were high and comparable primarily because of the moderate number of available edge sites. However, for CY-gCN, the competing oxygen evolution reaction is more prominent on the edge sites than on the other gCN surfaces.

The figure 4.7 shows that the local isotherms can reveal the relative proportions of various sites and faces in the total adsorption isotherms. Notably, the differences in the adsorption energies at the basal and edge sites allowed the assignment of local isotherms to specific faces, providing direct insights into the surface sites of the carbon nitride material.

4.2.5 Field Emission Scanning Electron Microscopy (FESEM)

Field Emission Scanning Electron Microscopy (FESEM) images offer invaluable insights into the morphological characteristics of graphitic carbon nitride (g-CN) samples prepared using various precursors. Distinctive surface structures observed in the FESEM images are consistent with crystalline and grain size variations, as indicated by X-ray Diffraction (XRD) analysis. The porous nature of the samples, identified through adsorption analysis, was visually apparent in the FESEM micrographs (Figure 4.8).

The XRD data provided further evidence of the crystalline nature of the materials, which was also demonstrated by FESEM images. Notably, the FESEM images of U-gCN revealed its low density, reduced crystallinity, and porous structure (Figure 4.8). The pore size and distribution, which are crucial aspects of material porosity, are shown in Figure 4.8. The presence of well-defined pores with a relatively uniform distribution aligns with the findings of the adsorption analysis, in which the porous nature of the samples was quantified. The need to add more material for B.E.T analysis to attain a specific weight highlights the porous nature of U-gCN,

which implies a higher surface area compared to the other samples.

Figure 4.8 depicts the particle size distribution of the samples, exhibiting both individual particles and clusters, suggesting varying degrees of agglomeration. The agglomerated regions may affect the overall structural integrity and properties of the material.

The heterogeneous nature of the material is highlighted in Figure 4.8, which shows variations in the surface characteristics and particle arrangements, indicating localized differences in the synthesis process or precursor materials.

The mortaring process for U-gCN samples presents a unique challenge. Although they do not require additional force for mortaring, they tend to adhere to the mortar and pestle owing to their low density, which makes their removal difficult. Figure 4.8 illustrates that the grain size in all other samples was larger than that in U-gCN.

Sample	Element	Weight %	MDL	Atomic %	Net Int.	Error %
AT-gCN	C K	42.8	0.38	46.8	727.6	10.7
	N K	54.3	1.02	50.8	264.1	12.2
	O K	2.9	0.46	2.4	23.2	19.2
CY-gCN	C K	49.3	0.70	53.2	387.1	11.1
	N K	50.0	2.20	46.2	94.9	13.6
	O K	0.7	0.89	0.6	2.6	85.7
DC-gCN	C K	41.6	0.54	45.5	461.2	11.0
	N K	56.2	1.43	52.7	183.4	12.5
	O K	2.1	0.65	1.7	10.9	25.2
M-gCN	C K	48.9	1.13	52.8	247.9	11.4
	N K	50.5	3.51	46.8	62.5	15.0
	O K	0.6	1.43	0.5	1.3	100.0
TU-gCN	C K	52.4	0.24	56.5	1054.3	9.6
	N K	44.3	0.90	40.9	192.9	12.5
	O K	3.3	0.41	2.7	29.4	18.9
	S K	0.0	0.00	0.0	2.1	68.6
U-gCN	C K	60.1	0.53	63.9	646.3	10.7
	N K	37.9	2.02	34.5	78.2	14.3
	O K	2.1	0.94	1.7	10.1	30.6

Table 4.6: Energy-dispersive X-ray analysis (EDAX) results for the carbon nitride samples.

4.2.6 Energy Dispersive X-ray Analysis (EDXA or EDAX)

Energy-dispersive X-ray Analysis (EDAX) was employed to investigate the elemental composition of graphitic carbon nitride (g-CN) samples prepared using different precursors. Table 4.6 summarizes the weight percentage, atomic percentage, and associated errors for carbon (C), nitrogen (N), oxygen (O), and sulfur (S) in each sample. The EDAX results revealed distinct elemental compositions for each g-CN sample. AT-gCN and CY-gCN exhibited compositions comparable to those of carbon and nitrogen as major components. However, the percentage error of oxygen in

CY-gCN exceeded 30% (85.7%), suggesting caution when interpreting the presence of oxygen in this sample. DC-gCN exhibits a similar trend, indicating the presence of oxygen-containing functional groups. Simultaneously, the error for sulfur in TU-gCN was 100%, indicating the clear absence of sulfur in this sample. M-gCN showed an unexpected result with a 100% error in oxygen content, suggesting potential limitations in EDAX analysis for this particular sample. This anomaly can be attributed to the specific surface chemistry or structural characteristics of M-gCN, warranting further investigations. TU-gCN displayed a more complex composition, featuring carbon as the primary element, substantial nitrogen, and a notable presence of oxygen. However, the absence of sulfur in TU-gCN agrees with the findings of other techniques, indicating a limitation or anomaly in EDAX analysis for sulfur detection in this sample. U-gCN exhibited the highest carbon content and a lower nitrogen-to-carbon ratio than other samples. In contrast to the EDAX results, the presence of oxygen in U-gCN was confirmed, as indicated by the error percentage of 30.6%. This observation aligns with its low-density and porous nature, as evidenced by Scanning Electron Microscopy (SEM) images and supported by adsorption analysis. The carbon and nitrogen content variations among the samples suggest differences in the influence of the precursor and the synthesis conditions. Considering the error percentages and potential limitations, it is crucial to interpret the EDAX results cautiously. The consistent oxygen detection in most samples suggest the presence of oxygen-containing functional groups on the surfaces of the g-CN materials.

4.2.7 Solid State Ultraviolet-Visible Spectroscopy

The solid-state ultraviolet-visible (UV-Vis) spectra of the carbon nitride samples synthesized using various precursors offer valuable information regarding the electronic transitions and optical properties of the materials. The prominent absorption peaks observed in the spectra are attributed to different electronic transitions, which provide distinctive features associated with the carbon nitride structures.

The spectra were analyzed using three plots: absorption versus wavelength (nm), absorption versus energy (eV), and the absorption coefficient versus energy. Subsequently, Tauc plots were constructed for each sample using various exponents for the photon energy (hν): $(\alpha \mathrm{h}\nu)^{1/2}$, $(\alpha \mathrm{h}\nu)^{1/3}$, $(\alpha \mathrm{h}\nu)^{2/3}$, and $(\alpha \mathrm{h}\nu)^{2}$. The analysis of these plots revealed that all samples exhibited direct-bandgap semiconductor behavior.

Various techniques can be employed to determine the bandgap energy of materials. Linear regression and first- and second-derivative analyses were used to plot $(\alpha \mathrm{h}\nu)^2$ versus energy. The first-derivative plot aids in identifying the inflection point that corresponds to the maximum absorption energy. Conversely, the second-derivative plot provides the D parameter (DP), which represents the difference between the maxima and minima, and is indicative of the strength of absorption at a specific energy [34–38].

The generation of diffuse reflectance spectra for the six carbon nitride samples entailed the utilization of reflectance versus wavelength information, which was obtained step by step from the initial data. the molar absorption and scattering coefficients were manually calculated from the reflectance plot, and the derived

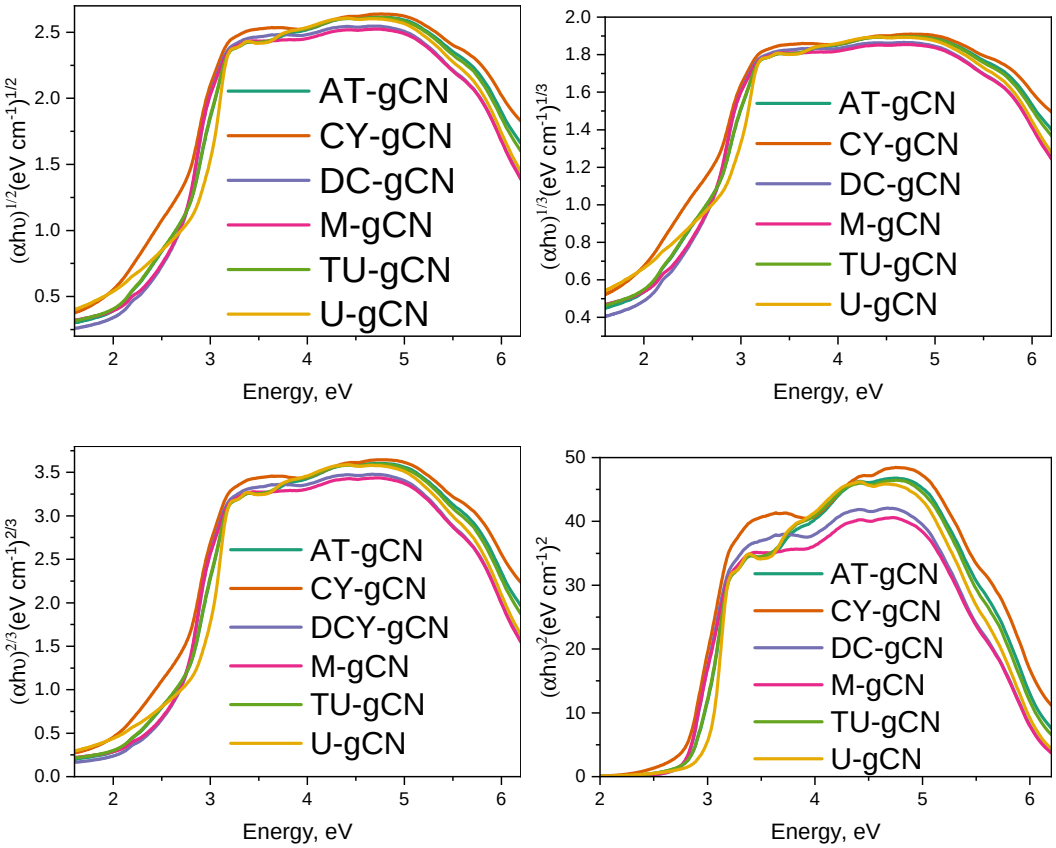

Figure 4.9: Tauc plots illustrating the bandgap characteristics of graphitic carbon nitrides, including directly allowed (r = 1/2), directly forbidden (r = 3/2), indirectly allowed (r = 2), and indirectly forbidden (r = 3) transitions.

K/S parameter yielded $F(R)$, indicating that all six samples were direct-bandgap semiconductors with bandgaps of approximately $3\,\mathrm{eV}$. This finding contrasts with the existing literature, which suggests a bandgap range of $2.5\,\mathrm{eV}$ to $2.7\,\mathrm{eV}$ for bulk carbon nitrides, casting doubt on the accuracy of curve-fitting methods. First- and second-derivative methods were employed to determine the band gap energy accurately, revealing bandgap values above $3\,\mathrm{eV}$. The second derivative spectra highlighted distinct features of the bonds and evidence of intermediate states near the bandgap energy, indicating the presence of shallow defect states in carbon nitrides. The nature of the precursors plays a crucial role in influencing the defect states, emphasizing the importance of selecting appropriate precursors for synthesizing defective carbon nitrides (Table 4.9).

The diffuse reflectance spectra of graphitic carbon nitride (g-CNx) exhibit a broad absorption band in the UV and visible regions, which is attributed to the π-π^* transitions of the conjugated carbon-nitrogen bonding network. This signature is indicative of the delocalized electronic states present in g-CNx, and is dependent on the degree of conjugation in the material. Conjugation refers to the alternating arrangement of single and double bonds in a carbon-based molecular structure, which results in continuous electron delocalization and a unique electronic band structure. In g-CNx, the conjugated carbon-nitrogen bonding network was responsible for the broad absorption band observed in the UV and visible regions.

Sample	Min.	Intensity	Max.	Intensity	D Parameter	S.A	D.P / S.A
AT-gCN	389	-0.03786	409	0.02158	0.05944	30.7	0.0019
CY-gCN	389	-0.02394	436	0.02157	0.04551	16.8	0.0027
DC-gCN	389	-0.02306	436	0.02258	0.04564	14.7	0.0031
M-gCN	389	-0.02269	437	0.02145	0.04414	14.8	0.0030
TU-gCN	389	-0.03576	409	0.01941	0.05517	16.3	0.0034
U-gCN	389	-0.06124	407	0.05642	0.11766	109.5	0.0011

Table 4.7: Summary of D parameter analysis for different g-CN samples derived from the second-derivative Tauc plot. S.A= Surface area, D.P= D parameter

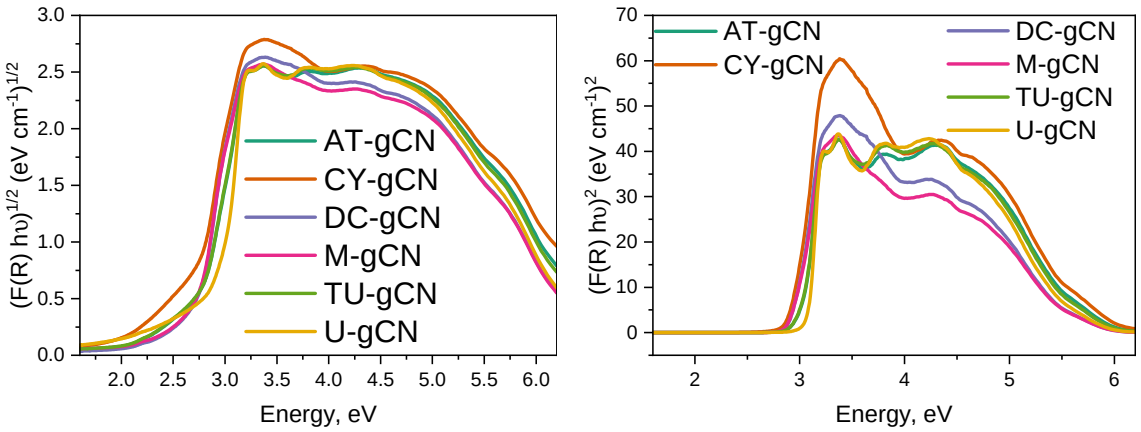

Figure 4.10: DRS UV spectra depicting bandgap characteristics of graphitic carbon nitrides, including indirectly allowed (r = 2) and directly allowed (r = 1/2) transitions.

The dimensions and surface area of the g-CN particles had a significantly affected the intensity and shape of the broad absorption band. In general, smaller particles with higher surface areas exhibit stronger absorption in the UV and visible light regions because of their increased surface-to-volume ratio, which results in a higher concentration of π–π^* transitions. In contrast, larger particles with smaller surface areas displayed weaker absorptions in these regions.

The extension of the spectra into the visible region reveals peaks attributed to n–π^* transitions involving non-bonding and anti-bonding orbitals. This suggests the presence of electronic transitions beyond the ultraviolet range, which contribute to the overall absorption characteristics of the material.

The onset of absorption, which corresponds to edge transitions, provides information on the bandgap energy. The second-derivative plots consistently exhibit bandgap values exceeding 3 eV for all samples, providing additional insight into the bandgap states of the carbon nitride samples. These plots reveal distinct surface-bond features and provide evidence of intermediate states close to the bandgap. Additional peaks or shoulders in the spectra may be attributed to defect-related absorption, indicating the presence of energy levels introduced by defects or impurities in the carbon nitride structure. The choice of precursor plays a crucial role in influencing the nature of defect states, particularly near the bandgap energy.

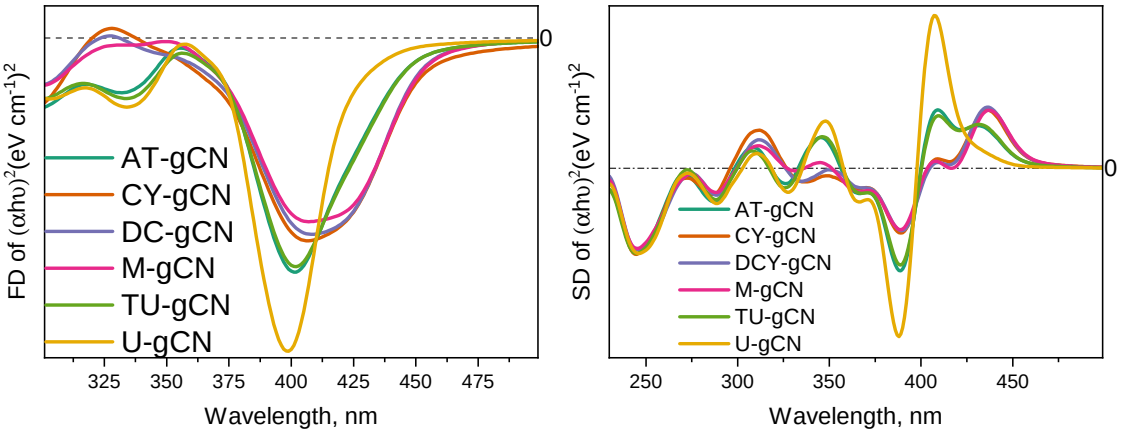

Figure 4.11: First and second derivative Tauc Plot analysis of carbon nitrides

This highlights the importance of selecting appropriate precursors to control defects in the carbon nitride structure, emphasizing their role in reactions aimed at synthesizing defective carbon nitrides.

The D parameter was examined in relation to the surface area of each sample to gain a deeper understanding of the relationship between the absorption and surface area. Subsequently, the D parameter was normalized to the surface area to obtain the D parameter per unit surface area, which represents the absorption efficiency per unit area of the sample.

The observation of the direct bandgap behavior in all samples is consistent with previous studies on similar materials. The D parameter, which reflects the absorption intensity at the maximum absorption energy, offers valuable insights into the light-harvesting capability of the material. A more accurate representation of the intrinsic absorption efficiency per unit area of the material was obtained by normalizing the D parameter to the surface area. This information is essential for optimizing the photon-assisted catalytic performance of a material by understanding the interplay between surface area, light absorption, and catalytic activity.

In the second-derivative plot, all the samples displayed distinct minima and maxima, indicating well-defined absorption bands. The widths of these absorption bands varied among the samples, with U-gCN exhibiting the highest D parameter, suggesting a broader range of absorbed energies. The surface area values, which represent the total area under the absorption curve, provide insight into the overall absorption capacity of each sample. The D Parameter per Unit Surface Area (DP/SA) ratio is a crucial metric for determining absorption efficiency per unit surface area. Elevated values of DP/SA indicate a heightened absorption efficiency, as a larger D parameter signifies a broader absorption band capable of encompassing a wider range of energies. Therefore, a higher DP/SA ratio suggests that a substantial portion of the surface area contributes to efficient light absorption, thereby highlighting the effective utilization of this material for this purpose.

The ranking of the DP/SA ratios among the six carbon nitride materials is TU-gCN > CY-gCN > DC-gCN > M-gCN > AT-gCN > U-gCN. The reason why TU-gCN, CY-gCN, DC-gCN, and AT-gCN exhibit higher activity towards methane and methanol production is due to the fact that a significant portion of their surface area contribute to efficient light absorption. Notably, AT-gCN displayed a

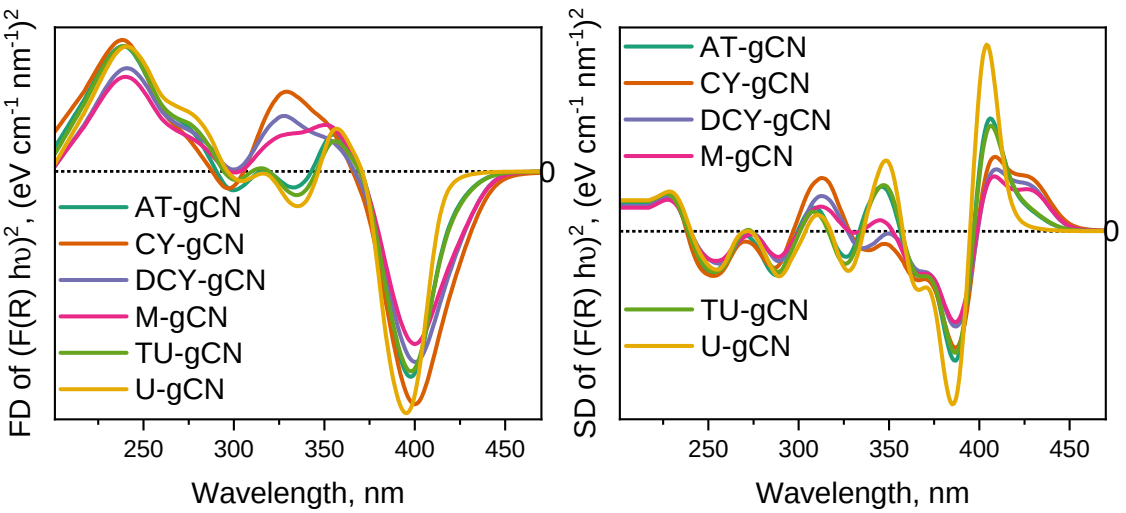

Figure 4.12: Derivative UV-visible diffuse reflectance spectroscopy analysis of carbon nitrides

Sample	Min.	Intensity	Max.	Intensity	D Parameter	SA	DP /SA
AT-gCN	387	-0.08256	406	0.07196	0.15452	30.7	0.005
CY-gCN	387	-0.0745	409	0.04745	0.12195	16.8	0.0073
DC-gCN	387	-0.06089	409	0.03946	0.10035	14.7	0.0068
M-gCN	387	-0.05803	408	0.03494	0.09297	14.8	0.0063
TU-gCN	387	-0.07766	406	0.06733	0.14499	16.3	0.0089
U-gCN	385	-0.11053	404	0.11909	0.22962	109.5	0.0021

Table 4.8: Summary of D parameter analysis for different g-CN samples derived from the second-derivative Kubelka-Monk plot. S.A= Surface area, D.P= D parameter

low DP/SA ratio compared to the other materials and is the best active catalyst for methanol production. To explain the abnormal behavior of AT-gCN, it was important to connect the DP/SA ratio to the B.E.T constant. The high C value of AT-gCN compensates for the low value of the DP/SA parameter by efficiently absorbing and utilizing light through better charge transfer to the adsorbate. This may be the reason for the enhanced methanol production over AT-gCN. The same explanation applies to TU-gCN.

4.2.8 Photoluminescence Spectroscopy

Graphitic carbon nitride (g-C_3N_4) exhibits blue-light emission in the $450\,\mathrm{nm}$ to $575\,\mathrm{nm}$ range, which can be attributed to its fundamental components [39]. Nitrogen vacancies and other defects act as light traps, capturing excited electrons and generating blue emissions[40]. The behavior of excitons is influenced by the edge states at the boundaries of g-C_3N_4, while surface modifications alter electronic interactions, enabling the manipulation of luminescence[41]. Although blue light is the dominant emission, other colors can be induced through techniques such as transition metal doping or modified synthesis procedures[42].

The photoluminescence spectra of various samples were analyzed to determine

Sample	Bandgap, eV						Urbach Energy, meV
	Tauc Plot			K-M Plot			
	L.R	F.D	S.D	L.R	F.D	S.D	L.R
AT-gCN	2.89	3.08	3.03	3.02	3.12	3.05	380
CY-gCN	2.76	3.04	2.84	2.95	3.10	3.03	430
DC-gCN	2.78	3.03	2.84	2.95	3.10	3.03	360
M-gCN	2.79	3.04	2.83	2.95	3.10	3.04	430
TU-gCN	2.84	3.08	3.03	3.02	3.12	3.05	390
U-gCN	2.99	3.11	3.05	3.08	3.14	3.07	750

Table 4.9: Bandgap energy values determined using different approaches along with Urbach energy. L.R = Linear Regression, F.D = First Derivative, S.D = Second Derivative.

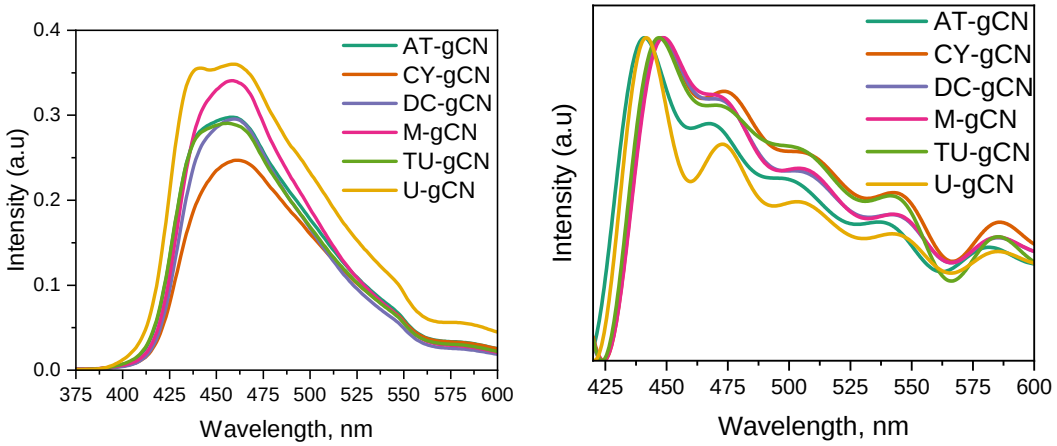

Figure 4.13: Photoluminescence (left) and deconvoluted (right) spectra of graphitic carbon nitrides prepared from various precursors.

their recombination rates. U-gCN exhibited the highest recombination rate, whereas CY-gCN displayed the lowest recombination rate. The low recombination rates of CY-gCN, TU-gCN, DC-gCN, and AT-gCN may have resulted in greater availability of charge carriers on the carbon nitride surface for CO_2 reduction. The high C value and improved utilization of charge carriers were attributed to the increased activity of these samples towards methane, methanol, and oxygen production.

According to the data presented in Figure 4.13, maximum recombination of charge carriers was observed for M-gCN and DC-gCN, whereas CY-gCN displayed the lowest recombination rate. The order of charge-carrier recombination was as follows: CY-gCN < AT-gCN < U-gCN < TU-gCN < DC-gCN < M-gCN. It should be highlighted here that although U-gCN exhibits a moderate level of electron-hole recombination as compared to other models such as TU-gCN or AT-gCN, its CO_2 conversion efficiency was lower. This disparity may be attributed to the ineffective transfer of the generated charge carriers to the CO_2 molecule, which may be due to the charge transfer resistance. CY-gCN, TU-gCN, and AT-gCN exhibited notable charge transfer efficiency and superior utilization of charge carriers for adsorbed CO_2. This could be attributed to the constant B.E.T values of these materials. As the C value increased, the adsorption of the respective gases increased, resulting in a significant charge transfer to the reactant molecule and a higher product

yield. Furthermore, as indicated by the derivative isotherm, TU-gCN exhibited the maximum number of edge sites and low recombination, which together contributed to improved charge generation, separation, and transfer. Additionally, the light absorption cross sections of TU-gCN and CY-gCN were high, as determined through diffuse reflectance spectroscopic analysis. The interplay between these factors is responsible for CO_2 photoreduction, indicating that the recombination process is not the sole determinant of photon-assisted catalytic performance.

The bandgap energy of g-C_3N_4, determined to be $3\,\mathrm{eV}$, corresponds to an emission wavelength of $413\,\mathrm{n\ m}$. Photoluminescence peaks often shifts because of Stokes shifts, and defects can introduce various emission wavelengths. The experimental peaks in the range of $450\,\mathrm{nm}$ to $575\,\mathrm{nm}$ align with this value, and the deconvolution suggests that the precursor influences the structure and luminescence. The presence of multiple peaks suggests the existence of diverse emission centers, which may be related to specific defects or vibronic couplings. The g-C_3N_4 molecules self-assembled into aggregates, with each aggregate contributing to a distinct peak, as evident from FESEM observations.

The presence of intrinsic defects, including nitrogen vacancies and antisite defects, significantly affected the luminescence of g-C_3N_4. Carbon doping, as indicated by the d value of the (120) reflection from XRD, could have an impact on the π-conjugation and result in blue-light emission.The broader luminescence peaks observed in the amorphous regions compared to those in the crystalline regions suggest that the former possesses a more complex relationship with the surface functional groups and luminescence. The introduction of new energy levels for tunable emissions is facilitated by the complex relationship between the surface functional groups and luminescence.

There may be a relationship between the shoulder peak observed in the second-derivative DRS spectrum of carbon nitride at approximately $440\,\mathrm{nm}$ and the main PL peak at $442\,\mathrm{nm}$ in the photoluminescence spectrum. The inflection point in the second-derivative spectrum at approximately $3\,\mathrm{eV}$ likely corresponds to the bandgap energy of carbon nitride. The shoulder peak extending towards $440\,\mathrm{nm}$ suggests the involvement of multiple electronic transitions in the absorption process. These additional transitions may originate from the following factors: (1) The shallow defect states reside near the bandgap and introduce new energy levels into the band structure. (2) High-energy electronic transitions within the π-electron system of the carbon nitride network. The primary cause of the peak at $442\,\mathrm{nm}$ in the photoluminescence (PL) spectrum can be attributed to the recombination of electron-hole pairs generated by light excitation at energies corresponding to the shoulder peak in the diffuse reflectance spectrum (DRS). This suggests that defect states are involved in the emission process.

The close relationship between the shoulder peak in the DRS spectrum and the main PL peak implied a possible connection between the electronic transitions involved in the respective processes. If the shoulder peak arises from the defect states, their participation in both the light absorption and emission can explain the observed correlation. However, other factors, such as surface states, impurities, or specific electronic configurations within the carbon nitride structure could also contribute to the PL peak and should be considered.

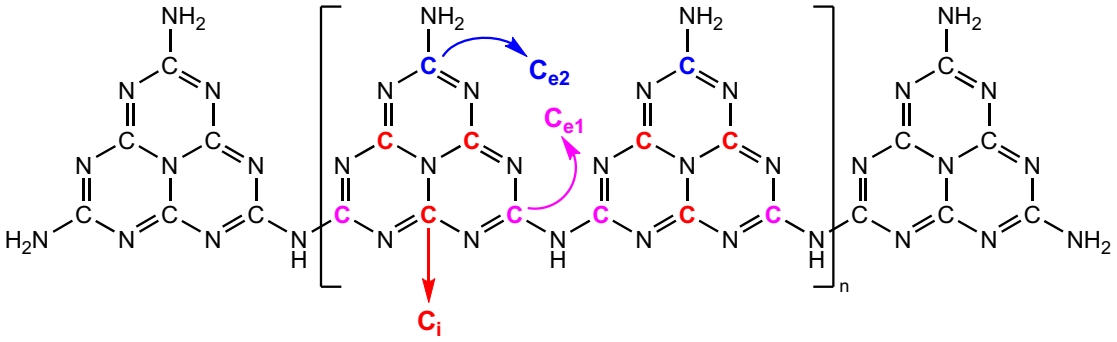

Figure 4.14: Possible C configurations

4.2.9 ^{13}C Solid State NMR Studies

The graphitic carbon nitride (g-C_3N_4) ^{13}C NMR spectrum presents notable characteristics that are essential for determining the structure of the compound. The presence of two prominent peaks around $156.4\,\mathrm{ppm}$ and $164.2\,\mathrm{ppm}$ in the spectrum corresponds to various carbon environments in the triazine units, which are the fundamental building blocks of g-C_3N_4. These peaks are crucial for providing information about the carbon environment in g-C_3N_4, which is necessary for structural elucidation[43, 44]. The peak at $156.4\,\mathrm{ppm}$, attributed to N_3-C, signifies a carbon atom bonded to three nitrogen atoms[45, 46]. Its lower chemical shift is indicative of its involvement in the aromatic π-system, resulting in stronger electron delocalization and shielding compared with other carbons. In contrast, the peak at $164.2\,\mathrm{ppm}$ corresponds to CN_2 (NHx) moieties, representing the carbon atom bonded to two nitrogen atoms and one hydrogen atom (N_2HxC). Its higher chemical shift suggests a less delocalized π-electron system influenced by the electron-withdrawing hydrogen atom[47, 48].

In addition to these prominent features, the relative intensities of the two peaks offer insight into the structural details of the g-C_3N_4. A weaker CN_2 (NHx) peak implies increased condensation and polymerization, which is indicative of fewer N_2Hx-type carbon atoms. Furthermore, the spectrum may show broadening or splitting of the peaks owing to factors such as chemical heterogeneity, structural defects, or interactions with neighboring atoms. Although the presence of two distinct peaks in the chemical shift values may be influenced by various factors, such as synthesis techniques, sample preparation, and measurement conditions, the overall consistent pattern of these peaks continues to reflect the fundamental structure of g-C_3N_4. The emergence of a shoulder peak at $162.7\,\mathrm{ppm}$ in the SSNMR spectrum of g-C_3N_4 provides valuable insights into the chemical environment of the material. The primary peak at $164.2\,\mathrm{ppm}$ is associated with CN_2-NH_x carbons within the heptazine cycles. The presence of a distinct peak at $162.7\,\mathrm{ppm}$ indicates a carbon environment with an increased electron density. This phenomenon can be explained by the incorporation of carbon dopants, as indicated by the d value of the (120) reflection from the XRD,which substituted the nitrogen atoms in the N−C=N units within the heptazine rings. The resulting higher electron density around the carbon atom suggests potential alterations in electronic properties. Depending on the specific dopant and its concentration, these carbon-doped g-C_3N_4 structures may exhibit modified electronic behavior and enhanced functionality. Therefore,

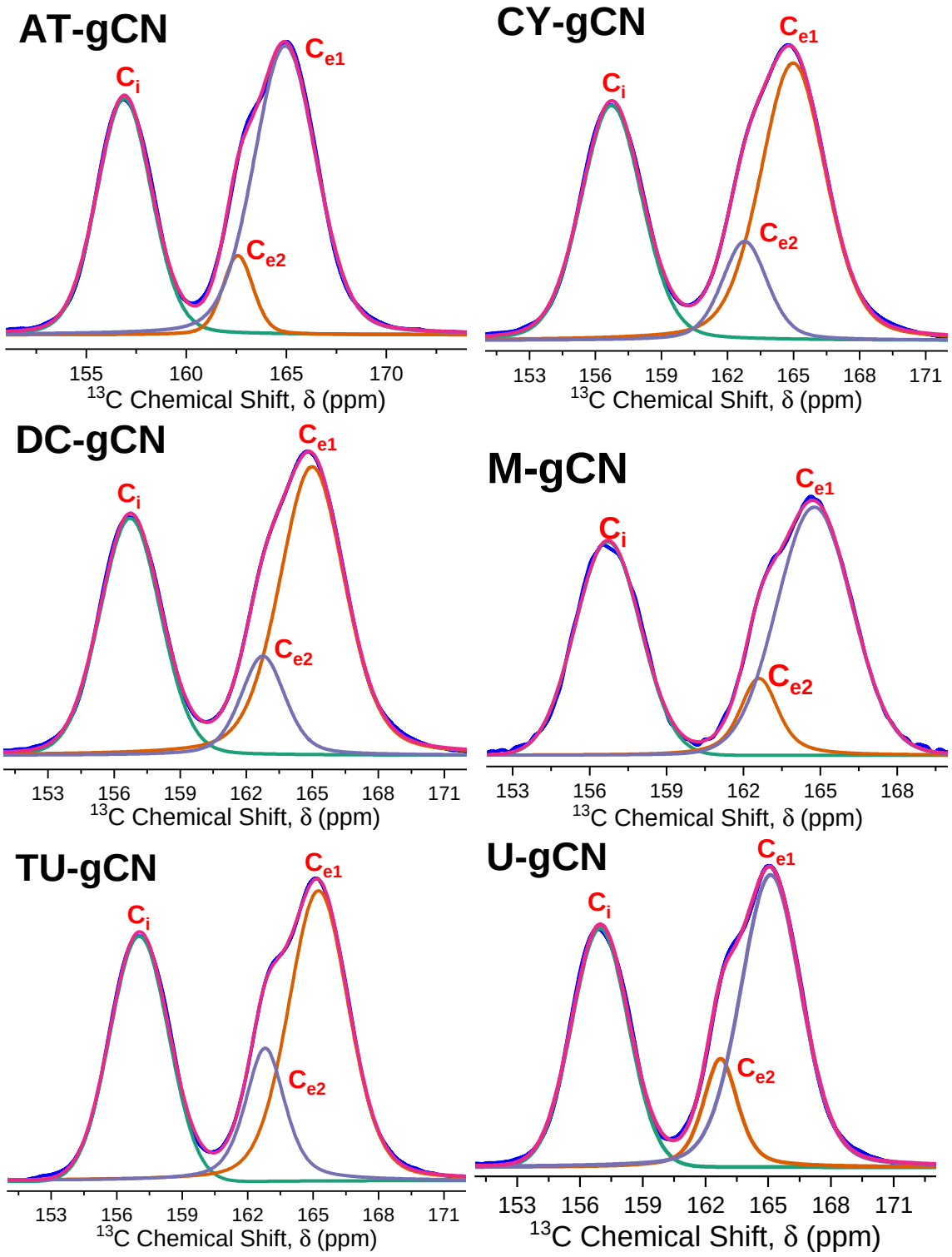

Figure 4.15: ^{13}C Solid state NMR spectra of carbon nitrides synthesized using various precursors

Table 4.10: ^{13}C NMR peak analysis

Sample	Intensity			Area			FWHM			R
	C_i	Ce_2	Ce_1	C_i	Ce_2	Ce_1	C_i	Ce_2	Ce_1	
AT-gCN	48758	60254	14641	187433	270581	36710	3.22	3.69	1.79	0.99
CY-gCN	61060	72652	23779	241629	321926	80819	3.26	3.51	2.42	0.99
DC-gCN	55445	68127	21550	209762	303140	72028	3.24	3.51	2.37	0.99
M-gCN	61704	71676	22192	196368	269223	51549	2.98	3.46	1.74	0.99
TU-gCN	47727	57044	24863	162347	226488	75382	3.12	3.24	2.12	0.99
U-gCN	86882	107232	37171	311412	445782	105170	3.19	3.42	1.95	0.99

the observation of NMR shifts has significant implications for the understanding of the chemical and electronic properties of g-C_3N_4.

Product Yield and ^{13}C NMR Area Trends

The evaluation of the trends in methane, methanol, and oxygen yields for the CO_2 photoreduction reaction across different carbon nitride samples revealed interesting results. The peak at $156\,\mathrm{ppm}$ associated with the C_i=N_3–C environment displayed an inverse relationship with the methane yield. Additionally, the trend in the area of the main peak at $164\,\mathrm{ppm}$, referred to as Ce_1, exhibited an inverse correlation with methane production, following the order U-gCN > CY-gCN > DC-gCN > AT-gCN > M-gCN > TU-gCN. Conversely, the trend in the area of the shoulder peak of Ce_1 at $162\,\mathrm{ppm}$, denoted as Ce_2, demonstrated an indirect correlation with methane production.

The methanol yield followed a distinct trend, with AT–gCN yielding the highest, followed by CY–gCN, TU–gCN, DC–gCN, M–gCN, and U–gCN. As with the methane yield, no precise correlation was observed between the methanol yield and distribution of carbon environments, indicating a complex relationship between the two variables.

Examination of the oxygen yield trend revealed that CY–gCN exhibited the highest yield, followed by DC–gCN, M–gCN, AT–gCN, TU–gCN, and U–gCN. Again, no straightforward linear relationship was observed between the oxygen yield and the areas of C_i, Ce_1, and Ce_2, suggesting that factors other than the individual carbon environments influence the observed trends.

There appears to be no straightforward connection between the results of ^{13}C NMR spectroscopy and the photon-assisted catalytic syntheses of methane, methanol, and oxygen. This is especially true given that the analysis indicates the presence of suitable carbon environments for CO_2 adsorption. Although ^{13}C NMR provides invaluable information regarding the carbon environment within g-CN, it is insufficient to fully comprehend the intricate surface catalytic processes responsible for the formation of specific products.

4.2.10 ^{15}N Solid State NMR Studies

The graphitic carbon nitride structure displayed four distinct nitrogen environments: $200\,\mathrm{ppm}$ (N_c-central triazine nitrogen), $157\,\mathrm{ppm}$ (N_i-imidic nitrogen), $137\,\mathrm{ppm}$ (NtH-bridged amine), and $110\,\mathrm{ppm}$ (NtH_2 - terminal amine)[43, 45]. The presence of these peaks serves as evidence of diverse nitrogen environments within the structure. The diagnostic nature of the $15\,\mathrm{N}$ chemical shifts was highlighted, with the $200\,\mathrm{ppm}$ peak indicating strong electron delocalization and sp^2 hybridization within the aromatic system. Conversely, the $110\,\mathrm{ppm}$ peak was attributed to the electron-donating nature of NH_2 owing to the availability of a lone pair[46].

The ^{15}N solid-state NMR (SSNMR) spectra of various graphitic carbon nitrides produced from different precursors show a clear distinction in the evolution of nitrogen environments influenced by the precursors (Figure 4.17). In samples derived from precursors other than M-gCN, the characteristic peak associated with the central triazine nitrogen, (N_c) separated into two sub-peaks, N_{ca} and N_{cb}. This

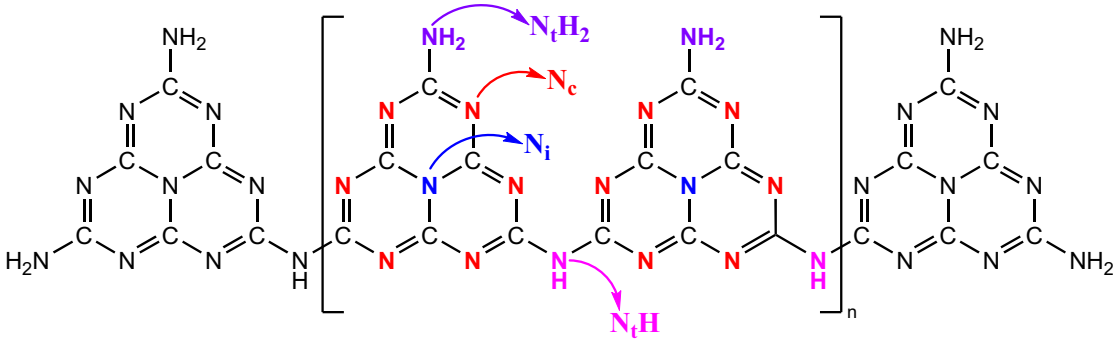

Figure 4.16: Possible N configurations present in graphitic carbon nitrides

Sample	N_{ca}	N_{cb}	N_i	N_tH	N_tH_2
AT-gCN	3.14×10^7	6.59×10^6	4.83×10^6	9.40×10^6	1.66×10^7
CY-gCN	5.00×10^6	2.24×10^7	2.58×10^6	6.44×10^6	1.17×10^7
DC-gCN	7.90×10^6	3.78×10^7	3.79×10^6	1.19×10^7	1.95×10^7
M-gCN	4.22×10^7	-	2.22×10^6	2.92×10^7	4.88×10^6
TU-gCN	7.12×10^6	2.12×10^7	1.74×10^6	9.63×10^6	1.18×10^7
U-gCN	2.78×10^7	9.72×10^6	2.99×10^6	1.16×10^7	9.21×10^6

Table 4.11: Peak area analysis of ^{15}N SSNMR spectra of graphitic carbon nitrides

intriguing observation suggests that there are two distinct chemical environments for Nc, implying subtle structural variations arising from the precursor selection.

Understanding the mechanism behind this process involves examining the relationship between the melamine precursor and the condensation pathways during thermal treatment. Melamine, which serves as the precursor for M-gCN, possesses the necessary triazine skeleton, allowing direct thermal condensation with minimal disruption of the N_c environment. This accounts for the appearance of a single distinct N_c peak in the ^{15}N SSNMR spectrum of M-gCN.

In contrast to other precursors, this process likely involves a two-step reaction. Initially, polymerization occurred with the triazine structure present in the melamine, followed by further condensation and network formation. Incomplete condensation results in the presence of residual functional groups or defects within the framework, leading to subtle variations in the local environment of the central triazine unit. These variations resulted in the emergence of the N_{ca} and N_{cb} sub-peaks, each representing a distinct chemical milieu for N_c.

The intensities of the N_{ca} and N_{cb} peaks offer further insight into the extent of incomplete condensation of each precursor. Additionally, the specific functional groups or defect types introduced by the individual precursors may influence the unique chemical environments reflected in the ^{15}N solid-state nuclear magnetic resonance (SSNMR) spectra. Although the triazine structure of melamine serves as a crucial structural motif, it is essential to consider the influence of precursor-specific moieties and the potential defects arising during incomplete condensation for a more comprehensive understanding. The results of ^{15}N solid-state nuclear magnetic resonance (SSNMR) analysis indicated a noteworthy connection between the selection of precursors and the complex nitrogen environment in graphitic carbon nitrides. In the context of CO_2 photoreduction, there was no direct correlation

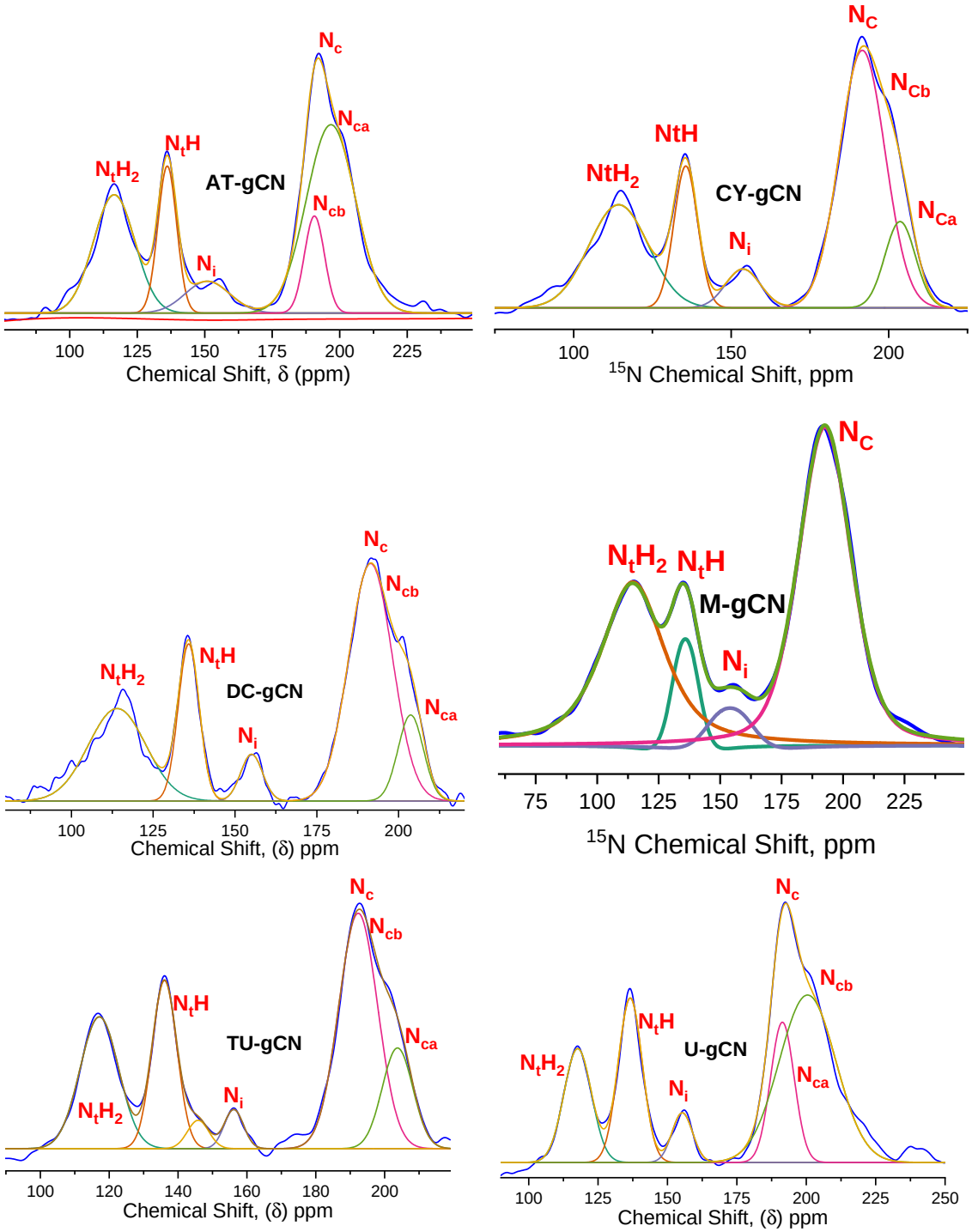

Figure 4.17: ^{15}N Solid State NMR Studies

between the ^{15}N dataset and yield of any product. This also highlights the intricacy of the reduction reaction, as mentioned in the ^{13}C section.

4.2.11 X-Ray Photoelectron Spectroscopy

In the survey spectrum (Figure 4.18), the dominant C 1s and N 1s peaks indicate the presence of carbon and nitrogen, which are the primary constituents of g-C_3N_4. However, additional peaks may appear depending on the synthesis method or the potential contamination of elements such as O 1s, B 1s, or Si 2p.

Upon examining the High-Resolution C 1s spectrum, deconvolution into multiple peaks revealed the following distinct components[16, 49–53]:

- $\approx 284.4\,\mathrm{eV}$ to $284.8\,\mathrm{eV}$: assigned to sp^2 hybridized carbon in aromatic C=N bonds within the tri-s-triazine rings, constituting the fundamental building block of g-C_3N_4.
- $\approx 288\,\mathrm{eV}$ to $289\,\mathrm{eV}$: Represents sp^2 hybridized carbon in C−N bonds.
- $285.5\,\mathrm{eV}$ to $286.5\,\mathrm{eV}$ (optional): May be present owing to C−NH_2 groups, contingent on the preparation method.

Similarly, the High-Resolution N 1s spectrum exhibits three main peaks upon deconvolution:

- $\approx 398.7\,\mathrm{eV}$: Corresponds to sp^2 hybridized nitrogen in tri-s-triazine rings (graphitic−N).
- $\approx 400.7\,\mathrm{eV}$: Pyrrolic-N, associated with edge sites or defects.
- $\approx 401.9\,\mathrm{eV}$: corresponding to pyridine-N, primarily found at defect sites or attributed to surface functional groups, such as amine (NH_2).
- Finally, the weaker band at BE = 404.2 eV was attributed to π-electron excitations in the heptazine rings.

Tables 4.12 and 4.13 present the surface concentrations and normalized surface concentrations of various functional aminities in the graphitic carbon nitrides. The six samples (AT-gCN, CY-gCN, DC-gCN, M-gCN, TU-gCN, and U-gCN) were analyzed for their (C)-N-Hx, N-C=N, C=N-C, N-$(C)_3$, C-(N)-Hx, and OH NSC% values, with a particular focus on methane, methanol, and oxygen production yields.

The normalized values for each catalyst were calculated by determining the normalized concentration per unit surface area, using the following formula:

$$\text{Normalized Surface Concentration, NSC\%} = \left(\frac{\text{XPS At\%}}{\text{SESAMI Surface Area}}\right) \times 100$$

This approach provides a normalized perspective on the concentration of specific elements or functional groups, considering the variations in surface area between different catalysts. The resulting normalized concentrations were subsequently used for comparative analysis, enabling a fair assessment of the relative abundances of the studied elements or functional groups across various catalysts. This method

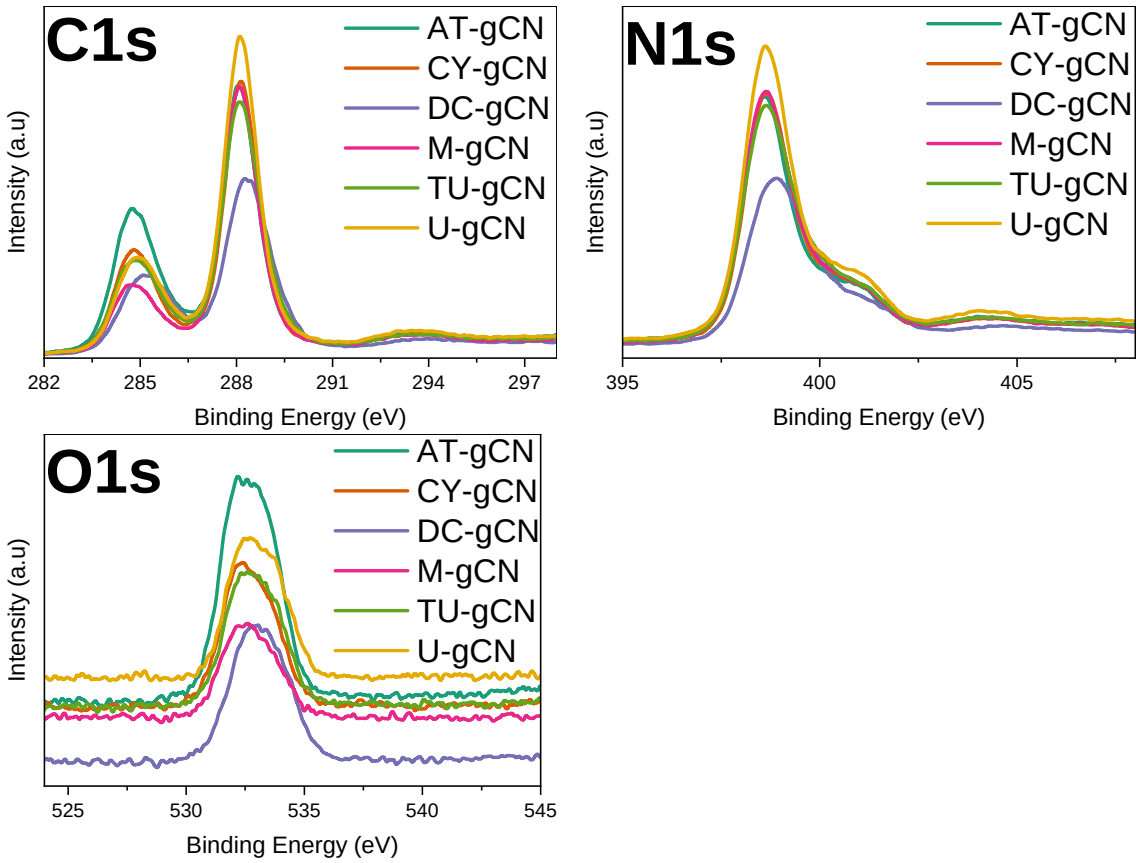

Figure 4.18: C*1s*, N*1s*, and O*1s* photoelectron spectra of graphitic carbon nitrides

Table 4.12: Surface concentrations of various functional groups in carbon nitride samples

Samples	SA	(C)-N-Hx	N-(C)=N	C=(N)-C	(N)-C_3	C-(N)-Hx	OH
AT-gCN	30.7	6.11	31	26.41	5.79	4.53	2.11
CY-gCN	16.8	3.47	33.47	28.99	6.28	6.15	1.87
DC-gCN	14.7	8.32	33.94	22.41	8.97	8.73	2.18
M-gCN	14.8	4.03	34.73	29.3	6.62	7.81	1.26
TU-gCN	16.3	5.12	34.76	25.09	7.91	8.3	1.47
U-gCN	109.5	4.37	34.02	30.51	5.63	5.43	1.26

Table 4.13: Normalized surface concentration (NSC%) for various functional groups in carbon nitride samples

Samples	(C)-N-Hx	N-(C)=N	C=(N)-C	(N)-C_3	C-(N)-Hx	OH
AT-gCN	19.90	100.98	86.03	18.86	14.76	6.87
CY-gCN	20.65	199.23	172.56	37.38	36.61	11.13
DC-gCN	56.60	230.88	152.45	61.02	59.39	14.83
M-gCN	27.23	234.66	197.97	44.73	52.77	8.51
TU-gCN	31.41	213.25	153.93	48.53	50.92	9.02
U-gCN	3.99	31.07	27.86	5.14	4.96	1.15

ensures that the observed differences are not solely attributable to variations in the surface area but rather reflect inherent disparities in the composition.

Table 4.13 highlights that U-gCN possesses the lowest amount of surface functionalities per unit surface area. Consequently, this leads to a lower yield of the reduction products. All samples, except AT-gCN, exhibited a significant surface functionalities per unit area. DC-gCN and CY-gCN had the highest concentrations of surface hydroxyl groups, which resulting in increased methanol production and oxygen evolution. TU-gCN demonstrated substantial concentrations of all surface functionalities, leading to a higher production of both methane and methanol. In contrast, AT-gCN exhibited a lower concentration of surface functionalities, resulting in increased methanol production and notable methane yields. This can be attributed to its moderate light absorption cross section and higher C value, which collectively produce a compensation effect towards lower surface functionalities.

Based on these observations, it is hypothesized that C-N-Hx groups actively participate in the formation of methanol, either through the adsorption and activation of CO_2 or by modifying the electronic structure and hydrogen availability. Additionally, the OH groups may facilitate water oxidation and oxygen release, potentially working together with other functionalities in a synergistic manner.

The effect of functional groups on carbon nitride catalysts in CO_2 photoreduction was apparent, with the presence of C-N-Hx groups demonstrating the potential to increase methanol production and OH groups, possibly contributing to the formation of oxygen. It is worth noting the similarity in the trend between the XPS NSC% (Table 4.13) and DP/SA (Table 4.8) values obtained from the UV-DRS analysis. This may be attributed to the fact that the surface functionalities inherently determine the light-absorption cross-section of the material. The introduction of the parameters NSC% and DP/SA enables a comparison of the light absorption characteristics of the materials with their surface functionalities.

4.2.12 Valence Band XPS

The X-ray photoelectron spectroscopy (XPS) valence-band spectrum of g-C_3N_4 displayed several well-defined peaks (Figure 4.19 & 4.20). A prominent peak near approximately $5.5\,\mathrm{eV}$ dominated the low-binding energy region (0-7 eV). This peak was attributed to the lone pair electrons of the nitrogen atoms and π-bonded electrons associated with the aromatic sp^2 C-N framework. Additionally, a shoulder located at approximately $1.8\,\mathrm{eV}$ within this peak can be further deconvoluted into contributions from the lone pair electrons and π-bonding states, shedding light on the hybridization and bonding scheme[54, 55].

The energy levels at which multiple overlapping peaks arise from the σ bonds between the C and N atoms, involving both 2s and 2p orbitals, are referred to as higher binding energies (7-20 eV). At these energies, a distinct peak centered at $13.5\,\mathrm{eV}$ can be assigned to C-N sp^2 σ bonds, while contributions from C-N sp^3 σ bonds and N-N bonds might be present in a broader feature centered at $17.5\,\mathrm{eV}$. These observations supported the expected hybridized configuration and bonding arrangement within the g-C_3N_4 framework.

The present study revealed the presence of weaker signals at binding energies greater than $20\,\mathrm{eV}$, which correspond to the deeper core-like states of C 2s and N 2s. The absence of significant satellite peaks or broadening of these core-level peaks

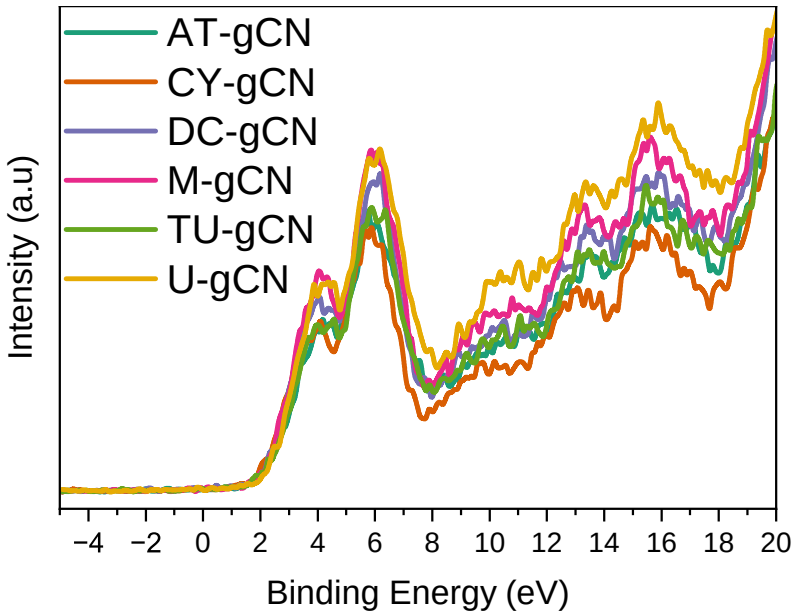

Figure 4.19: Valence band X-ray photoelectron spectroscopy (XPS) analysis of carbon nitrides

suggested that the sample exhibited minimal surface contamination or significant oxidation states.

The results obtained from the observed peak positions and intensities are consistent with theoretical predictions and previous experimental findings, confirming the presence of sp^2 hybridized N atoms and an aromatic C-N framework in the material. Moreover, the second-derivative valence band spectra of the low-binding-energy peak provide insights into the contributions of π-bonding and lone pair electrons, highlighting the significance of π-conjugation in the electronic properties of carbon nitrides.

The presence of distinct σ-bonding peaks, including sp^2 and sp^3 contributions, suggested the coexistence of both planar and nonplanar domains within the g-C_3N_4 structure. This raises the possibility that the charge carrier transport and photocatalytic performance may be influenced by the relative abundance and spatial distribution of these domains.

The valence-band position was determined using linear curve fitting and second-derivative valence-band spectroscopy. The latter method was found to be more accurate and reliable, allowing the precise measurement of the valence band position. This is because the second-derivative method can capture subtle features in the spectra, enabling more detailed analysis of the valence band structure.

Although the linear curve fitting method is commonly used, it has limitations in capturing intricate details within the valence band spectra. By contrast, the second-derivative method provides a more refined examination, particularly in areas where the valence band exhibits complex features. This enhanced accuracy of the second derivative method is crucial for obtaining precise measurements of the valence band position and building a solid foundation for further discussion of the electronic structure and properties of graphitic carbon nitride surfaces.

The second derivative valence-band spectra of graphitic carbon nitride offer valuable insights into the electronic structure of the material, revealing various features

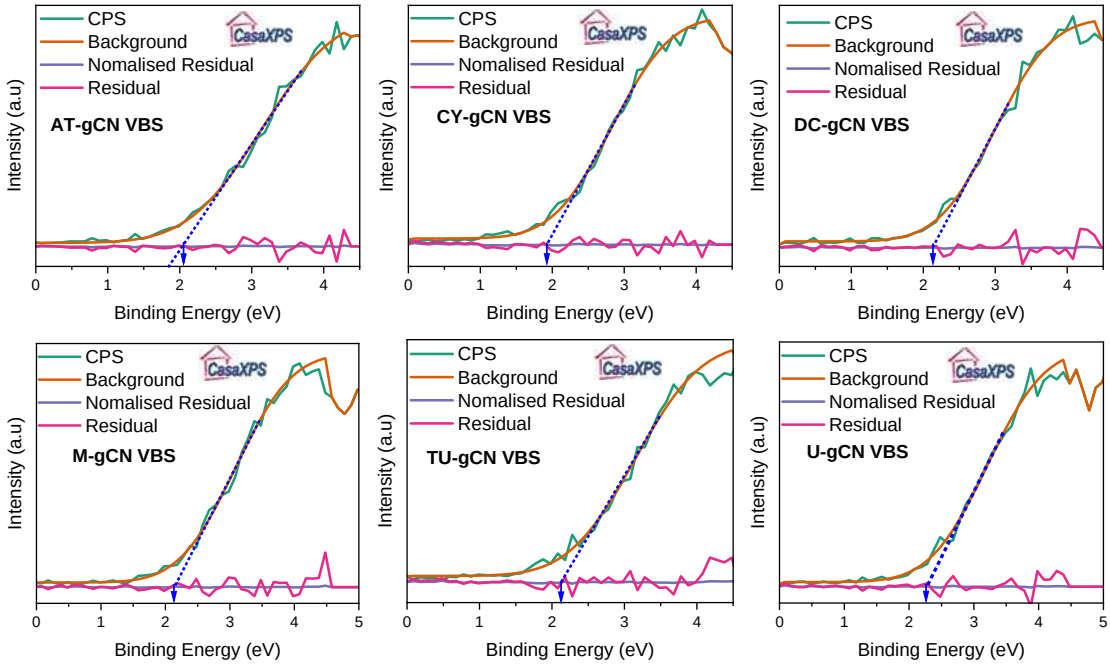

Figure 4.20: Valence band position estimation through curve fitting in carbon nitrides

corresponding to different electronic states. Although the binding energy values may vary depending on the experimental conditions and sample characteristics, several prominent features were identified in the spectra.

One such feature is the π-band of carbon (C 2p), which is typically centered in the binding energy range of $1\,\mathrm{eV}$ to $4\,\mathrm{eV}$. This feature signifies the presence of π orbitals associated with conjugated carbon within the graphitic structure of carbon nitride. These π orbitals significantly influence the electronic and optical properties of the material, contributing to its conductive behavior and interactions with the incident light.

Another salient feature is the σ-band of carbon (C 2s), which appears in the binding energy range $10\,\mathrm{eV}$ to $15\,\mathrm{eV}$. This feature corresponds to the σ orbitals of conjugated carbon within the graphitic carbon nitride structure. The σ orbitals contribute to the overall electronic configuration, thereby influencing the bonding characteristics and the stability of the material.

The participation of the electronic states of N is discernible in the N 2p states, which typically fall within the binding energy range of $8\,\mathrm{eV}$ to $15\,\mathrm{eV}$. These states underscore the role of N in the valence band of graphitic carbon nitride and its effect on the chemical reactivity and charge distribution.

Moreover, the spectra revealed hybridized carbon-nitrogen states, as evidenced by peaks at binding energy positions of approximately $-15\,\mathrm{eV}$ to $-20\,\mathrm{eV}$. These peaks signify the hybridized states of the carbon-nitrogen bonds within the material, which are crucial factors that influence its structural stability and contribute to its chemical and physical properties.

The reliable and reproducible nature of the identified features in the valence band spectra of the six carbon nitride samples are emphasized by their consistent presence. Although these samples were derived from various precursors, their valence band spectra exhibited a considerable degree of overlap, with noticeable

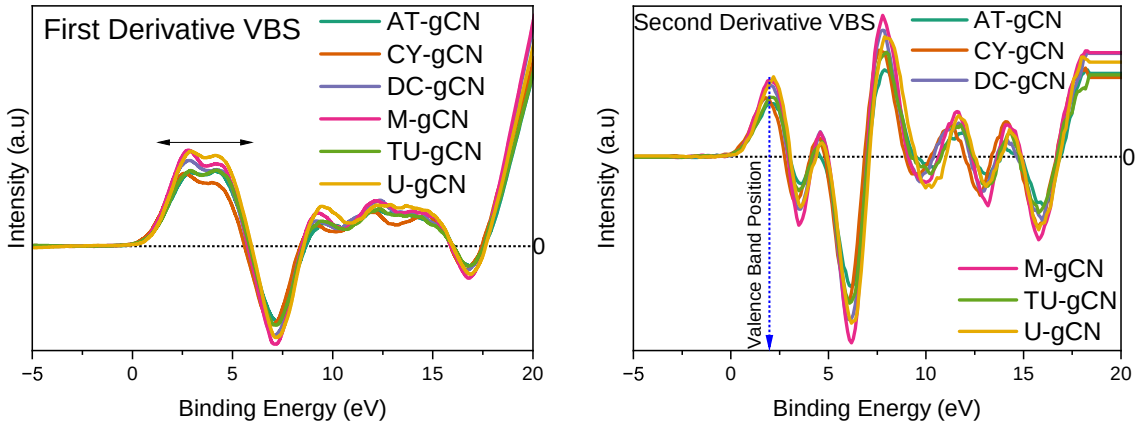

(a) (b)

Figure 4.21: Derivative valence band XPS plots and valence band position estimation through the second derivative method for carbon nitrides.

differences in intensity. This variation in intensity strongly implies that the choice of precursor has a remarkable impact on the electronic structure of graphitic carbon nitride.

The similarities in the valence band spectra of the diverse carbon nitride samples suggest a fundamental similarity in their electronic states and bonding configurations. The persistence of characteristic features, such as the π-band of conjugated carbon and hybridized carbon-nitrogen states, indicates a shared structural foundation among these materials. This consistency suggests that the core electronic properties of carbon nitride, as deduced from the valence band spectra, remain stable despite the variations in the precursor composition. The overlap in the valence band spectra implies a fundamental similarity in the electronic states and bonding configurations of the diverse carbon nitride samples. The persistence of characteristic features, including the π-band of conjugated carbon and hybridized carbon-nitrogen states, indicates a shared structural foundation among these materials.

Variations in the intensity of the overlapping spectra among the carbon nitride samples can be ascribed to the distinct chemical nature and makeup of the precursors utilized. Modifications in the structures of the precursors and their elemental compositions result in alterations in the concentrations of specific electronic states, culminating in observed variations in intensity. This intensity modulation effectively highlights the variations in the electronic structure of graphitic carbon nitride resulting from differences in precursor-dependent factors.

Second-derivative valence band spectra often exhibit a band tail near the valence band edge, indicating a gradual decrease in the density of electronic states beneath the main peak of the valence band. This phenomenon is typically attributed to the electronic disorder within the material, where impurities, defects, or structural imperfections create localized energy states within the bandgap. These localized states extend the valence band towards lower binding energies, giving rise to tail-like features observed in the spectrum.

The Urbach tail is a band tail commonly observed in amorphous materials and semiconductors. This reflects the disorder-induced broadening of density of states near the band edge (Table 4.9). In other words, the presence of disorder, such as

	Highest Occupied Molecular Orbital (HOMO), eV				
Sample	**Second Derivative**	**Curve Fitting**			
		Position	**Original Value**	**FWHM**	**STD**
AT-gCN	2.18	2	1.9957	1.91	1.302
CY-gCN	1.78	1.91	1.9138	1.52	1.224
DC-gCN	1.98	2.11	2.1113	1.47	1.157
M-gCN	1.98	2.11	2.1115	1.62	1.317
TU-gCN	1.98	2.12	2.1201	1.71	1.515
U-gCN	2.18	2.22	2.2199	1.64	1.305

Table 4.14: Valence position carbon nitrides derived from XPS

irregularities in the structure of the material, causes widening of the electronic states close to the valence band edge. This broadening effect contributes to the appearance of a band tail in the second-derivative valence-band spectra.

4.2.13 Elucidation of the Band Diagram

The band diagrams for all six carbon nitride samples were elucidated through a comprehensive approach utilizing the valence band position data obtained from derivative X-ray photoelectron spectroscopy (XPS) and bandgap values derived from second-derivative diffuse reflectance ultraviolet (DRD UV) measurements. This dual-source information allows for the calculation of both the valence and conduction band positions[56, 57]. Subsequently, the electron affinity and ionization energy of each sample were determined based on the calculated band positions.

Band diagrams for all samples were created using the data obtained from the valence-band XPS spectra and DRS UV measurements at both pH 0 and pH 8. To construct the band diagram at pH 0, the values obtained from these measurements were used to construct (Figure 4.22). Additional pH corrections were applied to the semiconductor band edge and CO_2 redox potential values to accurately represent the band diagram at pH 8 (Figure 4.23).

The valence and conduction bands of semiconductors are intrinsically related to their oxidation and reduction potentials. As shown in Table 4.15, the oxidation potentials varied across the carbon nitride samples in the following order: U-gCN>AT-gCN>T-gCN>DC-gCN>M-gCN>CY-gCN. Similarly, the reduction potentials varied in the following order: CY-gCN>TU-gCN>M-gCN>DC-gCN>U-gCN>AT-gCN. All carbon nitride systems have the necessary band-edge potential to reduce carbon dioxide to methane and methanol (Figure 4.23 & Equation 4.1 & 4.2). However, AT-gCN had a relatively low reduction potential compared to the others, although it had the highest yield of methanol and considerable methane yield. CY-gCN exhibited exceptional reducing power, as evidenced by its high methanol and methane yields. DC-gCN, M-gCN, and TU-gCN exhibited similar reduction potentials, but their methane and methanol production yields differed.

$$\begin{aligned} \mathrm{CO_2(g) + 3\,H_2(g) \longrightarrow CH_3OH\,(l) + H_2O\,(l)} \qquad & E^\circ = -0.39\,\mathrm{V} \\ \mathrm{6\,H^+\,(aq) + 6\,e^- \longrightarrow 3\,H_2(g)} \qquad & E^\circ = -0.41\,\mathrm{V} \\ \mathrm{CO_2\,(g) + 6\,H^+\,(aq) + 6\,e^- \longrightarrow CH_3OH\,(l) + H_2O\,(l)} \qquad & \mathrm{E}^\circ = -0.80\,\mathrm{V} \end{aligned} \tag{4.1}$$

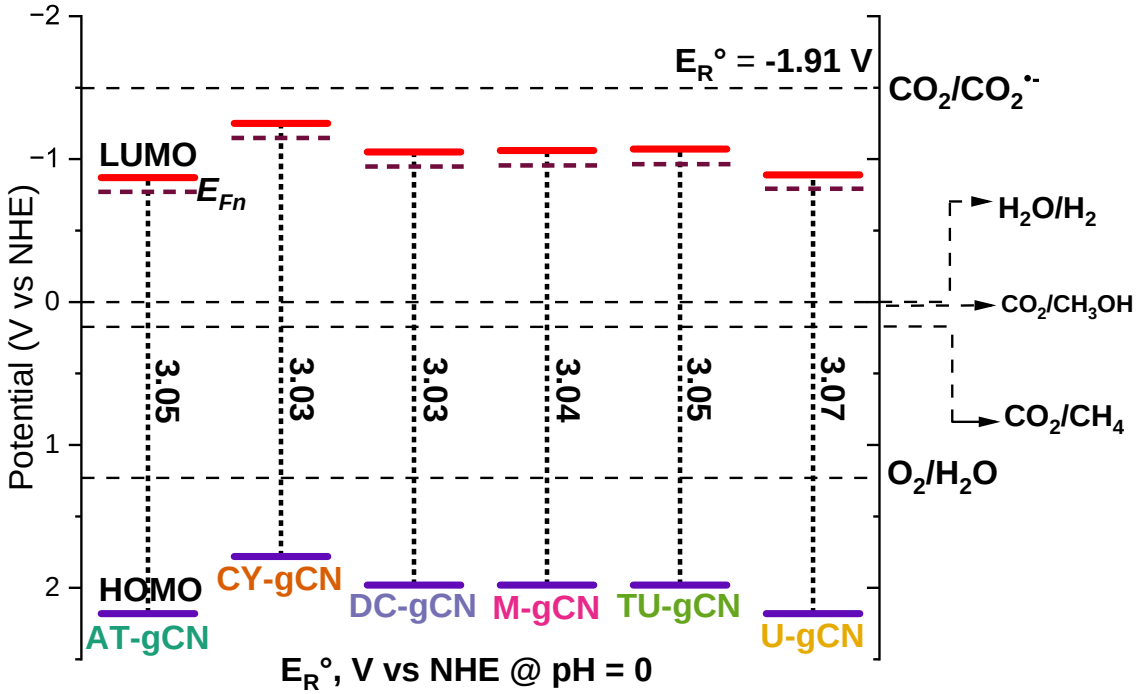

Figure 4.22: Band diagram of carbon nitrides at pH 0

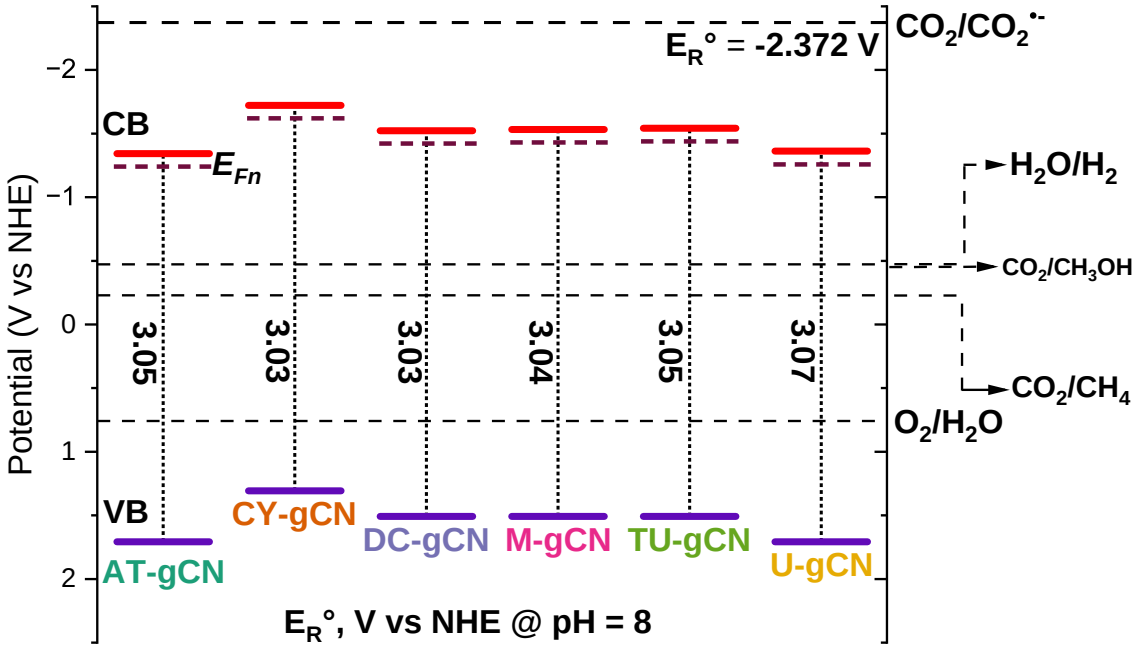

Figure 4.23: Band diagram of carbon nitrides at pH 8

$$\begin{aligned} \mathrm{CO_2(g) + 4\,H_2(g) \longrightarrow CH_4(g) + 2\,H_2O\,(l)} \quad & E^\circ = -0.24\,\mathrm{V} \\ \mathrm{8\,H^+\,(aq) + 8\,e^- \longrightarrow 4\,H_2(g)} \quad & E^\circ = -0.41\,\mathrm{V} \\ \mathrm{CO_2\,(g) + 8\,H^+\,(aq) + 8\,e^- \longrightarrow CH_4(g) + 2\,H_2O\,(l)} \quad & \mathrm{E^\circ = -0.65\,V} \end{aligned} \tag{4.2}$$

Regarding the oxidation potential, U-gCN has the highest oxidation potential among carbon nitrides and is expected to produce a high amount of oxygen, but its yield is poor. Conversely, CY-gCN produced a higher oxygen yield despite having a low oxidation potential compared to the others. This demonstrates that the product yield depends not only on the reduction or oxidation potential but also on other factors.

Sample	Bandgap	HOMO	LUMO	I.E	E.A	C	N	C/N
AT-gCN	3.05 eV	2.18 V	−0.87 V	6.62 eV	3.57 eV	31	41.29	0.7507
CY-gCN	3.03 eV	1.78 V	−1.25 V	6.22 eV	3.19 eV	33.47	45.91	0.7290
DC-gCN	3.03 eV	1.98 V	−1.05 V	6.42 eV	3.39 eV	33.94	44.68	0.7596
M-gCN	3.04 eV	1.98 V	−1.06 V	6.42 eV	3.38 eV	34.73	48.92	0.7099
TU-gCN	3.05 eV	1.98 V	−1.07 V	6.42 eV	3.37 eV	34.76	45.29	0.7674
U-gCN	3.07 eV	2.18 V	−0.89 V	6.62 eV	3.54 eV	34.02	46.53	0.7311

Table 4.15: Electronic properties of graphitic carbon nitrides

The ionization energy (IE) of carbon nitride plays a crucial role in its reactivity toward CO_2 reduction (Table 4.15). A higher IE indicates tightly bound electrons, resulting in reduced electron availability, and consequently, lower activity and slower reaction rates. Conversely, a lower IE facilitates electron transfer, initiating the reduction process and enhancing both the activity and reaction rates. This Table shows that a higher ionization energy favors the six-electron pathway to methanol over the eight-electron pathway to produce methane, and a lower ionization energy favors the opposite.

Similarly, the electron affinity (EA) of carbon nitride influences its CO_2 reduction performance (Table 4.15). A higher EA signifies a stronger attraction for electrons, leading to more robust binding of the CO_2 intermediate on the carbon nitride surface. Although this can impede further reduction and product release, it can also limit the overall efficiency of the process. However, a lower EA weakens the binding of the CO_2 intermediate, promoting its desorption and facilitating subsequent reduction steps, thereby improving the overall efficiency of CO_2 conversion. Therefore, the medium electron affinity values of carbon nitrides yielded appreciable amounts of methane and methanol. AT-gCN (higher methanol yield) exhibited a higher electron affinity and displayed an opposing trend with regard to the product yield, indicating that other factors are also involved in the process. U-gCN showed a higher electron affinity, ionization energy, and low product yield.

4.2.14 Possible Mechanism of Formation of Products

Methane Formation

In the process of CO_2 photoreduction on g-C_3N_4, where chemisorption favors C-C coupling over hydrogenation for methane formation, there are two primary scenarios for C-C coupling that can occur:

1. Direct C-C coupling between adsorbed CO_2 molecules: This pathway involves the formation of a carbon-carbon bond directly between two adsorbed CO_2 molecules on the g-C_3N_4 surface. The possible reaction sequence is as follows.

    - Step 1: Two CO_2 molecules chemisorb onto the g-C_3N_4 surface via strong bonds with specific functional groups or defect sites.

    $$CO_2(g) + \text{g-}C_3N_4 \xrightarrow{\text{Adsorption}} CO_2(\text{ad}) \tag{4.3}$$

    - Step 2: An electron transfer mechanism triggers the cleavage of a C-O bond in one CO_2 molecule, generating a CO* intermediate that remains adsorbed on the surface.

    $$CO_2(\text{ad}) + \text{g-}C_3N_4 \xrightarrow{\text{Light Excitation}} CO^*(\text{ad}) + O^*(\text{ad}) \tag{4.4}$$

    - Step 3: The remaining CO_2 molecule attacks the carbon atom of the CO* intermediate to form a C-C bond, which could involve a nucleophilic attack by the negatively charged oxygen atom on the carbon atom of CO*.

    $$CO_2(\text{ad}) + CO^*(\text{ad}) \xrightarrow{\text{C-C Bond Formation}} C_2O_2^*(\text{ad}) \tag{4.5}$$

    - Step 4: Subsequent hydrogenation steps involving H* transfer from water convert the C_2O_2* intermediate (formed from C-C coupling) into CH_4 through further C-O bond cleavage and H-C bond formation.

    $$C_2O_2^*(\text{ad}) + H \xrightarrow{\text{Hydrogenation}} CH_4 \tag{4.6}$$

2. C-C Coupling via CO Intermediates: The C-C coupling through CO intermediates entails the formation of such intermediates through a side reaction, followed by their interaction with another CO intermediate or an adsorbed CO_2 molecule.

    - Step 1: Initial chemisorption of CO_2 molecules on the g-C_3N_4 surface occurs.

    $$CO_2(g) + \text{g-}C_3N_4 \xrightarrow{\text{Adsorption}} CO_2(\text{ad}) \tag{4.7}$$

    - Step 2: A side reaction causes the dissociation of a C-O bond in one CO_2 molecule, resulting in the release of a free CO molecule and the formation of an O* intermediate on the g-C_3N_4 surface.

    $$CO_2(\text{ads}) + \text{g-}C_3N_4 \xrightarrow{\text{Side Reaction}} CO(\text{g}) + O^*(\text{ad}) \tag{4.8}$$

    - Step 3: The desorbed CO molecule is re-adsorbed onto the surface and reacts with the O* intermediate, forming a C-O bond and producing a CO_2* intermediate.

    $$CO(\text{g}) + O^*(\text{ad}) \xrightarrow{\text{C-O Bond Formation}} CO_2^*(\text{ad}) \tag{4.9}$$

    - Step 4: Alternatively, the CO molecule can directly react with another adsorbed CO_2 molecule to form a C-C bond.

    $$CO(\text{g}) + CO_2(\text{ad}) \xrightarrow{\text{Direct C-C Bond Formation}} C_2O_2^*(\text{ad}) \tag{4.10}$$

- Step 5: Subsequent hydrogenation steps convert the C_2O_2* or CO_2* intermediates into CH_4.

$$C_2O_2^*(ad) + H \xrightarrow{\text{Hydrogenation}} CH_4 \tag{4.11}$$

$$CO_2^*(ad) + H \xrightarrow{\text{Hydrogenation}} CH_4 \tag{4.12}$$

Methanol Formation

The formation of methanol on the surface of graphitic carbon nitride may have occurred through three processes.

1. The predominant adsorption mode in the CO_2 photoreduction process, which facilitates the formation of methanol, is physisorption with additional hydrogen bonding.

   - In the initial stage, CO_2 molecules interact with the lone pair electrons on the N atoms of g-C_3N_4 through weak van der Waals forces, allowing sufficient mobility for subsequent steps. This interaction was further strengthened through additional hydrogen bonding with amine, amide, or hydroxyl groups, which facilitated the charge transfer for activation.

$$CO_2(g) + \text{g-}C_3N_4 \xrightarrow{\text{Physisorption}} CO_2(ad) \tag{4.13}$$

$$CO_2(ad) + \text{g-}C_3N_4 \xrightarrow{\text{Hydrogen Bonding}} CO_2(ad)\cdots HN(ads) \tag{4.14}$$

   - In the second step, light excitation created electron-hole pairs in g-C_3N_4, which migrated to the adsorbed CO_2, reducing it to the radical anion (CO_2*-). The holes also contribute to C-O bond cleavage, generating CO* and O^-.

$$CO_2(ad) + \text{g-}C_3N_4 \xrightarrow{\text{Light Excitation}} CO_2^*(ad) + h^+(\text{hole}) + e^-(\text{electron}) \tag{4.15}$$

   - Subsequent sequential hydrogenation steps involve the transfer of protons (H^+) from water, ammonia, or other H* donors to CO_2*- and O- to form HCO_2* and OH*, respectively. Further hydrogenation occurs through similar H* transfer processes involving HCO* and CH_2O* intermediates.

$$CO_2^*(ad) + H_2O \xrightarrow{\text{H* Transfer}} HCO_2^*(ad) + H^+(aq) + e^-(\text{g-}C_3N_4) \tag{4.16}$$

$$HCO_2^*(ads) + H_2O \xrightarrow{\text{H* Transfer}} CH_2O^*(ad) + H^+(aq) + e^-(\text{g-}C_3N_4) \tag{4.17}$$

$$CH_2O^*(ads) + H_2O \xrightarrow{\text{H* Transfer}} CH_3OH^*(ad) + OH^-(aq) + H^+(aq) + e^-(\text{g-}C_3N_4) \tag{4.18}$$

- In the final step, the CH_2O^* intermediate is converted to CH_3OH^* via water formation and desorption. OH^* combines with another H^+ to form water, which is desorbed from the surface and CH_3OH^* is also desorbed from the g-C_3N_4 surface, completing the methanol formation cycle.

$$CH_3OH^*(ad) \xrightarrow{\text{H* Transfer}} CH_3OH(g) + H^+(aq) + e^-(\text{g-}C_3N_4) \quad (4.19)$$

$$OH^-(aq) + H^+(aq) \xrightarrow{\text{Combine}} H_2O(l) \quad (4.20)$$

- Potential side reactions that can arise during the reaction process include the formation of CO intermediates through C-O bond cleavage, which can participate in C-C coupling pathways and potentially lead to methane formation as a competing product. Additionally, the over-hydrogenation of CH_3OH may result in the formation of unwanted products, such as ethanol or ethane.

$$CO_2^*(ads) + CO_2(ad) \xrightarrow{\text{C-C Bond Formation}} C_2O_2^*(ad) \quad (4.21)$$

$$CH_3OH^*(ad) + H^+(aq) + e^-(\text{g-}C_3N_4) \xrightarrow{\text{Over-Hydrogenation}} C_2H_6O^*(ad) \quad (4.22)$$

2. The hydrogenation pathway leading to methanol:

- Initial CO_2 Adsorption: The interaction between the CO_2 molecules and g-C_3N_4 surface occurs through weak van der Waals forces between the quadrupole moments of the CO_2 molecules and the lone pair electrons of the nitrogen atoms on the g-C_3N_4 surface. This physisorption allows mobility, enabling access to the active sites for subsequent reactions. In addition, hydrogen bonding with functional groups, such as amides or hydroxyls, can further stabilize adsorbed CO_2 and facilitate hydrogen transfer.

$$CO_2(g) + \text{g-}C_3N_4 \xrightarrow{\text{Physisorption}} CO_2(ad) \quad (4.23)$$

$$CO_2(ad) + \text{g-}C_3N_4 \xrightarrow{\text{Hydrogen Bonding}} CO_2(ad)\cdots HN(ad) \quad (4.24)$$

- Hydrogenation to HCO_2^*: H^* is transferred from water to the adsorbed CO_2 molecule, reducing it to a formate (HCO_2^*) intermediate that remains adsorbed on the g-C_3N_4 surface. This step may involve multiple proton-electron transfer events through the g-C_3N_4 π-conjugated system.

$$CO_2(ad)\cdots HN(ad) + H_2O \xrightarrow{\text{H* Transfer}} HCO_2^*(ad) + OH^-(aq) + H^+(aq) + e^-(\text{g-}C_3N_4) \quad (4.25)$$

- Hydrogenation to HCO_2^* : The HCO_2^* intermediate receives another H^* and undergoes further reduction to form the formaldehyde (CH_2O^*) intermediate. Similar to the previous step, this may involve multiple proton-electron transfer events involving the g-C_3N_4 surface.

$$HCO_2^*(ad) + H_2O \xrightarrow{\text{H* Transfer}} CH_2O^*(ad) + OH^-(aq) + H^+(aq) + e^-(\text{g-}C_3N_4) \quad (4.26)$$

- Hydrogenation to CH_3OH^* : The CH_2O^* intermediate receives the final H^* to form a methanol (CH_3OH^*) molecule, which remains adsorbed on the g-C_3N_4 surface.

$$CH_2O^*(ad)+H_2O \xrightarrow{H^* \text{ Transfer}} CH_3OH^*(ad)+OH^-(aq)+H^+(aq)+e^-(\text{g-}C_3N_4) \tag{4.27}$$

- Desorption and Product Formation: The CH_3OH^* molecules desorb from the g-C_3N_4 surface, forming free methanol in the reaction medium.

$$CH_3OH^*(ad) \xrightarrow{H^* \text{ Transfer}} CH_3OH(g) + H^+(aq) + e^-(\text{g-}C_3N_4) \tag{4.28}$$

4.3 Summary

It is clear that the product yield in CO_2 photoreduction is influenced by several factors, including porosity, light absorption cross-section per unit surface area, surface functionalities per unit surface area, and the presence of surface sites such as edge sites and surface defects. All of these factors are interconnected and determine the overall yield of any particular product. This complicates the selection of improved catalyst systems. In the case of methane production, TU-gCN followed by CY-gCN and DC-gCN showed appreciable yields. AT-gCN, CY-gCN, TU-gCN, and DC-gCN afforded appreciable yields in the case of methanol. CY-gCN showed a higher yield than DC-gCN, M-gCN, AT-gCN, and TU-gCN did.

The transmission of light through the surface of a material is a critical factor that determines its catalytic efficacy. Owing to the presence of multiple particles in a colloidal system, light is likely to hit only a small fraction of the surface area at any given time and may even suffer from shadowing effects. Consequently, the most efficient catalyst should have the highest DP/SA and NSA% to ensure that the available light is utilized to the fullest extent possible. Therefore, the DP/SA and NSA% values can be directly used to compare a better catalyst system for water splitting or oxidation reactions such as pollutant degradation. However, in the case of CO_2 reduction, this will provide an idea for a better system, and caution should be exercised when selecting a better catalytic system. The DP/SA ratio can be used for CO_2 reduction when the selectivity is optimized for a specific product. In this study, TU-gCN, AT-gCN, and CY-gCN showed the highest activity for methane, methanol and oxygen production, respectively. If we consider the overall activity, CY-gCN is the best option because it is active towards all three reduction products. Additionally, CY-gCN may also be the highest producer of methanol, as the appreciable amount of oxygen produced suggests a high oxidizing power, which could lead to the reverse oxidation of methanol produced on the surface back to CO_2. The study primarily found that the majority of methanol originated from the vapor phase, whereas the detection of the methanol in the liquid reaction system was minimal, clearly indicating the possibility of reverse oxidation of the reduction products to CO_2. In addition, the methanol yield of CY-gCN was comparable to those of AT-gCN and TU-gCN. It is important to recognize that the development of surface functionalities aimed at a specific product enhances both the selectivity and yield of the reaction, while simultaneously accelerating the rate of competing reactions. Therefore, material design for CO_2 reduction should also consider competing chemical reactions.

This chapter explores the potential of graphitic carbon nitride (g-C_3N_4) to exploit its surface characteristics and enhance its capacity to capture and transform carbon dioxide (CO_2) into beneficial products using light energy. Specific functional groups, such as hydroxyl and amine groups serve as potent binding sites for CO_2, facilitating the capture and activation of CO_2 molecules by carbon nitrides. This leads to more efficient and selective CO_2 photoreduction. Furthermore, the surface characteristics of g-C_3N_4 can be used to adjust its electronic properties, enhance its light-absorption and electron-transfer capabilities, and improve its overall photocatalytic performance. Although g-C_3N_4 with tailored surface characteristics has significant potential for sustainable CO_2 utilization, challenges remain that need to be addressed, such as enhanced selectivity, stability, and conversion rates.

References

[1] Thomas, A.; Fischer, A.; Goettmann, F.; Antonietti, M.; Muller, J.-O.; Schlogl, R.; Carlsson, J. M. Graphitic carbon nitride materials: variation of structure and morphology and their use as metal-free catalysts. *Journal of Material Chemistry* **2008**, *18*, 4893–4908.

[2] Lakhi, K. S.; Park, D.-H.; Al-Bahily, K.; Cha, W.; Viswanathan, B.; Choy, J.-H.; Vinu, A. Mesoporous Carbon Nitrides: Synthesis, Functionalization, and Applications. *Chemical Society Review* **2017**, *46*, 72–101.

[3] Barrio, J.; Li, J.; Shalom, M. Carbon Nitrides from Supramolecular Crystals: From Single Atoms to Heterojunctions and Advanced Photoelectrodes. *Chemistry - A European Journal* **2023**, *29*, e202302377.

[4] Lan, H.; Li, L.; An, X.; Liu, F.; Chen, C.; Liu, H.; Qu, J. Microstructure of carbon nitride affecting synergetic photocatalytic activity: Hydrogen bonds vs. structural defects. *Applied Catalysis B: Environmental* **2017**, *204*, 49–57.

[5] Liebig, J. Annalen der Pharmacie. **1834**, *10*, 10–21.

[6] Teixeira, I. F.; Tarakina, N. V.; Silva, I. F.; López-Salas, N.; Savateev, A.; Antonietti, M. Overcoming Electron Transfer Efficiency Bottlenecks for Hydrogen Production in Highly Crystalline Carbon Nitride-Based Materials. *Advanced Sustainable Systems* **2022**, *6*, 2100429.

[7] Ajayan Vinu, T. M.; Ariga, K. New families of mesoporous materials. *Science and Technology of Advanced Materials* **2006**, *7*, 753–771.

[8] Zheng, Y.; Zhang, Z.; Li, C. A comparison of graphitic carbon nitrides synthesized from different precursors through pyrolysis. *Journal of Photochemistry and Photobiology A: Chemistry* **2017**, *332*, 32–44.

[9] Devthade, V.; Kulhari, D.; Umare, S. S. Role of precursors on photocatalytic behavior of graphitic carbon nitride. *Materials Today: Proceedings* **2018**, *5*, 6th National Conference on Nanomaterials and Nanotechnology, 11 to 13 February 2017, 9203–9210.

[10] Yew, Y. T.; Lim, C. S.; Eng, A. Y. S.; Oh, J.; Park, S.; Pumera, M. Electrochemistry of Layered Graphitic Carbon Nitride Synthesised from Various Precursors: Searching for Catalytic Effects. *ChemPhysChem* **2016**, *17*, 481–488.

[11] Ragupathi, V.; Panigrahi, P.; Ganapathi Subramaniam, N. Bandgap engineering in graphitic carbon nitride: Effect of precursors. *Optik* **2020**, *202*, 163601.

[12] Lee, H. L.; Sofer, Z.; Mazánek, V.; Luxa, J.; Chua, C. K.; Pumera, M. Graphitic carbon nitride: Effects of various precursors on the structural, morphological and electrochemical sensing properties. *Applied Materials Today* **2017**, *8*, 150–162.

[13] Zhang, W.; Zhang, Q.; Dong, F.; Zhao, Z. The Multiple Effects of Precursors on the Properties of Polymeric Carbon Nitride. *International Journal of Photoenergy* **2013**, *2013*, ed. by Zhang, P., Publisher: Hindawi Publishing Corporation, 685038.

[14] Bond, G., *Heterogeneous Catalysis: Principles and Applications*; Oxford chemistry series; Clarendon Press: 1974.

[15] Degen, T.; Sadki, M.; Bron, E.; Konig, U.; Nenert, G. The HighScore suite. *Powder Diffraction* **2014**, *29*, S13–S18.

[16] Miller, T. S.; Jorge, A. B.; Suter, T. M.; Sella, A.; Corà, F.; McMillan, P. F. Carbon nitrides: synthesis and characterization of a new class of functional materials. *Physical Chemistry Chemical Physics* **2017**, *19*, 15613–15638.

[17] Fina, F.; Callear, S. K.; Carins, G. M.; Irvine, J. T. S. Structural Investigation of Graphitic Carbon Nitride via XRD and Neutron Diffraction. *Chemistry of Materials* **2015**, *27*, 2612–2618.

[18] Hou, J.; Yang, M.; Dou, Q.; Chen, Q.; Wang, X.; Hu, C.; Paul, R. Defect engineering in polymeric carbon nitride with accordion structure for efficient photocatalytic CO_2 reduction and H_2 production. *Chemical Engineering Journal* **2022**, *450*, 138425.

[19] Tyborski, T.; Merschjann, C.; Orthmann, S.; Yang, F.; Lux-Steiner, M.-C.; Schedel-Niedrig, T. Crystal structure of polymeric carbon nitride and the determination of its process-temperature-induced modifications. *Journal of Physics: Condensed Matter* **2013**, *25*, 395402.

[20] Seyfarth, L.; Seyfarth, J.; Lotsch, B. V.; Schnick, W.; Senker, J. Tackling the stacking disorder of melon—structure elucidation in a semicrystalline material. *Physical Chemistry Chemical Physics* **2010**, *12*, 2227–2237.

[21] Melissen, S. T. A. G.; Le Bahers, T.; Sautet, P.; Steinmann, S. N. What does graphitic carbon nitride really look like? *Physical Chemistry Chemical Physics* **2021**, *23*, 2853–2859.

[22] Dong, G.; Zhang, L. Porous structure dependent photoreactivity of graphitic carbon nitride under visible light. *J. Mater. Chem.* **2012**, *22*, 1160–1166.

[23] Ismael, M.; Wu, Y.; Taffa, D. H.; Bottke, P.; Wark, M. Graphitic carbon nitride synthesized by simple pyrolysis: role of precursor in photocatalytic hydrogen production. *New Journal of Chemistry* **2019**, *43*, 6909–6920.

[24] Sing, K. S. W. Reporting physisorption data for gas/solid systems with special reference to the determination of surface area and porosity (Recommendations 1984). *Pure and Applied Chemistry* **1985**, *57*, 603–619.

[25] Rouquerol, J.; Llewellyn, P.; Rouquerol, F., Is the bet equation applicable to microporous adsorbents? In *Characterization of Porous Solids VII*, Llewellyn, P., Rodriquez-Reinoso, F., Rouqerol, J., Seaton, N., Eds.; Studies in Surface Science and Catalysis, Vol. 160; Elsevier: 2007, pp 49–56.

[26] Rouquerol, J.; Rouquerol, F.; Llewellyn, P.; Maurin, G.; Sing, K., *Adsorption by Powders and Porous Solids: Principles, Methodology and Applications*; Elsevier Science: 2013.

[27] Terrones, G. G.; Chen, Y.; Datar, A.; Lin, L.-C.; Kulik, H. J.; Chung, Y. G. SESAMI APP: An Accessible Interface for Surface Area Calculation of Materials from Adsorption Isotherms. *Journal of Open Source Software* **2023**, *8*, 5429.

[28] Osterrieth, J. W. M. et al. How Reproducible are Surface Areas Calculated from the BET Equation? *Advanced Materials* **2022**, *34*, 2201502.

[29] Datar, A.; Chung, Y. G.; Lin, L.-C. Beyond the BET Analysis: The Surface Area Prediction of Nanoporous Materials Using a Machine Learning Method. *The Journal of Physical Chemistry Letters* **2020**, *11*, 5412–5417.

[30] Sinha, P.; Datar, A.; Jeong, C.; Deng, X.; Chung, Y. G.; Lin, L.-C. Surface Area Determination of Porous Materials Using the Brunauer–Emmett–Teller (BET) Method: Limitations and Improvements. *The Journal of Physical Chemistry C* **2019**, *123*, 20195–20209.

[31] Thommes, M.; Kaneko, K.; Neimark, A. V.; Olivier, J. P.; Rodriguez-Reinoso, F.; Rouquerol, J.; Sing, K. S. *Pure and Applied Chemistry* **2015**, *87*, 1051–1069.

[32] Michot, L. J., 2 - Determination of surface areas and textural properties of clay minerals In *Surface and Interface Chemistry of Clay Minerals*, Schoonheydt, R., Johnston, C., Bergaya, F., Eds.; Developments in Clay Science, Vol. 9; Elsevier: 2018, pp 23–47.

[33] Michot, L.; Villieras, F., Chapter 2.10 - Surface Area and Porosity In *Handbook of Clay Science*, Bergaya, F., Lagaly, G., Eds.; Developments in Clay Science, Vol. 5; Elsevier: 2013, pp 319–332.

[34] Torrent, J.; Barron, V., Diffuse Reflectance Spectroscopy In *Methods of Soil Analysis Part 5-Mineralogical Methods*; John Wiley & Sons, Ltd: 2008; Chapter 13, pp 367–385.

[35] Scheinost, A. C.; Chavernas, A.; Barron, V.; Torrent, J. Use and Limitations of Second-Derivative Diffuse Reflectance Spectroscopy in the Visible to Near-Infrared Range to Identify and Quantify Fe Oxide Minerals in Soils. *Clays and Clay Minerals* **1998**, *46*, 528–536.

[36] Cao, W.; Jiang, Z.; Gai, C.; Barrón, V.; Torrent, J.; Zhong, Y.; Liu, Q. Re-Visiting the Quantification of Hematite by Diffuse Reflectance Spectroscopy. *Minerals* **2022**, *12*.

[37] Grekov, D.; Pre, P.; Grambow, B. On the use of manometry method for measurement of gas adsorption equilibria and characterization of clay texture with Derivative Isotherm Summation. *Applied Clay Science* **2020**, *184*, 105372.

[38] Villieras, F.; Michot, L. J.; Bardot, F.; Chamerois, M.; Eypert-Blaison, C.; Francois, M.; Gerard, G.; Cases, J.-M. Surface heterogeneity of minerals. *Comptes Rendus Geoscience* **2002**, *334*, 597–609.

[39] Zhang, Y.; Pan, Q.; Chai, G.; Liang, M.; Dong, G.; Zhang, Q.; Qiu, J. Synthesis and luminescence mechanism of multicolor-emitting g-C_3N_4 nanopowders by low temperature thermal condensation of melamine. *Scientific Reports* **2013**, *3*, 1943.

[40] Wu, P.; Wang, J.; Zhao, J.; Guo, L.; Osterloh, F. E. Structure defects in g-C_3N_4 limit visible light driven hydrogen evolution and photovoltage. *Journal of Material Chemistry A* **2014**, *2*, 20338–20344.

[41] Zuluaga, S.; Liu, L.-H.; Shafiq, N.; Rupich, S. M.; Veyan, J.-F.; Chabal, Y. J.; Thonhauser, T. Structural band-gap tuning in g-C_3N_4. *Physical Chemistry Chemical Physics* **2015**, *17*, 957–962.

[42] Yuan, Y.; Zhang, L.; Xing, J.; Utama, M. I. B.; Lu, X.; Du, K.; Li, Y.; Hu, X.; Wang, S.; Genc, A.; Dunin-Borkowski, R.; Arbiol, J.; Xiong, Q. High-yield synthesis and optical properties of g-C_3N_4. *Nanoscale* **2015**, *7*, 12343–12350.

[43] Hu, Y.; Shim, Y.; Oh, J.; Park, S.; Park, S.; Ishii, Y. Synthesis of ^{13}C-,^{15}N-Labeled Graphitic Carbon Nitrides and NMR-Based Evidence of Hydrogen-Bonding Assisted Two-Dimensional Assembly. *Chemistry of Materials* **2017**, *29*, 5080–5089.

[44] Jurgens, B.; Irran, E.; Senker, J.; Kroll, P.; Muller, H.; Schnick, W. Melem (2,5,8-Triamino-tri-s-triazine), an Important Intermediate during Condensation of Melamine Rings to Graphitic Carbon Nitride: Synthesis, Structure Determination by X-ray Powder Diffractometry, Solid-State NMR, and Theoretical Studies. *Journal of the American Chemical Society* **2003**, *125*, 10288–10300.

[45] Lotsch, B. V.; Doblinger, M.; Sehnert, J.; Seyfarth, L.; Senker, J.; Oeckler, O.; Schnick, W. Unmasking Melon by a Complementary Approach Employing Electron Diffraction, Solid-State NMR Spectroscopy, and Theoretical Calculations-Structural Characterization of a Carbon Nitride Polymer. *Chemistry - A European Journal* **2007**, *13*, 4969–4980.

[46] Liu, F.; Tong, Y.; Li, C.; Liu, X. One-Dimensional Conjugated Carbon Nitrides: Synthesis and Structure Determination by HRTEM and Solid-State NMR. *The Journal of Physical Chemistry Letters* **2021**, *12*, 10359–10365.

[47] Wirnhier, E.; Mesch, M. B.; Senker, J.; Schnick, W. Formation and Characterization of Melam, Melam Hydrate, and a Melam-Melem Adduct. *Chemistry - A European Journal* **2013**, *19*, 2041–2049.

[48] Makowski, S. J.; Kostler, P.; Schnick, W. Formation of a Hydrogen-Bonded Heptazine Framework by Self-Assembly of Melem into a Hexagonal Channel Structure. *Chemistry - A European Journal* **2012**, *18*, 3248–3257.

[49] Morgan, D. J. Core-level reference spectra for bulk graphitic carbon nitride (g-C_3N_4). *Surface Science Spectra* **2021**, *28*, 014007.

[50] Benedet, M.; Rizzi, G. A.; Barreca, D.; Gasparotto, A.; Maccato, C. XPS analysis of graphitic carbon nitride functionalized with CoO and $CoFe_2O_4$. *Surface Science Spectra* **2023**, *30*, 014004.

[51] Hellgren, N.; Haasch, R. T.; Schmidt, S.; Hultman, L.; Petrov, I. Interpretation of X-ray photoelectron spectra of carbon-nitride thin films: New insights from in situ XPS. *Carbon* **2016**, *108*, 242–252.

[52] Ronning, C.; Feldermann, H.; Merk, R.; Hofsass, H.; Reinke, P.; Thiele, J.-U. Carbon nitride deposited using energetic species: A review on XPS studies. *Physical Review B* **1998**, *58*, 2207–2215.

[53] Baker, M. A.; Hammer, P. A Study of the Chemical Bonding and Microstructure of Ion Beam-deposited CNx Films Including an XPS C 1s Peak Simulation. *Surface and Interface Analysis* **1997**, *25*, 629–642.

[54] Chen, Z. Y.; Zhao, J. P.; Yano, T.; Ooie, T. Valence band electronic structure of carbon nitride from X-ray photoelectron spectroscopy. *Journal of Applied Physics* **2002**, *92*, 281–287.

[55] Monclus, M.; Cameron, D.; Chowdhury, A.; Barkley, R.; Collins, M. Investigation of the valence band states of reactively sputtered carbon nitride films. *Thin Solid Films* **1999**, *355-356*, 79–84.

[56] Bui, D.-P.; Pham, M.-T.; Tran, H.-H.; Nguyen, T.-D.; Cao, T. M.; Pham, V. V. Revisiting the Key Optical and Electrical Characteristics in Reporting the Photocatalysis of Semiconductors. *ACS Omega* **2021**, *6*, 27379–27386.

[57] Maheu, C.; Cardenas, L.; Puzenat, E.; Afanasiev, P.; Geantet, C. UPS and UV spectroscopies combined to position the energy levels of TiO_2 anatase and rutile nanopowders. *Physical Chemistry Chemical Physics* **2018**, *20*, 25629–25637.

Chapter 5

On the Role of Nature of Crucible on the Properties of Graphitic Carbon Nitride ($g\text{-}C_3N_4$) Surface in the Photon-Assisted Reduction of Carbon Dioxide

Abstract

This chapter investigated the crucial role of crucible materials in shaping the structural, electronic, and photon-assisted catalytic properties of graphitic carbon nitride ($g\text{-}C_3N_4$) for CO_2 reduction. By employing melamine as a common precursor across various crucibles (Al, Si, Pt, graphite, Ni, Zr, and quartz), we isolated and elucidated the specific effects of the crucible choice on the resulting $g\text{-}C_3N_4$ materials. A comprehensive suite of characterization techniques, including X-ray diffraction (XRD), field emission scanning electron microscopy (FESEM), X-ray photoelectron spectroscopy (XPS), UV-visible diffuse reflectance spectroscopy (UV-Vis DRS), photoluminescence spectroscopy (PL), and solid-state nuclear magnetic resonance (NMR), were employed to thoroughly analyze the samples. Advanced data processing methods, such as second derivative analysis of UV-Vis and XPS data, have been utilized to extract more accurate and reliable results. Our findings reveal that the crucible materials significantly influence the crystallinity, surface area, pore structure, and defect chemistry of the resulting $g\text{-}C_3N_4$. XRD analysis showed variations in the lattice parameters and crystallite sizes among the samples, while FESEM images highlighted differences in the morphology and particle size distribution. XPS and solid-state NMR studies revealed variations in the chemical environments and bonding configurations. Notably, we observed that the photon-assisted catalytic activity for CO_2 reduction is not solely dependent on conventional parameters such as the bandgap and band edge positions. Instead, a complex interplay of factors, including surface functionalities, light absorption characteristics, and adsorption properties, governs catalytic performance. The normalized surface concentration (NSC%) derived from XPS analysis and the DP/SA ratio obtained from UV-DRS measurements emerged as crucial parameters correlating with photon-assisted catalytic activity. Among the studied samples, $g\text{-}C_3N_4$ synthesized in aluminum (Al-gCN)

and zirconium (Zr-gCN) crucibles exhibited superior performance in the photon-assisted CO_2 reduction to methane, methanol, and oxygen. This enhanced activity was attributed to their higher C values (indicating stronger adsorbate-adsorbent interactions), favorable distribution of surface functionalities on the edge sites, and optimal light absorption characteristics. This study provides valuable insights into the structure-property-performance relationship of g-C_3N_4 materials and offers guidance for optimizing their synthesis for CO_2 reduction applications. Our findings emphasize the importance of crucible selection in the design of efficient g-C_3N_4 catalysts for photon-assisted processes, and pave the way for further improvements in CO_2 reduction technologies.

5.1 Introduction

The choice of crucible can have a significant impact on the properties of the material being melted and solidified. This is due to the fact that the crucible material can react with the substance being melted, leading to changes in its composition and impurities. The crucible material can also affect the rate of heat transfer, which can in turn influence the solidification rate and the resulting microstructure of the solidified material. Furthermore, the thermal expansion coefficient of the crucible material affects the dimensional stability of the solidified material. These effects are a result of the differences in the thermophysical and chemical properties between the crucible material and the substance being melted[1].

To mitigate these effects, it is essential to select a crucible material that is chemically compatible with the substance being melted and that has a higher melting point. This prevents the crucible material from reacting with the melted substance, altering its composition and introducing impurities. In addition, using a crucible material with a higher melting point prevents it from partially or fully melting, which can also affect the composition of the melt and introduce impurities. These considerations are crucial for ensuring that the final product has the desired properties such as strength, ductility, and resistance to corrosion[2].

The transfer of heat from the heat source to the melted substance can also be influenced by the crucible material. The thermal conductivity and diffusivity of different crucible materials vary, which determines how quickly heat is transferred through the material. This can affect the solidification rate of the substance and the resulting microstructure of the solidified material[3].

For instance, if a material is melted in a crucible with a low thermal conductivity, the heat transfer rate to the material will be slow, leading to a longer solidification time. This can result in a coarser microstructure in the solidified material, with larger grain sizes and increased defects. Conversely, if the material is melted in a crucible with high thermal conductivity, the heat transfer rate will be faster, leading to a quicker solidification time and finer microstructure in the solidified material, with smaller grain sizes and fewer defects[4–7].

Thus, it is essential to carefully consider the thermal properties of the crucible material when selecting a crucible for a specific application because these properties can significantly affect the material properties of the final product[8]. The thermal expansion coefficient of a crucible is a measure of the extent to which a material expands or contracts as it is heated or cooled. This can affect the dimensional

stability of the solidified material in two ways[9]. First, as the melted substance began to solidify, it contracted in size. If the thermal expansion coefficient of the crucible differs from that of the solidifying material, the crucible may become deformed or distorted, as it attempts to accommodate the changing dimensions of the solidifying material. This can result in dimensional inaccuracies in the final product as well as defects such as cracks and warping. Second, as the solidifying material cooled, it continued to contract in size. If the thermal-expansion coefficient of the crucible differs from that of the solidifying material, the crucible can stress the solidifying material, causing additional contraction or even cracking. Therefore, it is essential to match the thermal expansion coefficient of the crucible material as closely as possible with that of the solidifying material to minimize these effects[1, 10].

The expansion coefficients of commonly used crucibles vary widely, depending on the material. Some of the most commonly used crucible materials and their approximate expansion coefficients include graphite ($4.5 \times 10^{-6}/K$), clay graphite ($3.5 \times 10^{-6}/K$), alumina (Al_2O_3) ($7.5 \times 10^{-6}/K$), zirconia (ZrO_2) ($10.6 \times 10^{-6}/K$), nickel ($13.6 \times 10^{-6}/K$), quartz (SiO_2) ($0.5 \times 10^{-6}/K$), and platinum ($9.6 \times 10^{-6}/K$)[†].

The properties of the carbon nitride formed depend on various factors, including the synthesis method, crucible material, and synthesis conditions[11]. The properties of carbon nitride formed in different crucibles are expected to vary in several ways. Alumina, zirconia, platinum, and quartz are crucible materials that can be used for the synthesis of carbon nitride. Carbon nitride formed in an alumina crucible is expected to have good thermal stability, but the crystallinity and particle size may be affected by the insulating properties of alumina, which can result in a slower cooling rate. Carbon nitride formed in a zirconia crucible is expected to have high thermal stability, good crystallinity, and small particle size. Carbon nitride formed in a platinum crucible is expected to have high thermal stability, good crystallinity, and small particle size. Carbon nitride formed in a quartz crucible is expected to have high thermal stability, good crystallinity, and small particle size. Graphite crucibles are also suitable materials for the synthesis of high-quality carbon nitride, owing to their good crystallinity, small particle size, and high surface area.

The present investigation utilized melamine as the precursor for the synthesis of carbon nitride owing to its remarkable stability in all crucibles. In contrast, other precursors, including urea, thiourea, ammonium thiocyanate, cyanamide, and dicyandiamide, were unstable in the existing volume of the laboratory crucible or required larger sizes for synthesis.

[†]Note that these values are approximate and may vary slightly depending on the crucible material and the manufacturer. Additionally, these values may change with temperature; therefore, it is important to consult a manufacturer or supplier to obtain accurate thermal expansion coefficient values for a specific crucible material.

5.2 Results and Discussions

5.2.1 Discussion on CO_2 Photoreduction Results

The results showed a clear hierarchy in the methane yields of the various materials tested. Al-gCN demonstrates the highest methane yield ($0.059\,12\,\mu\mathrm{mol\,g^{-1}\,h^{-1}\,m^{-2}}$), surpassing all other materials. Zr-gCN follows in second place with a moderately high methane yield ($0.017\,97\,\mu\mathrm{mol\,g^{-1}\,h^{-1}\,m^{-2}}$). In contrast, Si-gCN, Q-gCN, Pt-gCN, and Gr-gCN showed lower methane yields, with Q-gCN and Ni-gCN falling within the lower range, and Pt-gCN and Gr-gCN exhibited the lowest methane yields. The results suggest that Al-gCN and Zr-gCN are the most promising materials for methane synthesis, with Al-gCN demonstrating the most favorable performance.

The highest methanol yield was achieved by Zr-gCN. Al-gCN followed in second place with a moderately high methanol yield of $12.873\,65\,\mu\mathrm{mol\,g^{-1}\,h^{-1}\,m^{-2}}$. Ni-gCN showed a moderate methanol yield of $6.065\,56\,\mu\mathrm{mol\,g^{-1}\,h^{-1}\,m^{-2}}$, which was lower than Zr-gCN and Al-gCN but higher than Pt-gCN and Gr-gCN. Si-gCN also exhibited an intermediate methanol yield, similar to that of Ni-gCN. The lowest methanol yields were observed for Pt-gCN, Gr-gCN, and Q-gCN, with 2.24739, 1.02094, and 2.66548 $\mu\mathrm{mol\,g^{-1}\,h^{-1}\,m^{-2}}$, respectively.

In comparison with the methane yield, the methanol yield trend differed slightly. Zr-gCN and Al-gCN still achieved the highest yields, but Si-gCN and Ni-gCN showed better performance for methanol production compared to methane. Pt-gCN and Gr-gCN remained the least effective crucibles for both products.

Al-gCN exhibits the highest oxygen yield among the samples which is significantly higher than the others. Zr-gCN ranks second in oxygen yield while Q-gCN has a moderately low yield. Ni-gCN and Gr-gCN exhibited similar and relatively low oxygen yields, respectively. Si-gCN exhibited the lowest oxygen yield. Pt-gCN had the second-lowest oxygen yield. The trend in the oxygen yield was distinct from that of the methane and methanol yields. Al-gCN stands out with an exceptionally high oxygen yield, while the performance of other samples varies considerably. Zr-gCN appears to be versatile, as it achieves relatively high yields for both oxygen and methane.

5.2.2 X-ray Diffraction

XRD data were collected using a Bruker D8 Advance diffractometer equipped with Cu Kα radiation (wavelength = 1.5418 Å) in the 2θ range of 10–70°. The step size was 0.034° and each step was performed for 5 s. The acquired data were processed using the X'Pert HighScore Plus software (version 3.0), which involved subtracting the background and normalizing the data [12].

X-ray diffraction (XRD) is a widely used technique for determining the structures of crystalline and polymeric materials. Graphene-based materials, known as gCN, often exhibit characteristics that suggest an amorphous-to-nanocrystalline nature. The primary reflection at 2θ=26-28°, which is typically associated with a "graphitic" structure and an interplanar spacing of 3.2-3.4 Å, is not a conclusive criterion for determining the presence of graphitic sheets in gCN [13].

To examine the structure of the gCN materials, Rietveld refinement was performed using the PANalytical X'Pert HighScore Plus software (version 3.0). The

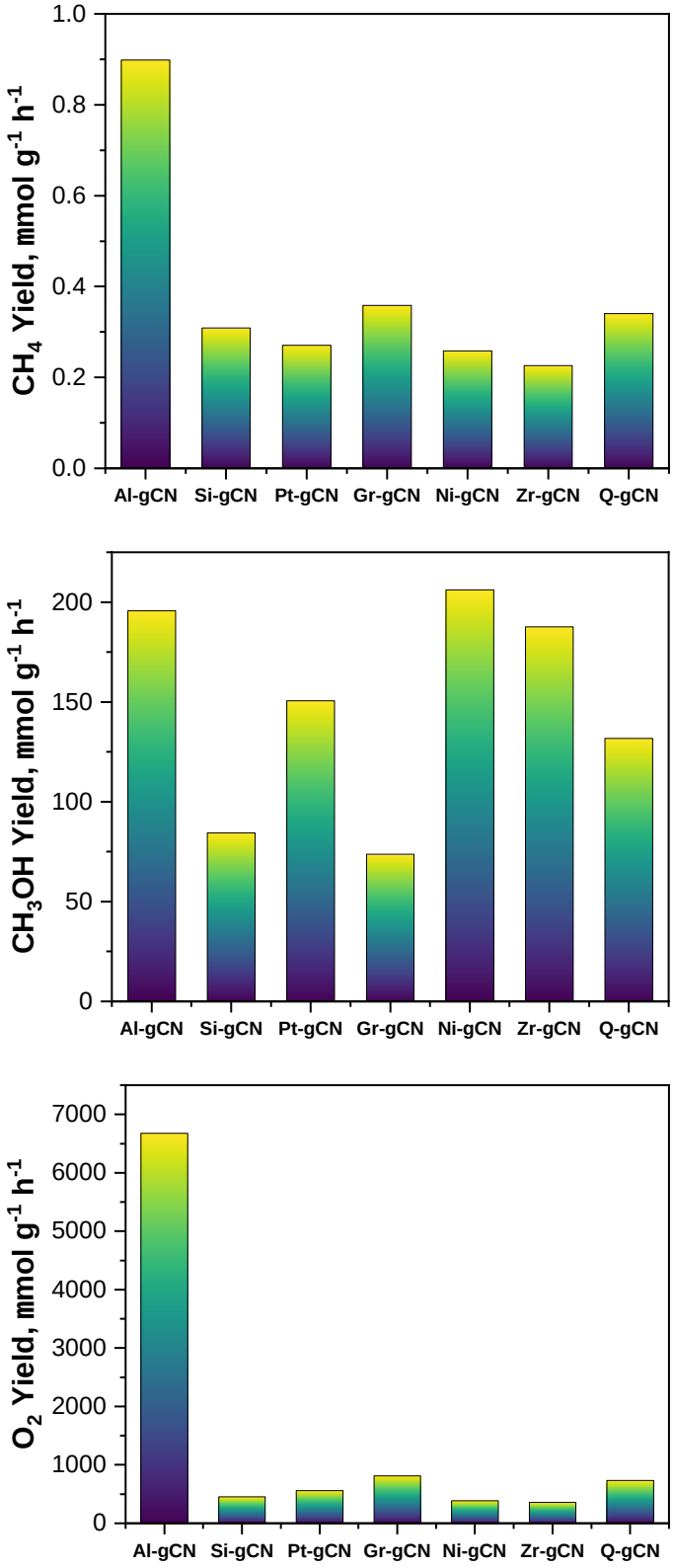

Figure 5.1: Product yields from the reduction of CO_2 over graphitic carbon nitrides, synthesized using various crucibles, activity reported with respect to total surface area.

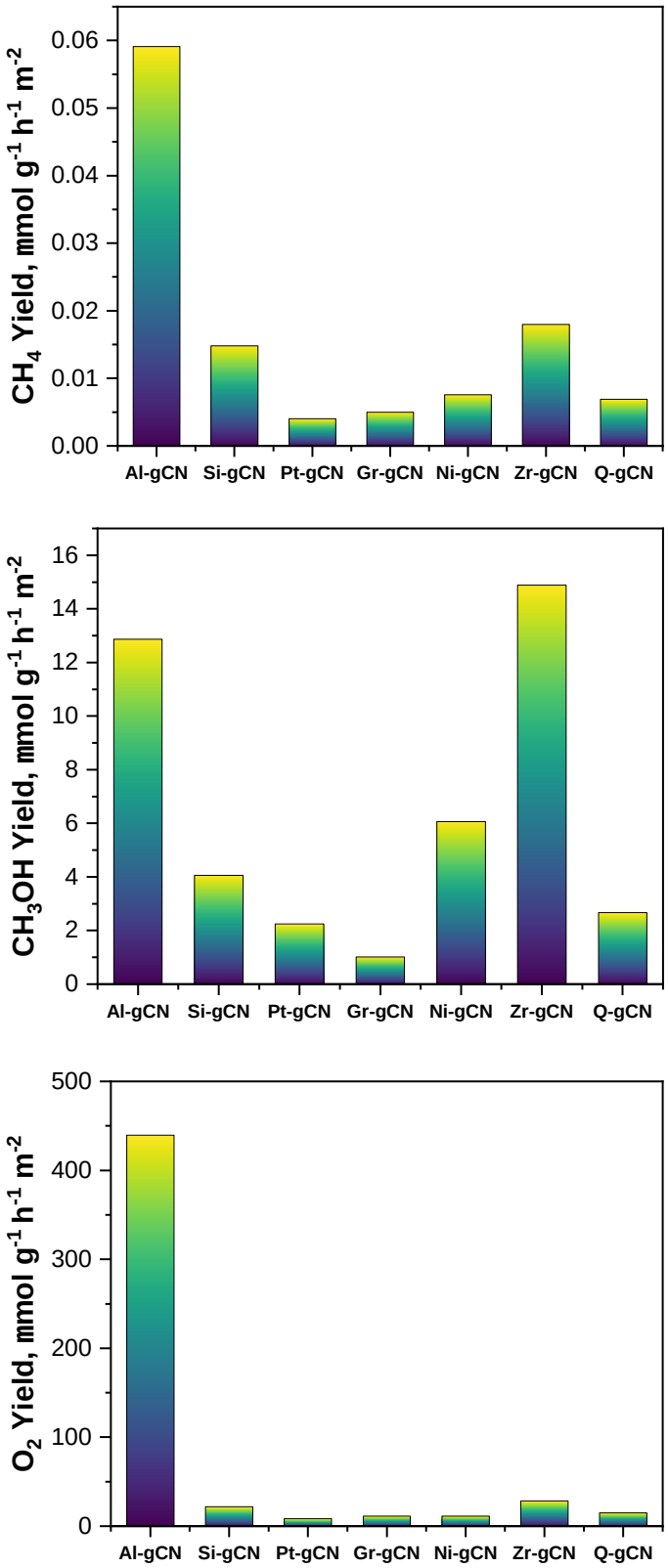

Figure 5.2: Product yields from the reduction of CO_2 over graphitic carbon nitrides, synthesized using various crucibles, activity reported in terms of unit surface area.

initial model was based on the reported crystal structure of $C_{24}H_{12}N_{36}$ (ICSD 194747; Structure: Carbon Nitride Amide; Space Group: $P2_12_12$; Cell: a= 16.4 Å, b= 12.4 Å, c= 6.49 Å, α = 90°, β = 90°, γ = 90°)), which is an orthorhombic crystal system [14]. The refinement process resulted in all single-digit agreement indices, indicating an excellent agreement between the calculated and observed data. The LeBail graph for each precursor-derived carbon nitride is shown in Figure. 5.3.

The XRD data presented in Figure 5.4 and Table 5.1 provide a thorough investigation of the influence of the nature of the crucible on the crystal structure of the g-CN. The presence of reflections corresponding to the (120) and (002) planes in all samples indicates the characteristic layered g-C_3N_4 motif featuring distinct in-plane and interlayer spacings.

XRD analysis confirmed the layered structure of g-C_3N_4 in all samples, as evidenced by the presence of the (120) and (002) reflections. Notably, the peak positions varied across the samples, indicating that the nature of the crucible influenced the stacking arrangement and the lattice parameters of the g-CN layers. The variation in the (002) reflection peak position of the g-C_3N_4 samples grown in different crucibles may be attributed to several factors, despite the absence of the crucible material in the final product. For instance, the interaction of metals with the growing g-C_3N_4 layer during synthesis can affect the interlayer spacing, leading to changes in peak position. Although not directly incorporated, metals such as nickel and platinum, owing to their strong metallic character, might cause slight contraction of the layers compared to other crucibles[15]. Moreover, the thermal conductivity and heat capacity of different crucibles influence the temperature distribution and heating/cooling rates during synthesis, affecting the crystal growth process and leading to variations in strain or lattice defects, which can also influence the peak position[10, 16]. Furthermore, crucibles may release trace amounts of other elements during synthesis even if they are not directly detected. These impurities, even in minute quantities, can subtly alter the g-C_3N_4 structure and affect its peak positions[16, 17]. The surface interactions between the crucible and precursor molecules can also influence the initial nucleation and orientation of the g-C_3N_4 layers, leading to slight differences in the packing arrangements and peak shifts. The observed increase in the peak position from 27.4° to 27.9° may indicate a gradual expansion of the interlayer spacing in the g-C_3N_4 structure, which could be due to increased strain, trace impurity incorporation, or subtle changes in the crystal packing, as discussed above. Crucibles with stronger interactions or higher thermal conductivities, such as platinum and graphite, appear to induce a larger shift, suggesting a more significant influence on the g-C_3N_4 structure.The observed trend shows a general decrease in the interlayer spacing from Al-gCN to Gr-gCN, with a slight increase in Zr-gCN and Q-gCN.

The intralayer spacing of g-C_3N_4, as reflected in the XRD pattern with (120) reflections, exhibited variations in the peak position ranging from 12.8865° to 13.18238°. These variations indicate the structural differences in the material. The interactions between the crucible and the growing g-C_3N_4 layers are influenced by factors such as the thermal conductivity, which affects the layer stacking and intralayer spacing. The expansion of the intralayer spacing is associated with the use of crucibles with higher thermal conductivity, such as Pt and Gr, suggesting their significant influence on the layer stacking and structure of g-C_3N_4. Additionally,

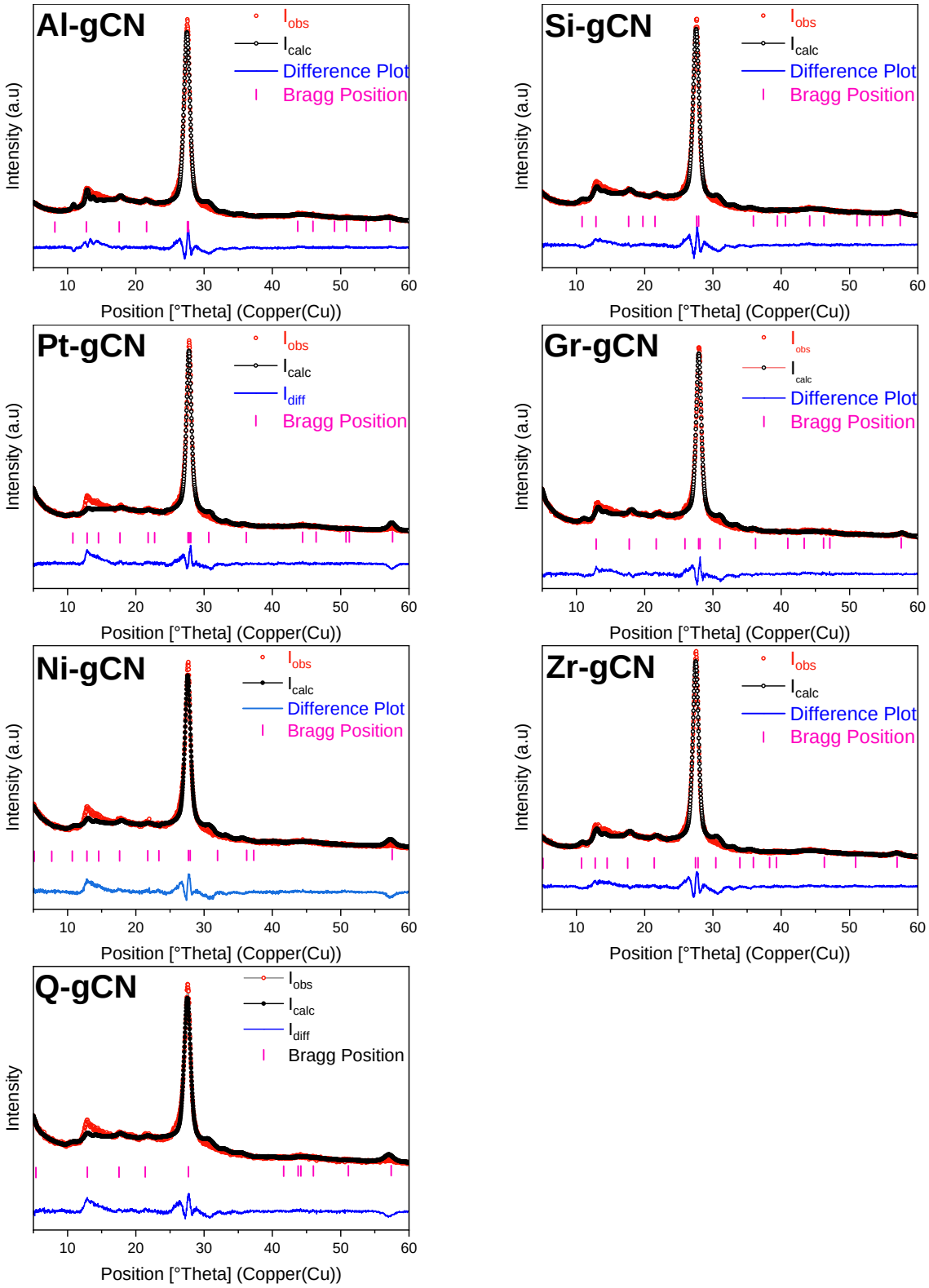

Figure 5.3: LeBail fits of graphitic carbon nitride derived from different crucibles.

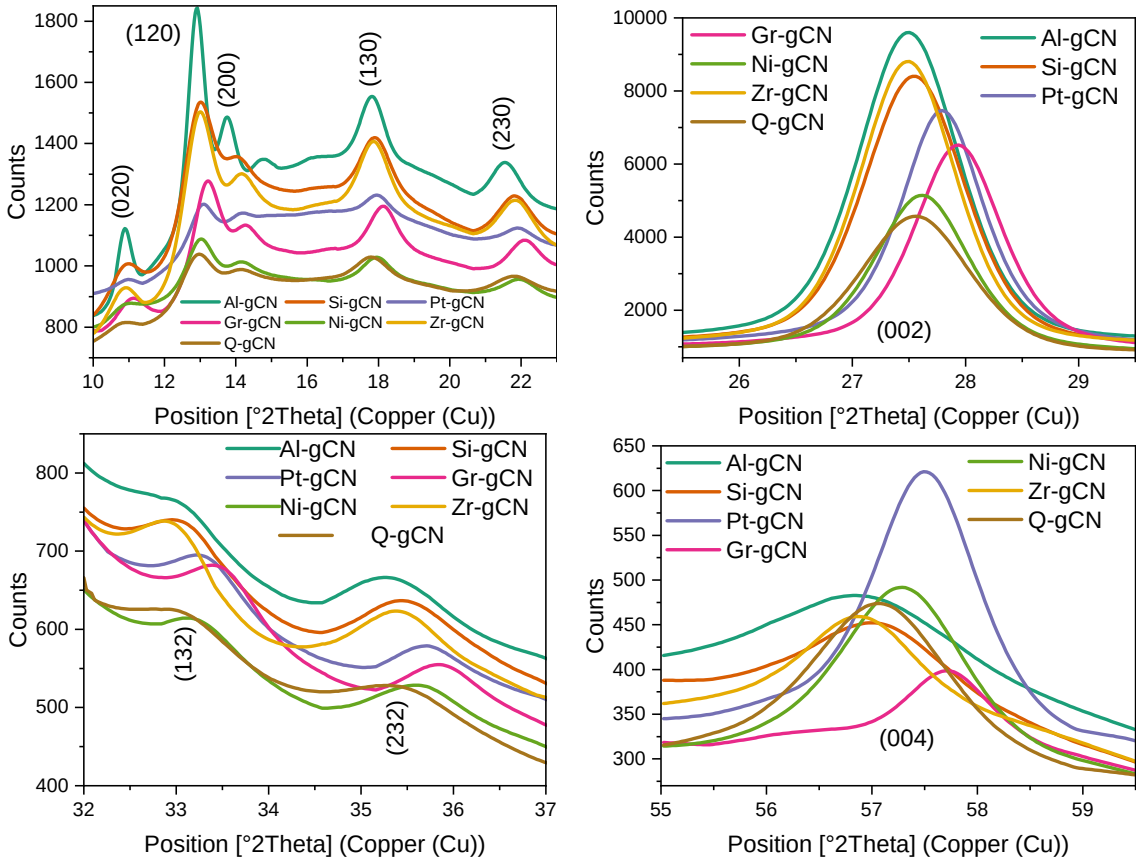

Figure 5.4: X-ray diffractogram of carbon nitrides synthesized from various precursors

although trace impurity release during synthesis is not directly detectable, it also plays a role in altering the intralayer spacing. The general trend of decreasing intralayer spacing from Al-gCN to Gr-gCN suggests compaction of the g-C_3N_4 structure in crucibles with a higher thermal conductivity.

The observed increase in the crystallite size from Si-gCN to Al-gCN and Gr-gCN suggests that these crucibles might facilitate faster crystal growth or the formation of larger nuclei. Crucibles may influence the nucleation and growth kinetics of g-C_3N_4 crystals during synthesis. Crucibles with higher thermal conductivities, such as Pt and Gr, might promote higher growth temperatures, potentially leading to larger crystallite sizes owing to the enhanced mobility and agglomeration of crystal domains. Surface interactions with crucibles can also affect the initial nucleation and orientation of the crystals, which can influence the crystallite size and shape. Trace impurities released from some crucibles, even if not directly detected, can subtly alter the growth process and affect crystallite size.

The trend of diminishing the microstrain from Al-gCN and Si-gCN to Pt-gCN and Gr-gCN suggests that these crucibles promote less defect formation and more stress-free growth in the g-C_3N_4 structure. It is possible that crucibles introduce thermal stress or strain during the growth of g-C_3N_4 owing to the differences in the thermal expansion coefficients. Crucibles with higher thermal conductivities such as Pt and Gr may cause faster heating or cooling, which can generate more strain in the crystal lattice. Additionally, surface interactions with crucibles can induce local lattice distortions and defects, contributing to variations in microstrain. Impurities

Table 5.1: X-ray diffraction data for carbon nitride samples prepared using different crucible

Sample	Position	FWHM	Area	h	k	l	d-spacing	Height	R.I[%]	Crystallite Size	Microstrain
Al-gCN	10.87	0.44	80	0	2	0	8.13147	145	2.56	9.84	2.11
	10.89	0.44	40	0	2	0	8.13112	72	1.27		
	12.88	0.54	325	1	2	0	6.86424	472	8.32		
	12.91	0.55	161	1	2	0	6.86399	234	4.13		
	27.47	1.04	7442	0	0	2	3.24404	5670	100		
	27.54	1.05	3701	0	0	2	3.24398	2815	49.64		
Si-gCN	10.89	0.93557	89	0	2	0	8.1174	77	1.58	7.57	1.82
	10.91	0.935712	44	0	2	0	8.1171	38	0.79		
	12.97	0.946774	355	1	2	0	6.81858	306	6.26		
	13.00	0.946957	177	1	2	0	6.81837	152	3.12		
	27.52	1.046915	6273	0	0	2	3.23751	4887	100		
	27.59	1.047489	3120	0	0	2	3.23747	2429	49.7		
Pt-gCN	10.94	0.803031	27	0	2	0	8.07465	24	0.56	8.81	1.59
	10.97	0.803081	13	0	2	0	8.0745	12	0.28		
	13.04	0.80744	110	1	2	0	6.78325	99	2.28		
	13.07	0.807518	55	1	2	0	6.78314	49	1.14		
	27.76	0.872745	5191	0	0	2	3.21007	4330	100		
	27.83	0.8732	2582	0	0	2	3.21004	2152	49.71		

(Continued)

Sample	Position	FWHM	Area	h	k	l	d-spacing	Height	R.I[%]	Crystallite Size	Microstrain
Gr-gCN	11.08	0.9085	71	0	2	0	7.97	59	1.6	9.39	1.29
	11.11	0.9085	35	0	2	0	7.97	29	0.80		
	13.18	0.9085	285	1	2	0	6.71	239	6.39		
	13.21	0.9085	142	1	2	0	6.71	119	3.18		
	27.91	0.9085	4467	0	0	2	3.19	3743	100		
	27.98	0.9085	2221	0	0	2	3.19	1861	49.73		
Ni-gCN	12.98	0.87	131.7356	1	2	0	6.81	115	4	7.89	1.84
	13.02	0.87	65	1	2	0	6.81	57	1.99		
	27.59	0.98	3689	0	0	2	3.23	2869	100		
	27.66	0.98	1834	0	0	2	3.23	1426	49.7		
Zr-gCN	10.86	0.94	101	0	2	0	8.13	86	1.67	8.09	1.58
	10.88	0.94	50	0	2	0	8.13	43	0.83		
	12.96	0.95	402	1	2	0	6.82	342	6.6		
	13.00	0.95	200	1	2	0	6.82	170	3.28		
	27.47	0.99	6410	0	0	2	3.24	5198	100		
	27.54	0.99	3187	0	0	2	3.24	2584	49.72		
Q-gCN	10.79	0.98	32	0	2	0	8.18	26	1.08	7.08	1.98
	10.82	0.98	16	0	2	0	8.18	13	0.54		
	12.90	0.99	134	1	2	0	6.85	108	4.39		
	12.93	0.99	66	1	2	0	6.85	53	2.18		
	27.53	1.11	3434	0	0	2	3.23	2472	100		
	27.60	1.11	1707	0	0	2	3.23	1228	49.7		

introduced by crucibles or precursor materials can disrupt the growth process and lead to lattice defects and local strain. Furthermore, variations in crystallite size can influence microstrain because smaller crystallites generally exhibit higher levels of strain owing to their larger surface-area-to-volume ratio.

The (002) reflection area of a material can offer insights into its crystallinity, orientation, and layer stacking order. A larger area is generally indicative of better crystallinity, preferred orientation, and organized layer-stacking arrangement. Al-gCN demonstrates an exceptionally high (002) reflection area, indicating an extraordinary degree of crystallinity, preferred orientation, and an orderly layer stacking arrangement. In contrast, Gr-gCN displayed the lowest (002) reflection area, suggesting a lower degree of crystallinity, less favored orientation, and potentially disordered layer stacking. The (002) reflection areas for Si-gCN and Zr-gCN were relatively high, indicating good crystallinity and a well-organized layer-stacking arrangement. Pt-gCN, Ni-gCN, and Q-gCN exhibited moderate (002) reflection areas, implying a balanced level of crystallinity and an organized layer-stacking arrangement.

The (120) reflection area in g-C_3N_4 may provide insight into the stacking order and domain size of aromatic carbon nitride layers. Generally, a larger area suggests more ordered stacking and larger in-plane crystallite size. Zr-gCN demonstrated the highest (120) reflection area, indicating highly ordered in-plane stacking and potentially a larger crystallite size. The results of the XRD analysis revealed that Si-gCN exhibited the second highest (120) reflection area, which suggests a well-ordered stacking pattern and a potentially large crystallite size. On the other hand, Al-gCN and Gr-gCN showed moderate 120 reflection areas, indicating moderate levels of order and crystallite size. Notably, Pt-gCN, Ni-gCN, and Q-gCN displayed the lowest (120) reflection areas, suggesting less ordered stacking and potentially smaller crystallite sizes.

Notably, the (020) peak was present in all the g-C_3N_4 samples, except for Ni-gCN. This can be attributed to the specific layer-stacking orientation of the crystal structure in a particular direction. The absence of this peak in Ni-gCN warrants further investigation to elucidate its underlying cause. It is possible that the Ni-gCN sample exhibited a preferred orientation, where the planes responsible for the (020) reflection were less exposed to the X-ray beam, resulting in a significantly weaker or undetectable peak. This could be due to the specific interaction between the Ni crucible and g-C_3N_4 layers during synthesis, which influences the crystal growth and orientation. Ni-gCN may exhibit less ordered stacking of the g-C_3N_4 layers, leading to the broadening or even disappearance of the (020) peak owing to the loss of long-range crystalline order. This could be related to factors such as faster growth in the Pt-gCN crucible, potentially causing less ordered stacking due to rapid temperature changes.

The d-spacing of the (020) plane differed slightly among the g-C_3N_4 samples prepared in various crucibles. This observation likely reflects variations in the layer-stacking arrangement within the crystal structure. Al-gCN and Q-gCN displayed the largest d-spacing values, suggesting a slightly larger interlayer distance along the (020) plane compared to the other samples. Conversely, Gr-gCN exhibited the smallest d-spacing, indicating a potentially denser packing of the layers in this direction. Pt-gCN and Si-gCN exhibited intermediate d-spacing values.

The relative intensities of the (020) plane in the g-C_3N_4 samples provided

additional insights into their structure and the potential impact of the crucibles. Al-gCN exhibits the highest relative intensity, which suggests the strongest (020) reflection and potentially the most ordered stacking or preferred orientation of planes contributing to this peak. Si-gCN, Zr-gCN, and Gr-gCN showed moderate intensities, indicating moderate levels of order or orientation related to the (020) plane. Pt-gCN and Q-gCN have the lowest intensities, which suggests weaker reflections and potentially less preferred orientation or less ordered stacking along this direction.

Analyzing the data on d-spacing and relative intensity can provide a more comprehensive understanding of layer stacking and arrangement within the samples. Al-gCN and Q-gCN, which have a slightly larger d-spacing and higher intensities, may exhibit a specific and well-defined stacking arrangement that leads to strong (020) reflections. However, Gr-gCN, which has the smallest d-spacing and moderate intensity, may display a slightly different packing arrangement compared to the other samples. Pt-gCN and Ni-gCN, which have lower d-spacings and weaker intensities, may have less ordered stacking or a less preferred orientation related to the (020) plane.

Notably, two prominent peaks emerged during the Rietveld refinement of the g-C_3N_4 samples. The presence of these peaks near the (002) and (120) reflections suggests the possibility of real doublet peaks arising from either twinned crystals or imperfections in the crystal structure. The twinned crystals may result in slightly shifted reflections, owing to the different orientations of the twin domains. However, imperfections or dislocations within the crystal structure can lead to local lattice distortions, resulting in the formation of doublet peaks. Moreover, significant microstrain variations across different crystal domains can contribute to the broadening of the reflections, appearing as shoulders or doublets.

	Al-gCN	Si-gCN	Pt-gCN	Gr-gCN	Ni-gCN	Zr-gCN	Q-gCN
Space Group	$P2_12_12$						
Crystal System	Orthorhombic						
a (Å)	12.71	12.48	12.46	12.41	12.33	12.45	12.45
b (Å)	15.99	16.00	16.02	15.97	15.94	16.14	16.16
c (Å)	6.44	6.44	6.40	6.39	6.40	6.46	6.44
α, β, γ (°)	90						
Rexp	3.06	3.78	3.90	4.07	4.23	3.82	4.26
Rp	6.28	5.59	6.21	5.30	6.13	5.82	6.13
Rwp	8.56	7.57	9.40	7.01	8.85	7.99	8.74
GOF	7.79	4.01	5.80	2.96	4.37	4.37	4.19

Table 5.2: Pertinent crystallographic data for graphitic carbon nitride synthesized using different crucibles. The table presents essential crystallographic parameters, including the space group, crystal system, unit cell parameters (a, b, c, α, β, γ), as well as R-factors (R_{exp}, R_p, R_{wp}) and the Goodness of Fit (GOF).

The lattice parameters exhibit variations along the a-axis, b-axis, and c-axis (Table 5.2). The a-axis values range from 12.33 Å in Ni-gCN to 12.71 Å in Al-gCN, which suggests potential differences in the in-plane packing arrangement of the

g-C_3N_4 layers. This could be attributed to the crucible material. The b-axis values show less variation, with the smallest value in Ni-gCN (15.94 Å) and the largest in Zr-gCN (16.14 Å), indicating generally consistent interlayer spacing but with subtle differences that could impact the overall structure. The c-axis values also vary moderately, ranging from 6.39 Å in Gr-gCN to 6.47 Å in Zr-gCN, reflecting changes in the stacking distance between adjacent layers, which could be influenced by interactions with the crucible materials.

The various lattice parameters of the g-C_3N_4 samples reveal significant differences in their crystal structures. Al-gCN demonstrated the largest a-axis and c-axis, indicating a more expanded structure than the other samples. This can be attributed to its high thermal conductivity, which promotes faster growth and larger crystallites. In contrast, Ni-gCN exhibits the smallest a-axis, suggesting a more compact in-plane packing arrangement. This could be associated with the strong metallic character, which may interact with the g-C_3N_4 layers and affect their structure. Zr-gCN exhibited the largest b-axis and c-axis, suggesting a slightly expanded interlayer spacing and stacking distance. This may be due to their distinct properties compared to other metals, which could influence the growth process differently. These variations in the lattice parameters highlight the crucial role of the crucible material in determining the crystal structure of g-C_3N_4. This has significant implications for understanding and optimizing the properties of these materials for various applications.

The relationship between the crystallite size and methane yield appears to be positive, as larger crystallite sizes are typically associated with higher methane yields. Al-gCN and Zr-gCN exhibit the largest crystallite sizes and highest methane yields. However, it is important to consider other factors, such as the microstrain and potentially specific characteristics of the Gr-gCN material, which might contribute to its lower methane yield despite its relatively large crystallite size. This suggests that well-organized layer stacking may enhance CO_2 adsorption and conversion, leading to increased methane production.

There is an apparent positive relationship between the (002) peak area, which is indicative of crystallinity, layer stacking order, and methane yield. Generally, samples with higher (002) peak areas exhibit higher methane yields. However, there are a few exceptions. For instance, Si-gCN, despite having a moderately high (002) peak area, exhibited a relatively low methane yield. In contrast, Gr-gCN and Q-gCN did not have the lowest methane yields, although their (002) peak areas were lower. A higher peak area for the (002) diffraction pattern suggests that the layers within the material are more well-organized and ordered, potentially providing a greater number of active sites and facilitating the efficient adsorption and conversion of CO_2 into methane. However, exceptions indicate that factors other than crystallinity may also play a role in determining methane yield. These factors could include microstrain, defects or impurities, and specific surface properties, such as variations in the surface area, porosity, and distribution of active sites, which can affect the accessibility of CO_2 molecules and influence methane production.

A positive association was observed between the crystallite size and methanol yield. Al-gCN and Zr-gCN, which exhibit the largest crystallite sizes, have the highest methanol yields. In contrast, Gr-gCN, which had the smallest crystallite size, had the second-lowest methanol yield. This trend suggests that the larger

crystallites provide more active sites for the conversion of CO_2 into methanol. It is worth noting that the relationship between the microstrain and methanol yield is less straightforward. Although Al-gCN and Zr-gCN have high methanol yields and relatively low microstrains, Si-gCN, with a moderate methanol yield, exhibits a low microstrain. Pt-gCN, with a low methanol yield, exhibited a moderate microstrain.

Similar to the methanol yield, there seems to be a positive correlation between larger crystallite size and higher oxygen yield. Al-gCN and Zr-gCN with the largest crystallite sizes and highest (002) peak areas also have the highest oxygen yields. This suggests that the larger and well-organized g-CN layers might provide more active sites for the desired reaction pathways involved in oxygen production. Similar to the methanol yield, the relationship between the microstrain and oxygen yield is less clear. While Al-gCN and Zr-gCN have high oxygen yields and relatively low microstrain, Si-gCN, with moderately high oxygen yield, has low microstrain, and Pt-gCN, with low oxygen yield, has moderate microstrain. Further investigations are needed to understand the nuanced role of microstrains in oxygen production.

The consistent interlayer distances observed across all the samples suggest that the fundamental building blocks of the g-CN layers remain largely unaffected by the nature of the crucibles (Figure 5.5). However, the variations in the intralayer packing and stacking arrangements highlight the potential of tailoring the structure of the g-CN materials by selecting appropriate crucibles.

5.2.3 Adsorption Isotherm Analysis

The nitrogen adsorption-desorption isotherms of all carbon nitride samples were classified as type III, indicating weak adsorbate-adsorbent interactions, the presence of adsorbed N_2 in the interlayer, or the presence of porous structures in the samples (Figure 5.6)[18–20]. The isotherms display type H3 hysteresis loops at $0.45 < \frac{p}{p_0} < 1.00$, a characteristic often observed in aggregates of plate-like particles, suggesting the existence of slit-shaped pores. The average pore sizes of all the carbon nitride samples were in the mesoporous regime. The results of the t-plot analysis revealed

	B.E.T SA	C
Al-gCN	11.86	-52.35
Si-gCN	15.21	-34.41
Pt-gCN	63.77	-242.77
Gr-gCN	70.25	-959.38
Ni-gCN	18.76	-37.09
Zr-gCN	14.39	-46.23
Q-gCN	46.04	-145.22

Table 5.3: B.E.T surface area and C values for graphitic carbon nitrides synthesized using different crucibles

that Pt-gCN exhibited the largest microporous area among all the g-CN samples (Pt-gCN > Q-gCN > Ni-gCN > Gr-gCN > Si-gCN > Al-gCN > Zr-gCN). When comparing the percentage of microporous area to the total surface area, it was observed that Al-gCN had the highest percentage, followed by Si-gCN, Zr-gCN, Ni-gCN, Q-gCN, Pt-gCN, and Gr-gCN. As anticipated, the quantity of adsorbed gas was highest in Gr-gCN because of its higher surface area. As the surface area increased,

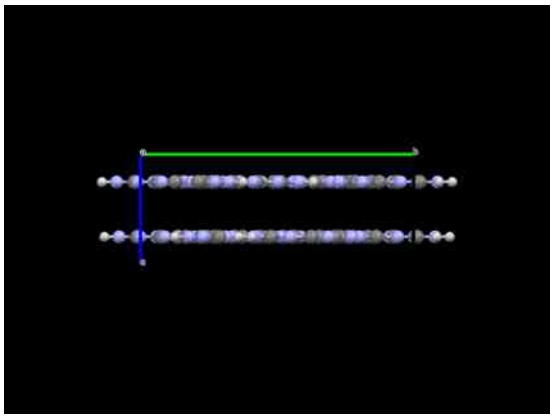

(a) 2D Layer Structure of Al-gCN

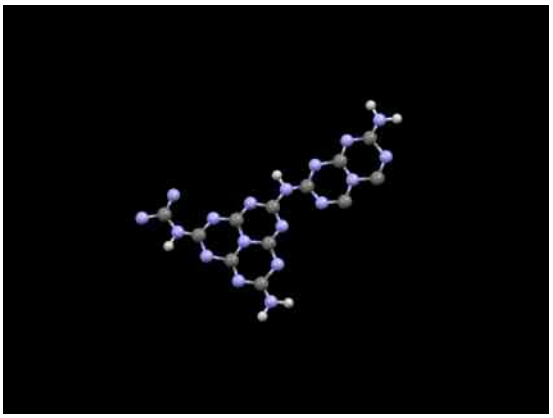

(b) Asymmetric Structure of Al-gCN

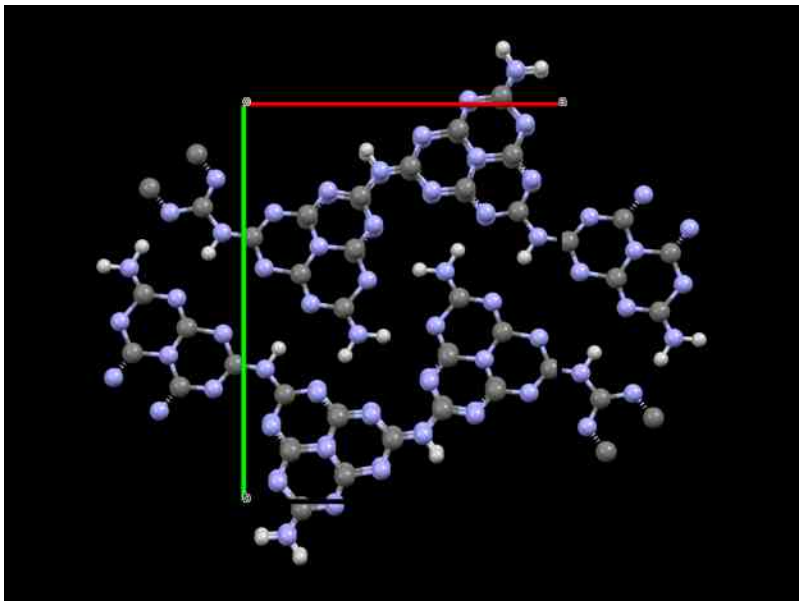

(c) Packing Structure of Al-gCN

Figure 5.5: Structural Features of Al-gCN: (a) 2D Layer Structure, (b) Asymmetric Structure, and (c) Packing Structure.

the quantity of the adsorbed gas also increased. The surface area of the sample was calculated using the B.E.T equation, as shown in Table 5.3. The B.E.T equation is often rearranged to linearize the isotherm and determine the slope and intercept of a specific plot. If the resulting value of C is negative, the linearized plot does not fit the assumed B.E.T model well [21]. This could be due to various reasons such as the non-ideal behavior of the adsorbate or limitations in the applicability of the BET model to a specific adsorption system. A negative C value suggests that the BET model may not accurately describe the adsorption isotherm for a given material or condition [22]. It is essential to interpret such results cautiously and consider alternative models or factors that might affect adsorption behavior [23–26]. All g-CN samples show negative C values, indicating that they do not follow the B.E.T equation, or corrections in the BET equation are recommended according to the Rouquerol equation [27]. The surface area data were fitted using BETSI and SESAMI techniques, and the results are presented in Table 5.4. Almost the same surface area was observed after correction; however, as the microporosity

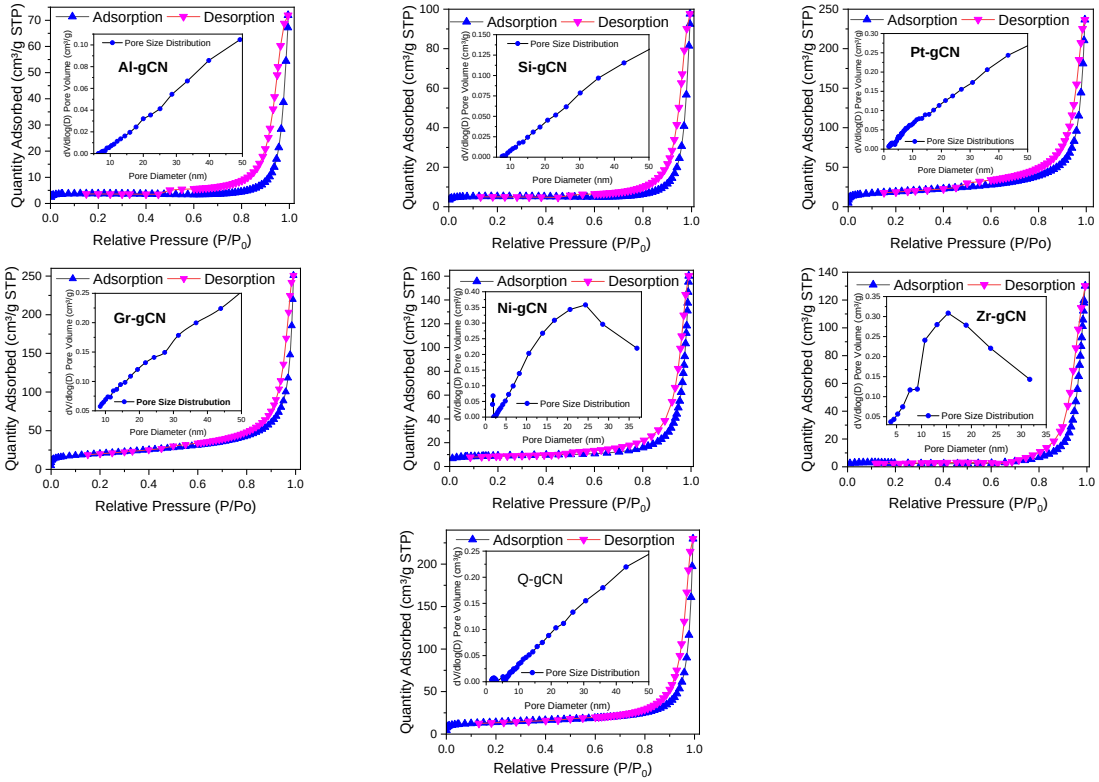

Figure 5.6: N_2 adsorption isotherms of graphitc carbon nitride synthesized from various crucibles

increased, the deviation became too large. In addition, it is well known that the B.E.T equation is not suitable for microporous materials or materials containing large numbers of micropores.

Surface Area, m^2/g				
	B.E.T	**BETSI**	**SESAMI**	C**, SESAMI**
Al-gCN	11.86	15	15.2	1093
Si-gCN	15.21	21	20.8	948.6
Pt-gCN	63.77	67	67	423.7
Gr-gCN	70.25	73	72.2	335.4
Ni-gCN	18.76	34	34	515.9
Zr-gCN	14.39	13	12.6	512.3
Q-gCN	46.04	50	49.4	530.7

Table 5.4: Recalculated surface area of g-CN samples using BETSI and SESAMI

The study of the surface area and porosity data, primarily utilizing the SESAMI method, yielded valuable insights into the relationship between these properties and the observed CO_2 reduction activity of g-CN samples (Table 5.5). This comprehensive interpretation considers the previously presented crystallographic data. Al-gCN show highest crystallinity, % microporous percentage and C value, and show higher activity towards methane, methanol and oxygen production. Zr-gCN showed higher methane and oxygen yields than Al-gCN and the highest methanol yield. In the case of Zr-gCN, the c value is almost half that of Al-gCN and Si-gCN.

	q_m, mol/kg	Pore Size, nm	t-plot M.A	% micropore
Al-gCN	0.16	37.53	12.43	81.78
Si-gCN	0.21	39.74	14.69	70.65
Pt-gCN	0.69	22.97	18.74	27.97
Gr-gCN	0.74	22.08	15.86	21.97
Ni-gCN	0.35	27.98	15.88	46.7
Zr-gCN	0.13	22.93	8.09	64.2
Q-gCN	0.51	30.88	16.89	34.19

Table 5.5: Quantity of gas asorbed, pore size and microporous properties of g-CN samples synthesized in various crucibles

The SESAMI method quantifies the interaction potential between the adsorbate and adsorbent surface by calculating C. A higher C value signifies stronger interactions, which can enhance CO_2 adsorption and activation. Al-gCN displayed the highest C value among the samples, which likely contributed to its exceptional CO_2 conversion performance. Enhanced micropore accessibility facilitates efficient CO_2 adsorption and interaction with active sites, contributing to the superior activity of Al-gCN towards methane, methanol, and oxygen yields. The results of this study suggest that the Brunauer–Emmett–Teller (B.E.T) surface area is not a reliable indicator of catalytic performance. Gr-gCN and Pt-gCN, which had the highest B.E.T surface areas, exhibited the lowest CO_2 conversion activity.The remarkable characteristics of Zr-gCN, specifically its high microporosity and crystallinity, may contribute to its ability to facilitate CO_2 reduction. Si-gCN showed a high C value as well as moderate crystallinity, and exhibited appreciable efficiency in methane and methanol production. In the case of methanol production, Ni-gCN exhibited moderate activity, which may be attributed to the higher % microporosity.

It is hypothesized that the reduced micropore volume and percentage of Gr-gCN and Pt-gCN limit the availability of active sites for CO_2 adsorption, thereby hindering overall activity. Although the pore sizes of all the samples were within the mesoporous range ($22\,\mathrm{nm}$ to $40\,\mathrm{nm}$), variations in their pore size distribution could affect the diffusion of CO_2 and accessibility to active sites. Further research using advanced adsorption isotherms is necessary to fully understand the relationship between the pore size distribution and catalytic performance.

The complex and multifaceted relationship between crystallinity and surface area suggests that other factors such as the formation of defects and surface chemistry significantly influence the overall surface properties of a material.

5.2.4 Derivative Adsorption Summation

In gas adsorption analysis, assessing the surface heterogeneity typically entails acquiring a significant number of experimental data points at low relative pressures, usually less than 0.15, during which monolayer filling occurs. The free energy of adsorption on the kT scale can be accurately determined by calculating the derivatives of the adsorption amount relative to the logarithm of the relative pressure, $(\ln(P/P_0))$[28, 29]. Figure 5.7 shows the derivative curve obtained from the $77\,\mathrm{K}$ nitrogen adsorption isotherm, which illustrates the gas adsorption energy on the surface. The second derivative was used to distinguish between the peaks

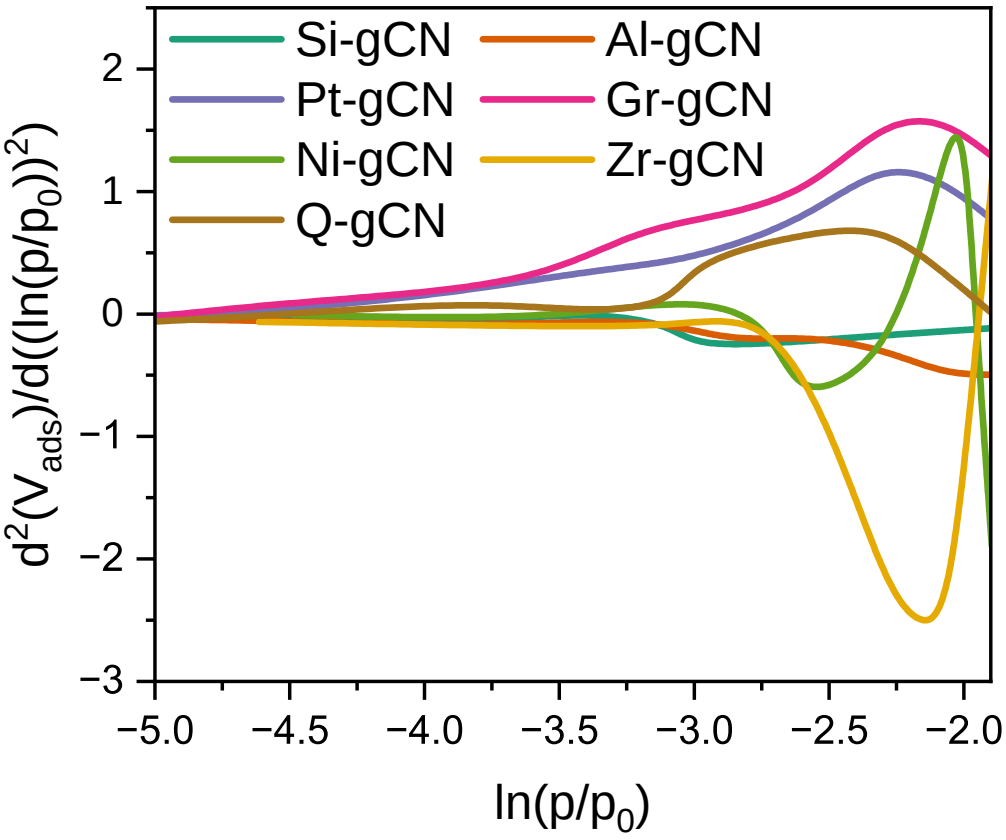

Figure 5.7: Second derivative isotherm summation (SDIS) plot of g-CN samples synthesized using various crucibles.

and shoulders in the derivative isotherm summation (DIS) plots. In the second-derivative isotherm summation (SDIS), noticeable peaks are observed as downward dips in the curve. This was because the DIS curve represented the second derivative of the adsorption isotherm. The minima in the second derivative correspond to the maxima in the original isotherm and represent the strongest binding sites. Two-dimensional materials are characterized by basal, edge, and high-energy adsorption surfaces, which correspond to low, medium, and high energies, respectively, [28, 29].

The second derivative, depicted in Figure 5.7 from the DIS, indicates that Gr-gCN, Q-gCN, and Pt-gCN exhibit significant peaks in the low-energy regime or in the area corresponding to the basal planes. The peak exhibited by Zr-gCN was broader, indicating dynamic adsorption behavior and the presence of moderate energy regimes, such as edge sites on the surface. The downward deviations in Ni-gCN, Si-gCN, and Al-gCN suggest the presence of moderate energy surfaces or edge sites. In the case of Zr-gCN, the edge sites dominate and display considerable activity towards methane and methanol production. The number of edge sites in Al-gCN was lower than that in Zr-gCN. The activity of Al-gCN can be attributed to the combined effect of high C values and moderate edge sites. It is worth noting that the oxygen evolution was also high in Al-gCN and Zr-gCN.

Sample	Element	Weight %	MDL	Atomic %	Net Int.	Error %
Al-gCN	C K	43.6	0.1	47.5	1758.3	9.2
	N K	54.9	0.3	51.3	593.9	11.1
	O K	1.5	0.2	1.2	25.8	19.3
	Al K	0.1	0.01	0	29.4	12.8
Si-gCN	C K	51	0.19	54.9	1152.6	9.3
	N K	48.8	0.75	45	243.5	11.8
	O K	0.1	0.35	0.1	0.8	100
	Si K	0.1	0.03	0	18.3	23.7
Pt-gCN	C K	62.7	0.2	66.6	777.9	8.6
	N K	36	1	32.8	79.9	12.6
	O K	0.8	0.45	0.6	4.4	32.6
	Pt L	0.6	0.6	0	2.6	54.8
Gr-gCN	C K	46.7	0.14	50.6	1451.7	9.2
	N K	53	0.47	49.2	403.2	11.3
	O K	0.2	0.25	0.2	3.1	89.7
Ni-gCN	C K	52.2	0.19	56.1	1163.1	9.3
	N K	47.7	0.78	43.9	227.3	11.8
	O K	0.1	0.36	0.1	0.6	100
	Ni K	0.1	0.08	0	3.8	59.9
Zr-gCN	C K	52.2	0.19	56.1	1163.1	9.3
	N K	47.7	0.78	43.9	227.3	11.8
	O K	0.1	0.36	0.1	0.6	100
	Ni K	0.1	0.08	0	3.8	59.9
Q-gCN	C K	54.9	0.06	59	4154.1	9
	N K	41.6	0.28	38.3	646.8	11.5
	O K	3.4	0.14	2.7	114.8	15
	Si K	0	0.01	0	44.1	8.5

Table 5.6: Elemental analysis data of graphitic carbon nitride (gCN) samples synthesized using various crucibles

5.2.5 Field Emission Scanning Electron Microscopy (FESEM)

FESEM images offer valuable insights into the morphological characteristics of graphitic carbon nitride (g-CN) samples prepared using various crucibles. These images revealed distinctive surface structures consistent with crystalline and grain size variations, as confirmed by X-ray Diffraction (XRD) analysis. The porous nature of the samples, determined by adsorption analysis, was also evident in the FESEM micrographs.

The XRD data provided further evidence of the crystalline nature of the materials, which was also demonstrated by the FESEM images. Notably, the FESEM images of Gr-gCN, Pt-gCN, and Q-gCN show low density, reduced crystallinity, and a porous structure. The pore size and distribution, which are essential aspects of the material porosity, are shown in Figure 5.8. The presence of well-defined pores with a relatively uniform distribution aligns with the adsorption analysis findings, which quantify the porosity of the samples. The need to add more material for B.E.T analysis to attain a specific weight highlights the porous nature of Gr-gCN,

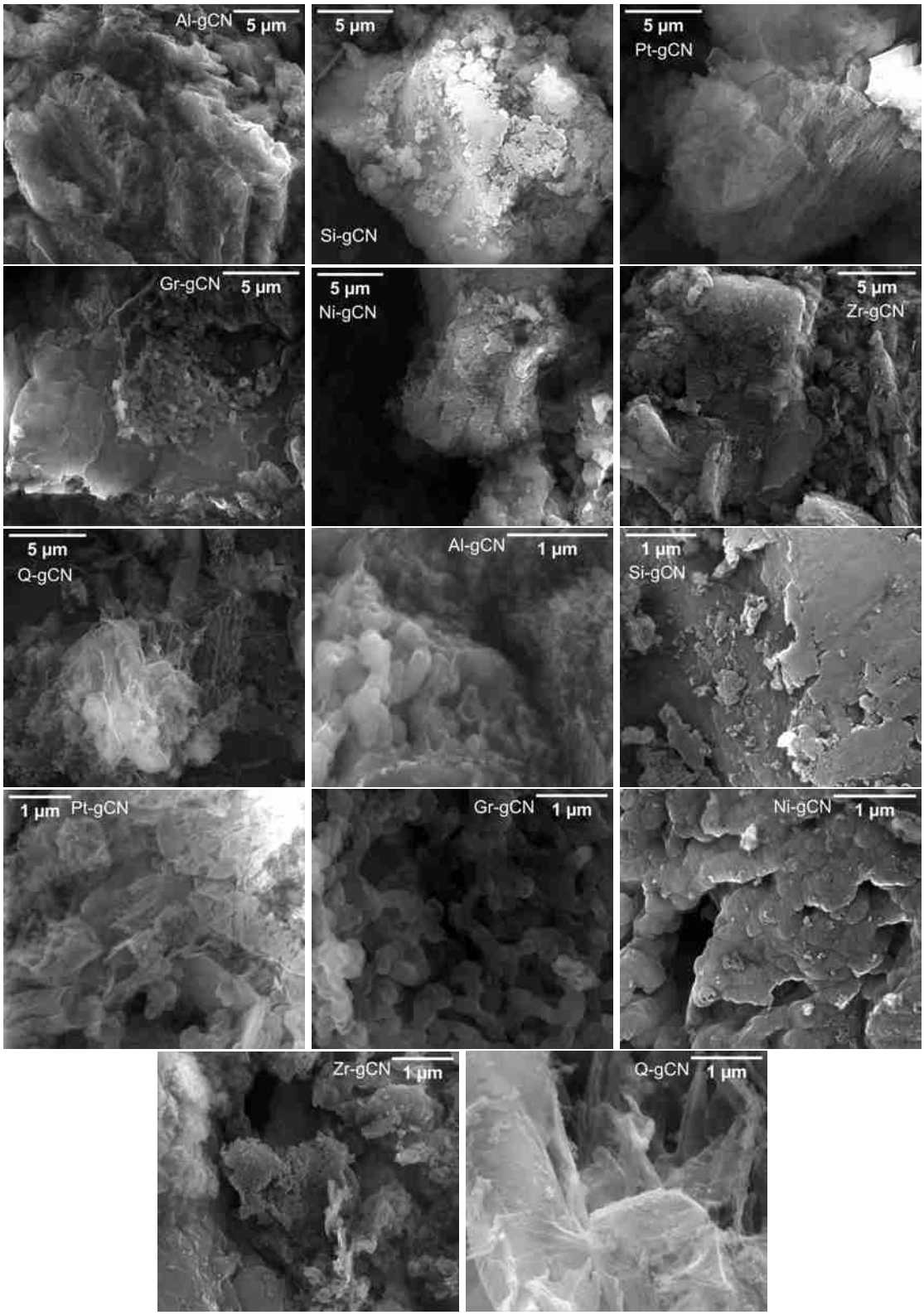

Figure 5.8: Field Emission Scanning Electron Microscopy (FESEM) images of the carbon nitride samples synthesized using various crucibles at $5\,\mu\mathrm{m}$ and $1\,\mu\mathrm{m}$ image resolutions.

Pt-gCN, and Q-gCN, implying a higher surface area compared to the other samples.

The distribution of the particle sizes in the samples is depicted in Figure 5.8, revealing both individual particles and clusters, indicating varying levels of agglomeration. The agglomerated regions may affect the overall structural integrity and properties of the material.

The surface characteristics and particle arrangements of the material exhibited heterogeneity, as shown in Figure 5.8, implying localized differences in the synthesis process.

The low density of the Gr-gCN, Pt-gCN, and Q-gCN samples makes them adhere to the mortar and pestle during the mortaring process, which presents a unique challenge. Although no additional force is required for mortaring, their removal is difficult because of their adhesion. Notably, Figure 5.8 illustrates that the grain sizes in all the other samples were larger than those in Gr-gCN, Pt-gCN, and Q-gCN.

High-resolution Scanning Electron Microscopy (HRSEM) images demonstrate the alterations in material properties that result from the use of different crucibles, as well as the effects of the thermal expansion coefficient and heating and cooling rates on these properties when the same precursor is employed.

5.2.6 Energy Dispersive X-ray Analysis (EDXA or EDAX)

Energy-dispersive X-ray Analysis (EDAX) was utilized to analyze the elemental composition of graphitic carbon nitride (g-CN) samples made using various crucibles (Table 5.6). The primary goal was to evaluate the elemental compositions of the synthesized materials and assess the potential effect of crucible choice on their composition.

All the samples primarily comprised carbon (C) and nitrogen (N), confirming the gCN structure. The nitrogen content displayed some variation, with Al-gCN having the highest (54.9 wt%) and Pt-gCN having the lowest (36 wt%). Oxygen (O) was also detected in varying amounts, but its significance was uncertain because of the relatively high error percentages exceeding 30% for Gr-gCN, Ni-gCN, and Zr-gCN.

Notably, trace amounts of elements related to the crucibles were observed in some samples. Al-gCN contained detectable aluminum (0.1 wt%), Si-gCN had measurable silicon (0.1 wt%), and Pt-gCN showed trace platinum (0.6 wt%), although the latter's significance was questionable due to its high error. Conversely, no Si was detected in Q-gCN despite the use of a Si crucible, potentially suggesting different interaction mechanisms with the substrate compared to other crucibles.

The quantitative significance of certain elements, particularly oxygen, is limited by their high error percentages. The localized elemental analysis provided by EDAX must be considered along with the potential variations in the distribution of elements within the samples. To gain a more comprehensive understanding of the surface composition and chemical state of the elements, complementary characterization techniques such as XPS are necessary.

The EDAX analysis revealed that the elemental compositions of the gCN samples synthesized with different crucibles were dissimilar. While C and N were the primary constituents in all the samples, variations in the O content and the presence of trace crucible elements were observed. Although the error percentages for some elements limited definitive conclusions, the findings suggest that the choice of

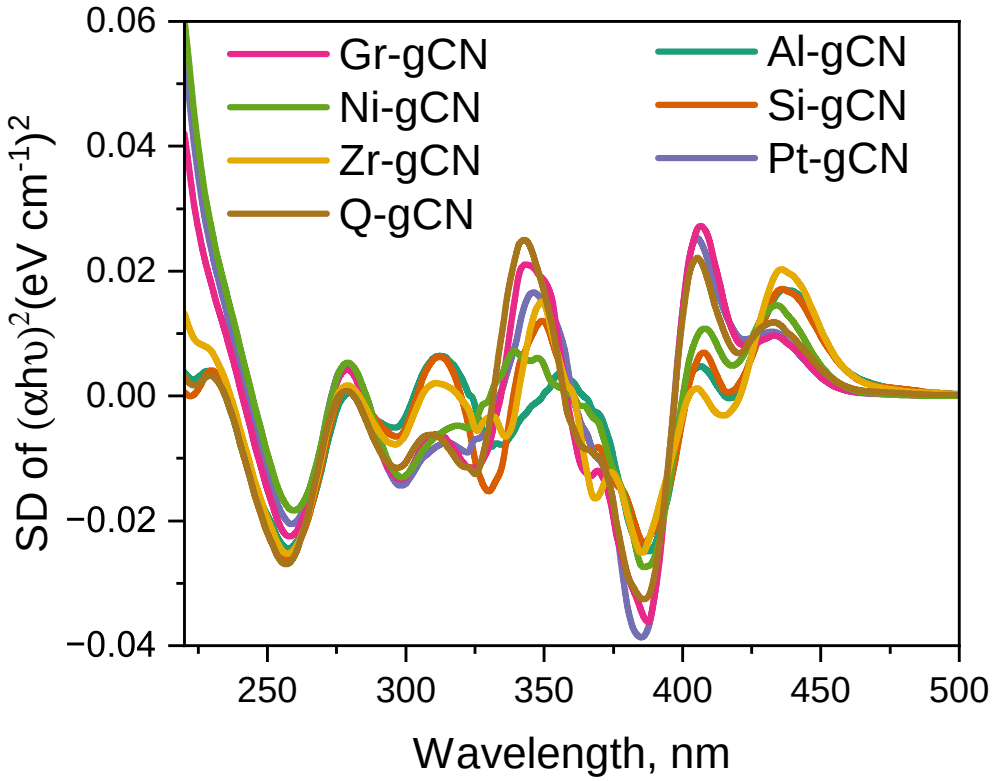

Figure 5.9: Second derivative Tauc plot for carbon nitrides synthesized in various crucibles

crucible might influence the composition of the gCN materials. Further investigations, including additional characterization techniques and correlation studies with catalytic properties, are recommended for a more detailed understanding of the relationship between the synthesis conditions and the structure and function of the gCN materials.

5.2.7 Solid State Ultraviolet-Visible Spectroscopy

Further insights into solid-state UV-visible spectroscopy of carbon nitrides can be found in detail in Chapter 4.2.7 of this thesis. The observations and analyses presented provide a comprehensive foundation for subsequent discussions in this chapter. For a thorough understanding of the experimental setup, results, and interpretation, readers are referred to the relevant sections in Chapter 4.

The results from the second derivative Tauc plot of the carbon nitride samples indicate that there are two distinct absorption maxima, one at $404\,\mathrm{nm}$ to $408\,\mathrm{nm}$ and another at $432\,\mathrm{nm}$ to $437\,\mathrm{nm}$. These findings suggest several potential explanations that are worth exploring.

One possible explanation is that the second absorption maximum (SAM) arises from the presence of shallow defect states within the bandgap [30, 31]. These defects can be attributed to factors such as vacancies, interstitials, or dopants[32]. The energy difference between the SAM and the main absorption edge, which is approximately $0.25\,\mathrm{eV}$ to $0.3\,\mathrm{eV}$, provides information regarding the energy level of the defect state. In this case, the shallow defect state was situated approximately $0.25\,\mathrm{eV}$ to $0.3\,\mathrm{eV}$ above the valence band [33]. Examining the shape and intensity

of SAM can provide further insights into the type of electronic transition associated with the defect state. This analysis can help identify whether the transition is allowed directly, allowed indirectly, or forbidden.

The decrease in the second-derivative signal as it approaches higher energies could be a result of band tailing, which is a phenomenon that arises owing to disorder or structural imperfections in the material[34–36]. This leads to fluctuations in the potential energy and creation of states within the bandgap[37, 38]. Analysis of the slope and energy distribution of the tail can provide valuable information about the type and extent of disorder in the material[39].

It is important to note that SAM may sometimes be related to phonon sidebands resulting from lattice vibrations. However, these features usually appear closer to the main absorption edge and have a specific energy spacing corresponding to phonon modes. In addition, the presence of impurities or dopants in the material can introduce extra peaks or modify the bandgap transition [40].

Analyzing the position and relative intensity of SAM in carbon nitride samples can provide useful information. Specifically, SAM are typically found closer to the absorption edge in samples with a higher defect density or shallower defect states[41]. Additionally, the relative intensity of the SAM is higher when there is a larger population of defect states contributing to absorption[42].

The UV region peaks observed in the second derivative Tauc plots of the carbon nitride samples, such as the peaks at $342\,\mathrm{nm}$, $310\,\mathrm{nm}$, and $278\,\mathrm{nm}$, likely correspond to different electronic transitions within the material.

1. Peak at $342\,\mathrm{nm}$: This peak could be associated with the interband electronic transitions from occupied states in the valence band to unoccupied states in the conduction band. In carbon nitride, several types of transitions can occur in this energy range depending on the specific electronic structure and configuration of the material. However, other contributions, such as charge-transfer transitions between different functional groups within the carbon nitride structure, should also be considered.

2. Peak at $310\,\mathrm{nm}$: This peak could be attributed to excitonic transitions involving the formation of bound electron-hole pairs within the material. Excitonic transitions often appear slightly lower in energy than the main interband transitions, owing to the binding energy of the exciton[43]. In addition, transitions involving defects or impurities within the bandgap can contribute to the peaks in this region.

3. Peak at $278\,\mathrm{nm}$: This peak may be related to deeper electronic transitions within the carbon nitride structure, potentially involving core levels or higher-energy bands. Transitions involving nitrogen lone pairs or functional groups, such as $-NH_2$ or $-OH$, can also contribute to the peaks in this ultraviolet region. Further investigation is required to fully understand the nature and implications of the observed peaks.

The results from the second-derivative K-M plots of the carbon nitride samples offer valuable insights into their defect states and light-matter interactions. The presence of the main absorption edge ($404\,\mathrm{nm}$ to $408\,\mathrm{nm}$) confirms that the bandgap energy of the samples is approximately $3\,\mathrm{eV}$, which is consistent with the typical values

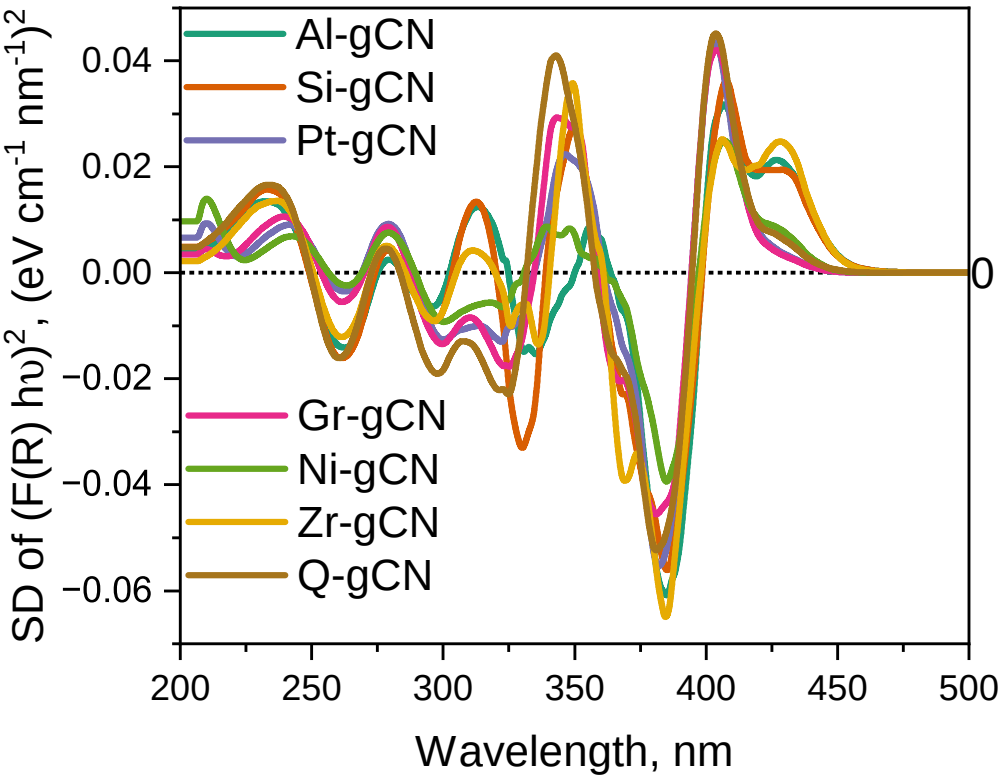

Figure 5.10: Second derivative diffuse reflectance spectra for carbon nitrides synthesized in various crucibles

for carbon nitride. Moreover, the shoulder peaks ($427\,\mathrm{nm}$ to $430\,\mathrm{nm}$) indicated the presence of shallow defect states within the bandgap, similar to those observed in the Tauc plot for some samples. The energy difference between the peak and main absorption edge ($\sim 0.2\,\mathrm{eV}$) suggests that shallow electron traps capture excited electrons slightly above the valence band. Additionally, the gradual extension of the four samples ($427\,\mathrm{nm}$ to $430\,\mathrm{nm}$) could be due to shallow hole traps, which capture holes just below the conduction band, or band tailing, that is, a gradual decrease in the density of states within the bandgap. Both defect states and band tailing influence light scattering, possibly contributing to the extended tail in the K-M plot. The sharpness of the drop may vary depending on the type and density of the defect states and the extent of disorder in each sample.

The K-M plot typically highlights the defect states that are closer to the bandgap edge because of their greater sensitivity to shallow states and light scattering. Both the Tauc and K-M plots exhibit shoulder peaks that confirm the existence of defect states; however, the distinctness of these peaks may vary depending on the sensitivity and focus on electronic transitions versus light-matter interactions.

- Peak at $342\,\mathrm{nm}$ to $350\,\mathrm{nm}$: This peak was possibly due to interband electronic transitions, similar to the Tauc plot peak at $342\,\mathrm{nm}$. However, it may also be influenced by light scattering by free carriers and defect states.

- Peak at $310\,\mathrm{nm}$ to $312\,\mathrm{nm}$: This peak can be attributed to excitonic transitions or contributions from defect states or impurities. The scattering processes might amplify the peak owing to enhanced sensitivity to localized states and interactions with light.

Sample	Band Gap, eV						U.E meV
	Tauc Plot			K-M Plot			
	L.R	F.D	S.D	L.R	F.D	S.D	L.R
Al-gCN	2.77	3.06	2.84	2.76	3.1	3.05	409
Si-gCN	2.78	3.06	2.84	2.77	3.12	3.04	365
Pt-gCN	2.94	3.12	3.06	2.95	3.14	3.08	163
Gr-gCN	2.94	3.12	3.05	2.95	3.14	3.07	163
Ni-gCN	2.83	3.08	2.86	2.84	3.12	3.05	165
Zr-gCN	2.78	2.97	2.84	2.77	3.1	3.05	198
Q-gCN	2.91	3.11	3.06	2.90	3.13	3.07	208

Table 5.7: Bandgap and Urbach energy determination using solid state UV-Visible spectroscopy technique

	Min	Intensity	Max	Intensity	D Parameter	SA	DP/SA
Al-gCN	386	-0.02504	437	0.01708	0.04212	15.2	0.0028
Si-gCN	386	-0.02366	436	0.01717	0.04083	20.8	0.002
Pt-gCN	385	-0.03872	405	0.02542	0.06414	67	0.00091
Gr-gCN	388	-0.03636	407	0.02731	0.06367	72.2	0.00088
Ni-gCN	386	-0.02748	434	0.01462	0.0421	34	0.0012
Zr-gCN	385	-0.02521	436	0.02031	0.04552	12.6	0.0036
Q-gCN	386	-0.03256	405	0.02216	0.05472	49.4	0.0011

Table 5.8: Derivative Tauc Plot Analysis

- Peak at $278\,\mathrm{nm}$ to $280\,\mathrm{nm}$: This peak aligns with the possible deeper electronic transitions and contributions from the core levels or higher-energy bands, as suggested for the Tauc plot at $278\,\mathrm{nm}$. Scattering, particularly by lattice vibrations (phonons), can also contribute to this peak in the K-M plot.
- Peak at $233\,\mathrm{nm}$ to $243\,\mathrm{nm}$: This peak is less common in carbon nitride and suggests potential contributions from higher-energy transitions beyond conventional bandgap excitations. Scattering processes and impurity-related transitions are increasingly likely at these shorter wavelengths[44].

The data presented in Table 5.7 reveal that the bandgap values for all carbon nitride samples synthesized using various crucibles are consistent and are derived from second-derivative plots. This implies that the choice of the crucible or pre-

	Min	Intensity	Max	Intensity	D Parameter	SA	DP / SA
Al-gCN	385	-0.06109	407	0.03189	0.09298	15.2	0.006
Si-gCN	385	-0.05629	408	0.03621	0.0925	20.8	0.004
Pt-gCN	382	-0.05562	403	0.04362	0.09924	67	0.0015
Gr-gCN	381	-0.04569	404	0.04213	0.08782	72.2	0.0012
Ni-gCN	385	-0.03963	407	0.02506	0.06469	34	0.0019
Zr-gCN	385	-0.06508	406	0.02561	0.09069	12.6	0.0072
Q-gCN	381	-0.0526	403	0.04524	0.09784	49.4	0.002

Table 5.9: Derivative Diffuse Reflectance Spectroscopic Analysis

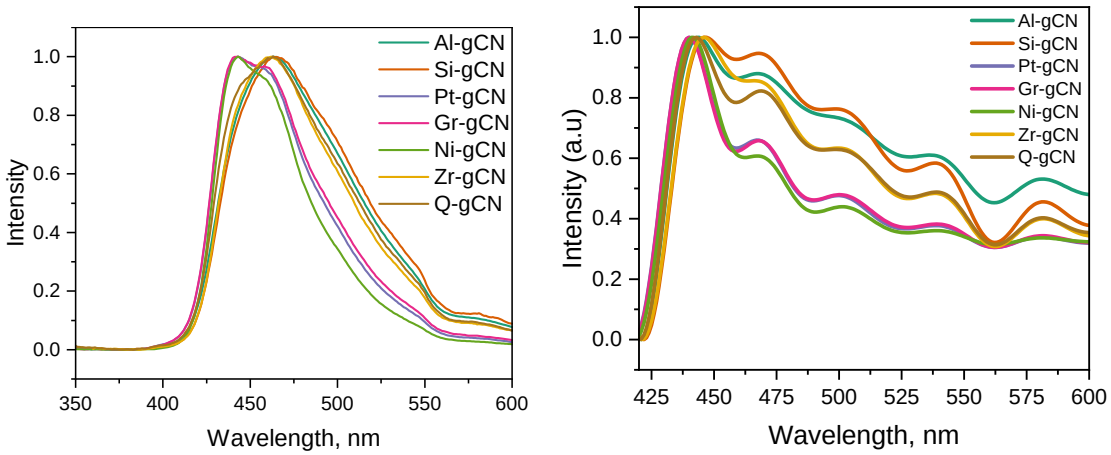

Figure 5.11: Photoluminescence (left) and deconvoluted (right) spectra of graphitic carbon nitride synthesized from various crucibles

cursor does not have a significant impact on the bandgap. Previous studies, as mentioned in Chapter 4.2.7, reported bandgap values of approximately $2.7\,\mathrm{eV}$. However, the observed deviation from this value is primarily due to incorrect fitting, which prevents the linear-fitting method from accurately determining the bandgap. The conventional linear fitting approach generally yields shoulder peak values, which are interpreted as the bandgap values. This suggests that the method may not be applicable in cases in which shallow defects are present. To ensure the accuracy of bandgap determination, it is recommended to use the second derivative K-M plot for validation purposes.

Derivative Tauc plot analysis provided some interesting observations (Table 5.8). The d parameter values of the high-surface-area samples, such as Gr-gCN, Pt-gCN, and Q-gCN, were almost similar to those of the rest of the carbon nitride samples. This indicates that the surface area was not linearly dependent on the light-absorption characteristics. It is interesting to note that the DP/SA ratios of Gr-gCN, Pt-gCN, and Q-gCN were low. Zr-gCN, Al-gCN,Si-gCN and Ni-gCN showing high DP/SA ratio respectively. This might be one of the reasons for the higher activities of Al-gCN and Zr-gCN, together with the high C value. The same can be observed in the second-derivative K-M plot analysis (Table 5.9).

5.2.8 Photoluminescence

The findings from the comparative analysis of the normalized photoluminescence (PL) spectra of the carbon nitride samples synthesized using different crucibles offer valuable insights into the impact of the synthesis conditions on their defect states and electronic structure (Figure 5.11). The main PL peak at $443\,\mathrm{nm}$ observed in the Gr-gCN, Ni-gCN, and Pt-gCN samples was likely due to the band-to-band recombination of photogenerated electrons and holes within the bulk material. The peak position ($\approx 2.8\,\mathrm{eV}$) aligns with the typical bandgap energy of graphitic carbon nitride ($\approx 3\,\mathrm{eV}$).

The shoulder peak around $459\,\mathrm{nm}$ observed in the Gr-gCN, Ni-gCN, and Pt-gCN samples suggests the presence of shallow defect states within the bandgap, slightly

above the valence band[33]. These states can act as trap sites for excited electrons, leading to additional emission pathways and an observed shoulder peak. The existence of these defect states in all three samples could be related to the specific interactions between the carbon nitride samples and their respective crucibles during synthesis.

Regarding the main PL peak at $463\,\mathrm{nm}$ observed in samples Al-gCN, Si-gCN, Ni-gCN, Q-gCN, and Zr-gCN, its slightly redshifted peak position ($\approx 2.68\,\mathrm{eV}$) can be attributed to several factors. These may include deeper defect states that serve as trap sites for photogenerated electrons located further within the bandgap, bandgap modifications caused by the influence of the crucible material on the electronic structure, or increased band tailing resulting from a broader distribution of states within the bandgap, which can lead to a less-defined peak and potentially mask the shoulder peak.

The band tail, which spans $600\,\mathrm{nm}$ in all the samples, suggests the presence of a broad distribution of electronic states that extend beyond the bandgap. This indicated the existence of defect states within the material. The extent and shape of the tail can provide valuable information on the type and density of these defect states. Crucibles can affect the synthesis process in various ways, including introducing impurities or dopants that create defect states, altering the growth kinetics and morphology of carbon nitride, and influencing its electronic structure through interactions with the precursors[45].

The normalized PL spectra for all carbon nitride samples exhibited similar intensities despite the variations observed in the peak positions and tailing. This suggests that the overall emission efficiency was similar for each sample. However, the differences in the peak positions and tailing indicate distinct recombination pathways and rates within each sample. The red-shifted peak in Al-gCN, Si-gCN, Ni-gCN, Q-gCN, and Zr-gCN indicates the presence of deeper trap states for photogenerated electrons. These deeper traps resulted in a slower overall recombination rate compared with the samples with a main peak at $443\,\mathrm{nm}$. Recombination occurred via shallow states in these samples. The similar overall PL intensities suggest that the population of deeper trap states may be smaller than that of shallow states in the other samples. This balance allows for similar total emissions, despite differing trap depths. This can be ascribed to the presence of charge carriers on the surface, in conjunction with the high C values of these samples, resulting in a more efficient utilization of the charge carriers and an increase in activity towards CO_2 reduction. The presence of a shoulder peak in Gr-gCN, Ni-gCN, and Pt-gCN suggests an additional recombination pathway through these shallow defect states. This contributes to the overall PL intensity, but may not significantly alter the average recombination rate owing to the relatively small population of these states.

The presence of a broadband tail in all samples suggests a diverse distribution of electronic states within the bandgap, resulting in various additional recombination pathways beyond the main and shoulder peaks. This increased complexity in recombination dynamics involves deeper and shallower states with different capture cross-sections and lifetimes. Despite the observed spectral variations, the overall PL intensity remained consistent, indicating a potential balance between the different trap state populations and recombination pathways across the samples. The presence of deeper trap states in some samples might lead to slightly slower overall recombination rates than those with shallower states. The complex influence of

band tailing on various states contributes to the recombination process.

The observed differences in the PL spectra of the carbon nitride samples synthesized using various crucibles provide valuable insights into the influence of the synthesis conditions on the defect states and electronic structure of the material. These findings contribute to a better understanding of the complex interplay between the crucible material and the synthesis process, which can aid in optimizing carbon nitride synthesis for specific applications.

5.2.9 ^{13}C Solid State NMR Studies

Further insights into the ^{13}C solid-state NMR of carbon nitrides can be found in detail in Chapter 4.2.9 of this thesis. The observations and analyses presented provide a comprehensive foundation for subsequent discussions in this chapter.

The absence of the shoulder peak at $162.7\,\mathrm{ppm}$ in Gr-gCN, Ni-gCN, Zr-gCN, and Q-gCN compared to Al-gCN, Si-gCN, and Pt-gCN offers valuable information regarding the influence of crucible material on the g-CN structure and properties (Figure 5.12 and 5.13). The absence of this peak in certain samples suggests that the crucibles hindered or prevented the incorporation of carbon dopants during the synthesis process. This phenomenon may be due to several factors, including chemical interactions between the crucible and precursors or intermediates, catalytic effects of the crucible material on reaction pathways or kinetics towards specific g-CN structures with less propensity for carbon doping, and differences in thermal conductivity or porosity of the crucibles affecting the diffusion of carbon-containing species onto the growing g-CN surface [46].

The shoulder peak at $162.7\,\mathrm{ppm}$ is commonly attributed to carbon dopants substituting for nitrogen atoms in the N−C=N units within the g-CN structure. Therefore, the absence of this peak in certain samples implies that these crucibles inhibited or suppressed the incorporation of carbon dopants during the synthesis process. This could be due to various factors such as chemical interactions, catalytic effects, and diffusion limitations.

Although carbon doping is a plausible explanation for the shoulder peak, other factors may also contribute to its absence from certain samples. This could include the presence of distinct structural defects, which might lead to the incorporation of carbon dopants into different carbon environments with slightly different chemical shifts. Additionally, variations in crystallinity due to differences in the ordering of the g-CN structures synthesized with different crucibles could affect the peak resolution and conceal the shoulder peak. Furthermore, instrumental factors, such as variations in experimental conditions or spectrometer sensitivity, may also impact the observed peak intensities and visibility of the shoulder.

Because ^{13}C NMR is primarily a bulk technique, as highlighted in Chapter 4, a comprehensive examination of the relationship between ^{13}C NMR analysis and CO_2 reduction has not been conducted in this context.

5.2.10 ^{15}N Solid State NMR Studies

In the ^{15}N NMR spectra of Gr-gCN and Q-gCN samples, the splitting of the N_c peak at 200 ppm is a noteworthy observation that highlights the distinct chemical environments for central triazine nitrogen in these two samples when compared to

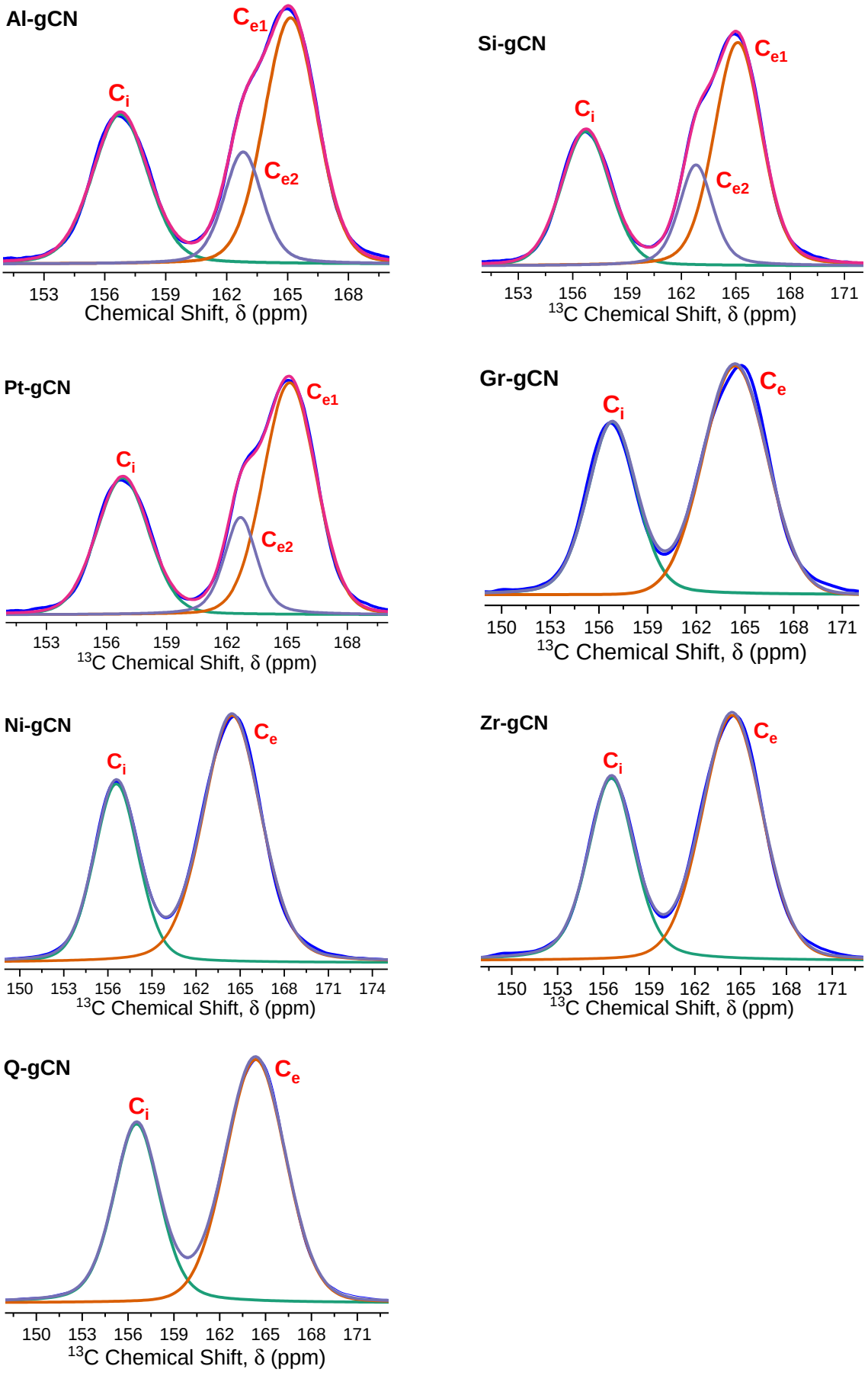

Figure 5.12: ^{13}C solid state NMR spectra of carbon nitride synthesized using various crucibles

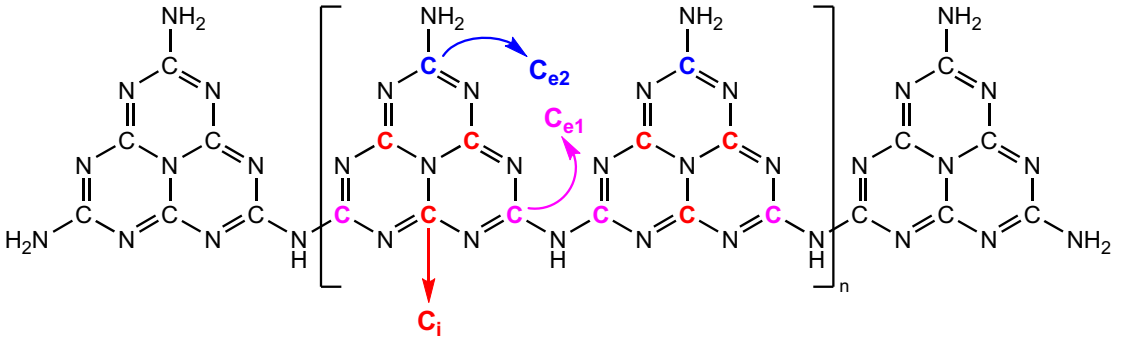

(a) ^{13}C NMR based structure of Al-gCN, Si-gCN and Pt-gcN

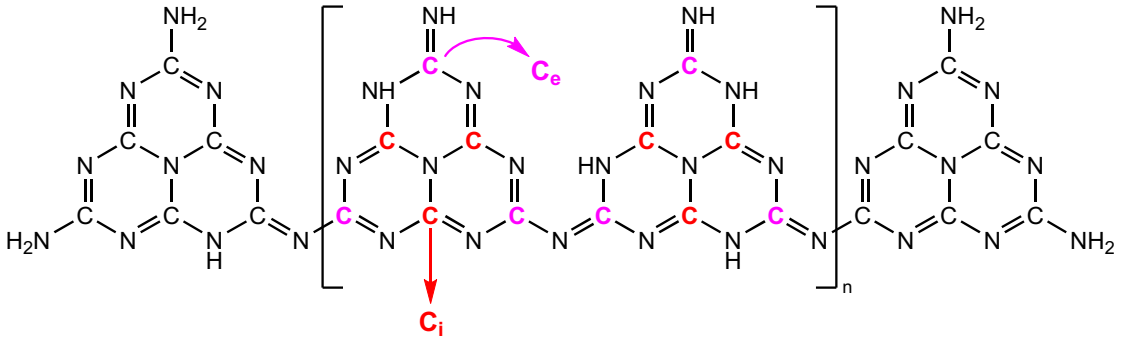

(b) ^{13}C NMR based structure of Gr-gCN, Ni-gCN, Zr-gCN and Q-gcN

Figure 5.13: Structural deviations observed in the ^{13}C NMR spectra of carbon nitrides

the single peak observed in Al-gCN, Si-gCN, Pt-gCN, Ni-gCN, and Zr-gCN samples. This may be due to precursor limitations, where the Gr and Q crucibles may impact the interaction with the precursor or affect the condensation pathways, hindering complete conversion to the triazine structure. Alternatively, kinetic factors may also play a role, where specific precursors may require different temperatures or durations for complete triazine formation, and the Gr and Q crucibles may alter the heat transfer or thermal gradients within the reaction mixture, leading to incomplete conversion in these samples. It should be noted that all samples exhibit most of the features of typical C_3N_4, except for N_c peak splitting, indicating that the basic framework of carbon nitride was intact in all samples.

Complete triazine formation can lead to local structural variations, which can result in peak splitting. Various factors, such as defects or vacancies in graphite and quartz crucibles, can affect the local bonding geometry and electronic character around the N_c units, leading to peak splitting. Additionally, interactions between the carbon nitride framework and the crucible material, specifically graphite or quartz, can alter the electron density distribution around the N_c sites, resulting in different chemical environments and peak splitting.

Although it is less probable, it is theoretically possible that the specific chemical nature of the precursors used for the synthesis of Gr-gCN and Q-gCN could contribute to N_c peak splitting. Certain precursors may comprise functional groups or impurities that interact with the forming network, locally modifying the environment around N_c and resulting in observed peak splitting.

In this study, melamine was used to synthesize carbon nitrides. Previous re-

search has shown that the use of melamine as a precursor results in the formation of distinct N_c peaks without any splitting. This suggests that complete triazine formation is achieved when melamine is used as the precursor because it already possesses the desired triazine skeleton, which requires minimal structural rearrangement during thermal condensation. Notably, only Gr-gCN and Q-gCN displayed N_c splitting among all the crucibles used in this study, indicating a specific interaction or influence exerted by these crucibles on the carbon nitride formation process.

Because ^{15}N NMR is primarily a bulk technique, as highlighted in Chapter 4, a comprehensive examination of the relationship between ^{15}N NMR analysis and CO_2 reduction has not been conducted in this context.

5.2.11 X-ray Photoelectron Spectroscopy

Upon examining the high-resolution C 1s spectrum, deconvolution into multiple peaks revealed the following distinct components[13, 47–51].

- $\approx 284.4\,\mathrm{eV}$ to $284.8\,\mathrm{eV}$: assigned to sp^2 hybridized carbon in aromatic C=N bonds within the tri-s-triazine rings, constituting the fundamental building block of g-C_3N_4.
- $\approx 288\,\mathrm{eV}$ to $289\,\mathrm{eV}$: Represents sp^2 hybridized carbon in C−N bonds.
- $285.5\,\mathrm{eV}$ to $286.5\,\mathrm{eV}$ (optional): May be present owing to C−NH_2 groups, contingent on the preparation method.

Similarly, the high-resolution N 1s spectrum exhibited three main peaks upon deconvolution.

- $\approx 398.7\,\mathrm{eV}$: Corresponds to sp^2 hybridized nitrogen in tri-s-triazine rings (graphitic−N).
- $\approx 400.7\,\mathrm{eV}$: Pyrrolic-N, associated with edge sites or defects.
- $\approx 401.9\,\mathrm{eV}$: corresponding to pyridine-N, primarily found at defect sites or attributed to surface functional groups, such as amine (NH_2).
- Finally, the weaker band at BE = 404.2 eV was attributed to π-electron excitations in the heptazine rings.

Tables 5.10 and 5.11 present the surface concentrations and normalized surface concentrations of various functional aminities in the graphitic carbon nitrides. The six samples (Al-gCN, Si-gCN, Pt-gCN, Gr-gCN, Ni-gCN, Zr-gCN and Q-gCN) were analyzed for their (C)-N-Hx, N-C=N, C=N-C, N-$(C)_3$, C-(N)-Hx, and OH NSC% values, with a particular focus on methane, methanol, and oxygen production yields.

The normalized values for each catalyst were calculated by determining the normalized concentration per unit surface area, using the following formula:

$$\text{Normalized Surface Concentration, NSC\%} = \left(\frac{\text{XPS At\%}}{\text{SESAMI Surface Area}}\right) \times 100$$

The use of this approach allows for a standardized perspective on the distribution of specific components or functional groups, considering the variations in the

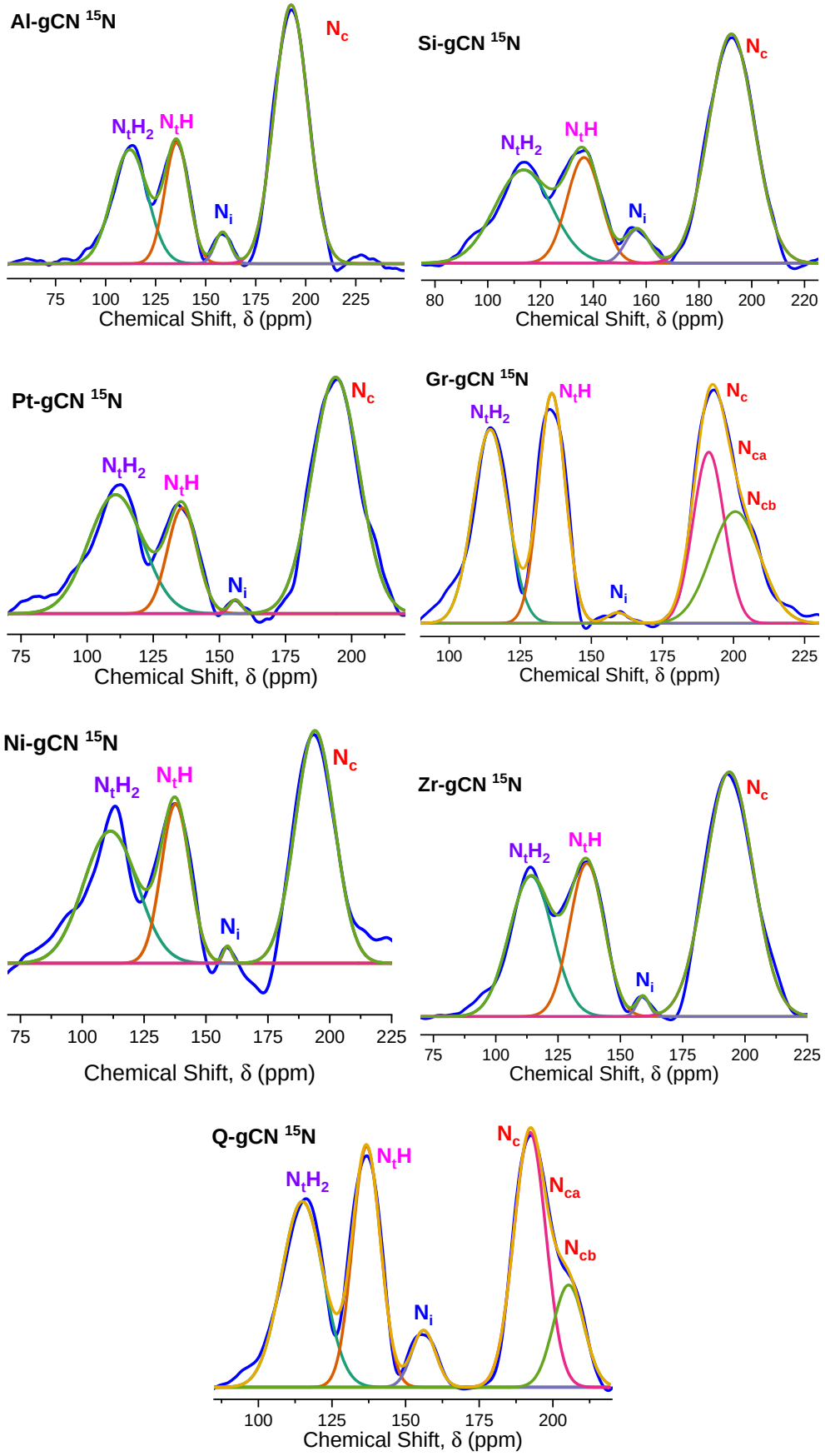

Figure 5.14: ^{15}N solid state NMR spectra of carbon nitride synthesized using various crucibles

surface area between various catalysts. By employing normalized concentrations, a comprehensive comparative analysis can be conducted, providing a fair evaluation of the relative abundance of the studied elements or functional groups across diverse catalysts. This method eliminates the influence of surface area variations and highlights the inherent discrepancies in composition.

Table 5.10: Atomic percentage of surface functional groups in carbon nitride prepared using various crucibles

Samples	SA	(C)-N-Hx	N-(C)=N	C=(N)-C	N-$(C)_3$	C-(N)-Hx	OH
Al-gCN	15.2	0.95	35.31	34.48	7.42	5.52	0.25
Si-gCN	20.8	3.48	32.85	34.42	10.47	2.37	0.05
Pt-gCN	67	0.62	35.5	33.71	7.81	5.91	0.02
Gr-gCN	72.2	1.27	35.21	34.94	6.5	5.71	0.9
Ni-gCN	34	1.1	35.08	34.6	8.21	4.72	0.51
Zr-gCN	12.6	1.1	34.82	35.16	5.37	6.52	0.79
Q-gCN	49.4	0.54	35.89	32.12	11.99	4.38	0.25

Table 5.11: Normalized surface concentration (NSC%) for various functional groups in carbon nitride samples synthesized from various crucibles

Samples	(C)-N-Hx	N-(C)=N	C=(N)-C	(N)-$(C)_3$	C-(N)-Hx	OH
Al-gCN	6.25	232.30	226.84	48.82	36.32	1.64
Si-gCN	16.73	157.93	165.48	50.34	11.39	0.24
Pt-gCN	0.93	52.99	50.31	11.66	8.82	0.03
Gr-gCN	1.76	48.77	48.39	9.00	7.91	1.25
Ni-gCN	3.24	103.18	101.76	24.15	13.88	1.50
Zr-gCN	8.73	276.35	279.05	42.62	51.75	6.27
Q-gCN	1.09	72.65	65.02	24.27	8.87	0.51

Table 5.11 shows that Gr-gCN, Pt-gCN, and Q-gCN have the lowest number of surface functionalities per unit surface area. This leads to a reduced product yield. In contrast, Zr-gCN, Al-gCN, and Ni-gCN exhibited high NSC% of C-(N)-Hx and OH. Additionally, Zr-gCN and Al-gCN show high NSC% values for N-(C)=N, C=(N)-C, and N-$(C)_3$, which suggests that these systems are highly active towards CO_2 reduction. Furthermore, the high C and d parameter values were also considered for the activities of Al-gCN and Zr-gCN. Based on these findings, the hypothesis suggests that C-N-Hx groups play an active role in the formation of methanol through either the adsorption or activation of CO_2 or by altering the electronic structure and hydrogen availability. Additionally, the OH groups may facilitate water oxidation and oxygen release, potentially working in conjunction with other functionalities in a synergistic manner.

The influence of the functional groups on the carbon nitride catalysts in the CO_2 photoreduction was evident. The presence of C-N-Hx groups indicated the potential to increase methanol production, whereas the OH groups may have contributed to the formation of oxygen. It is noteworthy that there is a similar trend between

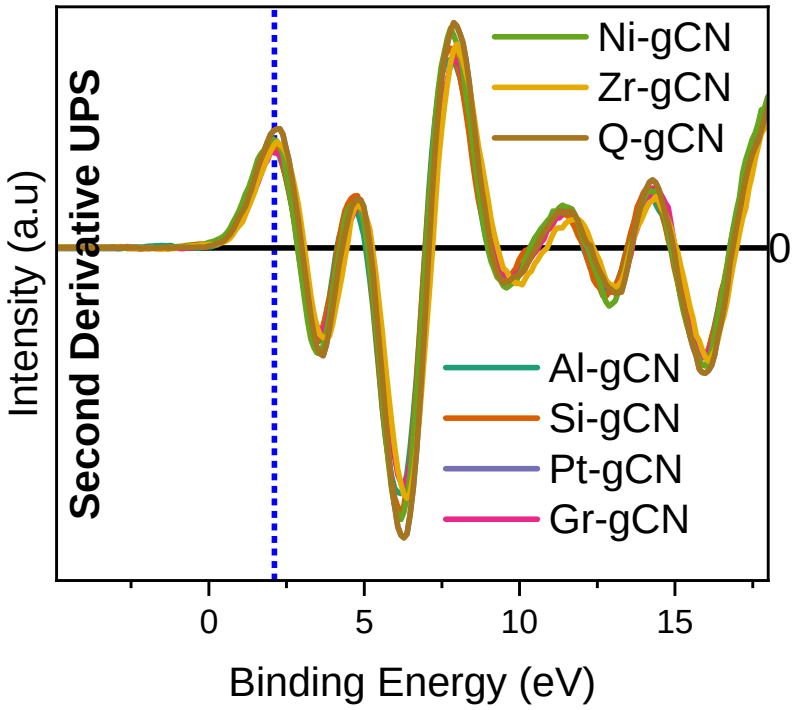

Figure 5.15: Second derivative valence band XPS of carbon nitrides prepared from various crucibles

the XPS NSC% (Table 5.11) and DP/SA (Table 5.9) values obtained from UV-DRS analysis. This can be attributed to the fact that the surface functionalities inherently determine the light-absorption cross-section of the material. The introduction of the parameters NSC% and DP/SA enables a direct comparison of the light absorption characteristics of the materials with their surface functionalities.

5.2.12 Valence Band XPS

The X-ray photoelectron spectroscopy (XPS) valence-band spectrum of g-C_3N_4 displayed a number of well-defined peaks (Figure 5.15). A prominent peak near $5.5\,\mathrm{eV}$ dominated the low-binding-energy region (0-7 eV). This peak is attributed to the lone pair electrons of the nitrogen atoms and π-bonded electrons associated with the aromatic sp^2 C-N framework. In addition, a shoulder located at approximately $1.8\,\mathrm{eV}$ within this peak can be further deconvoluted into contributions from the lone pair electrons and π-bonding states, shedding light on the hybridization and bonding scheme[52, 53].

The higher binding energies ($7\,\mathrm{eV}$ to $20\,\mathrm{eV}$) correspond to the energy levels at which multiple overlapping peaks arise from the σ bonds between the C and N atoms, involving both 2s and 2p orbitals. At these energies, a distinct peak centered at approximately $13.5\,\mathrm{eV}$ was assigned to C-N sp^2 σ bonds, whereas contributions from C-N sp^3 σ and N-N bonds may be present in a broader feature centered at approximately $17.5\,\mathrm{eV}$. These observations supported the expected hybridized configuration and bonding arrangement within the g-C_3N_4 framework.

The current investigation revealed the presence of weaker signals at binding energies greater than $20\,\mathrm{eV}$, which corresponded to the deeper core-like states of C

2s and N 2s. The absence of significant satellite peaks or broadening of these core-level peaks suggested that the sample exhibited minimal surface contamination or significant oxidation states.

The observed peak positions and intensities were consistent with theoretical predictions and previous experimental findings, confirming the presence of sp^2 hybridized N atoms and an aromatic C-N framework in the material. Additionally, the second-derivative valence band spectra of the low-binding-energy peak provided insights into the contributions of π-bonding and lone pair electrons, underscoring the significance of π-conjugation in the electronic properties of carbon nitrides.

The coexistence of planar and non-planar domains within the crystal structure of g-C_3N_4, as indicated by the presence of distinct σ-bonding peaks, including contributions from both sp^2 and sp^3 hybridization, suggests that the relative abundance and spatial distribution of these domains may influence the charge carrier transport and photocatalytic performance of the material.

To determine the valence-band position, both linear curve fitting and second-derivative valence-band spectroscopy were employed (Table 5.12). Although linear curve fitting is a commonly used approach, it has limitations in capturing the intricate details within the valence band spectra. By contrast, the second-derivative method offers a more refined examination, particularly in areas where the valence band exhibits complex features. Consequently, the second-derivative method provides a more accurate and reliable means of measuring the valence band position, enabling a more detailed analysis of the valence band structure, and a solid foundation for further discussion of the electronic structure and properties of graphitic carbon nitride surfaces. Variations in the valence band positions among the carbon nitride samples were observed, suggesting the influence of the crucible on the formation of well-defined bands. The XPS results indicated that the crucible caused a difference in the concentration of the chemical moieties, which in turn affected the positioning of the valence and conduction bands. To further elucidate the band diagram, the valence band position obtained from the second-derivative method was utilized (Table 5.12).

	Highest Occupied Molecular Orbital (HOMO), eV				
Sample	**Second Derivative**	**Curve Fitting**			
		Position	**Original Value**	**FWHM**	**STD**
AT-gCN	2.18	2	1.9957	1.91	1.302
CY-gCN	1.78	1.91	1.9138	1.52	1.224
DC-gCN	1.98	2.11	2.1113	1.47	1.157
M-gCN	1.98	2.11	2.1115	1.62	1.317
TU-gCN	1.98	2.12	2.1201	1.71	1.515
U-gCN	2.18	2.22	2.2199	1.64	1.305

Table 5.12: Valence position carbon nitrides derived from VB-XPS

The second-derivative valence-band spectra of graphitic carbon nitride provided valuable insights into the electronic structure of the material, revealing various features corresponding to different electronic states (Figure 5.15). Although the binding energy values may vary depending on the experimental conditions and sample characteristics, several prominent features are observed in the spectra.

One such feature is the π-band of carbon (C 2p), which is typically centered in the binding energy range of $1\,\mathrm{eV}$ to $4\,\mathrm{eV}$. This feature signifies the presence of π orbitals associated with conjugated carbon within the graphitic structure of carbon nitride. These π orbitals significantly influence the electronic and optical properties of the material, contributing to its conductive behavior and interactions with the incident light.

Another prominent feature is the σband of carbon (C 2s), which appears in the binding energy range of $10\,\mathrm{eV}$ to $15\,\mathrm{eV}$. This feature corresponds to the σ orbitals of conjugated carbon within the graphitic carbon nitride structure. The σ orbitals contribute to the overall electronic configuration, thereby affecting the bonding characteristics and the stability of the material.

Participation of the electronic states of nitrogen (N 2p) was discernible in the binding energy range of $8\,\mathrm{eV}$ to $15\,\mathrm{eV}$. These states underscore the role of nitrogen in the valence band of graphitic carbon nitride and its effect on chemical reactivity and charge distribution.

Additionally, the spectra revealed hybridized carbon-nitrogen states, as evidenced by peaks at binding energy positions of approximately $-15\,\mathrm{eV}$ to $-20\,\mathrm{eV}$. These peaks signify the hybridized states of the carbon-nitrogen bonds within the material, which are crucial factors that influence its structural stability and contribute to its chemical and physical properties.

The reproducible nature of the observed features in the valence band spectra of the seven carbon nitride samples was emphasized by their consistent presence, despite being derived from various crucibles. These samples exhibited a considerable degree of overlap in their valence band spectra with noticeable differences in intensity. The variation in intensity indicates that the choice of crucible has a significant impact on the electronic structure of graphitic carbon nitride. The presence of characteristic features, such as the π-band of conjugated carbon and hybridized carbon-nitrogen states, suggests a fundamental similarity in the electronic states and bonding configurations of these materials. This consistency implies that the core electronic properties of carbon nitride, as inferred from the valence band spectra, remain stable despite variations in the crucible used for synthesis. Therefore, the overlap in the valence band spectra suggests a fundamental similarity in the electronic states and bonding configurations of the diverse carbon nitride samples. The persistence of characteristic features, including the π-band of conjugated carbon and hybridized carbon-nitrogen states, indicates a shared structural foundation among these materials.

The variations in the overlapping spectral intensities among the carbon nitride samples can be ascribed to the distinct chemical natures and properties of the crucibles utilized. The intensity modulation effectively highlights the variations in the electronic structure of graphitic carbon nitride resulting from the differences in crucible-dependent factors.

Second-derivative valence-band spectra often exhibit a band tail near the valence-band edge, indicating a gradual decrease in the density of electronic states beneath the main peak of the valence band [34, 38]. This phenomenon is typically attributed to the electronic disorder within the material, where impurities, defects, or structural imperfections create localized energy states within the bandgap [35]. These localized states extend the valence band towards lower binding energies, giving rise to tail-like features observed in the spectrum.

Sample	Bandgap	HOMO	LUMO	I.E	E.A	C	N	C/N
Al-gCN	3.05 eV	2.08 V	−0.97 V	6.52 eV	3.47 eV	35.31	47.42	0.7446
Si-gCN	3.04 eV	2.08 V	−0.96 V	6.52 eV	3.48 eV	32.38	47.26	0.6851
Pt-gCN	3.08 eV	2.28 V	−0.8 V	6.72 eV	3.64 eV	35.5	47.43	0.7485
Gr-gCN	3.07 eV	1.98 V	−1.09 V	6.42 eV	3.35 eV	35.21	47.15	0.7468
Ni-gCN	3.05 eV	2.08 V	−0.97 V	6.52 eV	3.47 eV	35.08	47.53	0.7381
Zr-gCN	3.05 eV	2.18 V	−0.87 V	6.62 eV	3.57 eV	34.82	47.05	0.7401
Q-gCN	3.07 eV	2.28 V	−0.79 V	6.72 eV	3.65 eV	35.89	48.49	0.7402

Table 5.13: Electronic properties of graphitic carbon nitrides together with C/N ratio from XPS

The Urbach tail is a band tail commonly observed in amorphous materials and semiconductors [36, 41]. This reflects the disorder-induced broadening of the states near the band edge (Table 5.7). In other words, the presence of disorder, such as irregularities in the structure of the material, causes widening of the electronic states close to the valence band edge. This broadening effect contributes to the appearance of a band tail in the second-derivative valence-band spectra.

5.2.13 Possible Mechanism of Formation Products

The mechanisms discussed here are analogous to those described in Chapter 4. Therefore, for a detailed understanding of the mechanisms under consideration, the reader is advised to refer to the explanations provided in section 4.2.14.

5.2.14 Elucidation of the Band Diagram

The band diagrams for all seven carbon nitride samples were elucidated through a comprehensive approach, utilizing the valence band position data obtained from derivative X-ray photoelectron spectroscopy (XPS) and bandgap values derived from second-derivative diffuse reflectance ultraviolet (DRD UV) measurements. This dual-source information allows for the calculation of both valence and conduction band positions[54, 55]. Subsequently, the electron affinity and ionization energy of each sample were determined based on the calculated band positions.

Band diagrams for all the samples were created using the data obtained from the valence-band XPS spectra and DRS UV measurements at both pH 0 and pH 8. To construct the band diagram at pH 0, the values obtained from these measurements were used (Figure 5.16). Additional pH corrections were applied to the semiconductor band edge and CO_2 redox potential values to represent the band diagram at pH 8 accurately (Figure 5.17).

The relationship between the valence and conduction bands of semiconductors and their oxidation and reduction potentials is fundamental to their behavior. As shown in Table 5.13, the oxidation potentials varied among the carbon nitride samples in the following order: Q-gCN=Pt-gCN>Zr-gCN>Al-gCN=Si-gCN=Ni-gCN>Gr-gCN. Similarly, the reduction potentials decrease in the following order: Gr-gCN>Al-gCN=Ni-gCN>Si-gCN>Zr-gCN>Pt-gCN>Q-gCN. All carbon nitride systems had the necessary band-edge potential to reduce carbon dioxide to methane and methanol (Figure 5.17 & Equation 5.1 & 5.2). Despite these similarities, there

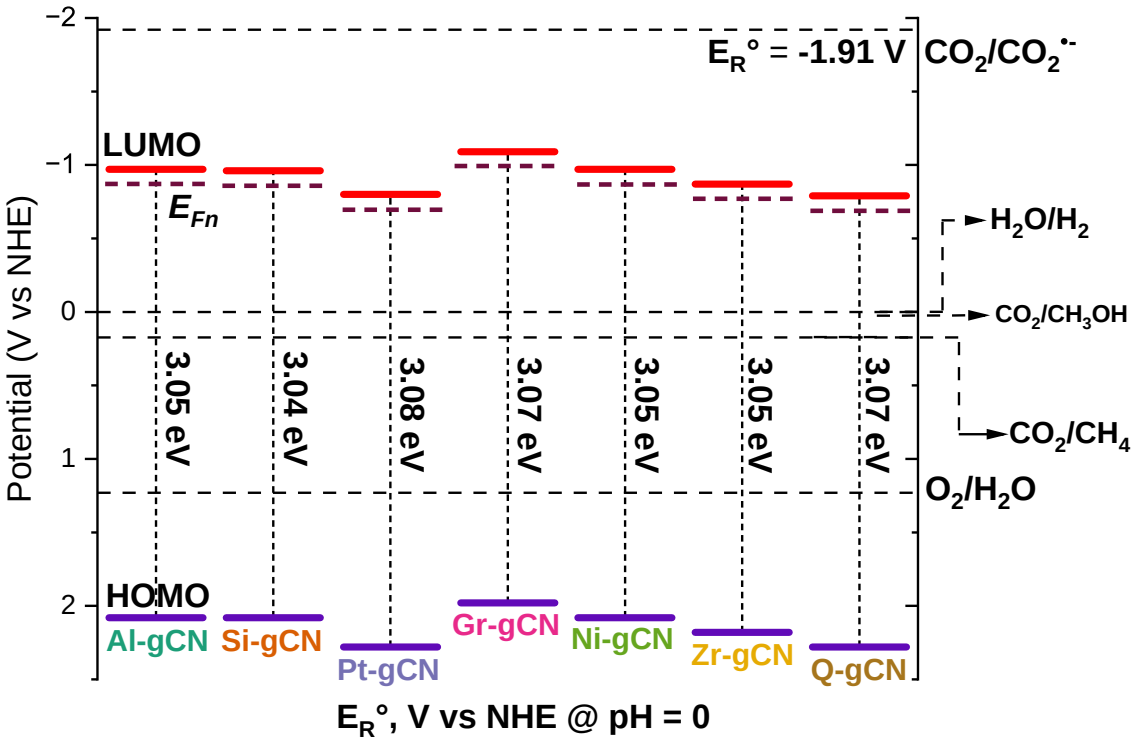

Figure 5.16: Band diagram of carbon nitrides at pH 0

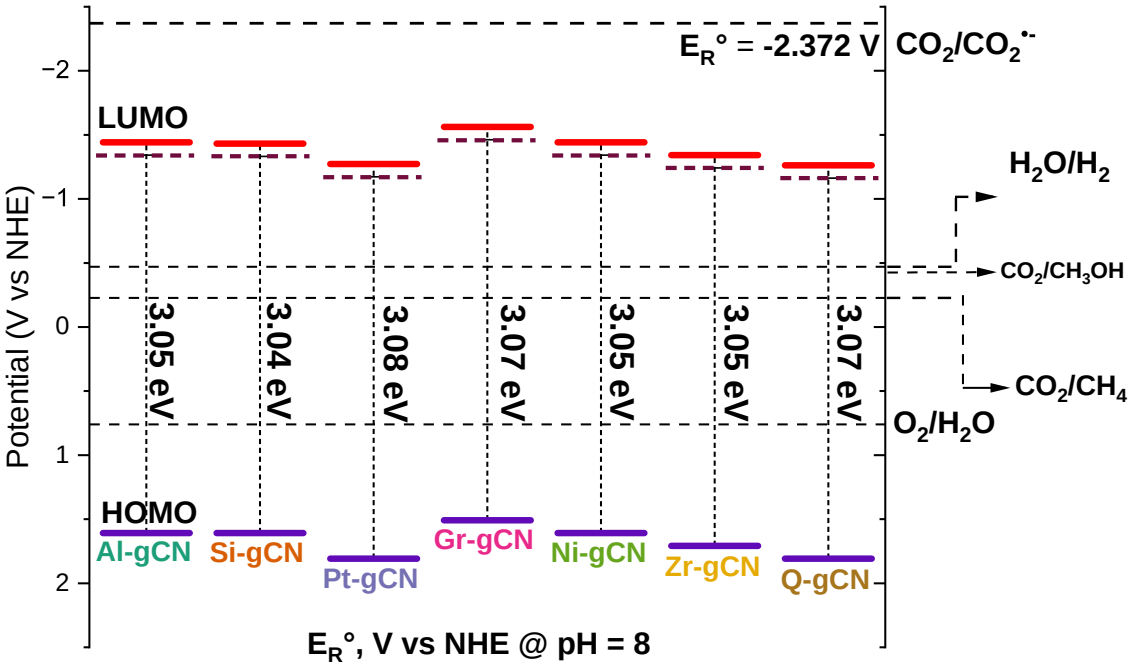

Figure 5.17: Band diagram of carbon nitrides at pH 8

are subtle variations in the reduction and oxidation potentials, electron affinity, and ionization energy among carbon nitrides. The higher C values of Al-gCN and Zr-gCN resulted in better adsorption of reactive species, such as carbon dioxide and water, on the surface. Additionally, the high DP/SA ratio among these samples ensures better utilization of the light irradiated on the surface and charge carriers. The higher oxidation potentials of Al-gCN and Zr-gCN also contributed to better water oxidation, producing more hydrogen ions on the surface, which can be utilized for CO_2 reduction. The presence of edge sites (derived from the second derivative, DIS) in Al-gCN, Zr-gCN, and Ni-gCN also contributed to the high product yield. This indicates that CO_2 reduction is interdependent on various parameters and does not solely depend on the band edge positions.

$$\begin{aligned} \mathrm{CO_2(g) + 3\,H_2(g) &\longrightarrow CH_3OH\,(l) + H_2O\,(l)} && E^\circ = -0.39\,\mathrm{V} \\ \mathrm{6\,H^+\,(aq) + 6\,e^- &\longrightarrow 3\,H_2(g)} && E^\circ = -0.41\,\mathrm{V} \\ \mathrm{CO_2\,(g) + 6\,H^+\,(aq) + 6\,e^- &\longrightarrow CH_3OH\,(l) + H_2O\,(l)} && \mathrm{E^\circ = -0.80\,V} \end{aligned} \tag{5.1}$$

$$\begin{aligned} \mathrm{CO_2(g) + 4\,H_2(g) &\longrightarrow CH_4(g) + 2\,H_2O\,(l)} && E^\circ = -0.24\,\mathrm{V} \\ \mathrm{8\,H^+\,(aq) + 8\,e^- &\longrightarrow 4\,H_2(g)} && E^\circ = -0.41\,\mathrm{V} \\ \mathrm{CO_2\,(g) + 8\,H^+\,(aq) + 8\,e^- &\longrightarrow CH_4(g) + 2\,H_2O\,(l)} && \mathrm{E^\circ = -0.65\,V} \end{aligned} \tag{5.2}$$

5.2.15 Summary

Carbon nitrides synthesized using melamine as a precursor in different crucibles were used to evaluate the effect of the material characteristics on the photoreduction of CO_2. The use of the same precursor, melamine, in the synthesis of carbon nitrides to evaluate their CO_2 photoreduction properties offers several advantages over the use of different precursors. By utilizing the same precursor, the influence of varying the precursor properties on the final carbon nitride structure and performance can be eliminated, allowing for a more focused examination of the specific impact of the crucible material on the material characteristics and the CO_2 photoreduction activity. The use of melamine-derived carbon nitrides enables a direct comparison of the influence of the crucible material on features such as surface area, pore structure, and defect chemistry within a relatively consistent structural framework. This approach facilitates the attribution of changes in CO_2 photoreduction activity to the specific differences caused by the crucible, providing clearer insights into the mechanisms involved in the crucible-material interaction and its influence on activity. Furthermore, using the same precursor ensures that the synthesis process is more likely to be reproducible, resulting in more consistent carbon nitride samples and potentially reducing experimental variability. This enhances the reliability and generalizability of the findings.

This study revealed the interconnection between the various parameters involved in the catalytic activity towards CO_2 photoreduction. The surface functionalities on the surface play an important role in enhancing the adsorbate–adsorbant interaction with light absorption and better utilization of the charge carriers. This is evident from the result that Zr-gCN and Al-gCN show higher activity towards CO_2 reduction. The high DP/SA ratios of these materials facilitated photon absorption. The photon absorption behavior of the material also depends on the

surface functionality, as is evident from the comparison between the NSC% and DP/SA values. The high C value observed in these materials is indicative of strong adsorbate-adsorbent interactions, which facilitate the optimal utilization of charge carriers for the respective adsorbent (water or CO_2). Derivative isotherm summation provides additional insight into the factors contributing to the high C value. Specifically, it suggests that the distribution of surface functionalities on the edge sites or moderate energy surfaces plays a significant role in this phenomenon. This, in turn, leads to moderate adsorption and desorption of the reaction intermediates, which ultimately enhances CO_2 conversion.

References

[1] Krishnamurthy, N., *Metal–Crucible Interactions*; CRC Press: 2022.

[2] Luxel Corporation RADAK® Crucible Selection Guide, Revision: 04-2022, 2022.

[3] Yan, Y.; Li, Z.; Liu, L.; Zhang, Y.; Zhou, G. Influence of Crucible Thermal Conductivity on Crystal Growth in an Industrial Directional Solidification Process for Silicon Ingots. *International Journal of Photoenergy* **2016**, *2016*, 8032709.

[4] Miyazawa, H.; Liu, L.; Kakimoto, K. Numerical Investigation of the Influence of Material Property of a Crucible on Interface Shape in a Unidirectional Solidification Process. *Crystal Growth & Design* **2009**, *9*, 267–272.

[5] Chen, X.; Nakano, S.; Kakimoto, K. 3D numerical analysis of the influence of material property of a crucible on stress and dislocation in multicrystalline silicon for solar cells. *Journal of Crystal Growth* **2011**, *318*, 259–264.

[6] Ding, C.; Huang, M.; Zhong, G.; Ming, L.; Huang, X. A design of crucible susceptor for the seeds preservation during a seeded directional solidification process. *Journal of Crystal Growth* **2014**, *387*, 73–80.

[7] Frenzel, J.; Neuking, K.; Eggeler, G. Induction Melting of NiTi Shape Memory Alloys – The Influence of the Commercial Crucible Graphite on Alloy Quality. *Materialwissenschaft und Werkstofftechnik* **2004**, *35*, 352–358.

[8] Yang, X.; Ma, W.; Lv, G.; Wei, K.; Zhang, C.; Li, S.; Chen, D. Effect of Heat Transfer during the Vacuum Directional Solidification Process on the Crystal Quality of Multicrystalline Silicon. *Metallurgical and Materials Transactions E* **2015**, *2*, 39–49.

[9] Shi, Y.; Wang, P.; Mu, H.; Kou, H.; Wu, A.; Su, L. Advances of interface, flow, and stress control for VB crystal growth: An overview. *Progress in Crystal Growth and Characterization of Materials* **2023**, *69*, 100605.

[10] Stand, N.; Mendoza, C. D.; Freire, F. L. Synthesis of WS_2 by Chemical Vapor Deposition: Role of the Alumina Crucible. *Crystals* **2022**, *12*.

[11] *Structure, Properties and Applications in Science and Technology*; Savateev, O., Antonietti, M., Wang, X., Eds.; De Gruyter: Berlin, Boston, 2023.

[12] Degen, T.; Sadki, M.; Bron, E.; Konig, U.; Nenert, G. The HighScore suite. *Powder Diffraction* **2014**, *29*, S13–S18.

[13] Miller, T. S.; Jorge, A. B.; Suter, T. M.; Sella, A.; Corà, F.; McMillan, P. F. Carbon nitrides: synthesis and characterization of a new class of functional materials. *Physical Chemistry Chemical Physics* **2017**, *19*, 15613–15638.

[14] Fina, F.; Callear, S. K.; Carins, G. M.; Irvine, J. T. S. Structural Investigation of Graphitic Carbon Nitride via XRD and Neutron Diffraction. *Chemistry of Materials* **2015**, *27*, 2612–2618.

[15] Xia, W.; Xu, B.; Duan, H.; Guo, Y.; Kang, H.; Li, H.; Liu, H. Ionic Conductivity and Air Stability of Al-Doped $Li_7La_3Zr_2O_{12}$ Sintered in Alumina and Pt Crucibles. *ACS Applied Materials & Interfaces* **2016**, *8*, 5335–5342.

[16] Schindler, F.; Michl, B.; Schon, J.; Kwapil, W.; Warta, W.; Schubert, M. C. Solar Cell Efficiency Losses Due to Impurities From the Crucible in Multicrystalline Silicon. *IEEE Journal of Photovoltaics* **2014**, *4*, 122–129.

[17] Wang, Y.; Yan, P.; Xiao, J.; Lu, X.; Zhang, J.-G.; Sprenkle, V. L. Effect of Al_2O_3 on the sintering of garnet-type $Li_{6.5}La_3Zr_{1.5}Ta_{0.5}O_{12}$. *Solid State Ionics* **2016**, *294*, 108–115.

[18] Dong, G.; Zhang, L. Porous structure dependent photoreactivity of graphitic carbon nitride under visible light. *J. Mater. Chem.* **2012**, *22*, 1160–1166.

[19] Ismael, M.; Wu, Y.; Taffa, D. H.; Bottke, P.; Wark, M. Graphitic carbon nitride synthesized by simple pyrolysis: role of precursor in photocatalytic hydrogen production. *New Journal of Chemistry* **2019**, *43*, 6909–6920.

[20] Sing, K. S. W. Reporting physisorption data for gas/solid systems with special reference to the determination of surface area and porosity (Recommendations 1984). *Pure and Applied Chemistry* **1985**, *57*, 603–619.

[21] Rouquerol, J.; Llewellyn, P.; Rouquerol, F., Is the bet equation applicable to microporous adsorbents? In *Characterization of Porous Solids VII*, Llewellyn, P., Rodriquez-Reinoso, F., Rouqerol, J., Seaton, N., Eds.; Studies in Surface Science and Catalysis, Vol. 160; Elsevier: 2007, pp 49–56.

[22] Rouquerol, J.; Rouquerol, F.; Llewellyn, P.; Maurin, G.; Sing, K., *Adsorption by Powders and Porous Solids: Principles, Methodology and Applications*; Elsevier Science: 2013.

[23] Terrones, G. G.; Chen, Y.; Datar, A.; Lin, L.-C.; Kulik, H. J.; Chung, Y. G. SESAMI APP: An Accessible Interface for Surface Area Calculation of Materials from Adsorption Isotherms. *Journal of Open Source Software* **2023**, *8*, 5429.

[24] Osterrieth, J. W. M. et al. How Reproducible are Surface Areas Calculated from the BET Equation? *Advanced Materials* **2022**, *34*, 2201502.

[25] Datar, A.; Chung, Y. G.; Lin, L.-C. Beyond the BET Analysis: The Surface Area Prediction of Nanoporous Materials Using a Machine Learning Method. *The Journal of Physical Chemistry Letters* **2020**, *11*, 5412–5417.

[26] Sinha, P.; Datar, A.; Jeong, C.; Deng, X.; Chung, Y. G.; Lin, L.-C. Surface Area Determination of Porous Materials Using the Brunauer–Emmett–Teller (BET) Method: Limitations and Improvements. *The Journal of Physical Chemistry C* **2019**, *123*, 20195–20209.

[27] Thommes, M.; Kaneko, K.; Neimark, A. V.; Olivier, J. P.; Rodriguez-Reinoso, F.; Rouquerol, J.; Sing, K. S. *Pure and Applied Chemistry* **2015**, *87*, 1051–1069.

[28] Michot, L. J., 2 - Determination of surface areas and textural properties of clay minerals In *Surface and Interface Chemistry of Clay Minerals*, Schoonheydt, R., Johnston, C., Bergaya, F., Eds.; Developments in Clay Science, Vol. 9; Elsevier: 2018, pp 23–47.

[29] Michot, L.; Villieras, F., Chapter 2.10 - Surface Area and Porosity In *Handbook of Clay Science*, Bergaya, F., Lagaly, G., Eds.; Developments in Clay Science, Vol. 5; Elsevier: 2013, pp 319–332.

[30] McCluskey, M. D.; Janotti, A. Defects in Semiconductors. *Journal of Applied Physics* **2020**, *127*, 190401.

[31] Pandey, S.; Shukla, A.; Tripathi, A. Elucidating the influence of native defects on electrical and optical properties in semiconducting oxides: An experimental and theoretical investigation. *Computational Materials Science* **2022**, *210*, 111037.

[32] Lau, V. W.-h.; Moudrakovski, I.; Botari, T.; Weinberger, S.; Mesch, M. B.; Duppel, V.; Senker, J.; Blum, V.; Lotsch, B. V. Rational design of carbon nitride photocatalysts by identification of cyanamide defects as catalytically relevant sites. *Nature Communications* **2016**, *7*, 12165.

[33] Wu, P.; Wang, J.; Zhao, J.; Guo, L.; Osterloh, F. E. Structure defects in g-C_3N_4 limit visible light driven hydrogen evolution and photovoltage. *Journal of Material Chemistry A* **2014**, *2*, 20338–20344.

[34] Li, M.; Huang, P.; Zhong, H. Current Understanding of Band-Edge Properties of Halide Perovskites: Urbach Tail, Rashba Splitting, and Exciton Binding Energy. *The Journal of Physical Chemistry Letters* **2023**, *14*, 1592–1603.

[35] Energy-band tails and the optical absorption edge; the case of a-Si:H. *Solid State Communications* **1982**, *44*, 1347–1349.

[36] Wolter, M. H.; Carron, R.; Avancini, E.; Bissig, B.; Weiss, T. P.; Nishiwaki, S.; Feurer, T.; Buecheler, S.; Jackson, P.; Witte, W.; Siebentritt, S. How band tail recombination influences the open-circuit voltage of solar cells. *Progress in Photovoltaics: Research and Applications* **2022**, *30*, 702–712.

[37] Nagpal, P.; Klimov, V. I. Role of mid-gap states in charge transport and photoconductivity in semiconductor nanocrystal films. *Nature Communications* **2011**, *2*, 486.

[38] Zarrabi, N.; Sandberg, O. J.; Meredith, P.; Armin, A. Subgap Absorption in Organic Semiconductors. *The Journal of Physical Chemistry Letters* **2023**, *14*, 3174–3185.

[39] Wong, J.; Omelchenko, S. T.; Atwater, H. A. Impact of Semiconductor Band Tails and Band Filling on Photovoltaic Efficiency Limits. *ACS Energy Letters* **2021**, *6*, 52–57.

[40] Stoneham, A., *Theory of Defects in Solids: Electronic Structure of Defects in Insulators and Semiconductors*; Oxford classic texts in the physical sciences; Clarendon Press: 2001.

[41] John, S.; Soukoulis, C.; Cohen, M. H.; Economou, E. N. Theory of Electron Band Tails and the Urbach Optical-Absorption Edge. *Phys. Rev. Lett.* **1986**, *57*, 1777–1780.

[42] Sarangapani, P.; Charles, J.; Kubis, T. Tuning Band Tails in Mono- and Multilayered Transition-Metal Dichalcogenides: A Detailed Assessment and a Quick-Reference Guide. *Phys. Rev. Appl.* **2022**, *17*, 024005.

[43] Cardona, M. Optical Properties and Electronic Density of States. *Journal of research of the National Bureau of Standards. Section A, Physics and Chemistry* **1970**, *74A*, 253–265.

[44] Spicer, W. E. Optical Density of States Ultraviolet Photoelectric Spectroscopy. *Journal of research of the National Bureau of Standards. Section A, Physics and Chemistry* **1970**, *74A*, 397–415.

[45] Zhang, Y.; Pan, Q.; Chai, G.; Liang, M.; Dong, G.; Zhang, Q.; Qiu, J. Synthesis and luminescence mechanism of multicolor-emitting g-C_3N_4 nanopowders by low temperature thermal condensation of melamine. *Scientific Reports* **2013**, *3*, 1943.

[46] Liu, F.; Tong, Y.; Li, C.; Liu, X. One-Dimensional Conjugated Carbon Nitrides: Synthesis and Structure Determination by HRTEM and Solid-State NMR. *The Journal of Physical Chemistry Letters* **2021**, *12*, 10359–10365.

[47] Morgan, D. J. Core-level reference spectra for bulk graphitic carbon nitride (g-C_3N_4). *Surface Science Spectra* **2021**, *28*, 014007.

[48] Benedet, M.; Rizzi, G. A.; Barreca, D.; Gasparotto, A.; Maccato, C. XPS analysis of graphitic carbon nitride functionalized with CoO and $CoFe_2O_4$. *Surface Science Spectra* **2023**, *30*, 014004.

[49] Hellgren, N.; Haasch, R. T.; Schmidt, S.; Hultman, L.; Petrov, I. Interpretation of X-ray photoelectron spectra of carbon-nitride thin films: New insights from in situ XPS. *Carbon* **2016**, *108*, 242–252.

[50] Ronning, C.; Feldermann, H.; Merk, R.; Hofsass, H.; Reinke, P.; Thiele, J.-U. Carbon nitride deposited using energetic species: A review on XPS studies. *Physical Review B* **1998**, *58*, 2207–2215.

[51] Baker, M. A.; Hammer, P. A Study of the Chemical Bonding and Microstructure of Ion Beam-deposited CNx Films Including an XPS C 1s Peak Simulation. *Surface and Interface Analysis* **1997**, *25*, 629–642.

[52] Chen, Z. Y.; Zhao, J. P.; Yano, T.; Ooie, T. Valence band electronic structure of carbon nitride from X-ray photoelectron spectroscopy. *Journal of Applied Physics* **2002**, *92*, 281–287.

[53] Monclus, M.; Cameron, D.; Chowdhury, A.; Barkley, R.; Collins, M. Investigation of the valence band states of reactively sputtered carbon nitride films. *Thin Solid Films* **1999**, *355-356*, 79–84.

[54] Bui, D.-P.; Pham, M.-T.; Tran, H.-H.; Nguyen, T.-D.; Cao, T. M.; Pham, V. V. Revisiting the Key Optical and Electrical Characteristics in Reporting the Photocatalysis of Semiconductors. *ACS Omega* **2021**, *6*, 27379–27386.

[55] Maheu, C.; Cardenas, L.; Puzenat, E.; Afanasiev, P.; Geantet, C. UPS and UV spectroscopies combined to position the energy levels of TiO_2 anatase and rutile nanopowders. *Physical Chemistry Chemical Physics* **2018**, *20*, 25629–25637.

Chapter 6

Exploring the Iono-Thermal Synthesis Route for Graphitic Carbon Nitride: Structural Insights and Solar Fuel Applications

Abstract

In this chapter, we describe the ionothermal synthesis of lithium polytriazine imide (Li-PTI) and its application in photon-assisted CO_2 reduction for solar fuel production. The research investigates the impact of synthesis atmosphere (air vs. nitrogen) on the structural, electronic, and catalytic properties of Li-PTI materials. The Li-PTI samples were synthesized using lithium chloride as the molten salt and melamine as the precursor. Comprehensive characterization techniques, including X-ray diffraction (XRD), UV-visible spectroscopy, X-ray photoelectron spectroscopy (XPS), and nitrogen adsorption-desorption analysis, were employed to elucidate the properties of the materials. XRD analysis revealed higher crystallinity in Li-PTI-N_2 than in Li-PTI-AIR, with crystallite sizes of 14.3 nm and 6.92 nm, respectively. UV-Vis spectroscopy revealed differences in the light absorption and band gap energies of the samples. XPS studies indicated variations in the surface chemical composition and valence band positions, while nitrogen adsorption-desorption analysis demonstrated differences in the surface area and pore characteristics. Photon-assisted CO_2 reduction experiments showed that Li-PTI-N_2 exhibited superior performance, with higher yields of methanol ($3.22\,\mu\mathrm{mol\,g^{-1}\,h^{-1}\,m^{-2}}$) and oxygen ($4.51\,\mu\mathrm{mol\,g^{-1}\,h^{-1}\,m^{-2}}$) than those of Li-PTI-AIR. The enhanced activity of Li-PTI-N_2 was attributed to its higher crystallinity, increased DP/SA value, moderate C value, and the presence of edge sites on the surface. Band diagrams were constructed using valence-band XPS and diffuse reflectance spectroscopy data to provide insights into the electronic structure of the materials and their suitability for CO_2 reduction. Possible reaction mechanisms for the formation of methane and methanol are proposed based on the experimental results. This study demonstrated the significant influence of the synthesis atmosphere on the properties and photon-assisted catalytic performance of Li-PTI materials. These findings contribute to the understanding of the structure-property-performance relationships in carbon nitride-based photon-assisted catalysts and offer insights for the design of efficient

materials for solar fuel production through CO_2 reduction.

6.1 Introduction

Molten-salt-assisted ionothermal synthesis (MSAIS) is a technique that utilizes molten salts to produce functional materials at high temperatures. This method offers several advantages, as molten salts act as both the solvent and reaction medium, allowing for precise control over temperature, pressure, and ion conductivity. Moreover, the high temperatures within the molten salt melt enable the rapid diffusion of ions and efficient chemical reactions, leading to the formation of complex materials with unique properties. Additionally, MSAIS typically uses environmentally friendly starting materials and avoids the use of organic solvents, making it a more sustainable and potentially scalable process than traditional synthesis methods.

The specific mechanism of MSAIS depends on the material and reaction conditions involved. However, certain key aspects were common. The precursor materials dissociate into ions or ionic complexes when dissolved in a molten salt, increasing the mobility of the ions and facilitating subsequent interactions. Ions from the precursors participate in various exchange and reaction processes driven by thermodynamics and the specific properties of the salt, leading to the formation of new ionic bonds and the assembly of the desired material structure. As the reaction progressed, the newly formed material nucleated and grew into crystals under the influence of factors such as temperature gradients, concentration changes, and inherent properties of the molten salt. Once the synthesis was complete, the reaction mixture was rapidly cooled to stabilize the final product, and the subsequent washing and purification steps removed any residual salts or unreacted precursors.

The factors that significantly impact the Molten Salt-Assisted Ionothermal Synthesis (MSAIS) process are the molten salt chosen, temperature, pressure, and the properties of the starting materials. Molten salt influences the solubility, reactivity, and stability of the precursors and final product, and factors such as the melting point, ionic conductivity, and chemical compatibility must be considered. The reaction kinetics, phase formation, and morphology of the synthesized material are also regulated by the temperature and pressure, which must be precisely controlled. The properties of the starting materials also play a significant role in determining the solubility, reactivity, and characteristics of the final product because they influence the properties of the precursor materials.

Selecting the appropriate molten salt and precursor for material synthesis using MSAIS is crucial for successful synthesis and control of the properties of the material. To avoid decomposition or unwanted side reactions, the melting point of the molten salt should be lower than the desired synthesis temperature, and its stability at the selected temperature should be considered. High ionic conductivity ensures efficient ion transport and reaction kinetics. Eutectic mixtures of salts are often used to achieve desired melting points and conductivity properties. The molten salt should not react with either the precursors or final product at a given temperature. It is important to select salts with negligible solubility as the target materials and precursors. In addition, for reactions involving oxidation or reduction, the redox behavior of the molten salt must be considered. Salts containing cations with

variable oxidation states, such as Mn^{2+}/Mn^{3+} or Ce^{3+}/Ce^{+}, can participate in redox reactions. Molten salts can exhibit Lewis acidic or basic properties owing to their cations and anions, which can influence the reaction mechanism and the morphology of the final product. Therefore, it is important to select salts that complement the desired acidic/basic environment for synthesis.

Precursor selection is critical to ensure a stable reaction environment and achieve the desired characteristics of the final product. Chemical compatibility is essential because the precursors do not react with each other or molten salt at the synthesis temperature. The morphology of the precursors also influences the crystallinity, grain size, and porosity of the final product. Therefore, it is crucial to select precursors with appropriate morphologies such as particles or powders.

In addition to chemical compatibility, the decomposition temperature of the precursors should be sufficiently higher than the synthesis temperature to avoid premature decomposition, which could negatively impact the quality of the final product. The cost and availability of the chosen precursors should also be considered for practical and scalable syntheses to ensure the feasibility of large-scale production. Other factors such as the environmental impact and safety of the selected precursors may also need to be considered.

Molten salt-assisted synthesis (MSAIS) is an essential approach for the generation of various carbon nitride materials that exhibit exceptional characteristics and show promise for numerous applications. Commonly used organic precursors include melamine, urea, thiourea, dicyandiamide, and cyanamide, which are frequently utilized because of their substantial nitrogen content and their capacity to decompose into CN_x intermediates at high temperatures. Inorganic precursors can also be used, such as cyanides of alkali metals (e.g., LiCN and NaCN) or metal salts (e.g., $FeCl_3$), combined with carbon sources such as graphite or melamine. Alkali metal halides, including NaCl, KCl, LiCl, and their eutectic mixtures, are commonly employed in carbon nitride synthesis due to their low melting points, good ionic conductivity, and minimal interaction with carbon nitride precursors. Other salts, such as $LiNO_3$, KNO_3, Na_2CO_3, and $CaCl_2$, have been explored for specific purposes and offer properties such as enhanced surface area or controlled morphology.

The formation mechanism of carbon nitride involves the decomposition of organic precursors at high temperatures within the molten salts, resulting in the release of CN_x intermediates and other volatile components. These intermediates react with each other to form triazine rings, which eventually polymerize into carbon nitride structures. The formation of carbon nitride crystals is influenced by temperature, concentration gradients, and salt properties, and the process is stabilized by rapid cooling and subsequent washing to remove residual salts and impurities.

The primary factor that determines the characteristics of carbon nitride is the nature of the molten salts, which can alter its morphology, crystallinity, and surface area during the synthesis process. Longer reaction times and higher temperatures generally lead to increased crystallinity and larger grain sizes. The type and purity of the precursor can affect the nitrogen content, surface functionality, and dopant incorporation possibilities, whereas introducing specific elements during the synthesis can tailor the electronic and catalytic properties of the resulting carbon nitride.

Molten salt-assisted ionothermal synthesis (MSAIS) is a promising approach for

generating carbon nitrides with tailored properties that may be valuable for CO_2 photoreduction. By adjusting the salt type, precursor, and synthesis conditions, the bandgap and electronic levels of carbon nitride can be optimized for efficient CO_2 conversion, light absorption, and charge-carrier dynamics. MSAIS often produces carbon nitrides with high crystallinity and well-defined pore structures, facilitating efficient mass transport of CO_2 molecules to the active sites on the surface of the material, thereby improving the photoconversion efficiency. Moreover, MSAIS allows for the incorporation of heteroatoms (dopants), such as Si, P, or S, during synthesis, which can further refine the bandgap and introduce additional active sites for CO_2 photoreduction, thereby enhancing the catalyst selectivity and activity. Additionally, MSAIS offers control over the morphology (nanosheets, nanotubes, etc.) of carbon nitride, with specific morphologies maximizing light harvesting and the surface area for CO_2 adsorption, leading to improved photoactivity. Compared to other synthesis methods, MSAIS is relatively cost-effective and adaptable for scaling up production, making it a suitable option for practical CO_2 utilization applications.

The challenges and considerations of carbon nitrides synthesized using MSAIS include enhancing their stability and durability under extended photocatalytic conditions. To achieve selective conversion of CO_2 into targeted products, such as hydrocarbons or methanol, further research is necessary on the selection of dopants and reaction tuning. Additionally, the development of cost-effective strategies for regenerating and recycling spent carbon nitride catalysts is essential for ensuring long-term sustainability and economic feasibility.

In this study, lithium chloride and melamine were used as the ionic salts and precursors, respectively. The high melting point of lithium chloride facilitates the dissolution of melamine into the molten salt at the synthesis temperature. The ionothermal synthesis of carbon nitrides was investigated by conducting the synthesis process in both air and nitrogen environments. The aim of this study is to examine the impact of the synthesis atmosphere on the formation of carbon nitrides and how it can be useful in the photon-assisted reduction of carbon dioxide to value-added chemicals and fuel.

6.1.1 Discussion on CO_2 Photoreduction Results

The figures 6.1 and 6.2 illustrate the photoreduction outcomes of carbon dioxide utilizing lithium polytriazine imide (PTI) synthesized under both air and nitrogen atmospheres. It is evident that Li-PTI-N_2 achieved significantly higher product yields, specifically in methanol ($3.22\,\mu\mathrm{mol\,g^{-1}\,h^{-1}\,m^{-2}}$) and oxygen ($4.51\,\mu\mathrm{mol\,g^{-1}\,h^{-1}\,m^{-2}}$), than Li-PTI-AIR. This finding implies that a nitrogen atmosphere considerably promotes the transformation of CO_2 into methanol during photoreduction.

The productivity of methanol in Li-PTI-N_2 is more than double that of Li-PTI-AIR, amounting to $3.22\,\mu\mathrm{mol\,g^{-1}\,h^{-1}\,m^{-2}}$ as opposed to $1.58\,\mu\mathrm{mol\,g^{-1}\,h^{-1}\,m^{-2}}$. This unequivocally demonstrates the advantageous effect of a nitrogen atmosphere on methanol production. Furthermore, Li-PTI-N_2 exhibits greater production of oxygen, amounting to $4.51\,\mu\mathrm{mol\,g^{-1}\,h^{-1}\,m^{-2}}$, as compared to Li-PTI-AIR, which amounts to $2.79\,\mu\mathrm{mol\,g^{-1}\,h^{-1}\,m^{-2}}$. This suggests higher efficiency of water oxidation, which is a critical component of the overall CO_2 photoreduction cycle. It is important to note that methane production was negligible in both cases, with values of less than

$0.004\,\mu\mathrm{mol\,g^{-1}\,h^{-1}\,m^{-2}}$. This finding indicates that the PTI catalyst exhibits high selectivity towards methanol and oxygen production, minimizing the formation of undesired byproducts.

6.1.2 X-ray Diffraction

XRD data were collected using a Bruker D8 Advance diffractometer equipped with Cu Kα radiation (wavelength = 1.5418 Å) in the 2θ range of 10–70°. The step size was 0.034° and each step was performed for 5 s. The acquired data were processed using the X'Pert HighScore Plus software (version 3.0), which involved subtracting the background and normalizing the data [1].

The X-ray diffraction pattern of PTI/Li^+Cl^- revealed that the compound was layered, with an interlayer spacing of $3.35\,$Å. This is indicated by the strongest reflection indexed as 002, analogous to that of graphite. The PTI/Li^+Cl^- sample exhibited numerous well-resolved and intense X-ray reflections, which suggests that the salt melt technique resulted in high crystallinity. The broadening of the single reflections was attributed to the nanocrystalline nature of the sample. PTI/Li^+Cl^- samples were prepared in both air and nitrogen atmospheres, resulting in the labels Li-TPI-AIR and Li-PTI-N_2, respectively. The crystallite sizes of these samples were determined to be $6.92\,\mathrm{nm}$ and $14.3\,\mathrm{nm}$ using the Scherrer equation to analyze X-ray diffraction data. Additionally, the microstrain of the samples was found to be 1.24 and 0.63 for Li-TPI-AIR and Li-PTI-N_2, respectively.

To investigate the structure of gCN materials, Rietveld refinement was carried out using the PANalytical X'Pert HighScore Plus software (version 3.0). The initial model was based on the reported crystal structure of [$(C_3N_3)_2(NH_xLi_{1-x})_3$·LiCl] (ICSD 422088; Structure: Poly(bis(triazine) triimide) lithium chloride; Space Group: $P6_3cm$, Cell: $a = 8.468\,24$ Å, $b = 8.468\,24$ Å, $c = 6.750\,20$ Å, $\alpha = 90°$, $\beta = 90°$, $\gamma = 119.99°$), which belongs to the hexagonal crystal system [2]. The refinement process yielded all single-digit agreement indices, indicating excellent agreement between the calculated and observed data. The refinement process was performed only for Li-PTI-N_2 because of its highly crystalline nature and the presence of distinct peaks (Figure 6.3). However, for Li-PTI-AIR, the observed broad reflections prevented the valid refinement of the data. Lithium polytriazine imide (L-PTI-N_2) is a carbon nitride material with a well-defined crystalline structure composed of triazine rings connected by imide groups with lithium ions inserted between the layers (Figure 6.3). This material forms a layered structure characterized by a 2D network of essentially planar layers that are stacked upon each other, with voids between them that are stacked upon each other to form channels running parallel to the c-axis. These channels are filled with lithium ions, which contributes to the unique properties of L-PTI-N_2. Lithium ions interact with the nitrogen atoms in the triazine rings and imide groups, establishing strong ionic bonds that influence the electronic properties of L-PTI. Each layer consists of triazine rings connected by imide bridges, forming a nearly flat, hexagonal pattern that optimizes intermolecular interactions and contributes to the good electrical conductivity of L-PTI-N_2. The layers stack in a specific orientation, creating channels along the c-axis of the crystal structure, which play a crucial role in applications such as gas separation and catalysis.

The X-ray powder diffraction (XRD) pattern of the Li-PTI-N_2 sample exhibits

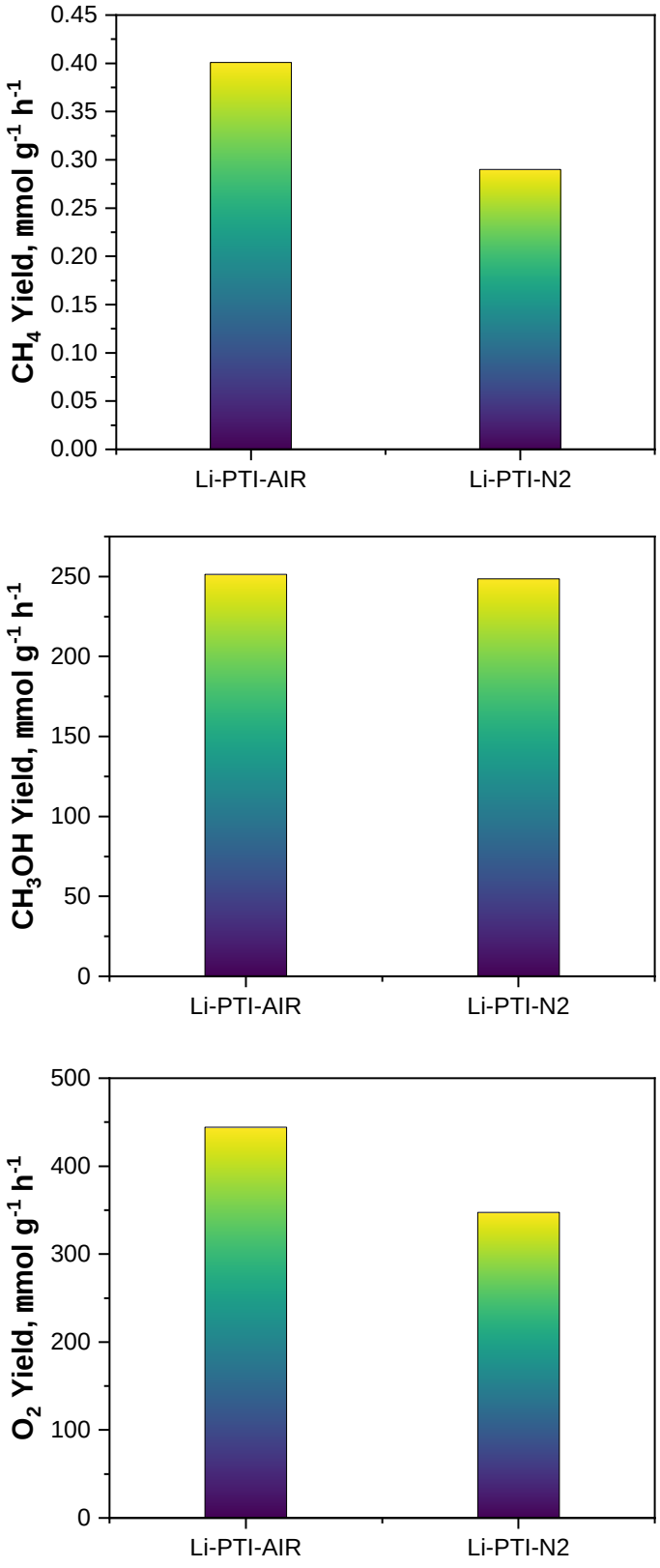

Figure 6.1: Product yields from the reduction of CO_2 over Li-PTI samples, activity reported with respect to total surface area.

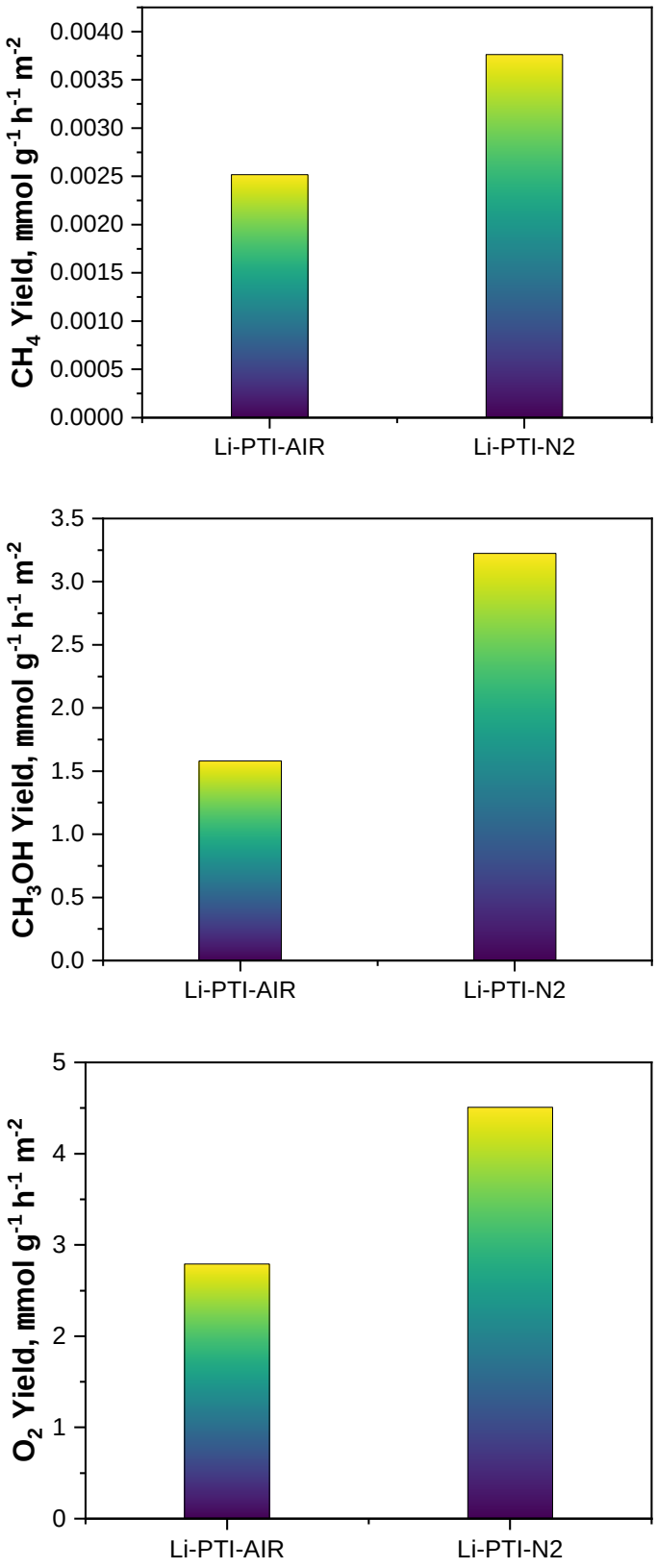

Figure 6.2: Product yields from the reduction of CO_2 over Li-PTI samples, activity reported in unit surface area.

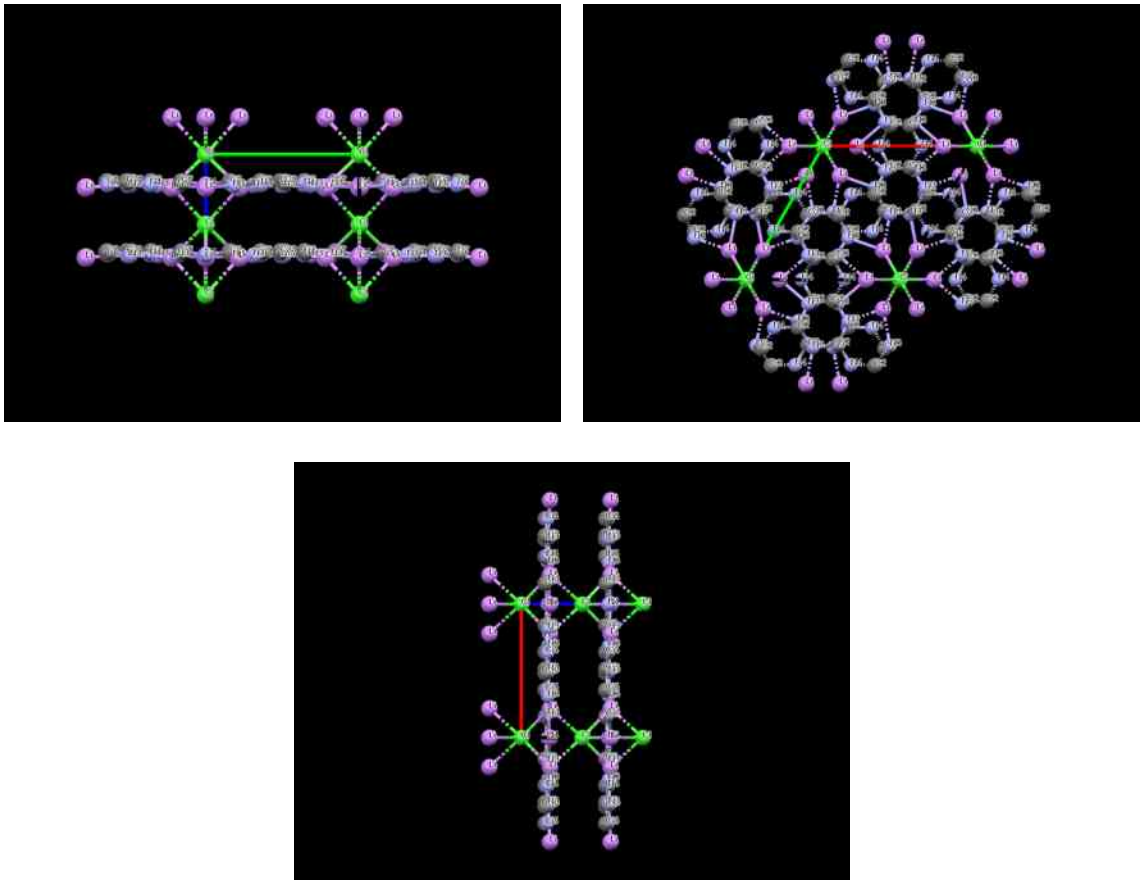

Figure 6.3: Structural features of Li-PTI-N_2

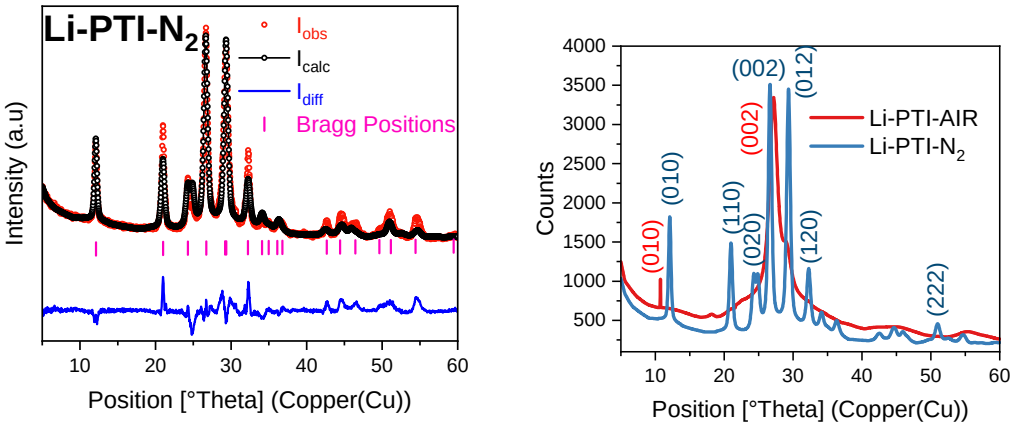

Figure 6.4: The LeBail fit of Li-PTI-N_2 and the X-ray diffraction pattern of Li-PTI-N_2 and Li-PTI-AIR.

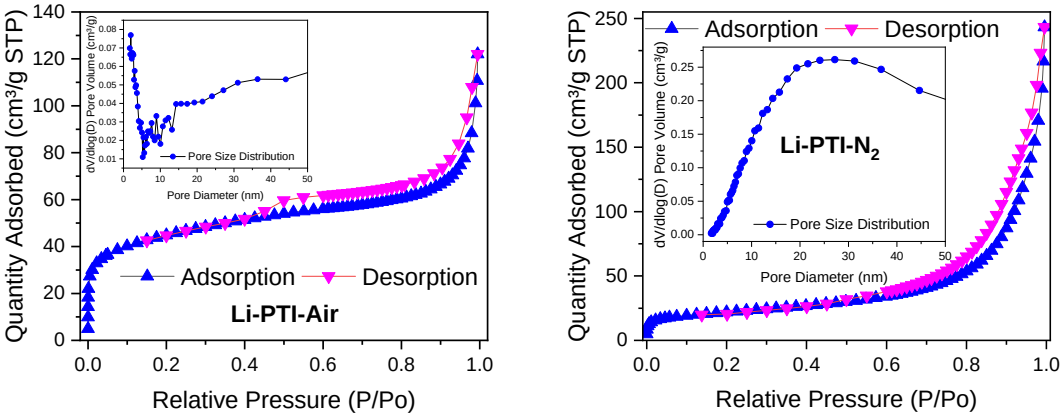

Figure 6.5: N_2 adsorption isotherms of Li-PTI-AIR and Li-PTI-N_2

sharp peaks, indicative of a high degree of crystallinity (Figure 6.4). In contrast, broad peaks or a halo pattern in the Li-PTI-AIR sample suggest a more disordered structure, which could be either amorphous or poorly ordered. Determining the phase purity of a sample by comparing its peak numbers and intensities to the reference patterns of known L-PTI polymorphs is common practice. The results of this analysis indicate that the phase purity of Li-PTI-N_2 was high, demonstrating the effectiveness of the synthesis method.

6.1.3 Adsorption Isotherm Analysis

The nitrogen adsorption-desorption isotherms of the Li-PTI-N_2 class of materials exhibit type-III characteristics, suggesting weak interactions between the adsorbate and adsorbent, the presence of adsorbed N_2 in the interlayer, or the presence of porous structures in the samples (Figure 6.5)[3–5]. These isotherms display type H3 hysteresis loops at $0.45 < \frac{P}{P_0} < 1.00$, which is a characteristic often observed in aggregates of plate-like particles, and suggests the existence of slit-shaped pores. The average pore sizes of all the carbon nitride samples were in the mesoporous regime. The Li-PTI-AIR classified as type II isotherm is characteristic of macroporous materials with relatively large open pores. It typically exhibits a gradual increase in gas uptake at low pressures, followed by a steeper rise owing to capillary condensation within the pores, and finally a plateau at high pressures as all available pores are filled. The pore size of $5.07\,\mathrm{nm}$ indicates that the Li-PTI sample has mesopores with diameters ranging from $2\,\mathrm{nm}$ to $50\,\mathrm{nm}$. The isotherm of Li-PTI-N_2 shows weak interactions between the surface and N_2 gas molecules, unlike type-II isotherms that have a well-defined capillary condensation step. This results in a more gradual and continuous increase in gas uptake over the pressure range. Compared to Li-PTI-AIR, the pore size of $20.16\,\mathrm{nm}$ indicates the presence of mesopores in Li-PTI synthesized in nitrogen. These differences in isotherm type and pore size emphasize the sensitivity of Li-PTI properties to synthesis conditions. The synthesis in the presence of nitrogen likely influenced the growth mechanism and pore structure of the material.

The B.E.T equation is often rearranged to linearize the isotherm and determine the slope and intercept of a specific plot. If the resulting value of C is negative, the

Table 6.1: Surface area characteristics of Li-PTI-AIR and Li-PTI-N_2

	B.E.T	**BETSI**	**SESAMI**	C**, SESAMI**
Li-PTI-AIR	148.94	160	159.1	421.1
Li-PTI-N_2	74.67	77	77.1	298.2

Table 6.2: Pore characteristics of Li-PTI-AIR and Li-PTI-N_2

	qm, $\mathrm{mol\,kg^{-1}}$	**Pore Size,** nm	**t-plot M.A**
Li-PTI-AIR	1.63	5.07	51.36
Li-PTI-N_2	0.79	20.16	17.32

linearized plot does not fit the assumed B.E.T model well [6]. This could be due to various reasons such as the non-ideal behavior of the adsorbate or limitations in the applicability of the B.E.T model to a specific adsorption system. A negative C value suggests that the B.E.T model may not accurately describe the adsorption isotherm for a given material or condition [7]. It is essential to interpret such results cautiously and consider alternative models or factors that might affect adsorption behavior [8–11]. All samples shown negative C values, indicating that they do not follow the B.E.T equation, or corrections in the BET equation are recommended according to the Rouquerol equation [12]. The surface area data were fitted using BETSI and SESAMI techniques, and the results are presented in Table 6.1. Almost the same surface area was observed after correction; however, as the microporosity increased, the deviation became too large. In addition, it is well known that the B.E.T equation is not suitable for microporous materials or materials containing large numbers of micropores.

The study of the surface area and porosity data, primarily utilizing the SESAMI method, yielded valuable insights into the relationship between these properties and the observed CO_2 reduction activity of the *g*-CN samples. The SESAMI method quantifies the interaction potential between the adsorbate and adsorbent surface by C. A higher C value signifies stronger interactions, which can enhance CO_2 adsorption and activation. Li-PTI-AIR exhibited the highest value of C among the samples, and its activity was found to be less than that of the Li-PTI-N_2. Moreover, Li-PTI-AIR had a high total micropore percentage and a high percentage of micropores per unit surface area (Table 6.1). Further research using advanced adsorption isotherms is necessary to fully understand the relationship between the pore size distribution and catalytic performance. The complex and multifaceted relationship between microporosity and surface area suggests that other factors, such as the formation of defects and surface chemistry, significantly influence the overall surface properties of a material.

6.1.4 Derivative Adsorption Summation

In gas adsorption analysis, evaluating surface heterogeneity commonly involves obtaining numerous experimental data points at extremely low relative pressures, generally less than 0.15, during which the monolayer filling occurs. The free energy of adsorption on the kT scale can be precisely determined by computing

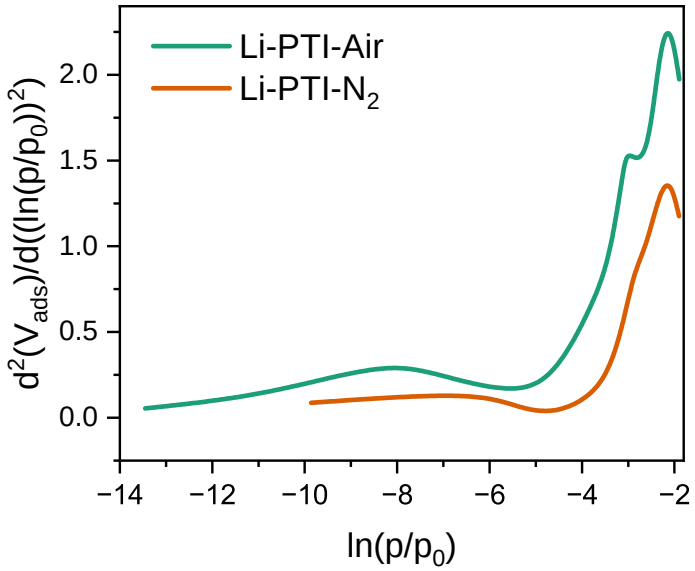

Figure 6.6: Second derivative isotherm summation plot of Li-PTI-AIR and Li-PTI-N_2

the derivatives of the adsorption amount relative to the logarithm of the relative pressure, $\ln \frac{p}{p_0}$ [13, 14].

The curve presented in Figure 6.6 demonstrates the gas adsorption energy on the surface, as derived from the nitrogen adsorption isotherm at $77\,\mathrm{K}$. The second derivative was employed to differentiate between the peaks and shoulders in the derivative isotherm summation (DIS) plots. In the second-derivative isotherm summation (SDIS), noticeable peaks can be observed as downward dips in the curve. The DIS curve represents the second derivative of the adsorption isotherm, and the minima in the second derivative correspond to the maxima in the original isotherm, indicating the strongest binding sites. Two-dimensional materials exhibit basal, edge, and high-energy adsorption surfaces, each corresponding to low, medium, and high energies, respectively, as reported in [13, 14].

The second derivative of the DIS isotherm reveals that Li-PTI-AIR and Li-PTI-N_2 exhibit notable peaks in the low-energy domain and in the region corresponding to the basal planes, as well as in the moderate-energy range or edge sites. The downward deviations observed in Li-PTI-AIR and Li-PTI-N_2 suggest the presence of moderate-energy surfaces or edge sites. In the case of Li-PTI-N_2, the edge sites dominate and demonstrate considerable activity towards methane and methanol production. The number of edge sites in Li-PTI-AIR is lower than that in Li-PTI-N_2. The activity of Li-PTI-N_2 can be attributed to the combined effect of its high crystallinity and moderate C values, as well as the presence of edge sites. It is important to note that the oxygen evolution was also relatively high in Li-PTI-AIR and Li-PTI-N_2.

6.1.5 Energy Dispersive X-ray Analysis

The elemental compositions of Li-PTI-Air and Li-PTI-N_2 were analyzed to evaluate their chemical makeup. Both samples consisted mainly of carbon (C), nitrogen (N), oxygen (O), and trace amounts of chlorine (Cl) (Table 6.3). Upon comparing

	Element	Weight %	MDL	Atomic %	Net Int.	Error %
Li-PTI-Air	C K	57.1	0.35	61.6	488.5	9.9
	N K	34.7	1.34	32.1	64.7	13.8
	O K	7.6	0.52	6.1	34.6	14.8
	Cl K	0.7	0.05	0.2	66.7	8.4
Li-PTI-N_2	C	56.6	1.06	61.2	-	11.6
	N	34.4	3.20	31.9	-	16.3
	O	8.1	1.10	6.6	-	18.3
	Cl	0.9	0.07	0.3	-	7.8

Table 6.3: Elemental analysis of Li-PTI-Air and Li-PTI-N_2

the two samples, Li-PTI-Air exhibited slightly higher weight percentages of carbon (57.1%) and nitrogen (34.7%) than Li-PTI-N_2 (56.6% and 34.4%, respectively). However, these differences were marginal and may have been within the experimental error. It is interesting to note that the weight percentage of oxygen was slightly higher in Li-PTI-N_2 (8.1%) than in Li-PTI-Air (7.6%), possibly indicating a minor difference in the synthesis conditions or the presence of oxygen-containing species in the nitrogen atmosphere.

Both samples contained trace amounts of chlorine, with similar weight percentages (0.7-0.9%) and atomic percentages (0.2-0.3%). The detection of chlorine suggested potential contamination or the presence of chlorine-containing compounds in the samples. It is important to mention that the error percentages for some elements, particularly oxygen, were relatively high (14.8-18.3%), which may affect the accuracy of their quantification. Nonetheless, qualitative detection of elements provides valuable insights into the overall composition of the samples.

Notably, lithium (Li) was not detected in either sample by energy-dispersive X-ray analysis (EDAX). The absence of lithium detection can be attributed to its low atomic number and the limitations of the EDAX technique, which may have insufficient sensitivity to detect elements with low atomic numbers or concentrations. Additionally, Li may have been present at concentrations below the detection limit of the EDAX instrument. Elemental analysis revealed minor differences in the compositions of the two samples, likely attributable to experimental variability or subtle differences in the synthesis conditions.

6.1.6 Solid State Ultraviolet Visible Spectroscopy

Solid-state ultraviolet-visible (UV-Vis) spectroscopy is an indispensable tool for characterizing the electronic structures and potential functionalities of Lithium Polytriazine Imide (Li-PTI) samples. This technique allows for detailed analysis of the triazine ring absorption, bandgap absorption, impurity and defect peaks, and charge transfer transitions in Li-PTI materials. The primary component of Li-PTI is the triazine ring structure, which exhibits strong π-π^* transitions in the ultraviolet (UV) region (approximately 200-250 nm). The intensity and position of these transitions can be influenced by specific substitution patterns and conjugation within the triazine rings. As a semiconductor, Li-PTI has a bandgap in the visible or near-UV range. The onset of absorption in the spectrum, characterized by a steep increase in absorbance, corresponds to the bandgap energy (Eg). The UV-Vis

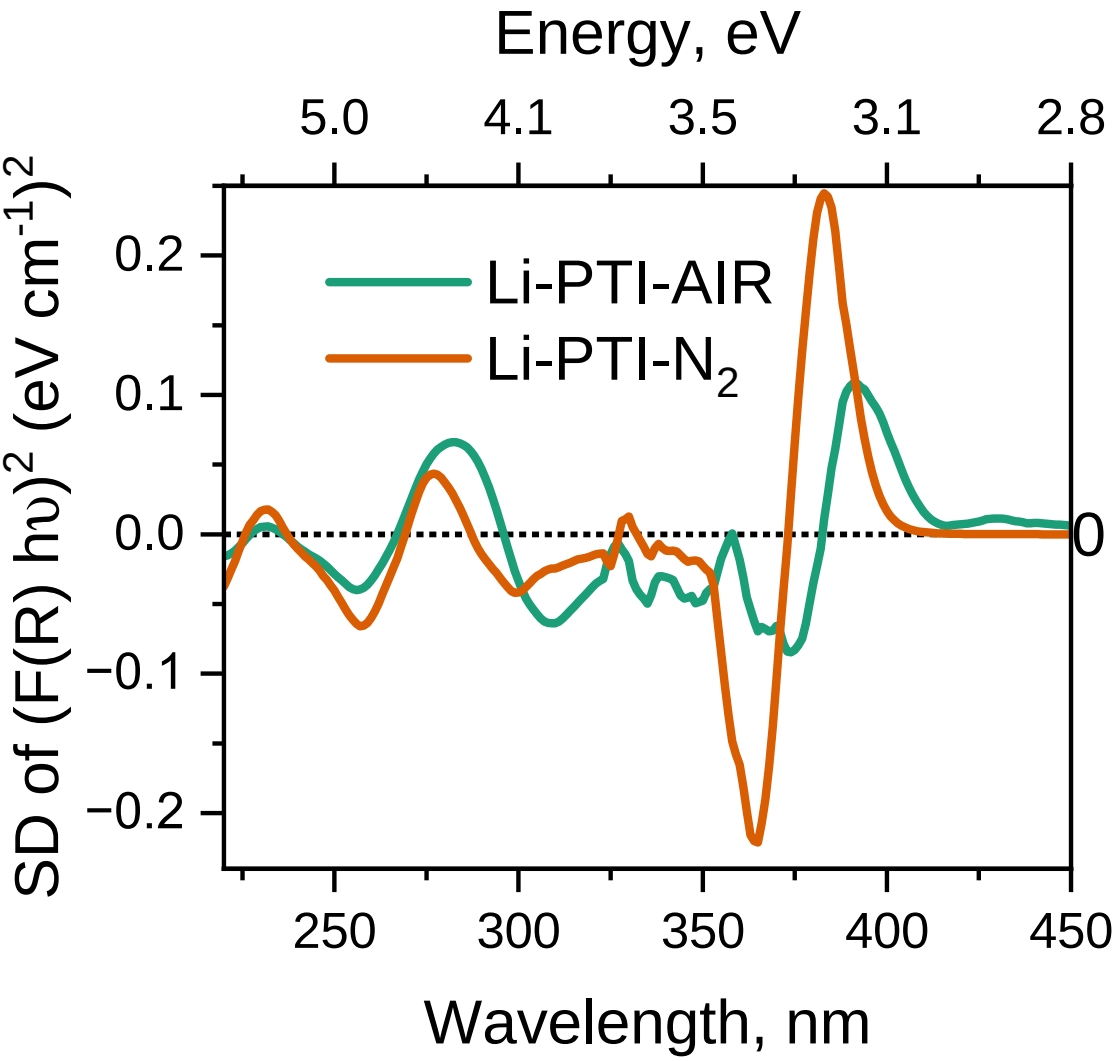

Figure 6.7: Second derivative of Kubelka-Munk plot of Li-PTI-AIR and Li-PTI-N_2

spectrum of Li-PTI synthesized in nitrogen exhibits a sharper peak near the band edge compared to that of the air-prepared sample, suggesting various potential reasons with consequent implications. The use of nitrogen during synthesis might have resulted in the better crystallinity of Li-PTI, as sharper peaks in the UV-Vis spectrum typically indicate well-defined electronic transitions within a more ordered crystalline structure. This improved crystallinity may lead to enhanced electronic properties and superior performance in applications, such as photocatalysis and photovoltaics. Additionally, the nitrogen environment during the synthesis may have minimized the introduction of defects within the Li-PTI structure. Defects can act as trap states for electrons, resulting in broader and weaker absorption peaks in the spectrum. The presence of a sharper peak suggests fewer defects, which can result in improved charge transport and higher photocatalytic activity. In some instances, nitrogen atoms may be directly incorporated into the Li-PTI framework during synthesis in a nitrogen environment. This nitrogen doping can create new energy levels within the bandgap, leading to additional absorption peaks or influencing the position and sharpness of the band edge peak. The specific impact depends on the doping level and the location of the nitrogen atoms. The presence

of nitrogen during synthesis might influence the local environment surrounding the Li^+ ions within the Li-PTI structure. This can slightly alter the electronic transitions responsible for the band edge absorption, potentially leading to a sharper peak owing to more consistent interactions within the material.

The UV-Vis spectra of your Li-PTI samples display distinct peaks at 200 nm and 275 nm, which are likely attributed to π-π* transitions within the triazine rings, a structural element in Li-PTI. These peaks were expected to appear regardless of the sample synthesis environment, whether in nitrogen or air. However, a noticeable deviation occurs near the band edge, with the sample prepared in air exhibiting a sharper deviation than the sample prepared in nitrogen. This deviation could be due to differences in the molecular packing or the presence of impurities, which affect the electronic properties of the samples and lead to variations in the UV-Vis spectra. The most intriguing and potentially applicable observation was the sharp peak near the band edge (beyond 340 nm) in the nitrogen-prepared Li-PTI. The sharper peak observed in the nitrogen-synthesized sample can be attributed to various factors. One possibility is that nitrogen synthesis led to a more ordered crystal structure with fewer defects, resulting in sharper electronic transitions and a more distinguishable band edge peak. Defects, such as missing atoms or structural imperfections, act as electron traps, causing broadening and weakening of the absorption peaks. Therefore, the reduced number of defects in the nitrogen-prepared sample led to a sharper band-edge peak. In addition, nitrogen atoms may be incorporated into the Li-PTI structure during nitrogen synthesis, which could introduce new energy levels within the bandgap. This doping could potentially shift or sharpen the band edge peak. The nitrogen environment may also influence the arrangement of Li^+ ions within the structure, subtly altering the electronic transitions and resulting in a sharper peak.

The observation that the Li-PTI prepared in air has a band edge extending to 500 nm, whereas the band tail of the nitrogen-prepared sample stops near 440 nm, presents several interesting possibilities regarding its optical properties and potential applications. One possible explanation for this difference is the variation in bandgap energy between the two samples. The air-prepared Li-PTI may have a wider bandgap, leading to absorption up to higher wavelengths (500 nm), compared to the nitrogen-prepared sample with a potentially narrower bandgap (absorption ending near 440 nm). The discrepancy in the bandgap can be attributed to various factors that arise during the synthesis process; for example, the crystal structure and defect formation may be influenced by different conditions, which in turn affects the bandgap. Furthermore, the presence of unintentional dopants or impurities during the air synthesis can slightly broaden the bandgap. Additionally, if nitrogen is directly introduced into the Li-PTI structure during nitrogen synthesis, it may create new energy levels that narrow the bandgap. Another possibility is that the air-prepared sample may have more defects that act as trap states for electrons. These trap states can introduce additional absorption at lower energies (longer wavelengths), extending the apparent band edge in the UV-Vis spectrum, even if the intrinsic bandgap is similar. Nitrogen synthesis may have resulted in fewer defects, leading to a sharper band edge without additional low-energy absorption tails. Light scattering within the material can affect the UV–Vis spectrum. If the air-prepared Li-PTI has a rougher surface or a larger particle size, it might scatter more light, potentially contributing to the extended tail in the spectrum.

Sample	Band Gap, eV						U.E meV
	Tauc Plot			K-M Plot			
	L.R	F.D	S.D	L.R	F.D	S.D	L.R
Li-PTI-AIR	2.88	3.67	3.12	3.08	3.24	3.17	447
Li-PTI-N_2	3.16	3.28	3.21	3.28	3.33	3.24	184

Table 6.4: Bandgap and urbach energy determination of Li-PTI samples

The bandgap value was determined using the second derivative method and was subsequently utilized in calculations to elucidate the positions of the band edges (Table 6.4). As expected from the band tail, the Urbach energy of Li-PTI-AIR is greater than that of Li-PTI-N_2. This indicates that there will be a greater number of defects in the Li-PTI-AIR, resulting in non-uniform recombination of charge carriers.

	D Parameter	SA	C	DP /SA
Li-PTI-AIR	0.1935	159.1	421.1	0.0012
Li-PTI-N_2	0.46593	77.1	298.2	0.0060

Table 6.5: Derivative diffuse reflectance spectroscopic analysis

The results of the second-derivative diffuse reflectance spectroscopy analysis demonstrated that Li-PTI-N_2 exhibits a higher value of the D parameter and DP/SA ratio than Li-PTI-AIR (Table 6.5). The elevated DP/SA value of Li-PTI-N_2 indicated superior light absorption by the surface, which compensated for its lower C value. This enhanced absorption cross-section facilitates the distribution of charge carriers at the edge sites, ultimately leading to an improved CO_2 reduction performance.

6.1.7 X-ray Photoelectron Spectroscopy

X-ray photoelectron spectroscopy (XPS) analysis was conducted on the Li-PTI sample. The C 1s peaks reveal information regarding the carbon atoms present in the sample. The sp^3 C ($284.72\,\mathrm{eV}$) peak corresponds to carbon atoms in a hybridized sp^3 state, which likely represents aliphatic carbons within triazine rings or other organic groups. The C in the C-N-Hx ($286.62\,\mathrm{eV}$) peak indicates carbon atoms bonded to nitrogen in the amine-like (C-N-H) groups. The strongest peak, C in N-C=N ($287.58\,\mathrm{eV}$), represents carbon atoms directly involved in the triazine rings (C=N-C). Two weaker peaks, C 1s Satellites ($289.62\,\mathrm{eV}$ and $292.08\,\mathrm{eV}$), were observed and were associated with shake-up transitions during photoemission from C 1s electrons.

The spectroscopic analysis of the sample revealed the presence of chlorine and lithium, as indicated by the Cl 2p and Li 1s peaks, respectively. The Cl 2p peaks, at energies of $198.25\,\mathrm{eV}$ and $199.88\,\mathrm{eV}$, suggest the presence of chlorine in different chemical environments. The weaker Cl 2p satellite peak ($202.89\,\mathrm{eV}$) is associated with a shake-up transition during photoemission from the Cl 2p electrons. The relatively high intensity of the Li 1s peak ($54.89\,\mathrm{eV}$) confirms the significant Li content in the sample.

The N 1s peaks provided information on the nitrogen atoms in the sample. The strongest peak, at $397.98\,\mathrm{eV}$, corresponds to the nitrogen atoms directly involved in

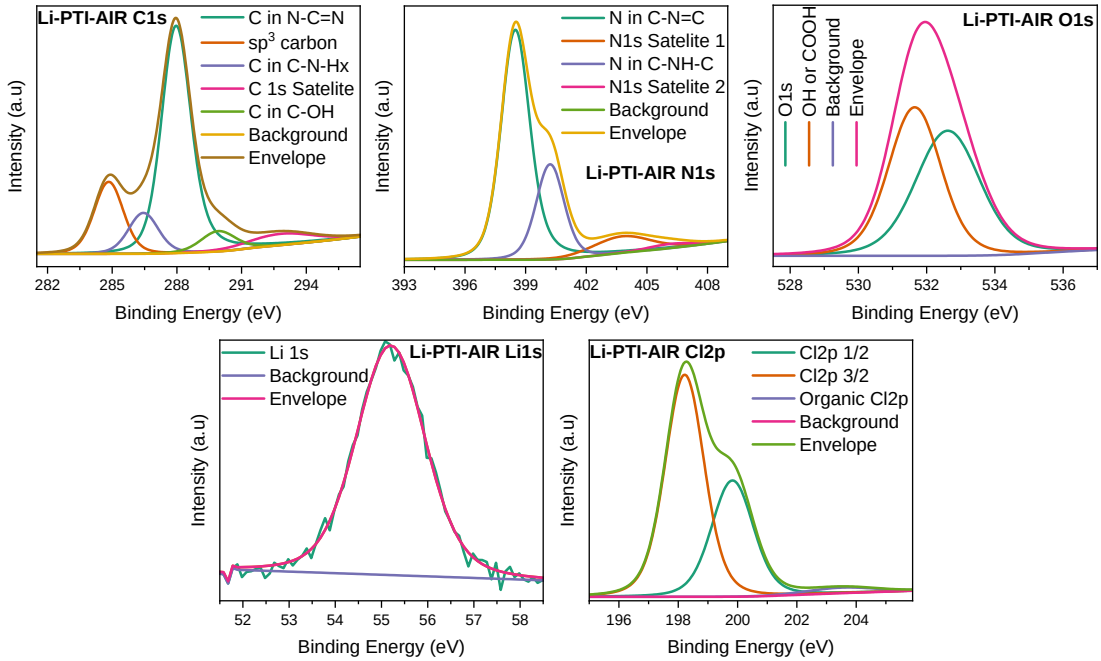

Figure 6.8: X-ray Photoelectron Spectra of Li-PTI-AIR

the triazine rings (C=N-C). The peak at $399.85\,\mathrm{eV}$ represents the nitrogen atoms in the amine-like groups (C-N-H). The weaker N 1s Satellite peaks, at $403.18\,\mathrm{eV}$ and $405.96\,\mathrm{eV}$, are associated with shake-up transitions during photoemission from N 1s electrons.

The O 1s peak at $531.41\,\mathrm{eV}$ corresponds to the hydroxyl groups (O-H) present on the surface of the sample. The O 1s peak at $532.71\,\mathrm{eV}$ was attributed to oxygen atoms participating in other functional groups within the Li-PTI structure, including C=O or N-O groups.

Upon analyzing the XPS data for the Li-PTI samples prepared in air compared with the previously mentioned Li-PTI-N_2 samples, several notable dissimilarities were observed. Both samples exhibited peaks corresponding to carbon (C 1s), primarily from the triazine rings (N-C=N) and amine-like groups (C-N-Hx). The Nitrogen (N 1s) peaks were primarily from the triazine rings (C=N-C) and amine-like groups (C-NH-C). The Oxygen (O 1s) peaks were attributed to hydroxyl groups (OH) and other groups such as C=O or N-O. Additionally, both samples showed the presence of Lithium (Li 1s), confirming its presence in both samples.

In terms of carbon peaks, the Li-PTI-N_2 sample displays a stronger signal for sp^3 C (aliphatic carbons), which could indicate the presence of more organic groups or surface contamination. Additionally, the sample showed a higher intensity of C in C-N-Hx, possibly indicating the presence of more amine-like groups. However, the relative intensity of the main C in the N-C=N peak was higher in the air-prepared sample, suggesting that a larger proportion of carbon was directly involved in the triazine rings in that sample. Regarding the chlorine peaks, the air-prepared sample showed a significantly lower intensity for the Cl 2p peaks, implying a much lower chlorine content compared to the Li-PTI-N_2 sample. This highlights the key difference in their preparation. For the lithium peaks, the air-prepared sample had a slightly higher intensity for the Li 1s peak, suggesting a potentially higher lithium content than that of Li-PTI-N_2. In terms of the nitrogen peaks, the relative

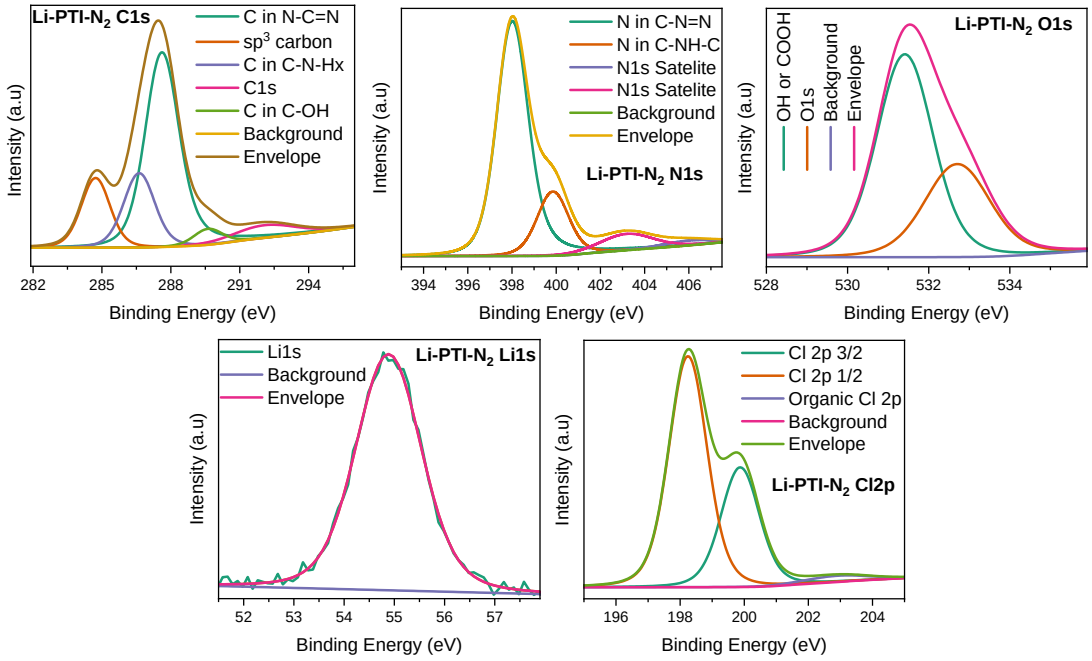

Figure 6.9: X-ray Photoelectron Spectra of Li-PTI-N_2

intensity of the main N in the C=N-C peak was higher in the air-prepared sample, suggesting that a greater proportion of nitrogen was directly involved in the triazine rings in that sample. Table 6.6 provides a comparison of the Normalized Surface

Table 6.6: Normalized surface concentration (NSC%) for Li-PTI Samples

Sample	(C)-N-Hx	N-(C)=N	C=(N)-C	C-NH-C	OH	Li	Cl 2p	Cl 2p
Li-PTI-AIR	2.608	15.116	14.412	5.487	3.086	7.744	0.823	0.459
Li-PTI-N_2	9.001	27.211	45.318	8.327	6.005	21.167	3.333	1.738

Concentration (NSC%) for the Li-PTI samples exposed to different atmospheres, specifically Li-PTI-AIR and Li-PTI-N_2. The results revealed significant variations in the NSC% values for various surface functional groups, thereby highlighting the substantial influence of the surrounding atmosphere on the surface composition of the material. The NSC% results for (C)-N-Hx showed a substantial increase in Li-PTI-N_2 (9.001%) compared to Li-PTI-AIR (2.608%), indicating a higher presence of carbon-nitrogen-hydrogen configurations under a nitrogen atmosphere. The comparison between Li-PTI-N_2 (27.211%) and Li-PTI-AIR (15.116%) for N-(C)=N revealed a notable elevation in the NSC% under a nitrogen atmosphere, suggesting a modification in the nitrogen-carbon bonding environment. The results for C=(N)-C displayed a significant increase in NSC% in Li-PTI-N_2 (45.318%) compared to Li-PTI-AIR (14.412%), indicating a notable alteration in carbon-nitrogen-carbon triple bonds on the surface. The NSC% values for C-NH-C showed a higher presence in Li-PTI-N_2 (8.327%) than in Li-PTI-AIR (5.487%), suggesting an increased presence of specific carbon-nitrogen-hydrogen-carbon configurations under a nitrogen atmosphere. The NSC% results for OH revealed an elevated value in Li-PTI-N_2 (6.005%) compared to Li-PTI-AIR (3.086%), indicating changes in the surface chemical reactivity or interaction with the surrounding species. The obtained data

highlight the pronounced susceptibility of the Li-PTI surface composition to the nitrogen content in the surrounding atmosphere. The presence of an increased number of nitrogen-containing groups, triple bonds, and lithium, in conjunction with a nitrogen atmosphere, could impact the reactivity and practical features of the material. The observed increase in the OH group concentration in Li-PTI-N_2 may signify modifications in the surface chemical reactivity or interactions with neighboring elements.

The NSC% values for Li-PTI-N_2 and Li-PTI-AIR, as presented in Table 6.6, provide valuable insights into their respective surface compositions and can be utilized to discuss the enhanced activity of Li-PTI-N_2 towards CO_2 reduction to methane and methanol. Li-PTI-N_2 demonstrates a higher NSC% for (C)-N-Hx (9.001%) in comparison to Li-PTI-AIR (2.608%). This indicates a greater presence of carbon-nitrogen-hydrogen configurations, potentially offering additional active sites for CO_2 adsorption and subsequent reduction. Li-PTI-N_2 shows a higher NSC% for N-(C)=N (27.211%) compared to Li-PTI-AIR (15.116%). The noticeable increase in nitrogen-carbon double bonds suggests a modification in the nitrogen-carbon bonding environment, which may influence the electronic properties of the material. Li-PTI-N_2 displays a higher NSC% for C=(N)-C (45.318%) compared to Li-PTI-AIR (14.412%). This substantial increase in the number of carbon-nitrogen-carbon triple bonds indicates a notable alteration in the surface composition, potentially enhancing the reactivity of the material. Li-PTI-N_2 exhibits a higher NSC% for C-NH-C (8.327%) compared to Li-PTI-AIR (5.487%). The increased presence of nitrogen amino groups facilitates interactions with CO_2 and contributes to more effective reduction reactions. Li-PTI-N_2 shows a higher NSC% for OH (6.005%) compared to Li-PTI-AIR (3.086%). The elevated concentration of hydroxyl groups may contribute to the generation of oxygen as a byproduct of CO_2 reduction. Li-PTI-N_2 exhibits a significantly higher NSC% for Li (21.167%) in contrast to Li-PTI-AIR (7.744%). The increased concentration of lithium on the surface may play a crucial role in catalyzing CO_2 reduction reactions.

The data indicate that the NSC% values for Li-PTI-N_2 changed, suggesting a customized surface composition with a higher concentration of nitrogen-containing groups, double and triple bonds, amino groups, and lithium. These alterations likely strengthen the attraction of the material to CO_2 and facilitate the multistep reduction processes, thereby promoting the production of methane and methanol. The added hydroxyl groups may also play a role in the generation of oxygen during the reduction of CO_2, further supporting the enhanced activity of Li-PTI-N_2.

6.1.8 Valence Band XPS

To determine the valence-band position, both linear curve fitting and second-derivative valence-band spectroscopy were employed (Table 6.7). Although linear curve fitting is a commonly used approach, it has limitations in capturing the intricate details within the valence band spectra. By contrast, the second-derivative method offers a more refined examination, particularly in areas where the valence band exhibits complex features. Consequently, the second-derivative method provides a more accurate and reliable means of measuring the valence band position, enabling a more detailed analysis of the valence band structure, and a solid foundation for further discussion of the electronic structure and properties of

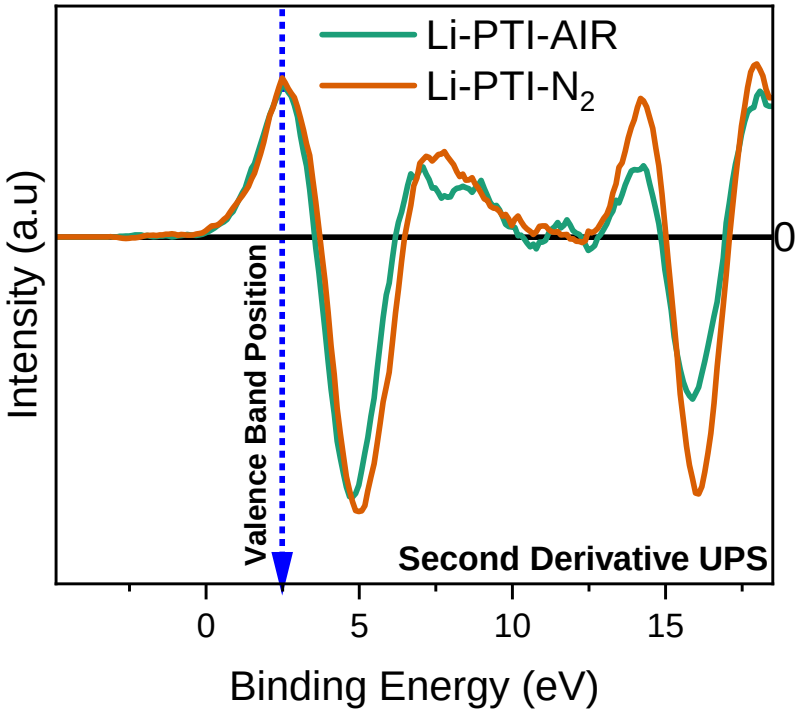

Figure 6.10: Derivative valence band XPS spectra of Li-PTIs

graphitic carbon nitride surfaces. Variations in the valence band positions among the carbon nitride samples were observed, suggesting the influence of the crucible on the formation of well-defined bands. The XPS results indicated that the crucible caused a difference in the concentration of the chemical moieties, which in turn affected the positioning of the valence and conduction bands. To further elucidate the band diagram, the valence band position obtained from the second-derivative method was utilized (Table 6.7).The valence band spectra of the Li-PTIs exhibit a high degree of similarity, with only slight variations in intensity that highlight their similar electronic structures (Figure 6.10).

Second-derivative valence-band spectra often exhibit a band tail near the valence-band edge, indicating a gradual decrease in the density of electronic states beneath the main peak of the valence band [15, 16]. This phenomenon is typically attributed to the electronic disorder within the material, where impurities, defects, or structural imperfections create localized energy states within the bandgap [17]. These localized states extend the valence band towards lower binding energies, giving rise to tail-like features observed in the spectrum.

	Highest Occupied Molecular Orbital (HOMO), eV				
Sample	**Second Derivative**	**Curve Fitting**			
		Position	**Original Value**	**FWHM**	**STD**
Li-PTI-AIR	2.48	2.41	2.4108	1.96	1.253
Li-PTI-N_2	2.48	2.39	2.3856	2.23	1.939

Table 6.7: Valence band positions of Li-PTIs

6.1.9 Possible Mechanism of Formation Products

Formation of Methane

1. **Multi-electron Reduction:** This pathway involves a series of reduction steps of CO_2 adsorbed on the Li-PTI surface, each requiring multiple electrons and protons:

   $$CO_2 \rightarrow CO \rightarrow HCHO \rightarrow CH_3OH \rightarrow CH_4$$

   Each step requires appropriate energies for efficient conversion and avoids undesired side reactions. Li-PTI can act as a photocatalyst under light irradiation or an electrocatalyst in an electrochemical setup to provide these electrons.

2. **C-C Coupling:** This pathway involves two CO molecules coupling to form a C_2 intermediate, which then undergoes further hydrogenation to methane:

   $$2CO \rightarrow C_2O_2 \rightarrow C_2H_2 \rightarrow CH_4$$

   This pathway might be less prominent due to higher energy barriers involved in C-C bond formation.

3. **Formate-Mediated Pathway:** In this pathway, CO_2 is first reduced to formate ($HCOO^-$), which then undergoes dehydrogenation and coupling to form methane:

   $$CO_2 \rightarrow HCOO^- \rightarrow CHOOH \rightarrow CH_2OH \rightarrow CH_3OH \rightarrow CH_4$$

   The presence of active sites for both CO_2 reduction and formate conversion on the Li-PTI surface is crucial for this pathway.

Formation of Methanol

1. **Multi-electron Reduction:** Similar to methane formation, this pathway involves a series of reduction steps of CO_2 adsorbed on the Li-PTI surface:

   $$CO_2 \rightarrow CO \rightarrow HCHO \rightarrow CH_3OH$$

   Each step requires one electron and one proton per molecule. Li-PTI can act as a photocatalyst under light irradiation or an electrocatalyst in an electrochemical setup to provide these electrons and protons.

2. **Formate-Mediated Pathway:** In this pathway, CO_2 is first reduced to formate ($HCOO^-$), which then undergoes further hydrogenation to methanol:

   $$CO_2 \rightarrow HCOO^- \rightarrow CH_2OH$$

   The presence of active sites for both CO_2 reduction and formate conversion on the Li-PTI surface is crucial for this pathway. This pathway can be more selective for methanol compared to the multi-electron reduction due to fewer competing side reactions.

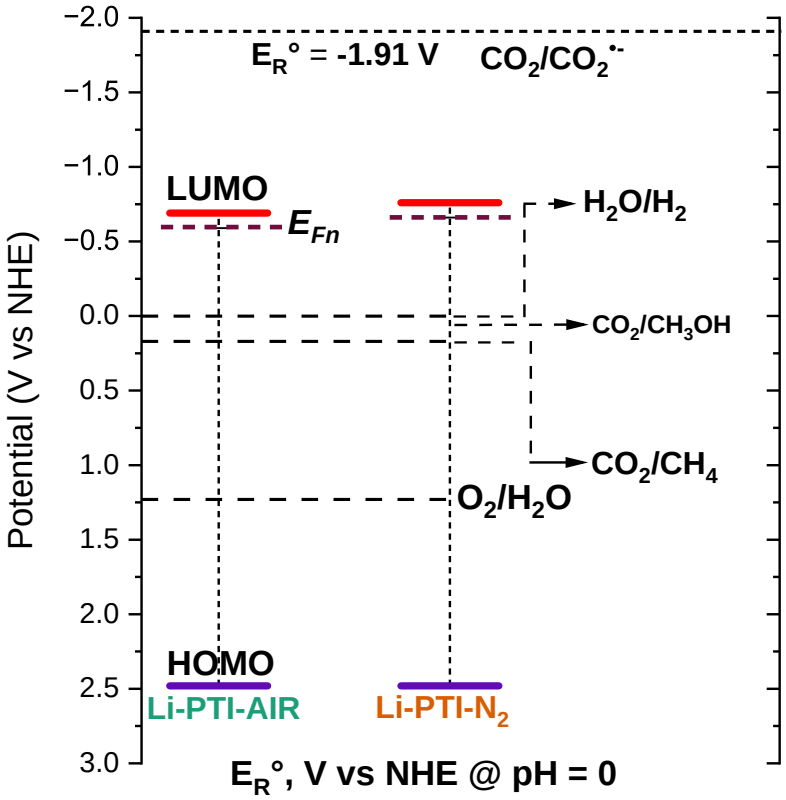

Figure 6.11: Band diagram of Li-PTI at pH 0

3. **Hydrogenation of CO:** CO, formed as an intermediate in other pathways, can directly react with H_2 to form methanol:

$$CO + 2H_2 \rightarrow CH_3OH$$

This pathway requires efficient activation of both CO and H_2 on the Li-PTI surface. It can be more energy-efficient than the multi-electron reduction but might compete with other CO consumption pathways.

6.1.10 Elucidation of Band Diagram

The band diagrams for all seven carbon nitride samples were elucidated through a comprehensive approach, utilizing the valence band position data obtained from derivative X-ray photoelectron spectroscopy (XPS) and bandgap values derived from second-derivative diffuse reflectance ultraviolet (DRD UV) measurements. This dual-source information allows for the calculation of both valence and conduction band positions[18, 19]. Subsequently, the electron affinity and ionization energy of each sample were determined based on the calculated band positions.

Band diagrams for all the samples were created using the data obtained from the valence-band XPS spectra and DRS UV measurements at both pH 0 and pH 8. To construct the band diagram at pH 0, the values obtained from these measurements were used (Figure 6.11). Additional pH corrections were applied to the semiconductor band edge and CO_2 redox potential values to represent the band diagram at pH 8 accurately (Figure 6.11). The band diagram clearly shows that the redox potentials of the two Li-PTIs are nearly identical. Thus, the greater

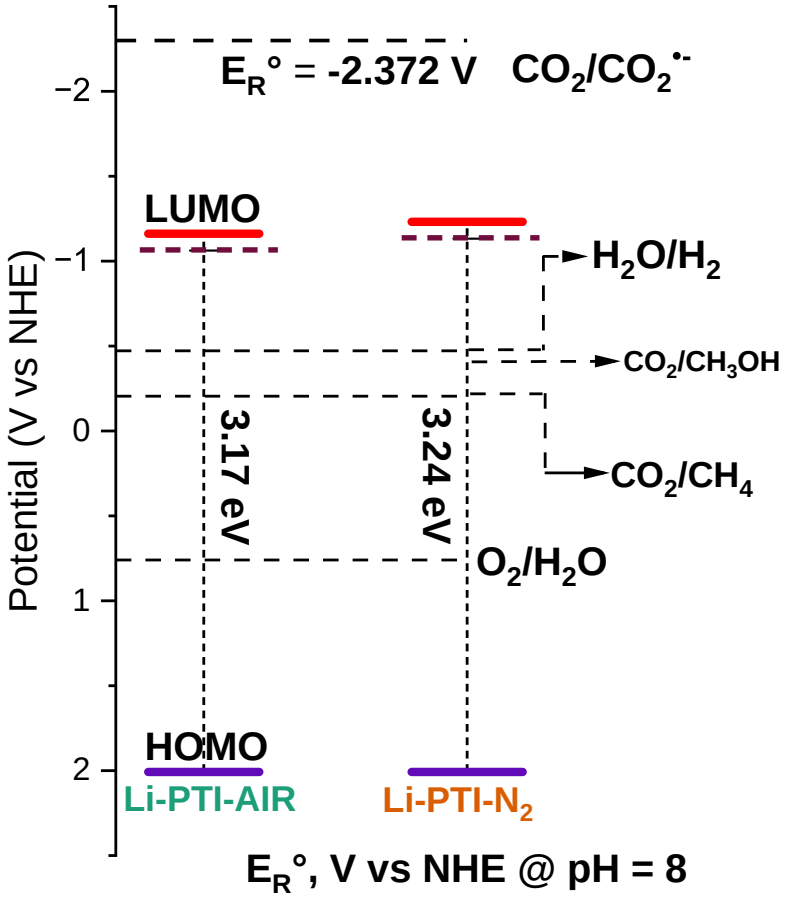

Figure 6.12: Band diagram of Li-PTI at pH 8

activity of Li-PTI-N_2 is due to the cumulative effect of several factors, including its crystallinity, high DP/SA value, and moderate C value. Additionally, the presence of edge sites on the surface contributed to enhanced surface functionalities. Furthermore, the high NSC% of Li-PTI-N_2 accommodates all of these factors and is responsible for the improved activity towards methane, methanol, and oxygen in the CO_2 photoreduction reaction.

6.1.11 Summary

Molten salt ionothermal method presents an opportunity to design materials for catalytic applications. By carefully selecting the necessary moltan salt and precursor, it is possible to incorporate in situ functionalities. This will result in either a single crystal or powder sample with a well-defined framework. Consequently, it becomes possible to explore different precursors and moltan salts for synthesizing new compounds. The synthesis of in situ metal-incorporated materials will be beneficial in catalysis, and the design should be appropriate for the concerned reaction. In the case of synthesis, temperature, atmosphere, and other conditions are optimized to achieve good surface functionality and active material.

References

[1] Degen, T.; Sadki, M.; Bron, E.; Konig, U.; Nenert, G. The HighScore suite. *Powder Diffraction* **2014**, *29*, S13–S18.

[2] Wirnhier, E.; Doblinger, M.; Gunzelmann, D.; Senker, J.; Lotsch, B. V.; Schnick, W. Poly(triazine imide) with Intercalation of Lithium and Chloride Ions : A Crystalline 2D Carbon Nitride Network. *Chemistry - A European Journal* **2011**, *17*, 3213–3221.

[3] Dong, G.; Zhang, L. Porous structure dependent photoreactivity of graphitic carbon nitride under visible light. *J. Mater. Chem.* **2012**, *22*, 1160–1166.

[4] Ismael, M.; Wu, Y.; Taffa, D. H.; Bottke, P.; Wark, M. Graphitic carbon nitride synthesized by simple pyrolysis: role of precursor in photocatalytic hydrogen production. *New Journal of Chemistry* **2019**, *43*, 6909–6920.

[5] Sing, K. S. W. Reporting physisorption data for gas/solid systems with special reference to the determination of surface area and porosity (Recommendations 1984). *Pure and Applied Chemistry* **1985**, *57*, 603–619.

[6] Rouquerol, J.; Llewellyn, P.; Rouquerol, F., Is the bet equation applicable to microporous adsorbents? In *Characterization of Porous Solids VII*, Llewellyn, P., Rodriquez-Reinoso, F., Rouqerol, J., Seaton, N., Eds.; Studies in Surface Science and Catalysis, Vol. 160; Elsevier: 2007, pp 49–56.

[7] Rouquerol, J.; Rouquerol, F.; Llewellyn, P.; Maurin, G.; Sing, K., *Adsorption by Powders and Porous Solids: Principles, Methodology and Applications*; Elsevier Science: 2013.

[8] Terrones, G. G.; Chen, Y.; Datar, A.; Lin, L.-C.; Kulik, H. J.; Chung, Y. G. SESAMI APP: An Accessible Interface for Surface Area Calculation of Materials from Adsorption Isotherms. *Journal of Open Source Software* **2023**, *8*, 5429.

[9] Osterrieth, J. W. M. et al. How Reproducible are Surface Areas Calculated from the BET Equation? *Advanced Materials* **2022**, *34*, 2201502.

[10] Datar, A.; Chung, Y. G.; Lin, L.-C. Beyond the BET Analysis: The Surface Area Prediction of Nanoporous Materials Using a Machine Learning Method. *The Journal of Physical Chemistry Letters* **2020**, *11*, 5412–5417.

[11] Sinha, P.; Datar, A.; Jeong, C.; Deng, X.; Chung, Y. G.; Lin, L.-C. Surface Area Determination of Porous Materials Using the Brunauer–Emmett–Teller (BET) Method: Limitations and Improvements. *The Journal of Physical Chemistry C* **2019**, *123*, 20195–20209.

[12] Thommes, M.; Kaneko, K.; Neimark, A. V.; Olivier, J. P.; Rodriguez-Reinoso, F.; Rouquerol, J.; Sing, K. S. *Pure and Applied Chemistry* **2015**, *87*, 1051–1069.

[13] Michot, L. J., 2 - Determination of surface areas and textural properties of clay minerals In *Surface and Interface Chemistry of Clay Minerals*, Schoonheydt, R., Johnston, C., Bergaya, F., Eds.; Developments in Clay Science, Vol. 9; Elsevier: 2018, pp 23–47.

[14] Michot, L.; Villieras, F., Chapter 2.10 - Surface Area and Porosity In *Handbook of Clay Science*, Bergaya, F., Lagaly, G., Eds.; Developments in Clay Science, Vol. 5; Elsevier: 2013, pp 319–332.

[15] Li, M.; Huang, P.; Zhong, H. Current Understanding of Band-Edge Properties of Halide Perovskites: Urbach Tail, Rashba Splitting, and Exciton Binding Energy. *The Journal of Physical Chemistry Letters* **2023**, *14*, 1592–1603.

[16] Zarrabi, N.; Sandberg, O. J.; Meredith, P.; Armin, A. Subgap Absorption in Organic Semiconductors. *The Journal of Physical Chemistry Letters* **2023**, *14*, 3174–3185.

[17] Energy-band tails and the optical absorption edge; the case of a-Si:H. *Solid State Communications* **1982**, *44*, 1347–1349.

[18] Bui, D.-P.; Pham, M.-T.; Tran, H.-H.; Nguyen, T.-D.; Cao, T. M.; Pham, V. V. Revisiting the Key Optical and Electrical Characteristics in Reporting the Photocatalysis of Semiconductors. *ACS Omega* **2021**, *6*, 27379–27386.

[19] Maheu, C.; Cardenas, L.; Puzenat, E.; Afanasiev, P.; Geantet, C. UPS and UV spectroscopies combined to position the energy levels of TiO_2 anatase and rutile nanopowders. *Physical Chemistry Chemical Physics* **2018**, *20*, 25629–25637.

Chapter 7

Supramolecular Assisted Eutectic Synthesis of Graphitic Carbon Nitride for Photon-Assisted Reduction of Carbon Dioxide

Abstract

This chapter presents a novel approach to the synthesis of carbon nitride (CN) materials for photon-assisted catalysis, specifically focusing on the reduction of carbon dioxide. In this study, a supramolecular-assisted eutectic synthesis method was developed utilizing melamine cyanurate (CAM) as a precursor and incorporating nickel through eutectic salt mixtures ($NiCl_2$-CsCl and $NiCl_2$-KCl). This innovative synthesis route resulted in the formation of Ni-incorporated CN frameworks with unique structural and electronic properties. The synthesized materials, denoted gCN-NiCs and gCN-NiK, were thoroughly characterized using a suite of analytical techniques, including X-ray diffraction (XRD), X-ray photoelectron spectroscopy (XPS), nitrogen adsorption-desorption isotherms, and UV-visible spectroscopy. The results revealed significant modifications in the CN structure upon Ni incorporation, including alterations in the surface area, pore characteristics, and electronic properties. Photon-assisted CO_2 reduction experiments demonstrated the superior performance of Ni-incorporated materials compared to of that bulk g-CN. Notably, the CN-NiCs exhibited the highest yield for methane and methanol production, whereas CN-NiK showed enhanced oxygen evolution. This study elucidates the structure-property-activity relationships, correlating the observed catalytic performance with the electronic structure, surface properties, and band positions of the materials. Detailed mechanistic insights into the CO_2 reduction process are proposed, considering both direct and indirect pathways for methane and methanol formation. This research also presents a comprehensive analysis of the band structures of the materials, constructed using data from valence band XPS and diffuse reflectance spectroscopy, providing a crucial understanding of the charge transfer processes involved in photon-assisted catalysis. This work not only introduces a novel synthesis approach for tailoring CN materials but also offers valuable insights into the design principles for efficient photon-assisted CO_2 reduction catalysts. These findings underscore the potential of supramolecular-assisted eutectic syn-

thesis in developing advanced materials for solar fuel production and contribute significantly to the broader field of sustainable energy conversion technologies.

7.1 Introduction

Supramolecular-assisted synthesis is an effective method for producing carbon nitride materials with tailored properties[1]. This technique utilizes non-covalent interactions such as hydrogen bonding, π-π stacking, and electrostatic forces to pre-organize carbon nitride precursors into well-defined assemblies prior to their final polymerization[2]. This controlled pre-organization results in enhanced control over the morphology and porosity of the carbon nitride materials, which is crucial for applications such as catalysis and gas storage. Additionally, this technique allows tuning of the bandgap and electronic properties of carbon nitride materials, making them suitable for use in photocatalysis, electronics, and optoelectronic devices. The controlled porosity and ordered structure of carbon nitride materials also enhance the accessibility of active sites for guest molecules and light, boosting the efficiency in applications such as adsorption and photocatalysis[3].

Commonly used precursors include melamine, urea, cyanuric acid, and dicyandiamide, and their selection and combination significantly influences the final structure and properties of carbon nitride. Before self-assembly, the precursors were dissolved in suitable solvents and noncovalent interactions directed the assembly process[4]. The type of solvent and reaction conditions play a crucial role in this process. The preorganized assemblies underwent thermal treatment (calcination) at specific temperatures, resulting in condensation reactions that converted them into polymeric carbon nitride networks[5]. The supramolecular-assisted synthesis method offers several advantages, including precise control over the material properties at the molecular level, synthesis under mild conditions compared to traditional methods, and scalability, making it a promising candidate for industrial applications[6].

Carbon nitride (CN) is commonly synthesized using melamine cyanurate (CAM) as the precursor. CAM is produced through a condensation reaction between melamine and cyanuric acid, which typically occurs in aqueous solutions under mild conditions, ranging from room temperature to gentle heating. Melamine, a compound with the chemical formula $C_3N_6(OH)_6$, behaves as a weak base because of the presence of lone pairs of electrons on its nitrogen atoms. Under acidic conditions, these lone pairs were protonated, generating positively charged ammonium (NH_3^+) groups. Protonated melamine acts as a nucleophile by attacking the electron-deficient carbon atom of cyanuric acid, which is a triazine with three electronegative carbonyl groups[7].

Because of this nucleophilic attack, a tetrahedral intermediate was formed. The elimination of a water molecule then leads to the formation of a melamine-cyanuric acid adduct. The adduct molecules further self-assembled through hydrogen-bonding interactions between the remaining NH and NH_2 groups of melamine and the carbonyl groups of cyanuric acid. These hydrogen bonds organize the molecules into a well-defined crystal structure, forming melamine-cyanurate[8].

Upon thermal treatment (calcination) at temperatures ranging from 400 °C to 550°C, CAM was readily converted to carbon nitride. At elevated temperatures, the

CAM adduct begins to decompose. The amino groups of melamine and carbonyl groups of cyanuric acid lose water and ammonia molecules, respectively. The remaining fragments underwent cyclization to form the triazine rings. These triazine rings further condense with each other through the elimination of additional ammonia molecules, resulting in the formation of extended π-conjugated CN networks. As the condensation reactions continue, the CN network grows, eventually leading to the formation of a polymeric carbon nitride structure. The triazine rings underwent aromatization, which further stabilized the CN framework.

Utilizing melamine cyanurate (CAM) as a precursor for carbon nitride (CN) synthesis through eutectic molten salt-assisted ionothermal synthesis presents several potential advantages over conventional methods. The use of preformed CAM structures may facilitate the polymerization process within the molten salt medium, potentially resulting in more controlled pore structures and morphologies than those achieved using simple carbon nitride precursors, such as melamine or urea. This offers opportunities to tailor the material for specific applications, including catalysis with enhanced active site accessibility or gas adsorption with specific pore sizes.

The interaction between CAM and the specific eutectic salt mixture may influence the stacking arrangement and interactions between CN layers, potentially enabling precise tuning of the bandgap and electronic properties of the resulting material. This could be advantageous for optimizing photocatalytic activity, electrical conductivity, or other optoelectronic properties[9].

The use of molten salt environments in comparison to conventional thermal calcination typically results in lower operating temperatures, which enables more rapid condensation and polymerization reactions, potentially leading to shorter reaction times and increased yields of CN products. Eutectic salt melts provide a confined and controlled reaction space, offering enhanced mass and heat transfer compared with solid-state calcination methods.

Additional advantages include the possibility of forming more ordered and crystalline CN-structures within the confined and controlled environment of the molten salt melt, as opposed to traditional methods. Additionally, eutectic salt mixtures can potentially be loaded with dopants or functionalizing agents, facilitating the in-situ incorporation of desired functionalities into the CN material during the synthesis process.

7.2 Results and Discussion

In this chapter, owing to the large size of the sample codes within the figures, a condensed representation is employed for clarity. The abbreviated codes are provided separately as follows:

1. CAM-gCN: Represented as gCN.
2. CAM-gCN-$NiCl_2$-CsCl: Represented as gCN-NiCs.
3. CAM-gCN-$NiCl_2$-KCl: Represented as gCN-NiK.

This shorthand notation is utilized for conciseness, considering the limitations in figure editing owing to the size of the code.

7.2.1 Discussion on CO_2 Photoreduction Results

A thorough examination of various catalytic systems for methane, methanol, and oxygen production offers valuable insights into their effectiveness in catalyzing CO_2 reduction reactions (Figure 7.1& 7.2). gCN – NiCs was the most efficient catalyst for methane and methanol production, followed by gCN – NiK, and gCN. gCN – NIK outperformed the other catalysts in terms of oxygen production, followed by gCN – NiCs, and gCN. These findings demonstrate the significant impact of catalyst composition on the reaction outcomes. gCN – NiCs showed exceptional performance in methane and methanol production, indicating its potential for applications that require high yields of these compounds. In contrast, gCN – NiK excelled in oxygen production, making it suitable for processes that prioritize oxygen generation. Methane production was relatively low for all materials, indicating a high selectivity for methanol and oxygen production.

When selecting a catalyst, it is crucial to consider the specific requirements of the desired reaction and the desired product yield. Further optimization and characterization of these catalyst systems may provide a more comprehensive understanding of their catalytic mechanisms.

7.2.2 X-ray Diffraction

The outcomes obtained from the calcination of melamine cyanurate (CAM) using a KCl-$NiCl_2$ eutectic mixture at 450°C in nitrogen yielded a product that deviated from the typical characteristics of carbon nitride. X-ray photoelectron spectroscopy (XPS) analysis revealed unexpected atomic compositions, suggesting the formation of a complex derivative material. The presence of 3.58% Ni in the material may indicate some level of Ni incorporation into the carbon nitride structure; however, it is unlikely to significantly alter the overall appearance of the material compared to that of pure carbon nitride. The high chlorine content (11.92%) suggests the formation of a hybrid metal-organic framework (MOF) in which $NiCl_2$ interacts with the cyanurate groups of CAM, leading to the incorporation of chlorine atoms. Such hybrid MOFs exhibit unique morphologies and properties compared with those of pure carbon nitride [10]. The relatively high oxygen content (11.27% as OH) suggests the presence of hydroxyl groups in the material, which could be attributed to the partial oxidation of the carbon nitride framework during calcination or incomplete condensation reactions within the CAM molecules. It is also possible that the calcination process resulted in the formation of unwanted side products along with some carbon nitride derivatives.

The X-ray diffraction (XRD) pattern indicated that the product obtained from the reaction of melamine cyanurate with the KCl-$NiCl_2$ eutectic mixture at 450°C was not pure carbon nitride (Figure 7.3). The absence of typical carbon nitride peaks and the presence of prominent peaks at 45° and 33° in the XRD pattern suggest a significant structural departure from pure CN. X-ray photoelectron spectroscopy (XPS) analysis suggested the incorporation of some nickel, and the complete absence of characteristic carbon nitride peaks in the XRD pattern indicated that the product was not purely carbon nitride. The incorporation of nickel might have disrupted the usual stacking of the triazine rings characteristic of carbon nitride, leading to the formation of a new and unknown phase with its own XRD signature.

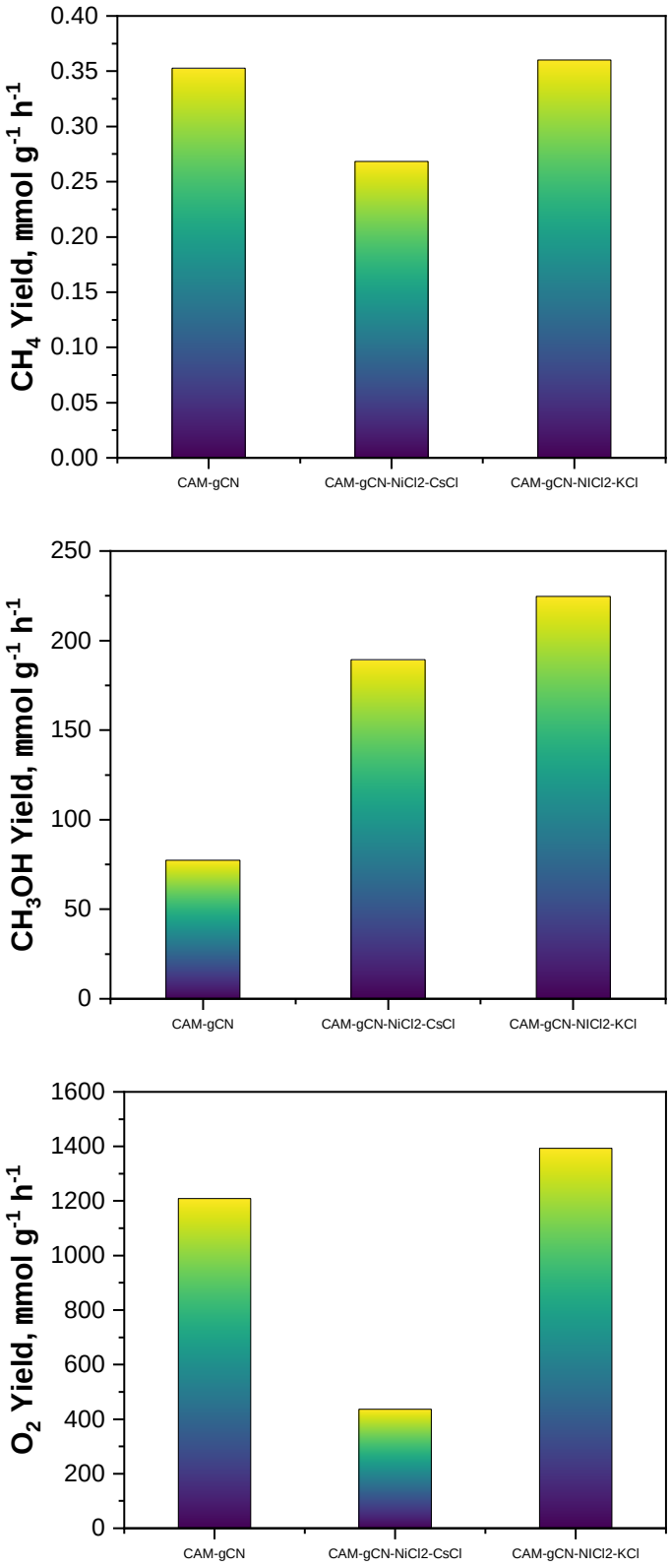

Figure 7.1: The yield of CO_2 reduction products with respect to total surface area

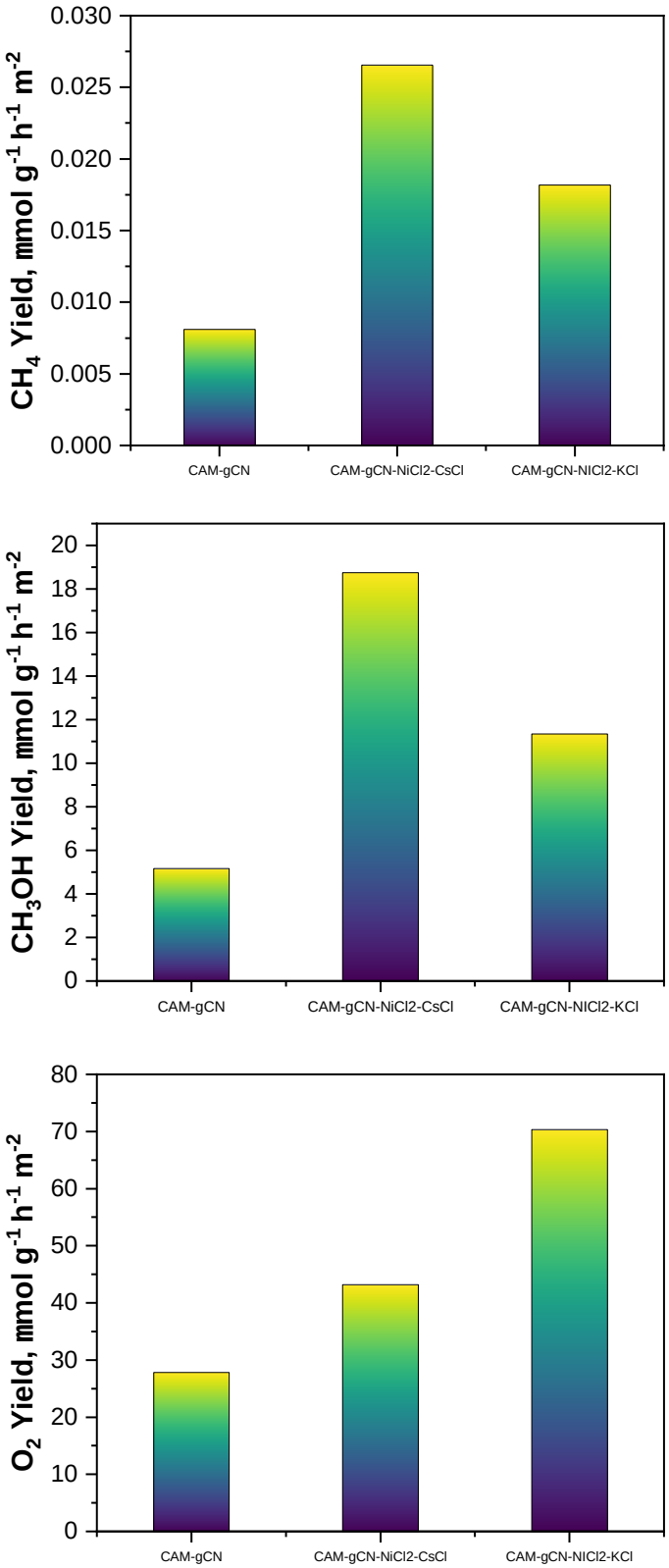

Figure 7.2: The yield of CO_2 reduction products with respect to unit surface area

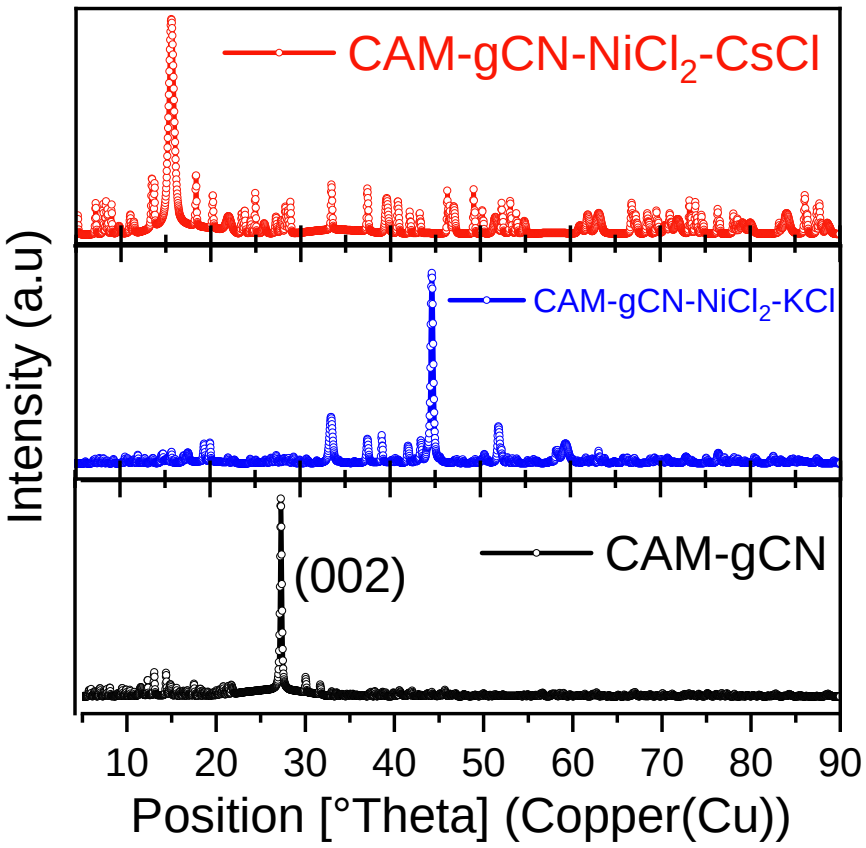

Figure 7.3: X-ray diffractogram of Ni-based carbon nitride systems

The ongoing absence of conventional carbon nitride peaks in the X-ray diffraction (XRD) patterns when melamine cyanurate was combined with various eutectic salt mixtures (in this case, $NiCl_2$-CsCl) further supports the conclusion that pure carbon nitride does not form under these conditions. The principal peak at 15° in the XRD spectrum adds an additional intrusion layer to the reaction and product. Both $NiCl_2$ and CsCl contain metal cations (Ni^{2+} and Cs^{+}, respectively). Their interaction with the cyanurate groups of melamine cyanurate could result in the formation of complex metal-organic frameworks (MOFs) or other hybrid materials with distinct crystal structures and XRD patterns [10]. The peak at 15° may indicate one of these phases.

7.2.3 Adsorption Isotherm Analysis

The nitrogen adsorption-desorption isotherms of the two samples (gCN and gCN-NiK) were classified as type III, indicating weak adsorbate-adsorbent interactions, the presence of adsorbed N_2 in the interlayer, or the presence of porous structures in the samples (Figure 5.6)[11–13]. The adsorption isotherm of the gCN-NiCs can be considered as type III, but a negative deviation is observed in the low-pressure region. The isotherms displayed type H3 hysteresis loops at $0.45 < \frac{P}{P_0} < 1.00$, a characteristic often observed in aggregates of plate-like particles, suggesting the existence of slit-shaped pores. The average pore sizes of the gCN and gCN-NiK samples were in the mesoporous regime and the pore size of the gCN-NiCs

was in the macroporous regime. A type III isotherm typically indicates weak

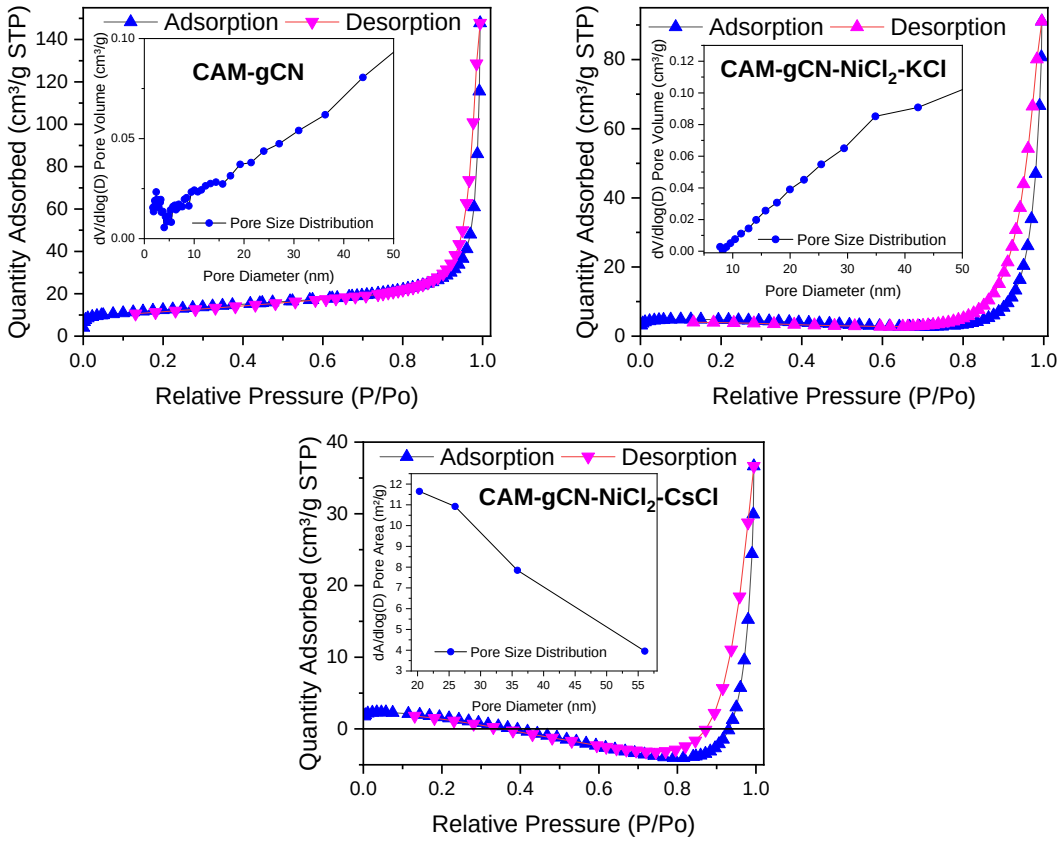

Figure 7.4: N_2 adsorption isotherms of bulk and Ni-based carbon nitrides

interactions between the adsorbate molecules and the adsorbent surface. In the case of gCN-NiK, the initial near-parallel adsorption suggests minimal interaction with the surface up to a high relative pressure ($0.8\frac{P}{P_0}$). This implies the presence of large, nonporous, or macroporous structures with limited access to internal areas. The progressive increase in adsorption above ($0.8\frac{P}{P_0}$) suggests the presence of an additional adsorption mechanism. This can be attributed to the following factors:

1. Micropore filling: If the material contains hidden micropores that are not easily accessible at lower pressures, they may start filling at higher relative pressures, contributing to the observed increase in adsorption.

2. Multilayer adsorption: Beyond a certain threshold, even weak interactions may become sufficient for multilayer adsorption to occur on existing adsorbed molecules, resulting in a gradual increase in the total adsorption.

3. Specific interactions: Although overall weak, specific interactions between the adsorbate and certain functional groups or defect sites on the surface may start contributing at higher pressures, leading to the observed increase in adsorption.

The results of the gCN-NiCs experiments showed negative adsorption and hysteresis. The initial decrease in adsorption with increasing pressure, as indicated by the negative values on the y-axis, suggests a phenomenon known as negative

adsorption[14–16]. This occurs when the adsorbent preferentially adsorbs gas molecules from the surrounding environment rather than releases them. The observation of an adsorption isotherm with a negative loop is atypical and requires careful interpretation. This phenomenon can be caused by several factors, including chemisorption, capillarity, and expulsion.

Chemisorption occurs when there is strong chemical bonding between the adsorbate and specific active sites on the surface, resulting in irreversible adsorption and a net decrease in the measured gas volume. The capillarity in microporous materials can cause the adsorbate to fill and block the pores at low pressures, initially decreasing the apparent volume, as measured by the isotherm. The expulsion effect occurs when the adsorbate displaces the pre-adsorbed water molecules or other species from the surface, resulting in a net decrease in the total adsorbed volume.

The presence of hysteresis in the adsorption process, in which adsorption decreases before increasing again, is indicative of a lag between the adsorption and desorption processes. This resulted in different adsorption and desorption branches of the isotherm. Hysteresis can be attributed to pore blocking, where capillary condensation in micropores hinders desorption at lower pressures, and energy barriers, where releasing strongly chemisorbed molecules from the surface requires overcoming activation energy barriers, leading to a slower desorption rate and hysteresis. The precise cause of negative adsorption and hysteresis in the material necessitates further investigation.

Sample	**B.E.T S.A**	**C**
gCN	42.345	-623.684787
gCN-NiCs	2.1652	-10.087368
gCN-NiK	12.8343	-26.441754

Table 7.1: B.E.T surface area and respective C value of bulk and Ni-based carbon nitrides

The B.E.T equation is often rearranged to linearize the isotherm and determine the slope and intercept of a specific plot. If the resulting value of C is negative, the linearized plot does not fit the assumed B.E.T model well [17]. This could be due to various reasons such as the non-ideal behavior of the adsorbate or limitations in the applicability of the BET model to a specific adsorption system. A negative C value suggests that the BET model may not accurately describe the adsorption isotherm for a given material or condition [18]. It is essential to interpret such results cautiously and consider alternative models or factors that might affect adsorption behavior [19–22]. All gCN samples show negative C values (Table 7.1), indicating that they do not follow the B.E.T equation, or corrections in the BET equation are recommended according to the Rouquerol equation [23]. The surface area data were fitted using BETSI and SESAMI techniques, and the results are presented in Table 7.2. Almost the same surface area was observed after correction; however, as the microporosity increased, the deviation became too large. In addition, it is well known that the B.E.T equation is not suitable for microporous materials or materials containing large numbers of micropores.

The study of the surface area and porosity data, primarily utilizing the SESAMI method, yielded valuable insights into the relationship between these properties and the observed CO_2 reduction activity of g-CN samples (Table 7.2). The SESAMI

Surface Area, m^2/g				
	B.E.T	**BETSI**	**SESAMI**	**C, SESAMI**
gCN	42.35	44	43.5	377.8
gCN-NiCs	2.17	10	10.1	1002
gCN-NiK	12.83	20	19.8	777.8

Table 7.2: Recalculated surface area and C value of gCN samples.

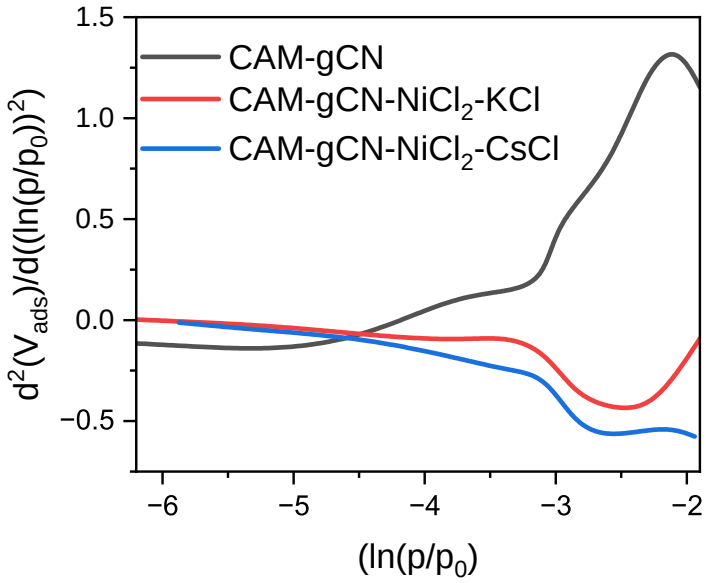

Figure 7.5: Second derivative isotherm summation plot of bulk and Ni-based carbon nitrides.

method quantifies the interaction potential between the adsorbate and adsorbent surface by calculating C. A higher C value signifies stronger interactions, which can enhance CO_2 adsorption and activation. gCN-NiCs displayed the highest C value among the samples, which likely contributed to its exceptional CO_2 conversion performance. Enhanced micropore accessibility facilitates efficient CO_2 adsorption and interaction with active sites, contributing to the superior activity of gCN-NiCs towards methane, methanol, and oxygen yields. The results of this study suggest that the Brunauer–Emmett–Teller (B.E.T) surface area is not a reliable indicator of photon-assisted catalytic performance. Owing to the presence of a negative isotherm in one of the cases, it was not possible to make comparisons between the other properties, except for the surface area.

7.2.4 Derivative Isotherm Summation

In gas adsorption analysis, assessing surface heterogeneity typically entails acquiring a significant number of experimental data points at low relative pressures, usually less than 0.15, during which monolayer filling occurs. The free energy of adsorption on the kT scale can be accurately determined by calculating the derivatives of the adsorption amount relative to the logarithm of the relative pressure ($\ln(P/P_0)$)[24, 25]. Figure 7.5 shows the derivative curve obtained from the $77\,K$ nitrogen adsorption isotherm that illustrates the gas adsorption energy on the sur-

face. The second derivative was used to distinguish between peaks and shoulders in the derivative isotherm summation (DIS) plots. In the second-derivative isotherm summation (SDIS), noticeable peaks are observed as downward dips in the curve. This was because the DIS curve represented the second derivative of the adsorption isotherm. The minima in the second derivative corresponded to the maxima in the original isotherm and represented the strongest binding sites. Two-dimensional materials are characterized by basal, edge, and high-energy adsorption surfaces, which correspond to low, medium, and high energies, respectively, [24, 25].

The second derivative in Figure 7.5 from the DIS demonstrates that the gCN displays significant peaks in the low-energy regime or in the region corresponding to the basal planes. The peak exhibited by the gCN-NiCs is broader, indicating dynamic adsorption behavior and the presence of moderate energy regimes, such as edge sites on the surface. The downward deviations in gCN-NICs and gCN-NiK suggest the presence of moderate-energy surfaces or edge sites. In the case of the gCN-NiCs, the edge sites dominate and exhibit considerable activity towards methane and methanol production. The number of edge sites in gCN-NiK is lower than that in gCN-NiCs. The activity of gCN-NiCs can be attributed to the combined effect of high C values and the presence of moderate energy surface or edge sites. Notably, oxygen evolution was also high in gCN-NiK and gCN-NiCs.

7.2.5 Energy-Dispersive X-ray Analysis (EDAX)

The elemental composition of two samples of carbon nitride (g-CN), namely gCN-NiK and gCN-NiCs, was analyzed using energy-dispersive X-ray analysis (EDAX) (Table 7.3). The main components of both samples were carbon (C) and nitrogen (N), in line with the characteristics of g-CN derivatives. However, the nitrogen content was higher in gCN-NiK (27.9 wt%) than in gCN-NiCs (24.9 wt%).

The presence of N, O, Cl, and Ni was also inferred to be at relatively high concentrations based on their weight percentages. Nevertheless, the high error percentage (62.6%) for K suggests that its detection may not be reliable, casting doubt on its presence in the sample. In comparison to gCN-NiK, gCN-CsK showed higher weight percentages of nitrogen and oxygen, and the high error percentage of Cs (56.9%) implies potential limitations in its detection.

The presence of oxygen (O) in both samples is notable, although its significance is uncertain because of the relatively high error percentages for some elements, exceeding 20% in some cases. The presence of oxygen suggests partial oxidation during synthesis or adsorption of oxygen-containing species from the environment.

In addition to carbon (C), nitrogen (N), and oxygen (O), trace amounts of other elements were detected in both the samples. gCN-NiK contained chlorine (Cl) and nickel (Ni), whereas gCN-NiCs also included cesium (Cs). However, the high error percentages for some elements, particularly oxygen, limit the quantitative significance of their presence. Nonetheless, qualitative detection of these elements provides valuable information about the overall composition of the samples.

7.2.6 Solid State Ultraviolet Visible Spectroscopy

Further insights into solid-state UV-visible spectroscopy of carbon nitrides can be found in detail in Chapter 4.2.7 of this thesis. The observations and analyses

	Element	Weight %	MDL	Atomic %	Net Int.	Error %
gCN-NiK	C K	31.6	1.73	43.0	55.9	13.9
	N K	27.9	1.81	32.6	40.2	14.5
	O K	15.9	0.72	16.3	55.0	13.6
	Cl K	7.1	0.12	3.3	374.8	4.0
	K K	0.1	0.14	0.0	2.7	62.6
	Ni K	17.5	0.39	4.9	250.3	3.6
gCN-NiCs	C K	25.9	2.05	37.9	40.5	14.7
	N K	24.9	1.66	31.3	40.8	14.5
	O K	17.6	0.65	19.4	71.7	13.2
	Cl K	10.0	0.12	4.9	565.8	3.8
	Ni K	21.4	0.39	6.4	333.7	3.3
	Cs L	0.3	0.48	0.0	3.8	56.9

Table 7.3: Elemental analysis data of bulk and Ni-based carbon nitrides

presented provide a comprehensive foundation for subsequent discussions in this chapter.

The absorption characteristics of the gCN-Ni derivative material were investigated using solid-state ultraviolet-visible (UV-vis) spectroscopy. These materials generally exhibit strong absorption in the UV region below $400\,\mathrm{nm}$ owing to π–π^* transitions within the conjugated carbon nitride network. However, the presence of Ni and Cl ions may introduce additional absorption bands depending on the oxidation state and coordination environment. Solid-state materials often exhibit broader absorption bands than isolated molecules because of the weaker electronic transitions and interactions between neighboring atoms.

In the gCN framework, π–π transitions can produce a broad band around $200\,\mathrm{nm}$ to $300\,\mathrm{nm}$, potentially extending further into the UV range depending on the specific structure. Nitrogen lone pair electrons can contribute to weaker n–π transitions at higher wavelengths (possibly around $350\,\mathrm{nm}$ to $400\,\mathrm{nm}$). Ni ions can display d–d transitions in the visible or near-UV region, depending on the Ni oxidation state and coordination environment (e.g., around $400\,\mathrm{nm}$ to $600\,\mathrm{nm}$ for Ni(II) complexes). Cl ions can exhibit charge-transfer transitions in the UV region (usually below $250\,\mathrm{nm}$) owing to electron transfer between Cl and the surrounding atoms.

The oxidation state and coordination environment of Ni can influence the observable spectral features. For Ni(II), electronic transitions in the visible range ($400\,\mathrm{nm}$ to $600\,\mathrm{nm}$) may occur owing to d–d transitions. However, a significant overlap with the broad gCN band in the same range may limit the visibility of these transitions in the $200\,\mathrm{nm}$ to $400\,\mathrm{nm}$ region. For Ni(III), if present, the d–d transitions may shift towards the UV region, potentially manifesting as shoulders or peaks within the $200\,\mathrm{nm}$ to $400\,\mathrm{nm}$ range. Information regarding the bandgap energy is highly relevant, as it is indicative of the onset of absorption and is associated with edge transitions. The bandgap values consistently exceeded 3 eV for all the samples in the second-derivative plots. Notably, gCN-NiK exhibited a bandgap value of 3.4, whereas that of the gCN-NiCs was 3.2. Furthermore, the gCN value was found to be 3.08.

The absorption bands for all samples displayed well-defined features, as evidenced by the presence of distinct peaks and valleys (Figure 7.6). The widths

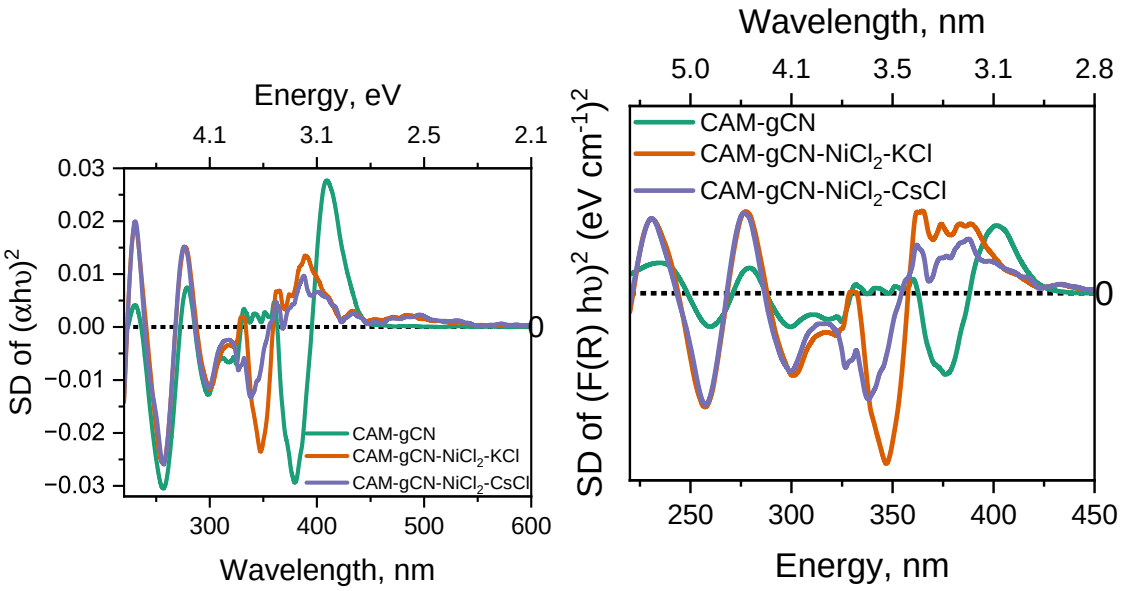

Figure 7.6: Second derivative Tauc and K-M plots

Sample	Band Gap, eV						U.E meV
	Tauc Plot			K-M Plot			
	L.R	F.D	S.D	L.R	F.D	S.D	L.R
gCN	2.96	3.14	3.03	3.06	3.19	3.08	229
gCN-NiK	2.82	3.42	3.19	3.43	3.12	3.4	1001
gCN-NiCs	2.66	3.42	3.2	2.98	3.43	3.2	1166

Table 7.4: Bandgap and Urbach energy values of bulk and Ni-based carbon nitrides

of these bands, as determined by the D value, varied among the samples, with gCN-NiCs showing the highest value, suggesting a broader range of absorbed energies. The D Parameter per Unit Surface Area (DP/SA) ratio is a critical metric for assessing absorption efficiency per unit surface area. A higher DP/SA ratio indicates enhanced absorption efficiency, suggesting a broader absorption band that can capture a wider range of energies. Therefore, a higher DP/SA ratio indicates that a larger portion of the surface area contributes to efficient light absorption, emphasizing the effectiveness of the material.

The gCN-NiCs exhibited higher DP/SA and C values than gCN-NiK. The gCN-NiCs were found to have higher DP/SA and C values than those of gCN-NiK. These characteristics, along with the numerous edge sites present in the derivative isotherm, make gCN-NiCs effective catalysts for CO_2 reduction.

7.2.7 X-ray Phototelectron Spectroscopy

The photoelectron spectrum indicates the presence of two nickel species with binding energies of $855.1\,\mathrm{eV}$ and $856.3\,\mathrm{eV}$, respectively, for the Ni $2\,p_{3/2}$ orbital. Furthermore, there was a broad shake-up satellite at $861.7\,\mathrm{eV}$. For instance, studies on nickel oxide particles decorated on carbon nitride polymers have also found multiple Ni species, with higher binding energies belonging to more oxidized Ni

	D Parameter	SA	Slope	DP/SA
gCN	0.09599	43.5	377.8	0.0022
gCN-NiK	0.12139	19.8	777.8	0.0061
gCN-NiCs	0.14529	10.1	1002	0.014

Table 7.5: Derivative K-M plot analysis

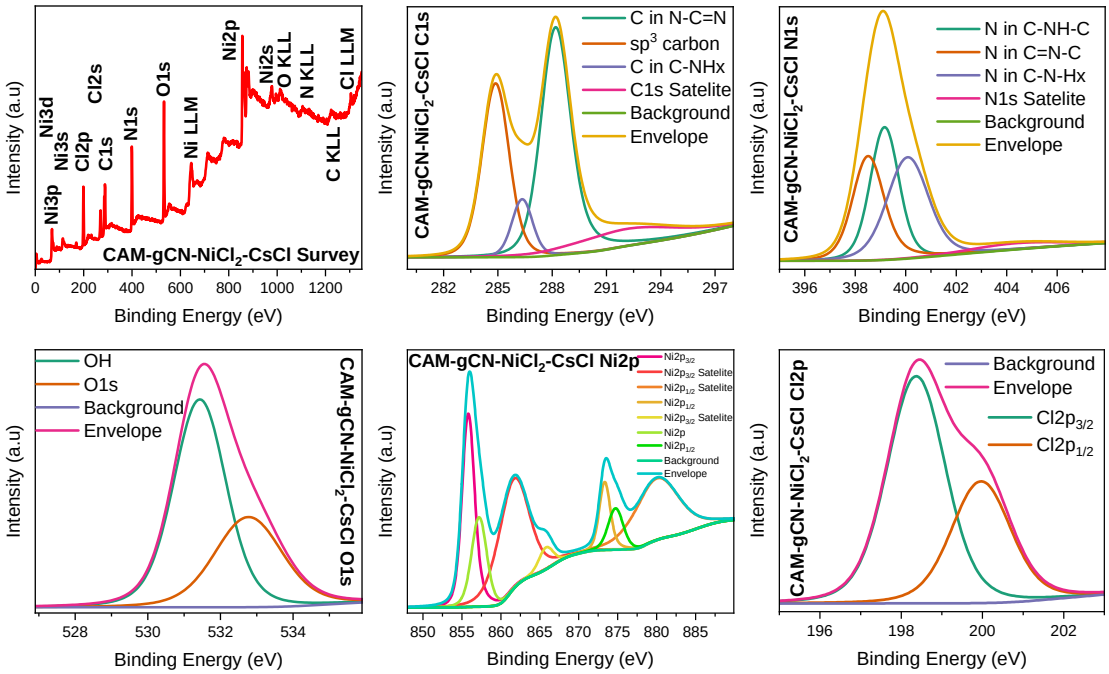

Figure 7.7: X-ray photoelectron spectra of gCN-NiCs

atoms. As a result, it is possible that there are various other nickel species in the same oxidation state, but with different coordination. Given the relatively high binding energies of both species, one might expect an octahedral environment for Ni. Nevertheless, this assignment should be taken with caution because the nonconductive nature of the Ni−CNx sample may have caused charging during the measurement, leading to a shifted binding energy. Moreover, it is challenging to assign the oxidation state of Ni, which further complicates the assignment[26].

In the XPS spectra of gCN-NiCs (Figure 7.7), the peak at $284.87\,\mathrm{eV}$ corresponds to the vast majority of the carbon atoms within the graphite-like carbon nitride framework. The presence of carbon atoms bonded to nitrogen and hydrogen, as indicated by the peak at $286.35\,\mathrm{eV}$, may be associated with the pyridine-like functionalities. The appearance of the peak at $288.15\,\mathrm{eV}$ suggested the presence of carbon atoms in the aromatic C=N groups in the framework.

According to the analysis, the dominant nitrogen signal in this peak is pyridinic-like nitrogen within the carbon nitride framework. Additionally, the presence of pyrrolic-like nitrogen functionalities is suggested by the C−NH−C peak. Another peak at $400.8\,\mathrm{eV}$ is attributed to nitrogen in the C−N−Hx functionalities, which may be associated with pyrrolic-like or amine-like groups. This suggests a more diverse nitrogen environment than the initial interpretation.

The Ni 2 p spectrum exhibits a complex nature, indicating the existence of multiple oxidation states. Ni(II) $(855.78\,\mathrm{eV})$ was the predominant species, suggesting

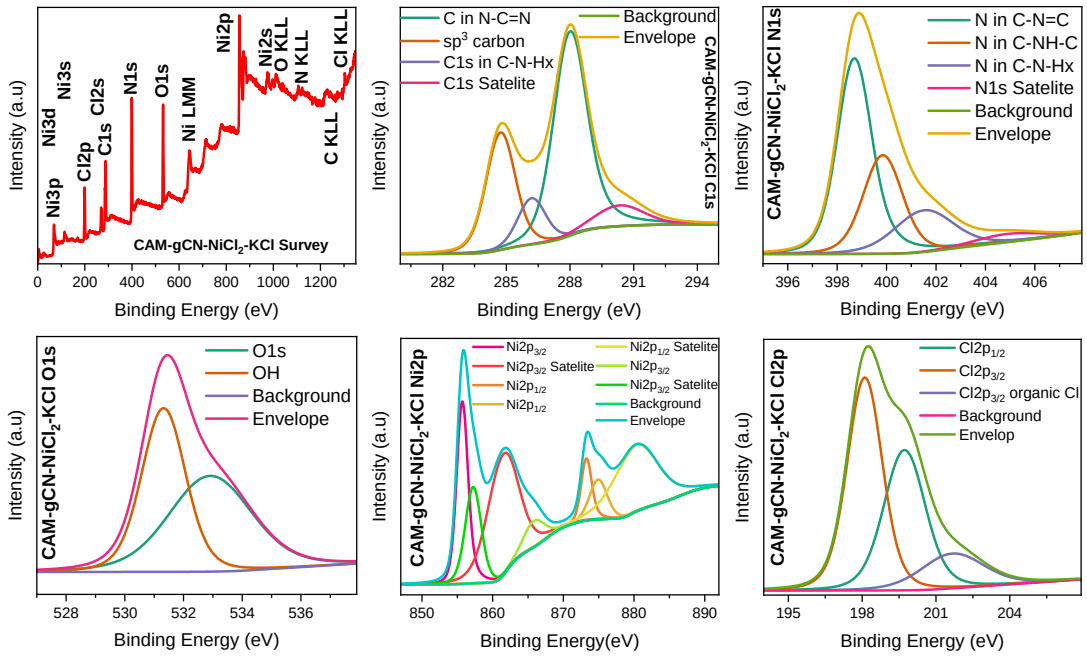

Figure 7.8: X-ray photoelectron spectra of gCN-NiK

a strong presence in the +2 oxidation state. A smaller contribution from Ni(III) (857.21 eV) is also observed. The satellite peaks at approximately 861 and 865 eV indicated the presence of both Ni(II) and Ni(III) oxidation states. The presence of Ni 2 $p_{1/2}$ peaks at 873.3 and 874.3 eV confirmed the existence of both Ni(II) and Ni(III) states. However, these peaks were relatively less intense than the Ni 2 $p_{3/2}$ peaks, indicating that Ni(II) was still the dominant oxidation state. The satellite peaks associated with Ni 2 $p_{1/2}$ further support this analysis[27–29].

The detection of a single peak at 198.37 eV unequivocally established the existence of chlorine ions within the material. Additionally, the observation of two peaks for Cl 2 p at 198.37 and 199.97 eV can be attributed to spin-orbit splitting, a common occurrence in XPS spectra. This further confirmed the presence of chlorine ions in the material[30–32].

The O 1 s peak, which may have an energy level of 532.77 eV, could originate from the presence of surface oxygen in the form of adsorbed water or oxygen. Alternatively, this peak may be attributed to hydroxyl groups located on the surface or chemisorbed water molecules.

The photoelectron spectra of gCN-NiK (Figure 7.8)aligned with previous analyses (Figure 7.7), confirming the presence of various nitrogen functionalities, mixed Ni oxidation states, and Cl ions. However, minor differences were observed. The N 1 s peak at 401.52 eV suggests the presence of additional nitrogen-containing groups compared to previous data. This peak suggests the presence of nitrogen-containing groups in addition to pyridinic and pyrrolic functionalities, possible candidates including amine-like groups (C–N–H), which could contribute to the enhanced CO_2 adsorption and activation through hydrogen bonding interactions. Quaternary nitrogen (N^+) can act as a Lewis acid center, potentially influencing adsorption and reaction pathways.

The Cl 2 p spectrum shows an additional peak at 201.68 eV, which may require further investigation for its origin. This could be related to surface contaminants

containing chlorine, such as chlorides, or organic chlorine-containing molecules. This might indicate different chlorine environments within the material; for example, chlorine bound to different elements or in varying oxidation states.

According to XPS analysis, the carbon nitride structure appears to exhibit characteristics similar to those of graphite, with various nitrogen functionalities present, including pyridinic, pyrrolic, and potentially amine-like groups. The Ni(II) oxidation state was the dominant state, with a smaller contribution from Ni(III). The presence of different nitrogen functionalities can affect the CO_2 interaction and proton transfer pathways during the reaction. Additionally, chlorine ions may contribute to the overall stability of the material and interact with other elements, thereby influencing its properties.

Table 7.6: Atomic percentage of surface functional groups in Ni-based carbon nitrides.

	(C)-N-Hx	N-(C)=N	C=(N)-C	N-(NH)-C	C-(N)-Hx	OH
gCN	1.38	35.34	35.36	7.65	6.26	0.24
gCN-NiCs	3.32	19.78	6.26	6.9	7.56	11.27
gCN-NiK	3.68	20.61	15.26	8.27	5.23	7.23

The data presented in Table 7.6 give a detailed analysis of the atomic structures of the surface functional groups in Ni-based carbon nitrides, including gCN, gCN-NiCs, and gCN-NiK. These functional groups are vital for determining the surface properties and potential reactivity of a material. The differences observed across the samples provided valuable insights into the impact of nickel modification on the surface chemistry of carbon nitrides. The increase in (C)-N-Hx groups in the gCN-NiCs and gCN-NiK suggests a higher abundance of these configurations, potentially influencing the surface reactivity and adsorption characteristics. Nitrogen-carbon double bonds were present in all samples, with reductions in gCN-NiCs and gCN-NiK, indicating potential changes in the electronic structure due to the incorporation of nickel. The significant decrease in the carbon-nitrogen-carbon triple bonds in the gCN-NiCs and gCN-NiK highlights the significant modification in the triple bond configurations with the introduction of nickel. Nitrogen-amino group-carbon configurations were present in all the samples, indicating the presence of these functional groups in comparable amounts. Variations in carbon-nitrogen-hydrogen configurations suggest potential impacts on the surface properties and reactivity of the samples. The increased presence of hydroxyl groups in gCN-NiCs and gCN-NiK indicates enhanced hydrophilicity, potentially impacting the surface wettability and interactions with water.

Table 7.7: Normalised surface concentration (NSC%) of surface functional groups in Ni-based carbon nitrides.

	(C)-N-Hx	N-(C)=N	C=(N)-C	N-(NH)-C	C-(N)-Hx	OH
gCN	3.17	81.24	81.29	17.59	14.39	0.55
gCN-NiCs	32.87	195.84	61.98	68.32	74.85	111.58
gCN-NiK	18.59	104.09	77.07	41.77	26.41	36.52

The data presented in Table 7.7 pertain to the normalized surface concentration (NSC%) of the surface functional groups in the Ni-based carbon nitrides (gCN, gCN-NiCs, and gCN-NiK). The NSC% values revealed that the (C)-N-Hx configurations exhibited a substantial increase in gCN-NiCs compared to gCN and gCN-NiK, suggesting a higher concentration of these groups on the surface. This may have influenced the surface reactivity owing to the increased concentration of these functional groups. N-(C)=N nitrogen-carbon double bonds were the dominant surface functional groups in all samples, with the highest NSC% observed in gCN-NiCs. This suggests a significant enhancement in this functional group, which may affect the electronic properties and reactivity of the material. Variations in the NSC% for C=(N)-C indicate changes in the abundance of carbon-nitrogen-carbon triple bonds, with gCN-NiCs showing a decrease. This modification of triple-bond configurations may influence the surface properties of the material. The substantial increase in NSC% for N-(NH)-C in gCN-NiCs suggests a higher concentration of these groups on its surface, which could have implications for the potential applications of the material, particularly in catalysis. The NSC% values for C–(N)–Hx suggest a significant increase in gCN-NiCs, reflecting a higher concentration of these configurations on its surface. This could influence the surface reactivity and adsorption characteristics of the material. The variation in NSC% for the hydroxyl groups was considerable, with gCN-NiCs showing a substantial increase.

Table 7.8: Atomic percentage of Ni 2 p and Cl 2 p in Ni-based carbon nitrides.

	Ni 2 $p_{3/2}$	Ni 2 $p_{3/2}$	Ni 2 $p_{1/2}$	Ni 2 $p_{1/2}$	Cl 2 p	Cl 2 p	Cl 2 p
gCN-NiCs	1.72	0.91	0.53	0.42	7.7	4.22	
gCN-NiK	1.37	0.96	0.43	0.44	4.95	3.86	1.44

Table 7.8 presents the atomic percentages of Ni 2p and Cl 2p in Ni-based carbon nitrides, providing insight into the chemical composition and presence of nickel and chlorine species on the surface of the material. In the gCN-NiCs, the atomic percentages of Ni 2 $p_{3/2}$ and Ni 2 $p_{1/2}$ were 1.72% and 0.53%, respectively. In gCN-NiK, Ni 2 $p_{3/2}$ is 1.37%, and Ni 2 $p_{1/2}$ is 0.43%. The presence of the Ni 2p peaks indicates the incorporation of Ni into the carbon nitride structure. The variations in the atomic percentages may suggest differences in the nickel bonding environments or oxidation states between the gCN-NiCs and gCN-NiK. The atomic percentage of Cl 2p in the gCN-NiCs was 7.7%. In gCN-NiK, the Cl 2p peak was 4.95%. The detection of Cl 2p peaks suggests the presence of chlorine-containing species on the surface of carbon nitrides. The lower atomic percentage of gCN-NiK indicates a relatively lower concentration of chlorine compared to that of gCN-NiCs. The presence of the Ni 2p peaks confirms the successful incorporation of Ni into the carbon nitride structure in both gCN-NiCs and gCN-NiK. Variations in the atomic percentages of the Ni 2p peaks between gCN-NiCs and gCN-NiK may suggest differences in the electronic states of the nickel species or coordination environments. The higher concentration of chlorine in gCN-NiCs may indicate a more significant interaction between chlorine and nickel in this sample.

Table 7.9 presents the normalized surface concentrations (NSC%) of Ni 2 p and Cl 2 p in Ni-based carbon nitrides, specifically gCN-NiCs and gCN-NiK. In the gCN-

Table 7.9: Normalised surface concentration (NSC%) of Ni 2 p and Cl 2 p in Ni-based carbon nitrides.

	Ni 2 $p_{3/2}$	Ni 2 $p_{3/2}$	Ni 2 $p_{1/2}$	Ni 2 $p_{1/2}$	Cl 2 p	Cl 2 p	Cl 2 p
gCN-NiCs	17.03	9.01	5.25	4.16	76.24	41.78	
gCN-NiK	6.92	4.85	2.17	2.22	25.00	19.49	98.46

NiCs, the NSC% for Ni 2 $p_{3/2}$ was 17.03%, and that for Ni 2 $p_{1/2}$ was 5.25%. The corresponding values for gCN-NiK were 6.92% and 2.17%, respectively. The higher NSC% values in the gCN-NiCs suggest a more substantial presence of nickel species on its surface compared to that of gCN-NiK. This difference may be attributed to variations in the nickel bonding environments or oxidation states. For the gCN-NiCs, the NSC% for Cl 2 p was 76.24%. For gCN-NiK, this value is 25.00%. The higher NSC% of Cl 2 p in the gCN-NiCs indicated a greater concentration of chlorine species on its surface. The elevated NSC% of Ni 2 p in the gCN-NiCs suggests a more pronounced presence of Ni on its surface, which could impact the electronic structure and catalytic properties of the material[33, 34]. The varied NSC% values for Cl 2 p indicate differences in the chlorine concentrations between gCN-NiCs and gCN-NiK, potentially influencing the surface reactivity and chemical interactions of these materials.

The results obtained from the XPS analysis can be used to elucidate the superior activity of gCN-NiCs as catalysts for CO_2 reduction to methane and methanol, as well as the significant production of oxygen. The higher NSC% values of Ni 2 p in gCN-NiCs (17.03% for Ni 2 $p_{3/2}$ and 5.25% for Ni 2 $p_{1/2}$) compared to those in gCN-NiK (6.92% and 2.17%, respectively) suggest the presence of nickel species on the surface of the gCN-NiCs. Ni is a well-known catalytic metal that can efficiently facilitate various reactions, including CO_2 reduction[35–37]. The increased concentration of Ni species on the surface of the gCN-NiCs might contribute to better catalytic performance. The higher NSC% of Cl 2 p in the gCN-NiCs (76.24%) compared to that of gCN-NiK (25.00%) indicates a greater concentration of chlorine species on the surface of the gCN-NiCs. Chlorine has been reported to have a positive effect on the catalytic activity by influencing the adsorption of reactants or stabilizing intermediates in CO_2 reduction[38–40]. The combined effect of the higher concentrations of nickel and chlorine species on the surface of the gCN-NiCs might lead to a synergistic catalytic effect, facilitating the efficient reduction of CO_2 to methane and methanol. Additionally, the presence of chlorine may contribute to the production of oxygen by participating in water oxidation, generating oxygen as a byproduct. Although gCN-NiK exhibited the second-best catalytic activity, it had a lower concentration of nickel and chlorine species than gCN-NiCs. This might explain its slightly lower performance in CO_2 reduction, but higher efficiency in oxygen generation. gCN, which is bulk carbon nitride with presumably lower concentrations of active sites, demonstrates the lowest activity in comparison.

7.2.8 Valence Band XPS

The valence band spectrum predominantly shows the involvement of carbon and nitrogen species. This can be attributed to the graphitic-like carbon nitride structure,

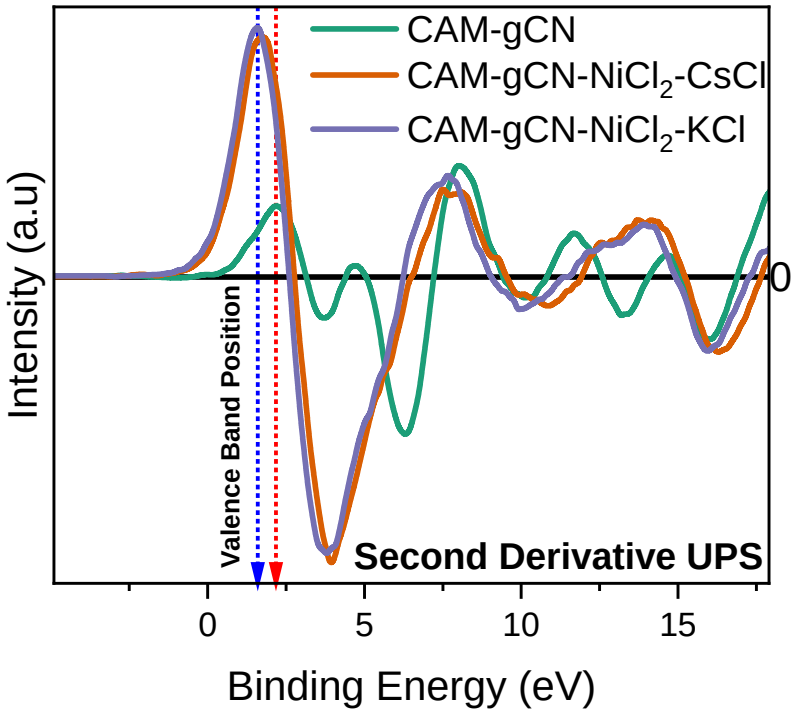

Figure 7.9: Valence band spectrum of Ni-based carbon nitrides

which led to the dominance of peaks arising from the C 2 p and N 2 p orbitals. The presence of Ni, however, introduces additional features stemming from the Ni 3 d orbitals, which may overlap with the C and N contributions. Depending on their abundance and bonding configurations, smaller contributions from the Cl 3 p and O 2 p orbitals may also be observed. It is worth noting that the valence band spectrum typically exhibits broader features than core-level spectra because of the delocalized nature of valence electrons and the influence of multiple overlapping electronic states. The results of the derivative valence band analysis indicate that graphitic carbon nitride exhibits the highest oxidation potential of +2.18 eV, followed by gCN-NiCs (+1.78 eV) and gCN-NiK (+1.58 eV) (Table 7.10). These values were used to elucidate the band diagrams of the respective materials. The valence band spectral peak assignments are given below.

- C–N σ-bonding states: These may be observed in the lower part of the valence band (VB) spectrum, generally ranging from approximately $6\,\mathrm{eV}$-$8\,\mathrm{eV}$ below the Fermi level (E_F).
- C–N π-bonding states: These may appear at a slightly higher binding energy than σ-bonding states and may overlap with Ni 3 d contributions.
- Ni 3 d states: Depending on the oxidation state and coordination environment of Ni, these states may be observed as broad features throughout the VB region, potentially overlapping with C–N π-bonding and Cl 3 p states.
- Cl 3 p states: If a significant amount of chlorine is present near the surface, a peak at approximately $2\,\mathrm{eV}$-$3\,\mathrm{eV}$ below E_F may be observed.
- O 2 p states: If surface oxygen species are present, a broad peak at approximately $5\,\mathrm{eV}$-$6\,\mathrm{eV}$ below E_F may be observed.

	Highest Occupied Molecular Orbital (HOMO), eV				
Sample	**SD**	**Curve Fitting**			
		Position	**Original Value**	**FWHM**	**STD**
gCN	2.18	2.28	2.2832	1.53	1.368
gCN-NiCs	1.78	1.74	1.7359	1.74	1.35
gCN-NiK	1.58	1.57	1.5701	1.67	1.818

Table 7.10: Valence band positions of Ni-carbon nitrides derived from VB-XPS.

7.2.9 Possible Mechanism of Formation of Products

Methane

1. **Direct CO_2 Reduction to Methane**: This mechanism describes the reduction of CO_2 to methane over the gCN-$NiCl_2$ framework. Light absorption generates electron-hole pairs, leading to CO_2 activation at the nickel sites. Subsequent multi-electron transfer steps result in the formation of methane, which desorbs from the active sites.

    - The gCN-$NiCl_2$ framework exhibits remarkable capability in absorbing photons with energy matching its bandgap, causing electrons from the valence band to transition to the conduction band. This energy transfer results in the formation of electron-hole pairs, with holes remaining in the valence band and electrons becoming mobile in the conduction band.

    $$\text{gCN-NiCl}_2 + \text{h}\nu \rightarrow \text{gCN-NiCl}_2^* + \text{e}^- + \text{h}^+$$

    - CO_2 adsorption and activation involve the migration of excited electrons to the surface of the material where they encounter adsorbed CO_2 molecules. In this process, Ni sites with appropriate oxidation states and coordination environments function as active centers for CO_2 adsorption and activation. This may involve Lewis acid-base interactions between Ni ions and the oxygen lone pairs of CO_2, which weaken the O-C bond and facilitate further reduction.

    $$\text{CO}_2 + \text{gCN-NiCl}_2^* \rightarrow \text{CO}_2^* + \text{gCN-NiCl}_2$$

    - The activation of carbon dioxide involves a series of proton-coupled electron transfer (PCET) processes. Electrons from the conduction band are transferred to the adsorbed CO_2 molecules, resulting in the formation of adsorbed CO_2 radical anions. Subsequent PCET steps, including H^+ addition and further electron transfer, lead to the formation of the adsorbed CO radical, adsorbed formaldehyde radical, adsorbed methanol radical, and adsorbed methane molecule. The presence of pyridine-like functionalities in the carbon-nitrogen framework may facilitate proton

transfer through hydrogen bonding interactions.

$$CO_2^* + e^- + H^+ \rightarrow CO^* + HCOOH^*$$
$$CO^* + H^+ + e^- \rightarrow HCHO^*$$
$$HCHO^* + H^+ + e^- \rightarrow CH_3OH^*$$
$$CH_3OH^* + H^+ + e^- \rightarrow CH_4^*$$

- Desorption and product formation involve the departure of adsorbed methane molecules from the active site and their discharge into the surrounding gaseous phase. This action concluded the catalytic cycle, allowing the newly formed holes in the valence band to engage in the oxidation of water, resulting in the formation of oxygen as a byproduct.

$$CH_4^* \rightarrow CH_4(g)$$

2. **Indirect Pathway via CO Production:** This mechanism describes the indirect pathway for CO_2 reduction to methane over the CAM-gCN-$NiCl_2$ framework. Initially, CO_2 is adsorbed and reduced to $CO\cdot$ and O^-. The $CO\cdot$ is then hydrogenated to methane through proton-coupled electron transfer (PCET) steps. Meanwhile, the holes generated in the valence band participate in water oxidation, producing oxygen as a byproduct.

   - The gCN-$NiCl_2$ framework exhibits remarkable capability in absorbing photons with energy matching its bandgap, causing electrons from the valence band to transition to the conduction band. This energy transfer results in the formation of electron-hole pairs, with holes remaining in the valence band and electrons becoming mobile in the conduction band.

$$\text{gCN-NiCl}_2 + h\nu \rightarrow \text{gCN-NiCl}_2^* + e^- + h^+$$

   - The adsorption of CO_2 molecules on Ni active sites may lead to one-electron transfer, resulting in the formation of $CO\cdot$ and O^- species. This one-electron transfer mechanism differs from the multi-electron transfer mechanism that occurs in the first mechanism.

$$CO_2 + \text{gCN-NiCl}_2^* \rightarrow CO_2^* + \text{gCN-NiCl}_2$$

$$CO_2^* + e^- \rightarrow CO^* + O^-$$

   - The adsorbed CO molecule desorbs and undergoes a series of PCET steps on another active site, potentially on the carbon-nitrogen framework. These steps involve the addition of H^+ and electron transfer, ultimately resulting in the formation of $CH_2\cdot$, $CH_3\cdot$, and $CH_4\cdot$.

$$CO^* + H^+ + e^- \rightarrow CH_2^* + OH^-$$

$$CH_2^* + H^+ + e^- \rightarrow CH_3^* + H_2O$$

$$CH_3^* + H^+ + e^- \rightarrow CH_4^*$$

- The holes in the valence band of the material surface can directly oxidize water molecules, producing oxygen and protons. The protons participate in the hydrogenation steps for CO conversion to methane.

$$h^+ + H_2O \rightarrow \frac{1}{2}O_2 + H^+ + e^-$$

The presence of alkali metals (Cs or K) might be affecting the product selectivity. XPS studies indicate that no alkali metals were detected in the final materials, suggesting their possible removal during the synthesis process. This could explain the relatively low methane production, as alkali metals are known to promote methane formation in CO_2 photoreduction.

Methanol

This mechanism describes the steps involved in the reduction of CO_2 to methanol over the gCN-$NiCl_2$ framework. Light absorption generates charge carriers, which are then separated and transferred to the surface for catalytic reactions. CO_2 adsorption, proton reduction, and intermediate formation lead to the eventual production of methanol.

- Upon exposure to light with an energy higher than the bandgap of gCN-$NiCl_2$, electrons were promoted from the valence band to the conduction band. Consequently, electron holes are formed in the valence band.

$$h\nu + \text{gCN-NiCl}_2 \rightarrow \text{gCN-NiCl}_2^*$$
$$\text{gCN-NiCl}_2^* \rightarrow e^- + h^+$$

- Adsorption of carbon dioxide (CO_2) molecules onto the surface of photocatalysts can occur because of Lewis acid-base interactions with exposed Lewis acid sites, such as Ni(II) or undercoordinated nitrogen atoms in the carbon nitride framework.

$$CO_2(g) + \text{Catalyst} \longrightarrow {CO_2}^*$$

- When the adsorbed carbon dioxide accepts an electron from the excited electron in the CB, it forms a $^{-\bullet}CO_2$. This initial electron transfer is a critical step in activating the CO2 molecules and initiating the conversion process.

$$CO_{2\text{ads}} + e^- \longrightarrow {}^{-\bullet}CO_2$$

- Proton reduction involves the conversion of protons (H^+) from water molecules or other sources into hydrogen atoms (H*) at the surface of the photocatalyst. This occurs through the acceptance of electrons from excited electrons in the conduction band (CB) or directly from the valence band (VB) via photogenerated holes. The efficiency of proton reduction is influenced by the availability of protons and the presence of suitable active sites on the photocatalyst surface.

$$H_2O\,(l) + e^- \longrightarrow H\cdot + OH^-$$

- The response provided is a technical description of chemical reactions involving the $^{-\bullet}CO_2$. The anion can react with a CO_2 molecule or hydrogen ion to produce various intermediates, including formic acid, formaldehyde, and methoxy. The intermediates subsequently undergo further reduction and coupling reactions to form methanol (CH_3OH). These processes may involve several hydrogenation and coupling steps that involve additional electrons and protons.

  Reaction with another CO_2 molecule:

  Pathway 1 (dimerization)

  $$2CO_2^{\bullet} \rightarrow {C_2O_4}^{2-} \text{ (adsorbed oxalate)}$$
  $${C_2O_4}^{2-} + 2H^+ + 2e^- \rightarrow HCOOH \text{ (formic acid)} + H_2O$$

  Pathway 2 (carboxylation)

  $$CO_2^{\bullet} + CO_2 \rightarrow {CO_3}^{\bullet} - \text{ (adsorbed carbonate)}$$
  $${CO_3}^{\bullet} - + 3H^+ + 3e^- \rightarrow HCOOH \text{ (formic acid)} + H_2O$$

  Reaction with H ;

  Pathway 1 (protonation)

  $$CO_2^{\bullet} + H^+ \rightarrow HCOO^{\bullet} \text{ (adsorbed formate)}$$
  $$HCOO^{\bullet} + 2H^+ + 2e^- \rightarrow HCHO \text{ (formaldehyde)} + H_2O$$

  Pathway 2 (hydrogenation):

  $$CO_2^{\bullet} + 2H^+ + 2e^- \rightarrow CHO^{\bullet} \text{ (adsorbed formyl)}$$
  $$CHO^{\bullet} + H^+ + e^- \rightarrow CH_2O^{\bullet} \text{ (adsorbed hydroxymethyl)}$$
  $$CH_2O^{\bullet} + H^+ + e^- \rightarrow CH_3O^{\bullet} \text{ (methoxy)}$$

  Further steps to methanol formation:

  Formate ($HCOO^-$) pathway:

  $$HCOO^- + H^+ + e^- \rightarrow HCHO \text{ (formaldehyde)} + H_2O$$
  $$HCHO + H^+ + e^- \rightarrow CH_2OH \text{ (methanol)}$$

  Formaldehyde (HCHO) pathway:

  $$HCHO + H^+ + e^- \rightarrow CH_2OH \text{ (methanol)}$$

  Methoxy (CH_3O) pathway: $CH_3O^{\bullet} + H^+ + e^- \rightarrow CH_3OH \text{ (methanol)}$

- To maintain charge balance, it is necessary to consume the photogenerated holes in the VB. This is typically accomplished by oxidation of water molecules to produce O_2 and H^+. However, this process is less efficient than desired, which can result in competition with CO_2 reduction for available electrons, ultimately hindering the overall production of methanol.

$$2\,H_2O\,(l) \longrightarrow O_2(g) + 4\,H^+ + 4\,e^-$$

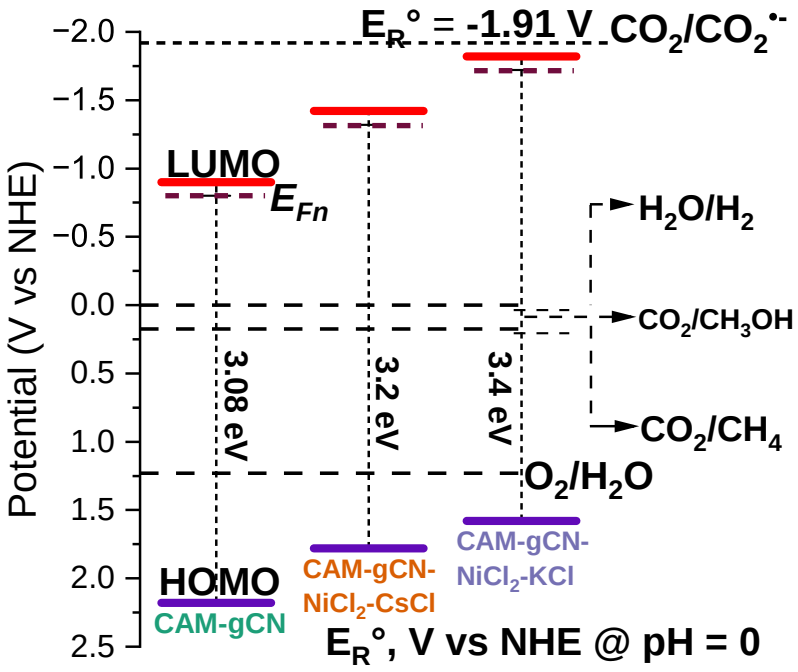

Figure 7.10: Band diagram of bulk and Ni-based carbon nitrides at pH 0

7.2.10 Elucidation of the Band Diagram

The band diagrams for all seven carbon nitride samples were elucidated through a comprehensive approach, utilizing the valence band position data obtained from derivative X-ray photoelectron spectroscopy (XPS) and bandgap values derived from second-derivative diffuse reflectance ultraviolet (DRD UV) measurements. This dual-source information allows for the calculation of both valence and conduction band positions[41, 42]. Subsequently, the electron affinity and ionization energy of each sample were determined based on the calculated band positions.

Band diagrams for all the samples were created using the data obtained from the valence-band XPS spectra and DRS UV measurements at both pH 0 and pH 8. To construct the band diagram at pH 0, the values obtained from these measurements were used (Figure 7.10). Additional pH corrections were applied to the semiconductor band edge and CO_2 redox potential values to represent the band diagram at pH 8 accurately (Figure 7.11).

$$\begin{aligned} \mathrm{CO_2(g) + 3\,H_2(g) &\longrightarrow CH_3OH\,(l) + H_2O\,(l)} && E^\circ = -0.39\,\mathrm{V} \\ \mathrm{6\,H^+\,(aq) + 6\,e^- &\longrightarrow 3\,H_2(g)} && E^\circ = -0.41\,\mathrm{V} \\ \mathrm{CO_2\,(g) + 6\,H^+\,(aq) + 6\,e^- &\longrightarrow CH_3OH\,(l) + H_2O\,(l)} && \mathrm{E^\circ = -0.80\,V} \end{aligned} \tag{7.1}$$

$$\begin{aligned} \mathrm{CO_2(g) + 4\,H_2(g) &\longrightarrow CH_4(g) + 2\,H_2O\,(l)} && E^\circ = -0.24\,\mathrm{V} \\ \mathrm{8\,H^+\,(aq) + 8\,e^- &\longrightarrow 4\,H_2(g)} && E^\circ = -0.41\,\mathrm{V} \\ \mathrm{CO_2\,(g) + 8\,H^+\,(aq) + 8\,e^- &\longrightarrow CH_4(g) + 2\,H_2O\,(l)} && \mathrm{E^\circ = -0.65\,V} \end{aligned} \tag{7.2}$$

The band diagrams for all seven carbon nitride samples were analyzed in detail using X-ray photoelectron spectroscopy (XPS) and second-derivative diffuse reflectance ultraviolet (DRD-UV) measurements. This information allowed for the calculation of both the valence and conduction band positions, which were used

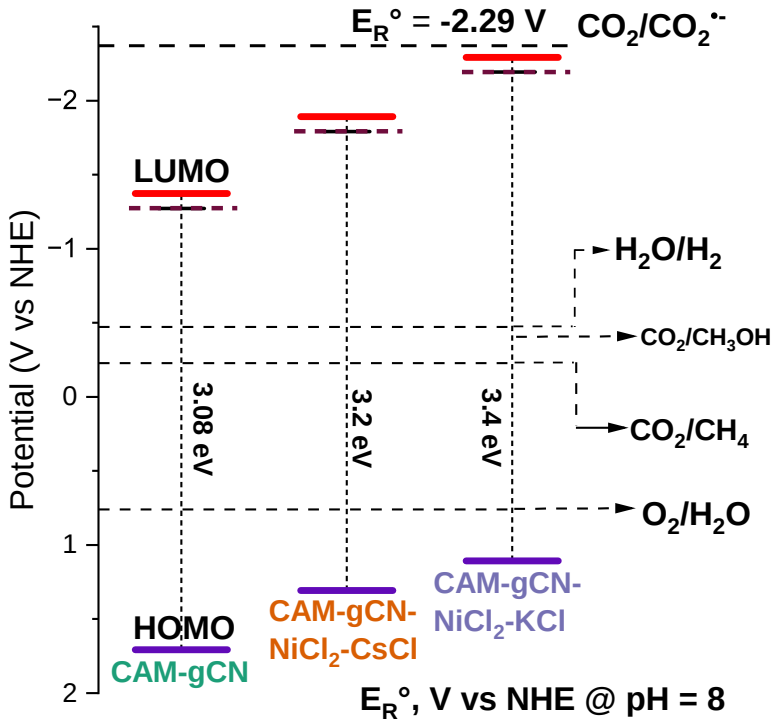

Figure 7.11: Band diagram of bulk and Ni-based carbon nitrides at pH 8

to determine the electron affinity and ionization energy of each sample[41, 42]. Band diagrams were constructed using valence-band XPS spectra and DRS UV measurements taken at both pH 0 and pH 8. The band diagram for pH 0 (Figure 7.10) was created using the data obtained from these measurements, and additional pH corrections were applied to accurately represent the band diagram at pH 8 (Figure 7.11).

The relationship between the valence and conduction bands of semiconductors and their oxidation and reduction potentials is of great significance in determining their behavior. The oxidation potentials of the carbon nitride samples varied in the following order: gCN>gCN-NiCs>gCN-NiK, as shown in Table 7.10. Similarly, the reduction potentials decreased in the following order: gCN-NiK>gCN-NiCs>gCN. All Ni-based carbon nitride systems had the necessary band-edge potential to reduce carbon dioxide to methane and methanol (Figure 7.11 & Equation 7.1 & 7.2). Despite having similar structural features, there were subtle differences in the reduction and oxidation potentials, electron affinities, and ionization energies of Ni-based carbon nitrides compared to those of bulk graphitic carbon nitride. gCN-NiK exhibited the highest potential for reducing CO_2 to $^{-\bullet}CO_2$. However, the gCN-NiCs exhibited a higher product yield than gCN-NiK. The low oxidation potential of gCN-NiK limits the production of hydrogen ions via water oxidation. The reduced number of protons on the surface decreased the proton-coupled electron transfer and, consequently, the product yield. The greater amount of $^{-\bullet}CO_2$ formed on the gCN-NiK surface may have initiated other free-radical reactions, producing carbon monoxide, formic acid, and formaldehyde, where the proton requirement is lower. However, the high oxygen yield in the case of gCN-NiK suggests that water oxidation is higher in gCN-NiK, which may explain the lower activity of the material. This may also be due to the reverse oxidation of the reduced products on

the surface.

gCN-NiCs possess a relatively high potential for oxidizing water and significant reduction potential for converting CO_2 into $^{-\bullet}CO_2$. They exhibited high values for C and DP/SA, which correspond to the presence of active surface sites or functionalities, making them a superior catalyst system for producing methane and methanol. This finding indicates that the reduction in CO_2 depends on multiple parameters and is not solely determined by the band-edge positions.

7.2.11 Summary

Supramolecular-assisted eutectic synthesis has emerged as a promising method for the design of materials for solar fuel applications. This method allows for the in-situ synthesis of metal-incorporated structures, either as frameworks or hybrids. The advantage of this approach is that many structures of the synthesized materials remain unknown, such as the gCN-Ni framework discussed in this chapter. Supramolecular chemistry enables engineering of the precursor for synthesis, which allows for the incorporation of necessary functionalities in the precursor stage itself. However, this also highlights the complexity of designing a catalyst for a specific reaction because numerous factors must be considered simultaneously. The factors affecting CO_2 reduction are interconnected in various ways, resulting in changes in material design according to the reaction of concern.

References

[1] Barrio, J.; Shalom, M. Rational Design of Carbon Nitride Materials by Supramolecular Preorganization of Monomers. *ChemCatChem* **2018**, *10*, 5573–5586.

[2] Ham, R.; Nielsen, C. J.; Pullen, S.; Reek, J. N. H. Supramolecular Coordination Cages for Artificial Photosynthesis and Synthetic Photocatalysis. *Chemical Reviews* **2023**, *123*, 5225–5261.

[3] Jordan, T.; Fechler, N.; Xu, J.; Brenner, T. J. K.; Antonietti, M.; Shalom, M. "Caffeine Doping" of Carbon/Nitrogen-Based Organic Catalysts: Caffeine as a Supramolecular Edge Modifier for the Synthesis of Photoactive Carbon Nitride Tubes. *ChemCatChem* **2015**, *7*, 2826–2830.

[4] Ishida, Y.; Chabanne, L.; Antonietti, M.; Shalom, M. Morphology Control and Photocatalysis Enhancement by the One-Pot Synthesis of Carbon Nitride from Preorganized Hydrogen-Bonded Supramolecular Precursors. *Langmuir* **2014**, *30*, 447–451.

[5] Shalom, M.; Inal, S.; Fettkenhauer, C.; Neher, D.; Antonietti, M. Improving Carbon Nitride Photocatalysis by Supramolecular Preorganization of Monomers. *Journal of the American Chemical Society* **2013**, *135*, 7118–7121.

[6] Wan, S.; Ou, M.; Zhong, Q.; Zhang, S.; Cai, W. Supramolecular Synthesis of Multifunctional Holey Carbon Nitride Nanosheet with High-Efficiency Photocatalytic Performance. *Advanced Optical Materials* **2017**, *5*, 1700536.

[7] Nalwa, H., *Supramolecular Photosensitive and Electroactive Materials*; Elsevier Science: 2001.

[8] Van Leeuwen, P.; Raynal, M., *Supramolecular Catalysis: New Directions and Developments*; Wiley: 2022.

[9] Wang, L.; Su, C., *Supramolecular Catalysts: Design, Fabrication, And Applications*; Series On Chemistry, Energy And The Environment; World Scientific Publishing Company: 2020.

[10] MacGillivray, L.; Lukehart, C., *Metal-Organic Framework Materials*; EIC Books; Wiley: 2014.

[11] Dong, G.; Zhang, L. Porous structure dependent photoreactivity of graphitic carbon nitride under visible light. *J. Mater. Chem.* **2012**, *22*, 1160–1166.

[12] Ismael, M.; Wu, Y.; Taffa, D. H.; Bottke, P.; Wark, M. Graphitic carbon nitride synthesized by simple pyrolysis: role of precursor in photocatalytic hydrogen production. *New Journal of Chemistry* **2019**, *43*, 6909–6920.

[13] Sing, K. S. W. Reporting physisorption data for gas/solid systems with special reference to the determination of surface area and porosity (Recommendations 1984). *Pure and Applied Chemistry* **1985**, *57*, 603–619.

[14] Negative adsorption in the isotherm adsorption experiments of low-adsorption coal and shale. *Natural Gas Industry B* **2019**, *6*, 44–50.

[15] Vanduyfhuys, L.; Van Speybroeck, V. Unraveling the thermodynamic conditions for negative gas adsorption in soft porous crystals. *Communications Physics* **2019**, *2*, 102.

[16] Krause, S.; Hosono, N.; Kitagawa, S. Chemistry of Soft Porous Crystals: Structural Dynamics and Gas Adsorption Properties. *Angewandte Chemie International Edition* **2020**, *59*, 15325–15341.

[17] Rouquerol, J.; Llewellyn, P.; Rouquerol, F., Is the bet equation applicable to microporous adsorbents? In *Characterization of Porous Solids VII*, Llewellyn, P., Rodriquez-Reinoso, F., Rouqerol, J., Seaton, N., Eds.; Studies in Surface Science and Catalysis, Vol. 160; Elsevier: 2007, pp 49–56.

[18] Rouquerol, J.; Rouquerol, F.; Llewellyn, P.; Maurin, G.; Sing, K., *Adsorption by Powders and Porous Solids: Principles, Methodology and Applications*; Elsevier Science: 2013.

[19] Terrones, G. G.; Chen, Y.; Datar, A.; Lin, L.-C.; Kulik, H. J.; Chung, Y. G. SESAMI APP: An Accessible Interface for Surface Area Calculation of Materials from Adsorption Isotherms. *Journal of Open Source Software* **2023**, *8*, 5429.

[20] Osterrieth, J. W. M. et al. How Reproducible are Surface Areas Calculated from the BET Equation? *Advanced Materials* **2022**, *34*, 2201502.

[21] Datar, A.; Chung, Y. G.; Lin, L.-C. Beyond the BET Analysis: The Surface Area Prediction of Nanoporous Materials Using a Machine Learning Method. *The Journal of Physical Chemistry Letters* **2020**, *11*, 5412–5417.

[22] Sinha, P.; Datar, A.; Jeong, C.; Deng, X.; Chung, Y. G.; Lin, L.-C. Surface Area Determination of Porous Materials Using the Brunauer–Emmett–Teller (BET) Method: Limitations and Improvements. *The Journal of Physical Chemistry C* **2019**, *123*, 20195–20209.

[23] Thommes, M.; Kaneko, K.; Neimark, A. V.; Olivier, J. P.; Rodriguez-Reinoso, F.; Rouquerol, J.; Sing, K. S. *Pure and Applied Chemistry* **2015**, *87*, 1051–1069.

[24] Michot, L. J., 2 - Determination of surface areas and textural properties of clay minerals In *Surface and Interface Chemistry of Clay Minerals*, Schoonheydt, R., Johnston, C., Bergaya, F., Eds.; Developments in Clay Science, Vol. 9; Elsevier: 2018, pp 23–47.

[25] Michot, L.; Villieras, F., Chapter 2.10 - Surface Area and Porosity In *Handbook of Clay Science*, Bergaya, F., Lagaly, G., Eds.; Developments in Clay Science, Vol. 5; Elsevier: 2013, pp 319–332.

[26] Schlomberg, H. Ionothermal synthesis opening new avenues towards highly crystalline carbon nitrides for artificial photosynthesis, 2021.

[27] Mansour, A. N. Characterization of NiO by XPS. *Surface Science Spectra* **1994**, *3*, 231–238.

[28] Pagot, G.; Benedet, M.; Maccato, C.; Barreca, D.; Di Noto, V. XPS study of NiO thin films obtained by chemical vapor deposition. *Surface Science Spectra* **2023**, *30*, 024028.

[29] Miller, A. C.; Simmons, G. W. Nickel by XPS. *Surface Science Spectra* **1992**, *1*, 312–317.

[30] Bello, I.; Chang, W. H.; Lau, W. M. Mechanism of cleaning and etching Si surfaces with low energy chlorine ion bombardment. *Journal of Applied Physics* **1994**, *75*, 3092–3097.

[31] Militello, M. C.; Simko, S. J. Palladium Chloride ($PdCl_2$) by XPS. *Surface Science Spectra* **1994**, *3*, 402–409.

[32] Wagner, C. D.; Naumkin, A. V.; Kraut-Vass, A.; Allison, J. W.; Powell, C. J.; Rumble, J. R. J. NIST Standard Reference Database 20, Version 3.4 (web version), Web Version.

[33] Cao, A.; Norskov, J. K. Spin Effects in Chemisorption and Catalysis. *ACS Catalysis* **2023**, *13*, 3456–3462.

[34] Liu, X.; Xiao, J.; Peng, H.; Hong, X.; Chan, K.; Norskov, J. K. Understanding trends in electrochemical carbon dioxide reduction rates. *Nature Communications* **2017**, *8*, 15438.

[35] Zhou, Y.; Martín, A. J.; Dattila, F.; Xi, S.; Lopez, N.; Perez-Ramirez, J.; Yeo, B. S. Long-chain hydrocarbons by CO_2 electroreduction using polarized nickel catalysts. *Nature Catalysis* **2022**, *5*, 545–554.

[36] Liu, X.-H.; Jia, X.-L.; Zhao, Y.-L.; Zheng, R.-X.; Meng, Q.-L.; Liu, C.-P.; Xing, W.; Xiao, M.-L. Recent advances in nickel-based catalysts for electrochemical reduction of carbon dioxide. *Advanced Sensor and Energy Materials* **2023**, *2*, 100073.

[37] Ismail, F.; Abdellah, A.; Lee, H.-J.; Sudheeshkumar, V.; Alnoush, W.; Higgins, D. C. Impact of Nickel Content on the Structure and Electrochemical CO_2 Reduction Performance of Nickel–Nitrogen–Carbon Catalysts Derived from Zeolitic Imidazolate Frameworks. *ACS Applied Energy Materials* **2022**, *5*, 430–439.

[38] Hsieh, Y.-C.; Senanayake, S. D.; Zhang, Y.; Xu, W.; Polyansky, D. E. Effect of Chloride Anions on the Synthesis and Enhanced Catalytic Activity of Silver Nanocoral Electrodes for CO_2 Electroreduction. *ACS Catalysis* **2015**, *5*, 5349–5356.

[39] Li, S.; Dong, X.; Zhao, Y.; Mao, J.; Chen, W.; Chen, A.; Song, Y.; Li, G.; Jiang, Z.; Wei, W.; Sun, Y. Chloride Ion Adsorption Enables Ampere-Level CO_2 Electroreduction over Silver Hollow Fiber. *Angewandte Chemie International Edition* **2022**, *61*, e202210432.

[40] Masana, J. J.; Peng, B.; Shuai, Z.; Qiu, M.; Yu, Y. Influence of halide ions on the electrochemical reduction of carbon dioxide over a copper surface. *Journal of Material Chemistry A* **2022**, *10*, 1086–1104.

[41] Bui, D.-P.; Pham, M.-T.; Tran, H.-H.; Nguyen, T.-D.; Cao, T. M.; Pham, V. V. Revisiting the Key Optical and Electrical Characteristics in Reporting the Photocatalysis of Semiconductors. *ACS Omega* **2021**, *6*, 27379–27386.

[42] Maheu, C.; Cardenas, L.; Puzenat, E.; Afanasiev, P.; Geantet, C. UPS and UV spectroscopies combined to position the energy levels of TiO_2 anatase and rutile nanopowders. *Physical Chemistry Chemical Physics* **2018**, *20*, 25629–25637.

Chapter 8

Conclusion and Perspectives

The efficient and selective capture of carbon dioxide (CO_2) molecules by carbon nitrides (g-C_3N_4) is facilitated by the presence of functional groups such as hydroxyl and amine groups, which act as potent binding sites. The enhanced photoreduction of CO_2 is a result of the tailored surface characteristics of g-C_3N_4, which can be used to adjust its electronic properties, enhance its light absorption and electron transfer capabilities, and improve its overall photocatalytic performance. Although g-C_3N_4 has significant potential for sustainable CO_2 utilization, challenges remain, such as enhanced selectivity, stability, and conversion rates.

The role of surface functionalities in enhancing the adsorbate-adsorbant interactions and promoting light absorption is well established. This is evident from the results obtained with Zr-gCN and Al-gCN, which showed higher activities towards CO_2 reduction owing to their high DP/SA ratios. The photon absorption behavior of the material was also influenced by the surface functionality, as evidenced by the comparison between the NSC% and DP/SA values. The high C value observed in these materials indicates strong adsorbate-adsorbent interactions, which facilitate the optimal utilization of charge carriers for the respective adsorbent (water or CO_2). The derivative isotherm summation provides additional insights into the factors contributing to the high C value, suggesting that the distribution of surface functionalities on edge sites or moderate-energy surfaces plays a significant role in this phenomenon. This, in turn, leads to moderate adsorption and desorption of reaction intermediates, which ultimately enhances the conversion of CO_2.

The application of molten salt ionothermal synthesis for the development of catalytic materials presents a unique opportunity to incorporate in-situ functionalities. By carefully selecting the molten salt and precursor, it is possible to produce either a single crystal or a powder sample with a well-defined framework. This approach allows for the exploration of different molten salts and precursors for the synthesis of novel compounds. The synthesis of in-situ metal-incorporated materials can be beneficial for catalytic applications, and the design should be appropriate for the specific reaction of interest. The temperature, atmosphere, and other conditions can be optimized during the synthesis to achieve good surface functionality and active materials.

Supramolecular-assisted eutectic synthesis presents a promising avenue for the design of materials for solar fuel applications. This technique enables the in-situ synthesis of metal-incorporated structures, either as frameworks or hybrids. The complexity of designing a catalyst for a specific reaction is highlighted by the

fact that many of the structures of the synthesized materials remain unresolved. For example, the gCN-Ni framework discussed in this chapter demonstrates the intricate interplay of factors that must be considered simultaneously when designing a material for CO_2 reduction. The interconnected factors affecting the reaction result in a material design change according to the specific reaction of concern.

Supramolecular-assisted eutectic synthesis has emerged as a highly promising approach for designing materials for solar fuel applications. This method allows for the in-situ synthesis of metal-incorporated structures, which can be either frameworks or hybrids. One of the advantages of this approach is that many structures of the synthesized materials, such as the gCN-Ni framework discussed in this chapter, remain unknown. Supramolecular chemistry enables engineering of the precursor for synthesis, which allows for the incorporation of necessary functionalities in the precursor stage itself. However, this also highlights the complexity of designing a catalyst for a specific reaction because numerous factors must be considered simultaneously. The factors affecting CO_2 reduction are interconnected in various ways, resulting in changes in material design according to the reaction of concern.

Efficient operation of photon-assisted catalytic systems is a pressing issue that requires immediate attention. While previous research has primarily focused on catalyst characteristics, such as per gram or per m^2 or the extent of illumination (photon flux or total illumination power), these measures are insufficient for assessing the true activity of the system. A more comprehensive approach is necessary, considering both the catalyst and the effective illumination. Additionally, not all of the exposed illumination is utilized for the photon-assisted catalytic reaction, owing to factors such as scattering and recombination. Assessing the activity based on the total photon flux is therefore inadequate and may impede the development of efficient photocatalysts. Therefore, a new independent measure is required to reflect the reactivity of the system accurately. The commonly reported apparent (formal) Quantum Efficiency (FQE) does not directly reflect the efficiency of a photocatalyst or the number of effective photons absorbed. A more nuanced understanding of the activity of photocatalysts is required to improve the development of photon-assisted catalytic systems, taking into account both the catalyst and effective illumination. This study highlights the potential of incorporating derivative diffuse reflectance spectroscopy and adsorption isotherm summation to address the issue of efficiency measurement. The combination of both methods considers the surface and light absorption characteristics. Derivative photoluminescence spectroscopy will provide insight into the amount of charge carriers lost due to recombination. The ratio of the D parameters of SD-UVDRS to those of PL provides the effective photons absorbed by the photocatalyst. This can be further correlated with NSC%. However, additional research is required to fully understand this relationship and unlock the full potential of photon-assisted catalytic systems.

Our research group has been exploring carbon nitride materials for CO_2 photoreduction, but thus far, we have not achieved satisfactory results. Despite the numerous materials tested in the literature, no other substance has effectively converted CO_2 into valuable products through photoreduction. Despite our attempts to modify the catalysts, we did not observe a significant improvement in CO_2 photoreduction yields. This led me to question the validity of our approach, which applies the principles of heterogeneous catalysis to photon-assisted catalysis. It is clear that we must also consider the wavelength and intensity of the photon when designing

photon-assisted catalytic systems, in addition to bandgap irradiation. Therefore, the wavelength of the photon must be monochromatic, and the selection process should not be arbitrary but rather tailored to the material and its modifications.

To design materials that optimize the efficiency of CO_2 reduction and water splitting, it is necessary to base them on the specific wavelength of the intense photons rather than just the bandgap. A monochromatic photon source with a precise wavelength must be used for the photoconversion reactions. The penetration depth of photons must correspond to the length of the depletion region of the semiconductor. If these two values are equal, the material behaves as an efficient light-absorbing material, and the energy from light can be utilized effectively. Thus, the wavelength of photons should be carefully chosen and tailored to the material and its modifications, rather than being arbitrary. It is crucial to consider the wavelength of intense photons for efficient CO_2 reduction and water splitting, as this will ensure that the energy from the light is used effectively and that the material acts as an efficient light-absorbing material.

The dimensions of the depletion region in a substance depend on the properties of its surface interface. If the substance is modified, the depletion region length will change and the photon wavelength used for irradiation must be adjusted accordingly. Under dark conditions, the semiconductor reached equilibrium with the surface adsorbate. The density of states and semiconductor-adsorbate interactions change when the first photon hits the surface. It is necessary to determine whether the interaction will become more pronounced (photo-adsorption) or less pronounced (photo-desorption) and what will happen to adsorption under constant irradiation. Wide-bandgap semiconductors offer numerous advantages for research purposes, particularly in photon-assisted catalysis. They have well-defined energy bands that make them suitable for various applications, and they are generally more stable than narrow-bandgap semiconductors. The use of stable materials for accurate and reliable results in any study is crucial, and wide-bandgap semiconductors are preferable. In the last 50 years, we have been testing materials for solar fuel generation using design criteria. However, none of them were successful, and we must re-evaluate whether we have followed the right track. We must include interfacial parameters, along with the wavelength and intensity of the photons, in the design criteria. There is an urgent need to modify the existing design criteria by considering interfacial parameters with proper experimental validation.